MAGMATIC-HYDROTHERMAL EVOLUTION AND POST-ORE MODIFICATIONS OF THE HALILAĞA PORPHYRY CU-AU DEPOSIT, NW TURKEY

by
Paula Brunetti

B.Sc., Universidad de Chile 2011

A THESIS SUBMITTED IN PARTIAL FULFILLMENT OF
THE REQUIREMENTS FOR THE DEGREE OF

MASTER OF SCIENCE

in

THE FACULTY OF GRADUATE AND POSTDOCTORAL STUDIES

(Geological Sciences)

THE UNIVERSITY OF BRITISH COLUMBIA
(Vancouver)

December 2016

© Paula Brunetti, 2016

Abstract

The Biga Peninsula of northwest Turkey is an emerging copper-gold province characterized by numerous epithermal and porphyry-type deposits and prospects associated with Eocene to Oligocene calc-alkaline post-collisional magmatism. Neotectonics in the Biga Peninsula are dominated by a NE-SW dextral strike slip regime that is associated with the southern branch of the North Anatolian Fault System (NAF) and a N-S extensional regime. The Halilağa Cu-Au deposit, in central Biga Peninsula, is a porphyry system that also includes other mineralization types such as high-sulfidation and skarn prospects. The deposit is bounded by two transtensional faults, which have a relevant post-mineralization role.

The Halilağa porphyry Cu-Au system comprises two dominant intrusive phases: a mineralized quartz monzonite porphyry with crowded phenocrysts of plagioclase and rounded quartz, and a poorly-mineralized, phenocryst-poor, quartz monzonite to granodiorite porphyry. Andesitic dykes cut and post-date the porphyry intrusions. Porphyry Cu-Au mineralization is spatially associated with biotite + magnetite ± K-feldspar alteration and intense quartz veining. This alteration assemblage has been variably overprinted by pervasive sericite±quartz alteration, in particular at shallow levels. At depth, selective pervasive chlorite+sericite alteration has overprinted the early biotite + magnetite ± K-feldspar assemblage. Epidote + chlorite + calcite alteration occurs at the edges of the system. Sulphide mineralogy is dominated by chalcopyrite, pyrite, and minor pyrrhotite as inclusions in pyrite. Faults that bound the porphyry stock display evidence of syn- and post-mineral activity, suggesting that these faults have protracted displacement histories.

U-Pb zircon geochronology from the Halilağa district, in this study, constrained the emplacement of the porphyry intrusions to Middle Eocene (40 to 37 Ma) and also indicated another magmatic event of ca. 28 Ma is spatially related to a high-sulfidation epithermal system. Middle Eocene and Oligocene magmatism is coincident with the ages of epithermal and porphyry mineralization in the Biga Peninsula (e.g. Kuscayir, Kartaldağ, Ağı Dağı, Tepeoba), suggesting a favorable setting for porphyry systems generation during that time. In Halilağa, the porphyry mineralization is associated with the Eocene magmatic event, confirmed by a Re-Os analysis of molybdenite yielding a mineralization age of 39.56 ± 0.21 Ma.

Preface

This work is the result of the author's work from May 2013 to December 2015. Research objectives and program design was lead by Craig Hart and Aleksandar Mišković. This MSc thesis is part of the "Western Tethyan Metallogeny Project" (WTMP), a three year research initiative of the Mineral Deposit Research Unit (MDRU) of UBC. The WTMP was funded by: Alamos Gold Inc., Anglo American plc, AngloGold Ashanti Ltd., Avala Resources Ltd., Centerra Gold Inc., Dunav Resources Ltd., Dundee Metals Inc., Eczacıbaşı, Eldorado Gold, First Quantum Minerals Ltd., Kinross Gold, National Iranian Copper Industries Co, Pilot Gold Inc., Silver Standard Resources Inc., and Teck Resources Limited (Teck).

Data collection was carried out during summer of 2013 and 2014. During the field season logistics, accommodation and field support were provided by Teck Madencilik Sanayi Ticaret A.S, the Turkish subsidiary of Teck.

The author is responsible for sample selection intended for several analytical methods: petrography, geochronology, short-wave infrared spectroscopy (SWIR), and lithogeochemistry. Additionally, the author is responsible for drill core log and field data (including field descriptions) as well as the generation of figures and tables of this thesis unless otherwise noted.

Thin section preparation for petrographic analysis was done by Geotech Labs in Vancouver, BC. Petrographic observations were carried out by the author at the Mineral Deposit Research Unit (MDRU) at the University of British Columbia (UBC) in Vancouver. Sample preparation and analysis for U-Pb geochronology was conducted by the Pacific Centre for Isotope and Geochemical Research (PCIGR) at UBC. Re-Os geochronology sample preparation and analysis was done at the University of Alberta. SWIR analyses were conducted at MDRU and in the field site in Çanakkale, Turkey. Lithogeochemistry sample preparation was completed at the MDRU facilities and analysis were done by Bureau Veritas Commodities Canada Ltd. in Vancouver, BC.

Table of Contents

Abstract ii

Preface iii

Table of Contents iv

List of Tables viii

List of Figures ix

List of Abbreviations xv

Acknowledgments xvi

Dedication xvii

Chapter 1: Introduction 1

1.1. Rationale and Significance 1

1.2. Porphyry Copper Deposit Overview 3

1.3. Post-Mineralization Modifications 6

1.4. Metallogeny in the Tethyan Orogenic Belt 9

1.4.1. Metallogeny of Turkey and northern Aegean 10

1.5. Deposit Location 11

1.6. Thesis Objectives 11

1.7. Methodology 13

1.8. Regional Geological Setting 14

1.8.1. Tectonic setting in NW Turkey 14

1.8.1.1. Neotectonics in NW Turkey 16

1.8.2. Geology and geochronology of the Biga Peninsula 18

1.8.3. Structural framework of the Biga Peninsula 22

1.8.4. Mineral occurrences in the Biga Peninsula 23

1.9. Exploration History of Halilağa 25

1.10. Thesis Structure 26

Chapter 2: Geology of the Halilağa Cu-Au Deposit 27

2.1. Deposit Lithology 27

2.1.1. Stratified units . . . 27
2.1.1.1. Cretaceous basement: Çetmi mélange . . . 27
2.1.1.2. Middle Eocene lavas, volcano-sedimentary and conglomerates (40-37 Ma) . . . 27
2.1.1.3. Oligocene lavas and tuffs . . . 31
2.1.1.4. Miocene sequences . . . 35
2.1.1.5. Plio-Quaternary sediments . . . 35
2.1.2. Intrusive units . . . 38
2.1.2.1. Kestane stock . . . 38
2.1.2.2. Intermediate dikes . . . 39
2.1.2.3. Kocakışla stock . . . 39
2.1.2.4. Evçiler pluton . . . 46
2.2. Structural Geology . . . 46
2.2.1. Major lineaments and magnetic features . . . 48
2.2.2. Structural observations and measurements . . . 48
Chapter 3: Lithogeochemistry . . . 54
3.1. Dataset and Methodology . . . 55
3.2. Trace Element Classification . . . 58
3.3. Harker Variation Diagrams . . . 58
3.4. Rare Earth Elements (REE) and Multi-Element Classification . . . 58
3.5. Tectonic Discrimination . . . 61
3.6. Fertile Porphyry Signatures . . . 65
Chapter 4: Hydrothermal Alteration and Mineralization . . . 67
4.1. Methodology . . . 68
4.1.1. Geochemistry dataset and analysis . . . 68
4.1.2. Reflectance spectroscopy . . . 69
4.2. Alteration Assemblages . . . 70
4.2.1. Early biotite . . . 70
4.2.2. Biotite+ magnetite ± K-feldspar . . . 70
4.2.3. Chlorite + epidote + calcite . . . 75
4.2.4. Calcic skarn . . . 78
4.2.5. Chlorite ± sericite . . . 78
4.2.6. Sericite ± quartz . . . 78
4.2.7. Late clays . . . 80
4.2.8. Argillic alteration (Kunk) . . . 80
4.2.9. Advanced argillic alteration (Kunk) . . . 83

4.2.10. Advanced argillic alteration (Pirentepe) . . . 83
4.3. Porphyry Veins . . . 86
4.3.1. Early veinlets (E1). . . . 86
4.3.2. Quartz veins . . . 88
4.3.2.1. Quartz + magnetite + sulfides (Q1) . . . 88
4.3.2.2. Quartz ± K-feldspar ± sulfides (Q2) . . . 88
4.3.2.3. Quartz + pyrite + chalcopyrite (Q3) . . . 88
4.3.2.4. Quartz + molybdenite (Q4) . . . 92
4.3.3. Late veins . . . 92
4.4. Mineralization . . . 94
4.4.1. Hypogene mineralization . . . 94
4.4.2. Supergene mineralization . . . 94
4.5. Summary of Mineral Paragenesis . . . 97
4.6. Alteration Geochemistry . . . 100
4.6.1. Molar ratios . . . 100
4.6.2. Alteration mass balance . . . 101
4.6.2.1. Samples and analytical and calculation procedure . . . 101
4.6.2.2. Biotite + magnetite ± K-feldspar . . . 103
4.6.2.3. Chlorite + epidote + calcite . . . 104
4.6.2.4. Sericite ± quartz . . . 104
4.6.2.5. Chlorite ± sericite . . . 104
4.6.3. Alteration mass balance summary. . . . 106
4.6.4. Alteration mass balance limitations . . . 106
4.7. Reflectance Spectroscopy Analysis . . . 107
4.7.1. 2200 nm wavelength analysis . . . 107
4.8. Re-Os Geochronology . . . 110

Chapter 5: Discussions . . . 111
5.1. Magmatic Setting of the Halilağa District . . . 111
5.1.1. Relationship with geological evolution of the Biga Peninsula . . . 117
5.1.2. Petrogenesis of Eocene and Oligocene magmatism. . . . 119
5.2. Hydrothermal Evolution . . . 121
5.2.1. Alteration anatomy . . . 121
5.2.2. Porphyry and epithermal relationship . . . 123
5.2.2.1. Biga Peninsula . . . 125
5.2.2.2. Globally . . . 125
5.3. Structural Evolution and Deformation . . . 126

5.4. Deposit Evolution Summary 129

Chapter 6: Conclusions 132

6.1. Conclusions 132

6.1.1. Magmatism and stratigraphy 132

6.1.2. Alteration and mineralization 133

6.1.3. Structures 134

6.2. Exploration Implications 135

6.3. Future Work 136

Appendix A: Strip Logs 156

Appendix B: Sample Descriptions 182

Appendix C: Lithogeochemistry Results 217

Appendix D: Geochronology Results 266

List of Tables

Table 2.1 Stratified geological units in the Halilağa Deposit. Age references are (1) Beccaletto, 2007; (2) This Study; (3) Sanchez, 2012. Sample descriptions can be found in Appendix B 40

Table 2.2 Results of U-Pb in zircon geochronology 42

Table 2.3 Intrusive rocks in the Halilağa Deposit. Sample description can be found in Appendix B. 44

Table 2.4 Summary of faults and veins at the Halilağa District 50

Table 4.1 Summary of alteration assemblages at the Halilağa Deposit. 73

Table 4.2 SWIR measurements along fault zones 83

Table 4.3.Veins at the Halilağa Deposit 89

Table 4.4 Sample used in mass balance calculation 103

Table 4.5 Elements gain-loss in alterations in the Halilağa Deposit. 107

Table 4.6 Re-Os geochronology 110

List of Figures

Figure 1.1. Generalized alteration zoning for a porphyry copper deposit and location of other deposits. Modified after Sillitoe, 2010 2

Figure 1.2. Simplified geological map of the Biga Peninsula indicating major geological units, structures and selected mineral deposits. Modified after Yigit, 2012 and Duru et al., 2012. 5

Figure 1.3 a) Porphyry deposits in the Western Tethyan Belt. IAES: Izmir-Ankara Suture, ITS: Inter-Tauride Suture EAES: Ankara- Erizincan Surure b) Mineral occurrences in Western Turkey are represented by red dots. The Balya (Skarn Pb-Zn-Au), Ovacık (Au-Ag, low sulfidation epithermal), Efemçukuru (Au, low sulfidation epithermal) and Tepeoba (porphyry Cu-Au-Mo) mines, in addition to the Halilağa deposit are indicated by yellow dots. Metallogenic belts after Yiğit, 2006; Heinrich and Neubauer, 2002; Western Tethyan Metallogenic Project data, 2016. Basemap from ESRI. 8

Figure 1.4. a) Aerial image of the Halilağa District with roads and drill holes. B) View from the Pirentepe area to Kestane- Kunk-Bakırlık areas.. 12

Figure 1.5 Paleotectonic reconstructions during: a) 260 Ma (Late Permian); b) 230 Ma (Middle Triassic); c) 180 Ma (Middle Jurassic). Modified after Moix et al., 2008 and references therein. 15

Figure 1.6 Tectonic divisions of Turkey and major features in the Aegean and the Biga Peninsula. NAFZ=North Anatolian Fault Zone, EAFZ=East Anatolian Fault Zone. Dashed box indicate Biga Peninsula detailed in Figure 2.2. Modified from Okay, 2008; Yiğit 2009.17

Figure 1.7 Simplified geological map of the Biga Peninsula. Indicating major units and summarized geochronological results. Modified from Duru et al., 2012; Yigit, 2012. Geochronology from (1) Okay and Satır, 2000a, (2) Okay and Satır, 2000b, (3) Aygul et al., 2012, (4) Altunkaynak et al., 2012a, (5) Altunkaynak et al., 2012b, (6) Delaloye and Bingöl, 2000, (7) Black et al., 2012, (8) Kuşcu, 2009, (9) Aysal, 2015, (10) Yiğit, 2012, (11) Murakami et al., 2005, (12)Ünal et al., 2013, (13) Ercan, 1995, (14) Borsi et al., 1972 20

Figure 2.1 Geological Map of the Halilağa District, including U-Pb geochronology samples and stratigraphic column location (Appendix A2). Modified after Sanchez (2012) and Ceyhan and Avsan (2012). UTM projection, zone 35N, datum ED50. Legend in Figure 2.2 28

Figure 2.2 Generalized stratigraphic column for the Halilağa district with U-Pb geochronology samples for this study. Previous studies Ar-Ar samples are shown in Figure 2.1 (Kuşcu, 2009; Sanchez, 2012). Note that cross-cutting relationships are not always observed in the area. 29

Figure 2.3 a)HD-28 and HD-25 in the Bakırlık area. The surrounding rocks are carbonates (dolomite) with light green garnets attributed to the Çetmi Melange b) Yellow tuff agglomerate with a glassy horizon dipping NW attributed to the Çan Formation c) Outcrop in the Muratlar-Etili road with stratified sediments attributed to the Bayramiç Formation (PB2014112) 31

Figure 2.4 NNW cross section from Pirentepe to Kunk . The Pirentepe, Kestane, and Kunk domains are limited by transtensional faults. 2.5x vertical exaggeration. The porphyry mineralization is located in the Kestane domain, a local graben bounded by the North Kapkali and Kunk faults; however, the porphyry stock is cut by the North and South faults. Horizontal scale in UTM projection, zone 35N, datum ED50. Location of cross-section X-X' in Figure 2.1 32

Figure 2.5 a) Fine grained rock altered to hornfels. Pyrite vein with sericitic halo. Chalcopyrite is clustered. HD-78 431 m; b) Altered and stratified sandstone and quartz conglomerate in drill core (HD-78, 43.2 m); c) Green andesite, plagioclase- and quartz- phyric in microcrystalline ground mass from West Kestane (Sample PB2014106 with geochronology; d) Embayed quartz megacryst and altered plagioclase phenocryst in a fine micro-crystalline ground mass; e) Altered dacite from Kunk. Porphyritic texture. Plagioclase phenocrysts are intensely altered to white mica and pyrophyllite. Specular and earthy hematite are present in veins and after phenocrysts in a vuggy texture; (f) Volcano-sedimentary rock with fragmental texture and polylithic fragments, this rock unit is interbedded with andesites and appear to be the unaltered host rock of Kestane. 33

Figure 2.6 a) Total alkali silica (TAS) diagram for rock classification of Eocene volcanic suite (Le Maitre et al., 1989) b)Subdivision of sub-alkalic series in Eocene volcanic rocks using K_2O and SiO_2 (After Peccerillo and Taylor, 1976; Le Maitre et al., 1989; Rickwood, 1989) c) TAS diagram for Oligocene volcanic rocks (Le Maitre et. al, 1989) d) Subdivision of sub-alkalic series in Oligocene volcanic rocks using K_2O and SiO_2 (After Peccerillo and Taylor, 1976; Le Maitre et al., 1989; Rickwood, 1989) e)Total alkali silica (TAS) diagram for plutonic rocks (Middlemost, 1994) f) Subdivision of sub-alkalic series in intrusive rocks using K_2O and SiO_2. 34

Figure 2.7 Concordia diagrams for volcanic units. Refer to appendix E for complete results. The red circles are the calculated age for valid zircon, light blue shows concordia age. 36

Figure 2.8 Oligocene volcanic rocks a) Basaltic andesite to andesite from outcrops in west Kestane b) Dacitic crystal tuff. Sub euhedral to euhedral plagioclases, reddish lath- shape mafic (amphiboles), rounded quartz phenocrysts (482684, 4423254) c) Andesite flow. Biotite, hornblende, plagioclase- phyric in a trachytic ground mass d) Argillized andesite (feldespar-phyric) from Pirentepe (sample PB2014061 with U-Pb geochronology) e) Vitric tuff breccia with bomb sized clasts, magnetic rock of andesitic composition. (480838, 4423162) f) Vitric tuff thin section, hornblende, orthopyroxene and spherulites in a vitric ground mass. 37

Figure 2.9 Microphotographs (left) and cross polarized thin section photograph (right) of the intrusive units in the district a) Kestane stock- phase A b) Kestane stock- phase B c) Andesitic Dyke d) Kocakisla stock e) Evçiler pluton f) TiO_2 versus Y immobile elements plot for plutonic rocks. 43

Figure 2.10 Concordia diagrams for intrusions. Refer to appendix E for complete results. The red circles are the calculated age for valid zircon, light blue shows concordia age. . 45

Figure 2.11 Interpreted lineaments a) Hillshade from a 10 m resolution SRTM; b) Reduced to the pole Airborne magnetic data c) ASTER satellite image 47

Figure 2.12 a) HD-94A 217.75 South fault b) HD-79 190.9 (6120) Fault breccia with pinkish

hornblende-phyric igneous rock c) Tasyatak Tepe (SE Kunk) fault breccia with goethite matrix; d) Preferred orientation of quartz veins with 3 major sets; e) Tension gashes observed in HD-78 in hornfels. 49

Figure 2.13 a) This study vein measurements along two sides of the Çamtaşı Fault b) Rose diagrams for B-type (quartz-hematite) veins by Teck data 2008 c) Rose diagrams for D-type (limonites+quartz and sericite halo) veins by Teck data 2008 d) This study fault planes and poles (Kestane and Pirentepe) e) Bozkurt (2007) fault planes and poles (Kunk).. 51

Figure 2.14 A-A' cross-section with interpreted lithology based on drill core logging and interpretation. UTM projection, zone 35N, datum ED50. Cross section location in Figure 2.1. 53

Figure 3.1 Trace elements classification diagrams a) Winchester and Floyd (1977) volcanic rock classification b) Winchester and Floyd (1977) for intrusive rocks 56

Figure 3.2 Harker diagrams for major elements. Considering least altered dataset (LOI <3.5 % and S<0.35%) of 27 samples. 59

Figure 3.2 (cont) 60

Figure 3.3 Eocene rock diagrams. a) Multi-element digram for intrusive rocks; b)REE digram for intrusive rocks c) Multi-element digram for volcanic rocks; d) REE digram for volcanic rocks; Chondrite normalization by Boynton (1984) in REE diagrams and Primordial Mantle by McDonough et al. (1992) in multi-element. 62

Figure 3.4 Oligocene rock diagrams. a) Multi-element digram for intrusive rocks; b) REE digram for intrusive rocks; c) Multi-element digram for volcanic rocks; d) REE diagram for volcanic rocks. Chondrite normalization by Boynton (1984) in REE diagrams and Primordial Mantle by McDonough et al. (1992) in multi-element. . . . 63

Figure 3.5 a) $[La/Sm]_N$ versus $[Dy/Yb]_N$ b) Eu/Eu* versus SiO_2 c) La/Yb versus Yb. d) Sr/Y versus Y. e) La/Yb versus SiO_2. f): Sr/Y versus SiO_2. Normalization values from Sun and McDonough (1989), fields for adakitic-like rocks from Richards and Kerrich (2007) and Richards et al. (2012). 64

Figure 3.6. a) Tectonic classification Hf-Rb-Ta for granites, after Harris et al., (1986) b) Tectonic classification based in Ta and Yb (Pearce et al., 1984) 66

Figure 4.1 Alteration cross section A-A' , oriented WSW-ENE, including lithologies (patterns) and Cu grades (dashed lines) cross sections location in Figure 2.1 71

Figure 4.2 Alteration cross section B-B', oriented NNW-SSE, inlcuding lithologies (patterns) and Cu grades (dashed lines) cross sections location is shown in Figure 2.1. Legend of alteration in Kestane in Figure 4.1. 72

Figure 4.3 Biotite+magnetite ± k-feldspar alteration, a) HD-13A biotite hornfels hand sample b) HD-13A biotite hornfels thin section c) HD-37 112, Intense biotite+magnetite ± k-feldspar alteration; d) Same sample in thin section. Euhedral secondary biotite with high birefringence product of later chlorite replacement. It is associated with chalcopyrite and magnetite;e) HD-37 112, Stained sample, minor Na-plagioclase (red) and dominant K-bearing minerals in phenocrysts and ground mass (sericite and K-feldspar); f) HD-80 99, Altered phenocrysts; plagioclases to clays and secondary

biotite in mafic site. Ground mass is formed by quartz and k-feldspar. 76

Figure 4.4 a) (2Ca+Na+K)/Al versus K/Al diagram for 118 samples from Kestane Stock classified by alteration type during drill core logging. The letters B to E indicate samples with microphotographs and used in mass balance calculations in Figure 4.11; b) Sample HD-01 62 with intense k-silicate alteration; c) HD-80 661, epidote + chlorite + calcite alteration; d) HD-01 31, pervasive sericite alteration; e) HD-01 271 Sericite + chlorite alteration overprinting K-silicate alteration. 77

Figure 4.5 a) HD-78 16 Calcite and epidote veins in a altered volcanic rock; b) HD-78 16 thin section; c) PD-21; d)HD-78 39.4, Skarn alteration overprinted by clays in a fine grained wall-rock; e) HD-78 39.4, Isotropic and anhedral garnet are widely distributed in the sample associated with calcite; f) HD-78 39.4, fragmented pyroxenes, calcite, anhedral garnets and fine-grained aggregates of K-feldspar and quartz 79

Figure 4.6 Chlorite+sericite a)HD-13A 471, Chlorite+sericite alteration. Chlorite is observed after secondary biotite, while plagioclases are altered to white mica; b) HD-38 396, Quartz vein with chlorite and muscovite in halos. The ground mass is a fine aggregate of quartz+k-feldspar, locally altered to white micas; c) HD-13A 471, Plagioclase phenocryst with polysynthetic twinning replaced by white mica (sericite) d) HD-45 459, Sub-hexagonal phenocrysts (biotite?) replaced by secondary biotite (brown to yellowish) followed by chlorite. Also elongated crystals with same alteration mineralogy. 81

Figure 4.7 Quartz+sericite alteration a) HD-115 146, Pervasive muscovite+quartz alteration; b) Same sample than a in thin section. Fine quartz veins with rutile with pyrite and chalcopyrite, sericite+clays halos. Ground mass is intensely altered to sericite+clays; c) HD-115 146, Stained sample from a, yellow indicate dominate of K-bearing minerals (K-feldspar or K-rich mica) while red colour is indicative of Na bearing minerals (Na-plagioclase) ;d) HD-13A 106, Altered phenocrysts to muscovite with pyrite and chalcopyrite. 82

Figure 4.8 a) Mapped alteration model; b) Distribution of SWIR minerals in a 3D-model of the distribution of white micas and clays in the Kunk and Kestane structural blocks defined by the Kunk Fault, North Fault, and South Fault 84

Figure 4.9 Epithermal alteration in Kunk (a to c) and Pirentepe (d to e) a) PB2013018. Intense alteration of white mica and pyrophyllite in felsic site. Vuggy texture in mafic site (completely removed from the rock) and hematite in veins; b) Same sample in thin section. Phenocrysts altered to white mica (muscovite) and pyrophyllite, hematite in veins and phenocryst borders; c) HD-09 215 Moderate silicification associated with pyrophylllite and white mica (paragonite); d) PD-05 50 vuggy silica texture; e) PD-17 59 , Clay replacing plagioclase phenocrysts and ground mass, relicts of mafic minerals with rutile; f) Same sample in thin section. Fine grained kaolinite in ground mass. 85

Figure 4.10 Veins and mineralization distribution in cross section A-A' , oriented WSW-ENE, including lithologies (patterns). a) biotite + magnetite veins; b) quartz veins; c) pyrite veins. Cross-section location in Figure 2.3. 87

Figure 4.11 a) HD-13A 225, intense K-silicate alteration: biotite after hornblende in phenocrysts

and intense veining. Dominated by quartz+magnetite+sulfides vein and minor thin biotite+magnetite veins, both crosscut by fine pyrite veins ; b) HD-99A 385 90

Figure 4.12 Veins in sample HD-38 396 a)Photograph of rock-sample with chlorite + sericite alteration. Two quartz veins (Q2 and Q3) dominate the rock; b) PPL thin section scan, indicating location of photographs in thin section c) Quartz vein with pyrite crystals (Q2). 4 mm width quartz veins include traces of diverse minerals: calcite with anomalous pinkish interference colour and cleavage, brownish radial chlorite and green pleochroism, only traces of chalcopyrite and magnetite. This vein cross-cut a fine (0.3 mm) magnetite+pyrite+chalcopyrite vein (E1) d) Irregular and discontinuous brown chlorite veins associated with magnetite and pyrite (E1?). This vein is crosscut by Q3 vein; e) pyrite+chalcopyrite ± magnetite ± quartz (Q3) . Dominated by sulphides with patches of granular quartz aggregates and have brownish with blue tint chlorite and fine grained sericite in vein selvages f) Pyrite+magnetite+chalcopyrite in vein Q3(shown in e). 91

Figure 4.13 a) HD-13A 471 quartz+pyrite+chalcopyrite vein crosscut by pyrite with chlorite halo veins in a chlorite + sericite altered sample. Quartz vein contains sulfides in a central line. Pyrite veins also contain chalcopyrite inclusions; b) HD-94 402, quartz+molybdenite vein crosscut quartz+pyrite+chalcopyrite vein and quartz ± k-feldspar ± sulfide vein. 93

Figure 4.14. a)HD-80 99, Secondary biotite after hornblende, plagioclase altered to clays-sericite and associated with chalcopyrite, pyrite and magnetite; b) HD-13A 47,1 Magnetite-chalcopyrite mineralization related to chlorite (after biotite) veins; c) HD-01 39, Supergene enrichment blanket with copper oxides, pyrite, covellite, and digenite. The dominant alteration in the rock is sericite and yellow clays; d) HD-80 29, Covellite replacing chalcopyrite associated with coarse sericite crystals. 95

Figure 4.15.Grade distribution in cross-section A-A' a) Au; b) Cu; c) Mo 96

Figure 4.16. Paragenetic chart of the minerals in up: Halilağa porphyry Cu-Au deposit down: Kunk epithermal occurrence. 98

Figure 4.17 Temporal evolution chart for the Halilağa District , considering porphyry mineralization and epithermal mineralization at Kunk. 99

Figure 4.18. a) Chlorite-muscovite-K-feldspar scatterplot b) Conserved element scatterplots Al_2O_3 versus TiO_2 diagram. Most of the data fall on a single line from the origin suggesting that those elements are immobile. There is a significant system size change suggested from the trend between fresh samples to Cu-rich samples (Stanley and Madeisky, 1994). 102

Figure 4.19. Mass change calculations relative to a fresh sample (HD-60 720) a) K-silicate alteration (sample HD-01 62); b)Propylitic alteration (chlorite+ epidote +calcite) from sample HD-80 661.15 c) Sericite ± quartz alteration (from sample HD-01 31); d) Chlorite+sericite alteration (from sample HD-01 271). Note that y-axis are in different scales for each alteration group. See Figure 4.4 for samples pictures and position in the (2Ca+Na+K)/Al versus K/Al diagram. 105

Figure 4.20. a) Reflectance versus wavelength in the SWIR range for illite and white micas (paragonite, muscovite, phengite). Modified from Scott and Yang, 1997; b) Box plot for white micas and montmorillonite for the wavelength at 2200 nm (Al-OH

absorption feature); c) Box plot for white micas and montmorillonite relative to depth; d) Depth versus the wavelength of the Al-OH absorption feature scatter-plot for selected drill holes (HD-01, HD-04, HD05, HD-06, HD-08, HD-13A). 108

Figure 4.21. 2200 nm wavelength distribution in cross-section, sericite crystallinity index (CI) is indicated with dashed red line. a) A-A'; b) B-B'. 109

Figure 4.22 Re-Os sample from HD-94 402.. 110

Figure 5.1 Stratigraphic columns for a) Pirentepe, Kestane and Bakirlik-Kunk structural blocks including U-Pb geochronology; b) Pirentepe and Dereoba-Keciagili; c) Regional MTA Map (Duru et al., 2012), showing stratigraphic columns locations... 112

Figure 5.2 Compiled geochronology in the Biga Peninsula (n=48) for relevant magmatic and hydrothermal ages. Each point represents the age and 2-sigma error for each sample. 114

Figure 5.3 Compiled geochronology in the Halilağa District showing the results of this work and previous studies. 116

Figure 5.4 Deposit evolution model in plan view. a) Early Eocene; b) Middle Eocene; c) Late Oligocene-Early Miocene; d) Pliocene. Mineral occurrences in the Halilağa District (Pirentepe, Kestane, Kunk, and Bakirlik) are indicated in yellow squares. 127

Figure 5.5 Deposit evolution model in cross-section view. 130

List of Abbreviations

Mt: million tonnes

CI: crystallinity index

HFSE: high field strength elements

HREE: heavy rare earth elements

HS: high-sulfidation

IS: intermediate-sulfidation

lb: pounds

LILE: large-ion lithophile elements

LREE: light rare earth elements

LS: low-sulfidation

MREE: medium rare earth elements

MSWD: mean square weighted deviation

MTA: Mineral Research & Exploration of Turkey

NAF: North Anatolian Fault System

ppb: part per billion

ppm: part per million

REE: rare earth elements

RTP: reduced to pole

SRTM: Shuttle Radar Topography Mission

SWIR: short-wave infrared reflectance spectroscopy

TAS: total alkali silica

Tra: traces

Mineral Abbreviations

Ank:ankerite

Bt: biotite

Cal: calcite

Cct: chalcocite

Chl: chlorite

Cov: covellite

Cpy: chalcopyrite

Dig:digenite

Epi: epidote

Gar: garnet

Gyp: gypsum

Hem: hematite

Kfs:K-feldspar

Kln: kaolinite

Mgt: magnetite

Mo: molybdenite

Ms: muscovite

Prl: pyrophyllite

Py: pyrite

Qz: quartz

Ser: sericite

Sil: silicification

Acknowledgments

I would like to thank to my supervisors Dr. Craig Hart and Dr. Aleksandar Mišković for their guidance during this masters and also for the opportunity to work in this beautiful and exciting field area. I also want to thank to my committee members: Dr. Peter Winterburn, Dr. Andrew Davies, and Dr. Farhad Bouzari for their valuable comments, edits, and ideas.

I want to thank to all the team from Teck and Pilot Gold during the two field seasons in the Etili camp for their technical and logistic support, particularly to Mevlit Avsan, April Barrios, Osman Uluca, Nihal Yavuz, Bilhan Tekin, Özgür Sönmez, Hakan Boran, and Ugur Kiziltepe. Claire Chamberlain and Scott Smith are thanked for giving me support to start this MSc. Owen Hatton is thanked for his comments and suggestions on the manuscript.

I also want to acknowledge the support of everyone involved with Mineral Deposit Research Unit (MDRU) specially to Thomas Bissig and Sara Jenkins. Thank you not only for your help with data or the writing but also for your friendship and good advices.

I am very grateful of my friends and colleagues at MDRU. Special mention for Irene, Kaleb, Raja, Fabien, Jelena, Graham, Hildebrando, Carolina P., Martin, Carolina A., and Agustin. Thank you for your technical help, motivation, and more important for the sharing some of the best moments that I had in Vancouver. Finally, I want to thank my parents and my sisters for their support.

To my mother

Chapter 1: Introduction

1.1. Rationale and Significance

Porphyry deposits (Figure 1.1) typically form in extensive, orogen-parallel, magmatic belts (e.g. Andes, Banat-Srednogorie belts) in continental and island arc settings, as product of subduction-related magmatism (Sillitoe, 2000; Richards, 2003; Sillitoe, 2010). Favorable tectonomagmatic conditions such as oxidized, hydrous, sulfur-rich magmas enable the formation of fertile magmas, product of the efficient exsolution of magmatic volatiles from calc-alkaline magmas (Sillitoe, 1997; Richards, 2003; Mpodozis and Cornejo, 2012). Pre-mineral structures and the host-rock stratigraphy play a major role on the ascent of magmatic-hydrothermal fluids and the development of porphyry deposits (Richards, 2003; Gow and Walshe, 2005; Sillitoe, 2010). As a result of the optimization of those genetic processes, porphyry deposits present an extensive (several km) alteration and mineralization footprint, which in the global context presents a well-documented geometry of alteration and mineralization (e.g. Lowell and Gilbert, 1970; Gustafson and Hunt, 1975; Sillitoe, 2010). However, post-ore structures and hydrothermal overprinting may modify the primary geometry of the ore body and therefore the understanding of the geological evolution of the deposit is key to explain the current anatomy of a porphyry deposit.

The Biga Peninsula (Figure 1.2) in Western Turkey, is an emerging Cu-Au metallogenic province that is characterized by numerous skarn, epithermal and porphyry-type prospects (Öztürk and Helvaci, 2008; Yiğit, 2012; Ünal et al., 2013; Smith et al., 2014). The western propagation of the North Anatolian Fault System (NAF) during the Early Pliocene (Armijo et al. 1999) controlled the formation of transtensional and transpressional faults (Yiğit, 2012) and may have affected the geometry of mineral deposits in northwest Turkey. A further problem observed in many porphyry and epithermal districts in the world (e.g. Maricunga Belt, Muntean and Einaudi, 2001) and that also takes place in the Biga Peninsula, is the superposition of alteration styles (e.g. Balya, Agdemir et al., 1994; Kuşcayiri, Yilmaz, 2003). Those hydrothermal events are spatially, but not necessarily genetically, related. The Biga Peninsula is located in an area with a complex tectonic setting and poor geological constraints reflected in: scarce volcanic correlation and use of several names to refer the same geological unit (e.g., Ercan et al., 1995, Genç, 1998; Dönmez et al., 2005); geochronology of volcanic rocks that is largely based on cooling ages and not magmatic ages; and limited mineralization ages (Ercan et al., 1995; Delaloye and Bingöl, 2000; Murakami et al., 2005; Yiğit, 2012), indicating a

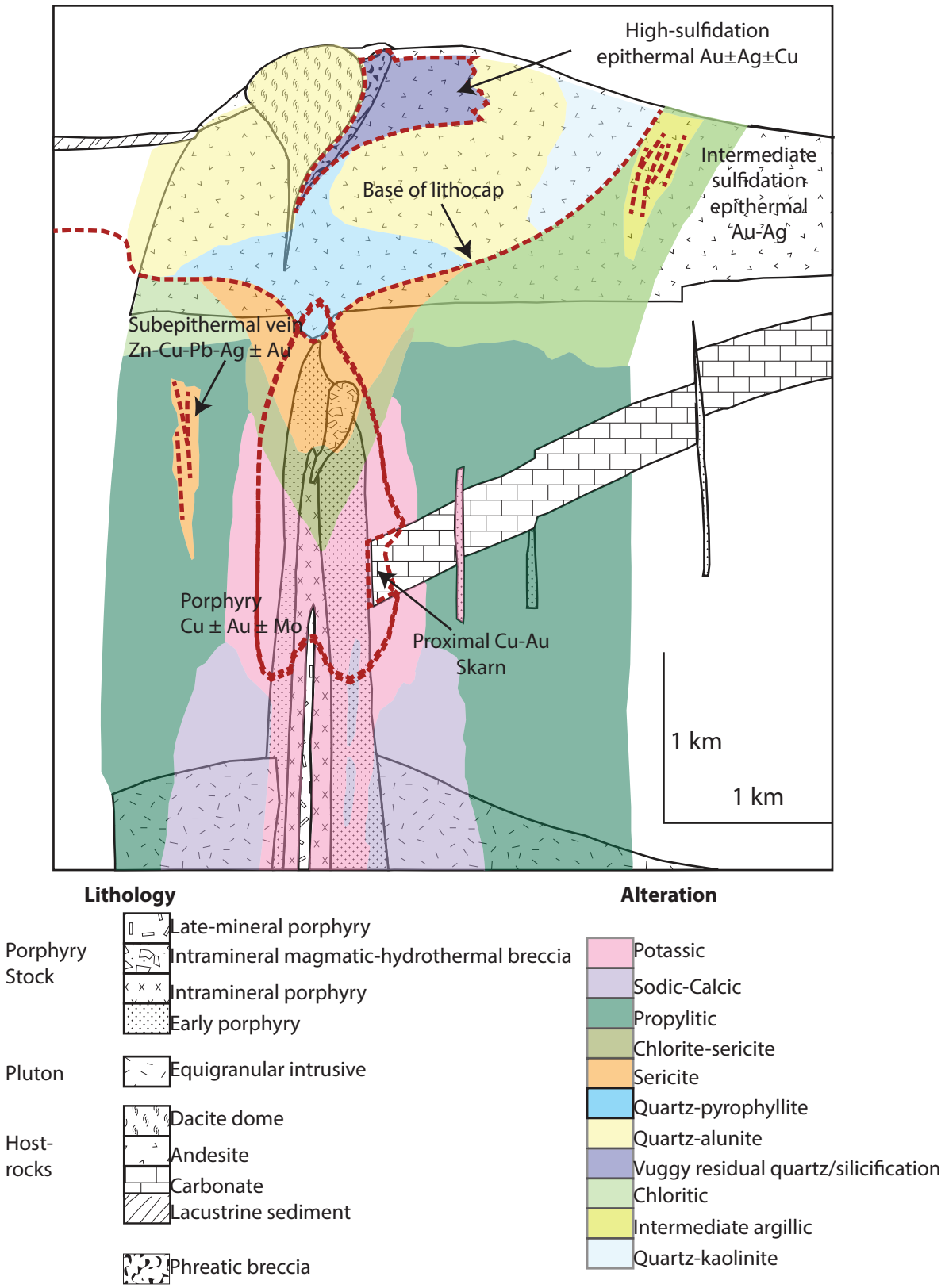

Figure 1.1. Generalized alteration zoning for a porphyry copper deposit and location of other deposits. Modified after Sillitoe, 2010

need to understand better the geology and metallogeny of the Biga Peninsula.

The Halilağa porphyry Cu-Au deposit is the largest porphyry system so far discovered in the Biga Peninsula (See 1.5). Cu and Au mineralization is genetically associated with Eocene porphyritic intrusions (Kestane stock) and correlated to the distribution of the biotite + magnetite + K-feldspar and sericite alteration. Mineralization decreases in the chlorite + sericite assemblages. The district also contains skarn and epithermal occurrences. However, the absolute or relative timing between spatially related lithocaps, skarn, and porphyry mineralization is not constrained by geochronology. In addition, present-day architecture of the Halilağa deposit is dominated by post-mineralization transtensional faulting that play a major role on defining the current geometry of the porphyry stock and potentially displaced mineralization. Those problems, observed in the Halilağa porphyry Cu-Au deposit, are also common in the Biga Peninsula and therefore the Halilağa deposit is a good candidate to understand the geological constraints and relationships for porphyry mineralization and to establish temporal and spatial connections with other deposits in the area, and establish comparisons between the district and the Biga Peninsula.

Knowledge of the temporal and spatial relationships among porphyry and epithermal deposits and post-ore deformation in the Halilağa porphyry deposit will contribute to the successful exploration for porphyry deposits in the Biga Peninsula. Additionally, new alteration distribution modeling, definition of volcanic stratigraphy, and the addition of detailed deposit scale mapping to previous structural models contributes to the understanding of the deposit.

1.2. Porphyry Copper Deposit Overview

Porphyry copper deposits represent the largest source of copper in the world contributing 70% of the total copper production and around 20% of gold, in addition to other commodities such as molybdenum, rhenium, lead, zinc, and silver (Sillitoe, 2010). The age of most porphyry copper deposits date from the Mesozoic to Cenozoic, although there are a few Paleozoic and Precambrian deposits (Seedorff et al., 2005). Porphyry copper deposits are high tonnage and low-grade magmatic-hydrothermal systems characterized by intermediate to felsic multistage porphyritic intrusions (Seedorff et al., 2005, Sillitoe, 2010). The porphyry intrusions are emplaced at shallow (1- 4 km) depth and linked to large mid- to upper crustal magma chambers (Cloos, 2001; Sillitoe, 2010). The intrusions are I-type and typically medium to high-K calc-alkaline, but may have a shoshonite or alkaline character (e.g. Lang et al., 1995; Sillitoe, 2010). Based on the relative abundance of gold or molybdenum, porphyry copper deposits can be divided in gold-rich with >0.4 g/t Au (e.g. Bingham,

Far Southeast, Bajo de la Alumbrera, Cerro Casale) or molybdenum-rich (e.g. Chuquicamata, Butte, Escondida) (Sillitoe, 1979; Sillitoe, 2000).

Porphyry copper deposits are spatially and genetically associated with other mineralization styles such as: epithermal, skarn, and carbonate-replacement. Epithermal deposits form at shallow depths (<1.5 km) at lower temperatures than porphyry deposits (<300°) and for the most part from subaerial hydrothermal systems. Based on gangue mineral assemblage, epithermal deposits are classified in quartz-alunite-pyrophyllite-dickite-kaolinite or high-sulfidation (HS) and quartz-calcite-adularia-illite or low-sulfidation types (LS) (Simmons et al., 2005; Tosdal et al., 2009). HS epithermal systems can occur above porphyry deposits (Figure 1.1) or can occur as tabular veins that overprint porphyry deposits (e.g., Rosario, Masterman et al., 2005). Shallower emplaced HS epithermal deposits share with porphyry deposits the magma-derived fluids from the same source in addition to the interaction with meteoric fluids, therefore the understanding of epithermal style is also an indicator of the initial magmatic source.

The regional tectonics and local stress regime during the intrusion play an important role on formation and location of porphyry deposits (e.g. Gruen et al., 2010; Harris and Holcombe, 2014). Several examples around the world suggest that there is a significant contribution of pre-mineral structures (faults, faults intersections, and lineaments) ascent of the magmatic-hydrothermal fluids involved in porphyry systems, particularly arc-parallel transcurrent faults (Richards, 2003). Regional tectonics and exhumation are responsible for porphyry deposit exposure and moreover have been indicated as quantifiers of exhumation rates in orogen (e.g. Maksaev and Zentilli, 1999; Kesler and Willkinson, 2006; Willkinson and Kesler, 2007; Yanites and Kesler, 2015). Local-scale structural stress fields on porphyry deposits are controlled by brittle fracturing and volume expansion due to changes in fluid pressure triggered by intrusion of multiphase stocks and dykes, exolution and phase separation of the hydrothermal fluids (Tosdal and Richards, 2001; Harris and Holcombe, 2014).

The magmatic-hydrothermal evolution of calc-alkaline porphyry copper deposits has widely been studied through the field description of intrusive types, alteration assemblages, vein types, and cross-cutting relationships (e.g. Lowell and Guilbert, 1970; Gustafson and Hunt, 1975; Muntean and Einaudi, 2001; Redmond and Einaudi, 2010). In addition, analytical techniques such as fluid inclusion microthermometry have aimed to clarifying the hydrothermal fluid evolution and the mechanism of ore deposition (e.g. Rusk et al., 2008; Landtwing et al., 2010). Lithogeochemistry and short-wave infrared spectroscopy (SWIR) assisted to model the spatial distribution of the alteration footprints (Halley et al., 2015). The result of those investigations suggests high variations in temperature with

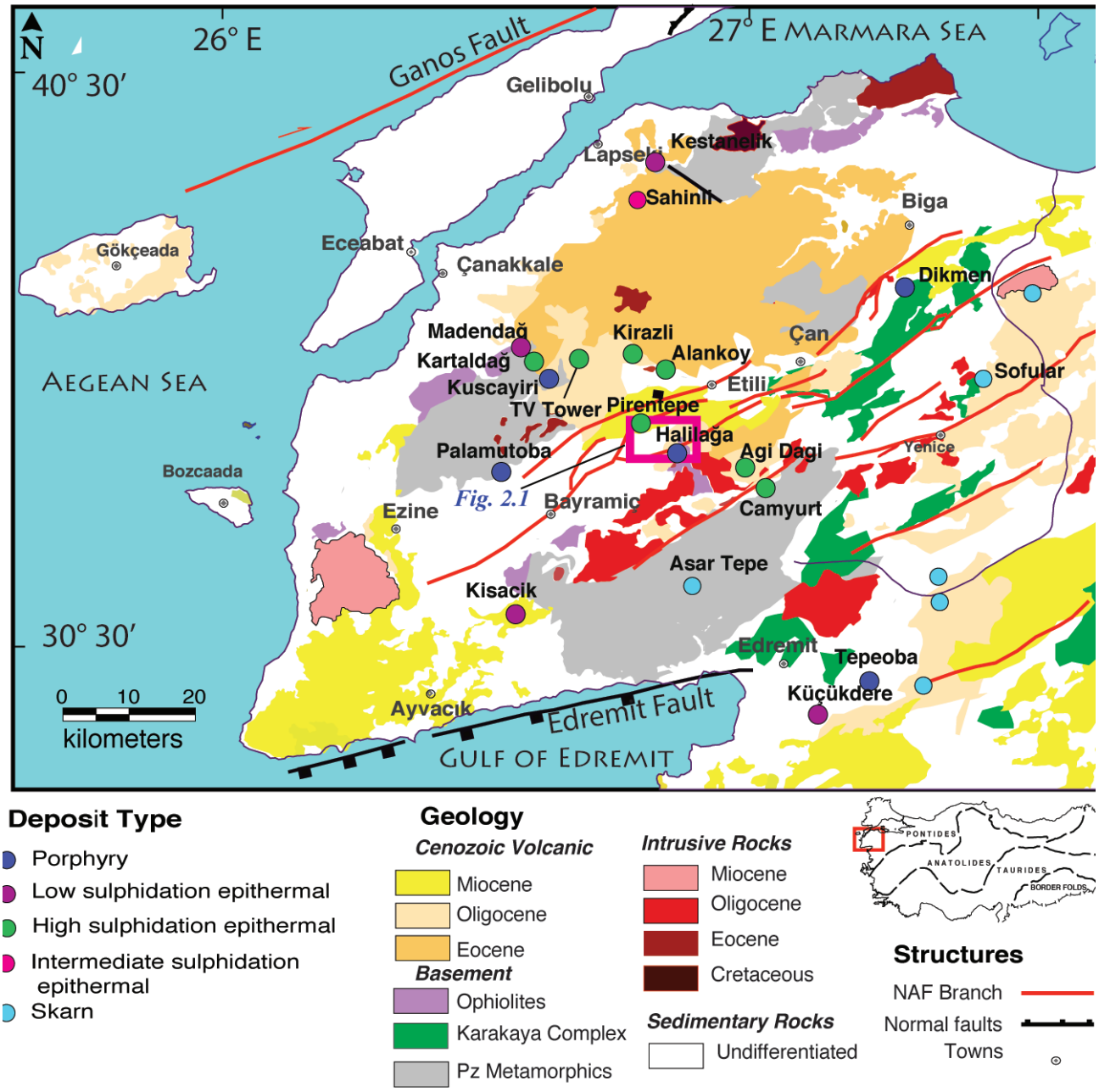

Figure 1.2. Simplified geological map of the Biga Peninsula indicating major geological units, structures and selected mineral deposits. Modified after Yigit, 2012 and Duru et al., 2012.

initial magmatic temperatures >500 °C where the progressive cooling of the system (to <300 °C) leads to brittle rock fracture, mineralization, and early high temperature alterations overprinting with younger and lower temperature alteration. Early alteration phases K-silicate, sodic-calcic, and propylitic (chlorite-epidote-albite-calcite) are followed by progressively more acidic alteration such as chlorite-sericite (SCC) and sericite (Sillitoe, 2010). Advanced argillic alteration characterized by quartz, pyrophyllite, alunite, and kaolinite may be associated with epithermal fluids. The distribution of the alteration assemblages laterally changes from K-silicate in the core of the system to propylitic at the periphery of the causative intrusions. In contrast, vertical variations of hydrothermal assemblages start with K-silicate and sodic-calcic in depth, changing to dominance of chlorite-sericite, grading out to sericite (Figure 1.1). Ore minerals are distributed and associated with specific alteration zones: bornite is present in K-silicate alteration with chalcopyrite and in the sericite zone with pyrite; chalcopyrite occur in K-silicate, chlorite-sericite, and sericite zones; pyrite is observed in all alterations zones but is characteristic of propylitic and sericite alterations; enargite associated with pyrite forms part of the ore mineralogy of advanced argillic zones (Sillitoe, 2010). Gold-rich porphyry copper deposits tend to have high magnetite content in K-silicate zones and a well-developed chlorite-sericite zone that overprints K-silicate alteration (Sillitoe, 2010). The gold is associated with earlier K-silicate alteration commonly hosted in bornite or chalcopyrite in deposits where bornite is scarce (Kesler et al., 2002). The lack of a high-grade bornite zone is common in gold-rich porphyry deposits (e.g Bajo de la Alumbrera; Kesler et al., 2002). The anatomy of a porphyry deposit in terms of hydrothermal alteration and mineralization reflects the hydrothermal fluid evolution and cooling.

1.3. Post-Mineralization Modifications

The anatomic model of porphyry deposits described in the previous section and shown in Figure 1.1, has been used as an exploration tool to identify and localize ore zones in porphyry systems. However, the primary alteration and mineralization zonation patterns and consequently the geometry of the ore body may be modified by; uplift and erosion; deformation; and hydrothermal overprinting. Those events might occur at different time scales following the primary alteration and mineralization stage.

The rates of uplift and erosion to a large extent control the exposure and preservation of porphyry systems (Cooke et al., 2005). Additionally, syn-hydrothermal uplift and erosion is often responsible for the superposition of porphyry and epithermal environment; (Sillitoe, 1994) or development of supergene enrichment on post-hydrothermal stages. Supergene enrichment is common in large

deposits in Central Andes and occurs due the interaction between tectonic uplift, erosion, variations in climate (controlling water supply), and burial. The supergene process is more efficient where uplift and erosion maintain a balance, such that hypogene sulphides are exposed to oxidation, but where erosion does not destroy supergene enriched ore (Clark et al., 1990; Bouzari and Clark, 2002; Hartley and Rice, 2005; Reich et al., 2009). Supergene enrichment can be important in some porphyry deposits because the supergene ore increases the economic potential of a deposit. A typical supergene profile is characterized from top to bottom by a leached zone represented by barren limonite; an oxide zone with "green" copper minerals such as atacamite, malachite, chrysocolla and other associated minerals such as azurite; and a supergene sulphide zone that consists of chalcocite and covellite (Chavez, 2000).

Post-mineralization extensional tectonics results in tilting or rotation of porphyry deposits leading to the exposure of vertical sections at surface. An example of extreme tilting is the Ann-Mason deposit in the Yerington district (Dilles and Einaudi, 1992), where a vertical section of >6 km is exposed at surface due to tilting of up to 90°; other examples are the Paleocene-Early Eocene porphyry deposits of the Laramide arc in Arizona where Tertiary normal faulting tilted the deposits 50° to 60° (Stavast et al., 2008). Major structures can divide and displace the ore body; a classical example is the Kalamazoo-San Manuel deposits in Arizona where normal faults tilted, bisected, and displaced the ore-body (Lowell, 1968; Guilbert and Lowell, 1995; Force et al., 1995).

Syn-mineral hydrothermal overprinting, or telescoping, may occur in porphyry deposits (e.g Sillitoe, 1994; Masterman et al., 2004; Sillitoe et al., 2013) and is the superimposition of epithermal style-alteration on the porphyry environment associated to the same magmatic-hydrothermal event (Sillitoe, 1994). However, the life span of the magmatic-hydrothermal system differs among deposits. Geochronology of alteration or mineralization minerals (e.g. alunite, molybdenite, muscovite) assisted to determine the porphyry-epithermal timing, suggesting 1 m.y. to <300.000 years life span of the hydrothermal system (Muntean and Einaudi, 2001; Masterman et al., 2004). In the Rosario Cu-Mo porphyry, Collahuasi District in northern Chile, geochronology indicates late epithermal Cu-Ag veins of 32.6 ± 0.3 Ma (Ar-Ar in alunite) overprint porphyry mineralization of 33.3 ± 0.2 (Masterman et al, 2004), suggesting that both events are related to the same magmatic-hydrothermal system. The Maricunga district contains porphyry Au-Cu and epithermal deposits that are spatially and genetically related (Muntean and Einaudi, 2001). Based on the description of veins and geochronology, Muntean and Einaudi (2001) established a synchronous origin of hydrothermal biotite and alunite, associated with K-silicate and advanced argillic assemblages respectively, at Aldebarán. Similar results were

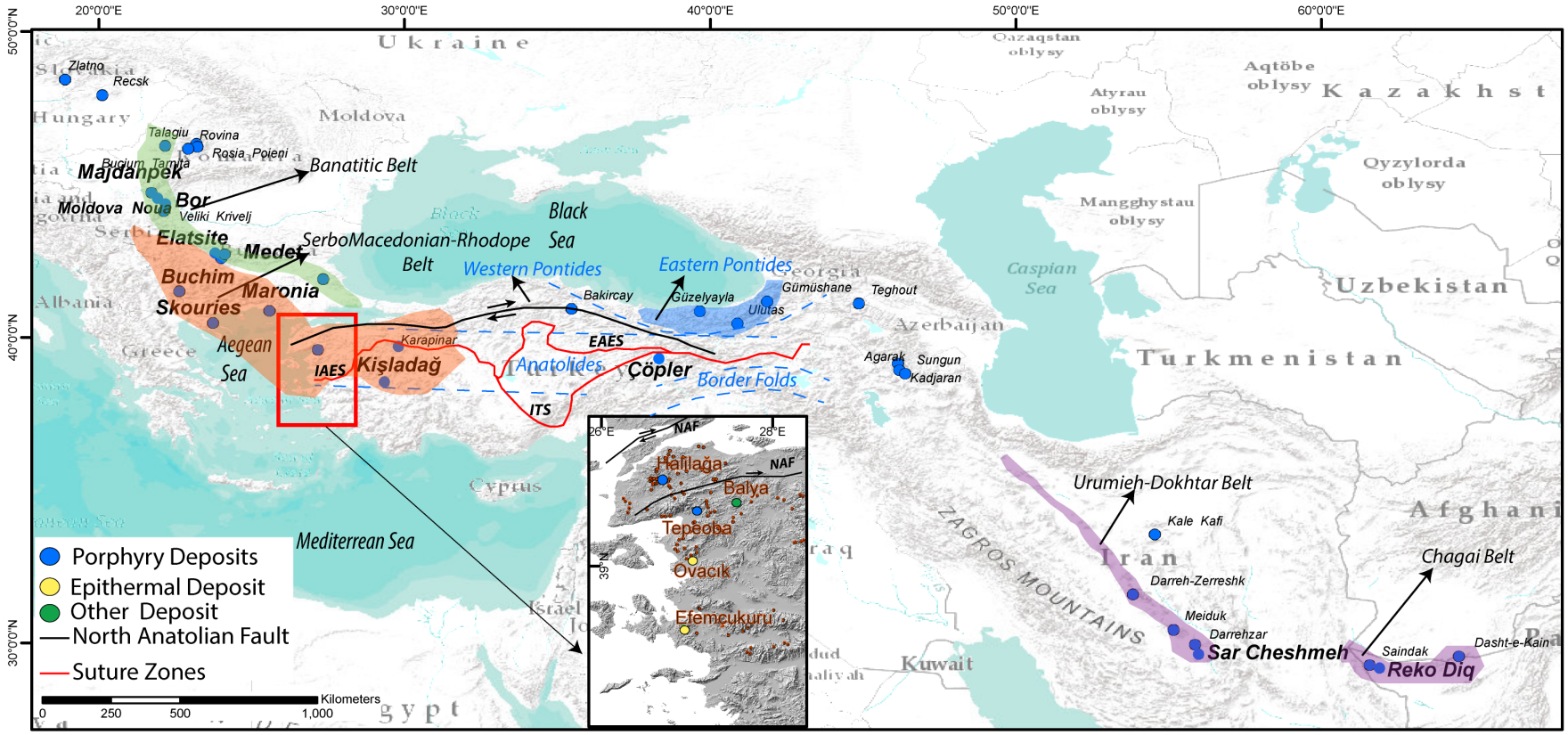

Figure 1.3 a) Porphyry deposits in the Western Tethyan Belt. IAES: Izmir-Ankara Suture, ITS: Inter-Tauride Suture EAES: Ankara-Erizincan Surure b) Mineral occurrences in Western Turkey are represented by red dots. The Balya (Skarn Pb-Zn-Au), Ovacık (Au-Ag, low sulfidation epithermal), Efemçukuru (Au, low sulfidation epithermal) and Tepeoba (porphyry Cu-Au-Mo) mines, in addition to the Halilağa deposit are indicated by yellow dots. Metallogenic belts after Yiğit, 2006; Heinrich and Neubauer, 2002; Western Tethyan Metallogenic Project data, 2016. Basemap from ESRI.

obtained in the Far Southeast porphyry and Lepanto epithermal systems in the Philipines (Hedenquist et al., 1998). The recently discovered Caspiche porphyry Cu-Au deposit presents extreme overprinting (or telescoping); advanced argillic lithocap overlies earlier potassic alteration (Sillitoe et al., 2013). Re-Os ages from molybdenite yielded 25.38 ± Ma for the porphyry mineralization (Sillitoe et al., 2013), while previous K-Ar in nearby deposits indicated 23 Ma at Refugio (Vila and Sillitoe, 1991) and U-Pb in zircon of the mineralized intrusion in Cerro Casale yields 13.9 Ma (Hollings et al., 2014). Those ages suggest synchronous epithermal and porphyry mineralization, but also the occurrence of several episodes of porphyry and epithermal alteration and mineralization in a district not necessarily simultaneous. Therefore is important to define the temporal relations between epithermal and porphyry-style alteration and mineralization to determine if single or multiple magmatic-hydrothermal events are responsible for cause alteration and mineralization types.

1.4. Metallogeny in the Tethyan Orogenic Belt

The Tethyan Metallogenic Belt (TMB) is a 10,000 km long orogen extending from Western Europe to Southeastern Asia (Figure 1.3a). The belt contains numerous porphyry, epithermal, and volcanogenic massive sulphide deposits, whose formation is genetically linked to Mesozoic and Cenozoic orogenic events, related to closure of the Tethyan Oceans and the collision of the African and Eurasian plates (Dixon and Pereira, 1974; Jankovic, 1977; Richards, 2014). The western segment of the TMB is composed of magmatic belts emplaced formed during subduction-related, collisional, and post-collisional events (Richards, 2014). Porphyry deposits of the TMB exhibit classical characteristics of worldwide porphyry deposits. Furthermore, Sar Cheshmeh (1,200 Mt) in Iran and Reko Diq (855 Mt) in Pakistan (Figure 1.3) are among the twenty-five largest known Au-rich porphyry Cu deposits in terms of contained Au (Cooke et al., 2005).

The most important magmatic-metallogenic belts, based on metal production, in the Tethyan Belt are: **The Banat-Srednogorie Metallogenic Belt** (also known as the Banatitic magmatic and metallogenic belt, BMMB) of Late Cretaceous age, which extends from Romania and Serbia to Bulgaria (Jankovic, 1977; Jankovic, 1997; Figure 1.3). This belt is associated with the subduction of the Vardar Ocean as a consequence of the closure of the northern Neotethys (Ciobanu et al., 2002). **The Serbomacedonian-Rhodope Metallogenic Belt** (Figure 1.3) of dominantly Late Eocene to Miocene age (Heinrich and Neubauer, 2002; Lips, 2002) extends from present day Bosnia to Serbia, Macedonia, Greece, and northwest Turkey. The origin of this belt is attributed to post-collisional magmatism (Heinrich and Neubauer, 2002; Richards, 2014). This belt considers multiple deposits

of different ages; the youngest of which are located in the Sumadija-Chalkidiki arc (25- 19 Ma; Lips, 2002) while the older porphyry and related epithermal deposits occur in the eastern Rhodopes (clustered between 33-29 Ma; Marchev et al., 2005; Moritz et al., 2010). **The Urumieh-Dokhtar Zone in Iran** (Figure 1.3) hosts multiple porphyry deposits mostly of Miocene age. This magmatic belt formed in a collisional tectonic setting (Richards, 2014). **The Chagai Belt in Western Pakistan** (Figure 1.3) includes Middle-Eocene to Early Pliocene porphyry deposits (Perelló et al., 2008) of continental arc affinity (Nicholson et al., 2010). These magmatic-metallogenic belts, host multiple Cretaceous to Miocene porphyry Cu-Au-Mo deposits (Figure 1.3a).

1.4.1. Metallogeny of Turkey and northern Aegean

In Turkey, the study of metallogenic provinces is still at an early stage generally due to the absence of systematic and reliable geochronology and geochemistry of host rocks and mineral deposits. Yiğit (2006, 2009, and 2012) published GIS inventories for deposits in Turkey and Biga Peninsula with major characteristics and their geographic distribution. Porphyry deposits in Turkey are generally Au-rich and associated with Late Cretaceous to Late Miocene granitoids. The Pontides belt (Figure 1.3a) includes porphyry prospects (Güzelyayla, Gümüshane, Bakırçay, and Ulutaş) of Late Cretaceous to late Eocene age (Yiğit, 2009). Despite the occurrence of younger deposits in the Pontides belt, it can be correlated with the Late Cretaceous Banatitic Belt in Eastern Europe (Yiğit, 2006). The Anatolides Belt comprises the most productive area for porphyry deposits in Turkey with deposits from Late Cretaceous to Late Miocene age (Yiğit, 2009, Kuşcu et al., 2013). Mines associated with this belt are the Eocene Çöpler epithermal Au deposit, which also includes a subeconomic porphyry Cu-Au, and the Middle Miocene Kışladağ porphyry Au, also associated with a barren HS epithermal system (Figure1.3a; Imer et al., 2012, Rabayrol, 2015) In Western Turkey, important LS deposits are the Ovacık Au-Ag mine and the Efemçukuru Au mine, both deposits are Middle Miocene (Figure 1.3b; Yiğit, 2009; Boucher, 2016).

Other relevant deposits in the northern Aegean, which are part of the Serbomacedonian-Rhodope Metallogenic Belt, are located in the Chalkidiki Peninsula in Greece and in the Trace region in Greece and Bulgaria. Examples of Oligocene porphyry deposits in the Rhodopes are the Maronia porphyry Cu-Mo, in the Thrace region, and the Buchim deposit (Figure 1.3b; Melfos et al., 2002; Lehmann et al., 2013). The Skouries porphyry Cu-Au, in the Chalkidiki Peninsula and part of the Kassandra mining district, corresponds to multi-stage alkalic porphyry intrusions of Early Miocene age that intrude the Serbo-macedonian Massif (Frei, 1995; Kroll, 2002).

1.5. Deposit Location

The Halilağa Cu-Au porphyry deposit is located in the Çanakkale region of the central Biga Peninsula, northwestern Turkey (Figure 1.2). Biga Peninsula, historically called Troas, hosted the Bronze Age city of Troy and is bounded by the Dardanelles to the northwest, by the Aegean Sea to the west, the Marmara Sea to the north, and it is separated from Anatolia to the east by the Kazdağ Mountains, historically known as Mount Ida. The Halilağa Deposit is located 55 Km southeast of the city of Çanakkale and near the villages of the Muratlar, Halilağa, and Hacıbekıler (Figure 1.4a). The resource estimation for the Halilağa porphyry deposit (Doerksen et al., 2015) has indicated mineral resource of 182.7 Mt, grading 0.30 g/t gold and 0.27% copper and inferred mineral resource of 178.7 Mt, grading 0.24 g/t gold and 0.23% copper, using a 0.43 g/t gold-equivalent cut-off.

In addition to the porphyry deposit, there are a number of other prospects in the Halilağa district: the Pirentepe and Kunk HS epithermal Au prospects and the Bakırlık Cu skarn prospect (Figure 1.4b). These mineral occurrences are located within three east-trending structural domains: Pirentepe, Kestane, and Bakırlık-Kunk. The porphyry mineralization located in the Kestane area (1.4b).

1.6. Thesis Objectives

The scientific problem that guided this study is to understand the effects in the geometry of the ore body of post-ore events such as faulting and hydrothermal alteration in a porphyry deposit. Research questions of this study are:

- What is the timing and the geological context of the Halilağa porphyry deposit?
- Are the mineral occurrences of the Halilağa District temporally related to porphyry mineralization?
- Was the deposit modified by post-mineral faults, that might have been active syn-mineralization?

Based on those questions, the objectives of this research are:

1. To determine the volcanic and plutonic setting of the Halilağa District to elucidate the geological evolution of the deposit.
2. Establish the timing of Halilağa hydrothermal events and nearby epithermal alteration.
3. Verify the role of post- mineralization faults in the current geometry of the Halilağa porphyry deposit and establish the timing of those structures.

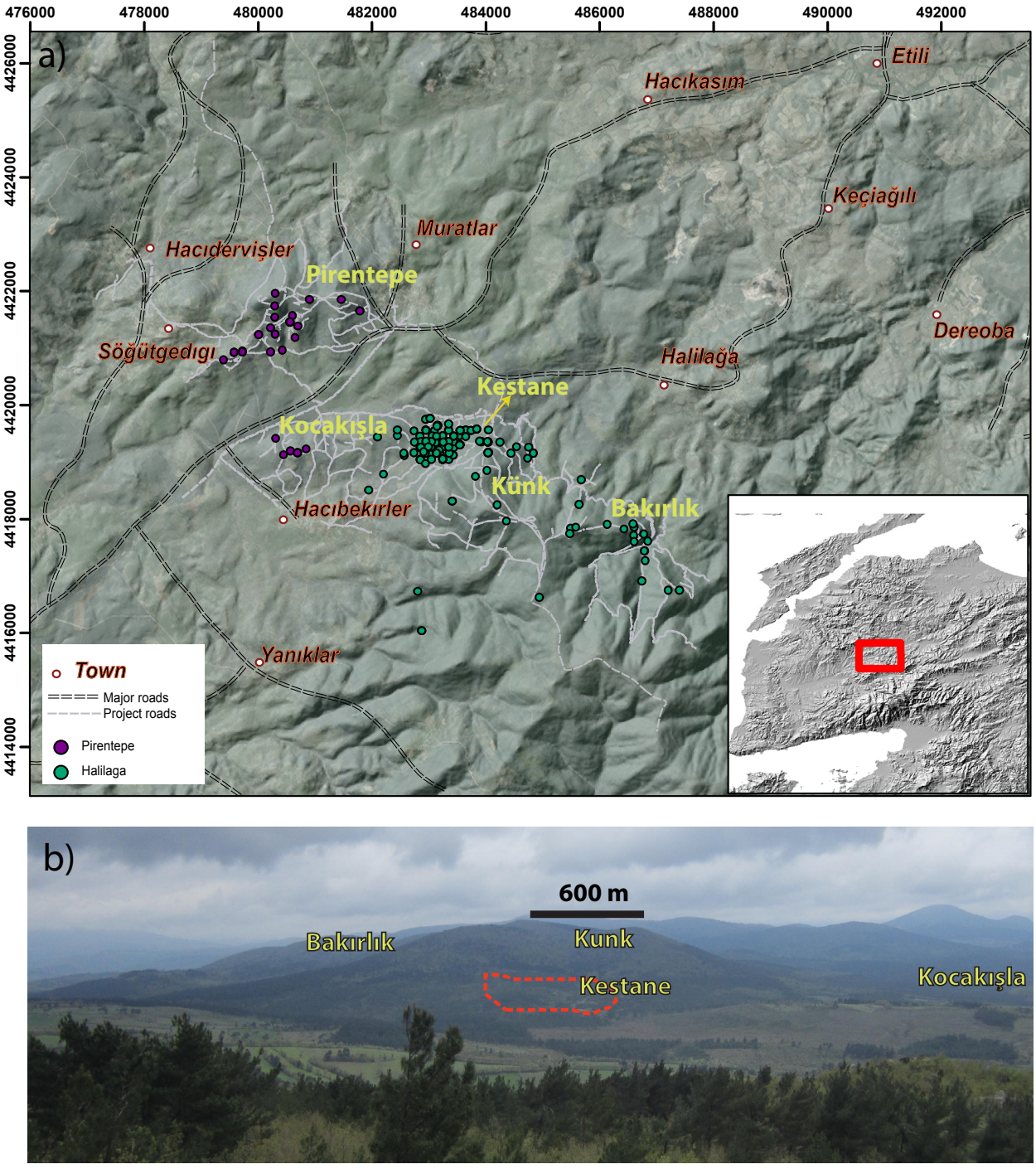

Figure 1.4. a) Aerial image of the Halilağa District with roads and drill holes. B) View from the Pirentepe area to Kestane- Kunk-Bakırlık areas.

Those problems, found locally at the Halilağa District, are also identified in the Biga Peninsula and consequently this study aims to contribute to the regional understanding of those problems.

1.7. Methodology

To accomplish the objectives proposed in the previous section, new geological mapping and core re-logging of Halilağa porphyry Cu-Au deposit was carried out. Furthermore, analytical techniques including geochemistry, geochronology, petrography, and spectral analyses were employed.

The first objective was achieved with fieldwork, cross-section and stratigraphic columns interpretation, petrography, and geochemistry. A total of five months were dedicated to fieldwork. The fieldwork was largely based on core logging due to limited rock outcrop exposure. More than 25 holes (approximate 10,000 m) were logged from the Pirentepe, Kunk and Kestane areas to establish lithology distribution, types of intrusions, and sample collection for analysis. Field mapping at the scale of 1:10.000 was executed along NNW sections at the Kestane, the Kunk hill, and the Kocakışla area to establish stratigraphic relationships of the geological units. The distribution and contact relations between them are reflected in cross-sections and stratigraphic columns (Chapter 2). Petrographic investigation enabled the description of lithological units. Geochemistry assisted with the rock classification and establish differentiation trends along the geological units.

The second objective was reached using U-Pb and Re-Os geochronology, paragenetic studies in macroscopic vein samples and thin section, petrography, SWIR mineral identification, and geochemistry of altered samples. Geochronology, allowed to establish temporal relations between the magmatic and hydrothermal events. Additionally, the petrographic examination of alteration types contributed to establish an alteration mineral paragenesis and consequently a relative hydrothermal temporal sequence. SWIR analyses assisted in identification of alteration minerals (particularly fine grained clays and white micas) and compositional variations in minerals due to hydrothermal overprinting. Geochemistry of altered samples assisted to quantify element enrichment or depletion related to hydrothermal alteration.

The third objective was achieved using interpretative cross-sections and a structural interpretation was carried out using remote sensing images (airborne magnetic data, hill-shade, and satellite images). Cross-section interpretation of lithology, structures, and alteration assisted to determine the role faults on the current geometry of the deposit.

1.8. Regional Geological Setting

The geological evolution of the Tethyan region results from successive subduction-related, collisional, post-collisional and rifting episodes. The Paleotethys Ocean opened in Ordovician to Silurian times and closed during the Triassic due to rifting and subsequent convergence between Laurasia and Gondwana that resulted in the formation of the Pangea supercontinent (Stampfli, 2000, Stampfli and Borel 2004). The rifting of the Cimmerian Continents (present day the areas of Turkey, Iran, Tibet, and Indochina) from Gondwana initiated the opening of the Neotethys Ocean from Permian to Early Triassic in southern Paleothethys (Figure 1.5a; Stampfli, 2000; Stampfli and Borel, 2004). In the Early Jurassic, the northward subduction of the Neotethys Ocean along the Laurasian margin resulted in magmatism in an active margin and rifting and opening of back arc basins and creation of oceans such as Vardar and Pindos (Figure 1.5; Stampfli and Borel, 2004).

The Aegean domain corresponds to the tectonics elements that are currently in and adjacent to the Aegean Sea, in eastern Mediterranean region (Figure 1.6). In the Aegean domain, the records of the closure of the Vardar and Pindos oceans by subduction define the current tectonic terranes separated by ophiolitic sequences (Robertson, 2002; Jolivet et al., 2013). Neotectonics in the Aegean tectonic domain are dominated by an extensional tectonic regime and the westward propagation of the NAF triggered by the roll-back of the Hellenic trench and the westward extrusion of Anatolia (Taymaz et al., 1991; Faccenna et al., 2006; Le Pichon and Kreemer, 2010; Jolivet et al., 2013).

The Biga Peninsula is a collage of tectonics terranes: the Sarkarya Zone, oceanic assemblages, and the Rhodope-Strandja Zone (Okay et al., 1991; Beccaletto and Jenny, 2004; Şengün et al., 2011). The geology is dominated by metamorphic basement and ophiolitic sequences overlaid by Cenozoic volcanic sequences and related intrusions (e.g. Genç, 1998; Altunkaynak and Genç, 2008). Recent discoveries of mineral deposits have highlighted the increased potential of Biga to host base and precious metals (e.g. Yiğit, 2012, Smith et al., 2014); emphasizing the need for better definition of Biga Peninsula stratigraphy and precise constraints on intrusions and the timing of mineralization.

1.8.1. Tectonic setting in NW Turkey

In Turkey, four major E-trending tectonic units were initially proposed by Ketin (1966) separated by major suture zones (Vardar-Izmir-Ankara suture, Bitlis suture): Pontides (Laurasia since Mesozoic), Anatolides-Tauride (Gondwana) and Border Folds (Gondwana). These were later re-classified into five major domains (Figure 1.6): Pontides, Anatolian terrane, Taurus-Cimmerian terrane, South-Taurides exotic units, and the peri-Arabian domain (Okay and Tüysüz, 1999; Bozkurt

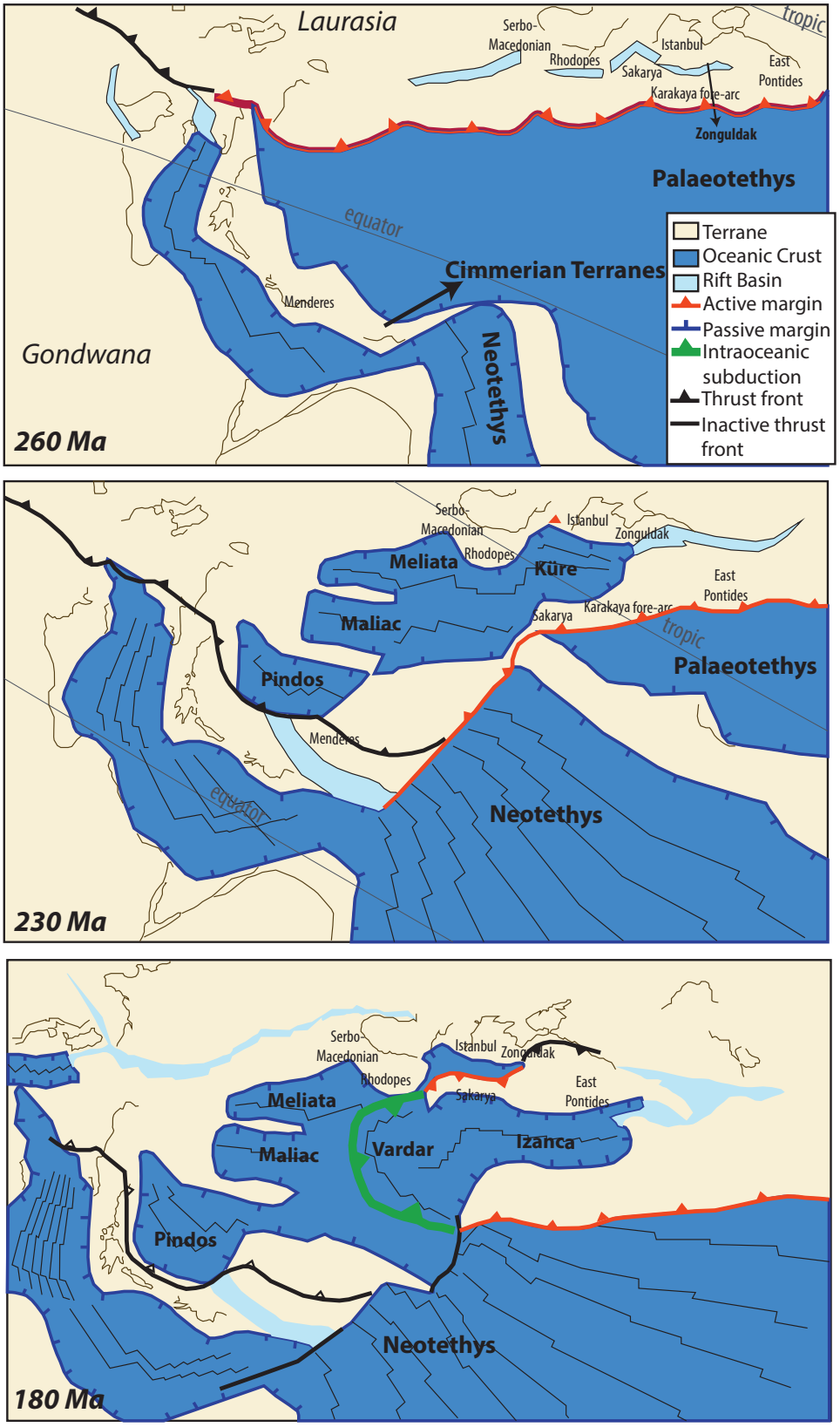

Figure 1.5 Paleotectonic reconstructions during: a) 260 Ma (Late Permian); b) 230 Ma (Middle Triassic); c) 180 Ma (Middle Jurassic). Modified after Moix et al., 2008 and references therein.

and Mittwede, 2001; Moix et al., 2008).

The Pontides, separated from the Anatolide-Tauride block by the Vardar-Izmir-Ankara suture zone, includes the Sakarya, Istanbul, Zonguldak, Rhodope-Strandja zones. Internally the Intra-Pontide suture delimits the Sakarya zone in the south from the Istanbul and Zonguldak zones in the north (Figure 1.6). Prior to the Late Triassic the Pontides were part of the active margin of Laurasia; the opening of the Küre Ocean in Late Triassic detached Sakarya and Eastern Pontides from Laurasia and formed a back arc basin between the northerly Rhodope, Istanbul, and Zonguldak zones, and the southerly Sakarya and Eastern Pontides (Figure 1.5; Moix et al., 2008). Sakarya and the Eastern Pontides were re-accreted to Laurasia during the mid-Cretaceous Balkan orogeny, constituting an active Laurasian margin and resulting in the production of subduction-related calk-alkaline magmatism (Figure 1.5; Moix et al., 2008). The opening of the Black Sea in Late Cretaceous initiated from the Pontides-Laurasia rifting and was followed by the Pontides-Anatolia collision in the Late Cretaceous along the Vardar-Izmir-Ankara Suture zone (Okay and Tüysüz, 1999).

The Biga Peninsula is located in the western Pontides domain. Several authors interpret a separate tectonic suture in the Biga Peninsula of which the Rhodope-Strandja zone in the northeast is separated from the Sakarya zone by an Alpine suture (Okay et al., 2001; Beccaletto and Jenny, 2004). In contrast, recent studies (Tunç et al., 2012) indicate a similar evolution in the metamorphic massifs in Biga Peninsula (Kazdağ and Çamlıca), which were subsequently affected by thermal events associated with Variscan and Alpine orogeny. Those studies disregard a tectonic suture between the Rhodope-Strandja zone and Sakarya zone.

1.8.1.1. Neotectonics in NW Turkey

The present-day morphology in the Biga Peninsula exhibits a NE-orientated horst and graben architecture that is a product of Cenozoic extensional tectonics (Çiftçi et al., 2010). The basins are bound by currently active strike-slip faults that are part of the NAF System (Kürçer et al., 2008) indicating that extensional faults were reactivated as strike-slip faults.

The causes of crustal extension, active since Eocene-Early Oligocene in the Aegean domain, have been subject of debate by several authors, of which the most popular theories are tectonic escape (Sengör et al., 1985, Sengör, 1987; Görür et al., 1995), orogenic collapse (Seyitoğlu and Scott, 1996) and the roll-back of the Hellenic arc (Bonev and Beccaletto, 2007; Ring et al., 2010). The tectonic escape model attributes the beginning of the extension to the westward extrusion of the Anatolian block. However, because the westward extrusion of Anatolia started not before ca. 12 Ma, tectonic

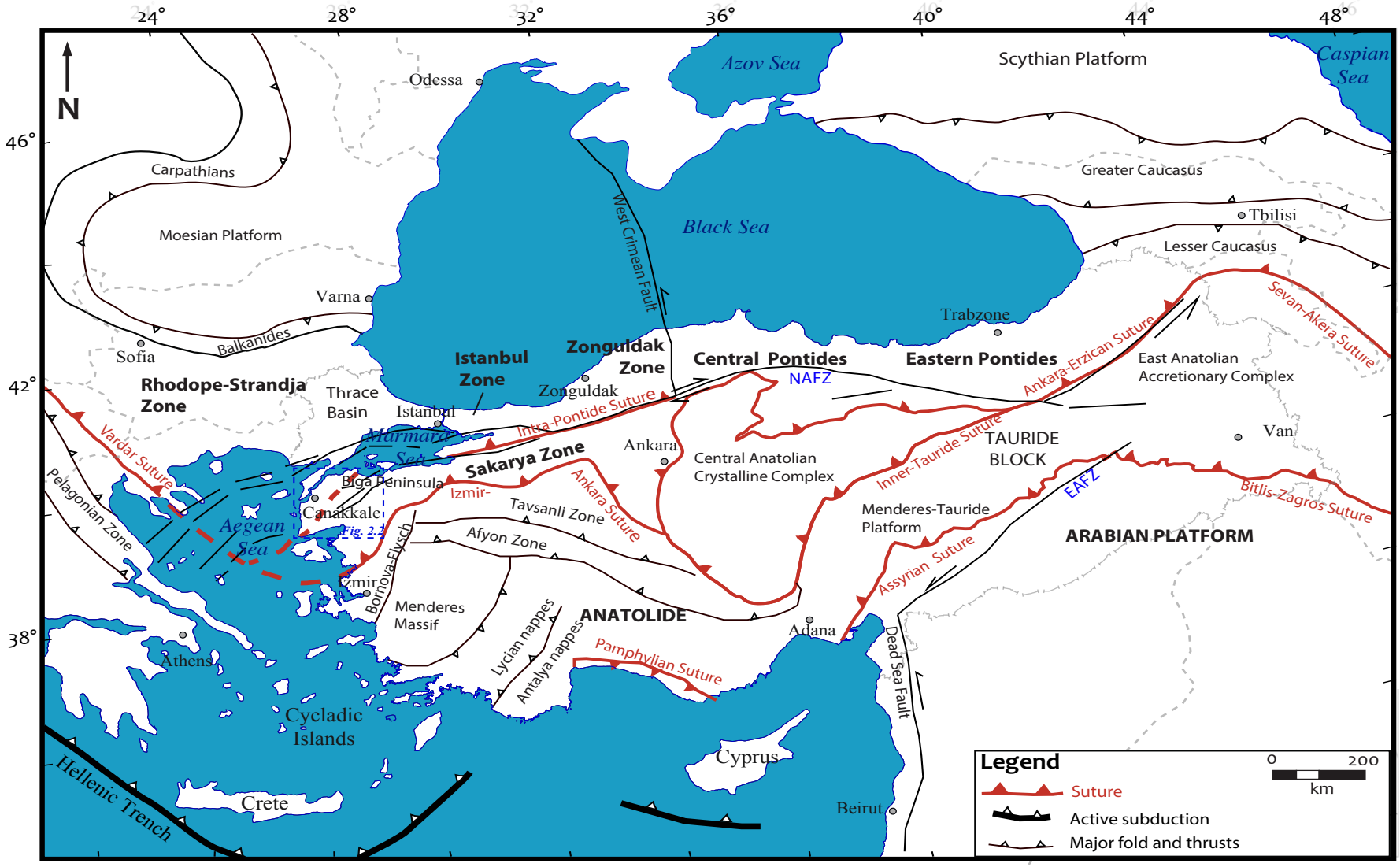

Figure 1.6 Tectonic divisions of Turkey and major features in the Aegean and the Biga Peninsula. NAFZ=North Anatolian Fault Zone, EAFZ=East Anatolian Fault Zone. Dashed box indicate Biga Peninsula detailed in Figure 2.2. Modified from Okay, 2008; Yiğit 2009.

escape cannot account for the Eocene-Early Oligocene onset of the extension (Bozkurt, 2001; Bozkurt and Mittwede, 2005). The orogenic collapse attributed to the N-S extension to spreading and thinning of an over-thickened crust, originated in a Paleogene compressive regime (Seyitoğlu and Scott, 1996). The roll-back of the Hellenic oceanic slab resulted in N-S extension across part of the Aegean domain since Eocene-Early Oligocene, causing core complex exhumation, crustal thinning and back arc basin formation (Jolivet and Faccenna, 2000; Jolivet and Brun, 2010, Menant et al., 2016). The southward migration of the subduction zone is evinced by magmatic arc south migration and southward shifting in the Aegean domain of high-pressure (HP) metamorphism; in the Rhodope Massif northeast of the Biga Peninsula, ultra HP metamorphism is Early Cretaceous to Eocene; while in the Cyclades basement south of Biga Peninsula HP metamorphism is dated Eocene; and in Crete HP metamorphism is Oligo-Miocene (Jolivet and Faccenna 2000; Ring et al., 2010; Jolivet and Brun, 2010; Jolivet et al., 2013).

The collision across the Zagros-Bitlis suture of the Arabian plate and Eurasia during Miocene resulted in the initiation of an intra-continental transform fault, the North Anatolian Fault System or NAF (Armijo et al., 1999; Bozkurt, 2001; Faccenna et al., 2006). The NAF is a dextral strike-slip fault that propagates for more than 1500 km from eastern Turkey to the Gulf of Corinth in Greece, running along the Intra-Pontide suture and accommodating the western extrusion of Anatolia (Jolivet et al., 2013; Faccenna et al., 2006). The motion rate ranges from 15-25 mm/yr based on GPS data (McClusky et al., 2000) for the entire fault zone, while the offset is estimated in a range of 80-100 km (Armijo et al., 1999; McClusky et al., 2000) from Pliocene to present-day. Several pull-apart basins formed along the NAF zone and in the western end, in the Dardanelle Strait, the NAF is responsible for the opening of the Marmara Sea pull-apart basin (Armijo et al., 1999, Okay et al., 2000; Armijo et al., 2002; Sengör et al., 2005). In the Marmara region, the NAF initiates in the Early Pliocene (Armijo et al., 1999) and bends into two main branches (Figure 1.6 and 1.7); through the Marmara Sea-Saros Gulf in the north and Biga Peninsula in the south (Armijo et al., 1999; Bozkurt et al., 2001). Both branches, Ganos and the Yenice-Gönen Fault in the southern branch, have active seismicity resulting in recent major earthquakes of magnitude > 6 (Okay et al., 2000; Kürçer et al., 2008).

1.8.2. Geology and geochronology of the Biga Peninsula

The earliest studies in the area were by the General Directorate of Mineral Research & Exploration of Turkey (MTA) who produced regional geology maps at scales of 1:100,000 and 1: 250,000 for the Biga Peninsula (Ercan et al., 1995; Dönmez et al., 2005; Duru et al., 2012).

The basement rocks in the Biga Peninsula are high- to medium- pressure metamorphosed blocks (Kazdağ Massif and Çamlıca Group) as well as metasedimentary and ophiolitic rocks from the Karakaya Complex and Çetmi Mélange, respectively (Figure 1.7). The northeast-trending Kazdağ massif, the highest elevation in the Biga Peninsula (1767 m.a.s.l.), is the oldest geological unit in the area and is associated with the Hercynian (Variscan) orogeny in Late Carboniferous. The Kazdağ Group includes felsic gneiss, marble, amphibolite, and meta-ultramafic rocks. Late Oligocene high-grade metamorphism in Kazdağ recorded by Rb-Sr and K-Ar systematics indicate that metamorphism is coeval with magmatism (Bingöl, 1969; Okay et al., 1996, Okay and Satır 2000a). The Çamlıca Group consists of quartz-feldspar schist, marble, and metabasites, which range from predominantly greenschist to amphibolite-egclogite facies (Okay et al., 1991; Okay and Satır, 2000b). The Kemer schists in the Marmara Sea, are a medium-grade northeast-trending metasedimentary sequence considered a northern extension of the Çamlıca metamorphics (Bonev and Beccaletto, 2007). The Kemer schists include mica schists, marble and minor metabasite and serpentinite (Beccaletto et al., 2007, Aygül et al., 2012). Metamorphism in Kemer and Çamlıca for the HP-LP metamorphism indicates a Late Cretaceous age similar to HP metamorphism in the Rhodope Massif (84-65 Ma; Rb-Sr phengite; Okay and Satır, 2000b, Aygül et al., 2012). The Permo-Triassic metasedimentary Karakaya Complex is divided into two major groups, namely the Lower and Upper Karakaya Complexes. The Lower unit includes highly-deformed metabasites interbedded with phyllite and marble, while arkosic sandstone, greywacke, basalts, and dark shales form the Upper unit (Okay and Göncüoğlu, 2004). The deposition of the Karakaya complex have been interpreted as either a late Permian rift to a marginal oceanic basin (Bingöl et al., 1975), as a subduction-accretion complex (Stampfli et al., 2003; Beccaletto and Jenny, 2004), or a combination of rifting and subduction-accretion (Göncüoğlu et al., 2000; Şayit et al., 2010, Şayit and Göncüoğlu, 2013). The ophiolitic Çetmi Mélange is in tectonic contact with the Kazdağ massif in the south and is also in tectonic contact with the Çamlıca micaschists in the north. The lithologies in the mélange include serpentinite, neritic and pelagic Triassic limestones, intermediate to mafic volcanics, radiolarite chert, grey-wacke and shale. The Çetmi Mélange ranges from Middle Triassic to Albian (Lower Cretaceous) and comprises marine, volcanic arc, and fore-arc sedimentation process (Beccaletto, 2003). These units have been frequently correlated with other units in the Rhodope Zone in the Balkans and Bulgaria (Okay and Satır, 2000a; Okay and Satır, 2000b; Bonev and Stampfli, 2003; Beccaleto and Jenny, 2004; Beccaletto et al., 2007).

Magmatism in the Biga Peninsula is widely distributed and principally Cenozoic; although the Sevketiye pluton in the northern Biga Peninsula may be Late Cretaceous (71.9 Ma by K/Ar;

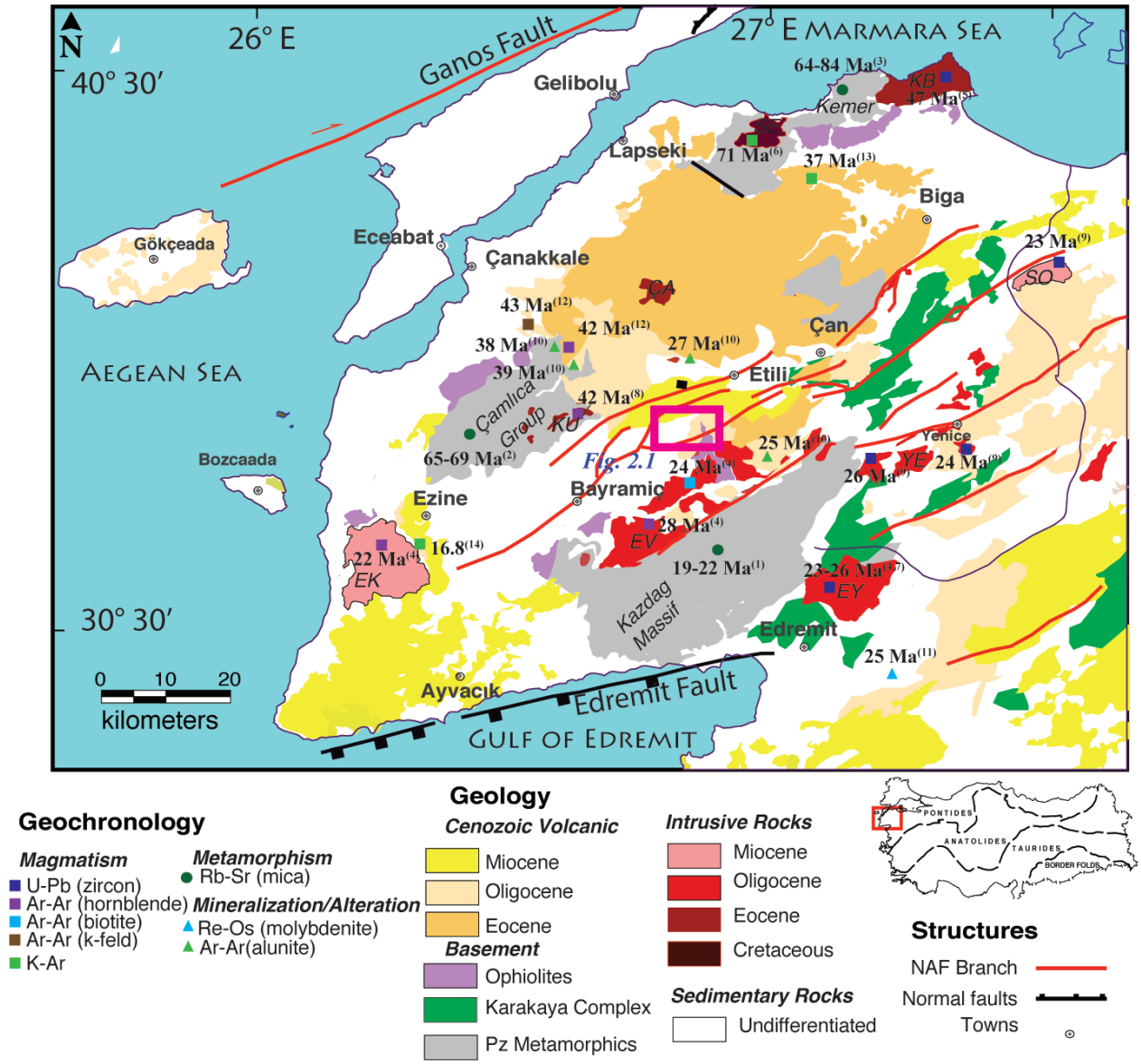

Figure 1.7 Simplified geological map of the Biga Peninsula. Indicating major units and summarized geochronological results. ÇA, Çamyayla granitoid, EV= Evciler Pluton, EK= Ezine-Kestanbol pluton, EY=Eybek Pluton, KB=Karabiga granitoid, KU= KU, Kuşçayırı granitoid, ŞE=Şevketiye granitoid, SO=Sarıoluk granitoid (Yenice North), YE=Yenice granitoids. Modified from Duru et al., 2012; Yigit, 2012. Geochronology from (1) Okay and Satır, 2000a, (2) Okay and Satır, 2000b, (3) Aygul et al., 2012, (4) Altunkaynak et al., 2012a, (5) Altunkaynak et al., 2012b, (6) Delaloye and Bingöl, 2000, (7) Black et al., 2012, (8) Kuşcu, 2009, (9) Aysal, 2015, (10) Yiğit, 2012, (11) Murakami et al., 2005, (12)Ünal et al., 2013, (13) Ercan, 1995, (14) Borsi et al., 1972

Delaloye and Bingöl, 2000), and in the Karakaya Complex and Çetmi Mélange intermediate to mafic volcanics are Mesozoic. Cenozoic magmatism in the Biga Peninsula ranges from Middle Eocene to Late Miocene, moving progressively southward. Similar to the origin of extensional tectonics in the Aegean domain, the onset of Cenozoic magmatism in Biga Peninsula is a subject of discussion (e.g., Pourteau et al., 2016). The most relevant models for western Turkey are: 1) single subduction along Hellenic arc and slab roll-back (Van Hinsbergen et al., 2010; Pourteau et al., 2013; Aysal, 2015) and 2) two-subduction model and slab break-off (Dilek and Altunkaynak, 2007; Altunkaynak et al., 2012b; Ersoy and Palmer, 2013). The single subduction model indicates continuous subduction of the Hellenic arc as supported by the southward migration of the magmatism and HP metamorphism through time across the Aegean domain (e.g., Ring et al., 2010; Jolivet and Brun, 2010; Jolivet et al., 2013). The two-subduction and slab break-off model suggests episodic subduction along two zones: a northerly subduction zone along the Izmir-Ankara Suture Zone and the southerly subduction corresponds to the modern Hellenic subduction (Dilek and Sandvol, 2009; Dilek and Altunkaynak, 2009). The slab break-off occurred at ca. 52 Ma accounts for the production of Eocene post-collisional magmatism following the Sakarya-Anatolia collision in the Late Cretaceous (Ersoy and Palmer, 2013).

The composition of Cenozoic plutons in the Biga Peninsula (Figure 1.7) ranges from granite to quartz diorite with high-K calc-alkaline affinities. In the north, the Karabiga (47.02 ± 0.82 Ma, U-Pb) and the Kapidağ (36.79 ± 0.67 and 45.3 ± 0.1 Ma, U-Pb and 40Ar/39Ar) intrudes metamorphic and Eocene volcanic sequences and form an E-trending magmatic belt (Altunkaynak et al., 2012b). The composition of those intrusions is diorite to granite with hypidiomorphic and porphyritic textures (Altunkaynak et al., 2012b). Another Eocene pluton in central Biga Peninsula, in the Çamilca range, is the Kuşcayir granitoid (38 Ma, 40K/39Ar; Delaloye and Bingöl, 2000). The Late Oligocene Evçiler (28-24 Ma, Ar-Ar; Altunkaynak et al., 2012a) and Eybek granodiorite (23-16 Ma, U-Pb; Altunkaynak et al., 2012a; Black et al., 2013) are located north and south of the Kazdağ Massif respectively. The Evçiler follows a NE-trend and compositionally ranges from monzodiorite to granodiorite with equigranular texture (Öngen, 1992; Genç, 1998). Early Miocene intrusions are represented by the Kestanbol granite (21 Ma, U-Pb; Altunkaynak et al., 2012a) and the Yenice plutons (25-22 Ma, U-Pb; Aysal, 2015).

The Cenozoic volcanic suites in the Biga Peninsula display different compositions ranging from basalts to rhyolites. There are contrasting nomenclatures over the geological units in the region, and many tend to have several names for the same unit (e.g., Ercan et al., 1995; Genç, 2008, Dönmez et al., 2005; Duru et al., 2012). However, from a geochemical perspective, Altunkaynak and Genç

(2008) divided the volcanism into five magmatic stages. Each of those stages has increasing alkalic character, from calc-alkaline in the Eocene to alkalic basalts in the Late Miocene, a decreasing subduction signature, and increasing crustal contamination (Altunkaynak and Genç 2008). The Eocene volcanism is represented by volcano-sedimentary and basaltic to dacitic volcanics (e.g. Balıklıçeşme Volcanics; Ercan, 1995) located primary in northern Biga Peninsula. Oligocene volcanism in central and eastern Biga Peninsula includes basaltic andesite, trachyandesites and andesitic volcanics with high-K calk-alkaline signatures (e.g. Çan Volcanics; Ercan, 1995; Hallaçlar Volcanics; Dönmez et al., 2005). Eocene to Late Oligocene magmatism is coeval with the emplacement of plutonic rocks (Genç, 1998; Altunkaynak and Genç, 2008). In the Early Miocene however, plutonic activity decreased while volcanism continued until the Middle Miocene. Early Miocene volcanics consist of tuffs, lavas and agglomerates ranging from andesitic to rhyolitic compositions and a high-K to shoshonitic calk-alkaline signature (e.g. Beheram Volcanics; Borsi et al., 1972; Ercan et al., 1995). Middle Miocene volcanic rocks are typically andesitic ignimbrites (Altunkaynak and Genç, 2008). In the Bayramiç area, Genç (1998) studied the Oligocene-Miocene volcanic rocks and based on geological mapping, geochemistry and Nd-Pb isotopes, defined two major volcanic association: the Lower Volcanic Association (Eocene-Oligocene) and the Upper Volcanic Association (Lower-Middle Miocene). Finally, the Late Miocene alkalic basalts dominate the last stage of volcanism characterized by OIB-type volcanism (e.g. Ezine Volcanics; Aldanmaz et al., 2000; Yılmaz et al., 2000; Altunkaynak and Genç, 2008).

The youngest rocks in the Biga Peninsula are Neogene sediments deposited in northeast-trending grabens that are the product of the active extension. The most extensive outcrops are localized in the Gallipoli Peninsula and near Çanakkale. The Early Miocene Küçükkuyu Formation includes lacustrine sediments marls, siltstones interlayed with tuffs (Inci, 1984). The Çan Formation (Siyako et al., 1989) consists of bituminous shale, sandstone, siltstone, tuffs, and lignite levels. The Pliocene-Quaternary Bayramiç Formation (Siyako et al., 1989) consists of conglomerates, claystone, and sandstone of fluvial origin with more extensive outcrops along the Bayramiç River, nearby the town of Bayramiç (Figure 1.7).

1.8.3. Structural framework of the Biga Peninsula

The record of crustal deformation in the Biga Peninsula is divided into three stages: the Cimmerian orogenesis, the Alpine orogenesis, and Neogene deformation (Kürçer et al., 2008). During the first two stages, the units in the Karakaya complex were deformed while ophiolitic mélanges

were obducted during the Alpine orogenesis. The Cenozoic stage is characterized by syn- and post-orogenic extension resulting in exhumation of metamorphic sequences and core complex formation as observed throughout the Aegean domain (Okay and Satır, 2000a; Beccaletto et al., 2007; Bonev and Beccaletto, 2007; Brun and Faccenna, 2008; Jolivet and Brun, 2010). In the Biga Peninsula, core complex exhumation started in the Paleocene in the Kemer michaschists and continued through the Oligocene in the Kazdağ Massif (Okay and Satır, 2000a, Bonev and Beccaletto, 2007). In Kemer, NE-directed extension related to ductile to brittle shearing occurred from the Late Cretaceous to Early Eocene (Beccaleto et al., 2007) while in the Kazdağ core complex, north- trending lineations indicate of Late Oligocene-Early Miocene E-W extension (Okay and Satır, 2000a, Cavazza et al., 2009).

The southern branch of the NAF in the Biga Peninsula includes several NE-trending strike slip "en echelon" faults, from north to south and are named: Etili, Çan-Biga, Ezine, Sariköy-Inova, Evçiler, Yenice-Gönen, Pazarköy, and Havran-Balıkesir faults (Figure 1.7). In the south, east-trending normal faults (e.g. Edremit fault) bound east-trending basins in the Western Anatolia Graben System that extends to the Aegean Turkish coast.

Sanchez (2012) studied the major structures and the Cenozoic tectonic evolution of the Biga Peninsula and proposed that mineral deposits are spatially associated with granitoids emplaced into the footwall of extensional faults. Sanchez (2012) also distinguished five extensional episodes from Paleocene to Late Miocene. The first phase occurred in the Paleocene, characterized by syn-orogenic extension; during the second phase in Middle Eocene extension and plutonism have related porphyry and epithermal mineralization; the third extensional phase took place in Late Oligocene and is associated with core complex formation and porphyry and epithermal mineralization; the fourth extensional phase in Early to Middle Miocene includes plutonism and low-sulfidation veins; the fifth and final extensional stage in Late Miocene is characterized by fissure-related basalts. The extensional phases were followed in the Pliocene to Holocene by a dextral strike-slip and transtensional faulting regime.

1.8.4. Mineral occurrences in the Biga Peninsula

Epithermal Au-Ag, porphyry Cu-Au, and base metal skarn mineralization are associated with Cenozoic calc-alkaline magmatism (Yiğit, 2012). Commonly, multiple types of mineralization occur in a district, suggesting not only spatial but also genetic connections (e.g. porphyry and epithermal mineralization at Kuşcayiri and Aladağ; Yılmaz, 2003; Yiğit, 2012; Smith et al., 2014).

The Eocene mineralization events includes porphyry and epithermal deposits and examples

include: Kartaldağ, Madendağ, Kuşcayiri, the TV Tower District, and Halilağa. With the exception of Halilağa, these deposits are aligned in a NW-trend along the contact between the Çamilca Group and the Eocene magmatism (Figure 1.2). The TV Tower District includes several mineral occurrences such as Camelback, Valley, and Columbaz porphyries (See Leroux, 2016). In the northern Biga Peninsula, the Kestanelik low-sulfidation (LS) and the Sahinli intermediate-sulfidation (IS) epithermal deposits are hosted by Eocene volcanic rocks (ignimbrites, basalts, andesites and rhyolitic lava domes), sedimentary rocks, and Paleozoic schists along northeast- and east- trending veins. High-sulfidation (HS) epithermal mineralization in Kuşcayiri (Kayaali) is associated with E-trending structures and consists of an early quartz-sericite stage followed by an advanced argillic hydrothermal event (Yılmaz, 2003) and is hosted in lava flows domes, andesitic to dacitic volcaniclastics, and quartz-feldspar porphyry intrusions (Yiğit, 2012). Recent drilling south of the TV Tower district intercepted porphyry-style quartz vein stockwork and phyllic alteration (Pilot Gold, 2015). Kartaldağ, located 5 km NNW of Kuşcayiri is another HS epithermal deposit hosted in Eocene dacite porphyry, and is characterized by several silica generations and alunite, dickite, diaspore, and kaolinite alteration associated with the Au-Ag mineralization (Ünal et al., 2013). Nearby, the Madendağ LS epithermal deposit is hosted in Paleozoic micaschists of the Çamilca Group and is also hosted in Eocene andesites and dacites. The mineralization occurs in E- to WNW-trending veins and breccias.

Oligocene porphyry, skarn and epithermal deposits include the currently mined deposits of Tepeoba (19.24 Mt at 0.33% Cu and 0.041% Mo; Yiğit, 2012), Balya (Remaining Reserves of 2.3 Mt at 8% Pb–Zn, 1.5 g/t Au, 200 g/t Ag; Yiğit, 2012), and the largest undeveloped epithermal deposits in the Biga Peninsula Ağı Dağı (measured and inferred resources 90 Mt at 0.59 g/t Au, 4.74 g/t Ag; Ferrigno, et al., 2012) and Kırazlı (measured and inferred resources 32 Mt at 0.72 g/t Au, 8.74 g/t Ag; Ferrigno, et al., 2012). The Tepeoba porphyry deposit, in southern Biga Peninsula, is genetically associated with the Late Oligocene Eybek granodiorite and intrudes Permo-Triassic metabasites and metasedimentary rocks. Hydrothermal alteration is characterized by K-silicate, sericite, and chlorite assemblages. The Ağı Dağı HS epithermal deposit is located 10 km SE of Halilağa and occurs in a northeast- trending altered and mineralized zone. The deposit is hosted by andesite to rhyolite volcanic rocks and quartz-feldspar porphyries with development of hydrothermal breccias associated with gold mineralization. Pervasive silicification, chalcedonic quartz, argillic, and advanced argillic alteration are the typical hydrothermal alteration assemblages at Ağı Dağı (Yiğit, 2012). The Kirazlı deposit, located to the north of the study area, lies in Middle Oligocene volcanic rocks; gold mineralization is associated with different stages of silicification and advanced argillic alteration (Yiğit, 2012). Other Oligocene

HS epithermal deposits are: Çamyurt located southeast of Ağı Dağı and Alankoy. The Balya Ag-Au-Pb-Zn (Figure 1.3b) skarn deposit lies within the Karakaya Complex and includes garnet, tremolite, and actinolite in the skarn zone with argillic, phyllic, and advanced argillic alteration with hypogene alunite suggesting an overprinting epithermal event (Yiğit, 2012). Fe-Au-Cu skarn are associated with the northeast-trending Evçiler pluton in contact with the Mesozoic limestones from the Çetmi Mélange (e.g. Asar Tepe).

Oligocene and Miocene plutons host several skarn deposits in the Biga Peninsula and are evenly distributed along the Evçiler-Yenice district (Figure 1.7). These skarn systems are typically Pb-Zn with less commonly Au-Cu and W-Mo (e.g. Sofular; Yiğit, 2012). In addition to the skarn mineralization, the Miocene includes some important LS epithermal deposits such as Kisacik and Küçükdere (measured and indicated resources of 1.276 Mt at 6.43 g/t Au; Yiğit, 2012). The Kisacik is hosted by Miocene lapilli tuff, ignimbrites, and quartz-feldspar porphyry, and the mineralization occurs in breccias and quartz veinlets. The Küçükdere Au-Ag deposit is hosted by Miocene feldspar-porphyries, the mineralized veins present classical LS textures (breccia, cockade, banded, and bladed quartz after calcite; Yiğit, 2012).

The age of magmatism and mineralization in the Biga Peninsula spans from the Middle Eocene to Middle Miocene, comparable to the Serbomacedonian-Rhodope Metallogenic Belt of the southern Balkan Peninsula (Lips, 2002; Yiğit, 2012). However, the earlier, Middle Eocene (40-37 Ma) mineralization pulse includes porphyry and epithermal mineralization that has no equivalent in the Rhodopes.

1.9. Exploration History of Halilağa

The Biga Peninsula is host to one of the first settlements in Turkey, the city of Troy (3000 B.C.). The mineral resources available in the region, coupled with its strategic location next to the sea, made Troy an important trading center with mineral deposits mined from ancient times (e.g. Madendağ and Kartaldağ; Yiğit, 2012). Early exploration for epithermal mineralization in the vicinity of Halilağa village was carried out by MTA between 1988 and 1991

The mineralization at Halilağa was discovered by-soil sampling anomalies and confirmed by rock chip samples of stockwork-vein and leached outcrops with gold values greater than 1 g/t (Avsan et al., 2012). From 2006 to 2012, over 53,000 m of core was drilled in the Halilağa property (including the Pirentepe epithermal system) in a joint venture between Teck Madencilik Sanayi Ticaret A.Ş. (Turkish subsidiary of Teck Resources Limited) with a participation of 60% and Pilot Gold Inc with a

40%. Geophysical surveys were carried out from 2005 to 2011 in the district. These surveys include induced polarization (IP), ground magnetics, and airborne magnetics.

1.10. Thesis Structure

This thesis comprises six chapters.

- Chapter 1 establishes the context and defines the purpose, states the goals, and describes the general methods employed in this study. Additionally it includes the literature review of the regional setting of the Halilağa deposit.
- Chapter 2 includes the results of core logging and geological mapping in the Halilağa district in terms of lithology and structures and structural interpretations are also included in this chapter to support field data. In addition, seven new U-Pb geochronology are presented for plutonic and volcanic units.
- Chapter 3 presents the igneous geochemistry results and Re-Os geochronology.
- In Chapter 4 are described the characteristics of hydrothermal alteration and mineralization of the porphyry deposit. Additionally, alteration geochemistry and SWIR analysis of alteration minerals are presented.
- Chapter 5 discusses the major implications of the new geochronology results in terms of the geological evolution of the deposit and the spatial relations between the different mineralization styles at the Halilağa District.
- Chapter 6 presents conclusions, exploration implications, and recommendation for future work.

Chapter 2: Geology of the Halilağa Cu-Au Deposit

The Halilağa porphyry Cu-Au deposit is the largest porphyry system yet discovered in the Biga Peninsula. Therefore the Halilağa District provides an excellent situation to address the stratigraphic setting, geochronology, and structural controls of porphyry deposits in the Biga Peninsula. The objective of this chapter is to present the deposit scale geological framework. To accomplish this field descriptions for volcanic and intrusive units and the results of the geochronology are provided. The structural geology section presents remote sensing interpretations in addition to field data.

The stratigraphy of the Halilağa District is dominated by pre-Eocene fine-grained continental sedimentary rocks (Figure 2.1). Eocene volcano-sedimentary rocks and Oligocene volcanic and subvolcanic rocks, which vary in composition from basaltic-andesite to rhyodacite. These rocks are interpreted as being the product of post-collisional magmatism controlled by slab-break off with continental arc signatures (Genç, 2008; Altunkaynak and Genç, 2008). The Paleogene stratified units are intruded by the Eocene to Oligocene Kestane stock, Kocakışla stock, and the Evçiler pluton that are dioritic to granitic in composition. A simplified stratigraphic column of the district including the geochronological results of this study is presented in Figure 2.2.

2.1. Deposit Lithology

2.1.1. Stratified units

2.1.1.1. Cretaceous basement: Çetmi mélange

Basement units are attributed to the Çetmi Mélange and these outcrops in the southeast of the study area around the Bakırlık hill (Figure 2.1). The age of the Çetmi mélange was constrained between Middle Triassic to Lower Cretaceous (Albian) by microfossils (Beccaletto, 2003). The Çetmi Mélange comprises marble, limestones, fine-grained marine sediments, and mafic volcanic rocks. Propylitic, kaolinite, and sericite alteration (Figure 2.3) in those rocks is generally intense and overprints original textures. The thickness of the mélange sequence is calculated to at least 300 m in the deposit area, though elsewhere is estimated to be > 500 meters (Beccaletto, 2003). A characteristic of the mélange at the Bakırlık hill is a 70 m thick level of marble seen in drill core and surface outcrop (Avsan et al., 2012).

2.1.1.2. Middle Eocene lavas, volcano-sedimentary and conglomerates (40-37 Ma)

These units have been identified at two principal locations: the Kestane graben and the Kunk

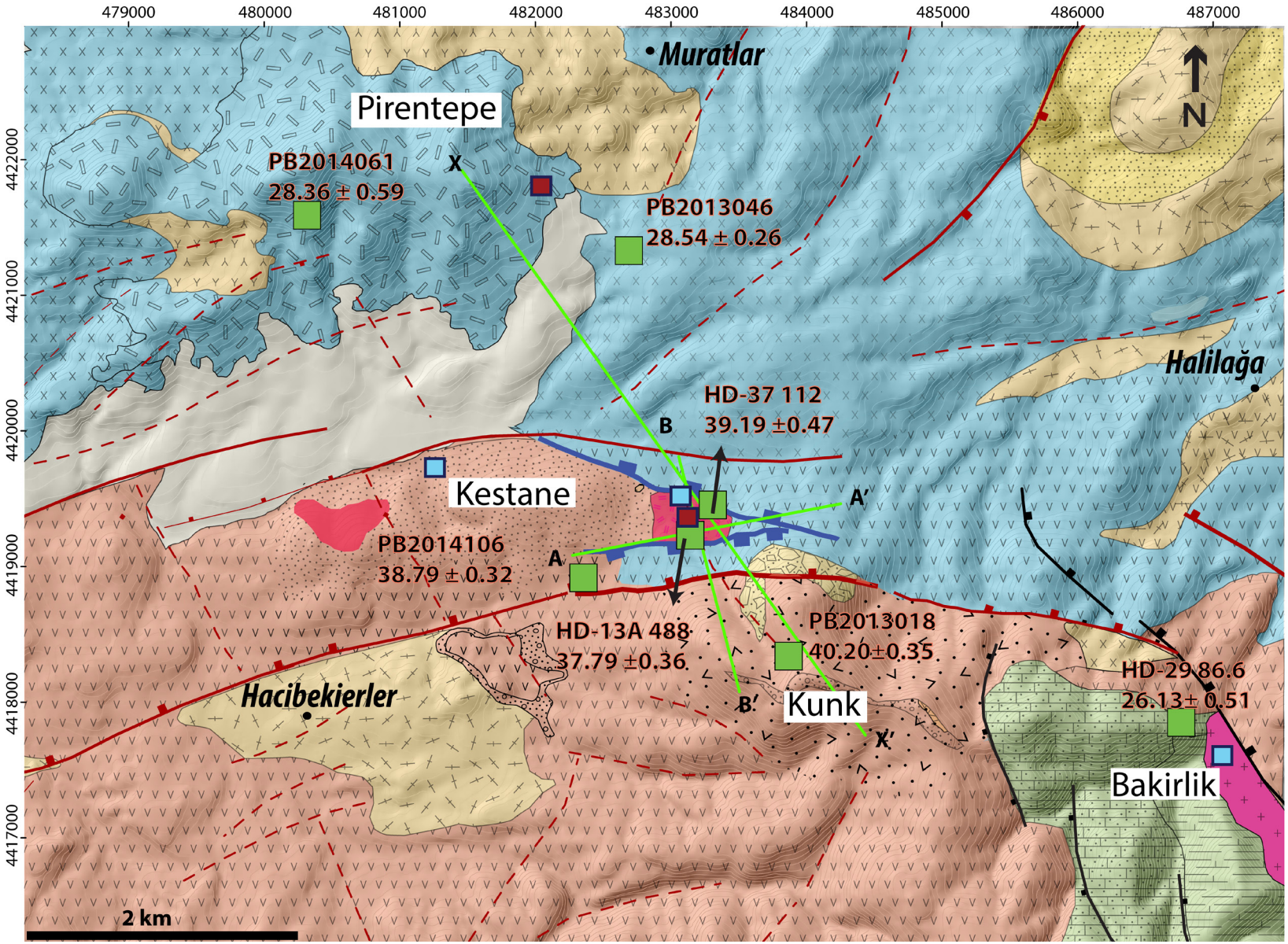

Figure 2.1 Geological Map of the Halilağa District, including U-Pb geochronology samples and stratigraphic column location (Appendix A2). Modified after Sanchez (2012) and Ceyhan and Avsan (2012). UTM projection, zone 35N, datum ED50. Legend in Figure 2.2

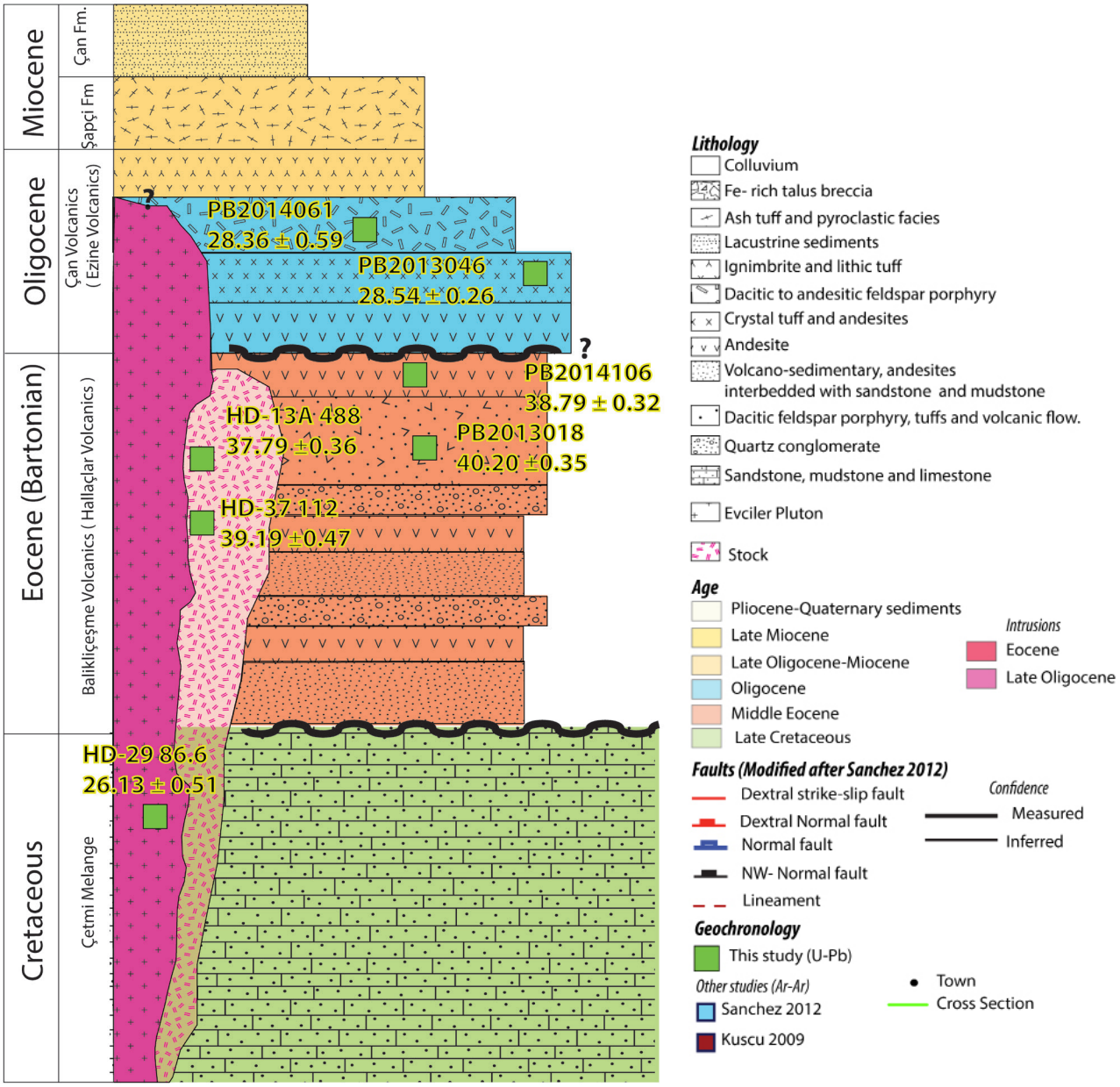

Figure 2.2 Generalized stratigraphic column for the Halilağa district with U-Pb geochronology samples for this study. Previous studies Ar-Ar samples are shown in Figure 2.1 (Kuşcu, 2009; Sanchez, 2012). Note that cross-cutting relationships are not always observed in the area.

hill (Figure 2.1 and 2.4) in the southern part of the study area. The contact with the Mesozoic Çetmi Mélange is unconformable. The contact between Eocene and Oligocene volcanics from drill core suggests that Oligocene volcanics overlies unconformably or by fault the Eocene volcanic sequence.

In the Kestane graben a 500 m–thick, W-dipping volcano-sedimentary sequence is the predominant unit. It consists of interbedded andesite lavas, volcanic siltstones, and volcanic sandstones, interbedded with centrimetric to metric-scale conglomerates (Figure 2.5). Accretionary lapilli are observed in volcanic sandstones suggesting genetic association with explosive volcanism. A 70 m thick marble level is interbedded with the volcano-sedimentary sequence. This volcano-sedimentary sequence has been subsequently intruded by the Kestane stock, which resulted in the development of hornfels in wall rocks adjacent to the contact obscuring many primary textures. The green andesite unit (Figure 2.5c) corresponds to porphyritic andesitic lavas, with abundant plagioclase (25%), hornblende (5%), biotite (7%) and rounded quartz (10%) phenocrysts in a green groundmass of feldspar (40%) and magnetite (3%) and with a typically high magnetic susceptibility, overlie the sequence.

The lithology at the Kunk hill section of the study is characterized by tuffs and lava flows of dacitic composition interbedded with volcanic sandstones and conglomerates containing characteristic pebble quartz clasts. The stratigraphy has an average northward dip of 28° coinciding with published regional observations (Sanchez, 2012). A characteristic aspect in the geophysics of this volcanic sequence is the low magnetic susceptibility measured in the field and also observed in ground and airborne magnetics due to magnetite destruction by hydrothermal alteration.

The petrographic investigations of this unit are summarized in Table 2.1. Dacitic lavas at Kunk (Figure 2.5e) comprise subhedral to anhedral plagioclases (30-35%), embayed quartz phenocrysts (5-10%), pseudomorphs after mafic minerals (5-7%) in a microcrystalline ground mass (quartz and feldspar aggregate, 40%). Fresher volcano-sedimentary levels include rounded quartz crystals, euhedral plagioclases, and lithic fragments.

Lithogeochemistry (Figure 2.6) reveals compositions ranging from andesite to rhyolite (61.12 - 75.74 wt% SiO_2). The green andesite unit has lower silica but higher alkali contents than the volcano-sedimentary unit or dacite from Kunk based on the total alkali silica diagram (TAS, Figure 2.6a).

U-Pb zircon geochronology in this study area has yielded two Middle Eocene ages of 40.20 ± 0.35 Ma and 38.79 ± 0.32 Ma for the dacite in Kunk and the green andesite respectively (Table 2.2). Concordia diagrams are shown in Figure 2.7. In published regional maps, numerous outcrops within the study area are assigned to the Late Oligocene-Early Miocene Hallaçlar Volcanics (Duru et al., 2012; Dönmez et al., 2005). Moreover, the volcano-sedimentary character of the sequence and

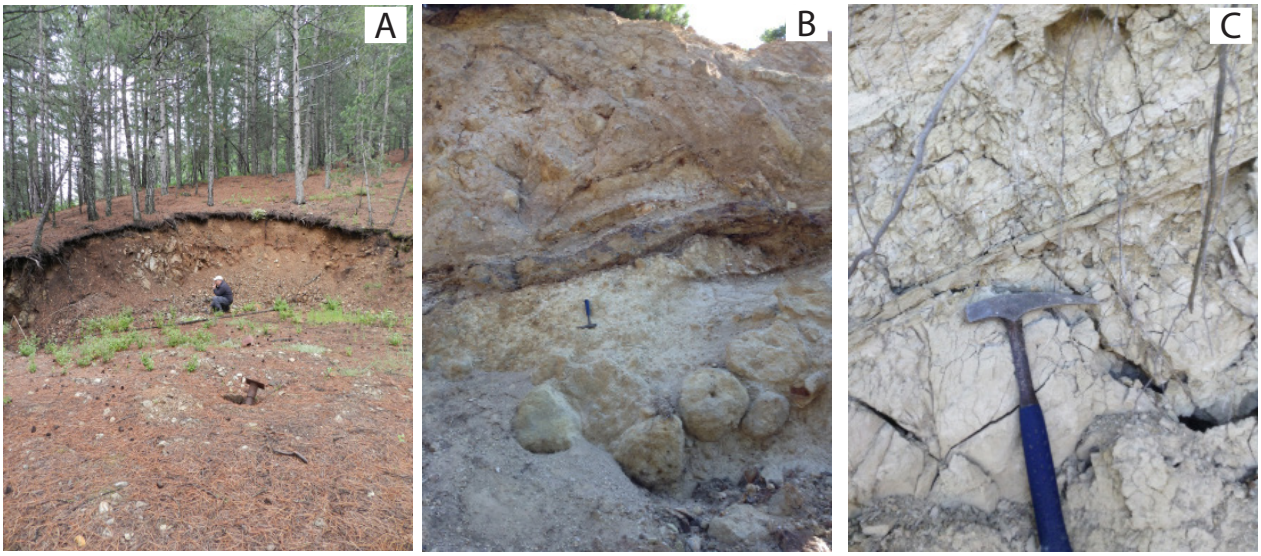

Figure 2.3 a)HD-28 and HD-25 in the Bakırlık area. The surrounding rocks are carbonates (dolomite) with light green garnets attributed to the Çetmi Melange b) Yellow tuff agglomerate with a glassy horizon dipping NW attributed to the Çan Formation c) Outcrop in the Muratlar-Etili road with stratified sediments attributed to the Bayramiç Formation (PB2014112)

the andesitic to dacitic composition of the lavas coincides with the published descriptions and age of Eocene Balıklıçeşme Volcanics (37.3 ± 0.9; Ercan et al., 1995), defined in northern Biga Peninsula.

2.1.1.3. Oligocene lavas and tuffs

Oligocene lavas and tuffs are located in the Pirentepe- Muratlar area, east of Kestane, and in the area nearby the villages of Keçiağılı, Dereoba, and Halilağa (Figure 1.3 and 2.1). The contacts of this unit is by fault contact with the Eocene volcano-sedimentary unit.

The Oligocene volcanic sequence is a variable sequence regarding volcanic facies and composition (Table 2.1). It includes lavas and pyroclastic deposits of dacitic to basaltic andesitic composition. The basal unit in Pirentepe observed in drill core, corresponds to the **basaltic andesite to andesite lavas** (Figure 2.8a), which are also observed at the top of the stratigraphic columns at Kestane, Bakırlık-Kunk, and Dereoba-Keçiağılı (Figure 1.4). The basaltic andesite corresponds to a dark grey-purple porphyritic fine-grained basaltic andesite with plagioclase phenocrysts in an aphanitic ground mass.

Basaltic andesite to andesite are locally overlain by **dacitic crystal tuffs** (Figure 2.5b), which has euhedral to subeuhedral plagioclase, hornblende, biotite, and quartz crystals and weak hydrothermal alteration. **Andesitic porphyries** (Figure 2.8d), with plagioclase, biotite, hornblende, and occasional quartz phenocrysts in a grey to purple groundmass overlie the dacitic crystal tuffs. The andesitic porphyries are also interbedded with highly altered and permeable volcaniclastic horizons

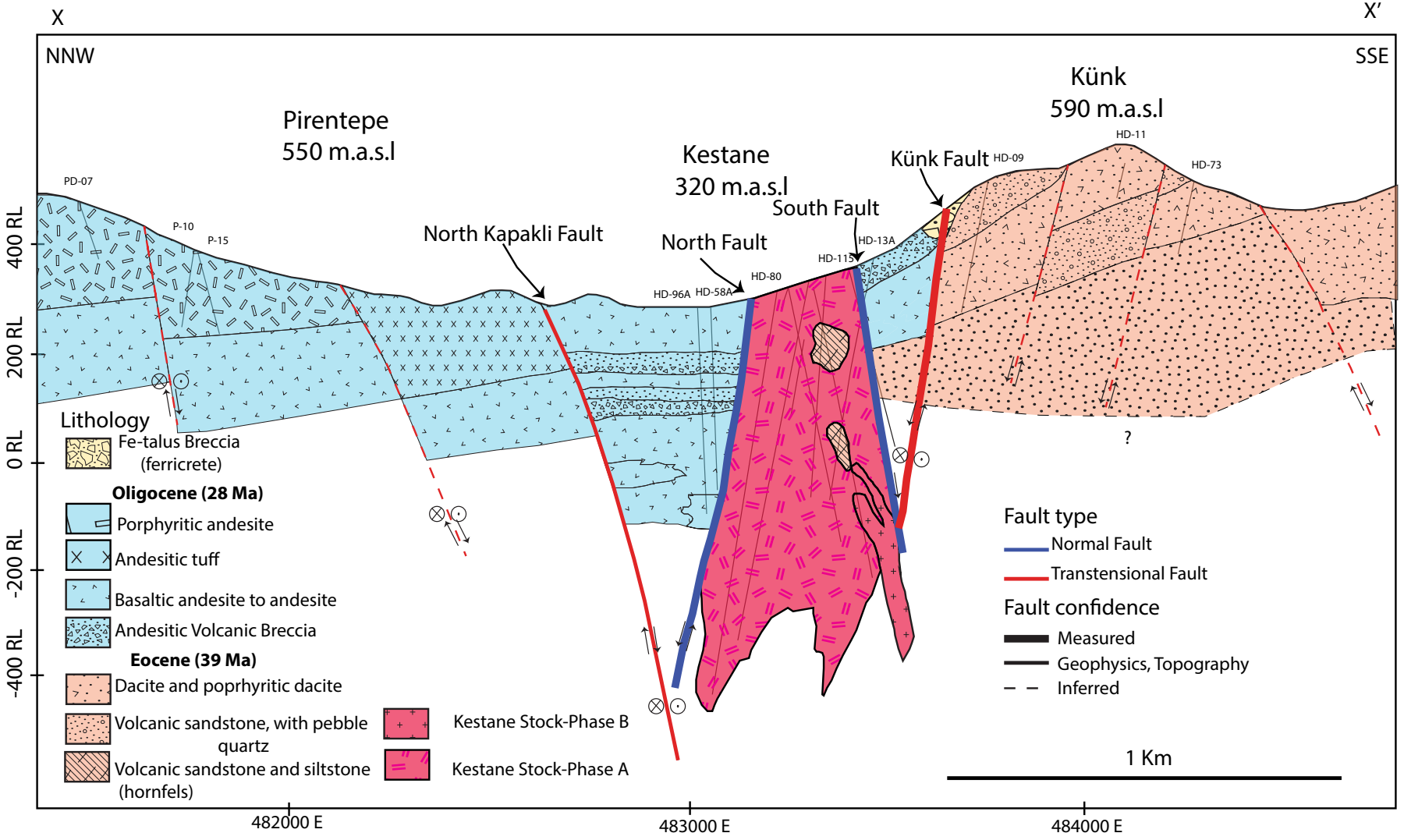

Figure 2.4 NNW cross section from Pirentepe to Kunk . The Pirentepe, Kestane, and Kunk domains are limited by transtensional faults. 2.5x vertical exaggeration. The porphyry mineralization is located in the Kestane domain, a local graben bounded by the North Kapkali and Kunk faults; however, the porphyry stock is cut by the North and South faults. Horizontal scale in UTM projection, zone 35N, datum ED50. Location of cross-section X-X' in Figure 2.1

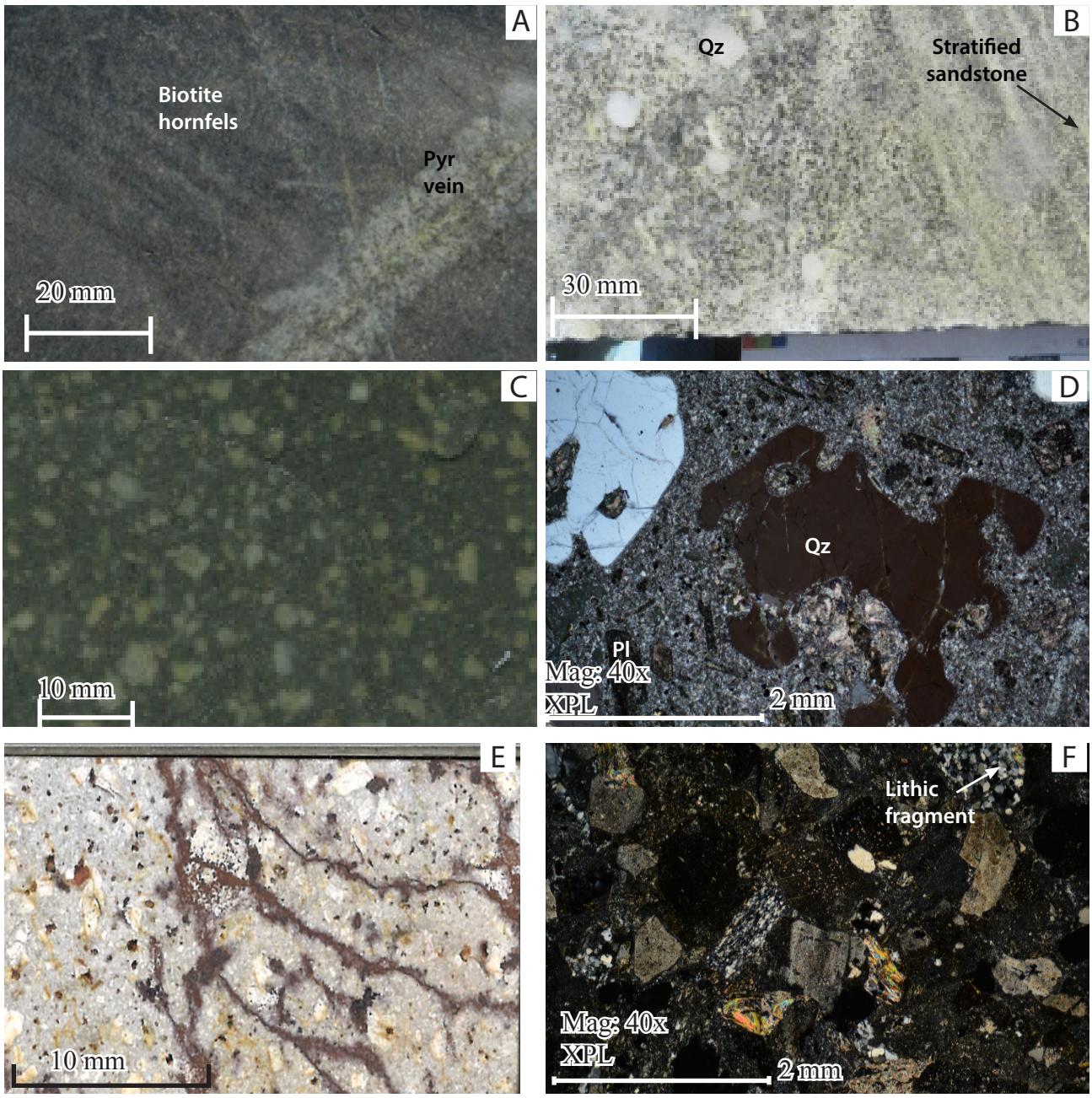

Figure 2.5 a) Fine grained rock altered to hornfels. Pyrite vein with sericitic halo. Chalcopyrite is clustered. HD-78 431 m; b) Altered and stratified sandstone and quartz conglomerate in drill core (HD-78, 43.2 m); c) Green andesite, plagioclase- and quartz- phyric in microcrystalline ground mass from West Kestane (Sample PB2014106 with geochronology; d) Embayed quartz megacryst and altered plagioclase phenocryst in a fine micro-crystalline ground mass; e) Altered dacite from Kunk. Porphyritic texture. Plagioclase phenocrysts are intensely altered to white mica and pyrophyllite. Specular and earthy hematite are present in veins and after phenocrysts in a vuggy texture; (f) Volcano-sedimentary rock with fragmental texture and polylithic fragments, this rock unit is interbedded with andesites and appear to be the unaltered host rock of Kestane.

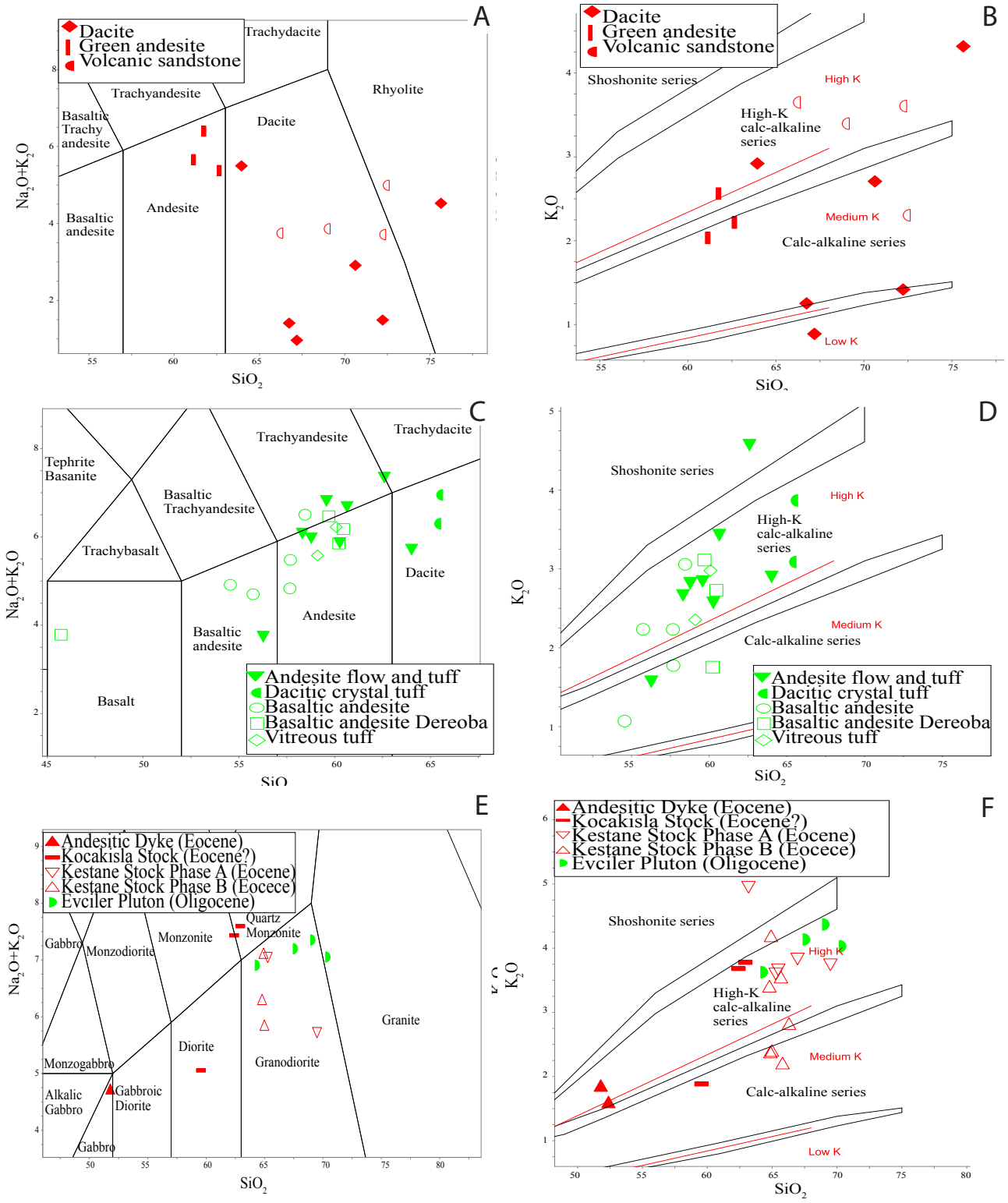

Figure 2.6 a) Total alkali silica (TAS) diagram for rock classification of Eocene volcanic suite (Le Maitre et al., 1989) b)Subdivision of sub-alkalic series in Eocene volcanic rocks using K_2O and SiO_2 (After Peccerillo and Taylor, 1976; Le Maitre et al., 1989; Rickwood, 1989) c) TAS diagram for Oligocene volcanic rocks (Le Maitre et. al, 1989) d) Subdivision of sub-alkalic series in Oligocene volcanic rocks using K_2O and SiO_2 (After Peccerillo and Taylor, 1976; Le Maitre et al., 1989; Rickwood, 1989) e)Total alkali silica (TAS) diagram for plutonic rocks (Middlemost, 1994) f) Subdivision of sub-alkalic series in intrusive rocks using K_2O and SiO_2.

that host gold mineralization in vuggy silica at Pirentepe. The top of the sequence is characterized by an extremely magnetic **vitric andesitic to dacitic tuff breccia** (Figure 2.8e-d), with lithic and ash-fall clasts (bombs). The andesitic porphyry is texturally and compositionally similar to the matrix of the vitric andesitic breccia.

Petrographic inspection of representative samples from each unit indicates abundant (ca. 10%) lithic fragments and subhedral to euhedral crystals of pyroxene (4-10%), plagioclase (20-30%), hornblende (3-10%), biotite (2-7%), quartz (in dacitic crystal tuff, up to 10%) in trachytic groundmass with variables contents of volcanic glass and magnetite. Geochemistry defined two major groups (Figure 2.6c): basalt andesite to andesite (ca. 57 wt% SiO_2) and andesite to dacite (ca. 61 wt% SiO_2). Both groups are primary high K calc-alkaline series (Figure 2.6d). Total alkali contents range from 3.74 to 7.34 wt%.

U-Pb geochronological data for this major unit have yielded two similar ages 28.36 ± 0.59 and 28.54 ± 0.26 Ma (Figure 2.7) for andesitic porphyry on the top of Pirentepe and an andesitic tuff near Muratlar respectively. However in regional maps, the outcrops of this unit were attributed to the Late Miocene Ezine Volcanics (Siyako et al., 1989; Duru et al., 2012).

Middle Oligocene ages of this sequence are similar to the ages of the Çan Volcanics (Ercan et al., 1995; Altunkaynak and Genç, 2008). Furthermore, in the Keçiağılı area (Figure 1.3), Sanchez (2012) obtained an $^{40}Ar/^{39}Ar$ (groundmass) plateau age of 28.63 ± 0.16 Ma in a porphyritic dacite (ignimbrite) comparable with the vitric tuff breccia.

2.1.1.4. Miocene sequences

Well-stratified sedimentary and volcaniclastic sequences are localized to the northeast of the study area and nearby the Hacibekierler village (southwest of Kestane) and are attributed to the Çan Formation (Siyako et al., 1989). The contact with Oligocene volcanic rocks is an unconformity observed in the Keçiağılı area (Sanchez, 2012). Palynological study has given a Burdigalian-Serravallian age of the Çan Formation, ranging between 20 and 12 Ma (Siyako et al., 1989). The sequences contain ash- fall tuffs, lacustrine deposits, and also include local coal horizons.

2.1.1.5. Plio-Quaternary sediments

Fluvial and alluvial sediments defining the Bayramiç Formation are located in the Kestane-Kocakışla graben and comprise pebble conglomerates, sandstones, and siltstone (Siyako et al., 1989).

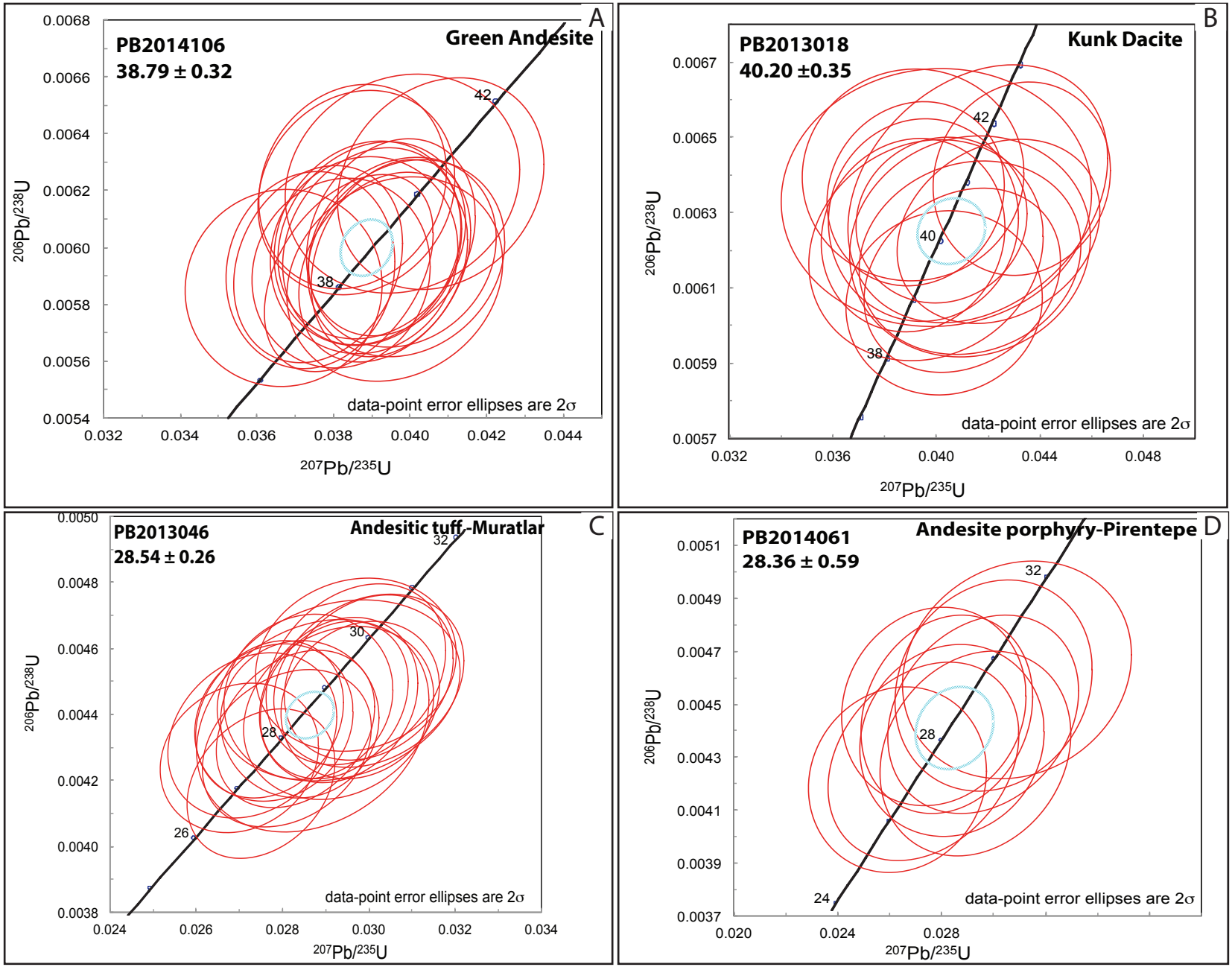

Figure 2.7 Concordia diagrams for volcanic units. Refer to appendix E for complete results. The red circles are the calculated age for valid zircon, light blue shows concordia age.

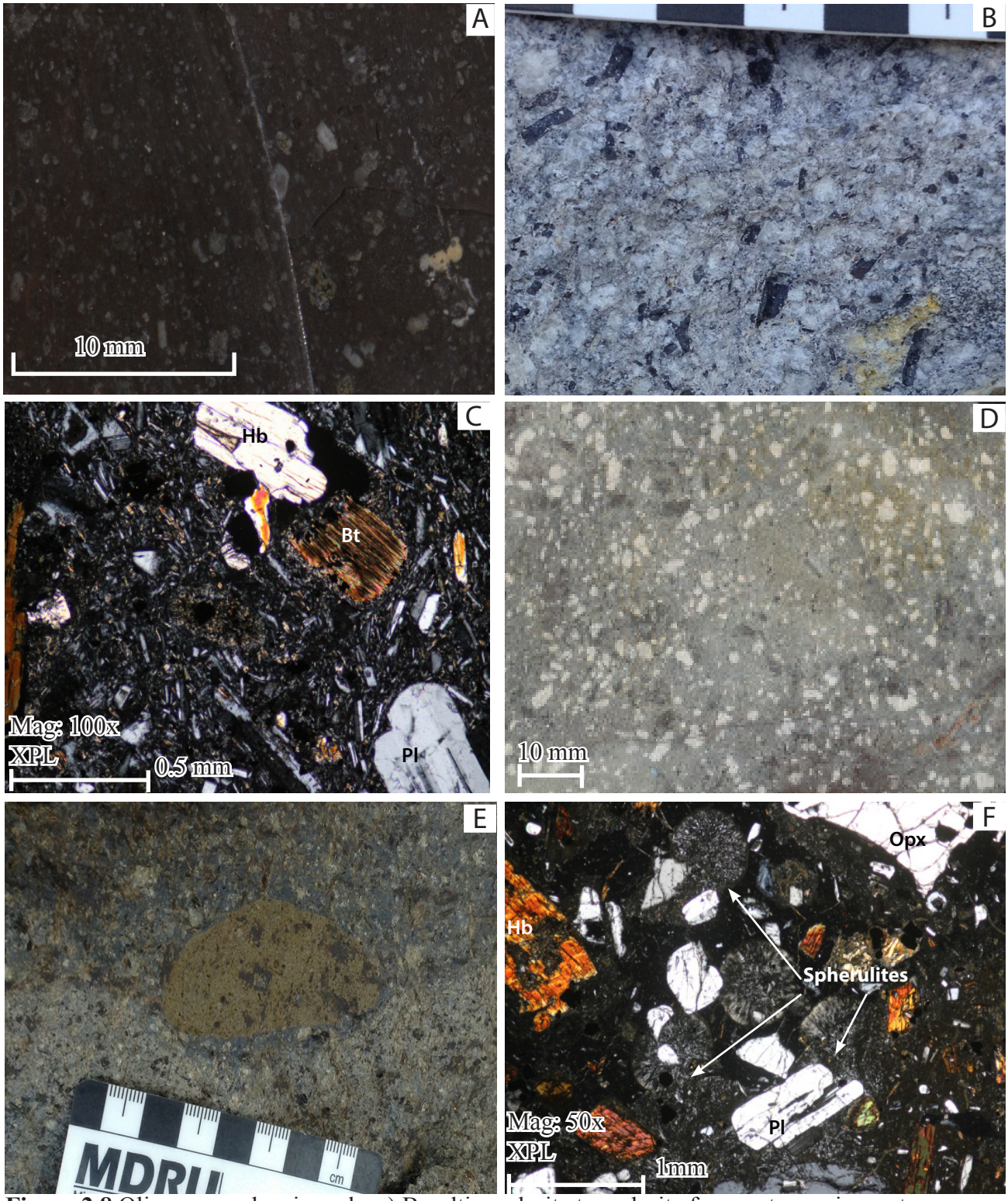

Figure 2.8 Oligocene volcanic rocks a) Basaltic andesite to andesite from outcrops in west Kestane b) Dacitic crystal tuff. Sub euhedral to euhedral plagioclases, reddish lath- shape mafic (amphiboles), rounded quartz phenocrysts (482684, 4423254) c) Andesite flow. Biotite, hornblende, plagioclase- phyric in a trachytic ground mass d) Argillized andesite (feldespar-phyric) from Pirentepe (sample PB2014061 with U-Pb geochronology) e) Vitric tuff breccia with bomb sized clasts, magnetic rock of andesitic composition. (480838, 4423162) f) Vitric tuff thin section, hornblende, orthopyroxene and spherulites in a vitric ground mass.

2.1.2. Intrusive units

Plutonic bodies are distributed along the central and southern parts of the study area. In the Halilağa District, there are at least two episodes of intrusive activity coeval with the volcanic episodes described in the previous section. Plutonism peaked in Middle Eocene (37-39 Ma) and the Late Oligocene (ca. 26 Ma). Porphyry mineralization is hosted in the Kestane stock, attributed to the Eocene plutonism, and the surrounding wall rock which is described in more detail below. In addition, other intrusions are causative of skarn mineralization in limestones.

2.1.2.1. Kestane stock

The Kestane stock is located in the Kestane-Kocakışla graben (Figure 2.1). The exposure in surface is limited to an area of 300 x 300 m and interpretation from drill core suggest a WNW-elongated porphyry stock controlled by two structures (North and South Faults).

The Kestane stock comprises two dominant intrusive phases that have similar compositions (quartz monzonite to granite): a mineralized phase with porphyritic texture (Phase A) and a poorly altered or mineralized (Phase B).

Phase A is a quartz monzonite to granite porphyry, phenocryst dominated with a fine-grained groundmass of K-feldspar and quartz, the groundmass: phenocrysts ratio is 50:50 to 60:40. The phenocrysts include plagioclase (25%), hornblende (10%), quartz (5%), and biotite (1%). Thin section studies of this unit revealed a mosaic textured ground mass, and weak to moderate alteration of plagioclase by white micas, as well as biotitization and later chloritization in mafic minerals (Figure 2.9a). Lithogeochemistry of these rocks indicated a granodiorite composition based in total alkalis silica classification for plutonic rocks with 65.27-69.49 wt.% SiO_2 and 5.71-7.12 wt% $Na_2O+ K_2O$ (TAS, Middlemost, 1994). In a classification diagram of sub-alkalic rocks, based on K_2O and SiO_2, Phase A represents a high K-calc-alkaline series (Middlemost, 1975).

Phase B is a quartz monzonite to granite porphyry that contains euhedral plagioclase (15-30%), subeuhedral hornblendes (7-15%), embayed rounded quartz (2-7%), and minor biotite (2-3%) phenocrysts in a mosaic aggregate of quartz and K-feldspar (Figure 2.9b), groundmass: phenocryst ratio is 70-60: 30-40. Thin section observations suggest less hydrothermal alteration compared with the Phase A, though biotitization and incipient chloritization affects hornblende. Similar to Phase A, the geochemistry indicates a granodiorite composition in the TAS diagram for plutonic rocks with 64.79-67.48 wt% SiO_2 and 5.70-7.11 wt% $Na_2O+ K_2O$ (Figure 2.6e).

The distinction between the porphyry phases is observed in the bivariate K_2O versus SiO_2

diagrams (Figure 2.9f). In the least altered samples, the Phase A presents higher K_2O signatures than the Phase B. This chemical differentiation is also observed in the immobile bivariate TiO_2 versus Y (Figure 2.9f), although the ratio Y/TiO_2 seems to be similar between the two porphyry phases and the contents of TiO_2 are slightly higher in phase B.

Previous $^{40}Ar/^{39}Ar$ plateau ages on muscovite and K-feldspar (Sanchez, 2012; Kuşcu, 2012) indicated a Late Oligocene cooling age, but new U-Pb geochronological data on zircon have yielded a Middle Eocene age (Table 2.2). The Phase A yielded a bimodal concordia age population at 39.19 ± 0.47 and 71.9 ± 1.3 Ma. The youngest age is interpreted to be the crystallization age of Phase A whereas the oldest age population to correspond to inherited zircon grains (Figure 2.10). The Phase B of the Kestane stock has yielded a concordia age of 37.79 ± 0.36 Ma (Figure 2.10).

2.1.2.2. Intermediate dikes

These units distributed throughout the Kestane graben correspond to narrow dikes that post-date and cut the Kestane stock. Due to the mafic composition of these rocks, U-Pb geochronology on zircon was not possible to obtain.

The dikes comprise plagioclase (30%), amphibole (15%), and pyroxene (5%) phenocrysts (Figure 2.9c); partially to completely altered to clays, epidote, chlorite and calcite, and are embedded in a microcrystalline ground mass of feldspars, mafic minerals, and magnetite. QAP diagram classification, based on modal percentages in thin section, indicates a monzodiorite composition. Geochemical classification based in major elements indicated gabbroic/basaltic composition (Middlemost, 1994) with 52.38-53.28 wt% SiO_2 and 4.8 wt% $Na_2O+ K_2O$ in high calc-alkaline series.

2.1.2.3. Kocakışla stock

The Kocakışla stock outcrops to the west of the Kestane graben, 1 km north of Hacibekirler village (Figure 2.1). Based on the drill hole intersections, it is interpreted as a sub-vertical, cylindrical body with a diameter of lesser than 400 m. The stock intrudes the Eocene volcanic sequence (hornfels, volcanic sandstone, and andesitic tuffs). The crystallization age of this intrusive is undetermined.

The Kocakışla stock corresponds to a dark fine-grained microcrystalline quartz monzonite to monzodiorite (2.9d). Mafic minerals represent a 35% of the rock; felsic minerals constitute the other 65%. Petrographic observations indicate a relatively equigranular and panidiomorphic texture (average crystal size is 1 mm). The rock contains biotite (15%), hornblende partially altered to clays (20%), euhedral plagioclases (35%), K-feldspar (20%), and quartz (10%). Geochemistry of unaltered, or weakly altered, samples of this intrusive are reveals high alkalis with 7.4-7.6 wt.% $Na_2O+ K_2O$ and

Table 2.1 Stratified geological units in the Halilağa Deposit. Age references are (1) Beccaletto, 2007; (2) This Study; (3) Sanchez, 2012. Sample descriptions can be found in Appendix B

Formation	Unit	Area	Description	Petrography	Geochemistry	Sample-type	Thickness	Timing/Age
Cetmi melange	Volcano-sedimentary	Bakirlik	dark and fine grained rock. Quartz conglomerate levels are interbedded within this sequence	-	-	-	>300 m	Middle Triassic to Lower Cretaceous (Albian) (1).
	Marble	Bakirlik	massive, white to pale grey.	-	-	-	70 m	Middle Triassic to Lower Cretaceous (Albian) (1).
Hallaclar/ Baliklicesme volcanics	Volcano-sedimentary	Kestane	fine grained volcano-sedimentary rock . Locally brecciated In fresher samples volcanic sandstone and siltstone with accretionary lapilli textures.	sedimentary texture with rounded quartz crystals, Other minerals exhibit euhederal shape (plagioclases, muscovite). Cryptocrystalline (probably rock flour) ground mass. Calcite is replacing plagioclases total and partially. Ocasionally present lithic fragments	TAS diagram: dacite to Rhyolite. (66.19-72.43 wt% SiO2 and 0.96-4.52 wt% Na2O+ K2O)	PB2014107c	500 m	Pre-Eocene (2)
	Marble	Kestane	massive, white to pale grey. Calcite crystals and hematite veins without sulphides.	-	-	-	70 m	Pre-Eocene (2)
	Conglomerate	Kestane-Kunk	rounded quartz clast in gray ground mass, ocasional jasperoid quartz	-	-	PB2013062	a few meters, interbedded	Pre-Eocene (2)
	Green andesite	Kestane	greenish ground mass andesite, plagioclase, quartz and biotite phyriric. Groundmass/ phenocrysts is 70?30.	plagioclase, rounded quartz phyric andsite to dacite. Pseudomorphs of biotite and hornblend, average size 2.5-3 mm. Cryptopcrystalline ground mass of feldspar and magnetite.	TAS diagram: andesite (61.12-62.63 wt% SiO2; 5.37-6.40 wt% Na2O+ K2O)	PB2014106	50 m (estimated)	38 Ma (U-Pb)
	Tuffs and lava flows of dacitic composition	Kunk	pinkish aphanitic dacites, dacitic tuffs with local pyrite in mafic site with pinkinsh ground mass. More porphyritic type has plagioclases, and quartz phenocrysts.	embayed quartz phenocrysts. Limonites disseminated in ground mass and in vuggy texture. Local brecciation with limonites matrix.	TAS Diagram: dacite to rhyolite. (66.74-75.74 wt% SiO2 and 0.96-4.52 wt% Na2O+ K2O)	PB2013018	160 m	40 Ma (U-Pb)

Table 2.1 (cont)

Formation	Unit	Area	Description	Petrography	Geochemistry	Sample-type	Thickness	Timing/Age
Ezine/Can Volcanics	Basaltic andesite to andesite lavas	Kestane/ Pirentepe/ Dereoba	purple andesite, phenocryst poor to aphanitic texture with hand lens observation. Intervals with andesitic breccia with local variations in colour: purple, gray, reddish. Generally monomictic	plagioclase, hornblende, pyroxene (Clinopyroxene) phyric in a microcrystalline to cryptocrystalline ground mass (plagioclase, rutile and probably pyxroxene). Mafic minerals are altered.	TAS diagram: basalt andesite to trachyandesite, including andesite (54.55-60.45 wt% SiO2 and 4.70-6.50 wt% Na2O+ K2O). High K calc-alkaline series	PB2013021; PD-23 186.7	50 m	32 Ma (Ar-Ar) in andesites from Dereoba (3)
	Dacitic crystal tuff	Pirentepe/ Dereoba	lght grey coeherent dacitic crystal-rich tuff . Plagioclases 5 mm su- ehudral to ehudral , opaque and reddish tabular mafic (amphibol shape), rounded to anhedral quartz, hexagonal biotite. Pale grey to yellowish ground mass, tufficeous?	plagioclase, embayed quartz, biotite, and diamond shape hornblende crystals. Groundmass is cryptocrystalline.	TAS diagram: dacite (65.38-65.48 wt% SiO2 and 6.29-6.95 wt% Na2O+ K2O). High K calc-alkaline series	PB2014004	-	Older than 28 and probably younger than 32
	Andesitic porphyry and tuffs	Pirentepe	andesitic porphyry; plagioclase, biotite, amphibole sub-euhedral phenocrysts in a purple groundmass. It can contain rounded quartz phenocrysts.	euhedral and fragmented plagioclases, caramel biotite, quartz, and hornblende. Ground mass contains crystals, magnetite, and volcanic glass	TAS diagram: andesite to trachyandesite (58.31-62.59 wt% SiO2 and 5.86-7.34 wt% Na2O+ K2O). High K calc-alkaline series	PD-07 101, PD-07 55	250 m	28 Ma (U-Pb); 28 Ma (Ar-Ar)
	Vitric tuff breccias	Pirentepe	strongly magnetic vitric tuff breccia. The matriz is the andesitic porphyry and the bomb size clast are yellow ash fall-tuff with some crystals.	plagioclases, biotite, hornblende, and lithic fragments in a vitric ground mass. Plagioclases present trahytic and anti-pertitic texture, altered diamond -shape hornblendes. Mafics exhibit replacement textures (clays and calcite).	TAS diagram: andesite. (59.10-60.08 wt% SiO2 and5.58-6.22 wt% Na2O+ K2O).High K calc-alkaline series	PB2013068, PB2013125	100 m	Younger than andesitic crystal tuff, and older than lacustrine deposits from Çan Fm.
Can Fromation/Sapçi Volcanics	Sedimentary and ash-fall deposits	E Muratlar	lacustrine sediments, ash tuff and pyroclastic facies	-	-			Miocene
Bayramic Formation	Continental sediments	Base of Pirentepe, Kestane graben	conglomerates, sandstones, siltstone	-	-			Plio-Quaternary

Table 2.2 Results of U-Pb in zircon geochronology

Sample	Unit	Area	Concordia age	2σ	MSWD	Probability
HD-29	Evçiler pluton	Bakirlik	26.32	0.61	0.12	0.72
PB2014061	Argillized feldspar porphyry	Pirentepe	28.36	0.59	0.2	0.66
PB2013046	Andesitic tuff	Pirentepe	28.54	0.26	1.02	0.31
PB2014106	Andesite (green andesite)	Kestane W	38.79	0.32	0.25	0.62
HD-37_112_Inher-itance	Inheritance	Kestane	71.9	1.3	1.5	0.21
HD-37_112	Kestane Stock- Phase A	Kestane	39.19	0.47	0.05	0.83
HD-13A_488	Kestane Stock- Phase B	Kestane	37.79	0.36	0.32	0.57

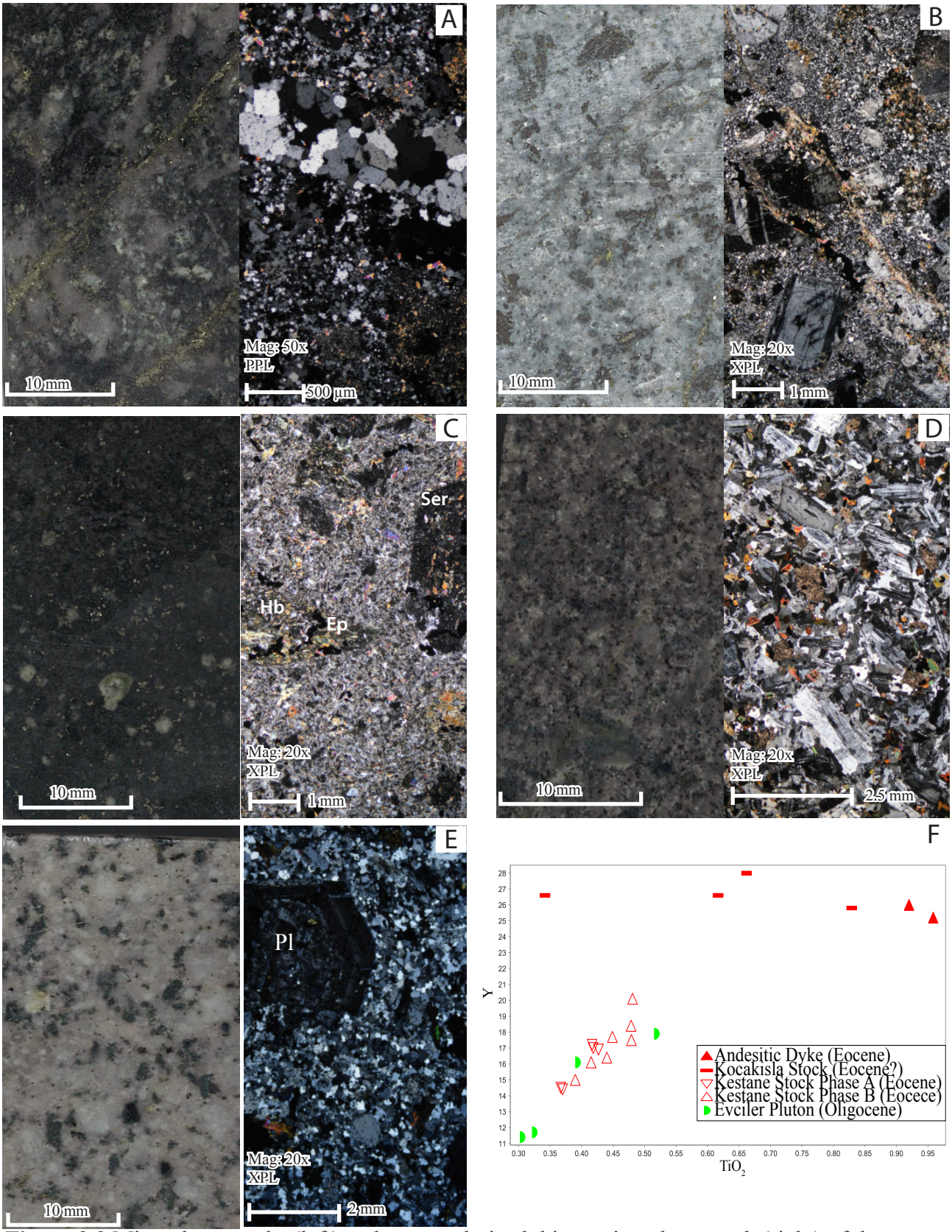

Figure 2.9 Microphotographs (left) and cross polarized thin section photograph (right) of the intrusive units in the district a) Kestane stock- phase A b) Kestane stock- phase B c) Andesitic Dyke d) Kocakisla stock e) Evçiler pluton f) TiO_2 versus Y immobile elements plot for plutonic rocks.

Table 2.3 Intrusive rocks in the Halilağa Deposit. Sample description can be found in Appendix B.

Major unit	Unit	Area	Description	Petrography	Geochemistry	Sample-type	Age
Kestane stock	Kestane stock-Phase A	Kestane	mineralized quartz monzonite to granite with porphyritic texture	ground mass: phenocrysts ratio is approximately 50/50. Phenocrysts are: plagioclases (10-25%), hornblende (7-10%), quartz (3-7%), and biotite (1-3%). The phenocrysts have two porpulations of phenocrysts size.	65.27-69.49 wt.% SiO_2; 5.71-7.12 wt% Na_2O+ K_2O	HD-37 112	39 Ma (U-Pb)
	Kestane stock - Phase B	Kestane	poorly altered or mineralized quartz monzonite to granite	ground mass: phenocrysts ratio is about 60: 40. Mosaic aggregate of 0.1 mm quartz and k-feldspar. Phernocrysts are plagioclases (15-30%), hornblendes (5-15%), quartz (3-7%), biotite (up to 3%)	64.79-67.48wt% SiO_2; 5.70-7.11 wt% Na_2O+ K_2O	HD-13A 488, HD-37 254	37 Ma (U-Pb)
Andesitic dyke	Andesitic dyke	Kestane	green andesitic porphyry, phenocryst poor (less than 30%) Plagioclase-pyric and pyritized mafics.	diamond shape hornblendes, plagioclases, clinopyroxene, and biotite phenocrysts in a microcrystaline groundmass (feldspar, magnetite, and mafics)	52.38-53.28 wt% SiO_2; 4.8 wt% Na_2O+ K_2O	HD-38 190, HD-01 297.5	-
Kocakisla stock	Kocakisla stock	Kocakisla	dark grey quartz monzonite to quartz monzodiorite with microcrystalline texture. Abundant mafic minerals (35%), quartz, plagioclase, and K-feldspar. (QAP: 16, 33, 58)	fine grained rock (average 1 mm), Mafic crystals are biotite (15%), hornblende(20%) overprinted by clays. Felsic crystals are plagioclases (35%), K-feldspar (20%), and quartz (10%).	62 wt.% SiO_2; 7.4-7.6 wt.% Na_2O+ K_2O	PD-21 229.5	-
Evciler pluton	Evciler intrusive	Bakirlik	Pinkish to greenish monzogranite, medium grained porphyrirtic texture. (QAP: 55, 33, 22)	porphyritic rock. Ground mass(70%) is a fine-grained granular aggregate of quartz and k-feldspar. Phenocrysts are: plagioclases (20%), biotite (3%), and quartz (7%,). The average size of phenocrysts is 3 mm.	64-70 wt.% SiO_2; 6.9-7.3-wt % Na_2O+ K_2O	HD-29 86	26 (U-Pb)

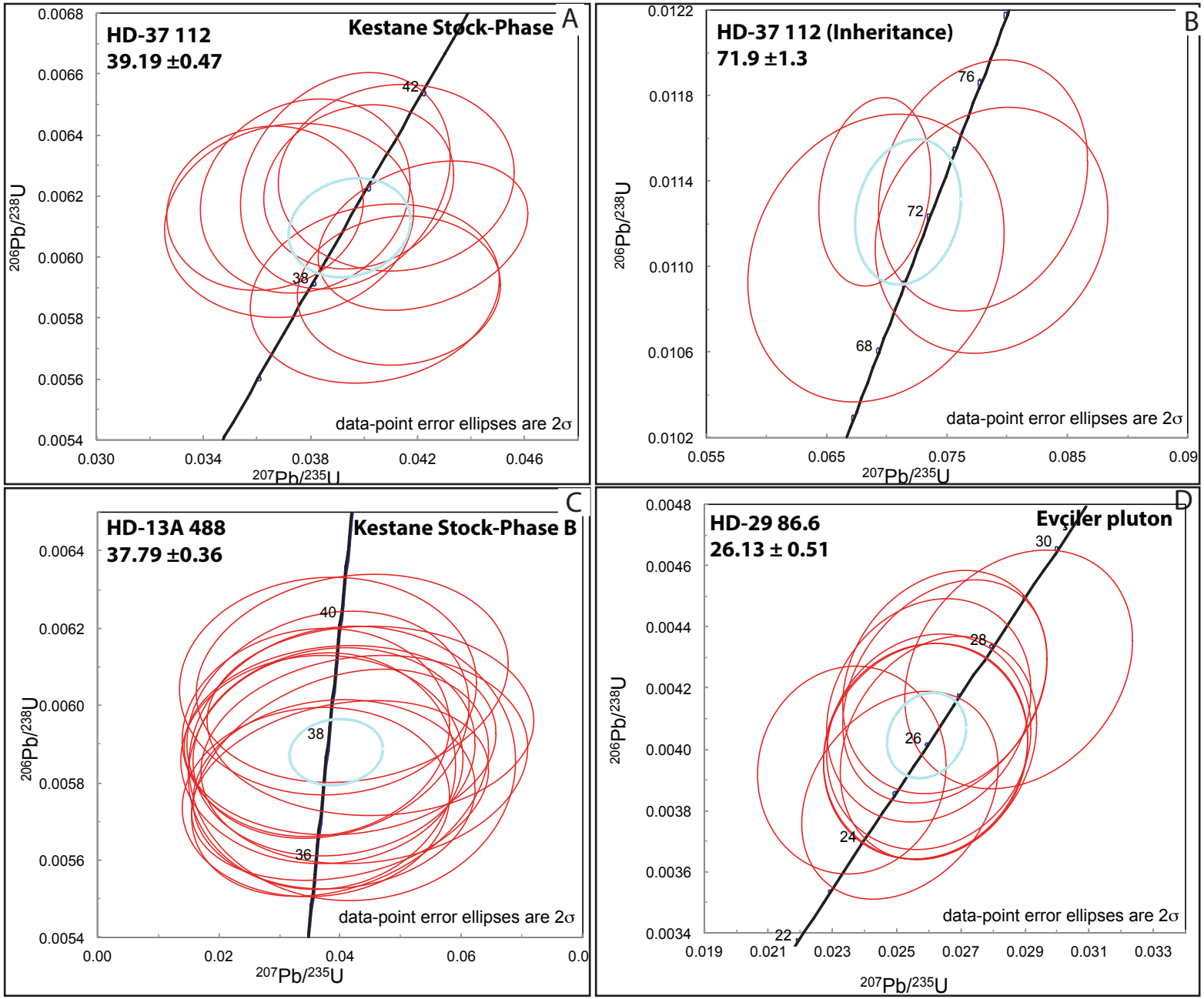

Figure 2.10 Concordia diagrams for intrusions. Refer to appendix E for complete results. The red circles are the calculated age for valid zircon, light blue shows concordia age.

an intermediate composition (62 wt.% SiO_2) pointing to diorite to quartz monzonite composition in the TAS Plutonic diagram (Figure 2.6e).

2.1.2.4. Evçiler pluton

The Evçiler pluton is a large batholith that outcrops in a in the northern flank of the Kazdağ Massif (Figure 1.7). In the Halilağa district, it outcrops in the southeast of the area in the Bakırlık hill (Figure 2.1) and intrudes with a NW orientation into limestones and siltstones of the Çetmi Mélange. Compositionally the Evçiler pluton corresponds to a porphyritic monzogranite (Figure 2.9e) with a fine-grained ground mass (quartz and K-feldspar aggregate with crystals up to 0.3 mm) and medium-grained phenocrysts of plagioclase (20%), biotite (3%) and quartz (7%). SiO_2 contents ranges from 64-70 wt.% and 6.9-7.3-wt % Na_2O+ K_2O suggesting granodiorite to granite in TAS diagram and high-K calc-alkaline series (Middlemost, 1975).

U-Pb in zircon yielded a late Oligocene age of 26.13 ± 0.51 Ma (Figure 2.10). Where previous $^{40}Ar/^{39}Ar$ hornblende ages of the Evçiler pluton yielded 28 ± 0.1 Ma and 27.7 ± 0.1 Ma (Altunkaynak et al., 2012), while $^{40}Ar/^{39}Ar$ biotite cooling ages indicated 24.8 ± 0.1 Ma (Altunkaynak et al., 2012a) and $^{40}Ar/^{39}Ar$ K-feldspar indicated 25.07 ± 0.14 and 26.38 ± 0.16 Ma (Sanchez, 2012).

2.2. Structural Geology

Structures are difficult to identify on surface due to poor rock exposure due to widespread quaternary cover, and farmlands. Consequently, the use of remote sensing tools was critical to interpret major orientations and the existence of possible faults; in addition to the limited collection of structural data from surface and drill core. Bozkurt (2007) conducted the first structural study in the area; interpreting major faults based on topographic lineaments in the Kunk area. Sanchez (2012) carried out a detailed structural study for the area and the Biga Peninsula based in geological mapping and remote sensing. In addition, in 2013 SRK also re-interpreted major lineaments based on: airborne and ground magnetic surveys, Lidar images, digital elevation models, and drill-core observations (Baker and Stenhouse, 2013).

In this study, the methodology for the structural analysis includes structural data from drill core and surface, re-interpretation of reduced to pole aerial (RTP) magnetic data (processed by Teck), 10 m resolution Shuttle Radar Topography Mission (SRTM) and 3.4 m resolution LIDAR topographic models, ASTER, and Landsat 7 ETM+. A skeleton map was first created based on major trends of topographic valleys observed in the hillshade, ASTER, and Landsat imagery and trends in the

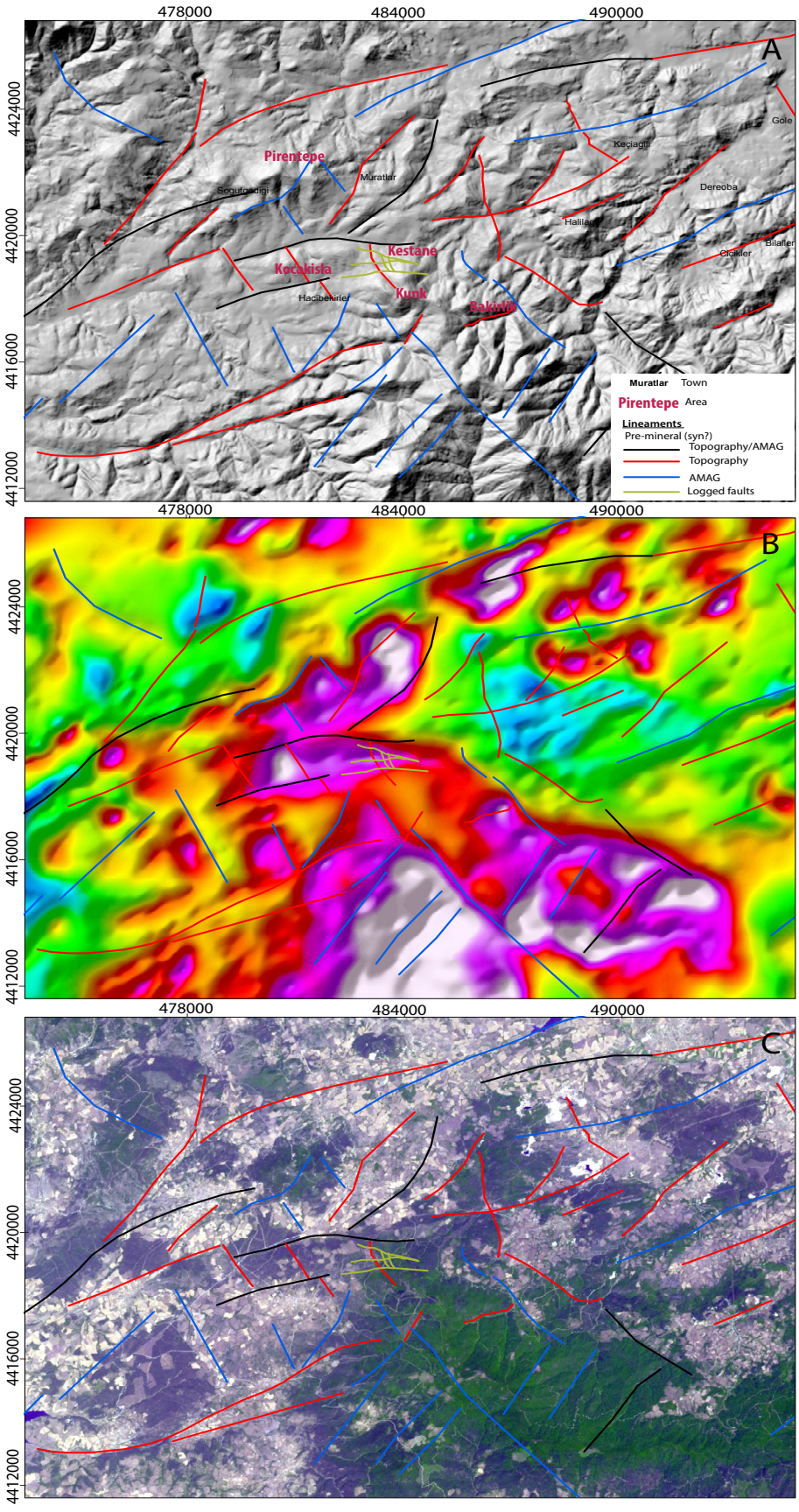

Figure 2.11 Interpreted lineaments a) Hillshade from a 10 m resolution SRTM; b) Reduced to the pole Airborne magnetic data c) ASTER satellite image

magnetic patterns. Following the interpretation for each separated dataset, the result was compiled and categorized and when lineaments occur in both datasets a higher confidence is given.

2.2.1. Major lineaments and magnetic features

Three main lineament trends have been identified in the study area based on magnetic and topographic datasets: a prominent ENE-trend, a secondary NNW- set, and a NE- trending set. The ENE-trending lineaments are the most important features in topography and are also present as distinct features in the magnetic survey and they define three major domains: the Pirentepe horst, Kestane graben, and Kunk-Bakırlık horst (Figure 2.4). The NNW trend is not observed in topography, but has an important signature in the aerial magnetometry. Finally, the NE lineaments are evidenced by both surveys, in addition to vegetation patterns (Figure 2.11c).

In geophysical surveys interpreted by Teck, high chargeability coincides with a semi-circular high magnetic anomaly in the Kestane porphyry Cu-Au deposit. Two major structural trends (E- and NW-) were observed in the magnetic interpretation and higher magnetic anomalies are located in the intersection of those trends (Avsan et al., 2012). Magnetic anomalies (“highs” in RTP) are broadly aligned NW in the southern border of the area and are associated with the Evçiler pluton intrusion. In Pirentepe the anomaly follows a NE orientation, while in the Kestane graben the NW trending anomaly bends E-W (Figure 2.11). At Kunk hill, the rocks exhibit lower magnetic susceptibility than Kestane, Bakırlık, or Pirentepe and it is also bounded by NW-trending structures.

2.2.2. Structural observations and measurements

Structural observations in drill core from the Kestane area showed 2-20 meter wide fault and damage zones characterized by cohesive cataclasites and incohesive fault breccias and gouges (Figure 2.12a-b), using the terminology of Woodcock and Mort (2008), and low temperature clays (kaolinite, smectite). Due to the lack of oriented core there is no possibility to confirm fault orientations or kinematics. In surface, only a few faults planes were measured and interpreted from drill core logging and modeling (n=10), those are mainly N-S and E-W oriented in Kestane and Pirentepe, while the dominant orientations in Kunk are: NNW- to NNE- and E- to WNW. However, Bozkurt (2007) measured fault orientations and rake in the Kunk area where he identified three major fault sets: An earlier NW and an associated NE, and a later E-W. In the first two sets he identified two successive kinematic regimes: an earlier strike-slip followed by a normal event.

The North Kapakli Fault (Figure 2.4, Table 2.4) is a major lineament observed in topography

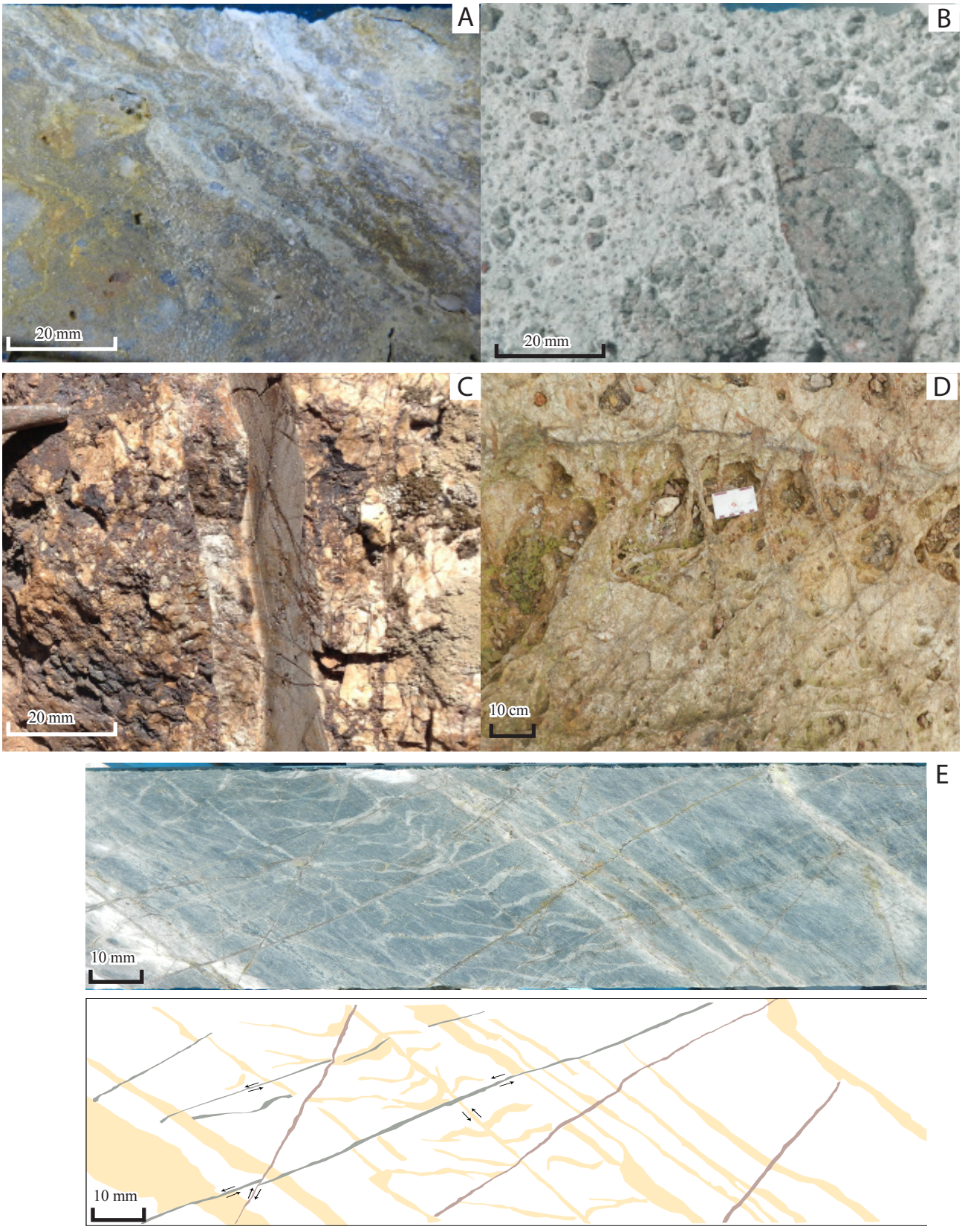

Figure 2.12 a) HD-94A 217.75 South fault b) HD-79 190.9 (6120) Fault breccia with pinkish hornblende-phyric igneous rock c) Tasyatak Tepe (SE Kunk) fault breccia with goethite matrix; d) Preferred orientation of quartz veins with 3 major sets; e) Tension gashes observed in HD-78 in hornfels.

and aerial magnetic images and the Kunk Fault is observed in drill- core and in a scarp where a Fe-rich breccia is also observed (Figure 2.4) Those E- to ENE-trending structures (Kunk fault in the south and the North Kapakli Fault) built graben morphology with three east-trending domains: the Pirentepe and Kunk horst and the Kestane graben (Fig 2.3 and 2.5). Those domains present differences in host-rocks type, age, mineralization, and structural orientations described below.

In the Kestane graben, the major faults interpreted from drill core, are two E- trending faults that bound the deposit to the north and south resulting in exhumation and tilting of the porphyry stock. A dominant normal kinematic indicator has been interpreted with probable strike-slip reactivation in Late Miocene; the stock and the altered (hornfelsed) volcano-sedimentary host-rocks lies in the footwall of these antithetic faults, while relatively unaltered post mineralization volcanic rocks are situated in the hanging wall. The North Fault has a dip/dip direction of 70/020 (modeled based on drill core) while the South Fault orientation is approximately 65/180. Another set of NNW- trending and sub-vertical normal faults is inferred from topographic lineaments, magnetic patterns and drill logs interpretations. The largest of these faults are the Çamtaşı and Karıncalı faults (Figure 2.13). The Çamtaşı Fault is the western-most fault in the stock and is extended to Kunk with a dip/dip direction of approximately 80/060. In the interpreted cross sections based on drill logs there is no major offsets observed. However, field measurements of quartz veins (B-type) and hematite-goethite-quartz veins (D-type) reveals differences to the east and west of this fault (Figure 2.13). To the west of the fault the dominant strike for B-type veins is ca. 280° and 045/225°, while to the east of the Çamtaşı Fault the veins trend ca. 025° and 105°. In the D-type vein sets the orientations are more diverse: 320°,

Table 2.4 Summary of faults and veins at the Halilağa District

Structure	Orientation	Dip	Kinematics
Faults			
North Kapakli	E-W to ENE-WSW	sub-vertical	Normal and strike slip
South Kapakli	E-W to ENE-WSW	sub-vertical	Normal and strike slip
North Fault	WNW-ESE	~70°	Normal and strike slip
South Fault	E-W	~65°	Normal and strike slip
Kunk Fault	E-W	sub-vertical	Normal and strike slip
Çamtaşı Fault	NNW	~80°	Normal
Karıncalı Fault	NNW	sub-vertical	Normal
Veins			
Quartz+limonite	Preferred E-W, secondary N to NNE, minor NNW	sub-vertical	-
Quartz+limonite+sericite halo	Preferred E-W, secondary N to NNE	sub-vertical	-

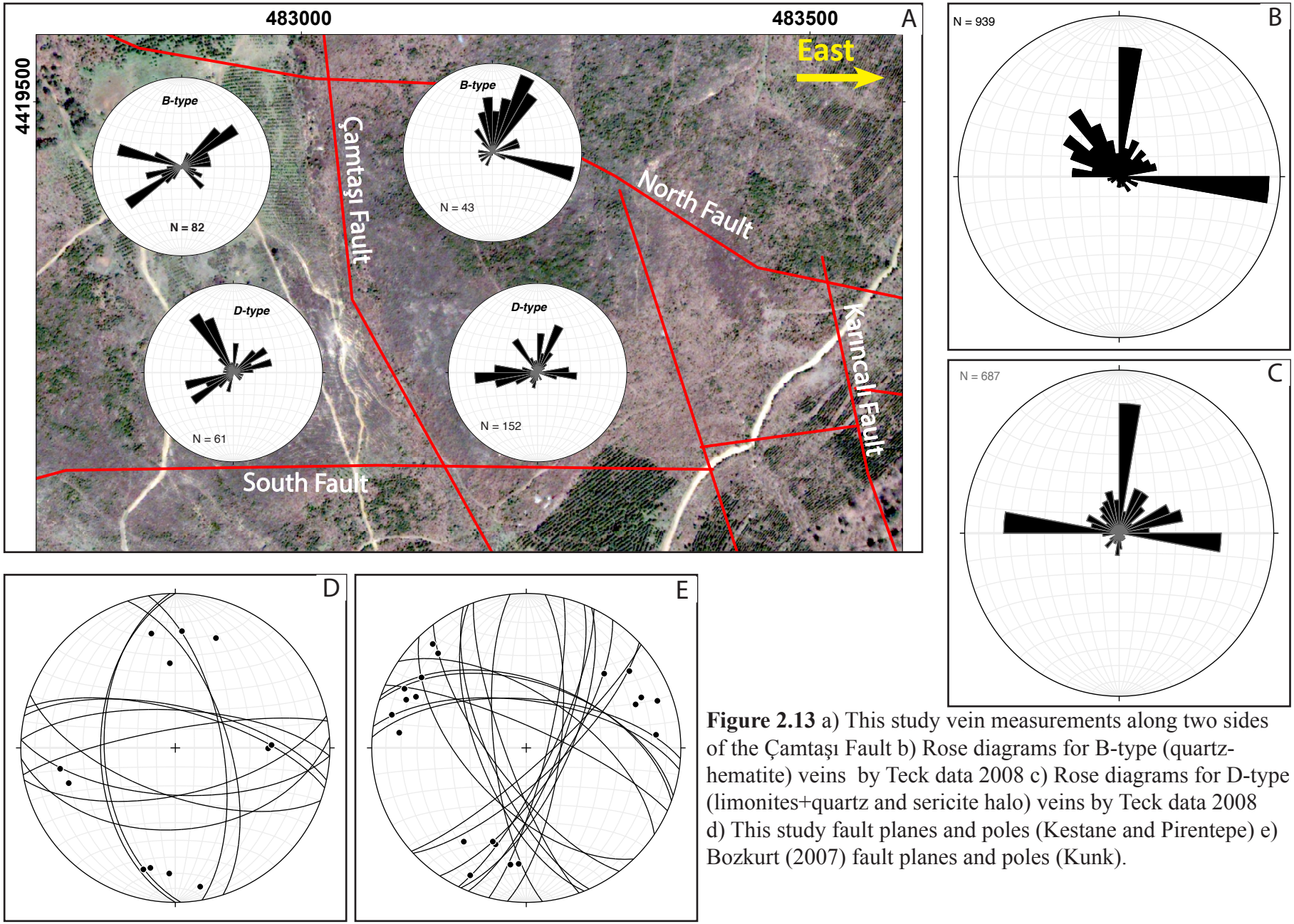

Figure 2.13 a) This study vein measurements along two sides of the Çamtaşı Fault b) Rose diagrams for B-type (quartz-hematite) veins by Teck data 2008 c) Rose diagrams for D-type (limonites+quartz and sericite halo) veins by Teck data 2008 d) This study fault planes and poles (Kestane and Pirentepe) e) Bozkurt (2007) fault planes and poles (Kunk).

260/80°, and 240/60° dominates the west, while 030°, 270/90° was observed to the east. Although it is not clear if the change in the vein orientations is relative to post-emplacement rotations or unidentified variations in the porphyry stock and different timings of emplacement.

The Karıncalı Fault in the east is not evident at surface due to cover from vegetation and recent sediments. Magnetic and topographic lineaments however, indicate a NNW trending structure. In addition, the thickness of the Oligocene volcanic sequence increases eastward, suggesting several normal structures controlling the development of this fault. In cross-sectional interpretation based on drill logs, this NNW (80/300) fault offsets the North Fault by 50 m (Figure 2.14).

In Halilağa, vein exposures are limited to an area of 300 m diameter. As previously mentioned, the mineralized quartz - sulfides (limonite), or B-type, veins and the later quartz + sulfides (limonite) with sericite halo, or D-type, are sheeted veins and exhibit a preferred orientation; historic measurements of B-type (n=939) and D-type (n=687) veins indicated a preferred E-W and secondary N to NNE orientations for both sets, and also a tertiary NNW for the B-type veins (Figure 2.13). In hornfels, en echelon tension gashes are observed in drill core (Figure 2.12e).

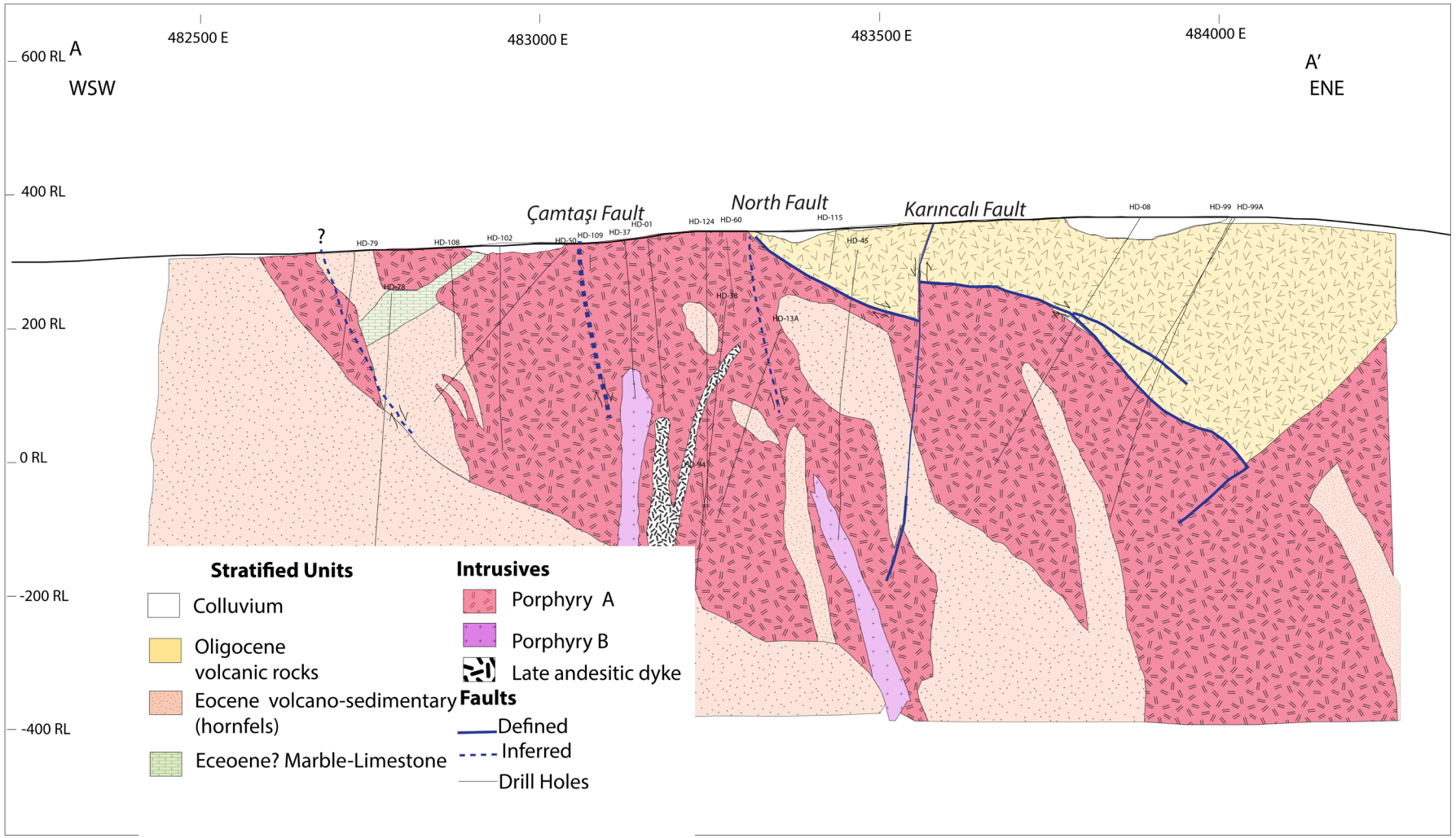

Figure 2.14 A-A' cross-section with interpreted lithology based on drill core logging and interpretation. UTM projection, zone 35N, datum ED50. Cross section location in Figure 2.1.

Chapter 3: Lithogeochemistry

The tectono-magmatic setting of porphyry deposits plays a major role in their formation (e.g. Richards, 2003; Cooke et al., 2005). Porphyry deposits typically form in continental and island arc setting usually related to subduction. However, a large number of deposits previously interpreted to be formed in subduction zones have been re-interpreted to be formed in syn-collisional or post-collisional setting, suggesting a broader tectono-magmatic setting for their emplacement (Tosdal et al., 2009, Richards, 2009). Porphyry deposits in the Aegean and NW Turkey are the result of post-collisional magmatism; which started by a retreating-slab (Hellenic arc) or by slab-break off. In addition, since the Eocene-Early Oligocene, extensional tectonics product of slab roll-back dominate the Aegean domain (See Chapter 1). As a result, porphyry deposits in the Serbomacedonian-Rhodope Belt exhibit variations in their geochemical features, based on age and geographic location, from having calc-alkaline to shoshonitic affinities (e.g. Skouries; Kroll et al., 2002; Marchev et al., 2005). In NW Turkey, little is known about the Eocene magmatism associated with porphyry deposits in the Central Biga Peninsula.

The Halilağa porphyry Cu-Au deposit is the largest porphyry system so far discovered in the Biga Peninsula. As mentioned in Chapter 2, the Halilağa District comprises two groups of magmatic rocks of Middle Eocene and Oligocene age. Furthermore, the new Eocene age for the quartz monzonite intrusions associated with the Halilağa porphyry Cu-Au deposit brings into question the geochemical characteristics of causative intrusions of the Eocene mineralization, which appear to be very productive on the context of ore deposit formation (e.g. Yiğit, 2012). Therefore, the study of the magmatic sequences in the Halilağa District provides an excellent opportunity to study Eocene and Oligocene magmatism responsible for porphyry mineralization in NW Turkey

Sr/Y, La/Yb and Eu_N/Eu^* ratios are employed in the exploration of porphyry copper deposits to determine the presence of characteristic lithogeochemical signatures indicating: hornblende fractionation as result of hydrous magma; suppression of plagioclase crystallization; and adakitic affinities (Richards et al., 2012). The term "adakites" identifies a specific type of magmatic rocks which have: intermediate to high silica concentrations ($\geq$ 56% wt% SiO_2), Sr/Y $\geq$ 20, La/Yb $\geq$ 20, Cr $\geq$ 20 ppm, high Mg number, and Ni $\geq$ 20 ppm (Richards and Kerry, 2007). The initial use of the term implied a specific genesis from melting of the subducted slab (Kay, 1978; Defant and Drummond, 1990). However, it has been demonstrated that rocks with adakite-like composition can originate by multiple process and do not necessarily reflect the initial source process (Richards and Kerry, 2007;

Castillo, 2012). However, because an adakite is more oxidized and has higher water contents; many porphyry deposits present adakite-like signatures reflected in high Sr/Y and La/Yb ratios. Hence without implying genesis those ratios still have value to indicate potentially fertile intrusions that may host economic deposits (Thieblemont et al., 1997; Oyarzún et al., 2001).

Lithogeochemistry of the plutonic and volcanic rocks present in the Halilağa District is examined herein in order to characterize the magmatism and to evaluate porphyry-like features.

3.1. Dataset and Methodology

The geochemical database utilized in this study consists of data from the (a) samples collected and processed for this thesis (50 samples) and (b) Teck whole-rock lithogeochemical dataset (26 samples) Samples collected and reported in this thesis (a) were prepared and analyzed as follows:

- Following crushing to <6mm samples were pulverized to 95% <75microns in a ceramic bowl pulverizer. The ceramic bowl is "washed" in between samples by pulverizing silica sand followed by washing with acetone to ensure no sample carry over.
- Major element composition was determined by the Bureau Veritas Lithogeochemical package (LF700). Sample pulp was digested by a lithium metaborate fusion and cast into glass disks. Glass disks were analysed by X-ray fluorescence (XRF).
- Trace elements were determined by the Bureau Veritas method LF100. Samples were digested using a lithium metaborate fusion, with aqua-regia digestion of the fusion bead. The solution was analyzed by inductively coupled plasma - mass spectrometry (ICP-MS).
- Total carbon and sulfur were determined by Combustion Furnace - non-dispersive infrared analysis (Bureau Veritas Code TC00).
- Base and precious metals were determined by hot modified aqua-regia digestion (1:1:1 Nitric acid:hydrochloric acid:water) coupled with ICP-MS analysis. (Bureau Veritas Labs Code AQ200).
- Gold was additionally determined by 30g fire assay fusion with previous digestion in aqua regia coupled with ICP-MS (Code FA130).

Samples reported in this thesis from Teck whole-rock lithogeochemical dataset (b) were prepared and analyzed as follows:

- Crushing and sample preparation was done in Ankara by ACMELabs (now Bureau Veritas). The samples were crushed to 2mm size in an oscillating steel jaw crusher.

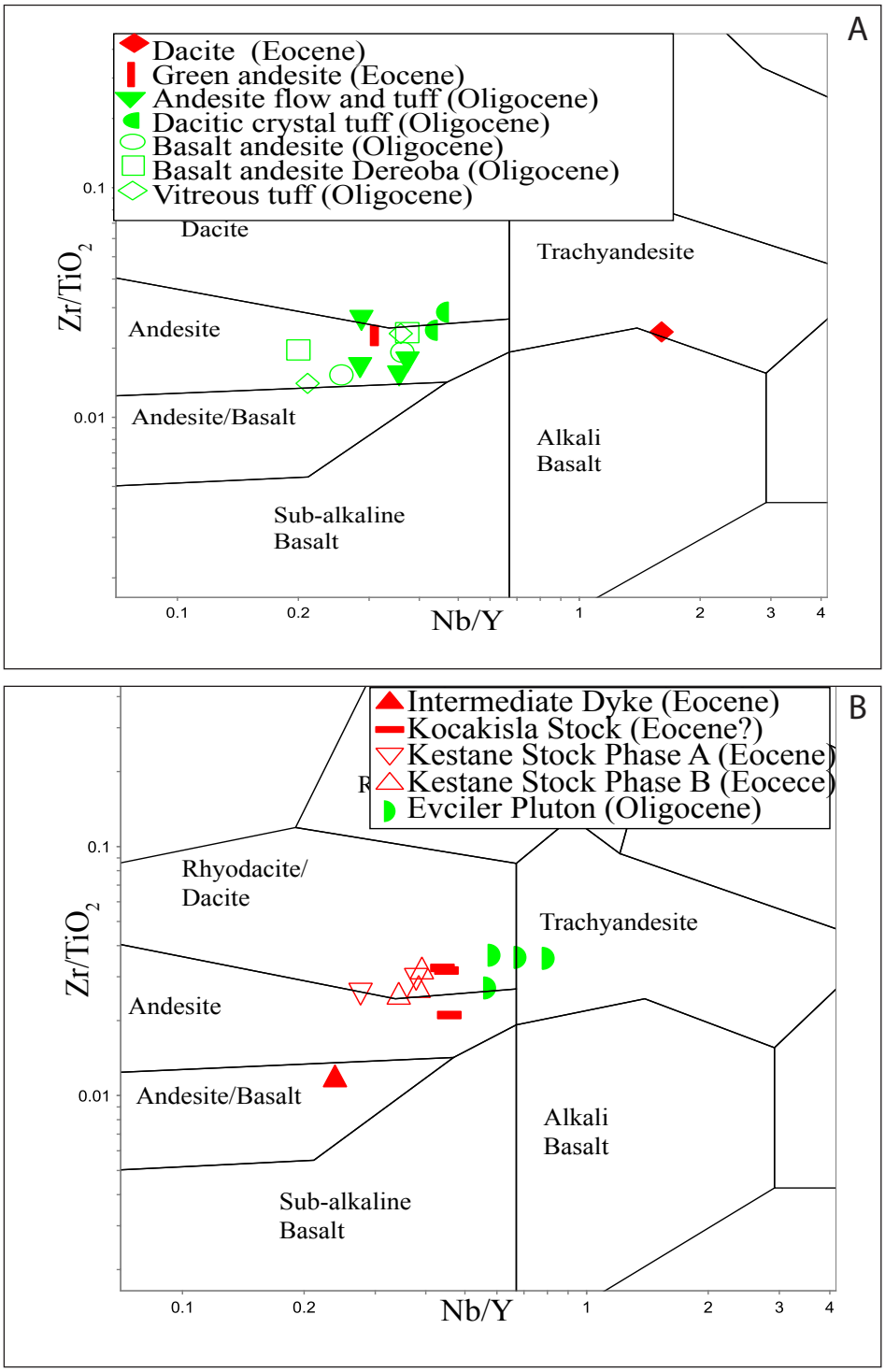

Figure 3.1 Trace elements classification diagrams a) Winchester and Floyd (1977) volcanic rock classification b) Winchester and Floyd (1977) for intrusive rocks

Approximately a 1000g split is pulverized in a chrome steel ring mill to 85% passing 200 mesh.

- Major element composition was determined by the classical Bureau Veritas Lithogeochemical package (former 4A, current LF302).). Sample pulp was digested by a lithium borate fusion and a dilute acid. The solution was analyzed by inductively coupled plasma – emission spectroscopy (ICP-ES).
- Trace elements were determined by Bureau Veritas method LF100. Samples are digested using a lithium borate fusion, with aqua-regia digestion of the fusion bead. The solution was analyzed by inductively coupled plasma - mass spectrometry (ICP-MS).
- Total carbon and sulfur were determined by Combustion Furnace - non-dispersive infrared analysis (TC003).
- Base and precious metals were determined by hot modified aqua-regia digestion (1:1:1 Nitric acid:hydrochloric acid:water) coupled with ICP-MS analysis. (AQ200).

Details of the elements analyzed, detection limits and corresponding methods of Bureau Veritas Laboratories are provided in Appendix C.1. The results of the analyses executed by Teck and the analysis carried out in this study are detailed in Appendix C.2. Test of precision and accuracy for the dataset is explained in Appendix C and specifically in Appendix C.4 to C.6.

In order to characterize the original geochemical signatures of the units described in the previous sub-section, major elements oxides were recalculated to eliminate volatiles using the formula:

$$\text{Concentration}_{\text{volatile-free}} = \text{Concentration}_{\text{reported}} * \text{Total (\%)} / [\text{Total (\%)} - \text{LOI (\%)}].$$

The different sample preparation between both datasets might result in a source of error. In preparation (a) pulverization was done in a ceramic bowl and in (b) a chrome steel ring mill is used to pulverized. Chrome steel mill introduces Cr and Fe and moderate amount of Mn and traces of Dy (Rollinson, 1993). In addition, due to the hydrothermal alteration present in the majority of the samples, the dataset was reduced to the least altered samples on the basis of <3.5 % loss on ignition (LOI) and < 0.35 % sulfur. This screening left 27 samples of which 13 are intrusive (6 Eocene and 7 Oligocene) and 14 are volcanic (2 Eocene and 12 Oligocene). From those 27 samples, 23 (85%) are samples collected in this study and pulverizer in a ceramic bowl, while only 4 samples (15%) were pulverized in a chrome steel ring. Therefore the majority of the samples have the same sample preparation.

3.2. Trace Element Classification

The main limitation of the rock classification based on major elements, presented in the previous section, is the high mobility of SiO_2, Na_2O, and K_2O during hydrothermal alteration. High Field Strength Elements such as Zr, Ti, Nb, and Y are generally considered to be immobile during hydrothermal alteration and weathering (Pearce, 1996; Winchester and Floyd, 1977).

In the Zr/Ti versus Nb/Y classification diagram (Winchester and Floyd (1977) for volcanic rocks (Figure 3.1a) the majority of the samples are classified as andesite; two samples are rhyodacite to dacite; and one sample (Eocene) lies in the trachyandesite field.

In the case of intrusive rocks (Figure 3.1b), most of the samples fall towards the lower-right border of the rhyodacite - dacite field; two samples from the Evçiler pluton fall in the trachyandesite field; one sample from the Kocakışla stock is classified as an andesite; and samples previously identified as an intermediate dyke fall in the andesite or basalt field.

The Winchester and Floyd (1977) classification diagrams indicate that intrusive rocks are compositionally more evolved than the volcanic suite. The Evçiler pluton and the Eocene dacite presents higher Nb/Y ratio than the rest of the lithological units.

3.3. Harker Variation Diagrams

Bivariate Harker diagrams (Harker, 1909) were applied to examine specific variations in the full igneous suite (both volcanic and plutonic rocks). In general, the dataset exhibits continuous trends: increasing K_2O; and decreasing TiO_2, Al_2O_3, MgO, Fe_2O_3, MnO, and CaO with increasing SiO_2 contents (Figure 3.2). The trend for Na_2O is more complex and increases to a peak at ~65.5 % SiO_2 after which it starts to decrease.

Exceptions to these general trends are observed in the Kestane stock, which does not display continuous trends. Despite the similar SiO_2 compositions of the two phases of the Kestane stock, Al_2O_3, MgO, CaO, K_2O, and Na_2O are variable in each sample of both units, suggesting effects of hydrothermal alteration. In addition, the least altered sample from the Eocene dacite exhibits high SiO_2 and TiO_2 contents relative to the suite and low Na_2O; this indicates SiO_2, addition to the system and K_2O metasomatism resulting in Na_2O depletion.

3.4. Rare Earth Elements (REE) and Multi-Element Classification

Multi-element and REE spider diagrams are shown in Figures 3.3 and 3.4 for the Eocene and

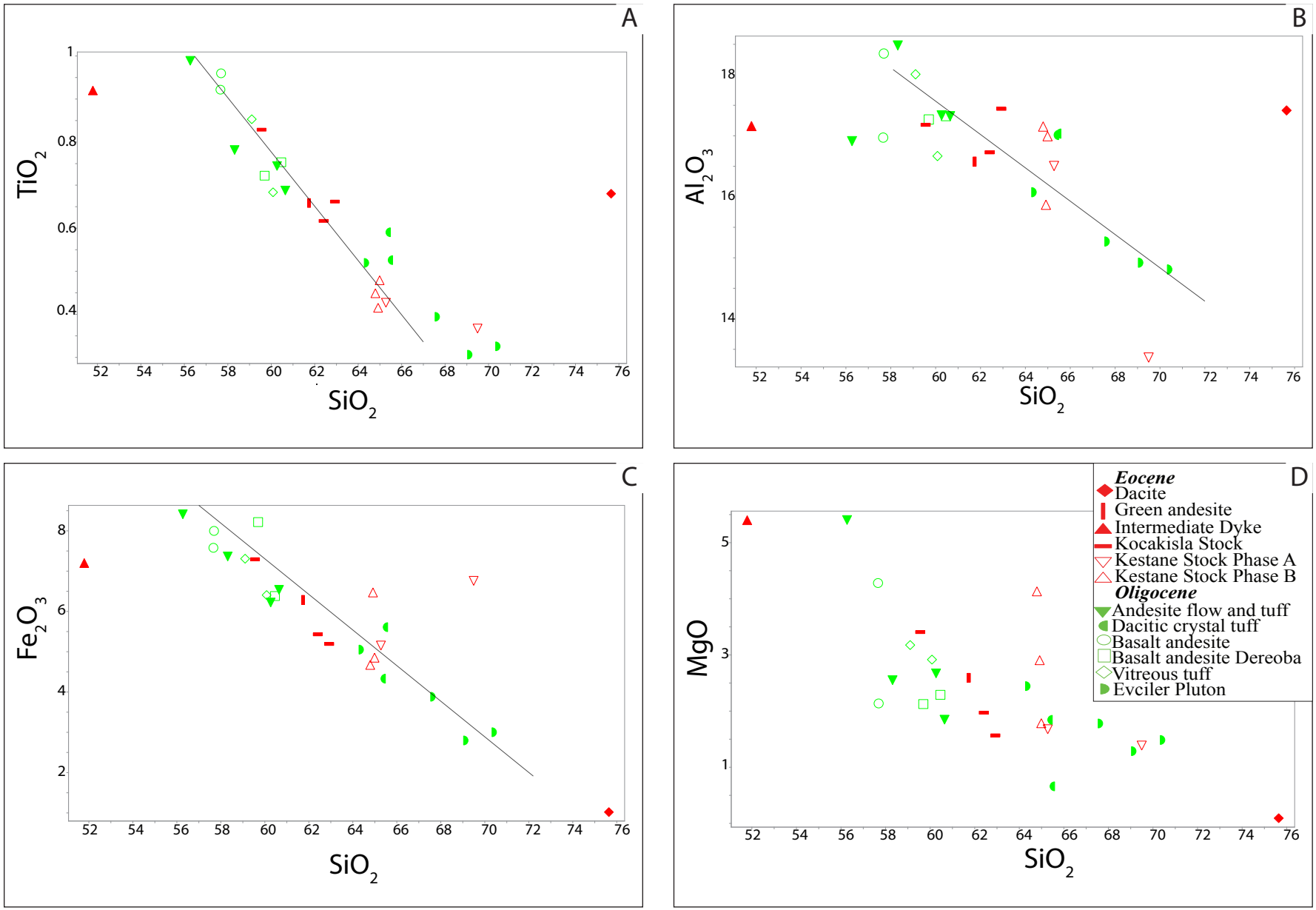

Figure 3.2 Harker diagrams for major elements. Considering least altered dataset (LOI <3.5 % and S<0.35%) of 27 samples.

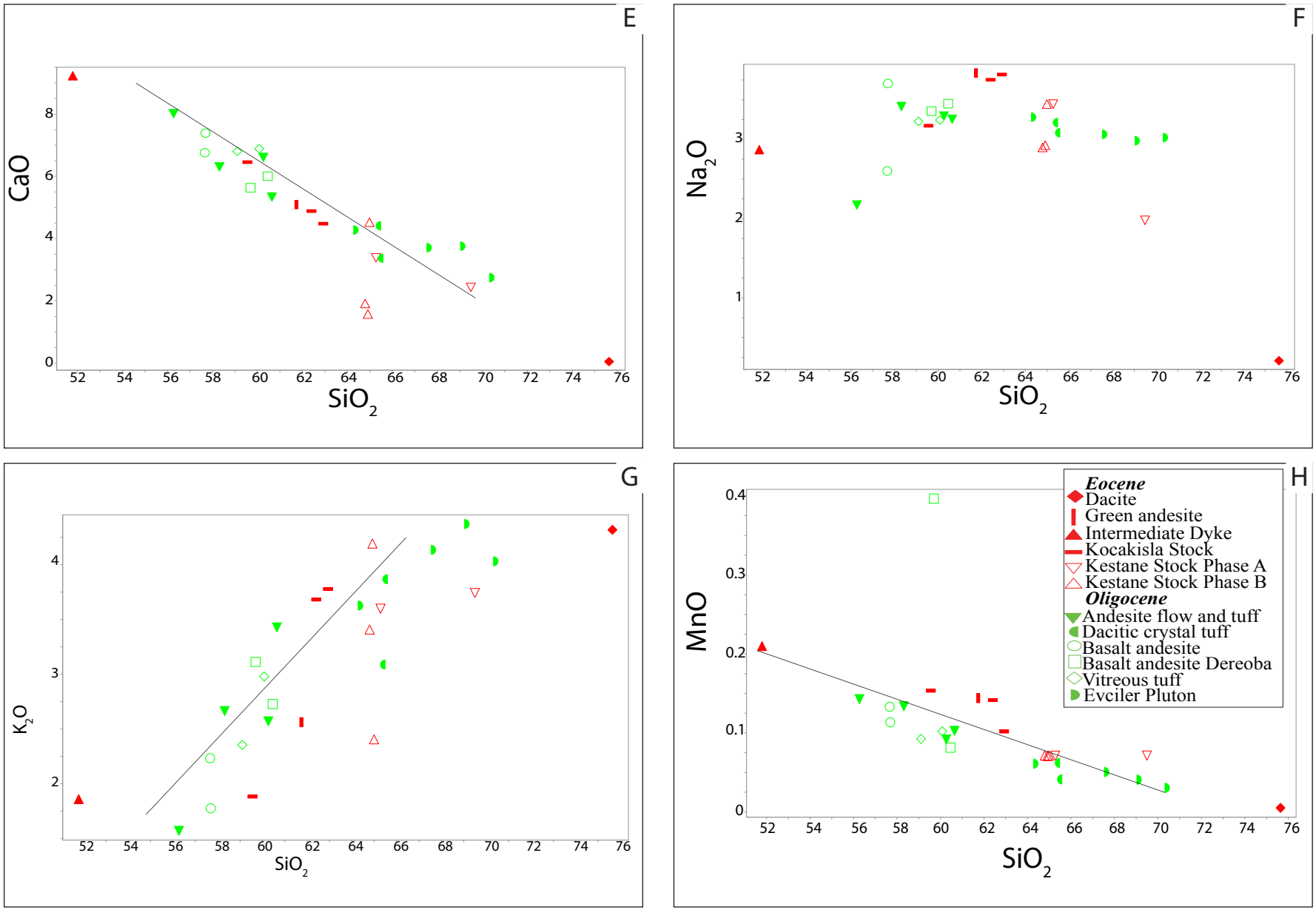

Figure 3.2 (cont)

Oligocene suites respectively. Data are normalized to primitive mantle (McDonough et al. 1992) and chondrite (Boynton 1984). In general, major negative anomalies for Ba, Ti, Nb, Ta and a slightly positive anomaly in Zr and Hf are observed in all samples. Both groups exhibit enrichment in large ion lithophile elements (LILE: Cs, Rb, Ba, K, Sr) and light rare earth elements (LREE). Eocene samples display anomalies in Sr; negative in dacite and slightly positive in the Kestane Stock and intermediate dyke. The enriched values for the LILE and LREE, and also the negative anomalies of Nb, Ti and Ta are consistent with a magma source in a subduction zone setting (McCulloch and Gamble, 1991).

In the REE diagram normalized to chondrite, LREE are enriched in both suites (average $[La/Sm]_N$ 4.27 for Eocene rocks and 4.48 for Oligocene rocks). The HREE present slightly concave-upward to planar trends. The positive concavity is best observed in the Oligocene dataset. The average MREE/HREE determined as $[Dy/Yb]_N$ is 1.06 and 1.12 for the Eocene and Oligocene suites respectively. In both magmatic suites Dy/Yb ratio decreases with the increase of SiO_2 (Figure 3.5a).

Europium anomalies are quantified using $Eu_N/Eu^* = Eu_N/\sqrt{[(Sm_N)(Gd_N)]}$ (Taylor and McLennan, 1985). Most of the samples display slightly negative Eu/Eu* anomalies, except for two Eocene samples (intermediate dyke and dacite) where the ratio is ~1. The Eu/Eu* ratio for the remainder of the samples ranges from 0.83 to 0.91 for the Kestane stock, 0.72 to 0.82 for the Kocakışla stock, and 0.85 to 0.95 for the Evçiler pluton. The Eu/Eu* ratio for the Oligocene volcanic sequence ranges from 0.67 to 0.87 (Figure 3.5). These minor to insignificant Eu_N/Eu^* ratios indicate that plagioclase fractionation and removal was not particularly important in these rocks, but also could represent a highly oxidized melt (Rollinson, 1993).

Despite the efforts to avoid altered samples, it seems that hydrothermal alteration affects the Eocene dacite trace elements. In addition to the higher SiO_2 (>75%) compared with the rest of the dataset, the dacite presents extreme concave-upward REE patterns and Sr negative anomaly, suggesting fractionation of amphibole and plagioclase respectively.

3.5. Tectonic Discrimination

Tectonic affinity diagrams were applied to distinguish the tectono-magmatic signatures of the various lithological units in the study area based on trace elements. Given the intermediate to felsic composition of the dataset; optimal trace elements to discriminate tectono-magmatic environments are: Y, Yb, Rb, Ba, K, Nb, Ta, Ce and Sm (Rollinson, 1993).

The trivariate diagram Hf: Rb/30: 3Ta (Figure 3.6a) distinguishes rocks from volcanic arcs and syn- or post-collisional granites (Harris et al., 1986). Tantalium, a HFSE, typically has low

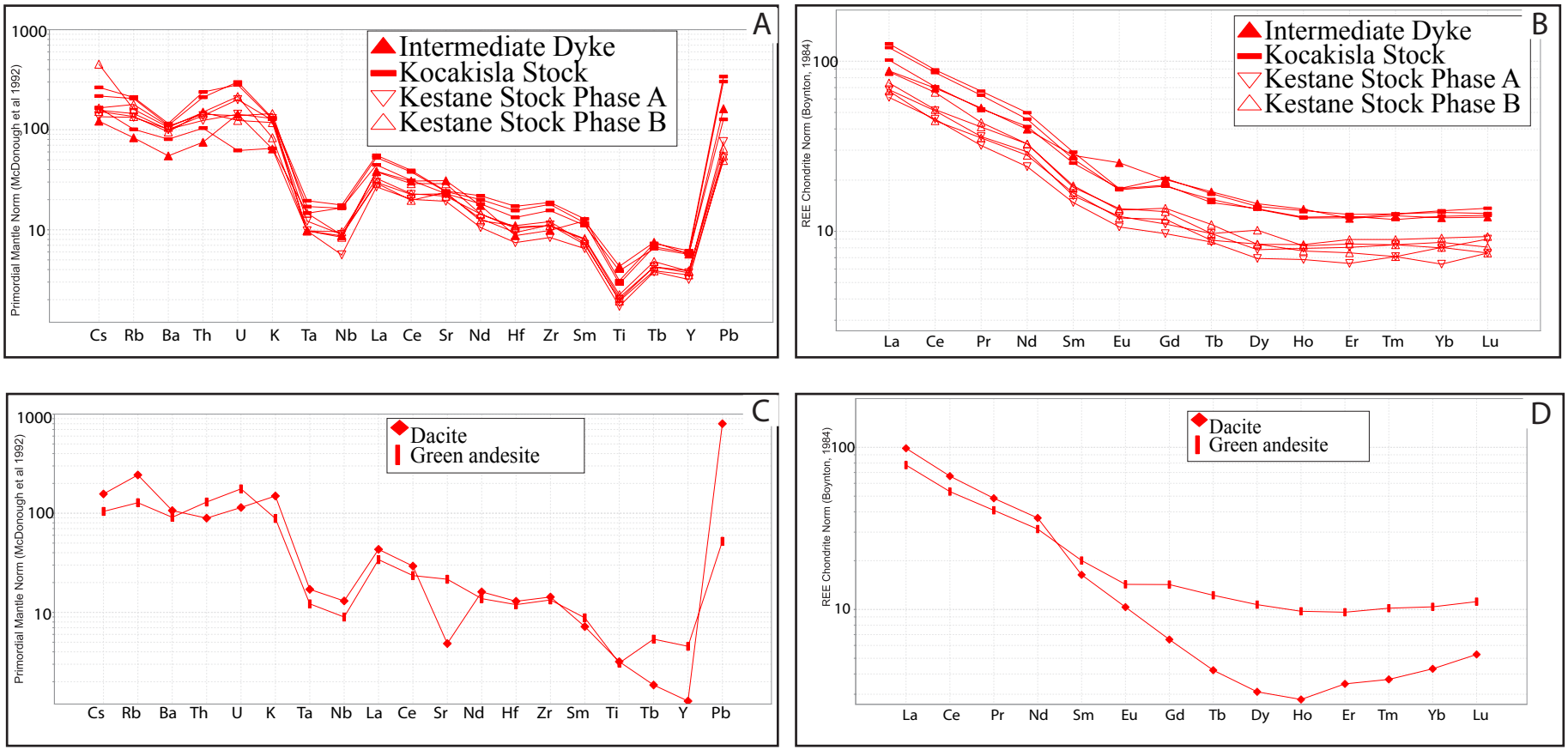

Figure 3.3 Eocene rock diagrams. a) Multi-element digram for intrusive rocks; b)REE digram for intrusive rocks c) Multi-element digram for volcanic rocks; d) REE digram for volcanic rocks; Chondrite normalization by Boynton (1984) in REE diagrams and Primordial Mantle by McDonough et al. (1992) in multi-element.

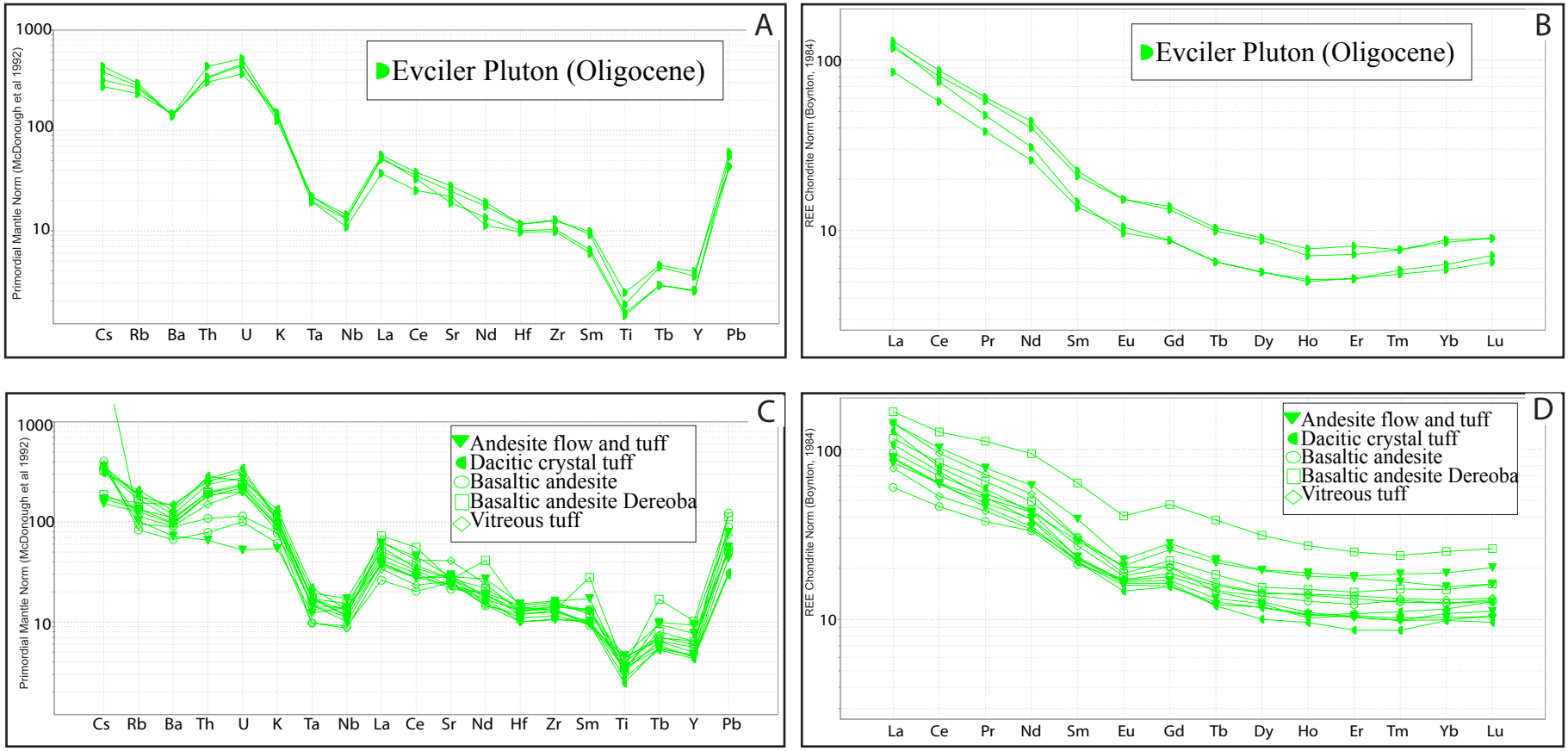

Figure 3.4 Oligocene rock diagrams. a) Multi-element digram for intrusive rocks; b) REE digram for intrusive rocks; c) Multi-element digram for volcanic rocks; d) REE diagram for volcanic rocks. Chondrite normalization by Boynton (1984) in REE diagrams and Primordial Mantle by McDonough et al. (1992) in multi-element.

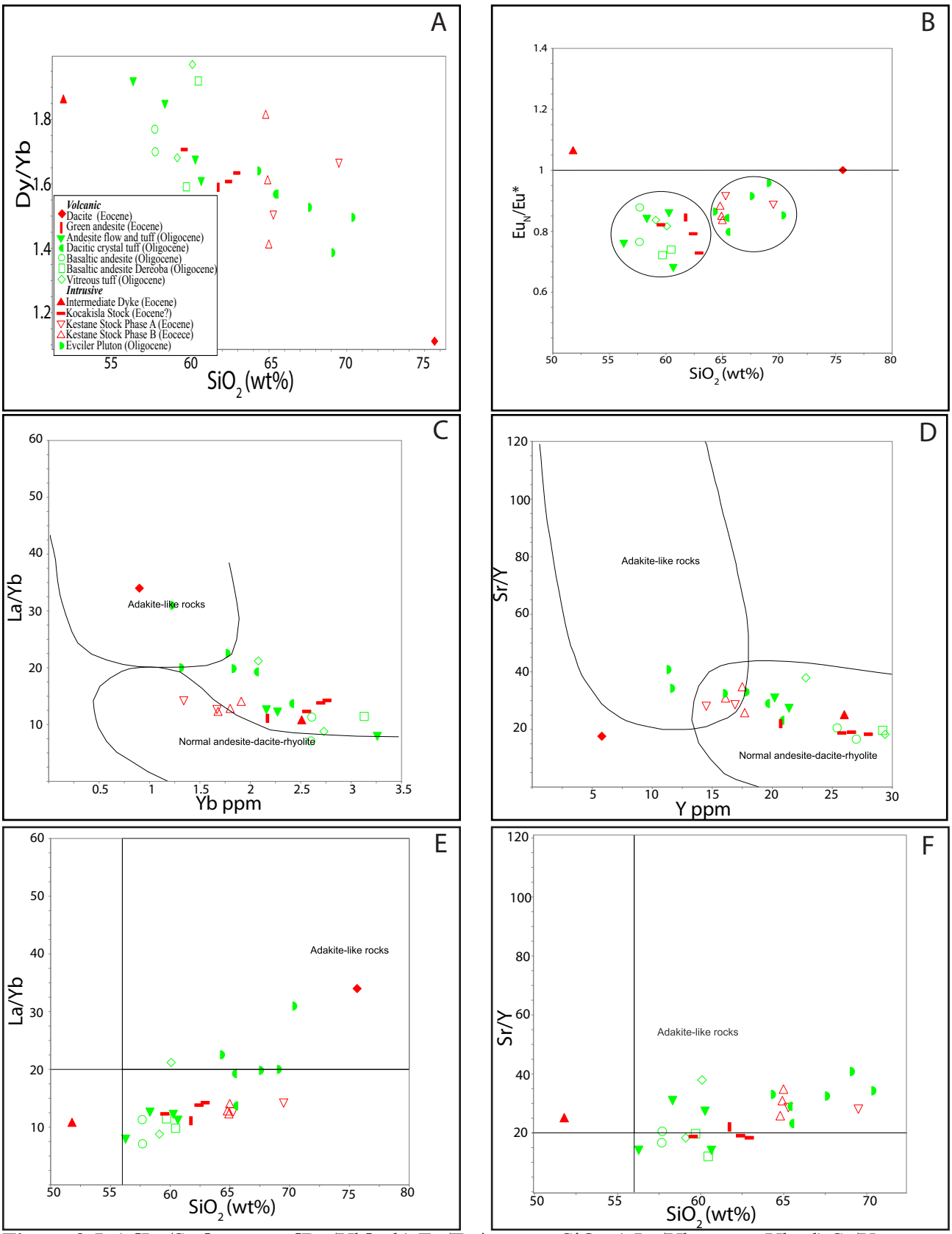

Figure 3.5 a) $[La/Sm]_N$ versus $[Dy/Yb]_N$ b) Eu/Eu* versus SiO_2 c) La/Yb versus Yb. d) Sr/Y versus Y. e) La/Yb versus SiO_2. f): Sr/Y versus SiO_2. Normalization values from Sun and McDonough (1989), fields for adakitic-like rocks from Richards and Kerrich (2007) and Richards et al. (2012).

concentrations in subduction- related igneous rocks; Hafnium being highly incompatible is indicator of an enriched source; Rubidium is a low field strength element (LFSE or LILE), used in tectonic classifications of granitic rocks. In this diagram all samples have a volcanic arc affinity. Similarly, in the bivariate Ta versus Yb (Pearce et al., 1984; Figure 3.6b) the samples exhibit volcanic arc signatures (low Ta and Yb).

3.6. Fertile Porphyry Signatures

The magmatic suites at Halilağa exhibits La/Yb ratios from 7.5 to 35 and Sr/Y ratios range from 15 to 44. La/Yb ratios in the samples from this study are relatively low compared to adakite-like rocks even for the Kestane stock intrusions. Samples from the Evçiler pluton and the Eocene dacite present higher La/Yb than the rest of the units (Figure 3.5c-d). Contrary, in the Sr/Y diagram versus SiO_2 and Y, samples from the Kestane stock and the Evçiler pluton overlaps the field of adakite-like.

La/Yb and Sr/Y ratios increase with the SiO_2 contents, while Yb and Y decrease with increase of SiO_2 (Figure 3.5e-f). Increases of La/Yb and Sr/Y ratios relative to SiO_2 reflect the fractionation of amphibole, titanite, or garnet (Davidson et al., 2007; Castillo, 2012; Richards et al., 2012). Furthermore, HREE concave upward patterns and decreasing Dy/Yb (MREE/HREE) with SiO_2 support fractionation of amphibole rather than garnet (Davidson et al., 2007).

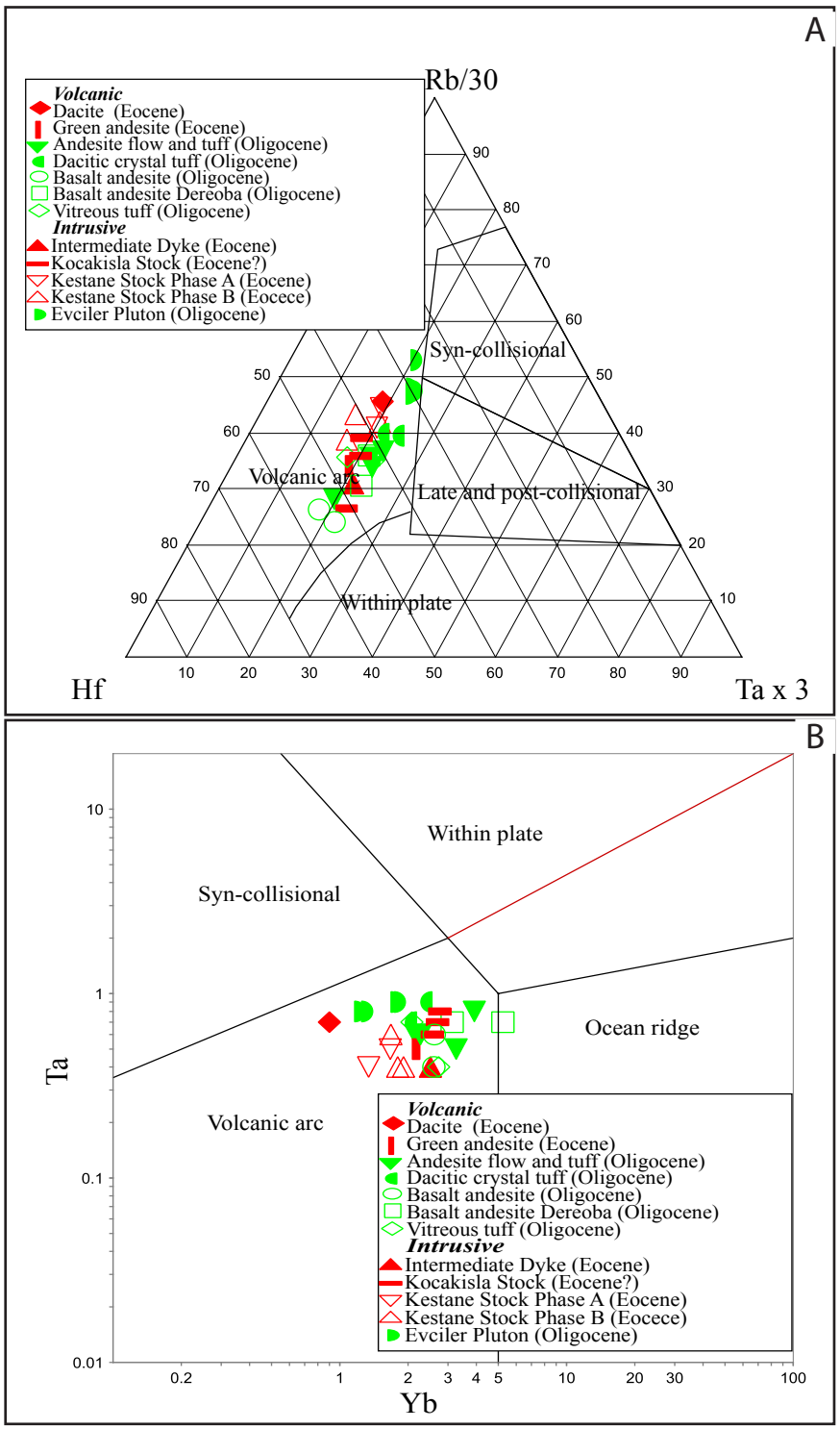

Figure 3.6. a) Tectonic classification Hf-Rb-Ta for granites, after Harris et al., (1986) b) Tectonic classification based in Ta and Yb (Pearce et al., 1984)

Chapter 4: Hydrothermal Alteration and Mineralization

Hydrothermal alteration in porphyry systems provides a link to characterize the chemical and physical conditions of ore formation and the overall evolution of the hydrothermal system. Field observation of minerals present in the altered rock, their texture, and the paragenetic relationship yields to a mineral assemblage. Each mineral assemblage represents a specific fluid type or event in the evolution of the hydrothermal system and can occur in specific, well defined physical and chemical zones or overprint previous ones. Porphyry deposits are typically characterized by: potassic (K-silicate), calc-sodic, propylitic (epidote + chlorite + calcite), chlorite ± sericite, phyllic (sericite ± quartz), and argillic (clays and white micas) alteration assemblages (Sillitoe, 2010) developed at different depths and distance of the hydrothermal center.

At Halilağa, the earliest stage of alteration is biotite + magnetite ± K-feldspar, overprinted by pervasive sericite ± quartz alteration closer to the present-day surface, while at depth the phenocrysts have been selectively replaced by sericite and chlorite. Porphyry Cu-Au mineralization at Halilağa is commonly associated with biotite + magnetite ± K-feldspar alteration with associated intense quartz veining. Chlorite + epidote +calcite and skarn assemblages occur on the margins of the deposit. Clays partially overprint earlier alteration assemblages and occurs in fault zones. Additionally, epithermal style alteration assemblages were developed in two areas: Kunk and Pirentepe. Epithermal alteration at Kunk has two zones: an advanced argillic zone dominated by pyrophyllite and an argillic zone dominated by white mica and clays. In Pirentepe, the alteration is typically pervasive silica in volcaniclastic rocks and pervasive to selective clay and white mica.

Four paragenetic stages of the hypogene fluid evolution are defined based on lithological description; vein cross-cutting relationships and alteration mineral assemblages observed in drill core. The hypogene stages are named Early, Main, Transitional, and Late. In addition to the hypogene events, a supergene event occurred in Kestane forming a chalcocite blanket in the central segment of the Kestane stock. Six of those alteration assemblages are associated with the magmatic-hydrothermal fluids associated with the porphyry intrusion.

In addition to the U-Pb geochronology for magmatic rocks presented in Chapter 2, Re-Os molybdenite dating was carried out to confirm the Eocene mineralization age at the Halilağa porphyry Cu-Au. The epithermal alteration at Kunk is ambiguous in terms of genetic association with porphyry style alteration; as there are no age constraints and spatial relations are inconclusive. Radiometric age dates indicate that host rock are similar to intrusions at Kestane (ca. 40 Ma, Table 2.2). However

alteration age relationships are complex in the Biga Peninsula. This topic will be discussed with more detail in Chapter 5. On the contrary, the epithermal alteration at Pirentepe is associated with a younger magmatic-hydrothermal event, evidenced by the Oligocene age of host-rocks (ca. 28 Ma, Table 2.2).

4.1. Methodology

Description of alteration assemblages is based on field observations backed by petrography, SWIR, and geochemistry for a sub-set of samples. More than 25 holes (approximate 10,000 m) were logged from the Pirentepe, Kunk and Kestane areas to establish alteration paragenesis and define intervals for sample collection. Core logging was executed using the Anaconda method for core logging (Einaudi, 1997); an example of a core-logging sheet is shown in Appendix A. The intensity of the alteration is expressed in terms of weak (5%), moderate (5-30%), and intense (>30%), based on percentages per volume of rock. To assist mineral identification, amaranth red and Na-cobaltinitrite were used to stain plagioclase red and K-feldspar and muscovite in yellow, respectively.

In the alteration assemblages subsection the alteration geochemistry data and SWIR analysis are used to complement field descriptions. Lithogeochemical description is based on K/Al and (2Ca+Na+K)/Al molar ratios to estimate K, Ca, and Na metasomatism and other Al-rich alterations. SWIR was employed to identify fine-grained minerals and also to establish specific spectral characteristics that differ among alteration types in all the altered lithologies.

4.1.1. Geochemistry dataset and analysis

The geochemical database utilized for the alteration consists of samples from the Teck whole-rock dataset from logged drill core and also samples collected in this study, resulting in a total of 130 samples. Preparation and analysis of samples collected in this study is described in Chapter 3. Samples collected previously by Teck and used in this thesis were prepared and analyzed as indicated in Chapter 2. Geochemistry diagrams of altered samples in this chapter consider the lithology of the porphyry stock of Teck dataset, so there are not issues relative to sample preparation (See Chapter 3).

Details of the elements analyzed, their detection limits and corresponding methods of Bureau Veritas are provided in Appendix C. Due to the chemical variations between the lithologies, and the intense alteration of the volcano-sedimentary wall rock, the alteration geochemistry dataset considers only the quartz monzonite porphyry stock (phases A, B) without considering samples in the volcano-sedimentary wall rock or volcanic units. The hydrothermal alteration in the dataset includes: fresh, biotite + magnetite ± K-feldspar, chlorite + epidote + calcite, chlorite ± sericite, and sericite ± quartz.

To avoid the effect of volatiles, major elements oxides were recalculated similarly to the igneous geochemistry dataset explained in Chapter 3. The geochemical dataset was used to calculate molar ratios and mass transfer during the hydrothermal alteration.

4.1.2. Reflectance spectroscopy

Reflectance spectroscopy analyses are used to recognize minerals, particularly fine-grained white micas and clays. The method is based on the spectral response of minerals to photon stimulation. The response is dependent on the wavelength and is displayed in terms of reflectance or the proportion of light reflected by the mineral. The wavelength is divided in three bands: visible and near infrared or VNIR (0.72-1.3 μm), short-wave infrared or SWIR (1.3-2.5 μm), and thermal infrared or TIR (6.0-14.5 μm). In the SWIR this range there are a number of absorption features that assist to recognize white micas, clays, carbonates, and chlorites making SWIR analysis very useful to identify minerals in Halilağa.

Particularly, the position of the absorption features (peaks) in SWIR is related to variations in mineral compositions. Typical absorption features occur at: 1400 nm (OH+ H_2O), 1900 nm (H_2O), 2200 nm (Al-OH), and 2300 nm (Fe-Mg-OH). Absorption features have quantitative parameters, calculated with The Spectral Geologist software (TSG), such as depth and width of the spectra.

White micas are the general term used to describe illite, muscovite, phengite, and paragonite. Compositional variations in white micas can be identified with wavelength changes in the absorption feature at 2200 nm from: paragonite, Al-rich and Na-bearing with Al-OH band near 2,190 nm; muscovite, K-rich and Al-rich, Al–OH band at around 2,200 nm; and phengite, Al-poor and Mg-rich or Fe^{2+} -rich, with Al–OH band >2,210 nm (Halley et al., 2015). Illite exhibits a deeper peak at 1900 nm due to higher water contents of illite compared with other micas or due the interlayering with montmorillonite. White micas are widely distributed in Halilağa in all types of alterations due to hydrothermal overprinting. Clays and white micas are indicators of variations in temperature and pH and are usually associated with specific hydrothermal environments (e.g. Thompson et al., 1999; Yang et al., 2005). The 2200 nm wavelength obtained with TSG is a scalar calculation to determine the wavelength at the minimum point where the spectra have an absorption feature in the neighborhood of 2200 nm. Another scalar calculation is the sericite crystallinity index (CI), calculated as the ratio between the depth of the Al–OH peak (2200 nm) and the depth of the water peak (1900 nm).

Reflectance spectroscopy analysis was applied on 82 samples (from drill core and surface) using an ASD Terraspec4® at UBC. The quantitative parameters for major spectral absorption features

such as: wavelength, width, and length were obtained with "The Spectral Geologist" software (TSG). Mineral identification obtained by TSG was corrected based on spectra observation. In addition, more than 12,000 (3,350) samples of SWIR data from 43 (25) drill holes (measured during drilling programs by Teck) were reinterpreted using TSG to observe variations in the 3D-distribution of alteration minerals in the Kestane and Kunk areas.

4.2. Alteration Assemblages

The distribution of the hydrothermal alteration in the Kestane and Kunk areas is shown in two cross-sections: A-A' and B-B' in Figure 4.1 and 4.2. The location of those cross-sections is shown in Figure 2.1. A summary of the field observations, petrography, SWIR, and geochronology for each alteration type is shown in Table 4.1.

4.2.1. Early biotite

This alteration assemblage consists of secondary biotite alteration that occurs in two types of locations and lithologies:

- location a: in the Kestane quartz monzonite stock at depths greater than 200 m
- location b: in volcano-sedimentary wall rocks resembling a fine-grained biotite hornfels texture (Figure 4.3a-b).

In the Kestane quartz monzonite stock (location a), this alteration is dominated by selective biotite after hornblende and primary biotite while in the wall rock (location b) occurs as a pervasive to "patchy" alteration with occasional silicification. In the volcano-sedimentary wall rock petrography indicates 25% of fine-grained biotite and 7% silica replacement in groundmass (Appendix B3, HD-13A 311) and in the Kestane stock biotite alteration corresponds to 10-15% of the rock. In the porphyry stock alteration (location a), only in few samples contained phlogopite (Mg- rich biotite) identified with SWIR. In contrast, in volcano-sedimentary wall rocks (location b), phlogopite is more common.

The variations among lithologies in the intensity and style of the alteration suggest lithological controls on the alteration intensity.

4.2.2. Biotite+ magnetite ± K-feldspar

Consists of secondary biotite after hornblende, accompanied with magnetite, chalcopyrite, and minor K-feldspar in groundmass and phenocrysts (Figure 4.3). The alteration is dominantly pervasive. Biotite+ magnetite ± K-feldspar alteration affects the Kestane quartz monzonite stock and is distributed

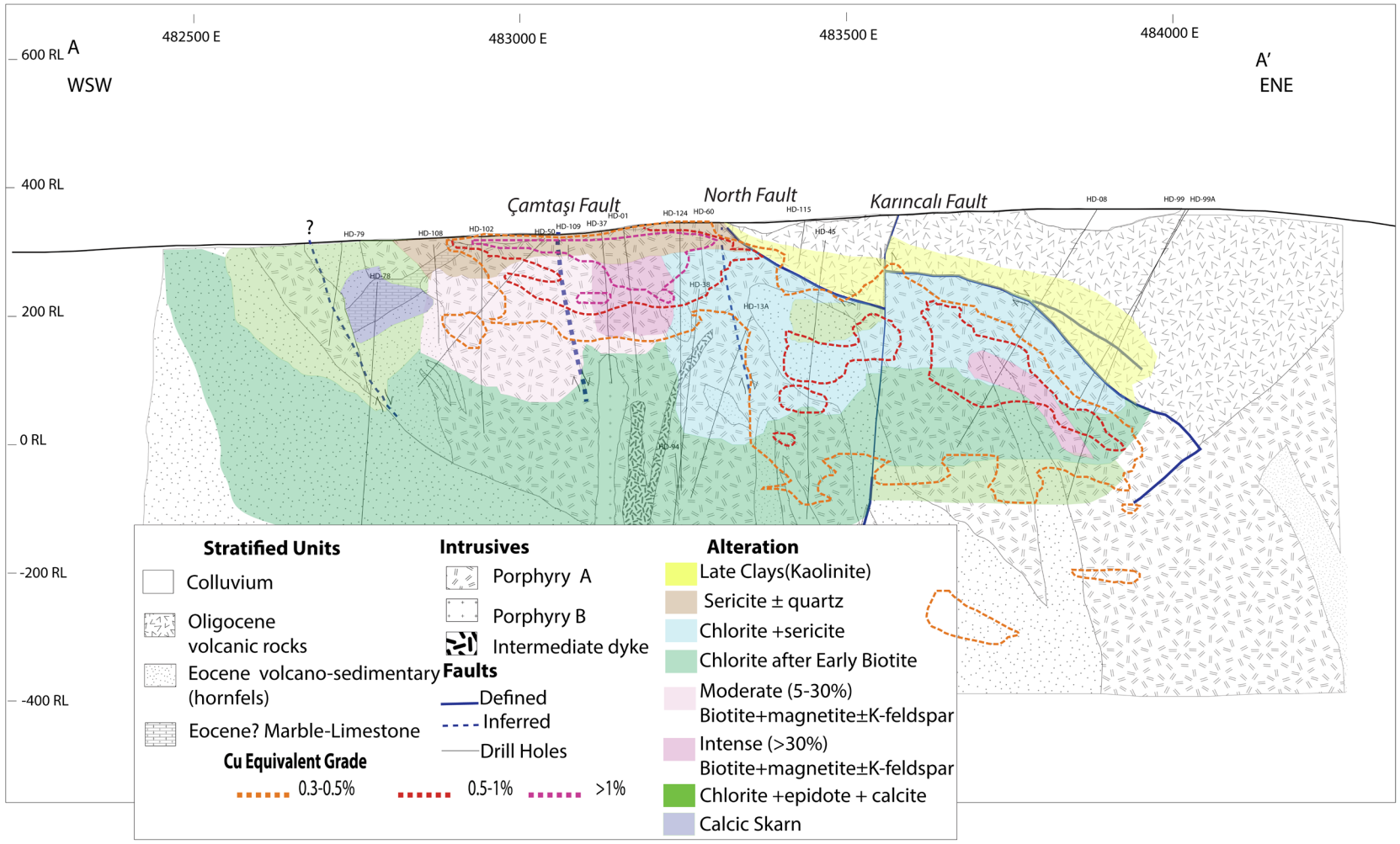

Figure 4.1 Alteration cross section A-A' , oriented WSW-ENE, including lithologies (patterns) and Cu grades (dashed lines) cross sections location in Figure 2.1

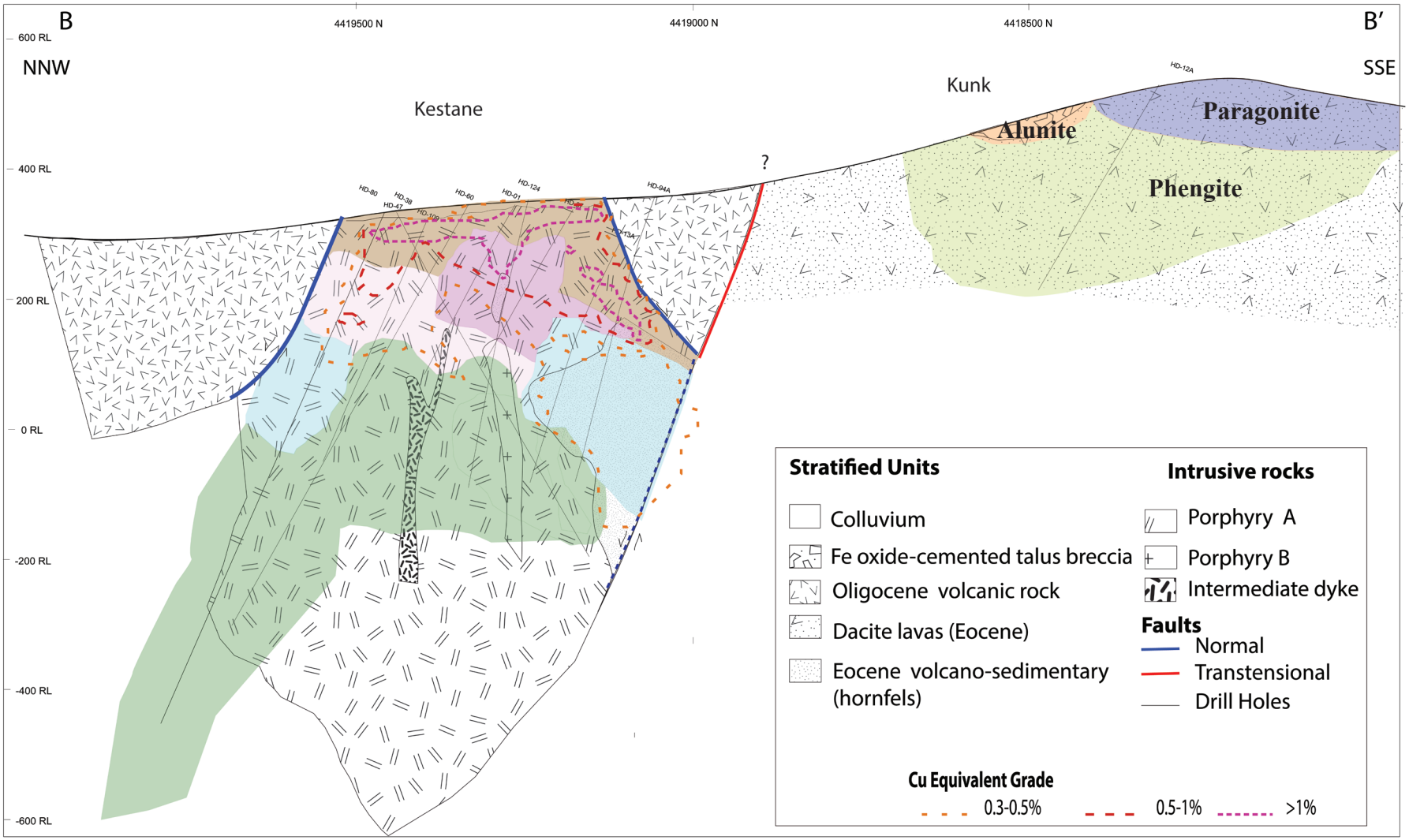

Figure 4.2 Alteration cross section B-B', oriented NNW-SSE, inlcuding lithologies (patterns) and Cu grades (dashed lines) cross sections location is shown in Figure 2.1. Legend of alteration in Kestane in Figure 4.1.

Table 4.1 Summary of alteration assemblages at the Halilağa Deposit.

Alteration	Distribution	Minerals	Style	Textures/petrography	Geochemistry	SWIR	Timing
Early Biotite	Kestane stock and volcano-sedimenraty wall rocks, at depth or distal to mineralized core	biotite	Selective/ pervasive replacement in host rocks	Biotite after hornblende	-	In biotite hornfels phologopite.	syn- porphyry mineralization (39 Ma)
Biotite+magnetite ±K-feldspar	Kestane stock. More intense in the first 200 m.	biotite, magnetite, K-feldspar, rutile.	pervasive, selective and in veins	biotite after hornblende and K-feldspar after plagioclase. In intense altered samples (e.g. HD_80 99) an incipient brecciation is observed with bt+mgt cement	higher K/Al ratios (0.4-0.55) migrating to muscovite node.	-	syn- porphyry mineralization (39 Ma)
Chlorite+epidote+calcite	distal	chlorite, epidote, calcite	pervasive, selective and in veins	carbonates reeplace phenocrysts also are distributed in veins. Epidote and chlorite after mafics	low K/Al ratios (0.25-0.10) and (2Ca+Na+K)/Al higher than 1	chlorite (interlayered with illite and peaks at 1414 nm, 2250 nm, and 2345 nm) and epidote (peaks at 1407 nm and 2257 nm)	syn- porphyry mineralization (39 Ma)
Calcic Skarn	distal. In limestones in West Kestane	calcite, garnet, epidote	pervasive	original texture obliterated, intense garnet alteration	Albite node: enrichment of Na and Ca.	smectite, epidote and dolomite, and minor actinolite. Smectite spectra indicate Mg- rich contents with Mg peaks at 2320 nm	syn- intrusion (39 Ma)
Chlorite ± sericite	overprinting the Kestane stock. Medial zones	sericite, chlorite	Selective	chlorite brown to blue interference colours (indicate Mg -rich composition)	intermediate K/Al (0.3-0.15) and (2Ca+Na+K)/Al (0.67-0.83).	muscovite, chlorite, phengite, and illite. Al-OH feature ranges from 2200-2010 indicating K, Mg, Al enriched micas. Chlorite spectra have peaks in 2250 and 2350 (Appendix B2).	~39 Ma-37 Ma
Sericite ± quartz	overprinting the Kestane stock. Surface	sericite, quartz, rutile	Pervasive and vein halos.	coarse muscovite in high grade zones.	high K/Al (greater than 0.34) ratios and high (2Ca+Na+K)/Al ratios	muscovite white mica (2200-2210 nm) with sericite crystalline index of 1.3-2.5	~39 Ma-37 Ma
Clays	fault zones and surface.	montmorillonite, kaolinite, white micas	Pervasive	-	weak gechemical response for smectites (weak alteration). In Kaolinite altered samples the shifting to the Kaolinite node and advanced argillic alteration is important.	phengite, montmorillonite, kaolinite, muscovite, paragonitic illite. The spectral response for samples identified as montmorillonite show peaks at 1450 nm, 2253 nm, and 2340 nm and deep H2O feature.	26 Ma? (Ar-Ar geochronology)

Table 4.1 (cont)

Alteration	Distribution	Minerals	Style	Textures/petrography	Geochemistry	SWIR	Timing
Argillic (Kunk)	West Kunk	white mica, montmorillonite, and smectite	Selective	fine grained white mica with orange interference colour, colorless to pale green colour. Some coarser acicular crystals replacing plagioclases.	low to moderate K/Al reflecting more interlayering with illite-smectite than the advanced argillic assemblage	paragonite and phengite white micas dominant.	undetermined
Advanced Argillic (Kunk)	East Kunk	alunite, pyrophyllite, diaspore, and dickite	Selective	pyrophyllite is observed similar to any white mica replacing plagioclase phenocrysts. Alunite was not observed In thin section	low K/Al ratios indicating more affinity with Kaolinite than illite-smectite.	alunite, pyrophyllite, diaspore, and dickite with strong features at 1393 and 2168	undetermined
Argillic Pirentepe	Buyukdag/Çeldiren	kaolinite, dickite	Pervasive	fine kaolinite replacement in veins, phenocrysts and ground mass	low K/Al ratios indicating more affinity with Kaolinite than illite-smectite.	kaolinite peak 1400 nm, very deep feature at 2208. Variable depth of water. Double peak in 1780 and 1900 could indicate presence of dickite.	younger than 28 Ma (host rocks age)

in two zones. The first zone is a narrow sub-vertical intense biotite + magnetite ± K-feldspar zone near the Çamtaşı Fault (Figure 4.1) and a 45° dipping alteration zone east of the Karıncalı Fault (Figure 4.1) in the eastern zone. Both zones are coincident with grades higher than 0.5 % Cu and 0.5 ppm Au, suggesting a genetic link of biotite+ magnetite ± K-feldspar alteration with mineralization. Modal percentages observed in thin sections for alteration minerals indicate 10-15% biotite, 1-7% magnetite, 1-5% K-feldspar, 2%. pyrite, and 3% chalcopyrite. Staining in altered samples indicates dominance of K-feldspar in phenocrysts and groundmass (Appendix B3, HD-80 99 and HD-37 112), while in fresher samples (e.g. Appendix B3, HD-38 310) albitic plagioclase is dominant in phenocryst and K-feldspar dominates groundmass, suggesting that K-feldspar in phenocrysts in the biotite + magnetite ± K-feldspar alteration is secondary.

Due to pervasive alteration and overprint SWIR mineral identification was not representative of this assemblage. Whole rock geochemistry of this alteration shows intermediate K/Al ratios between 0.4-0.55 (Figure 4.4).

4.2.3. Chlorite + epidote + calcite

The chlorite + epidote + calcite alteration assemblage is distributed in three lithologies:

- Predominantly, in the volcano-sedimentary wall rock in western Kestane (Figure 4.1a-b)
- Less important, in the Kestane stock in distal segments of the mineralized core (Figure 4.4c),
- Associated to the Kocakışla stock (Figure 4.5c).

The style of alteration is phenocryst replacement (feldspars, biotite, and hornblende) and also fine (~1 mm) veinlets of calcite and epidote (Figure 4.5a). Petrographic observations indicate that anhedral phenocrysts of epidote (3-5%) are associated with pyrite grains (5%). Epidote also occurs in 1mm veins (5%), while calcite and pyrite occur in quartz veins (1-3%). Similarly to the early biotite alteration, the intensity of this alteration is controlled by the lithology. The Kestane stock exhibits weak (<5%) to moderate (5-30%) intensities; in the volcano-sedimentary wall rock this alteration is more intense (>30%) and pervasive.

SWIR analysis indicated chlorite and epidote in these samples, with peaks at 1407 nm and 2257 nm for epidote and features at 1414 nm, 2250 nm, and deep feature at 2345 nm for chlorite interlayered with illite (See Appendix B2, PB2014106). Whole-rock geochemistry of this alteration reveals low values of K/Al ratios (0.25-0.10) and (2Ca+Na+K)/Al higher than 1, reflecting the addition of Ca to

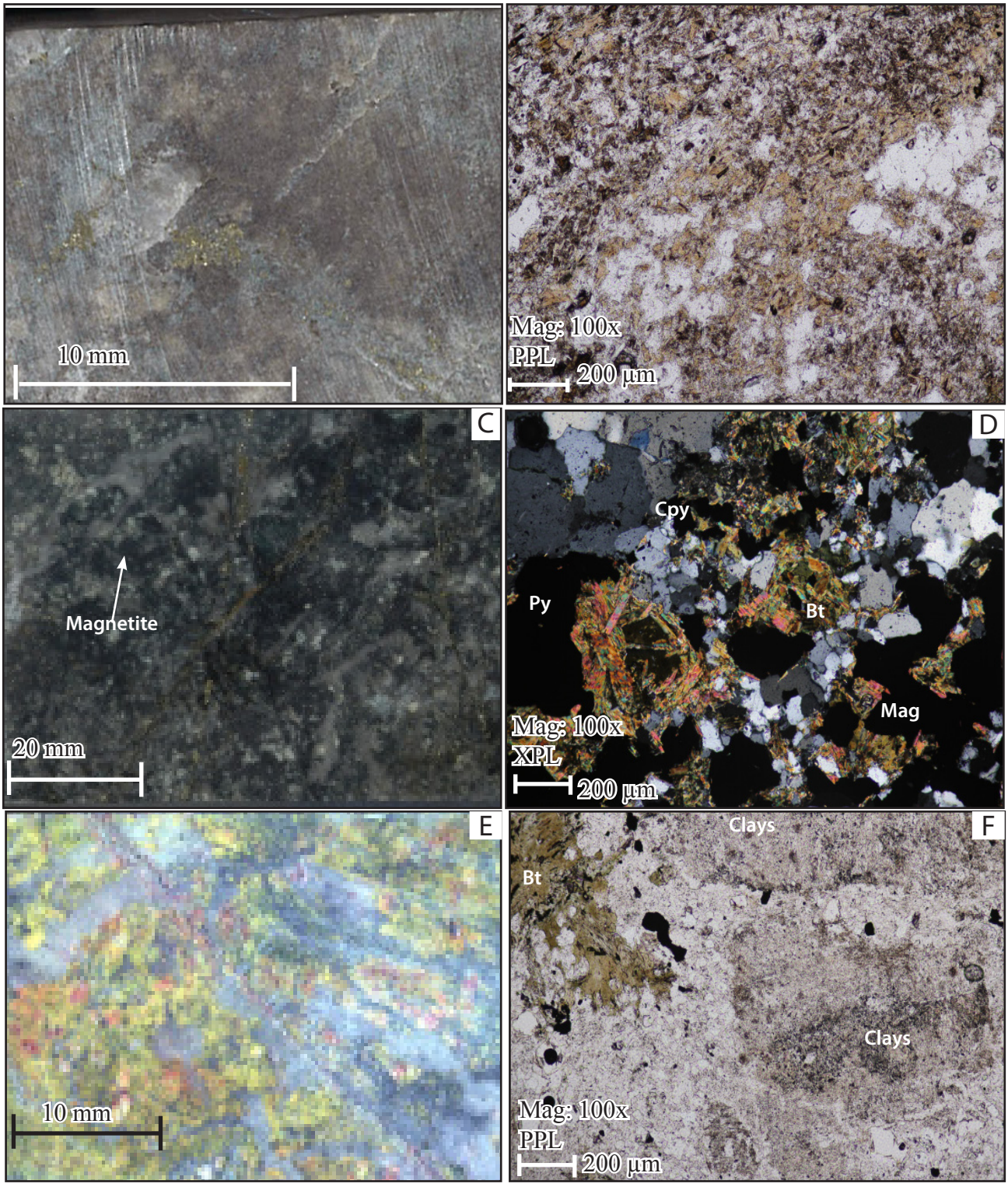

Figure 4.3 Biotite+magnetite ± k-feldspar alteration, a) HD-13A biotite hornfels hand sample b) HD-13A biotite hornfels thin section c) HD-37 112, Intense biotite+magnetite ± k-feldspar alteration; d) Same sample in thin section. Euhedral secondary biotite with high birefringence product of later chlorite replacement. It is associated with chalcopyrite and magnetite;e) HD-37 112, Stained sample, minor Na-plagioclase (red) and dominant K-bearing minerals in phenocrysts and ground mass (sericite and K-feldspar); f) HD-80 99, Altered phenocrysts; plagioclases to clays and secondary biotite in mafic site. Ground mass is formed by quartz and k-feldspar.

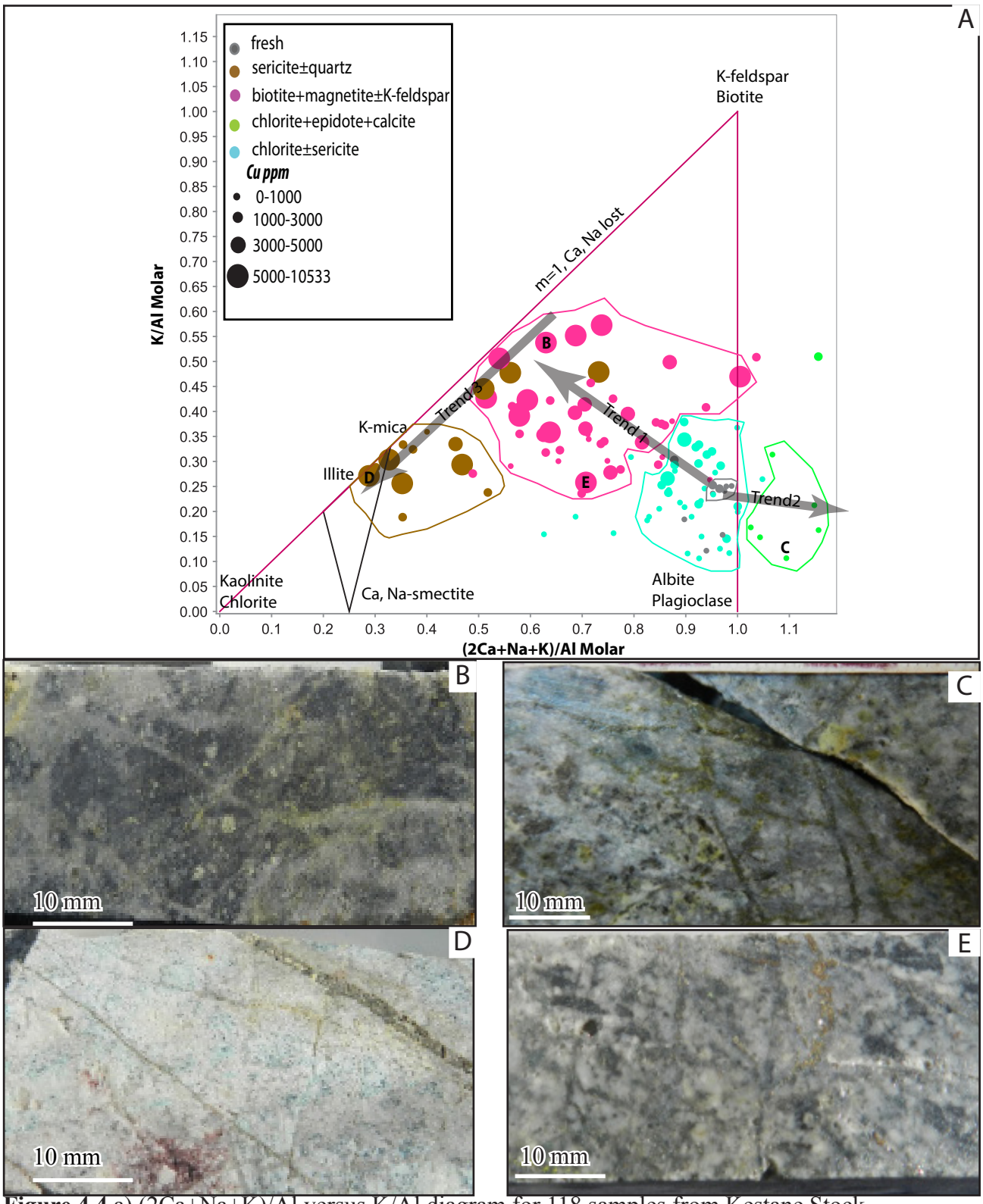

Figure 4.4 a) (2Ca+Na+K)/Al versus K/Al diagram for 118 samples from Kestane Stock classified by alteration type during drill core logging. The letters B to E indicate samples with microphotographs and used in mass balance calculations in Figure 4.11; b) Sample HD-01 62 with intense k-silicate alteration; c) HD-80 661, epidote + chlorite + calcite alteration; d) HD-01 31, pervasive sericite alteration; e) HD-01 271 Sericite + chlorite alteration overprinting K-silicate alteration.

the system, in Figure 4.4a calcite plots in the (1, 0) node and epidote in the (2,0) node, suggesting influence of both minerals in the chlorite +epidote + calcite alteration assemblage. Petrographic observations indicate low percentages (~1%) of carbonates. However, calcite is more abundant in the volcano-sedimentary wall rock altered to chlorite +epidote + calcite (See Appendix B2, PB2014106).

4.2.4. Calcic skarn

The calcic skarn alteration mineralogy is composed of pervasive garnet, epidote, quartz, and pyrite (Figure 4.5e). Calcic skarn alteration occurs within the western Kestane area, in limestone, calcareous volcanic sandstone and mudstone wall rock (Figure 4.1). Petrographic investigation shows a destruction of the original texture (Figure 4.5f) and a dominance of colourless and anhedral garnet (20-25%), interstitial quartz (35-40%), epidote (5%), clinopyroxene (5%), and calcite (10-15%).

The mineral identification in this zone based on SWIR spectra is dominated by smectite, epidote and dolomite, and minor actinolite. Smectite spectra indicate Mg- rich contents with Mg peaks at 2320 nm.

4.2.5. Chlorite ± sericite

Chlorite ± sericite alteration assemblage is distributed along the Kestane stock in medial zones and overprints earlier alteration (Figure 4.1 and 4.2). Sericite is more abundant at shallower zones (<200 m); while it decreases or disappears at deeper (>200 m) zones where the dominant mineral is chlorite. Sericite and chlorite are generally replacing phenocrysts, chlorite after biotite and sericite after plagioclase (Figure 4.6). Chlorite and sericite are also present in pyrite vein envelopes. In biotite hornfels, sericite overprints earlier biotite. Modal percentages of alteration minerals, based on petrographic description, indicate 12% of chlorite (sometimes exhibiting brown with blue tints interference colours), 2 % of coarse muscovite (up to 0.4 mm), and 10% of clays and undifferentiated white micas.

SWIR mineralogy in the chlorite ± sericite alteration indicates the presence of muscovite, chlorite, phengite, and illite. The wavelength in the Al-OH feature ranges from 2200-2010 indicating K, Mg, Al enriched micas (muscovite and phengite). Chlorite spectra have peaks in 2250 and 2350 nm indicating similar composition of Fe and Mg. The geochemistry of this alteration is shown in Figure 4.4 and indicate intermediate values of molar K/Al (0.3-0.15) and (2Ca+Na+K)/Al (0.67-0.83).

4.2.6. Sericite ± quartz

At Halilağa, sericite ± quartz alteration is distributed mainly in the surface-exposed central zone,

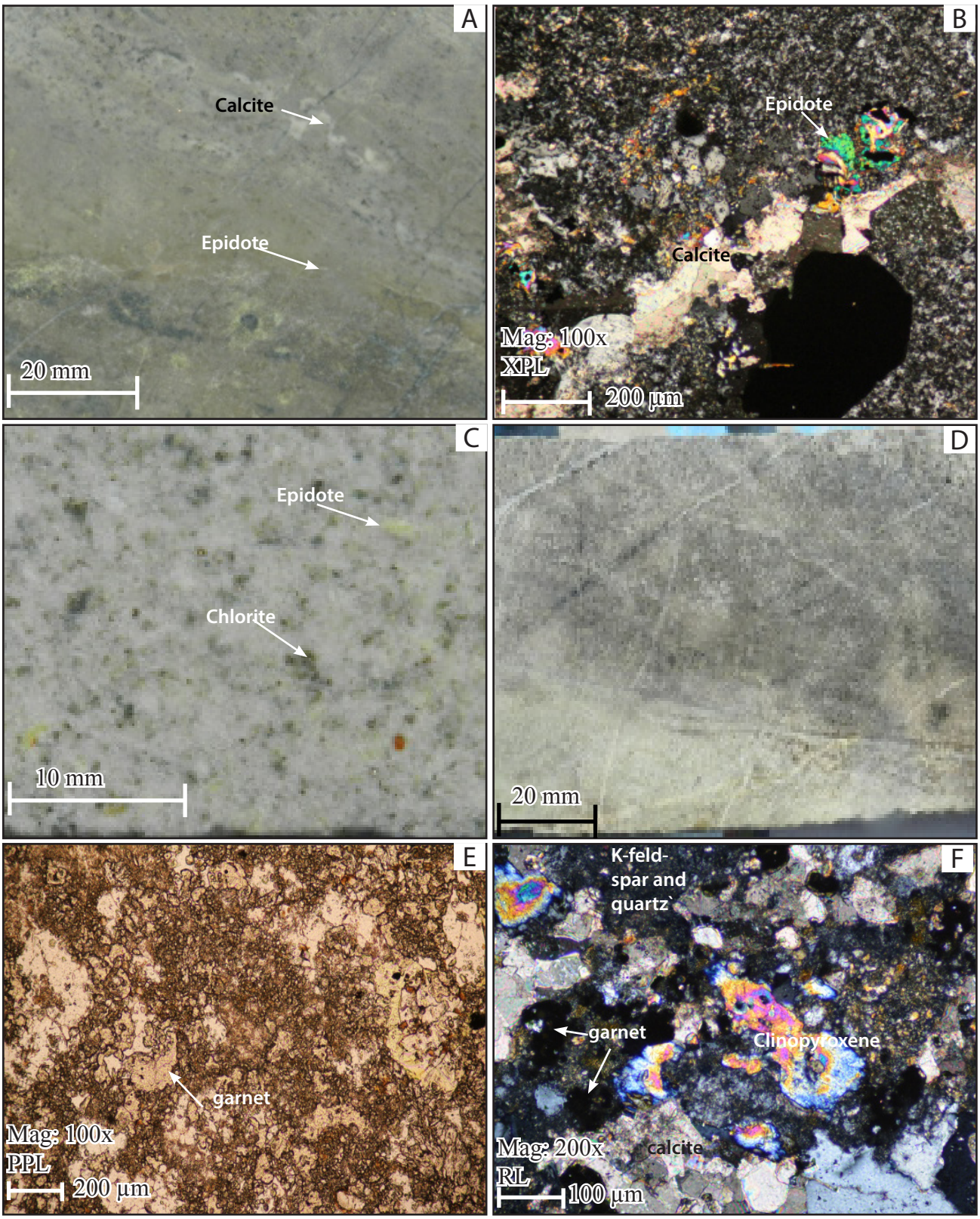

Figure 4.5 a) HD-78 16 Calcite and epidote veins in a altered volcanic rock; b) HD-78 16 thin section; c) PD-21; d)HD-78 39.4, Skarn alteration overprinted by clays in a fine grained wall-rock; e) HD-78 39.4, Isotropic and anhedral garnet are widely distributed in the sample associated with calcite; f) HD-78 39.4, fragmented pyroxenes, calcite, anhedral garnets and fine-grained aggregates of K-feldspar and quartz

overprinting K-silicate zones in Kestane, but also there are short intervals with sericite alteration in the covered portions of the Kestane stock in the zone east of the Karıncalı Fault (Figure 4.1). Microscopic observation of this alteration reveals coarse-grained muscovite (30-50%) and silica in ground mass with sericite patches. This alteration is associated with sulfides and rutile (3-4%), particularly in quartz veins (10-30%) and pyrite vein (5%) envelopes (Figure 4.7). Quartz veins (5-10%) contain interstitial acicular muscovite grains (3-5%). Staining of an altered sample shows patches of K-bearing alteration (in yellow) related to vein halos (Figure 4.7c).

SWIR analysis indicates dominant muscovite white mica (Al-OH absorption feature of 2200-2210 nm) with sericite crystalline index of 1.3-2.5. Paragonite is identified in a few drill holes in the Kestane area, but paragonitic-illite is common in the central portions of the porphyry and overprinting biotite-hornfels in unmineralized or poorly mineralized zones (Cu grades lower than 0.3%). In mineralized portions of the porphyry stock, the dominant white mica is muscovite after plagioclase. K- rich micas have a theoretical K/Al molar ratio of 0.3, whole-rock geochemistry of this alteration reflects K/Al molar ratios between 0.34 and 0.45 (Figure 4.4), suggesting that micas from the sericite ± quartz are slightly more enriched in K.

4.2.7. Late clays

Pervasive clays are commonly distributed along fault and fractures zones in the deposit and are present in the Oligocene volcanic unit. Based on SWIR analysis the clay mineralogy corresponds to kaolinite and smectite (montmorillonite). Kaolinite and montmorillonite are distributed in shallow levels (<100 m). The spectral response for samples with clays identified as montmorillonite show peaks at 1450 nm, 2253 nm, and 2340 nm and deep H_2O feature. SWIR measurements along fault zones, suggest the presence of white micas (phengite, paragoniticillite and muscovite) in addition to montmorillonite and kaolinite (Table 4.2). Phengite is generally observed along the South Fault, while montmorillonite is dominant along the North Fault (Figure 4.8). In the Oligocene volcanic unit, dickite is identified in the first 150 m of the HD-08 drill core (see Figure 4.1) and pervasive paragonitic illite.

Late clay alteration overprints earlier alterations, post-dating porphyry-related alterations.

4.2.8. Argillic alteration (Kunk)

Epithermal-style hydrothermal alteration assemblages occur at Kunk hill, 1 km SE of Kestane and affects the dacitic volcanic sequence (Figure 4.2). The mineralogy exhibits a zonation of argillic and advanced argillic assemblages.

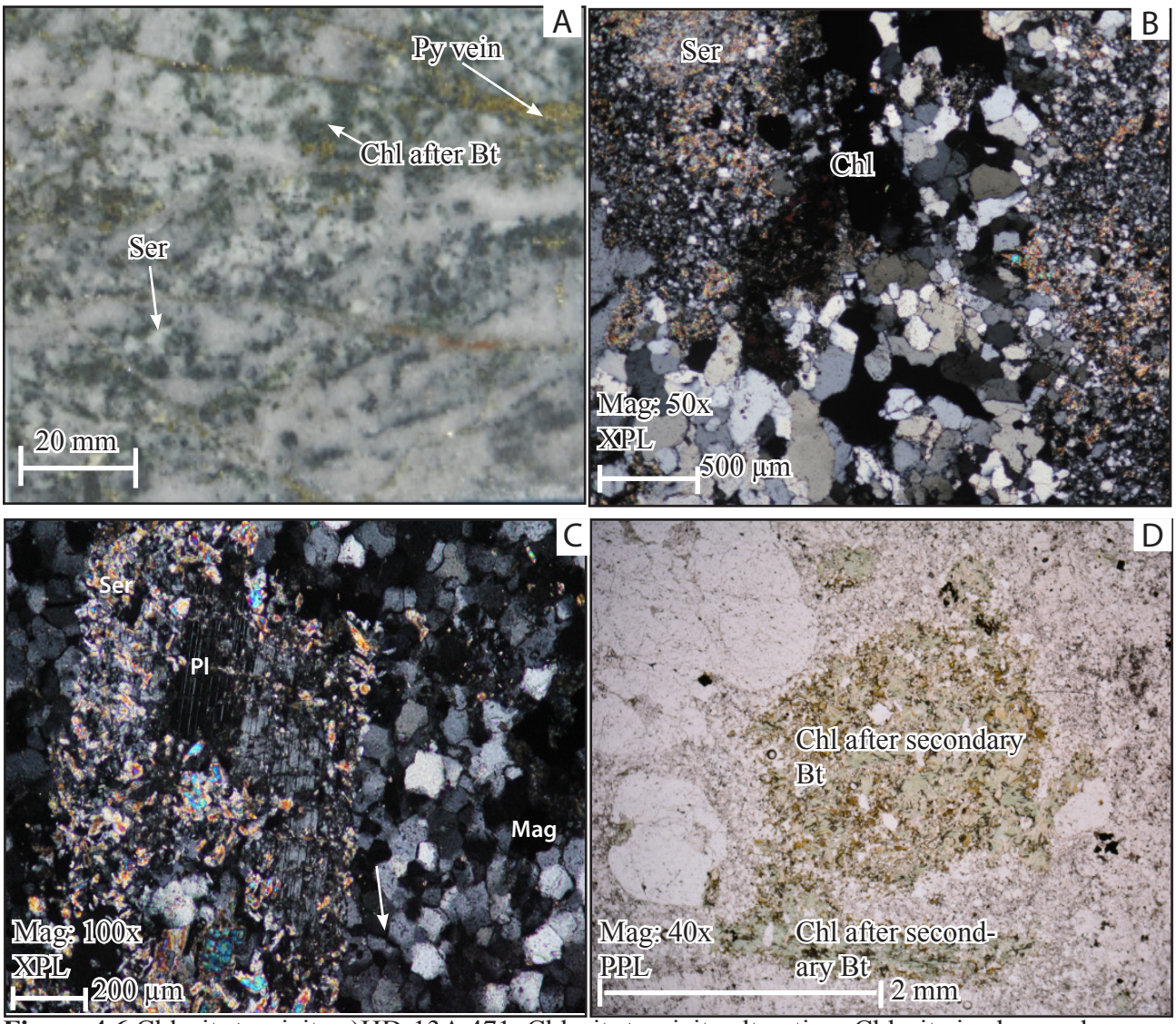

Figure 4.6 Chlorite+sericite a)HD-13A 471, Chlorite+sericite alteration. Chlorite is observed after secondary biotite, while plagioclases are altered to white mica; b) HD-38 396, Quartz vein with chlorite and muscovite in halos. The ground mass is a fine aggregate of quartz+k-feldspar, locally altered to white micas; c) HD-13A 471, Plagioclase phenocryst with polysynthetic twinning replaced by white mica (sericite) d) HD-45 459, Sub-hexagonal phenocrysts (biotite?) replaced by secondary biotite (brown to yellowish) followed by chlorite. Also elongated crystals with same alteration mineralogy.

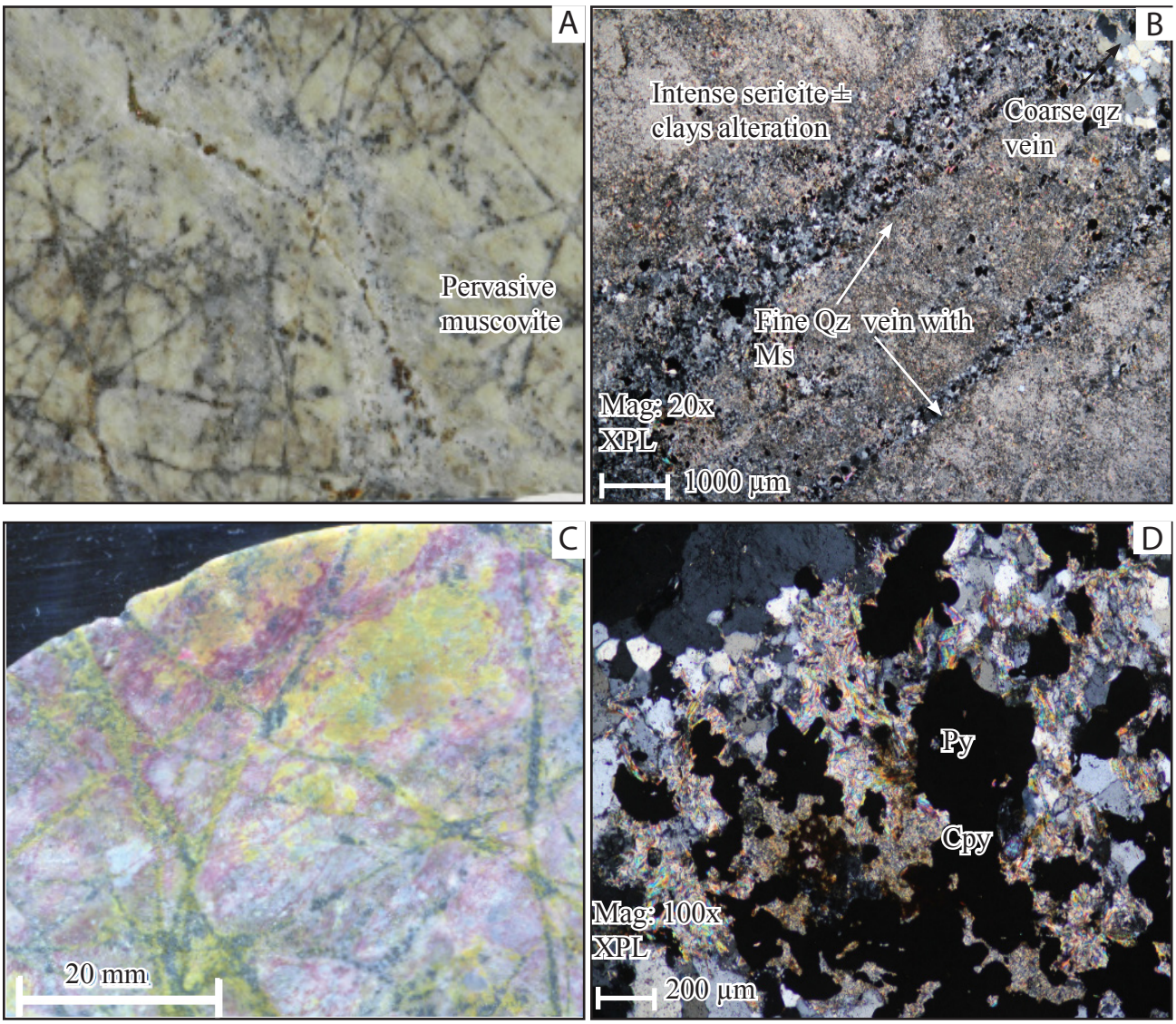

Figure 4.7 Quartz+sericite alteration a) HD-115 146, Pervasive muscovite+quartz alteration; b) Same sample than a in thin section. Fine quartz veins with rutile with pyrite and chalcopyrite, sericite+clays halos. Ground mass is intensely altered to sericite+clays; c) HD-115 146, Stained sample from a, yellow indicate dominate of K-bearing minerals (K-feldspar or K-rich mica) while red colour is indicative of Na bearing minerals (Na-plagioclase) ;d) HD-13A 106, Altered phenocrysts to muscovite with pyrite and chalcopyrite.

Table 4.2 SWIR measurements along fault zones

Holeid	Depth	1st Mineral	2nd Mineral	w2200	hqd2200	width2200	hqd1900	Sericite Crystallinity
HD-13A	90	Phengite		2221.72	0.15	10.05	0.16	0.95
HD-13A	167	Phengite		2222.41	0.09	13.09	0.11	0.86
HD-13A	179	Phengite	Montmorillonite	2222.14	0.06	13.00	0.08	0.72
HD-13A	209.3	Phengite		2220.44	0.1	14.97	0.12	0.81
HD-13A	235.5	Montmorillonite	Phengite	2221.14	0.13	14.89	0.22	0.58
HD-115	172	Montmorillonite	Kaolinite	2205.27	0.16	12.73	0.43	0.39
HD-115	178	Muscovite		2204.97	0.21	15.56	0.16	1.34
HD-115	229	Muscovite	Kaolinite	2205.26	0.19	14.38	0.16	1.22
HD-124	44.5	ParagoniticIllite		2201.03	0.28	14.56	0.19	1.50
HD-124	49.1	ParagoniticIllite	Kaolinite	2205.55	0.26	14.12	0.29	0.89

The western side of Kunk (Figure 4.8) contains white mica (muscovite, paragonite, phengite), kaolinite, and minor pyrophyllite, suggesting an argillic assemblage. In surface this alteration coexists with hematite and goethite (Figure 4.9a). The most common white micas are paragonite, at shallower levels (<200m) and phengite at depths greater than 200 m (Figure 4.2). Petrographic analysis showed groundmass replaced by fine-grained silicification (~30%) and white mica (Figure 4.9) interlayered with clay (~5%), while phenocrysts of plagioclase are replaced by coarser and occasionally acicular white mica (~20%).

4.2.9. Advanced argillic alteration (Kunk)

In the east of Kunk (Figure 4.8), advanced argillic assemblages are dominant and include: pyrophyllite and minor alunite, paragonite, diaspore, and dickite. Fine-grained alunite, identified only with SWIR, is occasionally present in plagioclase phenocrysts in shallower levels (<100 m) and particularly in a Fe- rich talus breccia (Figure 2.4), while pyrophyllite is replacing felsic phenocrysts at depth (50-350 m). In the advanced argillic zone, paragonite is commonly associated with pyrophyllite; kaolinite is limited to fault zones. Diaspore is observed in two drill holes at depth higher than 300 m in HD-09 and 230 m in HD-10. Dickite is restricted to the Kunk fault zone.

4.2.10. Advanced argillic alteration (Pirentepe)

In Pirentepe, located 2.5 km NW of Kestane (Figure 2.1), the andesitic volcanic sequence is affected by hydrothermal alteration characterized by: vuggy silica (Figure 4.9d), silicification, white mica (illite, phengite, paragonite, muscovite), and clays (kaolinite). Alunite is scarce in drill core and more common to the western (Davulgali area). White micas selectively replace primary plagioclase phenocrysts.

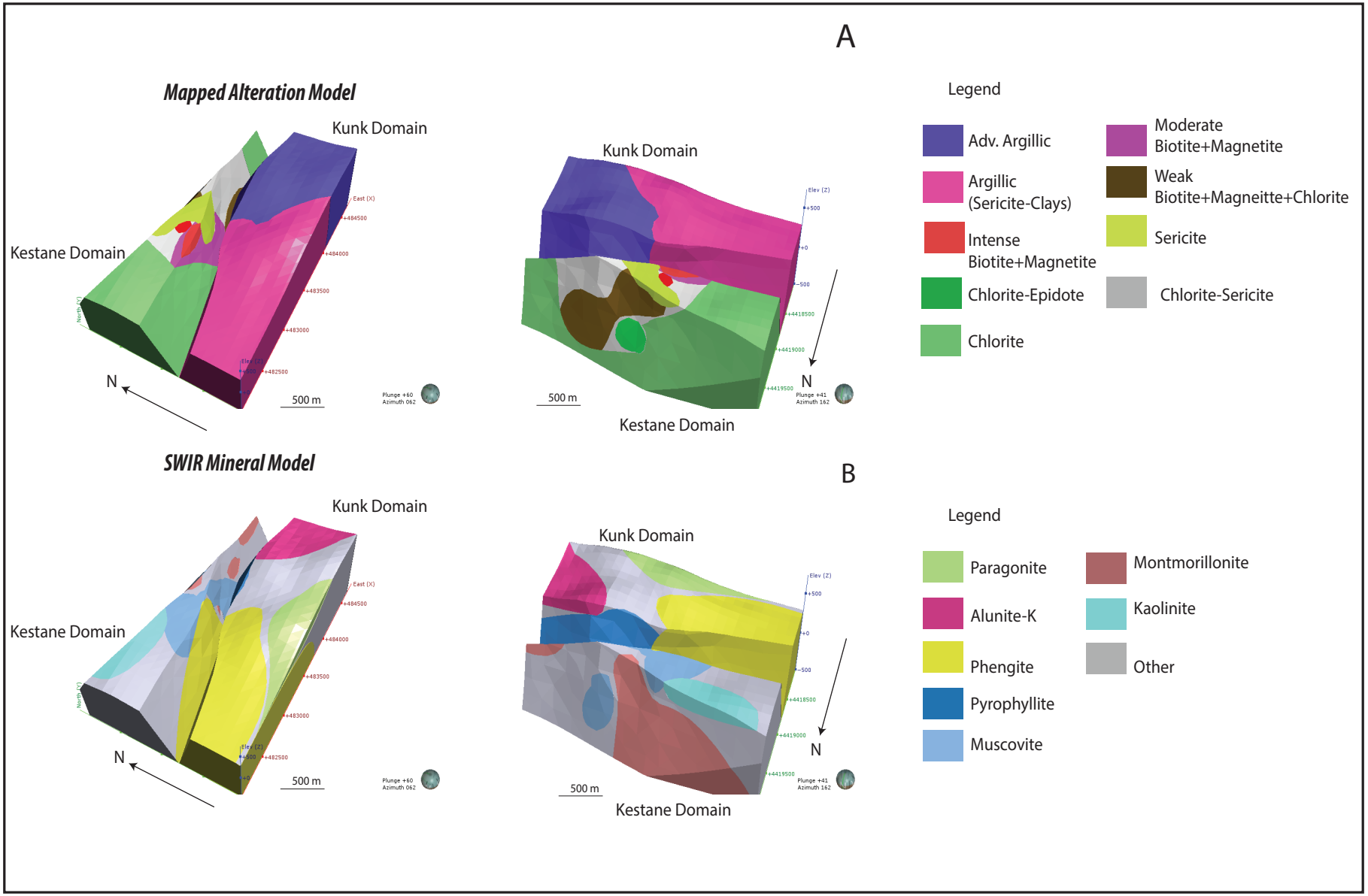

Figure 4.8 a) Mapped alteration model; b) Distribution of SWIR minerals in a 3D-model of the distribution of white micas and clays in the Kunk and Kestane structural blocks defined by the Kunk Fault, North Fault, and South Fault

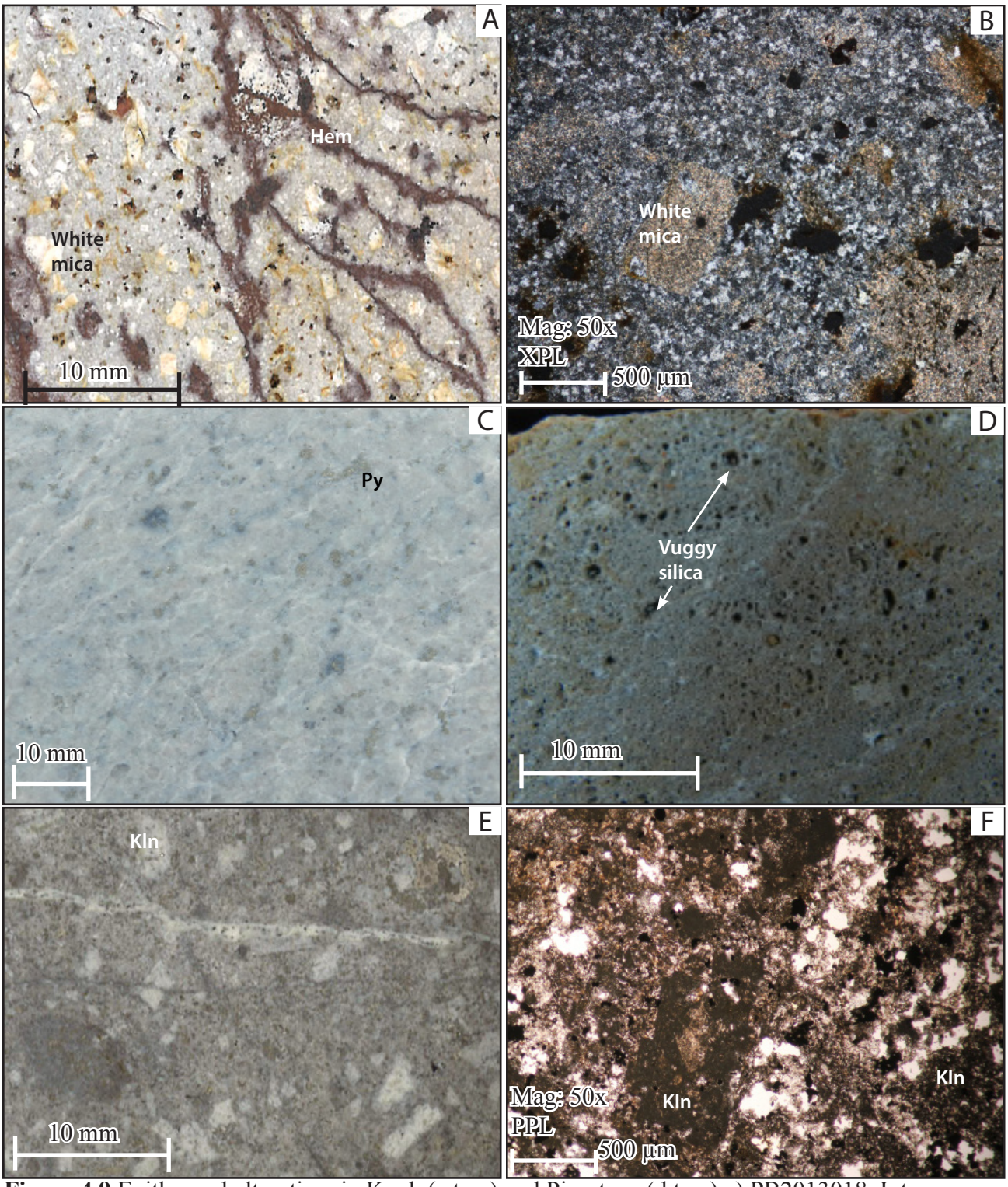

Figure 4.9 Epithermal alteration in Kunk (a to c) and Pirentepe (d to e) a) PB2013018. Intense alteration of white mica and pyrophyllite in felsic site. Vuggy texture in mafic site (completely removed from the rock) and hematite in veins; b) Same sample in thin section. Phenocrysts altered to white mica (muscovite) and pyrophyllite, hematite in veins and phenocryst borders; c) HD-09 215 Moderate silicification associated with pyrophylllite and white mica (paragonite); d) PD-05 50 vuggy silica texture; e) PD-17 59 , Clay replacing plagioclase phenocrysts and ground mass, relicts of mafic minerals with rutile; f) Same sample in thin section. Fine grained kaolinite in ground mass.

SWIR analysis indicate dominance of phengitic white mica with wavelength greater than 2215 nm in the Al-OH absorption feature. Kaolinite exhibits a peak at 1400 nm and a very deep feature at 2208 nm. Double peaks at 1780 nm and 1900 nm could indicate presence of dickite (Appendix B3, PD-17 59.8). Petrographic observations in altered rocks from Pirentepe (Figure 4.9e-f) suggest fine-grained kaolinite (~45) in ground mass and phenocrysts accompanied by limonites (~20%).

4.3. Porphyry Veins

Veins in porphyry deposits has been widely studied and assigned to stages in the evolution of the porphyry deposit (e.g. Gustafson and Hunt, 1975; Gustafson and Quiroga, 1995, Rusk and Reed, 2008). Classical vein nomenclature from the "El Salvador" deposit in northern Chile is the most commonly used and widely accepted and is as follows: early magnetite-biotite veins (EB-type), early quartz veins (A-type), transitional quartz veins with central sulfides (B-type), and pyrite with sericite halos (D-type) (Gustafson and Hunt, 1975; Gustafson and Quiroga, 1995). The classical nomenclature has been used for decades to denote veins assemblages and furthermore vein temporal relations. However, in many cases is better to name veins based on the mineral assemblage and this description style is used to describe veins in the following paragraphs.

A summary with field observations and description for each vein type of the Halilağa deposit is detailed in Table 4.3. Similarly to the alteration assemblages described in a previous sub-section, the vertical distribution of veins changes significantly when the post-mineral andesites cover the porphyry stock in the eastern area, increasing the depth in 300 m (Figure 4.10).

4.3.1. Early veinlets (E1)

Biotite + magnetite veins are fine veinlets (1-2 mm) associated with intense to moderate K-silicate alteration zones and are cross-cut by quartz veins (Figure 4.11a). In Kestane the highest density (>4 veins per meter) of these veinlets are commonly at shallower depths (above 100 m), similarly to the extension of K-silicate alteration, and in the center of the deposit extends to 250 m depth (Figure 4.10). Petrographic observation of these veins shows brown to green pleochroic biotite and anhedral magnetite.

The occurrence of this veining in high-grade zones in K-silicate altered zones but also in un-mineralized zones associated only with secondary biotite after hornblende suggests pre-mineralization timing for this event.

In Figure 4.12 two early veins are cross-cut by quartz veins (Q1 and Q2). The chlorite + magnetite

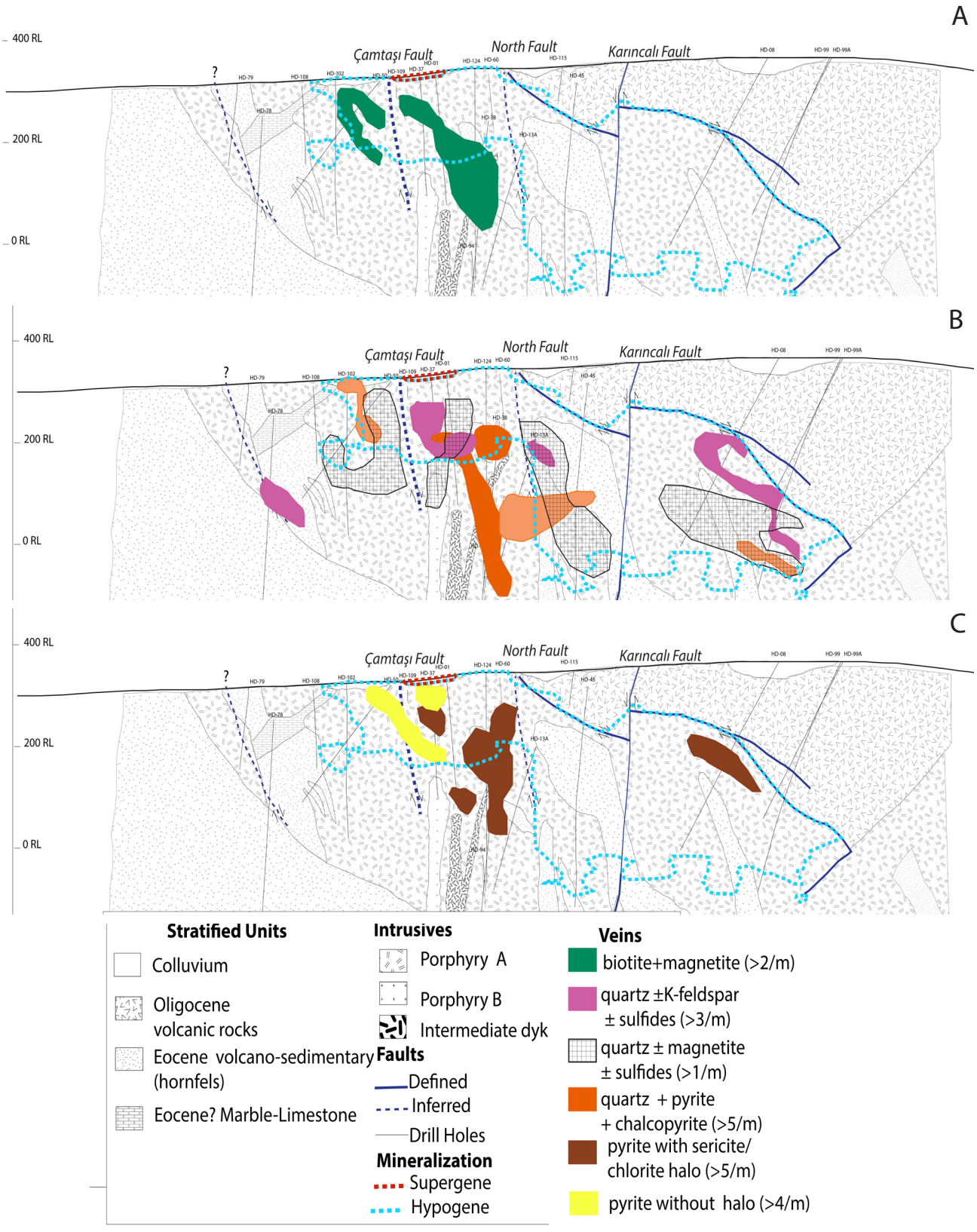

Figure 4.10 Veins and mineralization distribution in cross section A-A' , oriented WSW-ENE, including lithologies (patterns). a) biotite + magnetite veins; b) quartz veins; c) pyrite veins. Cross-section location in Figure 2.3.

+ pyrite vein (Figure 4.12d) can be correlated with the biotite + magnetite veins, with biotite being replaced by chlorite and probably reflecting vein re-opening.

4.3.2. Quartz veins

Quartz veins host most of the Cu-Au mineralization. According to vein geometry, mineral assemblages, and cross-cutting relations four different stages have been identified. Those veins have variations in the density and their spatial distribution. .

4.3.2.1. Quartz + magnetite + sulfides (Q1)

Quartz + magnetite + sulfides veins are 5 mm thick,on average with maximum of 7 mm (Figure 4.11a), distributed in high grade zones (>0.5% Cu and >0.5ppm Au) associated with intense biotite + magnetite ± K-feldspar alteration assemblages where they can have densities higher than 4 veins per meter. In quartz + magnetite + sulfides veins, magnetite and quartz are banded (Figure 4.11a) and sulfides are pyrite and chalcopyrite. In thin sections is possible to observe the association magnetite + chalcopyrite in those veins. Cross-cutting relationships with other quartz veins are scarce, but some evidences from drill core, suggests than quartz + magnetite + sulfides veins are cross-cut by quartz ± K-feldspar ± sulfides

4.3.2.2. Quartz ± K-feldspar ± sulfides (Q2)

Quartz ± K-feldspar ± sulfides veins are usually magnetite poor and contain chalcopyrite and pyrite. Quartz ± K-feldspar ± sulfides are 3-10 mm thick (Figure 4.11b); densities higher than 4 veins per meter are distributed at shallow to moderate depths <300 m relative to the intrusion depth. Based on their morphology two groups are identified: a) straight borders characterized by pink colour due to the abundance of K-feldspar b) sinuous borders with milky colour quartz generally barren and more frequent than the previous veins. Petrographic observations indicate coarse-grained quartz up to 1 mm with traces of anhydrite, epidote and calcite. The absence of cross-cutting relationships between both groups and the scarce mineralization suggests that both veins occur at the same time. In Figure 4.12b, a 4 mm Q2 vein, consisting of quartz and pyrite with traces of calcite, chlorite, magnetite and chalcopyrite cross-cut a biotite + magnetite vein (E1 in Figure 4.12 b).

4.3.2.3. Quartz + pyrite + chalcopyrite (Q3)

Quartz + pyrite + chalcopyrite veins are distributed in the highly mineralized portion of the porphyry stock at depths betwwen 150-300 m. Quartz + pyrite + chalcopyrite vein are up to 8 mm thick with averages of 4 mm; and average density of 4 veins per meter with ranges from 1 to 15 veins

Table 4.3.Veins at the Halilağa Deposit

Vein Type	Assemblage	Halo	Gangue	Sulfides or Oxides	Alteration Zone	Thickness	Morphology	Cross-Cutting relationships	Distribution
Early	biotite-magnetite (E1)	-	bio	cpy, mgt	biotite+magnetite±K-feldspar	fine, 0.2-1 mm	fine and irregular	earliest, quartz veins cross-cut biotite-magnetite veins	central mineralized zone, in shallow to moderate depths (50-300 m)
Quartz	quartz+magnetite+sulfides (Q1)	-	qz	cpy, py, mgt	biotite+magnetite±K-feldspar	up to 7 mm, average 5 mm	banded, irregular	cross-cut by quartz-+k-feldspar veins	ore-body, in the central area at shallow depth (40-150) and deeper in the eastern zone (~400 m)
	quartz±K-feldespar±sulfides (Q2)	-	qz, kfs	tra of cpy and py	5	3-10 mm	a) straight borders (dominance of K-feldspar) b) sinous walls ("milky colour")	often crosscut biotite+-magnetite veins, but sometimes biotite+magnetite veins crosscut and displace quartz-±K-feldespar±sulfides veins	higher densities at moderate to shallow depth, from (70-250 m)
	quartz + pyrite + chalcopyrite (Q3)	-	qz	cpy, py	biotite+magnetite±K-feldspar; chlorite ± sericite	up to 8 mm thickness, average 5 mm	straight borders, sulfides often in central suture, often present "sugary" or mosaic grains	cross-cut biotite+magnetite veins	ore-body, at moderate depth (150-300 m)
	quartz+molibdenite (Q4)	-	qz	cpy, py, mo	biotite+magnetite±K-feldspar; chlorite + sericite	average thickness 1 mm	straight borders, molybdenite in vein walls	cross-cut the quartz-pyrite-chalcopyrite	southern and western margins of the intrusion
Late veins	pyrite (L1)	without/ sericite/ chlorite	qz, hl, ser	py, minor cpy	chlorite±sericite, sericite±quartz	average 5-8 mm (including halo)	fine center with thicker, irregular halo	cross-cut quartz veins, ankerite veins cross-cut and displace pyrite with sericite halos veins	widely distributed
	calcite/ankerite (L2)		cal/ank	-	chlorite+epidote+calcite	fine, less than 0.5 mm	fine and irregular	cross-cut all veins	usually at the edges of the system

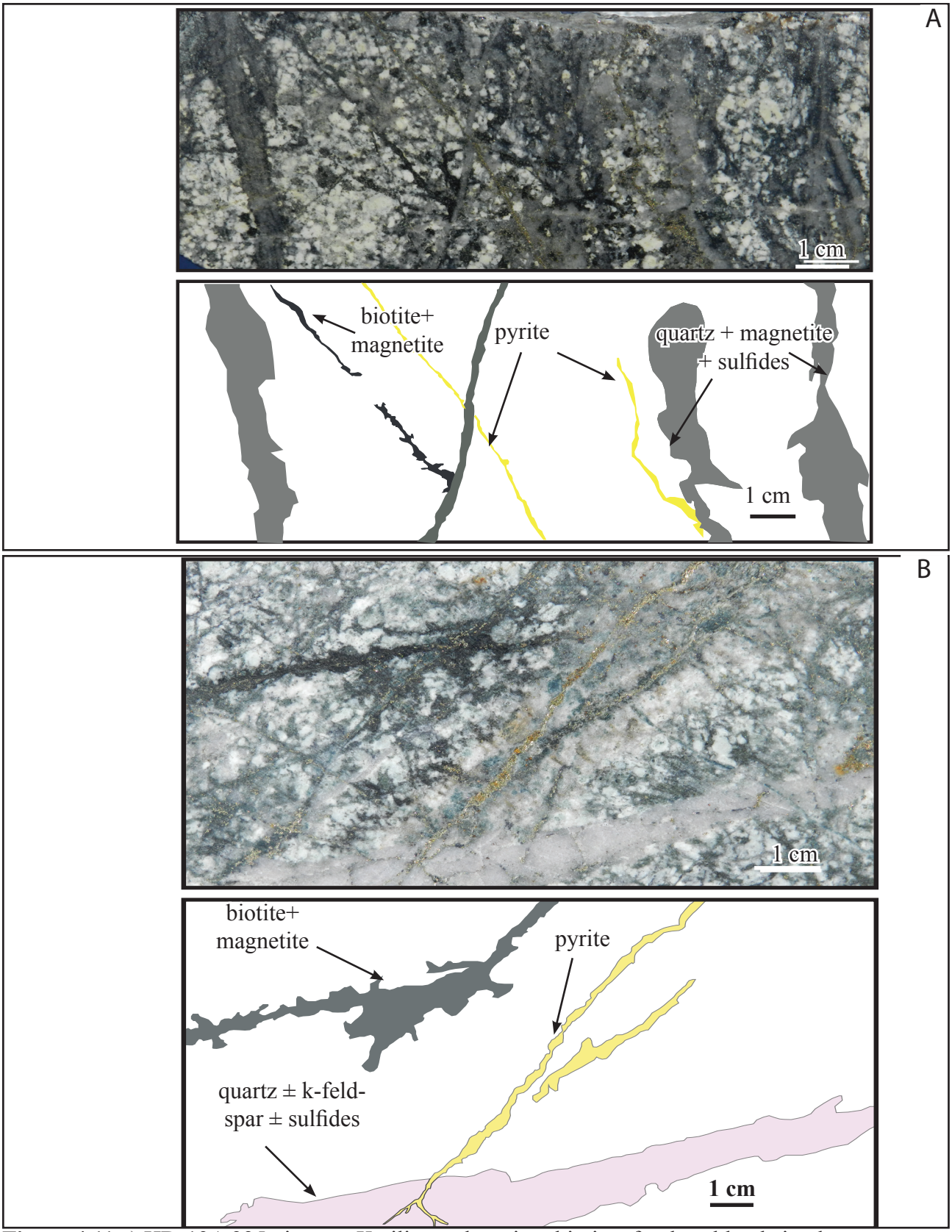

Figure 4.11 a) HD-13A 225, intense K-silicate alteration: biotite after hornblende in phenocrysts and intense veining. Dominated by quartz+magnetite+sulfides vein and minor thin biotite+magnetite veins, both crosscut by fine pyrite veins ; b) HD-99A 385

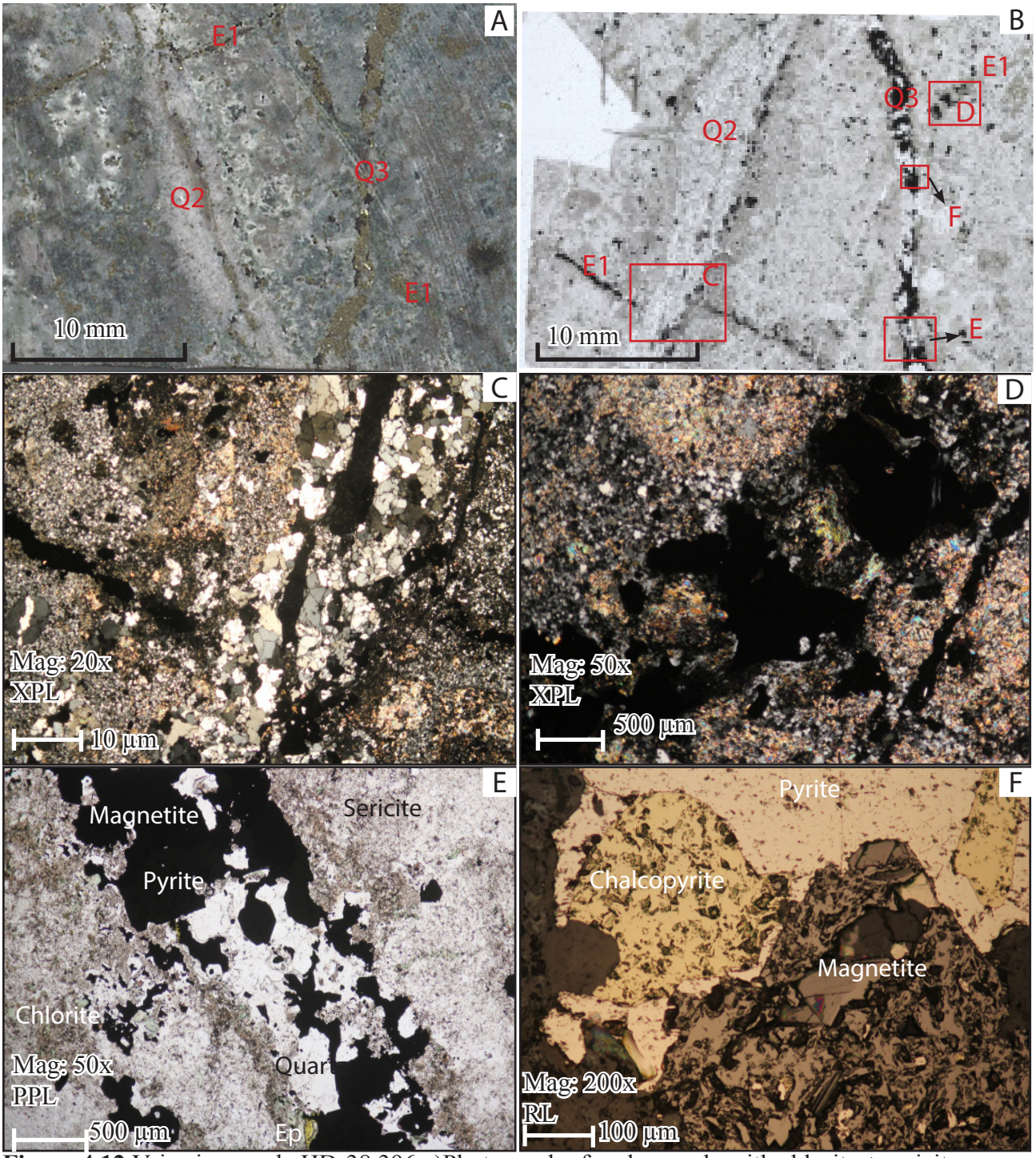

Figure 4.12 Veins in sample HD-38 396 a)Photograph of rock-sample with chlorite + sericite alteration. Two quartz veins (Q2 and Q3) dominate the rock; b) PPL thin section scan, indicating location of photographs in thin section c) Quartz vein with pyrite crystals (Q2). 4 mm width quartz veins include traces of diverse minerals: calcite with anomalous pinkish interference colour and cleavage, brownish radial chlorite and green pleochroism, only traces of chalcopyrite and magnetite. This vein cross-cut a fine (0.3 mm) magnetite+pyrite+chalcopyrite vein (E1) d) Irregular and discontinuous brown chlorite veins associated with magnetite and pyrite (E1?). This vein is crosscut by Q3 vein; e) pyrite+chalcopyrite ± magnetite ± quartz (Q3) . Dominated by sulphides with patches of granular quartz aggregates and have brownish with blue tint chlorite and fine grained sericite in vein selvages f) Pyrite+magnetite+chalcopyrite in vein Q3(shown in e).

per meter. Quartz + pyrite + chalcopyrite veins have straight borders and a sulfide central line with magnetite associated with chalcopyrite (Figure 4.13a). In other examples pyrite veins, including gold inclusions, grow perpendicular to quartz vein margins. Petrographic observations show two types of veins according with the grain size of the quartz: fine grained quartz crystals (0.1 mm) with pyrite, and chalcopyrite (chalcopyrite>pyrite) and coarser grained (0.5-1 mm) with pyrite, chalcopyrite, and less frequently minor biotite in selvages. Fine-grained quartz + pyrite + chalcopyrite cross-cut the coarser quartz + chalcopyrite veins. Cross-cutting relationships with other veins are shown in Figure 4.12, where a quartz + pyrite + chalcopyrite vein, containing chalcopyrite in pyrite grains, cross-cuts a discontinuous chlorite + magnetite + pyrite veins, that corresponds to a re-opened E1 vein.

4.3.2.4. Quartz + molybdenite (Q4)

Quartz + molybdenite veins are 1 mm thick and usually with a low density (3 per meter). Quartz + molybdenite veins have straight borders; usually have a pyrite ± chalcopyrite central line, and molybdenite in the vein margins. The distribution of quartz + molybdenite veins is restricted to the western zone (in hornfels) and in the southern border of Kestane, near the South Fault. Due to the scarcity of quartz+ molybdenite veins cross-cutting relationships is limited, but they cross-cut the quartz + pyrite + chalcopyrite veins (Figure 4.13b) suggesting a late timing compared with other quartz veins.

4.3.3. Late veins

Pyrite veinlets with or without sericite envelopes (L1) cross-cut all of the previous veins at shallower levels (<150 m). At deeper levels, they are associated with sericite or chlorite halos (particularly chlorite after biotite, Figure 4.13a). The density of these veins ranges from 2-3 per meter in average to highly dense zones with more than 8 veins per meter. The average width is 1 mm of pyrite with a 1-6 mm sericite/chlorite halo. Pyrite veins include variable contents of chalcopyrite inclusions, especially in presence of chlorite after biotite. Petrographic observations indicate muscovite grains no larger than 0.2 mm in vein selvages.

Lastly, late calcite (L2) occurs in the edges of the porphyry system overprinting earlier veins. The thickness of calcite veins is less than 0.4 mm and an average 0.2 mm. Densities of calcite veins range from 3 to 8 veins per meter.

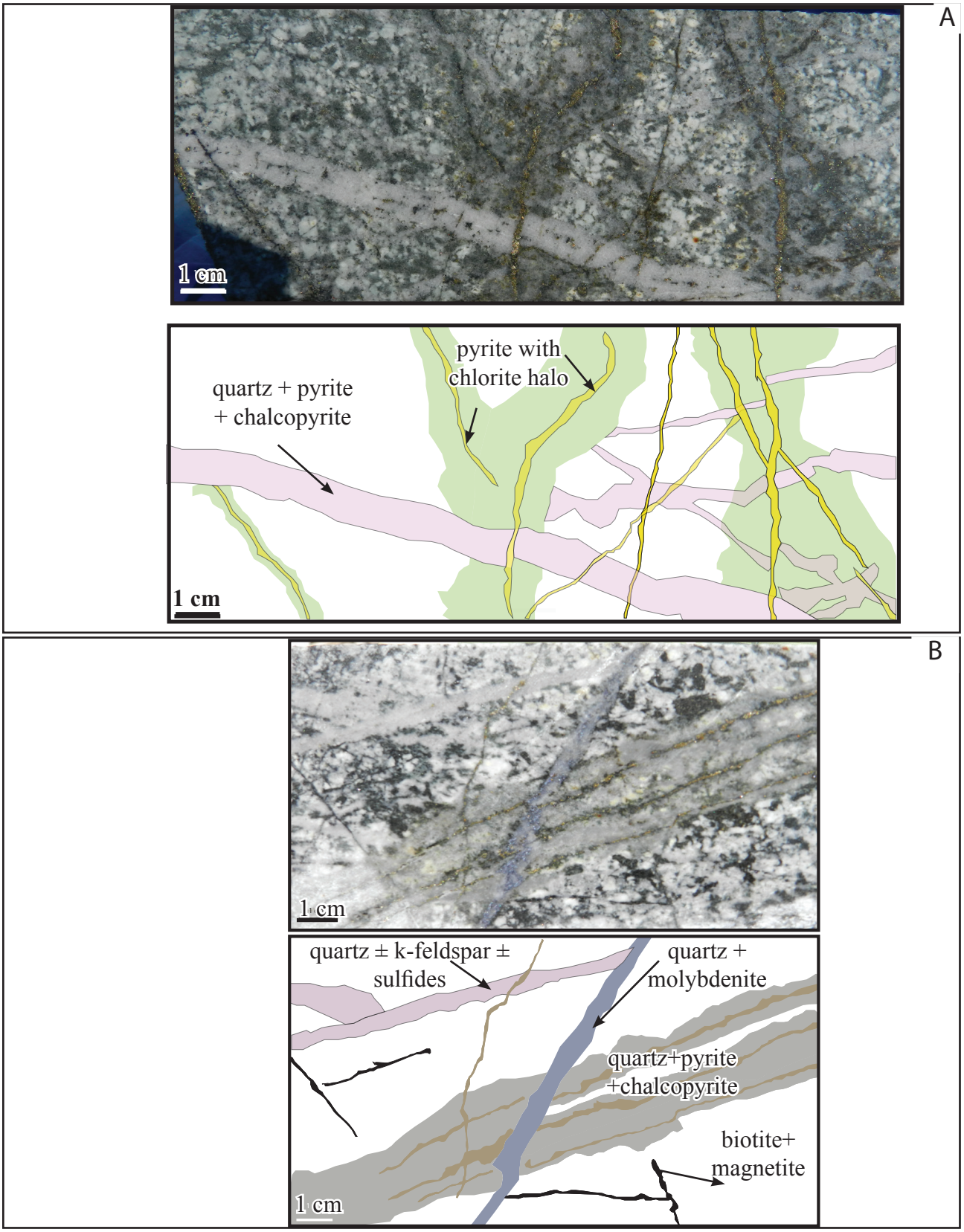

Figure 4.13 a) HD-13A 471 quartz+pyrite+chalcopyrite vein crosscut by pyrite with chlorite halo veins in a chlorite + sericite altered sample. Quartz vein contains sulfides in a central line. Pyrite veins also contain chalcopyrite inclusions; b) HD-94 402, quartz+molybdenite vein crosscut quartz+pyrite+chalcopyrite vein and quartz ± k-feldspar ± sulfide vein.

4.4. Mineralization

4.4.1. Hypogene mineralization

The majority of mineralization in the deposit consists of hypogene sulfides (Figure 4.10). The geometry of the ore-body follows an E-W direction with approximately 40-45° plunge (Figure 4.10). Hypogene ore in the quartz monzonite stock consists of chalcopyrite with pyrite and magnetite (Figure 4.14) in veins and disseminated. In hornfels, the mineralization is predominately disseminated and only minor mineralization (less than 1%) is distributed veins.

The copper grades are proportional to the intensity of K-silicate alteration; grades higher than 0.5 % Cu are observed in the intense (>30%) biotite + magnetite ± K-feldspar altered stock, while moderate and low copper grades (0.1-0.3 % Cu) are distributed in weak (5%) biotite + magnetite ± K-feldspar alteration and in chlorite ±sericite alteration (Figure 4.15a). Sulfide mineralization occurs as veinlets, quartz stockwork and finely disseminated crystals. In addition to pyrite and chalcopyrite, pyrrhotite occurs as inclusions in pyrite.

Gold mineralization (grades > 0.5 ppm) coincides with intense biotite + magnetite +K-feldspar alteration and early quartz veinlets (Figure 4.15b). Molybdenite is restricted to disseminations and minor veining in the western area (in hornfels) or in the outer margins of quartz veins with straight borders in hornfels and in the quartz monzonite stock, particularly near the South Fault. Figure 4.15c indicate zones were Mo is higher than 90 ppm.

Cu and Au grades are intimately related and controlled by lithology and alteration; higher grades (>0.5% Cu or 0.5 ppm Au) are distributed in the Kestane stock and associated with biotite + magnetite ± K-feldspar alteration and sericite ± quartz alteration (Figure 4.15 a-b). Particularly, Au is extremely well correlated with the intensity of biotite + magnetite ± K-feldspar, grades between 0.5-1 ppm follow the same geometry of the intense K-silicate alteration (Figure 4.15a), Cu has 0.3-0.5% in that zone but it does not follow the alteration geometry (Figure 4.15b). Mo exhibits a different distribution controlled by structures and with higher grades (>90 ppm) in biotite hornfels instead of the Kestane stock (Figure 4.15c).

4.4.2. Supergene mineralization

A supergene blanket is observed in the central area of the deposit, restricted to a small area where the stock is exposed on surface and consists of 20-50 m of supergene mineralization (Figure 4.10). From top to bottom the sequence consists in a) up to 25 m of leached goethite ± hematite zone

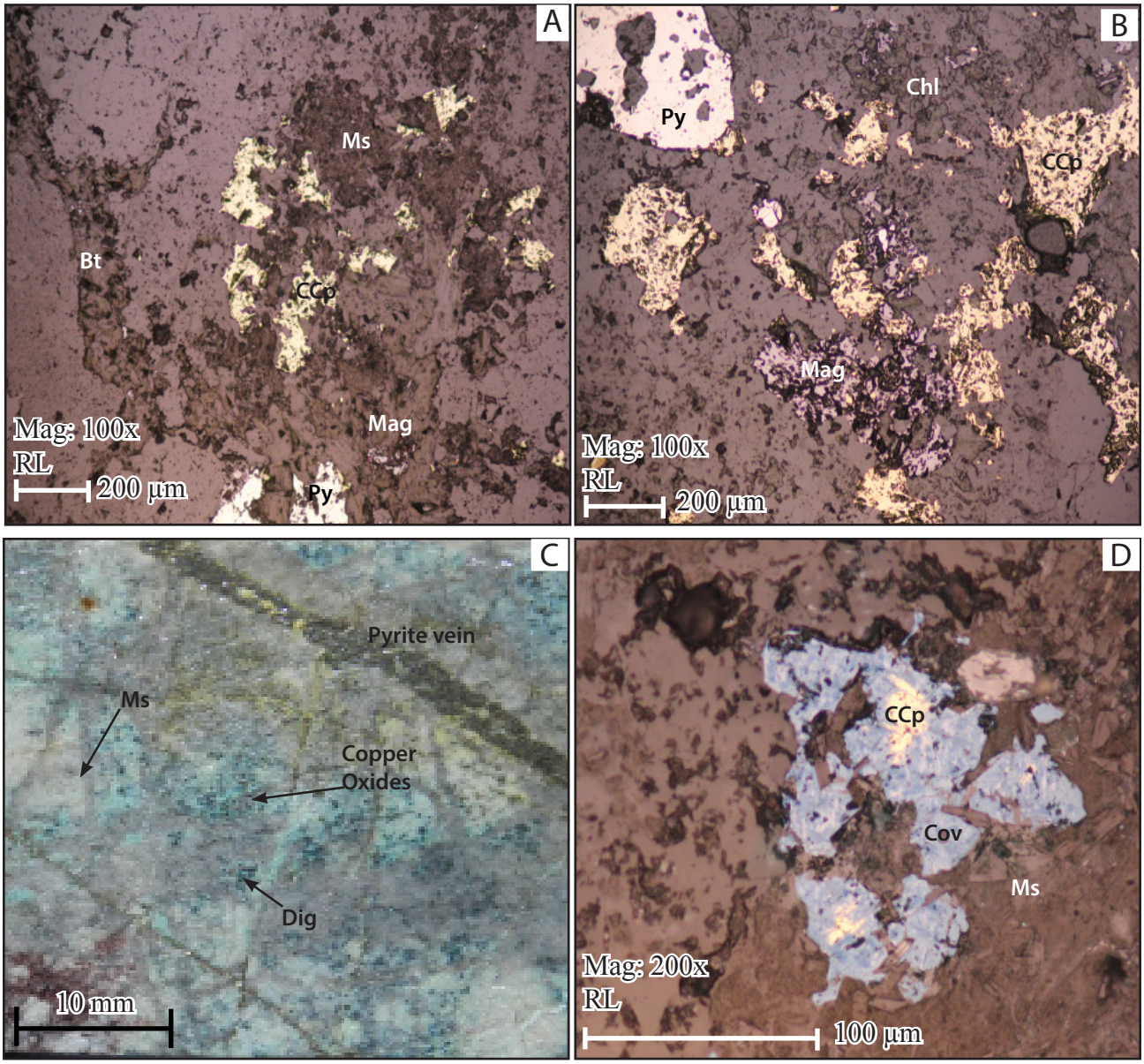

Figure 4.14. a)HD-80 99, Secondary biotite after hornblende, plagioclase altered to clays-sericite and associated with chalcopyrite, pyrite and magnetite; b) HD-13A 47,1 Magnetite-chalcopyrite mineralization related to chlorite (after biotite) veins; c) HD-01 39, Supergene enrichment blanket with copper oxides, pyrite, covellite, and digenite. The dominant alteration in the rock is sericite and yellow clays; d) HD-80 29, Covellite replacing chalcopyrite associated with coarse sericite crystals.

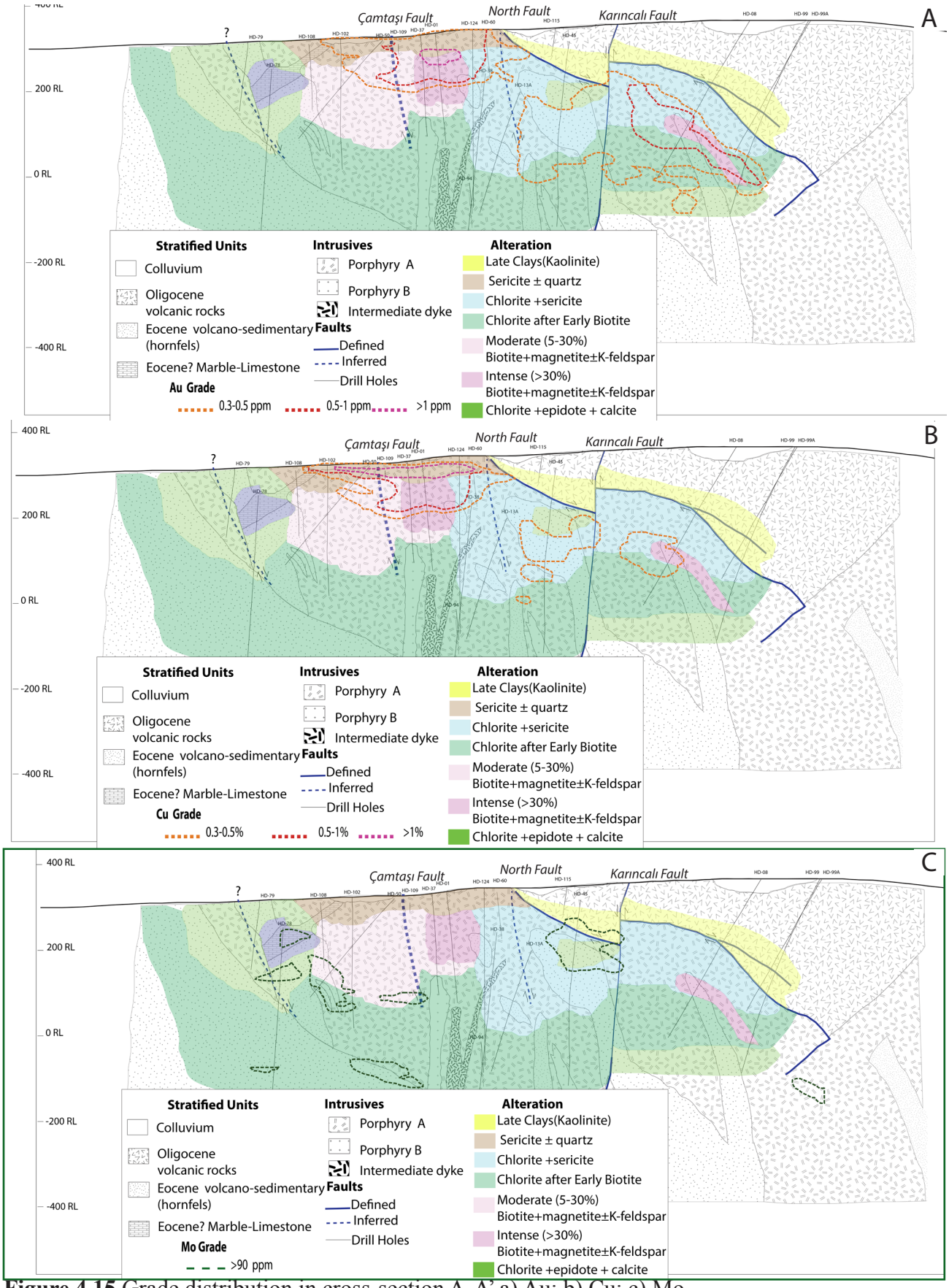

Figure 4.15.Grade distribution in cross-section A-A' a) Au; b) Cu; c) Mo

in the sericite + quartz (-kaolinite) alteration, with elevated gold values (>0.3 ppm) and anomalous copper values (< 1000 ppm); b) supergene copper-enriched zone with disseminated covellite, digenite and chalcocite (with copper grades > 1 % and elevated gold grades >0.5 ppm). These sulfides are often associated with copper oxides and hematite in an intense sericite-quartz altered rock (Figure 4.14c-d).

4.5. Summary of Mineral Paragenesis

The Early Stage (Figure 4.16-4.17) is characterized by biotite replacement and biotite + magnetite veins. As a product of this alteration, the volcano-sedimentary host rock is altered to a biotite hornfels-like rock. The onset of propylitic (chlorite + epidote +calcite) and calcic skarn alteration is related to early stages of the system, but calcic skarn developed in the biotite hornfels indicate that calcic skarn post-dates the early biotite stage. In the stock, early alteration is restricted to distal zones of the mineralized core, where a non-mineralized porphyry stock and without quartz veining presents secondary biotite alteration after hornblende.

The Main Stage is K-rich and related to intense biotite and magnetite addition with moderate K-feldspar (Figure 4.16) and also addition of chalcopyrite, and molybdenite restricted to more permeable zones near fault zones (Figure 4.15c). Quartz veins (Q1 to Q4) occur during this stage in the core of the mineralized system. In the margins of the system chlorite, epidote, calcite and the calcic skarn alteration occur in favorable host rocks (such as limestones or near limestones).

The Transitional Stage is characterized by the overprint of sericite and chlorite in felsic and mafic phenocrysts, respectively following the main ore bearing pulse. In addition, those minerals are distributed in veins halos or as replacement of biotite veins. In this alteration pyrite is intense-to moderate (5-7%) and minor chalcopyrite (3%) is also present in quartz veins with coarse muscovite grains. In the upper portions of the system sericite ± quartz alteration overprints earlier K-silicate assemblages and destroys magnetite.

The Late Stage alteration is dominated by clays such as montmorillonite and kaolinite, but also includes white micas. Veins in this stage are typically calcite or ankerite veins and also minor pyrite veins with sericite halo.

During the Supergene Stage, limonites and ore minerals such chalcocite and Cu oxides are generated from hypogene minerals and are associated with white micas and clays.

Two zones characterize the Epithermal Stage at Kunk an advanced argillic zone dominated by pyrophyllite, alunite, and dickite; and an intermediate argillic zone dominated by white micas and kaolinite.

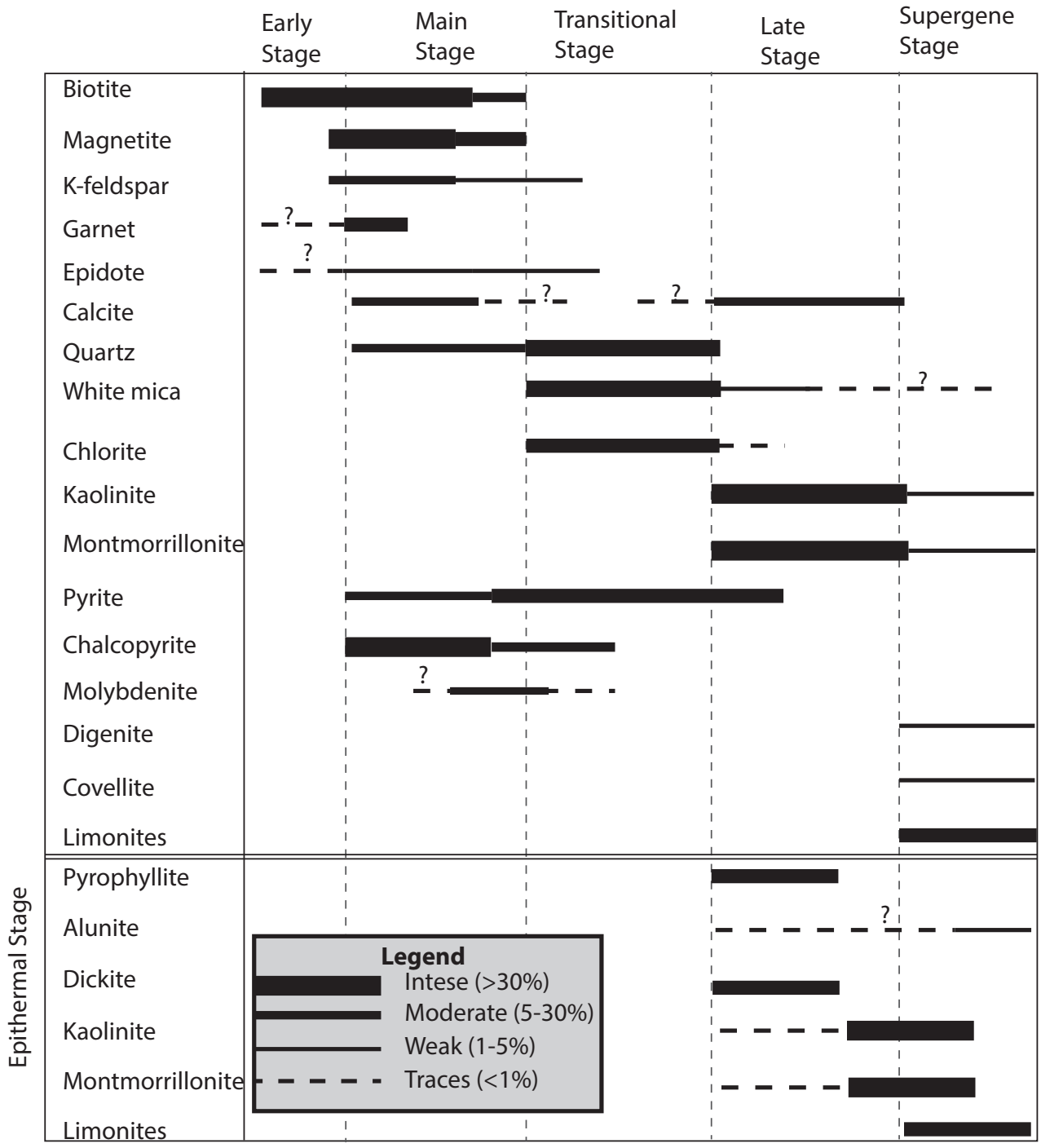

Figure 4.16. Paragenetic chart of the minerals in up: Halilağa porphyry Cu-Au deposit down: Kunk epithermal occurrence.

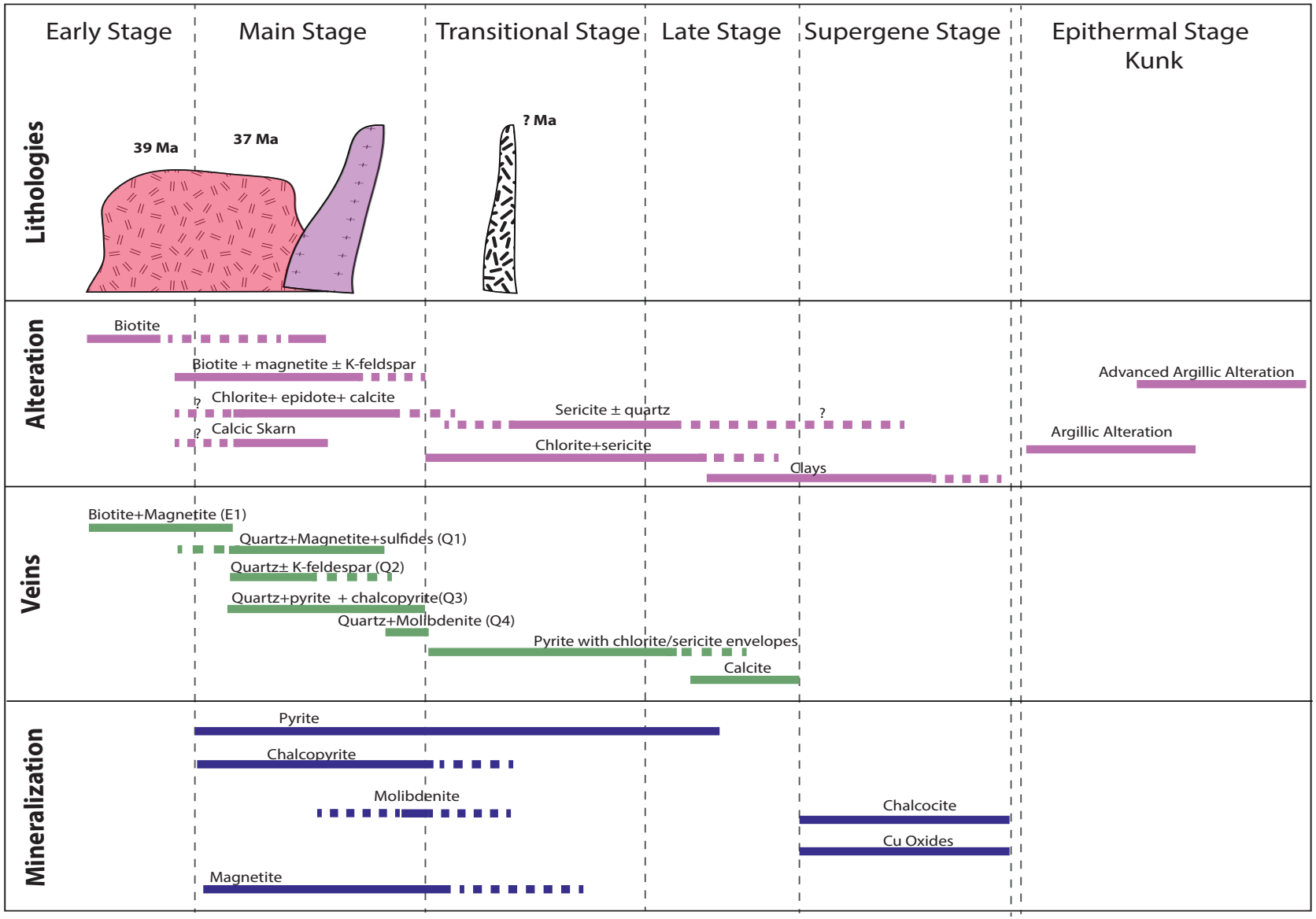

Figure 4.17 Temporal evolution chart for the Halilağa District , considering porphyry mineralization and epithermal mineralization at Kunk.

4.6. Alteration Geochemistry

4.6.1. Molar ratios

Lithogeochemistry has been widely applied to volcanic-hosted massive sulfides deposits (VHMS, e.g., Gemmell and Large, 1992; Madeisky and Stanley, 1993) and in lesser extent to porphyry and epithermal deposits (Warren et al., 2007; Urqueta et al., 2009; Davies and Whitehead, 2010). Particularly, molar ratios plots have proved to be an effective method to identify alterations types in mineral deposits (e.g., Warren et al., 2007; Davies and Whitehead, 2010) and moreover they allow the quantification of compositional changes due to the hydrothermal process. To evaluate hydrothermal alteration, Pearce element ratios or PER (Pearce, 1968) use an immobile element denominator (e.g., Ti, Zr, Al) and a mobile element (Na, K, Ca), during hydrothermal alteration, as numerator. The slope of this scatterplot is function of the material transfer process stoichiometry. If the denominator is not an immobile element, this ratio is named general element ratio (GER). The slope on a GER scatterplot is only function of the initial composition of the rocks (Madeisky and Stanley, 1993). Specific hydrothermal phases plot in nodes whereas the addition or loss of that phase results in displacement from those nodes.

In order to characterize hydrothermal alteration in the deposit a GER diagram using molar (2Ca+Na+K)/Al geochemical concentrations versus molar K/Al (Warren et al., 2007) is used as a tool to graphically evaluate K, Ca, and Na metasomatism and other Al-rich alterations. The mineral nodes are in function of the K, Ca, Na, and Al ratios: (1,1) for K-feldspar and biotite, (1,0) for albite plagioclase, (0,0) for Al-bearing phases without K, Ca or Na (chlorite, kaolinite), and (0.33, 0.33) for K-mica. If Al is immobile during the hydrothermal alteration the displacement of the altered samples from fresh rock compositions is proportional to K, Ca, and Na hydrothermal metasomatism and the displacement towards those nodes reflects the evolution of the hydrothermal system in the deposit (Madeisky and Stanley, 1993; Warren et al., 2007).

In the (2Ca+Na+K)/Al versus K/Al (Figure 4.4) fresher samples exhibit two trends: trend 1 towards K-enrichment and therefore higher K/Al ratios and trend 2 towards Na and Ca enrichment and therefore higher (2Ca+Na+K)/Al. Another trend (trend 3, Figure 4.4) is defined due to overprinting of biotite + magnetite ± K-feldspar by sericite ± quartz alteration; resulting in migration from intermediate K/Al ratios due to K-silicate alteration to the K-mica (muscovite) node. Mineralized samples (>3000 ppm Cu) correspond to samples in the biotite + magnetite ± K-feldspar (Figure 4.4b) and sericite ± quartz alterations, along trend 3. In contrast, poorly mineralized samples (<1000 ppm Cu) exhibit

lower K/Al and are classified as chlorite ± sericite (Figure 4.4e) or propylitic (chlorite + epidote + calcite, Figure 4.4b).

The diagram (Fe+Mg)/Al versus K/Al permit the classification of chlorite, muscovite, and biotite, the most common alteration minerals in Halilağa. The results shown in Figure 4.18a, suggest two major trends indicated with gray arrows. Biotite + magnetite ± K-feldspar altered samples range from moderate (Fe+Mg)/Al ratios (~1.5) towards the muscovite node, suggesting control on the muscovite overprinting of biotite alteration. On other hand, most of the chlorite ± sericite altered samples contain low K/Al and (Fe+Mg)/Al ratios moving towards the origin without showing a clear trend between chlorite and muscovite nodes.

K-enriched samples (biotite + magnetite ± K-feldspar and sericite ± quartz altered) exhibit lower compositions of Al_2O_3 and TiO_2 (Figure 4.18b). In contrast, chlorite ± sericite and chlorite + epidote + calcite alteration contain higher Al_2O_3 and TiO_2. Those higher contents in Al, partially explain the low (Fe+Mg)/Al s and K/Al molar ratios observed in Figure 4.18a.

4.6.2. Alteration mass balance

4.6.2.1. Samples and analytical and calculation procedure

Mass transfer calculation was used to quantify metasomatism and fluid composition within each alteration assemblage. The first step consisted of selecting homogeneous and representative samples from the same lithology, in this case the quartz monzonitic stock. The selection of sample pairs was difficult due to alteration overprinting and intense veining that affect the alterations and change results in calculations. The samples were chosen with extreme precaution to avoid those issues. One fresher sample (Appendix B3, HD-60 720) and four representative samples from the biotite + magnetite ± K-feldspar (Figure 4.4b), chlorite + epidote + calcite (Figure 4.4c), sericite ± quartz (Figure 4.4d), and chlorite ± sericite (Figure 4.4e) assemblages were selected to compare the gain or loss for specific elements compared with the fresher sample. A brief sample description is included in Table 4.4.

Following the sample selection stage, it is necessary to evaluate immobile elements during the hydrothermal alteration. Classical elements that are immobile during the hydrothermal alteration are Al, Ti, and Zr. Using the Al_2O_3 versus TiO_2 (Figure 4.18b) diagram is observed that linear trends can be projected through the origin indicating that both elements are immobile (Madeisky and Stanley, 1993; Warren et al., 2007).

Because Al participates in all hydrothermal alterations and can be easily mobilized, in the next

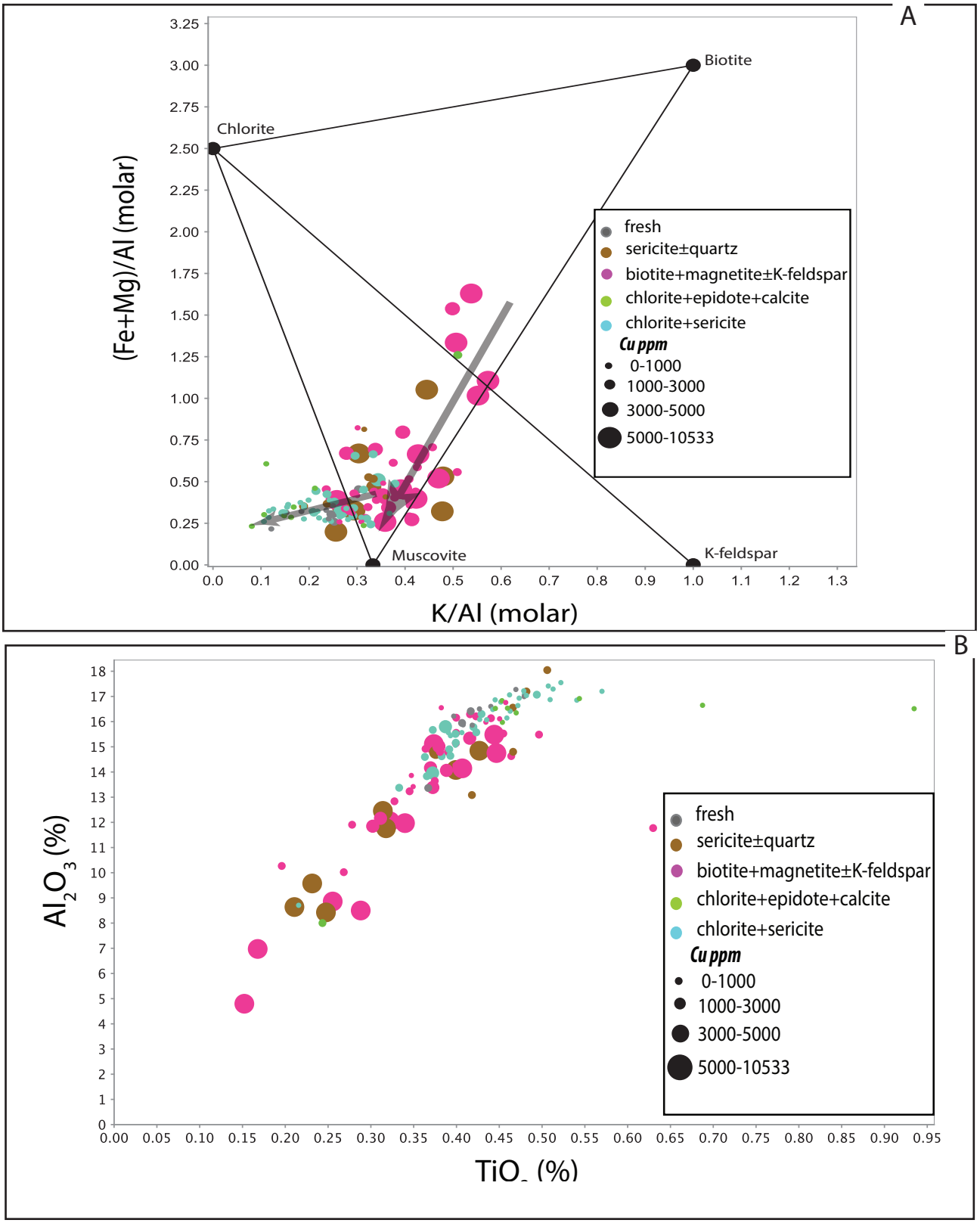

Figure 4.18. a) Chlorite-muscovite-K-feldspar scatterplot b) Conserved element scatterplots Al_2O_3 versus TiO_2 diagram. Most of the data fall on a single line from the origin suggesting that those elements are immobile. There is a significant system size change suggested from the trend between fresh samples to Cu-rich samples (Stanley and Madeisky, 1994).

calculation TiO_2 was used as the immobile element. Gains and losses were calculated following the Grant's equation (Grant, 1986):

$$\Delta C=(C_i^A)/(C_i^B)\ C^B-C^A$$

Where ΔC= mass change per 100g of rock for major elements or in parts per million (ppm) for trace elements and parts per billon (ppb) for Au, C^A = fresh sample, C^B = altered sample, i=immobile element.

This procedure was performed for the four main types of alterations in the Halilağa porphyry stock. The results for K-silicate (biotite + magnetite ± K-feldspar), propylitic (chlorite + epidote + calcite), sericite ± quartz, and chlorite ± sericite assemblages can be observed in column plots in Figure 4.19 and also in Table 4.5. For the purpose of major gains and losses estimation, a graphical approach is used (Figure 4.19). Volume changes can also be determined based on mass changes if density is measured from the parent and altered rock. In this study, density was not therefore volume implications cannot be quantitative determined.

4.6.2.2. Biotite + magnetite ± K-feldspar

K-silicate alteration has a considerable gain of Si and Fe and lesser gains of K, S, Cu, and Zn; removed elements are Ba, Ca, Na, and Sr. No variation was observed in C, Rb, Mo, Pb, Ni, As, Bi, Tl, and Se (Table 4.5). Inevitably for this alteration, the sample has quartz veins (20%), so the increase of Si is partially attributed to quartz veins. In K-silicate alteration the gain of K and losses of Ca are product of replacement of primary hornblende with secondary biotite. Fe addition is explained by the magnetite, present in this alteration. Increases in S are due to the sulfides addition (chalcopyrite and pyrite). Na losses reflect the albitic-plagioclase replacement by K-feldspar, this change in mineralogy

Table 4.4 Sample used in mass balance calculation

Alteration	Sample	Description	Veins
Fresher	HD-60 720	Ground mass/phenocrysts is 70/30. Phenocrysts are: plagioclases (20%), quartz (5%), hornblende (15%). Replacement textures in mafics: chlorite after secondary biotite after hornblende.	-
biotite+magnetite±K-feldspar	HD-01 61	intense replacement of biotite + magnetite ± K-feldspar (Figure 4.4b) observable in phenocrysts and groundmass	Quartz 20%
chlorite+epidote+-calcite	HD-80 661.15	Selective epidote in felsic site and chlorite in mafic site only minor calcite is observed in the rock (Figure 4.4c).	-
sericite ± quartz	HD-01 31	Selective alteration; sericite replaces plagioclases and chlorite overprints secondary biotite (Figure 4.4e).	Pyrite (5%), Quartz (10%)
chlorite +sericite	HD-01 271	Pervasive sericite alteration, quartz veins, and limonites (Figure 4.4d).	-

is observed in stained samples; fresher samples contain more Na-plagioclase (Appendix B3, HD-38-310) and biotite + magnetite ± K-feldspar altered samples contain less Na-plagioclase and more K-feldspar (Appendix B3, HD-80-99). Removal of Ba and Sr is due to feldspar destruction.

4.6.2.3. Chlorite + epidote + calcite

In propylitic assemblages elements gained are Ca, S and minor Na; removed elements are K, Si, Al, Ba, Rb, Sr, Cu and Au (Figure 4.11c-d). Elements without major variations in this assemblage are: Fe, Mg, Na, C, V, Pb, Zn, Ni, As, Bi, Tl, and Se. Ca is added in calcite, epidote and gypsum. Increases in S occur due to pyrite increase, because this is the only assemblage depleted in Cu relative to the less altered sample. Desilicification is typical of propylitic assemblages and indicates a prograde path (Ulrich and Heinrich, 2002). Depletion of K, Rb, Ba, and Sr indicates major feldspar destructive alteration overprint.

4.6.2.4. Sericite ± quartz

Sericite assemblage has increases of Si, Fe, S, Cu, Au, Pb, As (Figure 4.19e-f). Na, Ca, Sr, and Mg are lost due the muscovite replacement of plagioclases and biotite. Silicification, pyrite veins (5%), and quartz veining (10%) explain the increase of Si. Fe, S, and Cu are explained by the addition of pyrite and maybe chalcopyrite into the system, but chalcopyrite could also be part of the K-silicate alteration overprinted by sericite ± quartz alteration. Sr and Ba reflect plagioclase breakdown by sericite. K contents in this alteration are not particularly high compared with fresher samples resulting in a relatively immobility of K, instead Rb is depleted (Rb substitutes for K in minerals). This is confirmed by a stained sample (Appendix B3, HD-38-310) where K-rich zones are associated with vein halos and patches, while most of the ground mass is more Na-rich. Increase of V has been observed in sericite from this alteration in other deposits (e.g. Halley et al., 2015).

4.6.2.5. Chlorite ± sericite

Chlorite ± sericite assemblage is largely depleted in Si, Na, Ba, Ca, Al, and Sr (Figure 4.19g-h). In contrast, chlorite ± sericite assemblage gains Fe, S, Cu, Au, and Zn. K, Mg, Rb, Pb, V, Ni, As, Bi, Tl, and Se continue without major variations. The increase of Fe is controlled by chlorite replacement after mafics and also by the increase of pyrite and chalcopyrite, reflected in increases in Cu and S. Na, Ba and Sr reflects plagioclase breakdown and replacement by sericite.

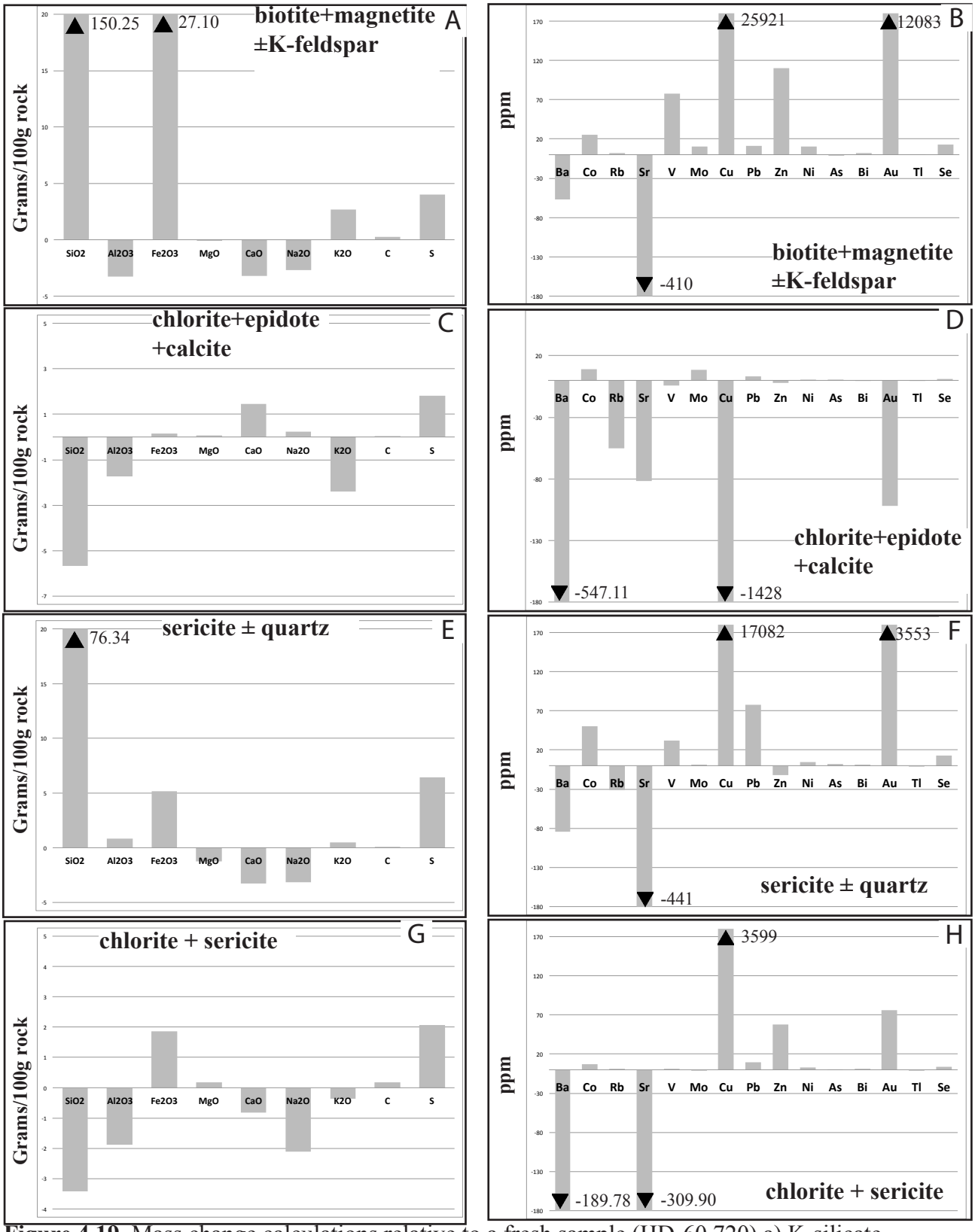

Figure 4.19. Mass change calculations relative to a fresh sample (HD-60 720) a) K-silicate alteration (sample HD-01 62); b)Propylitic alteration (chlorite+ epidote +calcite) from sample HD-80 661.15 c) Sericite ± quartz alteration (from sample HD-01 31); d) Chlorite+sericite alteration (from sample HD-01 271). Note that y-axis are in different scales for each alteration group. See Figure 4.4 for samples pictures and position in the (2Ca+Na+K)/Al versus K/Al diagram.

4.6.3. Alteration mass balance summary

A common pattern for all alterations is Sr depletion caused by feldspar destructive alteration that overprints all alterations. Pathfinder elements that remained constant during the four alterations are: Ni, As, Bi, Tl, and Se.

4.6.4. Alteration mass balance limitations

Alteration mass balance calculations in this study has demonstrated important mass changes between the alteration types. However, there are many limitations and assumptions of the approach used in this study.

First, mass addition has density and volume implications. Specifically for biotite +magnetite±K-feldspar 150g of silica are added per 100 g of rock, in this case an increase of volume is more likely than a variation in density.

Second, the use of only one representative sample of each hydrothermal alteration is not the best scenario for comparing element interaction due to specific features of each sample (veins, intensity of alteration). Furthermore, because only one sample was used to determine the elements variation in each alteration type it was not possible to estimate quantitative errors or give a confidence interval for the gains or losses (e.g. Bouzari and Clark, 2006). A solution for this issue would be having a group of altered samples and background, in order to have a valid statistic confidence interval for mass changes that does not rely in a single sample.

Third, the assumption that the starting composition is in fact completely unaltered is not completely accurate. In porphyry deposits most of the samples present some degree of hydrothermal alteration, therefore a "fresh" sample is not completely unaltered making this calculation procedure even more challenging. An approach would be considering mass and volume changes between pair of alteration, rather than from a non-altered sample.

Fourth, veins in altered rocks indicate that there was space in the rock before the hydrothermal alteration occurred and the original volume was lower, therefore large mass addition is possible with increase in volume. In this study, biotite+magnetite±K-feldspar and sericite ± quartz assemblages exhibit larger mass changes and also contain vein infill suggesting that there was an important change in volume as well.

Table 4.5 Elements gain-loss in alterations in the Halilağa Deposit.

Alteration	Gain	Loss	No variation
biotite + magnetite ± K-feldspar	Si, Fe, K, S, Zn, V	Ba, Ca, Na, Sr	C, Rb, Mo, Pb, Ni, As, Bi, Tl, Se
chlorite + epidote + calcite	Ca, S	Si, K, Rb, Sr, Zn, Ba, Al, Cu	Fe, Mg, Na, C, V, P, Zn, Ni, As, Bi, Tl, Se
sericite ± quartz	Si, Fe, S, Co, V, Cu, Pb, Au	Na, Ca, Mg, Ba, Sr, Rb	K, C, Mo, Ni, As, Bi, Tl, Se
chlorite + sericite	Fe, S, Cu, Zn, Au	Si, Na, Ca, Al, Ba, Sr	Mg, Ca, K, C, Rb, V, Pb, Ni, As, Bi, Tl, Se

4.7. Reflectance Spectroscopy Analysis

4.7.1. 2200 nm wavelength analysis

To evaluate quantitative parameters box plots were created using the wavelength around the Al-OH absorption feature and the depth for samples that displayed muscovite, paragonite, paragonitic-illite, phengite, and phengitic-illite as the primary mineral. Figure 4.20b shows that the mineral classification is consistent with the theoretical values expected for the minerals (Figure 4.20a); paragonite has the lower wavelength (mean=2195, median=2194) and phengite has the higher wavelength (mean=2217, median=2219) compared with the rest of the minerals (muscovite, paragonitic-illite, phengitic-illite). Relative to drill core depth (Figure 4.20c) the distribution of these white micas and clays has some variations. Muscovite and paragonite are located at shallower depths (from 80 m) and muscovite has a wider range until almost 250 m. In contrast, phengite is located at higher depths (from 160 to 320 m).

A sample depth versus the wavelength of the Al-OH absorption feature scatterplot (Figure 4.20d), for six drill holes and with size relative to Cu contents, indicate that Cu is commonly associated with muscovite and at depths shallower than 300 m. Exceptions are observed in HD-13A located in the southern Kestane area, crossing the South Fault and in HD-08 located to the east of Kestane and where more than 150 m volcanic covers the porphyry stock. In HD-13A there are two intervals with higher mineralization associated with phengite between 100-200m and 325-475m. In HD-08 the mineralization occurs between 275 to 375 m associated with muscovite and lesser to paragonitic-illite.

The 2D distribution of the 2200 nm wavelength for white micas and the sericite crystallinity index (CI) is shown in Figure 4.21. In general, the core of the hydrothermal system that host Cu and Au mineralization (Figure 4.1 and 4.2) coincides with zones in the range of 2202-2205 nm and sericite crystallinity index higher than 0.89 CI, coinciding with muscovite compositions and therefore more

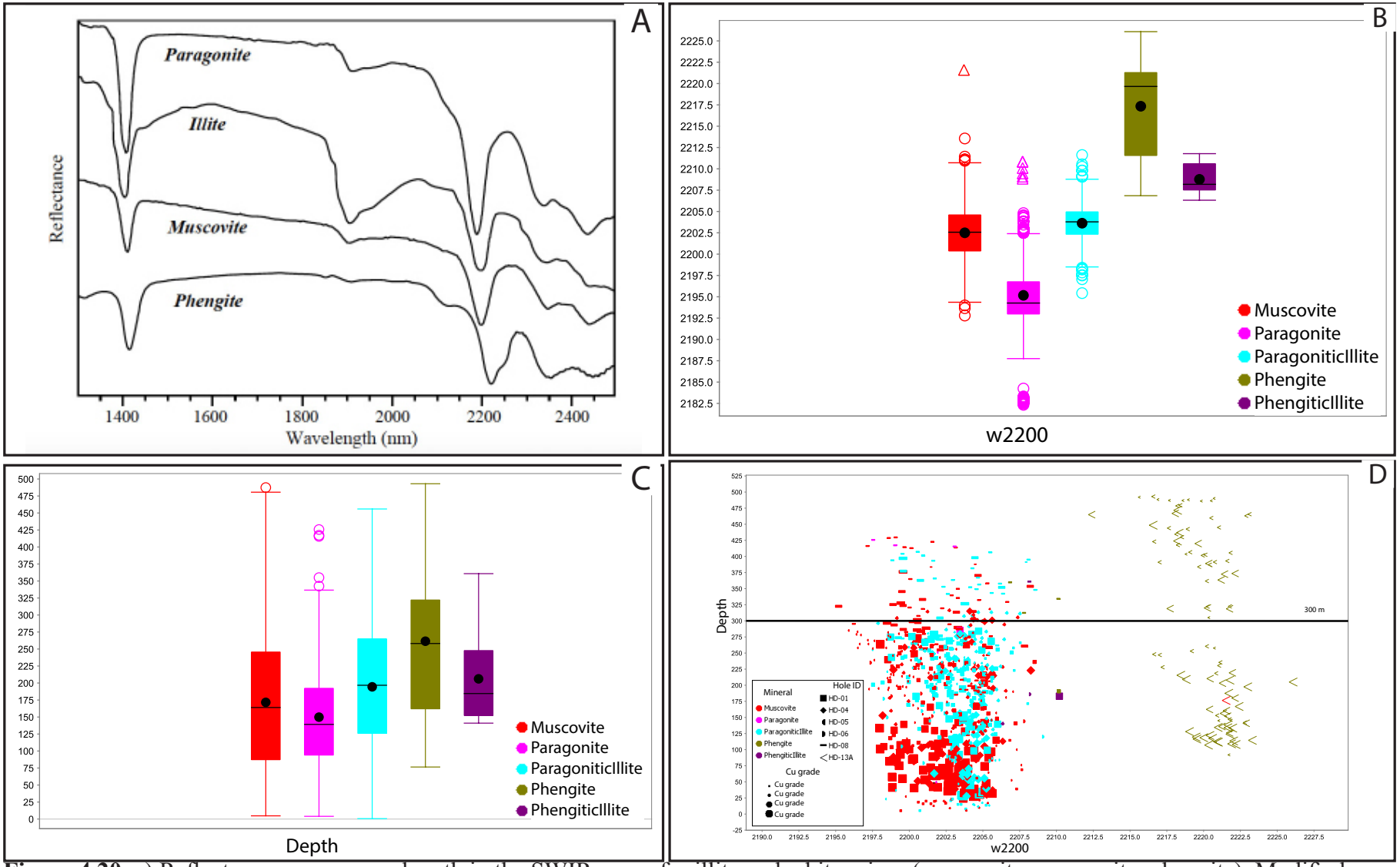

Figure 4.20. a) Reflectance versus wavelength in the SWIR range for illite and white micas (paragonite, muscovite, phengite). Modified from Scott and Yang, 1997; b) Box plot for white micas and montmorillonite for the wavelength at 2200 nm (Al-OH absorption feature); c) Box plot for white micas and montmorillonite relative to depth; d) Depth versus the wavelength of the Al-OH absorption feature scatter-plot for selected drill holes (HD-01, HD-04, HD05, HD-06, HD-08, HD-13A).

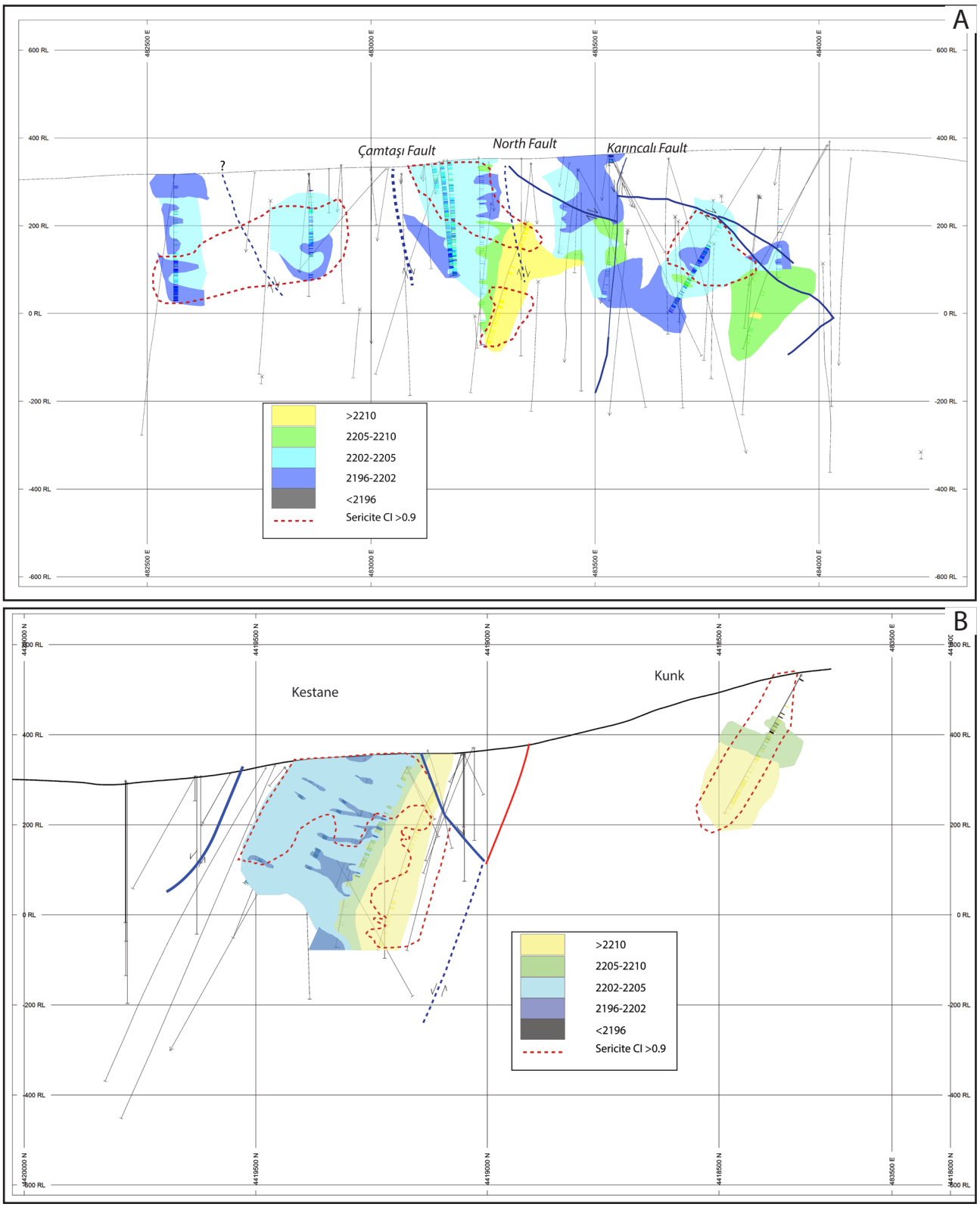

Figure 4.21. 2200 nm wavelength distribution in cross-section, sericite crystallinity index (CI) is indicated with dashed red line. a) A-A'; b) B-B'

acidic pH than other white micas (Scott and Yang, 1997). However, not all zones with high CI or >2202 nm wavelength spectra for white micas correspond to mineralized areas.

4.8. Re-Os Geochronology

The age of the mineralized intrusions in Halilağa has been obtained with U-Pb geochronology and indicated 39 and 37 Ma for the two phases of the porphyry stock (Table 2.2.) However, these ages might not represent the age of mineralization. Re-Os in molybdenite is considered a robust geochronological method to study porphyry deposits (Chiaradia et al., 2013) and in this study is used to determine the mineralization age in Halilağa.

Re-Os in molybdenite was analyzed at the University of Alberta in Edmonton (See Appendix D for details on analytical methods). The sample was taken from drill core HD-94 402, located in the southern border of the porphyry mineralization. Molybdenite occurs in a quartz + molybdenite vein that crosscut a quartz + pyrite + chalcopyrite vein (Figure 4.22), suggesting that molybdenite postdate Cu mineralization. The hydrothermal alteration of the sample is selective to phenocrysts: sericite after plagioclase and biotite after hornblende and incipient chlorite replacement with intense quartz veining. Re-Os geochronology yielded an age of 39.56 ± 0.21 Ma (Table 4.6), confirming the Eocene age of the porphyry mineralization in Halilağa and indicating a maximum Cu mineralization age.

Table 4.6 Re-Os geochronology

Sample	Re ppm	± 2σ	^{187}Re ppm	± 2σ	^{187}Os ppb	± 2σ	Model Age (Ma)	± 2σ (Ma)
HD-94 402	1555	5	977.1	2.9	644.2	1.9	39.56	0.21

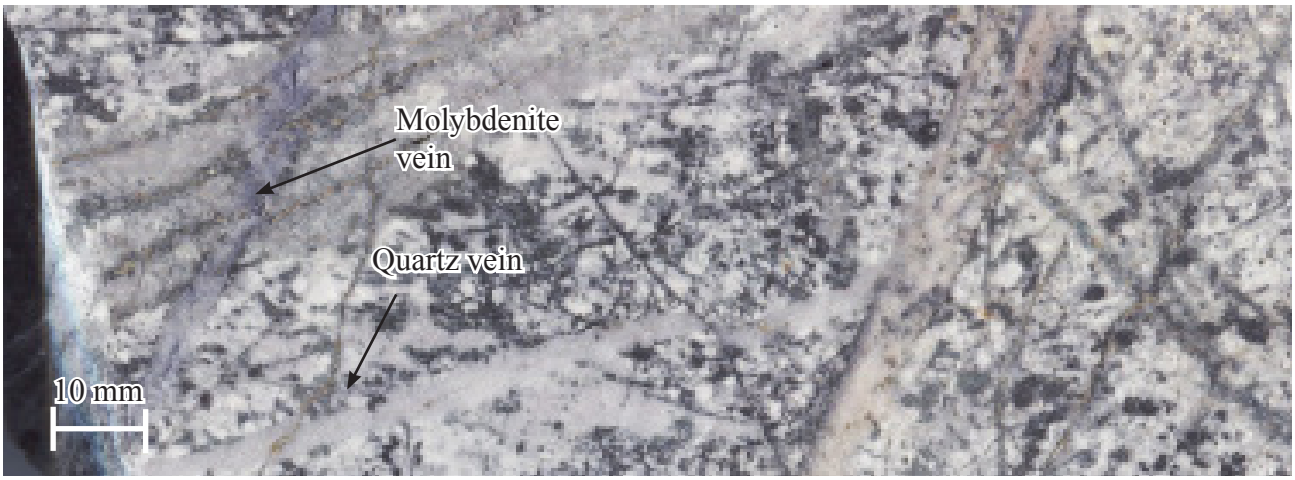

Figure 4.22 Re-Os sample from HD-94 402.

Chapter 5: Discussions

In order to determine the evolution and understand post-mineral modifications of the Halilağa deposit, three specific objectives were defined: 1) To determine the volcanic and plutonic setting of the Halilağa District to elucidate the geological evolution and the role of magmas in mineralization; 2) Establish the timing of Halilağa hydrothermal events and nearby epithermal mineralization; 3) Verify the role of post- mineralization faults in the current geometry of the Halilağa porphyry deposit.

Herein, the results of the volcanic and plutonic setting of the Halilağa District are revised and correlated with units in the district and in the context of the geological evolution of Biga Peninsula. The temporal and spatial relationships of magmatic rocks, Cu-Au mineralization and hydrothermal processes in the Halilağa District are compared with other porphyry deposits in Biga Peninsula and globally. The effects of post-mineral hydrothermal overprinting and deformation are examined in the context of the current anatomy of the deposit.

5.1. Magmatic Setting of the Halilağa District

The geology of the Halilağa District is dominated by volcanic and sub-volcanic rocks and associated plutonic rocks of Eocene and Oligocene age. To facilitate the description of the stratigraphic correlations and discussions four localities are employed: Pirentepe, Kestane, Bakırlık- Kunk, and Dereoba-Keçiağılı (Figure 5.1). Previous maps of the area (Duru et al., 2012), suggested two major volcanic packages that are attributed to the Oligocene Hallaçlar Volcanics and the Miocene Ezine Volcanics. $^{40}Ar/^{39}Ar$ biotite geochronological data from Pirentepe andesites, interpreted as part of the Ezine Volcanics, yielded two contrasting age plateaus at 26.3 ± 2.5 Ma and 36.9 ± 0.83 Ma (Kuşcu, 2009). Sanchez (2012) obtained a 27.2 Ma for andesites (groundmass) considered to host porphyry mineralization and part of the Hallaçlar Volcanics. However, new U-Pb age data obtained in this study indicated Oligocene and Eocene ages for those volcanic packages respectively with ages of 40-38 Ma for the sequence attributed to the Hallaçlar Volcanics and of 28 Ma for the Ezine Volcanics. For intrusions, Sanchez (2012) dated the Kestane stock ($^{40}Ar/^{39}Ar$ on K-feldspar) and the Evçiler pluton ($^{40}Ar/^{39}Ar$ on K-feldspar and biotite) and obtained plateau ages of 24.81 ± 0.14 Ma and 25.15 ± 0.15 Ma for both intrusions. Similarly, Kuşcu (2009) obtained a plateau age of 26.27 ± 0.19 Ma at the Kestane stock ($^{40}Ar/^{39}Ar$ on muscovite). As a result, the porphyry mineralization was considered to be Late Oligocene whereas this study indicated an Eocene age for the causative intrusions of porphyry mineralization.

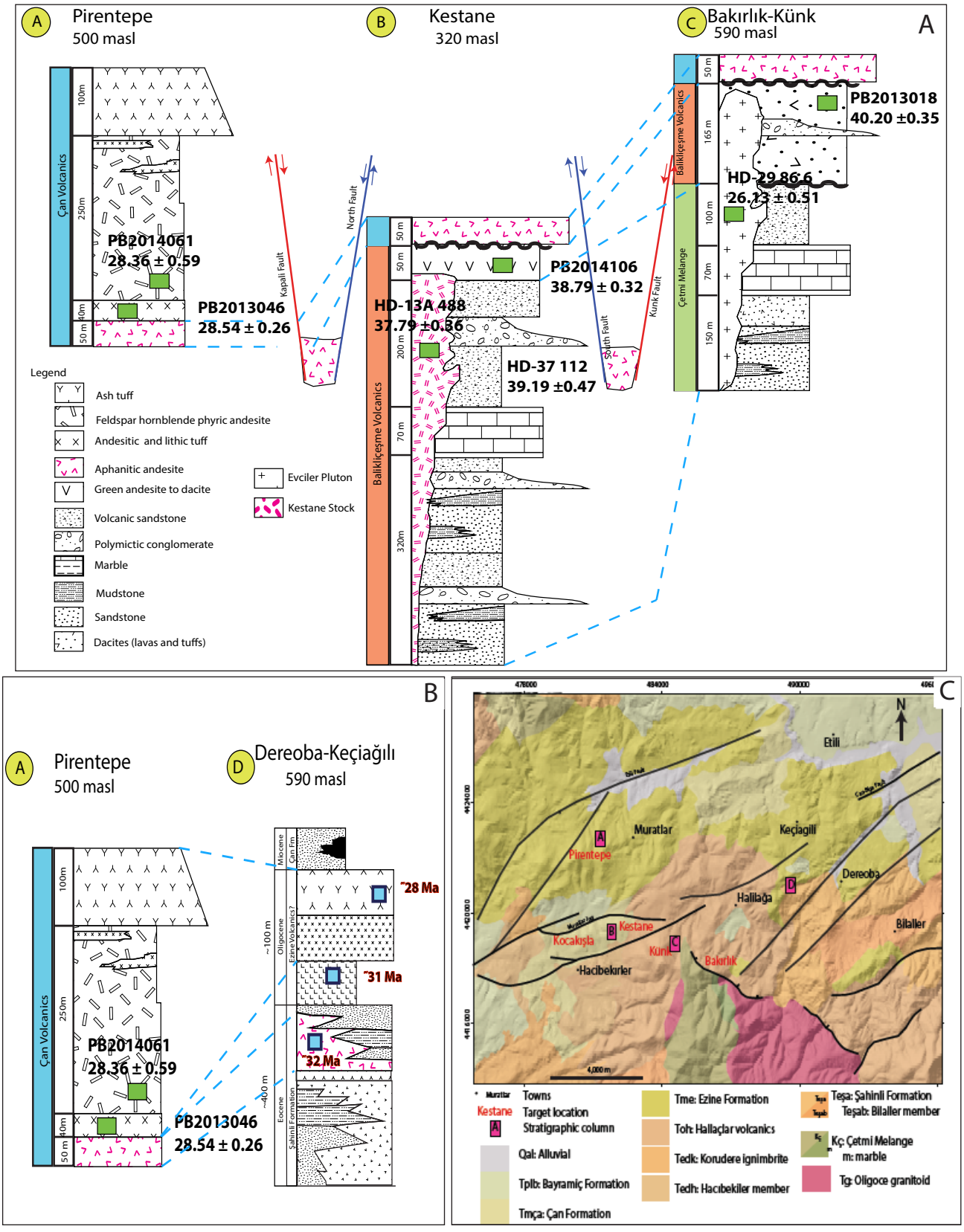

Figure 5.1 Stratigraphic columns for a) Pirentepe, Kestane and Bakirlik-Kunk structural blocks including U-Pb geochronology; b) Pirentepe and Dereoba-Keciagili; c) Regional MTA Map (Duru et al., 2012), showing stratigraphic columns locations..

The Eocene volcano-sedimentary sequence includes limestones, volcanic sandstone and mudstone, and andesitic to dacitic lavas. Volcano-sedimentary rocks at the Kestane graben present a sequence similar to the volcano-sedimentary sequence at Bakırlık- Kunk stratigraphic column (Figure 5.1a, columns B and C). Despite the potential different age of those sequences, the first is considered Eocene while the later is attributed to the Cretaceous Çetmi Mélange, correlations between both sequences can be made due to: similar lithology and the presence of a limestone level with similar thickness (ca. 50 m) in both locations. There are not further evidences, such as geochronology or fossils, to confirm correlations between those units. Furthermore, in the Biga Peninsula limestones occurred during the Mesozoic (in the Çetmi Mélange) and the younger limestones known belong to the Soğucak Formation of Middle Eocene age (Beccaletto, 2007; Siyako and Huvaz, 2007), indicating that these sequences could be attributed to different formations. Other correlations can be made between the volcanic units that overlie the volcano-sedimentary sequence in the Kestane and the Bakırlık-Kunk. There are two lithologies outcropping these locations: the green andesite in the Kestane graben and the dacite in Kunk hill. These lithologies are product of different hydrothermal alterations: intense chlorite and epidote in the green andesite and intense white mica, silicification, and pyrophyllite in the dacite; resulting in two dissimilar units. However, their primary composition and textures, with the same phenocryst minerals (plagioclases and variable rounded quartz), and comparable age dates, suggest that both lithologies are part of the same volcanic to sub-volcanic sequence that is temporally related to the intrusion of the Kestane stock. Because of the predominance of volcano-sedimentary rocks in the Eocene sequence, particularly at the Kestane graben, the depositional environment for the Eocene volcanic sequence is an alternation of volcanic rocks intercalated with shallow marine sediments, evinced by marble in western Kestane (Appendix A2).

The Oligocene volcanic sequence is slightly more mafic ranging from basaltic andesite to dacite and present coherent lavas and pyroclastic facies (e.g. Figure 2.8e). The basaltic andesite to andesite unit is stratigraphically positioned in the base of the Pirentepe column and is correlated with the unit observed on the top of the Kestane and Bakırlık- Kunk columns and furthermore a similar unit outcrops 8 km east in the village of Dereoba indicating a lateral continuity of the Oligocene volcanics. Similarly, the overlying sequence dominated by porphyritic sub-volcanics and tuffs also can be correlated with sequences in the Dereoba- Keçiağılı column. In the Oligocene unit, the fragmented crystals and re-worked clasts indicate a subaerial pyroclastic origin consistent with the Çan Volcanics (Ercan 1995) of Middle Oligocene age (Ercan et al., 1995; Altunkaynak and Genç, 2008). The basaltic andesite to andesite represents a coherent unit compared with the overlying sub-volcanic to tufficeous sequence;

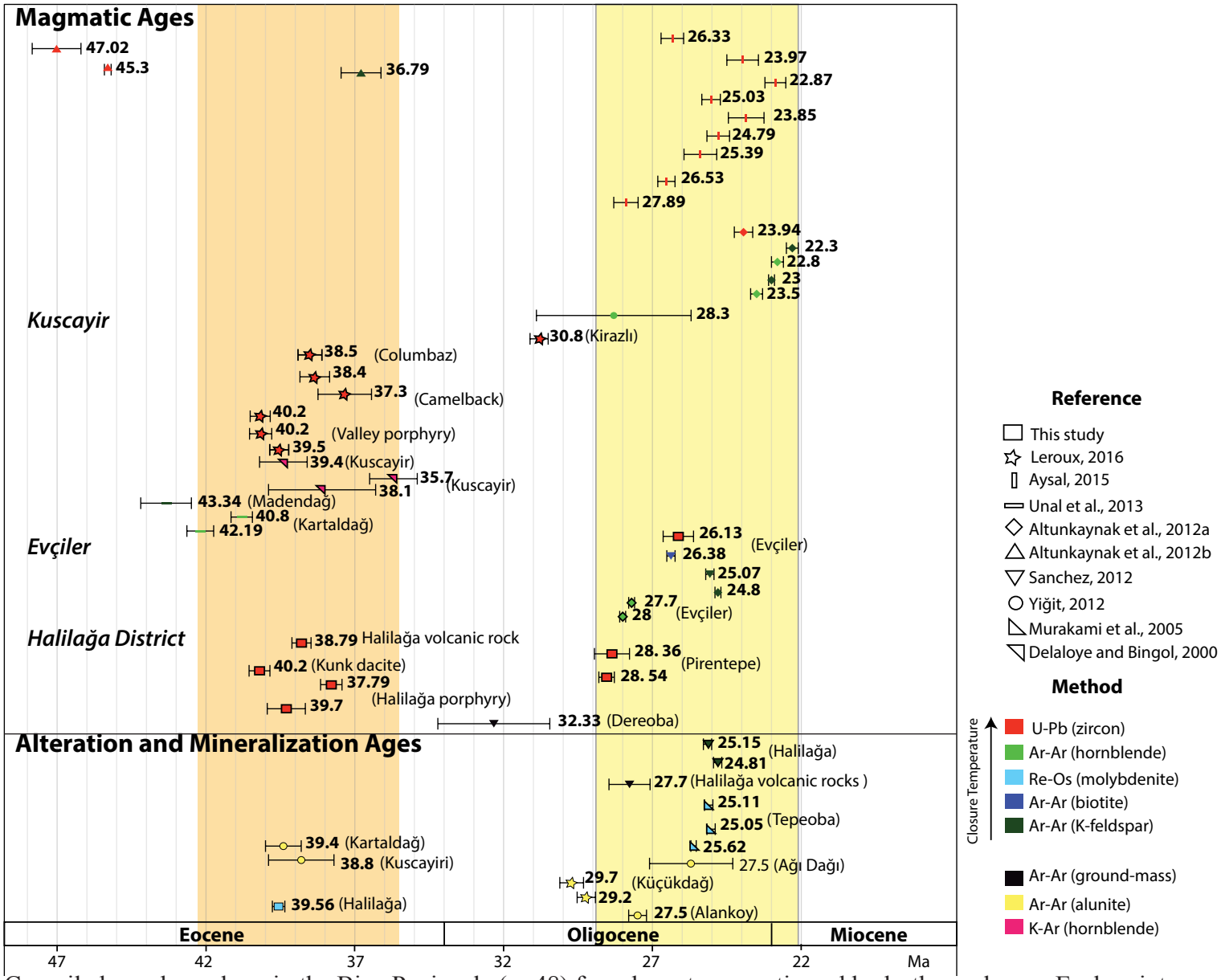

Figure 5.2 Compiled geochronology in the Biga Peninsula (n=48) for relevant magmatic and hydrothermal ages. Each point represents the age and 2-sigma error for each sample.

coherent lavas and pyroclastic rocks suggests episodes of explosive and effusive volcanism in the area during the Oligocene. A common characteristic between the Eocene and Oligocene volcanic sequences in the Halilağa District is the abundance of sub-volcanic intrusive rocks suggesting shallow emplacement and relatively rapid cooling of those rocks.

The three intrusions present in the area: the Kestane stock, the Kocakışla stock, and the Evçiler pluton, differ in age, geochemical signatures, and texture. The Kestane stock includes three intrusive phases of which two are mineralized. The compositions of the mineralized intrusions range from granodiorite to granite, while the later phase is of dioritic-gabbroic composition. Intrusive contacts between the mineralized intrusions are diffuse, but there is a correlation of the intrusions with alteration intensity, Cu grades, and immobile elements ratios (Figure 2.11 f). The geometry of the mineralized intrusive body, considering Phase A and Phase B is controlled by faults following the E-trending North and South Fault. The latest dioritic-gabbroic dikes are narrow and pencil-shaped dikes. The younger Evçiler pluton is texturally and compositionally similar to the Kestane stock and despite the different age between the Middle Eocene Kestane stock and the Late Oligocene Evçiler pluton, immobile classification diagram for the intrusive units (Y versus TiO_2; Figure 2.10 f) suggest one group that includes the both intrusions, and excludes dykes and the Kocakışla stock, indicating a similar evolution trend for those intrusions. The age of the equigranular Kocakışla stock in the western Kestane area is undetermined. However, geochemical, textural, hydrothermal alteration differences with the Kestane stock as presented herein suggest a different timing of this intrusion.

Geochronology of the Kestane stock and nearby volcanic rocks documents a previously unrecognised Middle Eocene age (40 to 37 Ma) magmatic event as well as supporting the previously recognised Oligocene (~28 Ma) event. U-Pb geochronology indicates a minimum range of 40-38 Ma for the Eocene volcanic sequence. Specifically, the age obtained for the plagioclase and quartz-phyric "green andesite", in the Kestane area, is 38.79 ± 0.32 Ma (PB2014106, Table 2.2) and for the Kunk dacite is 40.2 ± 0.35 Ma (PB2013018). Similarly, the magmatic ages from the two phases of the porphyry stock range from 39.19 ± 0.47 to 37.79 ± 0.36 Ma (Samples HD-37-112 and HD-13A-488 respectively, Table 2.2), suggesting that the volcanic activity is pre- and syn- stock emplacement. Inherited zircons with a concordia age of 71.9 ±1.3 Ma in the sample HD-37-112 of 39 Ma register Cretaceous magmatism coincident with the Sevketiye pluton (71.9 ±1.8, Delaloye and Bingöl, 2000), the only record of Mesozoic plutonism in the Biga Peninsula. The basaltic andesite to andesite at the base of the Oligocene sequence lack zircons, but a groundmass $^{40}Ar/^{39}Ar$ age date by Sanchez (2012) from a micro-porphyritic andesite from the Dereoba area that correlates with the basaltic andesites

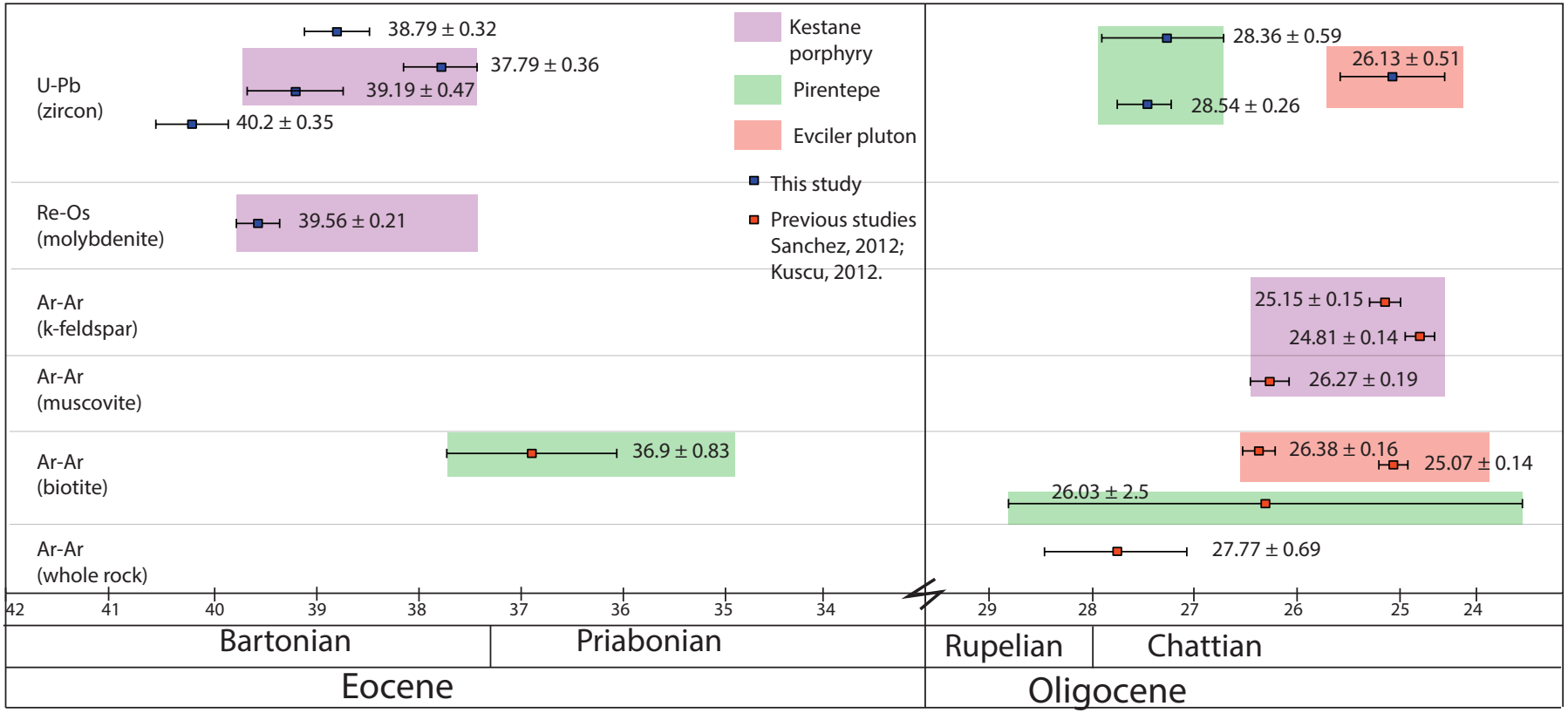

Figure 5.3 Compiled geochronology in the Halilağa District showing the results of this work and previous studies.

to andesites from the Kestane area gave a plateau of 32.33 ± 1.84 Ma, suggesting Early Oligocene magmatism. Geochronological results from the top and bottom of the Pirentepe volcanic sequence give a similar age of 28.36 ± 0.59 and 28.54 ± 0.26 Ma (samples PB2014061 and PB2013046 respectively, Table 2.2), indicating a single brief event. Similarly, in the Keçiağılı area, Sanchez (2012) obtained $^{40}Ar/^{39}Ar$ (groundmass) age of 28.63 ± 0.16 Ma in a porphyritic dacite (ignimbrite) that is texturally and temporally comparable with the vitric tuff breccia, on the top of the Pirentepe sequence (Figure 5.1). The youngest Oligocene age obtained in this study is 26.32 ± 0.61 Ma (sample HD-29, Table 2.2) in the Evçiler pluton, an extensive pluton with different intrusive phases ranging from granodiorite to monzodiorite (Öngen, 1992; Genç, 1998). Previous $^{40}Ar/^{39}Ar$ hornblende indicated a magmatic age of 28 Ma, while $^{40}Ar/^{39}Ar$ cooling ages in biotite returned ages of 24-25 Ma and K-feldspar of 26 Ma (Altunkaynak et al., 2012a; Figure 5.2). Therefore previous studies and geochronology presented in this study, based on the Halilağa District, suggest a range of 26-28 Ma for the Oligocene magmatism in this area and provides proof for the plutonic and volcanic temporal association during Late Oligocene (Chattian) suggested by many authors in the Biga Peninsula (e.g. Genç, 1998, Altunkaynak and Genç, 2008).

Previous $^{40}Ar/^{39}Ar$ K-feldspar geochronology in the Halilağa deposit indicated a late Oligocene age for the mineralized stock (24-26 Ma; Sanchez, 2012) suggesting genetic connections with the Evçiler pluton, located 2 km SE of the porphyry deposit. However, the Eocene age of the Halilağa porphyry deposit precludes a genetic link with the Evçiler pluton. In contrast, the age of the mineralization and magmatism in the Halilağa porphyry deposit is contemporaneous with the ages of the Kuşcayir District, located 13 km to the WNW where previous $^{40}K/^{39}Ar$ hornblende dates range from 38 to 39 Ma (Delaloye and Bingöl, 2000) suggesting a temporal connection between the Halilağa porphyry deposit and the Kuşcayir intrusion.

5.1.1. Relationship with geological evolution of the Biga Peninsula

Magmatic rocks of Eocene to Miocene age are widely distributed and in the Biga Peninsula. Previous studies in Biga Peninsula and Western Turkey indicated that post-collisional magmatism started in the Eocene and spans to Miocene. Geochemistry of those rocks reveals changes in the evolution of those suites from dominant subduction signatures (enrichment in incompatible elements) with calc-alkaline affinity in the Eocene to an alkaline bimodal magmatism with decreasing subduction signature in the Miocene (Altunkaynak and Genç, 2008; Dilek and Altunkaynak, 2009). Furthermore, Early Eocene intrusions in Biga Peninsula have adakite-like signatures, based on Sr/Y ratios, indicating

thickened crust at that time, while the Middle Eocene intrusions have normal arc signatures, suggesting thinned lithosphere product of extension (Altunkaynak et al., 2012b). Sr and Nd isotopes in sequences younger than 24 Ma present continuous decrease in $^{143}Nd/^{144}Nd$ and a concomitant increase in $^{87}Sr/^{86}Sr$ (Altunkaynak and Genç, 2008) reflecting a decrease in subduction signature and an increase in crustal contamination respectively. After the exhumation of the Kazdağ metamorphic complex from 20 to 10 Ma (Cavazza et al., 2009), the isotopic patterns observed in younger sequences gradually decrease in crustal contamination indicating more primitive signatures (Altunkaynak and Genç, 2008; Dilek and Altunkaynak, 2009). Those geochemical and isotopic variations reflect the transition from post-collisional magmatism highly influenced by inherited subduction signatures resulting in differentiated rocks during the Eocene to an asthenosphere-derived magmatism driven by extensional tectonics during the Miocene.

The volcanic sequences in the Halilağa District were attributed to the Oligocene Hallaçlar Volcanics and Miocene Ezine Volcanics in MTA maps (Duru et al., 2012). However, U-Pb zircon geochronology demonstrates that those sequences are older, and correlated with the Balıklıçeşme Volcanics ($^{40}K/^{39}Ar$ 37.3 ± 0.9; Ercan, 1995) and the Çan Volcanics ($^{40}K/^{39}Ar$; 27.3±0.6; Ercan, 1995). The geological evolution of the Halilağa District in agreement with previous observations in central Biga Peninsula where volcanic associations are characterized by andesitic to dacitic lavas and pyroclastic rocks that are spatially associated with plutonic rocks (Ercan, 1995; Genç, 1998). The widespread volcanism, and associated intrusive activity, indicates extensive magmatism during the Paleogene. However, the Eocene is dominated by volcano-sedimentary sequences interbedded with lavas and volcaniclastic rocks, while the Oligocene sequences have a wide compositional variation and a dominance of volcanic facies. The Eocene volcanic and sedimentary sequences in the Biga Peninsula are interpreted to be formed in a marine environment (Ercan 1995; Altunkaynak and Genç, 2008) with significant shallow marine transgression during Middle Eocene, where limestones were deposited (Soğucak Formation) in the Thrace Basin and northern Biga Peninsula interbedded with andesitic lavas and tuffs (Ercan, 1995).

Geochronological results of magmatism in the Halilağa District and the Biga Peninsula, suggests that Eocene and Oligocene magmatic sequences peaks at 47-35 Ma and 28-22 Ma (Figure 5.2). There is an apparent a gap of magmatism between 35-28 Ma Eocene to Early Oligocene; one $^{40}Ar/^{39}Ar$ age from a basalt andesite in the Dereoba area falls on this field, and a U-Pb age from Kirazli has 30 Ma (Figure 5.2; Sanchez, 2012; Leroux, 2016). This gap could be explained either for data paucity or due to complications in geochronology (e.g. lack of zircons and/or resetting of low temperature

geochronometers).

5.1.2. Petrogenesis of Eocene and Oligocene magmatism

The Eocene magmatism is fundamentally classified based on intrusive units due to the paucity of unaltered volcanic samples; two volcanic samples were used in this study, but one of those (the dacite from Kunk) presented several anomalies in major and trace elements indicating hydrothermal alteration. Geochemistry of porphyry-related intrusions at Halilağa indicates medium to high-K calc-alkaline series, comparable with Au-rich porphyry Cu deposits (Sillitoe, 1997). Trace elements of the two main intrusive phases are slightly different; the altered and mineralized Phase-A present lower TiO_2 contents than the less altered and un-mineralized Phase-B indicating minor variations in the geochemistry of both phases. Compositional variations between the two main phases are also noted in the Harker diagrams (Figure 3.2), where higher SiO_2, MgO, and Al_2O_3 are observed in Phase-A. However, those results might be influenced by hydrothermal alteration. The slope from the origin in the Y versus TiO_2 diagram (Figure 2.9f) is similar for both intrusive phases indicating a cogenetic origin for the sequence (Stanley and Madeisky, 1994). In contrast, andesitic dykes present completely different compositions and the slope in the immobile elements scatterplot (Figure 2.11 f) suggests no direct connections with the Kestane stock phases. On the other hand, due to the location nearby the Kestane stock, herein the Kocakışla stock was initially considered in the Eocene magmatic rocks, but it presents several geochemical differences with the rest of the Eocene rocks. The Kocakışla stock has flat REE patterns and negative europium anomalies (Figure 3.3 b) indicating plagioclase fractionation.

Intrusions at Halilağa present: abundant hornblende phenocrysts suggesting high magmatic water content, minimal europium anomalies ($Eu_n/Eu^* \approx 1$) indicating suppression of plagioclase crystallization and/or oxidized magma, and hornblende fractionation evinced by listric shape REE patterns; those features are commonly associated with fertile porphyry-related intrusions (e.g. Dilles, 1987; Cline and Bodnar, 1991; Richards et al., 2012). However, most of the units exhibit normal arc signatures with low La/Yb and moderate Sr/Y ratios (Figure 3.6), which differ from typical adakitic signatures in porphyry deposits (Thiéblemont et al., 1997; Chiaradia et al., 2012; Mpodozis and Cornejo, 2012; Richards et al., 2012). At Halilağa, the geochemistry of porphyry-related intrusions indicates non-adakitic signatures based on REE fractionation on La/Yb ratio and slightly adakitic signatures based on Sr/Y. Non-adakitic signatures consistent with large back-arc porphyry Cu-Au deposits such as Bajo de la Alumbrera and Bingham (Richards and Kerrich, 2007; Loucks, 2014).

REE listric-shape patterns reveal hornblende fractionation for the Oligocene rocks, particularly

for the Evçiler pluton, andesitic flows and tuffs, and the dacitic crystal tuff. Those observations are consistent with petrographic observations where dominant phenocrysts are euhedral hornblende, euhedral biotite, and lath-shape plagioclase phenocrysts. Hornblende fractionation in REE patterns together with the occurrence of hornblende crystals in the rock indicates abundance of water in the magma and potential for porphyry deposits (Dilles, 1987; Cline and Bodnar, 1991; Richards et al., 2001; Richards et al., 2012). Furthermore, the adakite-like signatures of the Evçiler pluton based on Sr/Y and slightly adakite-like in the La/Yb confirming the fractionation of hydrous hornblende. However, except for the Evçiler pluton, the Oligocene volcanic rocks display strong negative europium anomalies (Figure 3.6b) suggesting important plagioclase fractionation in the younger magmatic event.

Since the Biga Peninsula is more than 800 km far from the current Hellenic subduction, the tectonic setting for epithermal and porphyry mineralization is a subject of debate (e.g. Dilek and Altunkaynak, 2009; Ersoy and Palmer, 2013; Aysal, 2015). The origin of the post-collisional Cenozoic magmatism, particularly from Eocene to Oligocene, has been attributed to the slab-break off of a previous subduction zone below the Izmir-Ankara Suture Zone (IASZ, Altunkaynak and Genç, 2008, Dilek and Altunkaynak, 2009, Ersoy and Palmer, 2013) or a slab-roll back and back-arc extension of the Hellenic slab (e.g. Jolivet et al., 2013; Aysal, 2015). In this work, the results show continuous compositions of SiO_2 in Harker diagrams and subduction signatures in the Eocene and Oligocene aged magmatic suites. Subduction signatures are inferred from negative anomalies of Ta, Nb, Tl and enrichment in large ion lithophile elements (LILE: Cs, Rb, Ba, K, Sr) and light rare earth elements (LREE). Furthermore, the tectonic classification based on Ta versus Yb and the trivariate Hf, Ta, Rb indicates volcanic arc signatures for all magmatic rocks in the district. There are not enough evidence to indicate of if the Eocene and Oligocene magmatism was back-arc or due to slab break-off either of the Hellenic slab or a subduction zone below IASZ; but because of the large distance of Biga Peninsula from the Hellenic subduction zone, a nearby subduction (below the IASZ) is a plausible explanation for the magmatism in the Biga Peninsula. Oligocene-Miocene plutons in the Biga Peninsula suggest shallow emplacement product of crustal thinning in a back-arc extensional regime and slab roll-back of the Hellenic trench (Aysal, 2015). Herein, the absence of alkalic bi-modal volcanism does not favor the hypothesis of Eocene back-arc setting. However, the position of the Eocene magmatism is clearly behind the arc, either the Hellenic or the arc below IASZ. Some important porphyry and epithermal deposits developed in back-arc setting such as Çöpler, Bingham Canyon, and Bajo de la Alumbrera (Ulrich and Heinrich, 2001; Imer et al., 2013) but in the case of Halilağa there are not

enough evidences to attribute the origin of the magmatism to a back-arc extensional setting.

5.2. Hydrothermal Evolution

The Re-Os age of molybdenite (39.56 ± 0.21 Ma) at Halilağa is the first direct mineralization age that indicates an Eocene porphyry deposit in the Biga Peninsula. Additionally, it confirms the genetic relationship of the porphyry mineralization with the earlier phase of the porphyry stock (Phase A).

Previous Oligocene Ar-Ar age determinations at Halilağa from K-feldspar and muscovite yielded dates of 24-26 Ma, ca. 15 m.y. younger than the Eocene result from mineralization and magmatism (Figure 5.3; Kuşcu, 2009; Sanchez, 2012). The differences are attributed to a thermal event that followed the main porphyry alteration event at Middle Eocene. Closure temperature of Ar in K-feldspar ranges from 150-350° (Foland, 1994; Lovera et al., 1991; 1997) meaning that the systematics are easily affected by a low-temperature thermal event. The resetting of the $^{40}Ar/^{39}Ar$ muscovite age from Kuşcu (2009), indicate that the thermal overprint reached at least 300-350° (Robbins, 1972; Hames and Bowring, 1994). Furthermore, cooling ages of the Evçiler pluton are 24-25 Ma (Figure 5.3; Altunkaynak et al., 2012) similar to the Oligocene ages at Halilağa, indicating that the Oligocene intrusion of Evçiler caused the heat necessary to reset $^{40}Ar/^{39}Ar$ systematics in K-feldspar and muscovite.

5.2.1. Alteration anatomy

Hydrothermal fluid evolution at Halilağa based on geochronology, alteration geochemistry, mass balance calculations, and field observations, suggests four stages of hypogene hydrothermal alteration: Early, Main, Transitional, and Late.

The Early Stage at Halilağa is a widely distributed secondary biotite after hornblende, or weak biotite alteration in both phases of the stock is associated with low Cu or Au grades or un-mineralized zones, hence it could be a barren and the earliest alteration event. Examples of barren early biotite alteration are observed in other porphyry Cu deposits such as Cerro Colorado (Bouzari and Clark, 2006), where biotite alteration precedes the chalcopyrite bearing biotite + magnetite ± K-feldspar main hypogene event, and at Bajo de la Alumbrera (Ulrich and Heinrich, 2001) where weak potassic alteration is characterized by secondary biotite after hornblende.

During the Main Stage Cu and Au are added into the system during the biotite + magnetite ± K-feldspar alteration, which also results in addition of Si, Fe, K, and S and depletion of Ca and

Na, suggesting addition of sulfide minerals to the system and the replacement of Ca and Na by K. However, in K-rich assemblages, the relatively low K/Al ratio could result from the overprinting effect of white micas and chlorite in the original assemblage. The Main Stage comprises the majority of the mineralized veins: biotite + magnetite, and quartz veins. The sulfide minerals are chalcopyrite, molybdenite, and pyrite. Cu and Au grades are spatially correlated (Figure 4.15), suggesting that both elements co-precipitated at the same time during K-silicate assemblage, similarly to other porphyry Cu-Au (e.g. Kesler et al., 2002; Ulrich and Heinrich, 2001). Chalcopyrite is the main ore mineral in Halilağa, usually intergrown with magnetite and with no bornite. The lack of a bornite center is a characteristic of Halilağa. The absence or scarcity of bornite is observed in many other Au-rich porphyry Cu deposits (Kesler et al., 2002) and because of the level erosion present in Halilağa, that exposes K-silicate alteration and mineralization, the lack of bornite at Halilağa is interpreted as a primary feature and not related to post-ore faulting.

Propylitic (epidote + chlorite ± calcite) assemblages temporally overlaps the K-silicate event in the Main Stage, but is developed at the margins of the system. In this alteration, the addition of Ca into the system is attributed to the increase in epidote with moderate addition of calcite as indicated by petrographic observations.

The Transitional Stage consists of lower temperature alteration assemblages caused by the cooling of the hydrothermal system; at Halilağa the Transitional Stage assemblages include chlorite-sericite and sericite alteration. Chlorite-sericite assemblages are characterized by gains of Fe, Pb, and Zn and losses of Si and Na. Sericite alteration is associated with grades of Cu and Au greater than 1% and 1 ppm respectively in the core of the mineralized system. K/Al molar ratios portray the mineralogical and chemical changes associated with K-metasomatism. Sericite (K-mica) should have a K/Al ratio of 0.3, herein sericite alteration exhibit wide ranges of K/Al (0.2-0.47), which might be influenced by the compositions of the previous K-silicate alteration, increasing the K/Al ratios, and smectite overprint, which decreases K/Al ratios (Figure 4.4). Phengite (identified by SWIR) is distributed in the southern margin of the porphyry alteration and because phengite is associated with K-, Mg- and Fe- rich environments (Scott and Yang, 1997), phengite along the South Fault suggest that this fault acted as pathway for hydrothermal fluids.

In the Late Stage, alteration mineral paragenesis reveals intense overprinting of earlier high-temperature alteration with low-temperature clays. This late stage of alteration is indicated by Sr loss in all alteration assemblages product of post-mineral overprints of clays and white micas on plagioclase phenocrysts. The sericite that is spatially related to fault zones, on the eastern zone with

the North Fault, is considered to be part of this alteration stage and not part of the Transitional Stage. In addition to sericite, clays are present on this later stage; montmorillonite at the northern margin of the stock and in shallow zones, and kaolinite occurs near the surface. Late Stage assemblages could be result of the younger thermal event responsible for the resetting of the Ar-Ar ages.

The alteration zonation along the north margins of the porphyry (Figure 4.6) lack alteration zones outward from the biotite + magnetite core, indicating a possible fault truncation of the porphyry.

5.2.2. Porphyry and epithermal relationship

Spatial associations between HS epithermal deposits and porphyry deposits have been described in many deposits in the world (Hedenquist et al., 1998; Muntean and Einadi, 2001; Sillitoe, 2000). The spatial and temporal link between porphyry and HS epithermal deposits is typical in the Biga Peninsula in deposit such as Kuşcayir, Alankoy, Aladağ, and Halilağa (Yiğit, 2012). This feature is relevant for mineral exploration because the broad footprints of epithermal alteration can be associated with and indicate porphyry alteration, but also conceal porphyry potential through texturally destructive overprinting alteration events.

Spatially and temporally associated porphyry and epithermal deposits can result in both systems being mineralized (e.g. Far South East and Lepanto; Hedenquist et al., 1998) but can produce mineralized epithermal systems and barren porphyries deposits, and vice-versa, (e.g. Çöpler; Imer et al., 2013; Nevados de Famatina; Pudack et al., 2009). The formation of porphyry Cu-Mo or porphyry Cu-Au deposits has been attributed to the depth of mineralization (e.g. Sillitoe, 1997; Murakami et al., 2010). Furthermore, the precipitation of Cu or Au is controlled by the thermodynamic evolution of the ore-forming fluids; fluid pressure controls phase separation rates and consequently preference of a) Au precipitation at shallower levels and extreme phase separation, or b) Cu at depth with a slower phase separation and consequent residual Au available for epithermal mineralization (Murakami et al., 2010). The favorable preservation of epithermal deposits in the Biga Peninsula is controlled by the rates of uplift and erosion allowed the exposure and preservation of porphyry systems at a similar level than systems resulting in telescoped porphyry deposits. The favorable rates of uplift and erosion might be product of the transition from a post-collisional in the Cretaceous-Paleocene to the current extensional tectonic setting that started in the Oligocene.

A Biga Peninsula geochronology compilation (Figure 5.2) suggests two major pulses of Eocene and Oligocene porphyry and epithermal mineralization. Only a few direct mineralization and alteration ages (Re-Os dating on molybdenite, $^{40}Ar/^{39}Ar$ in alunite or adularia) are available in the area and the

geochronology of mineral deposits have been usually constrained using host rocks ages (e.g. Kuşcu, 2009, Unal et al., 2013). Eocene examples of HS epithermal systems are from the Kuşcayiri District, located 13 km NW of Halilağa, where HS epithermal alteration at Kuşcayiri and Kartaldağ based on $^{40}Ar/^{39}Ar$ step-heating of alunite indicate 38 to 39 Ma ages (Yiğit, 2012). Syn-mineralization porphyry intrusions are dated at ca. 40 Ma and $^{40}Ar/^{39}Ar$ cooling ages of host rock at the HS Kartaldağ and LS Madendağ epithermal systems NW of Kuşcayiri (Figure 1.2), yielded 40-43 Ma (Unal et al., 2013, Leroux, 2016). Oligocene mineralization occurs at Ağı Dağı (25.8 ± 1.4) and Alankoy (27.5 ± 0.3) based on $^{40}Ar/^{39}Ar$ step-heating age in alunite (Yiğit, 2012), $^{40}Ar/^{39}Ar$ hornblende of a causative granodioritic intrusion with propylitic alteration yielded 28.3 ± 2.6 (Yigit, 2012).

At Halilağa the spatial relationship between epithermal (Kunk) and porphyry systems suggests that those systems could be genetically connected. From a geochronological perspective, the similar age of the host rocks at Kunk (ca. 40 Ma) with the Kestane stock (ca. 39 Ma) do not exclude the possibility that this mineralization is related to the porphyry mineralization. In contrast, geochronology from the andesitic volcanic host rock sequence at Pirentepe epithermal system yielded ca. 28 Ma indicating a minimum age for the epithermal alteration (Figure 2.10, Table 2.2). This time is comparable with the younger HS mineralization of ca. 27 Ma.

There are no geochronological constraints on epithermal alteration at Kunk, therefore alteration patterns and cross-cutting relationships are crucial to establish a relative timing between epithermal and porphyry alterations. Epithermal alteration at Kunk is zoned: western Kunk is dominated by intermediate argillic alteration (white micas and illite); eastern Kunk has advanced argillic alteration (alunite, kaolinite, and pyrophyllite). In the advanced argillic zone fine-grained alunite replace phenocrysts above pyrophyllite zone (Figure 4.12). Hypogene alunite can be coarse-grained and white or pink, but alunite at Kunk, is fine-grained and replaces white micas, so is interpreted to be of supergene origin (Allen, 1996). Pyrophyllite is widely distributed, replaces feldspar phenocrysts and groundmass and confirms advanced argillic alteration at Kunk. In general, pyrophyllite forms at intermediate temperatures (~300°; Hemley et al., 1980; Allen, 1996) and is a typical product of low pH fluids. Isotopic studies in other deposits indicate that the origin of pyrophyllite can be related to cooling of fluids in equilibrium with sericite (Hedenquist et al., 1998) thus epithermal alteration indicated by pyrophyllite is genetically related to porphyry-related fluids. At Kunk, the alteration patterns of continuity of phengite from the southern border of the porphyry alteration and along the South Fault, is interrupted in the southern flank of the South fault, and continues to the intermediate argillic alteration zone in the Kunk Hill, suggesting a spatial and genetic connection between epithermal

alteration at Kunk and porphyry alteration at Kestane.

5.2.2.1. Biga Peninsula

Eocene porphyry mineralization ages in the Biga Peninsula are inferred from magmatic or cooling ages of the causative intrusions. The youngest porphyry occurrence in the Biga Peninsula is the Dikmen porphyry Au-Mo-Cu of ~47 Ma (Figure 1.2; Yiğit, 2009, 2012). Yılmaz (2003) suggested porphyry style mineralization at the Kuşcayir pluton (NW of Halilağa, Figure 1.2), where $^{40}Ar/^{39}Ar$ hornblende yielded 35-39 Ma (Delaloye and Bingöl, 2000). Other porphyry occurrences are found in northern Biga Peninsula are: Alankoy (Eurasian Minerals, 2015), and K2 in the TV Tower District (Kayali and Karaayi, Pilot Gold, 2014). Those occurrences are usually related to epithermal systems, similarly to Halilağa. None of those deposits have resource estimation and mostly correspond to porphyry-like alteration zones (quartz-sericite-pyrite) and quartz stockwork in porphyritic intrusions (Yiğit, 2012; Pilot Gold, 2014).

The Tepeoba Cu-Mo-Au mine, in southern Biga Peninsula, has a mineralization age of ca. 25 Ma based in Re-Os, thus it corresponds to a younger porphyry system, than the mentioned above, in the Biga Peninsula. A distinctive feature in Tepeoba is the hydrothermal breccia that host Cu-Au-Mo mineralization that is not observed in Halilağa (Murakami et al., 2005). However, as also seen at Halilağa, the alteration zoning consists of proximal K-silicate zone and biotite grading to muscovite and chlorite alteration zones in distal segments of the intrusion (Murakami et al., 2005).

Eocene porphyry deposits in Turkey occur to the southeast of the Biga Peninsula, in Central Anatolia. Eocene porphyry deposits are distributed in the Karapinar/Bursa District (e.g. Karapinar, Figure 1.3) and in the Çöpler/Kabataş magmatic complex (e.g. Çöpler; Figure 1.3). The magmatic and mineralization ages are Early Eocene ranging from 51 to 43 Ma (Marinov et al., 2011; Imer et al., 2013; Kuşcu et al., 2013; Rabaynol, 2015), older than the mineralization at the Biga Peninsula.

5.2.2.2. Globally

The Halilağa porphyry deposit shares many characteristics with other porphyry systems in the world. Regardless of the similar composition between the two phases of the stock, the differences in age and alteration suggests that at least two intrusive phases are associated with the porphyry system and cross-cut by a younger and more mafic intrusion. Alteration assemblages observed in Halilağa are common in Au-rich porphyry deposits; dominated by biotite + magnetite cores over K-feldspar and with intense quartz and quartz + magnetite + chalcopyrite veining (e.g. Bajo de la Alumbrera, Ulrich and Heinrich, 2001; Refugio Au District in the Maricunga Belt, Muntean and Einaudi, 2000)

in contrast with porphyry Cu-Mo deposits dominated by early granular quartz-chalcopyrite ± bornite veins (Sillitoe, 2010).

Veins at Halilağa are classical and typical features in many porphyry systems in the world; a paragenetic stage of veins and associated hydrothermal alteration is shown in Figure 4.17. Early magnetite or biotite veins are described in multiple deposits: magnetite + actinolite (e.g. M-type veins, Arancibia and Clark, 2006) and biotite without magnetite veinlets in Bingham (Redmond et al., 2010). Banded quartz and magnetite veins are common in the Maricunga belt porphyry Cu-Au systems (Muntean and Einaudi, 2001). Quartz + pyrite + chalcopyrite veins are correlated with B type veins observed in many porphyry deposits (Gustafson and Hunt, 1975; Sillitoe, 2010).

The Halilağa porphyry deposit represents a classical example of Au-rich porphyry Cu mineralization in terms of vein types and alteration assemblages. However, the alteration zonation suggests truncation product of faulting.

5.3. Structural Evolution and Deformation

Interpretation of structural measurements, geological map patterns, geophysics, and modeling based on drill hole reveals three major orientations for lineaments, faults, and veins: NW to NNW, E to ENE, and NE. Those orientations are widely observed throughout the Biga Peninsula with E-W and NE-SW being the most prominent structural feature revealing the current N-S extension and strike-slip regime (Yilmaz and Karacik, 2001; Gurer et al., 2006; Yilmaz et al., 2010).

NW-trending faults are the earliest fault set at the Halilağa District, because they correspond with discontinuous structures that are cross-cut by most of the other sets. At Halilağa, two NW-oriented faults are identified based on cross-section interpretation, but the cross-cutting relationships are ambiguous to determine timing because of later fault reactivation. On the Biga Peninsula, several mineral occurrences of different ages are aligned in a NW orientation (e.g. Kartaldağ, Kuscayir, TV Tower, Halilağa, and Ağı Dağı; Figure 1.3) suggesting that this fault orientation may be an important pathway for mineralizing magmas or that the structure existed prior to mineralization. Regionally, NW-trending faults are observed to pre-date E-trending faults (e.g. Yilmaz and Karacik, 2001) and were identified by Sanchez (2012) as the earliest structures in the Biga Peninsula that generated NW-trending half grabens and arc-parallel orientation. In northern Biga Peninsula, NW faults structures juxtapose basement with volcanic sequences (e.g. Çamlıca Group with Eocene volcanic; Figure 1.2; Okay and Satir, 2000b).

The ENE- trending North Kapakli Fault (Figure 2.5) was interpreted to be part of the North

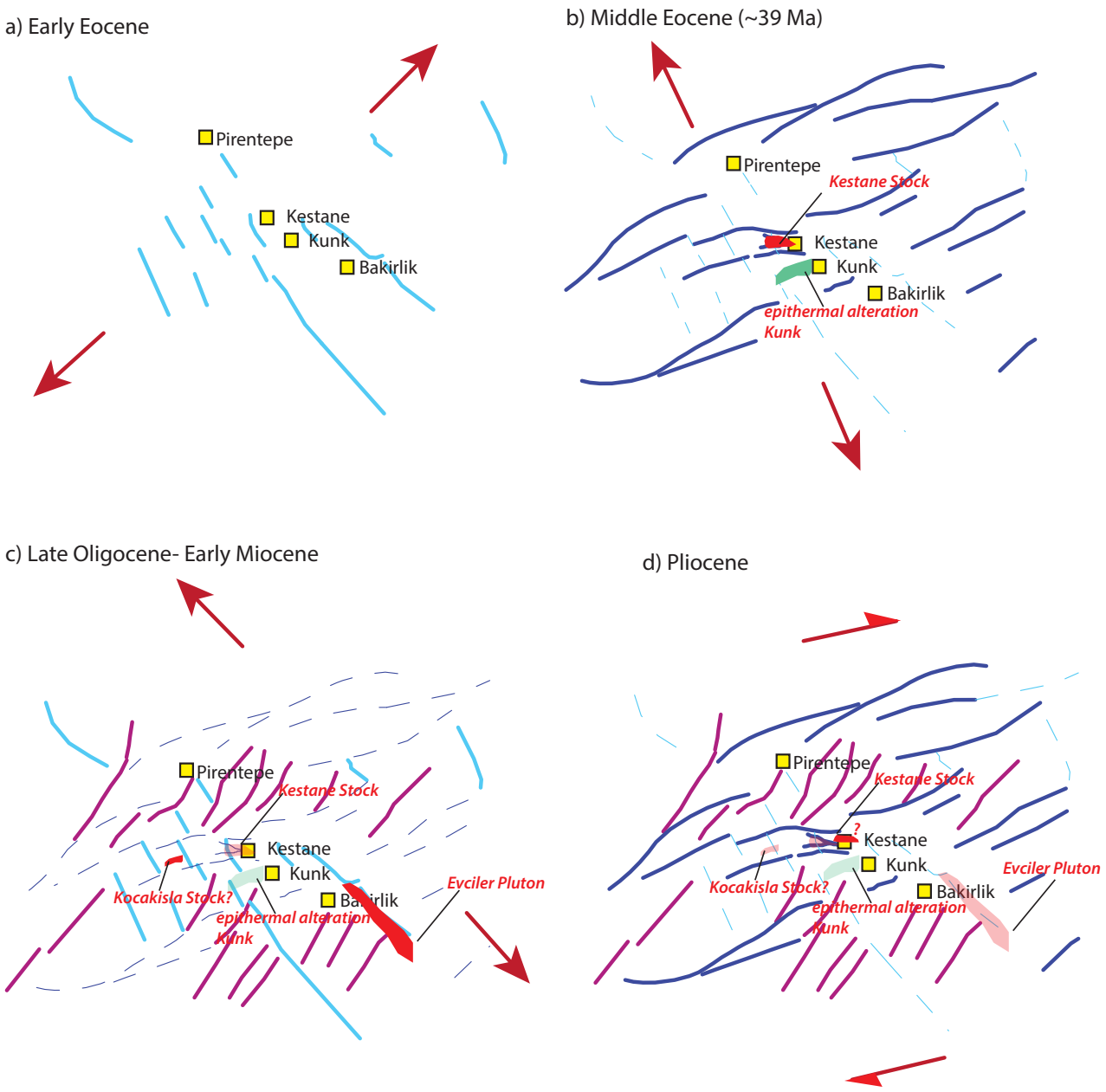

Figure 5.4 Deposit evolution model in plan view. a) Early Eocene; b) Middle Eocene; c) Late Oligocene-Early Miocene; d) Pliocene. Mineral occurrences in the Halilağa District (Pirentepe, Kestane, Kunk, and Bakirlik) are indicated in yellow squares.

Anatolian Fault system (Grieve, 2009, Sanchez, 2012). The North Kapakli Fault plays a major role in the district, separating the local horst-graben morphology, where Kestane is in the graben and Pirentepe is in the horst block (Figure 2.5). The southern edge of the Kestane graben is limited by the South Kapakli Fault (Sanchez, 2012) that also follows an ENE-orientation. Regionally, post-orogenic extension generated E- to ENE-trending faults (Sanchez et al., 2012) during the Oligocene, and controlled core complex exhumation. At the Halilağa District, the Kunk Fault (Figure 2.5) in the northern flank of the Kunk hill is spatially consistent and has the same orientation as the South Kapakli Fault hence both faults are interpreted to correspond to the same system.

In the scenario of a genetic association between porphyry and epithermal alteration at Kunk, meaning that the epithermal alteration at Kunk formed from the interaction between porphyry-related hydrothermal fluids and meteoric waters, the Kunk Fault seems to be responsible for uplifting and localizing the Kunk hydrothermal system. Additionally, a Fe-rich talus breccia along the fault scarp further supports a Miocene activation of the fault. Fe-rich talus breccias are typical features along ENE-fault zones in Biga Peninsula and are associated with lateritic iron deposits formed during Upper Miocene to Pliocene and linked to major uplift in the Biga Peninsula (Sanchez, 2012; Yigit, 2012). Therefore the Kunk Fault was an active extensional fault from Middle to Late Eocene (syn- or post-mineralization) until Pliocene.

The North and South faults cut and therefore bound the porphyry stock. The orientations of the North and South faults are WNW- ESE and E-W respectively. The North Fault separates the Eocene from the Oligocene volcanic sequence and its orientation differs from the dominant NNW-SSE, E-W to ENE-WSW, and NNE-SSW trends. Based on the fault geometry the North Fault is interpreted to be subsidiary of the major ENE trend.

The geometry of the porphyry stock is slightly tilted and parallel with the North Fault, resulting in a variation of approximately 30° with the vertical and a dip-direction of 020. The tilting of the porphyry could be a primary feature controlled by syn-porphyry faults, but the 30° tilting observed in Oligocene and Eocene stratified sequences (Figure 2.3; Sanchez, 2012) is consistent with the tilting of the porphyry stock, suggesting that tilting is a post-mineralization feature.

The geometry of the alteration zones is also relevant to determine the role and timing of the North and South faults. As mentioned in the previous section (see 5.2.1), the hydrothermal alteration zonation at Halilağa reveals that montmorillonite, phengite, and sericite occur within fault zones. Phengite along segments the South Fault evinces a ferromagnesian rich environment that could reflect previous K-silicate alteration. Furthermore, montmorillonite enrichments along the western segments

of the North Fault suggests post-mineralization movements along the North Fault because as part of the Smectite Group, it characterizes an environment of lower temperature and acid pH (Corbett and Leach, 1997). The presence of high and low temperature minerals in fault zones may suggest a syn-mineral origin of those structures used as a conduct for mineralization, followed by post- mineral reactivation. Additionally, abrupt changes in K-silicate zones particularly in the northern boundary where from intense biotite + magnetite ± K-feldspar in the core grades to moderate biotite + magnetite ± K-feldspar alteration also indicate post-mineralization activity that possibly truncated a segment of the porphyry along the northern side.

Sheeted quartz veins in porphyry systems form parallel to regional stresses (Tosdal and Richards, 2001; Cannel et al., 2005) and at Halilağa, quartz vein orientations suggests preferred E-W orientation that is sub-parallel to the North and South Faults and secondary N to NNE orientations for quartz + sulfides (limonites) veins and quartz + sulfides (limonites) veins with sericite halo. The main E-W trend, observed in both faults sets, coincides with the orientation of Kunk Faults and the South Fault, in terms of stresses suggesting a dominant N-S extension. However, because the tilting of the porphyry stock is post-mineral, those quartz veins are also tilted and their orientations do not represent a primary feature.

The role of NE-trending structures is not clear in the Halilağa District, but at regional scale, NE-trending structures controlled Miocene basin deposition (Okay et al., 1991; Yilmaz and Karacık, 2001; Gürer et al., 2006) and consequently NE structures are interpreted to be post-mineralization at Halilağa. However regionally, NE-SW structures are interpreted to pre-date E-W structures responsible for E-W trending Pliocene grabens (e.g. Edremit graben; Yilmaz and Karacık, 2001).

5.4. Deposit Evolution Summary

During Early Eocene, NE extension is recorded in the Kemer micaschists in northern Biga Peninsula from Palaeogene until 52 Ma (Beccaletto et al., 2007, Bonev and Beccaletto, 2007). The NE extension regime favours the development of NW faults, which are also indicated to be arc-parallel structures (Sanchez, 2012). Consequently, in the Halilağa District, the Early Eocene is characterized by NW-trending normal faults (Figure 5.4a).

During the Middle Eocene the N-S extension causes E-trending porphyry (quartz-limonite) veins and ENE-trending faults (Figure 5.4b). During this period, the Kestane stock's two magmatic phases at 39 Ma and 37 Ma intrudes the volcano-sedimentary host-rocks and also occurs associated andesitic to dacitic at Kunk (40 Ma) and at Kestane (38 Ma). Porphyry mineralization takes place

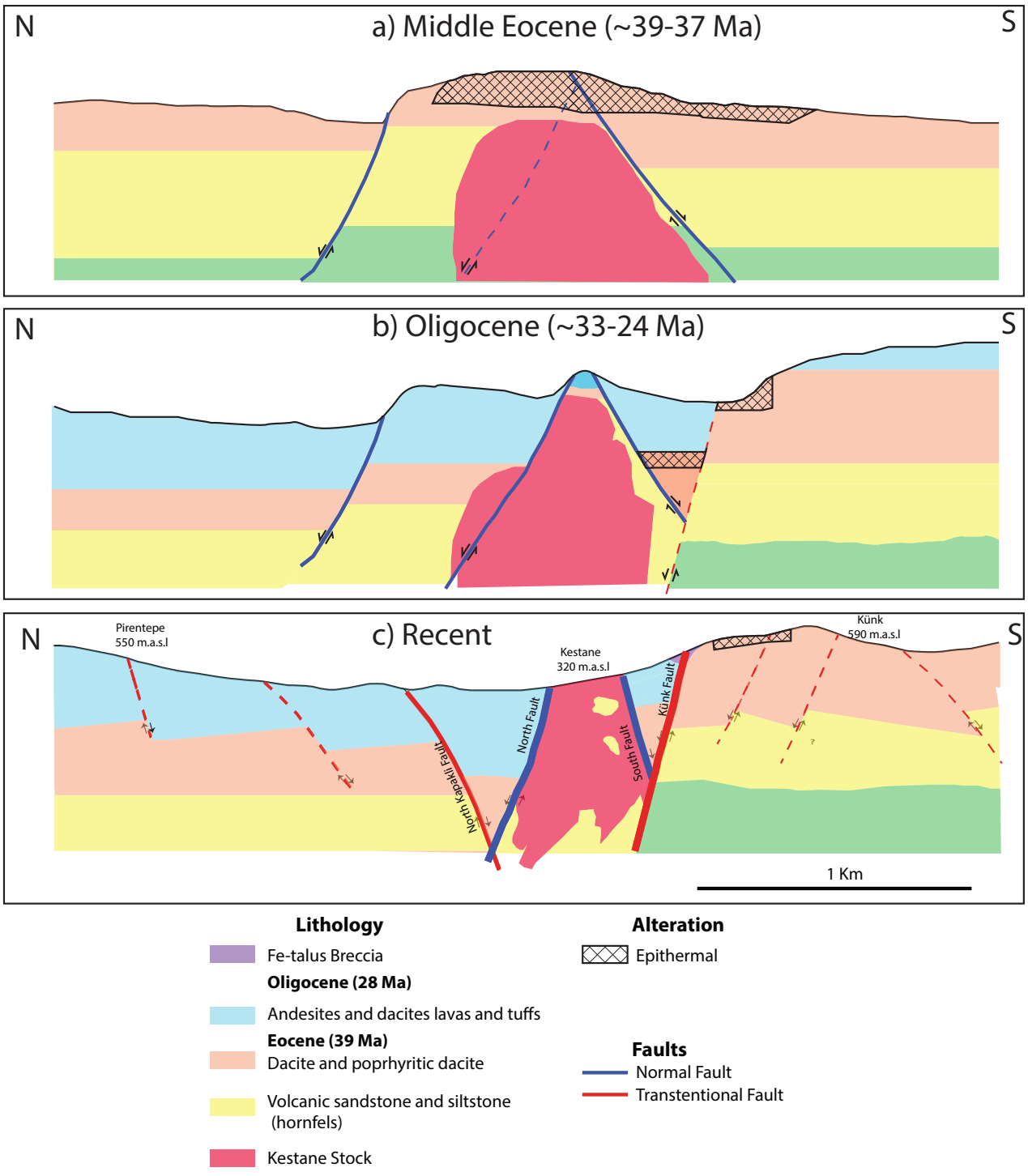

Figure 5.5 Deposit evolution model in cross-section view.

at 39 Ma and is temporal and spatial associated with biotite + magnetite ± k-feldspar alteration and quartz + sulfides veins or "B-type veins" (Figure 5.5a). Retrograde alteration includes chlorite + sericite and sericite ± quartz alteration and associated with quartz + sulfides with sericite halo or "D-type veins". The similar orientation of those earlier quartz veins or "B-type" and later quartz veins or "D-type veins" suggests similar conditions, N-S extension, during the formation of those veins. The hydrothermal alteration along fault zones, more notably along the South Fault, suggest that faults were active during porphyry intrusion and mineralization (syn-mineralization), but also porphyry tilting, alteration zoning and alteration truncation along the north margin indicate post-mineralization activity that possibly truncated a segment of the porphyry along the northern side

In the Late Oligocene to Early Miocene (Figure 5.4c), a dominant NE-trending faulting and the reactivation of NW-trending faults as conjugate set (Yilmaz and Karacik, 2001) that facilitate major regional features during this period such as the exhumation of Kazdağ Metamorphic Complex (20 to 10 Ma, Cavazza et al., 2009). Additionally, NE- to NNE-trending faults control Evçiler and Kestanbol emplacement (Yilmaz and Karacik, 2001). At the Halilağa District (Figure 5.5b), volcanic and sub-volcanic rocks at Pirentepe (28 Ma) hosts subsequent epithermal mineralization, while at Bakirlik the intrusion of the Evçiler pluton (26 Ma) produces skarn alteration; this thermal event resetted the 27-24 Ma Ar-Ar ages at Halilağa.

Finally, the current deposit geometry is modified and controlled by NE-treding strike-slip faulting linked to NAF westward propagation that arrived in the Pliocene (Armijo et al., 1999; Figure 5.4d and Figure 5.5c). Normal faulting associated with Aegean extension started in Late Pliocene originating E-trending faults, yielding to the reactivation of earlier faults (Gurer et al., 2006).

Chapter 6: Conclusions

6.1. Conclusions

The geological evolution of the Halilağa deposit was herein addressed using geological mapping and core logging, U-Pb and Re-Os geochronology, petrography, lithogeochemistry, and hydrothermal alteration description. The conclusions of this work can be summarized in three major topics: magmatism and stratigraphy, structures, and alteration and mineralization.

6.1.1. Magmatism and stratigraphy

Two major magmatic pulses are identified at the Halilağa District; A Middle Eocene magmatic pulse that ranges from 39 to 37 Ma and a Late Oligocene event that ranges from 28 to 26 Ma. Both magmatic events include volcanic and plutonic facies.

- The Eocene volcanic packages in the Halilağa District include coherent volcanic facies, volcanic sandstone, and volcanic siltstone of andesitic to dacitic composition. This unit is correlated with the Balikliçesme Volcanics. Igneous geochemistry indicates moderate K calc-alkaline for Eocene rocks.
- Eocene plutonism is represented by the quartz monzonitic to granitic Kestane stock. Geochemical signatures indicate characteristics common to fertile porphyry-related intrusions such as minimal europium anomalies, evidences of hornblende fractionation and high magmatic water content. However, non-adakitic signatures based on La/Yb are less common in Andean and Tethyan porphyry deposits with exception of Bajo de la Alumbrera and Bingham.
- Oligocene volcanic rocks are part of a more explosive cycle. Crystal and lithic tuffs of andesitic composition are the dominant lithology. This unit is correlated with the Çan Volcanics. Igneous geochemistry suggests higher K-calc-alkaline trends.
- Oligocene plutonism in the District is represented by the monzogranite Evçiler pluton. Geochemistry of the Evçiler pluton shows stronger fertile porphyry-related intrusions features than the Kestane stock suggesting potential for undiscovered porphyry mineralization.
- Despite the spatial relation, the Kestane stock is located less than 3 km SE of the Evçiler pluton; there is no genetic link between the Evçiler pluton (located at SW of Halilağa) and the Kestane stock. Furthermore, the age of magmatism of causative intrusions in the Halilağa porphyry deposit coincides with the cooling ages of the Kuscayir granitoids from 38 to 39 Ma

($^{40}K/^{39}Ar$ hornblende; Delaloye and Bingöl, 2000) suggesting a temporal connection between the Halilağa porphyry deposit and the Kusçayir intrusion.

6.1.2. Alteration and mineralization

- Hydrothermal evolution at Halilağa can be divided in four hypogene stages: Early, Main, Transitional and Late. A supergene event followed the hypogene stages.
- The Early Stage is characterized by secondary biotite after hornblende in the stock and in the volcano-sedimentary wall rock resembles a hornfels.
- The Main Stage is associated with chalcopyrite mineralization and is dominated by biotite + magnetite ± k-feldspar in the core of the hydrothermal system, grading to chlorite + epidote ± calcite at distal segments of the intrusion usually in the volcano-sedimentary host rocks. A calcic-skarn alteration is also developed in volcano-sedimentary and limestones at the western edge of the porphyry intrusion.
- The Transitional Stage is dominated by sericite ± quartz at shallow levels and chlorite ± sericite selective to phenocrysts in deeper portions.
- The Late Stage is represented by clays and minor white mica that overprints earlier alteration minerals and is also present along fault zones.
- The Supergene Stage is characterized by chalcocite, Cu oxides, and limonites in a pervasive sericite ± quartz alteration.
- HS epithermal alteration is identified in the Halilağa district at Pirentepe and Kunk located respectively to NNW and SSE of the porphyry mineralization. HS epithermal alteration includes white micas, clays (kaolinite and montmorillonite), pyrophyllite, silicification, and minor alunite.
- Based on the geological relations between alteration minerals, spatial association, and geology, the barren epithermal deposit at Kunk represents higher levels of the porphyry mineralization. K-silicate assemblages at Kestane are overprinted by sericite and chlorite alteration and pyrophyllite in the epithermal deposit might be genetically related to those fluids.
- The emplacement of the Middle Eocene Kestane stock controls hydrothermal alteration and mineralization at Halilağa. The genetic relationship was confirmed with U-Pb of the syn-mineral intrusions and Re-Os geochronology in molybdenite.
- The porphyry and epithermal mineralization along the structural blocks have different ages. From oldest to youngest, these are:

- Kestane: porphyry mineralization 39 Ma
- Kunk: host rock are 40 Ma, epithermal alteration could be cogenetic with porphyry or part of a younger epithermal event similar in age to Pirentepe.
- Pirentepe: epithermal mineralization is younger than 28 Ma (host-rock age)
- Bakirlik: Evçiler intrusion is 26 Ma (associated with skarn mineralization)

- The younger hydrothermal activity in the district of 26-24 Ma, recorded in previous $^{40}Ar/^{39}Ar$ ages of K-feldspar and muscovite, is associated with the hydrothermal alteration generated by the Evçiler intrusion.
- Two episodes of porphyry mineralization are recorded by Re-Os geochronology in the Biga Peninsula: a Middle Eocene (39 Ma in Halilağa) and Late Oligocene (25 Ma in Tepeoba, Murakami et al., 2005).
- There is no dominant metal zonation between the distribution of Au and Cu. Furthermore, the precipitation of both metals occur closely at the same depth, lithology, and alteration type, therefore is associated with the same event.

6.1.3. Structures

- NW- faults appear to control many mineralized systems in the Biga Peninsula, as many mineral occurrences, of different age, are aligned in that direction. At Halilağa, NW-oriented faults are interpreted to be the earlier structures, pre-dating mineralization.
- E-oriented structures are interpreted to be syn-mineral based on alteration zoning along the North Fault and the South Fault.
- E-oriented faults define three major structural corridors, composed of rocks of different ages and deposit types. From north to south the blocks are: Pirentepe, Kestane, and Kunk.
- The North and the South Fault bound the porphyry stock and both faults have evidences of syn- and post-mineral activity revealed by the intense K-silicate alteration and quartz veining along fault zones. Cross section interpretation based in core logging indicates that those systems have been subsequently reactivated and the deposit is truncated by post-mineralization movement along the North Fault.
- NE-trending faults do not play a relevant role on the Halilağa District, but appear to be post-mineral based on regional controls in Miocene basin deposition in the Biga Peninsula and reactivated during the Pliocene (Yilmaz and Karacık, 2001; Gürer et al., 2006).

6.2. Exploration Implications

The focus of this research was restricted to deposit-scale porphyry and nearby HS epithermal deposits. While regional applications are beyond the scope of this study, there are important implications for the metallogeny of the Biga Peninsula and NW Turkey.

The use of indirect exploration methods such as geophysics and geochemistry, require the knowledge of the geological setting on the regional context and an understanding of porphyry ore-forming process within the global and local scale. In the Biga Peninsula, porphyry and HS epithermal mineralization are associated with magmatic rocks from Middle Eocene to Middle-Late Oligocene in a post-collisional setting transitional to current the extension, indicating host-rock of those age are more favorable for mineralization. The two ages of magmatism observed in the Halilağa district are Middle Eocene (39-37 Ma) and Middle Oligocene (28-26 Ma), coinciding with the regional timing for mineralization. In a district scale, in addition to the known porphyry-style mineralization of Eocene age, there is potential for Oligocene porphyry-style mineralization in the Halilağa District. The Evçiler pluton presented adakite-like signatures, common in porphyry deposits around the world (e.g. Thiéblemont et al., 1997; Oyarzún et al., 2001), suggesting favorable magmatic conditions for porphyry type-mineralization associated with this magmatic event. Furthermore, the Oligocene age for the volcanic sequence that host HS epithermal alteration at Pirentepe indicates a prospective time for epithermal related fertile-porphyry intrusions at depth.

The NW-alignment of an Eocene porphyry belt in Central Biga and the mineral occurrences in the Halilağa District suggest a relevant a relevant role in the mineralization since the Eocene. In the Halilağa District E- trending faults are syn- and post-mineralization, therefore E-trending structures represent favorable areas for ascent of hydrothermal fluids, in addition to the pre- mineral NW structures.

Vein and alteration intensity has been demonstrated to be an effective technique to delineate high grades zones in porphyry Cu-Au deposits (e.g. Muntean and Einaudi, 2001; Redmond and Einaudi, 2010). At Halilağa, the highest Au and Cu concentrations are associated with quartz vein densities > 10 per m in intense K-silicate (>30%) or sericite ± quartz alteration, emphasizing the importance of veining and alteration intensity as indicators of porphyry mineralization in the Halilağa District. Other porphyry occurrences in the Biga Peninsula, are also characterized by Au and Cu mineralization in K-silicate zones (Tepeoba; Murakami et al., 2005) and sheeted or stockwork veins (Dikmen; Yiğit, 2012).

Because lithocaps, associated with HS epithermal alteration, are an evident topographic feature and are localized nearby porphyry deposits in the Biga Peninsula, the occurrence of lithocaps can be used in many cases as an indicator of porphyry mineralization at depth. However, the hydrothermal overprint must be considered to establish timing among those mineralization types. The intense magmatic and hydrothermal activity during the Eocene and Oligocene results in an overprint of earlier hydrothermal alteration, which in addition to the rapid core complex exhumation during the Oligocene, results in a resetting of $^{40}Ar/^{39}Ar$ ages in the Halilağa District. Therefore $^{40}Ar/^{39}Ar$ geochronology should be used with caution in the Biga Peninsula, specially in areas located nearby intrusions and metamorphism, particularly in the case of dating minerals with low closure temperatures which might reflect posterior events.

6.3. Future Work

Future work in the area should center in 1) establishing a genetic relationship between epithermal alteration and porphyry mineralization; and 2) characterizing the tectonomagmatic setting of Eocene-Oligocene porphyry mineralization in the Biga Peninsula. To address those questions isotopes, fluid inclusions, and mineralization age dating of epithermal systems are useful methodologies, described below.

To establish genetic relationships between epithermal and porphyry deposits it is key to compare: $^{40}Ar/^{39}Ar$ in alunite, $^{40}Ar/^{39}Ar$ in muscovite from epithermal and porphyry systems, $^{40}Ar/^{39}Ar$ in biotite (secondary biotite after hornblende) and Re-Os in molybdenite. Unfortunately, as observed at the Halilağa District, later hydrothermal alteration may affect $^{40}Ar/^{39}Ar$ age dating. Additionally, fluid inclusions can assist to determine the thermodynamic evolution of the fluids responsible for mineralization. Stable isotopes such as S, O, and H may help determine the nature and source of the hydrothermal fluids and describe the fluid evolution and connections between the epithermal and porphyry mineralization.

Systematic geochemistry using Nd and Sr isotopes of causative intrusions may help to establish the tectonomagmatic setting for emplacement of porphyry deposits in the Biga Peninsula. Previous studies have focused in older intrusions located in northern Biga Peninsula (e.g. Altunkaynak et al., 2012b), yet the mineralization-prospective Eocene stocks and plutons in central Biga Peninsula have not being included.

References

Agdemir, N., Kirikoğlu, M. S., Lehmann, B., Tietze, J., 1994, Petrology and alteration geochemistry of the epithermal Bayla Pb-Zn deposit, NW Turkey: Mineral Deposita, v. 29, p. 366-371.

Aldanmaz, E., Pearce, J., Thriwall, M.F., Mitchell, J., 2000, Petrogenetic evolution of late Cenozoic, post-collision volcanism in western Anatolia, Turkey: Journal of Volcanology and Geothermal Research, v.102, p. 67–95.

Altunkaynak, Ş., and Dilek, Y., 2006, Timing and nature of postcollisional volcanism in western Anatolia and geodynamic implications. Geological Society of America Special Papers, 409, 321-351.

Altunkaynak, S., and Genç, S., 2008, Petrogenesis and time-progressive evolution of the Cenozoic continental volcanism in the Biga Peninsula, NW Anatolia (Turkey). Lithos, v. 102, p. 316-340

Altunkaynak, Ş., Dilek, Y., Genç, C. Ş., Sunal, G., Gertisser, R., Furnes, H., and Yang, J., 2012a, Spatial, temporal and geochemical evolution of Oligo–Miocene granitoid magmatism in western Anatolia, Turkey. Gondwana Research, 21(4), 961-986.

Altunkaynak, Ş., Sunal, G., Aldanmaz, E., Genç, C. Ş., Dilek, Y., Furnes, H., ... and Yıldız, M., 2012b, Eocene granitic magmatism in NW Anatolia (Turkey) revisited: new implications from comparative zircon SHRIMP U–Pb and 40 Ar–39 Ar geochronology and isotope geochemistry on magma genesis and emplacement. Lithos, 155, 289-309.

Armijo, R., Meyer, B., Hubert, A., and Barka, A., 1999, Westward propagation of the North Anatolian fault into the northern Aegean: Timing and kinematics.Geology, 27(3), 267-270.

Armijo, R., Meyer, B., Navarro, S., King, G., and Barka, A., 2002, Asymmetric slip partitioning in the Sea of Marmara pull□apart: a clue to propagation processes of the North Anatolian Fault?. Terra Nova, 14(2), 80-86.

Arribas Jr, A., 1995, Characteristics of high-sulfidation epithermal deposits, and their relation to magmatic fluid. Mineralogical Association of Canada Short Course, 23, 419-454.

Audétat, A., and Pettke, T., 2003, The magmatic-hydrothermal evolution of two barren granites: a melt and fluid inclusion study of the Rito del Medio and Canada Pinabete plutons in northern New Mexico (USA). Geochimica et Cosmochimica Acta, 67(1), 97-121.

Avsan, M., Keles, S., Zeyrek, A., Isiklar, M., 2012, Halilaga Property Exploration 2012 Year-End

Report, Internal Teck Report, Ankara, Turkey, 68 p.

Aygül, M., Topuz, G., Okay, A. I., Satır, M., and Meyer, H. P., 2012, The kemer metamorphic complex (NW Turkey): A subducted continental margin of the Sakarya Zone. Turkish Journal of Earth Sciences, 21(1), 19-35.

Aysal, N., 2015, Mineral chemistry, crystallization conditions and geodynamic implications of the Oligo–Miocene granitoids in the Biga Peninsula, Northwest Turkey. Journal of Asian Earth Sciences, 105, 68-84.

Baker and Stenhouse, 2013, A Structural Evaluation of the Halilaga Project, Turkey, Internal Report by SRK for Teck Resources Limited, 55 p.

Beccaletto, L., 2003, Geology, correlations, and geodynamic evolution of the Biga Peninsula (NW Turkey). Doctoral dissertation, Université de Lausanne, Lausanne, Switzerland.

Beccaletto, L., and Jenny, C., 2004, Geology and correlation of the Ezine zone: a Rhodope fragment in NW Turkey?. Turkish Journal of Earth Sciences, 13(2), 145-176.

Beccaletto, L., Bonev, N., Bosch, D., and Bruguier, O., 2007, Record of a Palaeogene syn-collisional extension in the north Aegean region: evidence from the Kemer micaschists (NW Turkey). Geological Magazine, 144(02), 393-400.

Bingöl, E., 1969, Geology of the central and southeastern parts of the Kazdag Massif. Maden Tetkik ve Arama Enstitüsü Dergisi.

Bingöl, E., Akyürek, B., and Korkmazer, B., 1975, Geology of the Biga Peninsula and some characteristics of the Karakaya blocky series. In Proceedings of the Congress of Earth Sciences for the 50th Anniversary of the Republic of Turkey (pp. 70-7). Ankara: Mineral Resource and Exploration Institute Turkey (MTA).

Black, K. N., Catlos, E. J., Oyman, T., and Demirbilek, M., 2013, Timing Aegean extension: evidence from in situ U–Pb geochronology and cathodoluminescence imaging of granitoids from NW Turkey. Lithos, 180, 92-108.

Bonev, N. G., and Stampfli, G. M., 2003, New structural and petrologic data on Mesozoic schists in the Rhodope (Bulgaria): geodynamic implications. Comptes Rendus Geoscience, 335(8), 691-699.

Bonev, N., and Beccaletto, L., 2007, From syn-to post-orogenic Tertiary extension in the north Aegean region: constraints on the kinematics in the eastern Rhodope–Thrace, Bulgaria–Greece and the Biga Peninsula, NW Turkey. Geological Society, London, Special Publications, 291(1), 113-142.

Borsi, S., Ferrara, G., Innocenti, F., and Mazzuoli, R., 1972, Geochronology and petrology of recent volcanics in the eastern Aegean Sea (West Anatolia and Lesvos Island). Bulletin Volcanologique, 36(3), 473-496.

Boucher, K., 2016, The structural and fluid evolution of the Efemçukuru epithermal gold deposit, western Turkey. Unpublished PhD Thesis, Vancouver, Canada, The University of British Columbia, 452p.

Bouzari, F., and Clark, A. H., 2002, Anatomy, evolution, and metallogenic significance of the supergene orebody of the Cerro Colorado porphyry copper deposit, I Región, northern Chile. Economic Geology, 97(8), 1701-1740.

Bouzari, F., and Clark, A. H., 2006, Prograde evolution and geothermal affinities of a major porphyry copper deposit: the Cerro Colorado hypogene protore, I Región, northern Chile. Economic Geology, 101(1), 95-134.

Boynton, W.V., 1984, Geochemistry of the rare earth elements: meteorite studies. In: Henderson, P. (Ed.), Rare earth element geochemistry. Elsevier, Amsterdam, Netherlands, pp. 63–114

Bozkaya, G., Banks, D., Ozbas, F., and Wallington, J., 2014, Fluid processes in the Tesbihdere base-metal-Au deposit: Implications for epithermal mineralization in the Biga Peninsula, NW Turkey. Open Geosciences, 6(2), 148-169.

Bozkurt, E., and Mittwede, S. K., 2001, Introduction to the geology of Turkey—a synthesis. International Geology Review, 43(7), 578-594.

Bozkürt, E., 2001, Neotectonics of Turkey – a synthesis: Geodinamica Acta, v. 14, p. 3-30.

Bozkurt, E., 2007, On the Structural Geology of the Halilaga Project, Biga Peninsula, Western Turkey, Internal Report for Teck-Cominco Madencilik A.Ş, 41 p.

Brun, J. P., and Faccenna, C., 2008, Exhumation of high-pressure rocks driven by slab rollback. Earth and Planetary Science Letters, 272(1), 1-7.

Castillo, P. R., 2012, Adakite petrogenesis. Lithos, 134, 304-316.

Cavazza, W., Okay, A. I., and Zattin, M., 2009, Rapid early-middle Miocene exhumation of the Kazdağ Massif (western Anatolia). International Journal of Earth Sciences, 98(8), 1935-1947.

Ceyhan, N. and Avsan, M., 2012, Geological map in the Halilağa property. Internal Teck report.

Chávez, W.X., 2000, Supergene oxidation of copper deposits: Zoning and distribution of copper oxide minerals: Society of Economic Geologists Newsletter, no. 41, p. 1, 10–21.

Chiaradia, M., Ulianov, A., Kouzmanov, K., and Beate, B., 2012, Why large porphyry Cu deposits like high Sr/Y magmas?. Scientific reports, 2.

Chiaradia, M., Schaltegger, U., Spikings, R., Wotzlaw, J. F., and Ovtcharova, M., 2013, How Accurately Can We Date the Duration of Magmatic-Hydrothermal Events in Porphyry Systems?—An Invited Paper. Economic Geology, 108(4), 565-584.

Chouinard, A., Williams-Jones, A. E., Leonardson, R. W., Hodgson, C. J., Silva, P., Téllez, C., ... and Rojas, F., 2005, Geology and genesis of the multistage high-sulfidation epithermal Pascua Au-Ag-Cu deposit, Chile and Argentina. Economic Geology, 100(3), 463-490.

Çiftçi, N. B., Temel, R. O., and Iztan, Y. H., 2010, Hydrocarbon occurrences in the western Anatolian (Aegean) grabens, Turkey: Is there a working petroleum system?: AAPG bulletin, 94(12), 1827-1857.

Ciobanu, C., Cook, N. and Stein, H., 2002, Regional setting and geochronology of the Late Cretaceous Banatitic Magmatic and Metallogenetic Belt: Mineralium Deposita, v. 37, p. 541-567.

Clark, A. H., Tosdal, R. M., Farrar, E., and Plazolles, A., 1990, Geomorphologic environment and age of supergene enrichment of the Cuajone, Quellaveco, and Toquepala porphyry copper deposits, southeastern Peru. Economic Geology, 85(7), 1604-1628.

Cline, J. S., and Bodnar, R. J., 1991, Can economic porphyry copper mineralization be generated by a typical calc□alkaline melt?. Journal of Geophysical Research: Solid Earth, 96(B5), 8113-8126.

Cloos, M., 2001, Bubbling magma chambers, cupolas, and porphyry copper deposits. International geology review, 43(4), 285-311.

Cooke, D. R., Hollings, P., and Walshe, J. L., 2005, Giant porphyry deposits: characteristics, distribution, and tectonic controls. Economic Geology, 100(5), 801-818.

Davidson, J., Turner, S., Handley, H., Macpherson, C., and Dosseto, A., 2007, Amphibole “sponge” in arc crust?. Geology, 35(9), 787-790.

Davies, J. F., and Whitehead, R. E., 2010, Alkali/alumina molar ratio trends in altered granitoid rocks hosting porphyry and related deposits. Exploration and Mining Geology, 19(1-2), 13-22.

Defant, M. J., and Drummond, M. S., 1990, Derivation of some modern arc magmas by melting of young subducted lithosphere. Nature, 347(6294), 662-665.

Delaloye, M., and Bingol, E., 2000, Granitoids from western and northwestern Anatolia: geochemistry and modeling of geodynamic evolution. International Geology Review, 42(3), 241-268.

Dilek, Y., and Altunkaynak, Ş., 2007, Cenozoic crustal evolution and mantle dynamics of post-collisional magmatism in western Anatolia. International Geology Review, 49(5), 431-453.

Dilek, Y., and Altunkaynak, Ş., 2009, Geochemical and temporal evolution of Cenozoic magmatism in western Turkey: mantle response to collision, slab break-off, and lithospheric tearing in an orogenic belt. Geological Society, London, Special Publications, 311(1), 213-233.

Dilek, Y., and Sandvol, E., 2009, Seismic structure, crustal architecture and tectonic evolution of the Anatolian-African plate boundary and the Cenozoic orogenic belts in the Eastern Mediterranean region. Geological Society, London, Special Publications, 327(1), 127-160.

Dilles, J. H.,1987, Petrology of the Yerington Batholith, Nevada; evidence for evolution of porphyry copper ore fluids. Economic Geology, 82(7), 1750-1789.

Dilles, J. H., and Einaudi, M. T., 1992, Wall-rock alteration and hydrothermal flow paths about the Ann-Mason porphyry copper deposit, Nevada; a 6-km vertical reconstruction. Economic Geology, 87(8), 1963-2001.

Dixon, C. J., and Pereira, J., 1974, Plate tectonics and mineralization in the Tethyan region. Mineralium Deposita, 9(3), 185-198.

Doerksen, G; Freudigmann, S; Pilotto, D; Rykaart M; Abrahams, G; Simmons, G; Kirkham G; Gray, J., 2015, Revised Preliminary Economic Assessment Technical Report Halilağa Project, Turkey. Prepared for Pilot Gold Inc by JDS Energy and Mining Inc, Canadian National Instrument 43-101 Technical Report, 333 p.

Dönmez, M., Akçay, A.E., Genç, Ş.C. ve A.Ş., 2005, Biga yarımadasında Orta-Üst Eosen volkanizması ve denizel ignimbiritler: MTA Dergisi (MTA Magazine), v.13, p. 49-61.

Duru, M., Dönmez, M., Ilgar, A., Pehlivan, Ş. And Akçay, A. E., 2012, Geological map of the Biga Peninsula: Ankara: MTA (General Directorate of Mineral Research and Exploration of Turkey) Publications, scale: 1/250,000.

Einaudi, M. T., 1997, Mapping altered and mineralized rocks; an introduction to the "Anaconda method. Unpublished report. Stanford, CA: Stanford University Department of Geological and Environmental Sciences.

Ercan, T., Satir, M., Steinitz, G., Dora, A., Sarifakioglu, E., Adis, C., Walter, H.J. and Yildirim, T., 1995, Features of the Tertiary volcanism in the Biga Peninsula and in the islands of Gökçeada, Bozcaada and Tavsan adasi: Maden Tetkik ve Arama Dergisi (In Turkish), v. 114, p. 55-86.

Ersoy, E. Y., and Palmer, M. R., 2013, Eocene-Quaternary magmatic activity in the Aegean: implications for mantle metasomatism and magma genesis in an evolving orogeny. Lithos, 180, 5-24.

Faccenna, C., Bellier, O., Martinod, J., Piromallo, C., and Regard, V., 2006, Slab detachment beneath eastern Anatolia: A possible cause for the formation of the North Anatolian fault. Earth and Planetary Science Letters, 242(1), 85-97.

Ferrigno, D., Defilippi, C., Repetto, P., Welhener, H., Browne, R., Dobr , M., Jutras, M., 2012, Technical Report Kirazli and Ağı Dağı Gold Project, Çanakkale Province, Biga Peninsula of northwestern Turkey. Prepared for Alamos Gold by Kappes, Cassiday and Associates, Canadian National Instrument 43-101 Technical Report, 415 p.

Foland, K. A., 1994, Argon diffusion in K-feldspar, Feldspars and Their Reactions I. Parsons, 415–447.

Force, E. R., Dickinson, W. R., and Hagstrum, J. T., 1995, Tilting history of the San Manuel-Kalamazoo porphyry system, southeastern Arizona. Economic Geology, 90(1), 67-80.

Frei, R., 1995, Evolution of mineralizing fluid in the porphyry copper system of the Skouries Deposit, Northeast Chalkidiki (Greece); evidence from combined Pb-Sr and stable isotope data. Economic Geology, 90(4), 746-762.

Gemmell, J. B., and Large, R. R., 1992, Stringer system and alteration zones underlying the Hellyer volcanogenic massive sulfide deposit, Tasmania, Australia. Economic Geology, 87(3), 620-649.

Genç, Ş., 1998, Evolution of the Bayramiç magmatic complex, northwestern Anatolia. Journal of Volcanology and Geothermal Research, 85(1), 233-249.

Göncüoğlu, M. C., Turhan, N., Şentürk, K., Özcan, A., Uysal, Ş., and Yaliniz, M. K., 2000, A geotraverse across northwestern Turkey: tectonic units of the Central Sakarya region and their tectonic evolution. Geological Society, London, Special Publications, 173(1), 139-161.

Görür, N., Sengör, A. M. C., Sakinü, M., Akkök, R., Yiğitbaş, E., Oktay, F. Y., ... and Aykol, A., 1995, Rift formation in the Gökova region, southwest Anatolia: implications for the opening of the Aegean Sea. Geological Magazine, 132(06), 637-650.

Gow, P. A., and Walshe, J. L., 2005, The role of preexisting geologic architecture in the formation of giant porphyry-related Cu±Au deposits: Examples from New Guinea and Chile. Economic Geology, 100(5), 819-833.

Grant, J. A., 1986, The isocon diagram; a simple solution to Gresens' equation for metasomatic alteration. Economic Geology, 81(8), 1976-1982.

Gruen, G., Heinrich, C. A., and Schroeder, K., 2010, The Bingham Canyon porphyry Cu-Mo-Au

deposit. II. Vein geometry and ore shell formation by pressure-driven rock extension. Economic Geology, 105(1), 69-90.

Guilbert, J. M., and Lowell, J. D., 1995, Tilting history of the San Manuel-Kalamazoo porphyry system, southeastern Arizona; discussion. Economic Geology, 90(7), 2094-2096.

Gürer, Ö. F., Sangu, E., and Özburan, M., 2006, Neotectonics Of The SW Marmara Region, NW Anatolia, Turkey. Geological Magazine, 143(02), 229-241.

Gustafson, L. B., and Hunt, J. P., 1975, The porphyry copper deposit at El Salvador, Chile. Economic Geology, 70(5), 857-912.

Gustafson, L. B., and Quiroga, J., 1995, Patterns of mineralization and alteration below the porphyry copper orebody at El Salvador, Chile. Economic Geology, 90(1), 2-16.

Halley, S., Dilles, J., Tosdal, R., 2015, Footprints: Hydrothermal alteration and geochemical dispersion around porphyry copper deposits. – SEG newsletter, 100, January 2015, 1–17

Hames, W. E., and Bowring, S. A., 1994, An empirical evaluation of the argon diffusion geometry in muscovite. Earth and Planetary Science Letters, 124(1), 161-169.

Harker, A., 1909, The natural history of igneous rocks. Macmillam.

Harris, N. B., Pearce, J. A., and Tindle, A. G., 1986, Geochemical characteristics of collision-zone magmatism. Geological Society, London, Special Publications, 19(1), 67-81.

Harris, A. C., and Holcombe, R. J., 2014, Quartz vein emplacement mechanisms at the E26 porphyry Cu-Au deposit, New South Wales. Economic Geology, 109(4), 1035-1050.

Hartley, A. J., and Rice, C. M., 2005, Controls on supergene enrichment of porphyry copper deposits in the Central Andes: a review and discussion. Mineralium Deposita, 40(5), 515-525.

Hedenquist, J. W., Arribas, A., and Reynolds, T. J., 1998, Evolution of an intrusion-centered hydrothermal system; Far Southeast-Lepanto porphyry and epithermal Cu-Au deposits, Philippines. Economic Geology, 93(4), 373-404.

Hedenquist, J. W., and Taran, Y. A., 2013, Modeling the formation of advanced argillic lithocaps: volcanic vapor condensation above porphyry intrusions. Economic Geology, 108(7), 1523-1540.

Heinrich, C. A., and Neubauer, F., 2002, Cu-Au-Pb-Zn-Ag metallogeny of the Alpine-Balkan-Carpathian-Dinaride geodynamic province. Mineralium Deposita,37(6), 533-540.

Heinrich, C. A., 2005, The physical and chemical evolution of low-salinity magmatic fluids at the porphyry to epithermal transition: a thermodynamic study. Mineralium Deposita, 39(8), 864-889.

Hollings, P., Chen, H., and Cooke, D.R., 2014, Tectonic evolution of the Cerro Casale Au-Cu-porphyry system, Chile: using igneous geochemistry for exploration targeting. In 2014 SEG Conference,Keystone, Colorado.

İmer, A., Richards, J. P., and Creaser, R. A., 2013, Age and tectonomagmatic setting of the Eocene Çöpler–Kabataş magmatic complex and porphyry-epithermal Au deposit, East Central Anatolia, Turkey. Mineralium Deposita, 48(5), 557-583.

Inci, U., 1984, Demici ve Burhaniye bitümlü seyleri stratigrafisi ve organicözellikleri: TJK Bülletin, v. 5, p. 27 – 40.

Janković, S., 1977, The copper deposits and geotectonic setting of the Thethyan Eurasian metallogenic belt. Mineralium Deposita, 12(1), 37-47.

Jankovic, S., 1997, The Carpatho-Balkanides and adjacent area: a sector of the Tethyan Eurasian metallogenic belt: Mineralium Deposita, v. 32, p. 426-433.

Jolivet, L., and Faccenna, C., 2000, Mediterranean extension and the Africa□Eurasia collision. Tectonics, 19(6), 1095-1106.

Jolivet, L., and Brun, J. P. 2010. Cenozoic geodynamic evolution of the Aegean. International Journal of Earth Sciences, 99(1), 109-138.

Jolivet, L., Faccenna, C., Huet, B., Labrousse, L., Le Pourhiet, L., Lacombe, O., ... and Driussi, O., 2013, Aegean tectonics: Strain localisation, slab tearing and trench retreat. Tectonophysics, 597, 1-33.

Kay, R. W., 1978, Aleutian magnesian andesites: melts from subducted Pacific Ocean crust. Journal of Volcanology and Geothermal Research, 4(1), 117-132.

Kesler, S. E., Chryssoulis, S. L., and Simon, G., 2002, Gold in porphyry copper deposits: its abundance and fate. Ore Geology Reviews, 21(1), 103-124.

Kesler, S. E., and Wilkinson, B. H., 2006, The role of exhumation in the temporal distribution of ore deposits. Economic Geology, 101(5), 919-922.

Ketin, I., 1966, Tectonic units of Anatolia (Asia Minor). Min Res Expl Inst Turkey, 66, 22-34.

Kroll, T., Müller, D., Seifert, T., Herzig, P. M., and Schneider, A., 2002, Petrology and geochemistry of the shoshonite-hosted Skouries porphyry Cu–Au deposit, Chalkidiki, Greece. Mineralium Deposita, 37(1), 137-144.

Kürçer, A., Chatzipetros, A., Tutkun, S. Z., Pavlides, S., Ateş, Ö., and Valkaniotis, S., 2008, The Yenice–Gönen active fault (NW Turkey): Active tectonics and palaeoseismology. Tectonophysics, 453(1), 263-275.

Kuscu, I., 2009, Metallogenesis of the Tethyan Collage: Magmatic association and age of ore deposits in Turkey. Year-2 update to sponsor companies. Teck internal report, 45p.

Kuşcu, İ., Tosdal, R. M., Gencalioğlu-Kuşcu, G., Friedman, R., and Ullrich, T. D., 2013, Late Cretaceous to Middle Eocene magmatism and metallogeny of a portion of the Southeastern Anatolian orogenic belt, East-Central Turkey. Economic Geology, 108(4), 641-666.

Landtwing, M. R., Furrer, C., Redmond, P. B., Pettke, T., Guillong, M., and Heinrich, C. A., 2010, The Bingham Canyon porphyry Cu-Mo-Au deposit. III. Zoned copper-gold ore deposition by magmatic vapor expansion. Economic Geology, 105(1), 91-118.

Lang, J. R., Stanley, C. R., Thompson, J. F., and Dunne, K. P., 1995, Na-K-Ca magmatic-hydrothermal alteration in alkalic porphyry Cu-Au deposits, British Columbia. Mineralogical Association of Canada Short Course, 23, 339-366.

Le Maitre, R. W., 1989, A classification of igneous rocks and glossary of terms: Blackwell, Oxford, 193p.

Le Pichon, X., and Kreemer, C., 2010, The Miocene-to-present kinematic evolution of the Eastern Mediterranean and Middle East and its implications for dynamics. Annual Review of Earth and Planetary Sciences, 38, 323-351.

Lehmann, S., Barcikowski, J., Von Quadt, A., Gallhofer, D., Peytcheva, I., Heinrich, C. A., and Serafimovski, T., 2013, Geochronology, geochemistry and isotope tracing of the oligocene magmatism of the Buchim–Damjan–Borov dol ore district: Implications for timing, duration and source of the magmatism. Lithos, 180-181, 216-233. doi:10.1016/j.lithos.2013.09.002

Leroux, G., 2016, Stratigraphic and petrographic characterization of HS epithermal Au-Ag mineralization at the TV Tower district, Biga Peninsula, NW Turkey. Unpublished PhD Thesis, Vancouver, Canada, The University of British Columbia, 452p.

Lips, A.L.W., 2002, Correlating magmatic-hydrothermal ore deposit formation over time with geodynamic processes in SE Europe, In: Blundell, D.J., Neubauer, F., von Quadt, A. (Eds.), The Timing and Location of Major Ore Deposits in an Evolving Orogen. Geological Society London, Special Publication 204, pp. 69-79.

Loucks, R. R., 2014, Distinctive composition of copper-ore-forming arcmagmas. Australian Journal of Earth Sciences, 61(1), 5-16.

Lovera, O. M., Richter, F. M., and Harrison, T. M., 1991, Diffusion domains determined by 39Ar released during step heating. J. Geophys. Res, 96(B2), 2057-2069.

Lovera, O. M., Grove, M., Harrison, T. M., and Mahon, K. I., 1997, Systematic analysis of K-feldspar 40Ar39Ar step heating results: I. Significance of activation energy determinations. Geochimica et Cosmochimica Acta, 61(15), 3171-3192.

Lowell, J. D., 1968, Geology of the Kalamazoo orebody, San manuel district, Arizona. Economic Geology, 63(6), 645-654.

Lowell, J. D., and Guilbert, J. M., 1970, Lateral and vertical alteration-mineralization zoning in porphyry ore deposits. Economic Geology, 65(4), 373-408.

Lowenstern, J. B., 2001, Carbon dioxide in magmas and implications for hydrothermal systems. Mineralium Deposita, 36(6), 490-502.

Madeisky, H. E., and Stanley, C. R., 1993, Lithogeochemical exploration of metasomatic zones associated with volcanic-hosted massive sulfide deposits using Pearce element ratio analysis. International Geology Review, 35(12), 1121-1148.

Maksaev, V., and Zentilli, M., 1999, Fission track thermochronology of the Domeyko Cordillera, northern Chile: Implications for Andean tectonics and porphyry copper metallogenesis. Exploration and Mining Geology, 8(1/2), 65-90.

Marchev, P., Kaiser-Rohrmeier, M., Heinrich, C., Ovtcharova, M., von Quadt, A., and Raicheva, R., 2005, Hydrothermal ore deposits related to post-orogenic extensional magmatism and core complex formation: The Rhodope Massif of Bulgaria and Greece. Ore Geology Reviews, 27(1), 53-89.

Masterman, G. J., Cooke, D. R., Berry, R. F., Clark, A. H., Archibald, D. A., Mathur, R., ... and Durán, M., 2004, 40Ar/39Ar and Re-Os geochronology of porphyry copper-molybdenum deposits and related copper-silver veins in the Collahuasi district, Northern Chile. Economic Geology, 99(4), 673-690.

Masterman, G. J., Cooke, D. R., Berry, R. F., Walshe, J. L., Lee, A. W., and Clark, A. H., 2005, Fluid chemistry, structural setting, and emplacement history of the Rosario Cu-Mo porphyry and Cu-Ag-Au epithermal veins, Collahuasi district, northern Chile. Economic Geology, 100(5), 835-862.

McClusky, S., Balassanian, S., Barka, A., Demir, C., Ergintav, S., Georgiev, I., Gurkan, O., Hamburger, M., Hurst, K. and Kahle, H., 2000, Global Positioning System constraints on plate kinematics and dynamics in the eastern Mediterranean and Caucasus. Journal of Geophysical Research 105, 5695-5720.

McCulloch, M. T., and Gamble, J. A., 1991, Geochemical and geodynamical constraints on subduction

zone magmatism. Earth and Planetary Science Letters, 102(3), 358-374.

McDonough, W. F., Sun, S. S., Ringwood, A. E., Jagoutz, E., and Hofmann, A. W., 1992, Potassium, rubidium, and cesium in the Earth and Moon and the evolution of the mantle of the Earth. Geochimica et Cosmochimica Acta, 56(3), 1001-1012.

Melfos, V., Vavelidis, M., Christofides, G. and Seidel, E., 2002, Origin and evolution of the Tertiary Maronia porphyry copper-molybdenum deposit, Thrace, Greece: Mineralium Deposita, v. 37, p. 648-668.

Menant, A., Jolivet, L., and Vrielynck, B., 2016, Kinematic reconstructions and magmatic evolution illuminating crustal and mantle dynamics of the eastern Mediterranean region since the late Cretaceous. Tectonophysics, 675, 103-140.

Middlemost, E. A., 1994, Naming materials in the magma/igneous rock system. Earth-Science Reviews, 37(3), 215-224.

Moix, P., Beccaletto, L., Kozur, H.W., Hochard, C., Rosselet, F., and Stampfli, G.M., 2008, A new classification of the Turkish terranes and sutures and its implication for the paleotectonic history of the region: Tectonophysics, v. 451, p. 7–39.

Moritz, R., Marton, I., Ortelli, M., Marchev, P., Βουδούρης, Π., Bonev, N., ... and Cosca, M., 2010, A review of age constraints of epithermal precious and base metal deposits of the tertiary eastern Rhodopes: coincidence with late eocene-early oligocene tectonic plate reorganization along the tethys. Επιστημονική Επετηρίδα του Τμήματος Γεωλογίας (ΑΠΘ), 100, 351-358.

Mpodozis, C., and Cornejo, P., 2012, Cenozoic tectonics and porphyry copper systems of the Chilean Andes. Geology and Genesis of Major Copper Deposits and Districts of the World: A Tribute to Richard H. Sillitoe: Society of Economic Geologists Special Publication, 16, 329-360.

Muntean, J. L., and Einaudi, M. T., 2000, Porphyry gold deposits of the Refugio district, Maricunga belt, northern Chile. Economic Geology, 95(7), 1445-1472.

Muntean, J. L., and Einaudi, M. T., 2001, Porphyry-epithermal transition: Maricunga belt, northern Chile. Economic Geology, 96(4), 743-772.

Murakami, H., Watanabe, Y., and Stein, H., 2005, Re-Os ages for molybdenite from the Tepeoba breccia-centered Cu-Mo-Au deposit, western Turkey: Brecciation-triggered mineralization. In Mineral Deposit Research: Meeting the Global Challenge (pp. 805-808). Springer Berlin Heidelberg.

Murakami, H., Seo, J. H., and Heinrich, C. A., 2010, The relation between Cu/Au ratio and formation depth of porphyry-style Cu–Au±Mo deposits. Mineralium Deposita, 45(1), 11-21.

Nicholson, K. N., Khan, M., and Mahmood, K., 2010, Geochemistry of the Chagai–Raskoh arc, Pakistan: Complex arc dynamics spanning the Cretaceous to the Quaternary. Lithos, 118(3), 338-348.

Okay, A. I., Siyako, M., and Burkan, K. A., 1991, Geology and tectonic evolution of the Biga Peninsula, northwest Turkey: Bulletin of the Technical University of Istanbul, v. 44, p. 191-256.

Okay, A.I., Satir, M., Maluski, H., Siyako, M., Monie, P., Metzger, R. and Akyüz, S., 1996, Paleo-and Neo-Tethyan events in northwest Turkey: geological and geochronological constraints. Tectonics of Asia (eds A. Yin and M. Harrison), 420-441.

Okay, A, I., and Tuysuz, O., 1999, Tehtyan sutures of northern Turkey: In: Durand, B., Jolivet, L., Horvath, L., Serranne, M., (eds), The Mediterranean Basins: Tertiary extension within the Alpine Orogen: Geological Society of London, Special Publication no. 146, p. 475-515.

Okay, A. I., Kaşlılar-Özcan, A., Imren, C., Boztepe-Güney, A., Demirbağ, E., and Kuşçu, İ., 2000, Active faults and evolving strike-slip basins in the Marmara Sea, northwest Turkey: a multichannel seismic reflection study.Tectonophysics, 321(2), 189-218.

Okay, A. I., and Satir, M., 2000a, Coeval plutonism and metamorphism in a latest Oligocene metamorphic core complex in northwest Turkey. Geological Magazine, 137(05), 495-516.

Okay, A. I., and Satir, M., 2000b, Upper Cretaceous eclogite-facies metamorphic rocks from the Biga Peninsula, northwest Turkey: Turkish Journal of Earth Science, v. 9, p. 47-56.

Okay, A. L., Satır, M., Tüysüz, O., Akyüz, S., and Chen, F., 2001, The tectonics of the Strandja Massif: late-Variscan and mid-Mesozoic deformation and metamorphism in the northern Aegean. International Journal of Earth Sciences, 90(2), 217-233.

Okay, A. I., Tansel, I., and Tüyzüz O., 2001, Obduction, subduction and collision as reflected in the Upper Cretaceous–Lower Eocene sedimentary record of western Turkey. Geological Magazine, 138(02), 117-142.

Okay, A. I., and Göncüoglu, M.C., 2004, The Karakaya Complex: A review of data and concepts: Turkish Journal of Earth Science, v. 14, p. 77-95.

Okay, A. I., 2008, Geology of Turkey: a synopsis. Anschnitt, 21, 19-42.

Öngen, S., 1992, Les échances métasomatiques entre granitoides et encaissant particuliers (calcaires, dolomies, ultrabasites, series manganiferes): I'example de la Turquie-NW. Doctorat These. Université de Nancy, Faculté des Sciences de la Terre.

Oyarzun, R., Márquez, A., Lillo, J., López, I., and Rivera, S., 2001, Giant versus small porphyry copper deposits of Cenozoic age in northern Chile: adakitic versus normal calc-alkaline magmatism. Mineralium Deposita, 36(8), 794-798.

Öztürk, Y. Y., and Helvaci, C., 2008, Skarn Alteration and Au-Cu Mineralization Associated with Tertiary Granitoids in Northwestern Turkey: Evidence from the Evciler Deposit, Kazdağ Massif, Turkey. Economic Geology, 103(8), 1665-1682.

Pearce, T. H., 1968, A contribution to the theory of variation diagrams. Contributions to Mineralogy and Petrology, 19(2), 142-157.

Pearce, J. A., Harris, N. B., and Tindle, A. G., 1984, Trace element discrimination diagrams for the tectonic interpretation of granitic rocks. Journal of petrology, 25(4), 956-983.

Pearce, J. A., 1996, A user's guide to basalt discrimination diagrams, in Wyman, D.A. (ed) Trace element geochemistry of volcanic rocks: applications for massive sulphide exploration. Geological Association of Canada, Short Course Notes, 12(79), 113.

Peccerillo, A., and Taylor, S. R., 1976, Geochemistry of Eocene calc-alkaline volcanic rocks of the Kastamonu area, northern Turkey: Contributions in Mineral Petrology, v. 58, p. 63-81.

Perelló, J., Razique, A., and Schloderer, J., 2008, The Chagai porphyry copper belt, Baluchistan province, Pakistan. Economic Geology, 103(8), 1583-1612.

Pilot Gold, 2014, Extensive Supergene Copper Zone, indications of two porphyry Cu-Au systems along K2 trend. Press Release, January, 2014.

Pourteau, A., Oberhänsli, R., Candan, O., Barrier, E., and Vrielynck, B., 2016, Neotethyan closure history of western Anatolia: a geodynamic discussion. International Journal of Earth Sciences, 105(1), 203-224.

Rabayrol, F., 2015, Temporal and Spatial Distribution of Porphyry and Epithermal Systems in the Anatolian-Tauride Metallogenic Belt, Turkey: In Miskovic, A., Ed. Western Tethyan Metallogeny Project, Final Technical Report to Companies, MDRU, The University of British Columbia, 2015.

Redmond, P. B., and Einaudi, M. T., 2010, The Bingham Canyon porphyry Cu-Mo-Au deposit. I. Sequence of intrusions, vein formation, and sulfide deposition. Economic Geology, 105(1), 43-68.

Reich, M., Palacios, C., Vargas, G., Luo, S., Cameron, E. M., Leybourne, M. I., ... and You, C. F., 2009, Supergene enrichment of copper deposits since the onset of modern hyperaridity in the Atacama Desert, Chile. Mineralium Deposita, 44(5), 497-504.

Richards, J. P., Boyce, A. J., and Pringle, M. S., 2001, Geologic evolution of the Escondida area, northern Chile: a model for spatial and temporal localization of porphyry Cu mineralization. Economic Geology, 96(2), 271-305.

Richards, J. P., 2003, Tectono-magmatic precursors for porphyry Cu-(Mo-Au) deposit formation. Economic Geology, 98(8), 1515-1533. doi:10.2113/98.8.1515

Richards, J. P., and Kerrich, R., 2007, Special paper: adakite-like rocks: their diverse origins and questionable role in metallogenesis. Economic geology, 102(4), 537-576.

Richards, J. P., 2009, Postsubduction porphyry Cu-Au and epithermal Au deposits: Products of remelting of subduction-modified lithosphere. Geology, 37(3), 247-250.

Richards, J. P., Spell, T., Rameh, E., Razique, A., and Fletcher, T., 2012, High Sr/Y magmas reflect arc maturity, high magmatic water content, and porphyry Cu±Mo±Au potential: examples from the Tethyan arcs of Central and Eastern Iran and Western Pakistan. Economic Geology, 107(2), 295-332.

Richards, J. P., 2014, Tectonic, magmatic, and metallogenic evolution of the Tethyan orogen: From subduction to collision. Ore Geology Reviews.

Rickwood, P. C., 1989, Boundary lines within petrologic diagrams which use oxides of major and minor elements. Lithos, 22(4), 247-263.

Ring, U., Glodny, J., Will, T., and Thomson, S., 2010, The Hellenic subduction system: high-pressure metamorphism, exhumation, normal faulting, and large-scale extension. Annual Review of Earth and Planetary Sciences, 38, 45-76.

Robbins G., 1972, Radiogenic argon diffusion in muscovite under hydrothermal conditions. M.S. Thesis, Brown University. Providence, Rhode Island.

Robertson, A. H., 2002, Overview of the genesis and emplacement of Mesozoic ophiolites in the Eastern Mediterranean Tethyan region. Lithos, 65(1), 1-67.

Rollinson, H, 1993, Using geochemical data, 352 pp.

Rusk, B. G., Reed, M. H., and Dilles, J. H., 2008, Fluid inclusion evidence for magmatic-hydrothermal fluid evolution in the porphyry copper-molybdenum deposit at Butte, Montana. Economic Geology, 103(2), 307-334.

Sanchez, M. G., 2012, Tectonic and structural setting of porphyry Cu-Au and epithermal Au mineralization of the Biga Peninsula, NE Aegean: Unpublished PhD Thesis, London, England, Royal Holloway University.

Sayit, K., Göncüoglu, M. C., and Furman, T., 2010, Petrological reconstruction of Triassic seamounts/

oceanic islands within the Palaeotethys: geochemical implications from the Karakaya subduction/accretion Complex, Northern Turkey. Lithos, 119(3), 501-511.

Sayıt, K., and Göncüoglu, M. C., 2013, Geodynamic evolution of the Karakaya Mélange Complex, Turkey: a review of geological and petrological constraints. Journal of Geodynamics, 65, 56-65.

Scott, K. M., and Yang, K., 1997, Spectral reflectance studies of white micas. Australian Mineral Industries Research Association Ltd. report, 439, 35.

Seedorff, E., Dilles, J. H., Proffett, J. M., Einaudi, M. T., Zurcher, L., Stavast, W. J. A., and Barton, M. D., 2005, Porphyry deposits: characteristics and origin of hypogene features. Economic Geology 100th anniversary volume, 29, 251-298.

Şengör A.M.C., Görür N., Saroglu F., 1985, Strike-slip faulting and related basin formation in zones of tectonic escape: Turkey as a case study, in: Biddle K.T., Christie-Blick N. (Eds.), Strike-slip Faulting and Basin Formation, Soc. Econ. Paleontol. Mineral. Sp. Pub., 37, pp. 227–264.

Şengor, A.M.C., 1987, Tectonics of the Tethysides: Orogenic Collage Development in a Collisional Setting. Annual Reviews in Earth and Planetary Sciences 15(1), 213-244.

Şengör, A.M.C., Tüysüz, O., Imren, C., Sakinç, M., Eyidogan, H., Görür, N., Le Pichon, X. and Rangin, C., 2005, The North Anatolian Fault: a new look. Annu. Rev. Earth Planet Sci. 33, 37-112.

Şengün, F., Yiğitbaş, E., and Tunc, I. O., 2011, Geology and tectonic emplacement of eclogite and blueschists, Biga peninsula, northwest Turkey.Turkish Journal of Earth Sciences, 20(3), 273-285.

Seyitoglu, G., and Scott, B., 1991, Late Cenozoic crustal extension and basin formation in west Turkey. Geological Magazine, 128(2), 155-166.

Seyitoğlu, G., and Scott, B.C., 1996, The cause of N–S extensional tectonics in western Turkey: Tectonic escape vs back-arc spreading vs orogenic collapse: Journal of Geodynamics, v. 22, p. 145–153.

Sillitoe, R. H., 1979, Some thoughts on gold-rich porphyry copper deposits. Mineralium Deposita, 14(2), 161-174.

Sillitoe, R. H., 1994, Erosion and collapse of volcanoes: Causes of telescoping in intrusion-centered ore deposits. Geology, 22(10), 945-948.

Sillitoe, R. H., 1997, Characteristics and controls of the largest porphyry copper□gold and epithermal

gold deposits in the circum□Pacific region. Australian Journal of Earth Sciences, 44(3), 373-388.

Sillitoe, R. H., 2000, Gold-rich porphyry deposits, descriptive and genetic models and their role in exploration and discovery. SEG Reviews, 13, 315-345.

Sillitoe, R. H., 2010, Porphyry copper systems. Economic Geology, 105(1), 3-41.

Sillitoe, R. H., Tolman, J., and Van Kerkvoort, G., 2013, Geology of the caspiche porphyry gold-copper deposit, Maricunga Belt, Northern Chile. Economic Geology, 108(4), 585-604.

Simmons, S. F., White, N. C., and John, D. A., 2005, Geological characteristics of epithermal precious and base metal deposits. Economic Geology 100th anniversary volume, 29, 485-522.

Siyako, M., Bürkan, K.A. and Okay, A.I., 1989, Tertiary geology and hydrocarbon potential of the Biga and Gelibolu peninsulas: Turkish Association of Petroleum Geologists Bulletin, v. 1, p. 183–99.

Siyako, M., and Huvaz, O., 2007, Eocene stratigraphic evolution of the Thrace Basin, Turkey. Sedimentary Geology, 198(1), 75-91.

Smith, M. T., Lepore, W. A., Incekaraoğlu, T., Shabestari, P., Boran, H., and Raabe, K., 2014, Küçükdağ: A New, High Sulfidation Epithermal Au-Ag-Cu Deposit At The Tv Tower Property In Western Turkey: ECONOMIC GEOLOGY, v. 109, p. 1501-1511.

Stampfli, G. M., 2000, Tethyan oceans. Geological society, london, special publications, 173(1), 1-23.

Stampfli, G. M., Vavassis, I., De Bono, A., Rosselet, F., Matti, B. and Bellini, M., 2003, Remnants of the Paleotethys oceanic suturezone in the western Tethyan area. In: Cassinis, G. and Decandia, F. A. (eds), Stratigraphic and Structural Evolution on the Late Carboniferous to Triassic Continental and Marine Successions in Tuscany (Italy): Regional Reports and General Correlation. Bolletino della Societa Geologica Italiana, Volume speciale 2,1-23.

Stampfli, G.M., Borel, G.D., 2004, The TRANSMED transects in space and time: constraints on the paleotectonic evolution of the Mediterranean domain. In: Cavazza, W., Roure, F., Spakman, W., Stampfli, G.M., Ziegler, P. (Eds.), The TRANSMED Atlas: The Mediterranean Region from Crust to Mantle. Springer Verlag, Berlin, pp. 53–80.

Stanley, C. R., and Madeisky, H. E., 1994, Lithogeochemical exploration for hydrothermal ore deposits using Pearce element ratio analysis. Alteration and alteration processes associated with ore-forming systems: Geological Association of Canada, Short Course Notes, 11, 193-211.

Stavast, W. J., Butler, R. F., Seedorff, E., Barton, M. D., and Ferguson, C. A., 2008, Tertiary tilting

and dismemberment of the Laramide arc and related hydrothermal systems, Sierrita Mountains, Arizona. Economic Geology, 103(3), 629-636.

Sun, S. S., and McDonough, W. S., 1989, Chemical and isotopic systematics of oceanic basalts: implications for mantle composition and processes. Geological Society, London, Special Publications, 42(1), 313-345.

Taylor, S. R., and McLennan, S. M., 1985, The continental crust: its composition and evolution Blackwell Scientific Publications, Oxford, 312 p.

Taymaz, T., Jackson, J., and McKenzie, D., 1991, Active tectonics of the north and central Aegean Sea. Geophysical Journal International, 106(2), 433-490.

Thiéblemont, D., Stein, G., and Lescuyer, J. L., 1997, Gisements épithermaux et porphyriques: la connexion adakite. Comptes Rendus de l'Académie des Sciences-Series IIA-Earth and Planetary Science, 325(2), 103-109.

Thompson, A. J., Hauff, P. L., and Robitaille, A. J., 1999, Alteration mapping in exploration: application of short-wave infrared (SWIR) spectroscopy. SEG newsletter, 39(p. 1), 16-27.

Tosdal, R. M., and Richards, J. P., 2001, Magmatic and structural controls on the development of porphyry Cu±Mo±Au deposits. Reviews in Economic Geology, 14, 157-181

Tosdal, R. M., Dilles, J. H., and Cooke, D. R., 2009, From source to sinks in auriferous magmatic-hydrothermal porphyry and epithermal deposits. Elements, 5(5), 289-295.

Tunç, İ. O., Yiğitbaş, E., Şengün, F., Wazeck, J., Hofmann, M., and Linnemann, U., 2012, U-Pb zircon geochronology of northern metamorphic massifs in the Biga Peninsula (NW Anatolia-Turkey): new data and a new approach to understand the tectonostratigraphy of the region: Geodinamica Acta, v. 25, no. 3-4, p. 202-225.

Ulrich, T., Günther, D., and Heinrich, C. A., 2001, The evolution of a porphyry Cu-Au deposit, based on LA-ICP-MS analysis of fluid inclusions: Bajo de la Alumbrera, Argentina. Economic Geology, 96(8), 1743-1774.

Ulrich, T., and Heinrich, C. A., 2002, Geology and alteration geochemistry of the porphyry Cu-Au deposit at Bajo de la Alumbrera, Argentina. Economic Geology, 97(8), 1865-1888.

Ünal İmer, E., Güleç, N., Kuşcu, İ., and Fallick, A. E., 2013, Genetic investigation and comparison of Kartaldağ and Madendağ epithermal gold deposits in Çanakkale, NW Turkey. Ore Geology Reviews, 53, 204-222. doi:10.1016/j.oregeorev.2013.01.009

Urqueta, E., Kyser, T. K., Clark, A. H., Stanley, C. R., and Oates, C. J., 2009, Lithogeochemistry of the Collahuasi porphyry Cu–Mo and epithermal Cu–Ag (–Au) cluster, northern Chile:

Pearce element ratio vectors to ore. Geochemistry: Exploration, Environment, Analysis, 9(1), 9-17.

Van Hinsbergen, D. J., 2010, A key extensional metamorphic complex reviewed and restored: the Menderes Massif of western Turkey. Earth-Science Reviews, 102(1), 60-76.

Vila, T., and Sillitoe, R. H., 1991, Gold-rich porphyry systems in the Maricunga belt, northern Chile. Economic Geology, 86(6), 1238-1260.

Warren, I., Simmons, S. F., and Mauk, J. L., 2007, Whole-rock geochemical techniques for evaluating hydrothermal alteration, mass changes, and compositional gradients associated with epithermal Au-Ag mineralization. Economic Geology, 102(5), 923-948.

Wilkinson, B. H., and Kesler, S. E., 2007, Tectonism and exhumation in convergent margin orogens: Insights from ore deposits. The Journal of Geology, 115(6), 611-627.

Williams-Jones, A. E., and Heinrich, C. A., 2005, 100th Anniversary special paper: vapor transport of metals and the formation of magmatic-hydrothermal ore deposits. Economic Geology, 100(7), 1287-1312.

Winchester, J. A., and Floyd, P. A., 1977, Geochemical discrimination of different magma series and their differentiation products using immobile elements. Chemical geology, 20, 325-343.

Yang, K., Lian, C., Huntington, J. F., Peng, Q., and Wang, Q., 2005, Infrared spectral reflectance characterization of the hydrothermal alteration at the Tuwu Cu–Au deposit, Xinjiang, China. Mineralium deposita, 40(3), 324-336.

Yanites, B. J., and Kesler, S. E., 2015, A climate signal in exhumation patterns revealed by porphyry copper deposits. Nature Geoscience, 8(6), 462-465.

Yiğit, O., 2006, Gold in Turkey—a missing link in Tethyan metallogeny. Ore Geology Reviews, 28(2), 147-179.

Yiğit, O., 2009, Mineral deposits of Turkey in relation to Tethyan metallogeny: implications for future mineral exploration. Economic Geology, 104(1), 19-51.

Yiğit, O., 2012, A prospective sector in the Tethyan Metallogenic Belt: Geology and geochronology of mineral deposits in the Biga Peninsula, NW Turkey: Ore Geology Reviews, v. 46, p. 118-148.

Yilmaz, Y., Genç, Ş. C., Gürer, F., Bozcu, M., Yilmaz, K., Karacik, Z., and Elmas, A., 2000, When did the western Anatolian grabens begin to develop?.Geological Society, London, Special Publications, 173(1), 353-384.

Yilmaz, Y., and Karacik, Z., 2001, Geology of the northern side of the Gulf of Edremit and its tectonic

significance for development of the Aegean grabens: Geodinamica Acta, v. 14, p. 31-43.

Yilmaz, H., 2003, Exploration at the Kuscayiri Au (Cu) prospect and its implications for porphyry-related mineralization in western Turkey. Journal of Geochemical Exploration, 77(2), 133-150.

Yılmaz, Y., Gökaşan, E., and Erbay, A. Y., 2010, Morphotectonic development of the Marmara Region. Tectonophysics, 488(1), 51-70.

Appendix A: Strip Logs

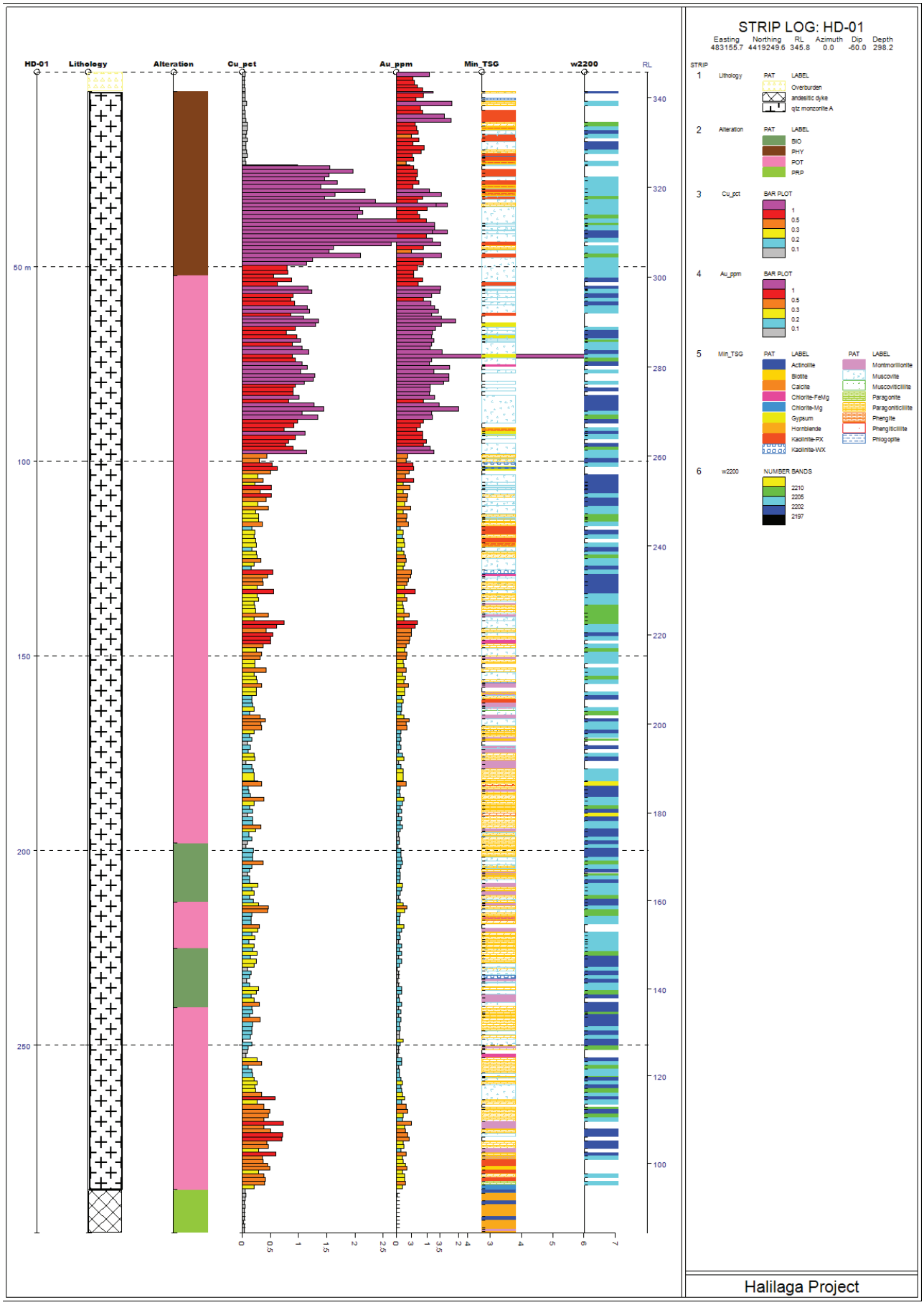
HD-01
Lithology
Alteration
Cu_pct
Au_ppm
Min_TSG
w2200
RL
50 m
100
150
200
250
340
320
300
280
260
240
220
200
180
160
140
120
100
STRIP LOG: HD-01
Easting 483155.7
Northing 4419249.6
RL 345.8
Azimuth 0.0
Dip -60.0
Depth 298.2
STRIP
1 Lithology
PAT
LABEL
Overburden
andesitic dyke
qtz monzonite A
2 Alteration
BIO
PHY
POT
PRP
3 Cu_pct
BAR PLOT
1
0.5
0.3
0.2
0.1
4 Au_ppm
5 Min_TSG
Actinolite
Biotite
Calcite
Chlorite-FeMg
Chlorite-Mg
Gypsum
Hornblende
Kaolinite-PX
Kaolinite-WX
Montmorillonite
Muscovite
Muscovitic/illite
Paragonite
Paragonitic/illite
Phengite
Phengitic/illite
Phlogopite
6 w2200
NUMBER BANDS
2210
2205
2202
2197
Halilaga Project

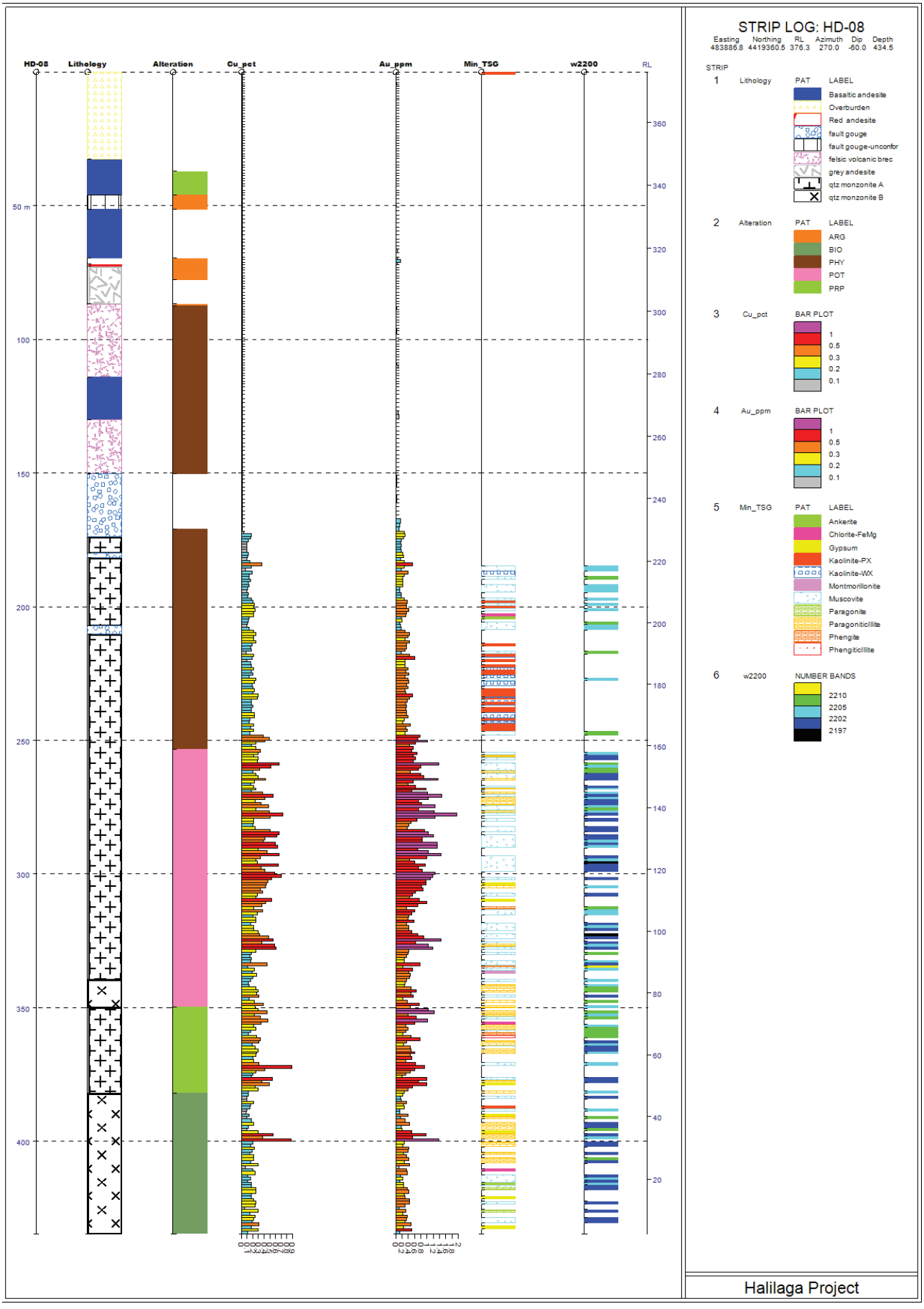
HD-08
Lithology
Alteration
Cu_pct
Au_ppm
Min_TSG
w2200
RL
50 m
100
150
200
250
300
350
400
360
340
320
300
280
260
240
220
200
180
160
140
120
100
80
60
40
20
STRIP LOG: HD-08
Easting 483886.8
Northing 4419360.5
RL 376.3
Azimuth 270.0
Dip -60.0
Depth 434.5
STRIP
1 Lithology
PAT
LABEL
Basaltic andesite
Overburden
Red andesite
fault gouge
fault gouge-unconfor
felsic volcanic brec
grey andesite
qtz monzonite A
qtz monzonite B
2 Alteration
PAT
LABEL
ARG
BIO
PHY
POT
PRP
3 Cu_pct
BAR PLOT
1
0.5
0.3
0.2
0.1
4 Au_ppm
BAR PLOT
1
0.5
0.3
0.2
0.1
5 Min_TSG
PAT
LABEL
Ankerite
Chlorite-FeMg
Gypsum
Kaolinite-PX
Kaolinite-WX
Montmorillonite
Muscovite
Paragonite
Paragoniticillite
Phengite
Phengiticillite
6 w2200
NUMBER BANDS
2210
2205
2202
2197
Halilaga Project

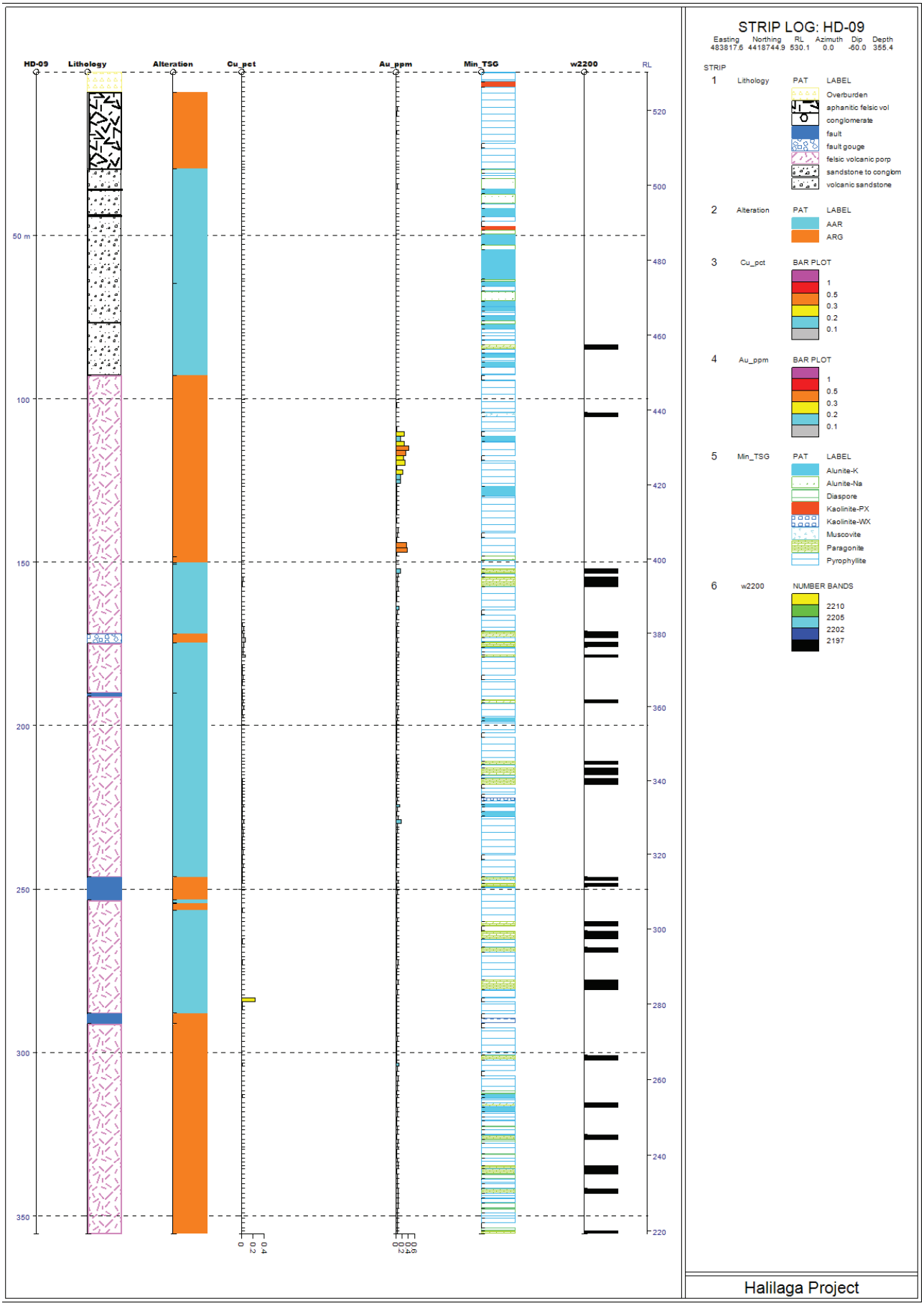
HD-09
Lithology
Alteration
Cu_pct
Au_ppm
Min_TSG
w2200
RL
50 m
100
150
200
250
300
350
520
500
480
460
440
420
400
380
360
340
320
300
280
260
240
220
0
0.2
0.4
2
4
6
STRIP LOG: HD-09
Easting 483817.6
Northing 4418744.9
RL 530.1
Azimuth 0.0
Dip -60.0
Depth 355.4
STRIP
1 Lithology
PAT
LABEL
Overburden
aphanitic felsic vol
conglomerate
fault
fault gouge
felsic volcanic porp
sandstone to conglom
volcanic sandstone
2 Alterstion
PAT
LABEL
AAR
ARG
3 Cu_pct
BAR PLOT
1
0.5
0.3
0.2
0.1
4 Au_ppm
BAR PLOT
1
0.5
0.3
0.2
0.1
5 Min_TSG
PAT
LABEL
Alunite-K
Alunite-Na
Diaspore
Kaolinite-PX
Kaolinite-WX
Muscovite
Paragonite
Pyrophyllite
6 w2200
NUMBER BANDS
2210
2205
2202
2197
Halilaga Project

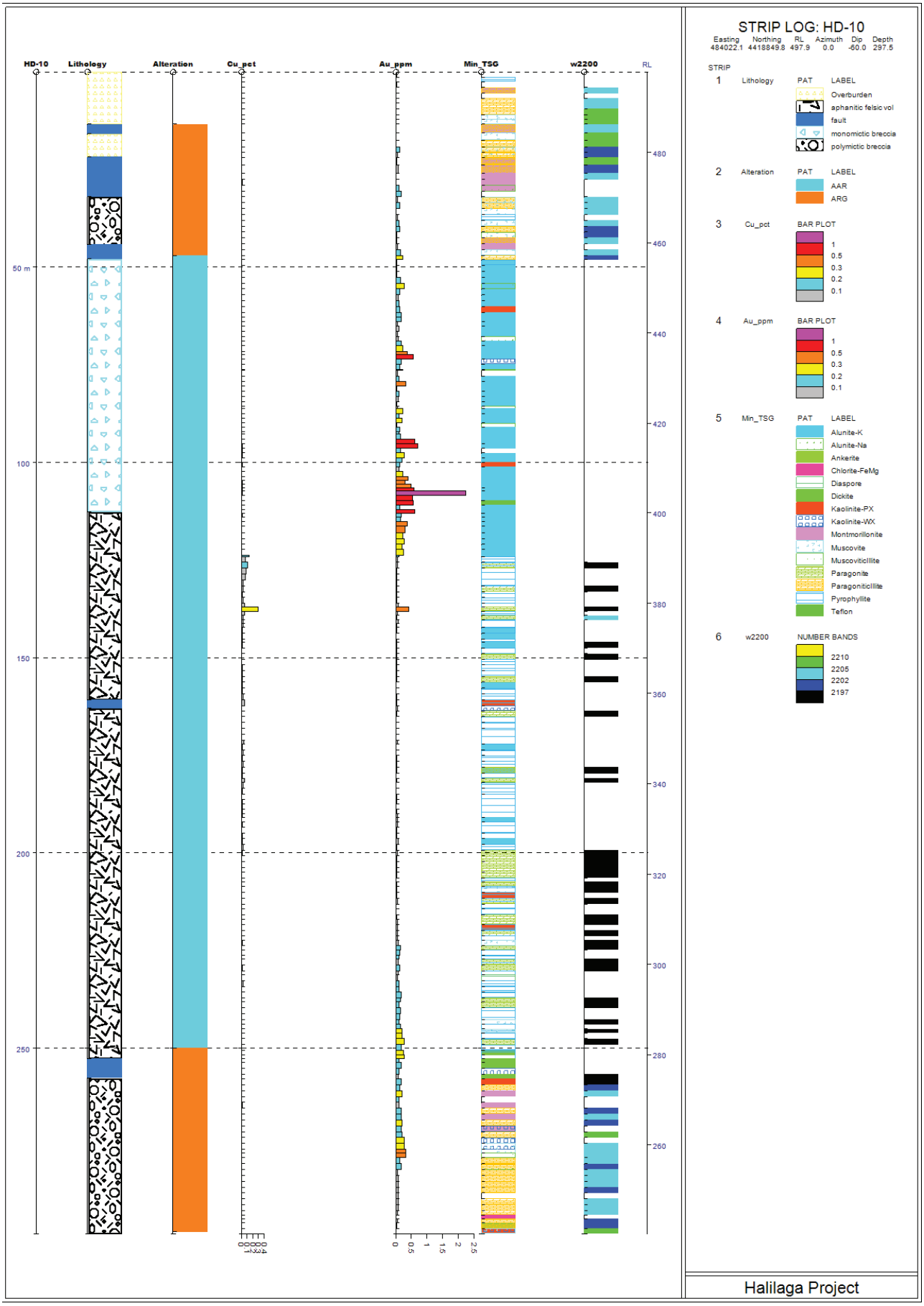
HD-10
Lithology
Alteration
Cu_pct
Au_ppm
Min_TSG
w2200
RL
50 m
100
150
200
250
480
460
440
420
400
380
360
340
320
300
280
260
0
0.5
1
1.5
2
2.5
STRIP LOG: HD-10
Easting 484022.1
Northing 4418849.8
RL 497.9
Azimuth 0.0
Dip -60.0
Depth 297.5
STRIP
1 Lithology
PAT
LABEL
Overburden
aphanitic felsic vol
fault
monomictic breccia
polymictic breccia
2 Alteration
PAT
LABEL
AAR
ARG
3 Cu_pct
BAR PLOT
1
0.5
0.3
0.2
0.1
4 Au_ppm
BAR PLOT
1
0.5
0.3
0.2
0.1
5 Min_TSG
PAT
LABEL
Alunite-K
Alunite-Na
Ankerite
Chlorite-FeMg
Diaspore
Dickite
Kaolinite-PX
Kaolinite-WX
Montmorillonite
Muscovite
Muscoviticillite
Paragonite
Paragoniticillite
Pyrophyllite
Teflon
6 w2200
NUMBER BANDS
2210
2205
2202
2197
Halilaga Project

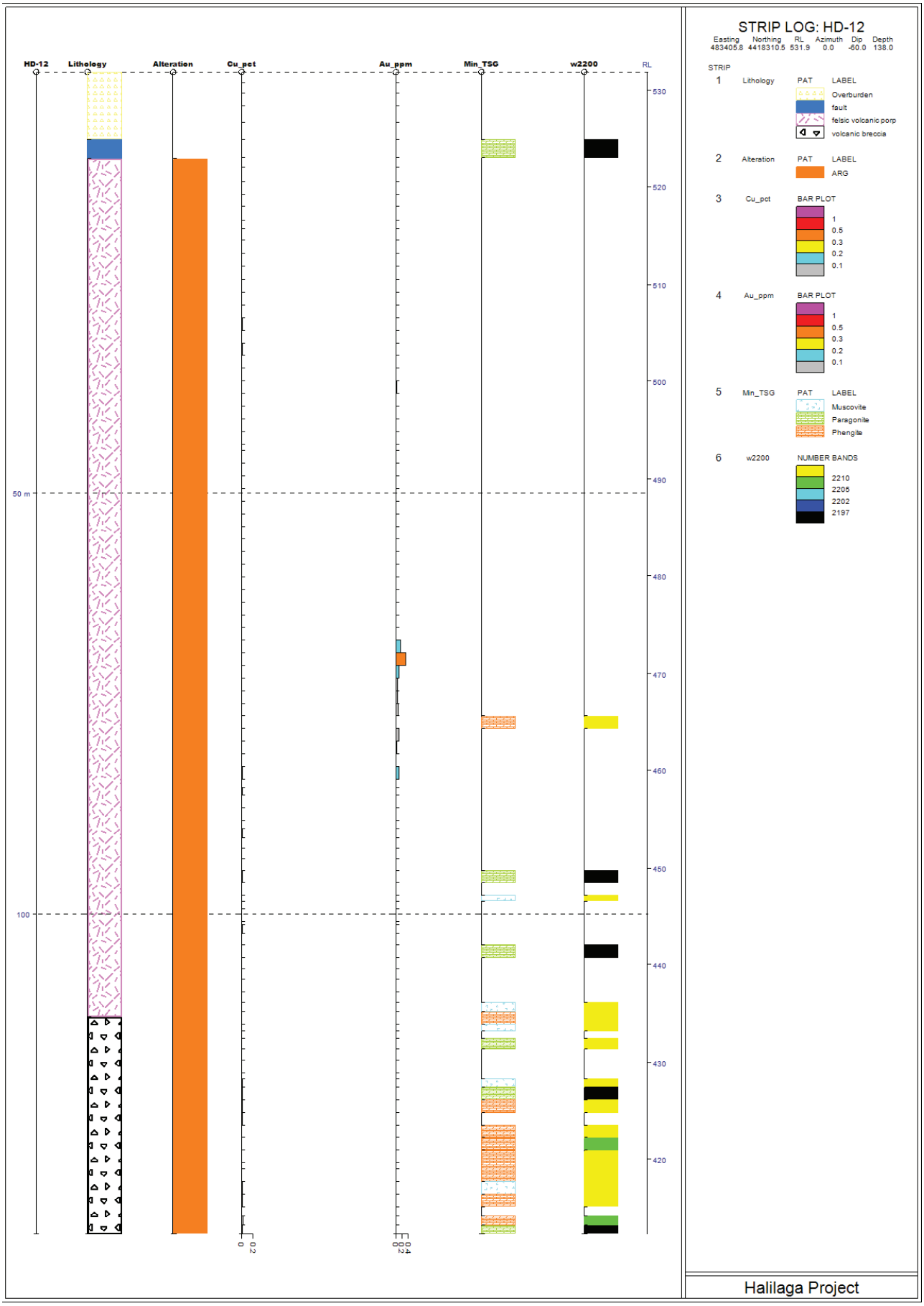
HD-12
Lithology
Alteration
Cu_pct
Au_ppm
Min_TSG
w2200
RL
530
520
510
500
490
480
470
460
450
440
430
420
50 m
100
0
0.2
0
0.2
0.4
STRIP LOG: HD-12
Easting 483405.8
Northing 4418310.5
RL 531.9
Azimuth 0.0
Dip -60.0
Depth 138.0
STRIP
1 Lithology PAT LABEL
Overburden
fault
felsic volcanic porp
volcanic breccia
2 Alteration PAT LABEL
ARG
3 Cu_pct BAR PLOT
1
0.5
0.3
0.2
0.1
4 Au_ppm BAR PLOT
1
0.5
0.3
0.2
0.1
5 Min_TSG PAT LABEL
Muscovite
Paragonite
Phengite
6 w2200 NUMBER BANDS
2210
2205
2202
2197
Halilaga Project

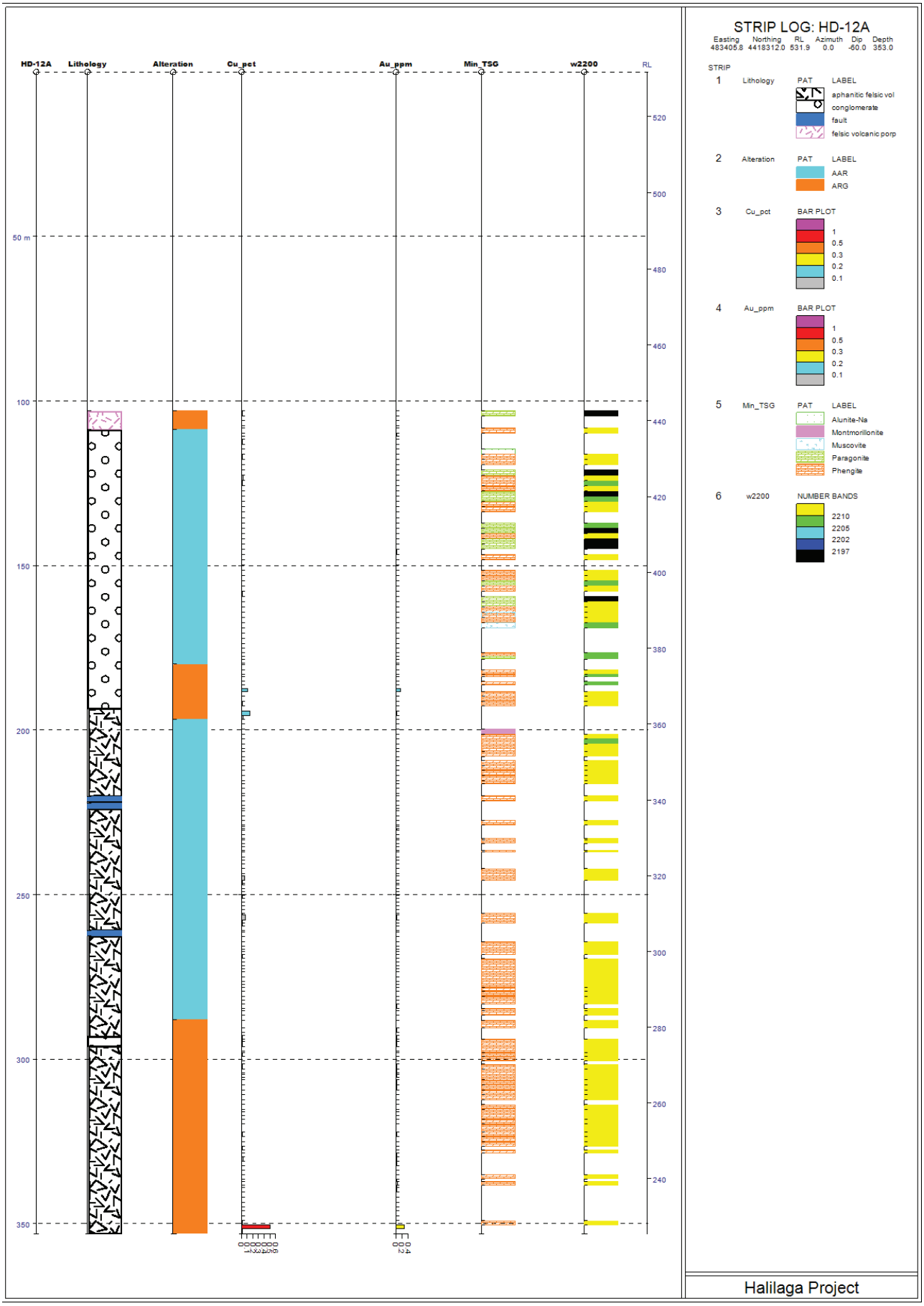
HD-12A
Lithology
Alteration
Cu_pct
Au_ppm
Min_TSG
w2200
RL
50 m
520
500
480
460
440
420
400
380
360
340
320
300
280
260
240
100
150
200
250
300
350
STRIP LOG: HD-12A
Easting 483405.8
Northing 4418312.0
RL 531.9
Azimuth 0.0
Dip -60.0
Depth 353.0
STRIP
1 Lithology PAT LABEL
aphanitic felsic vol
conglomerate
fault
felsic volcanic porp
2 Alteration PAT LABEL
AAR
ARG
3 Cu_pct BAR PLOT
1
0.5
0.3
0.2
0.1
4 Au_ppm BAR PLOT
1
0.5
0.3
0.2
0.1
5 Min_TSG PAT LABEL
Alunite-Na
Montmorillonite
Muscovite
Paragonite
Phengite
6 w2200 NUMBER BANDS
2210
2205
2202
2197
Halilaga Project

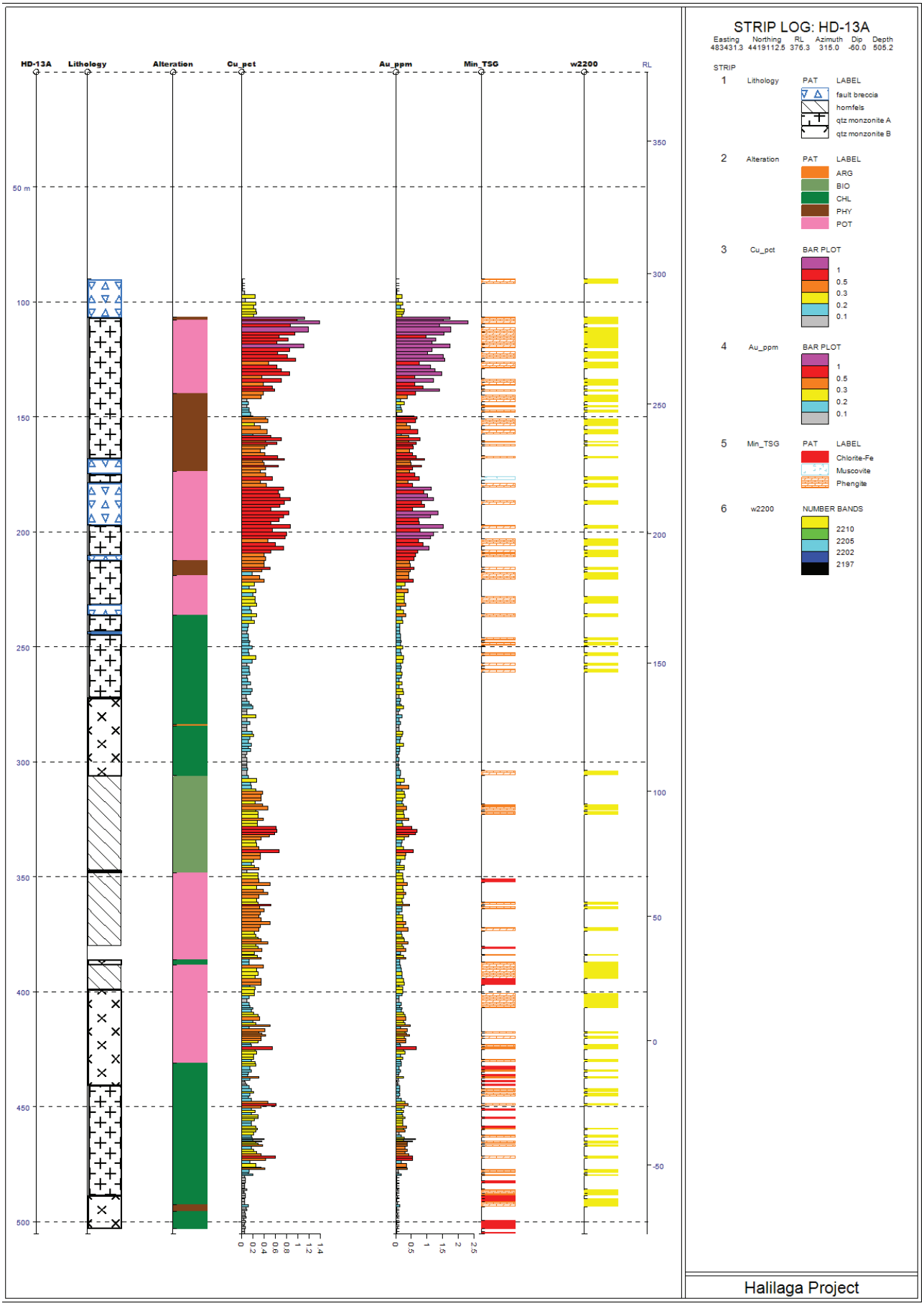
HD-13A
Lithology
Alteration
Cu_pct
Au_ppm
Min_TSG
w2200
RL
50 m
100
150
200
250
300
350
400
450
500
350
300
250
200
150
100
50
0
-50
0 0.2 0.4 0.6 0.8 1 1.2 1.4
0 0.5 1 1.5 2 2.5
STRIP LOG: HD-13A
Easting 483431.3
Northing 4419112.5
RL 376.3
Azimuth 315.0
Dip -60.0
Depth 505.2
STRIP
1 Lithology
PAT
LABEL
fault breccia
hornfels
qtz monzonite A
qtz monzonite B
2 Alteration
PAT
LABEL
ARG
BIO
CHL
PHY
POT
3 Cu_pct
BAR PLOT
1
0.5
0.3
0.2
0.1
4 Au_ppm
BAR PLOT
1
0.5
0.3
0.2
0.1
5 Min_TSG
PAT
LABEL
Chlorite-Fe
Muscovite
Phengite
6 w2200
NUMBER BANDS
2210
2205
2202
2197
Halilaga Project

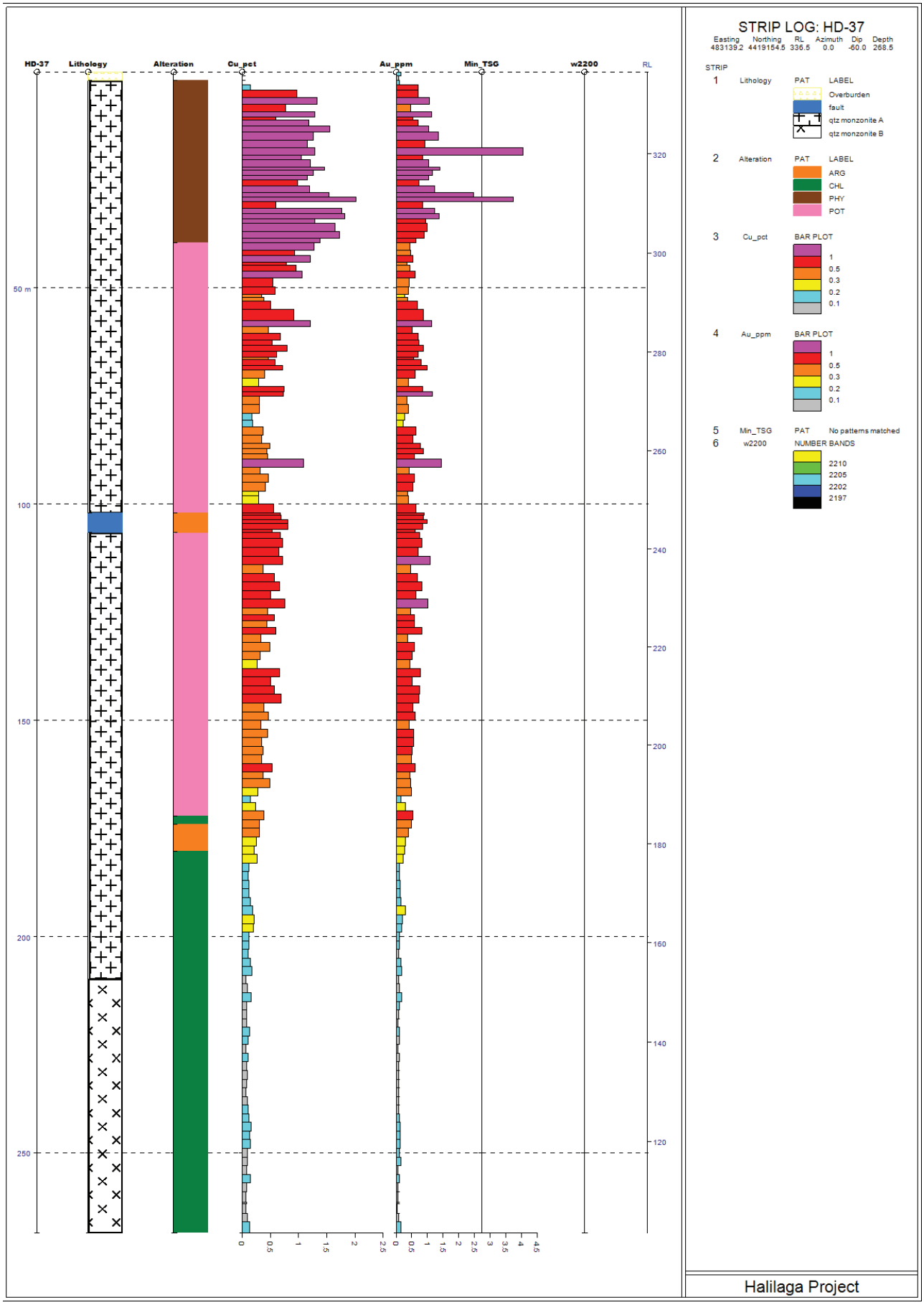
HD-37
Lithology
Alteration
Cu_pct
Au_ppm
Min_TSG
w2200
RL
50 m
100
150
200
250
320
300
280
260
240
220
200
180
160
140
120
0
0.5
1
1.5
2
2.5
3
3.5
4
4.5
STRIP LOG: HD-37
Easting 483139.2
Northing 4419154.5
RL 336.5
Azimuth 0.0
Dip -60.0
Depth 268.5
STRIP
1 Lithology PAT LABEL
Overburden
fault
qtz monzonite A
qtz monzonite B
2 Alteration PAT LABEL
ARG
CHL
PHY
POT
3 Cu_pct BAR PLOT
1
0.5
0.3
0.2
0.1
4 Au_ppm BAR PLOT
1
0.5
0.3
0.2
0.1
5 Min_TSG PAT No patterns matched
6 w2200 NUMBER BANDS
2210
2205
2202
2197
Halilaga Project

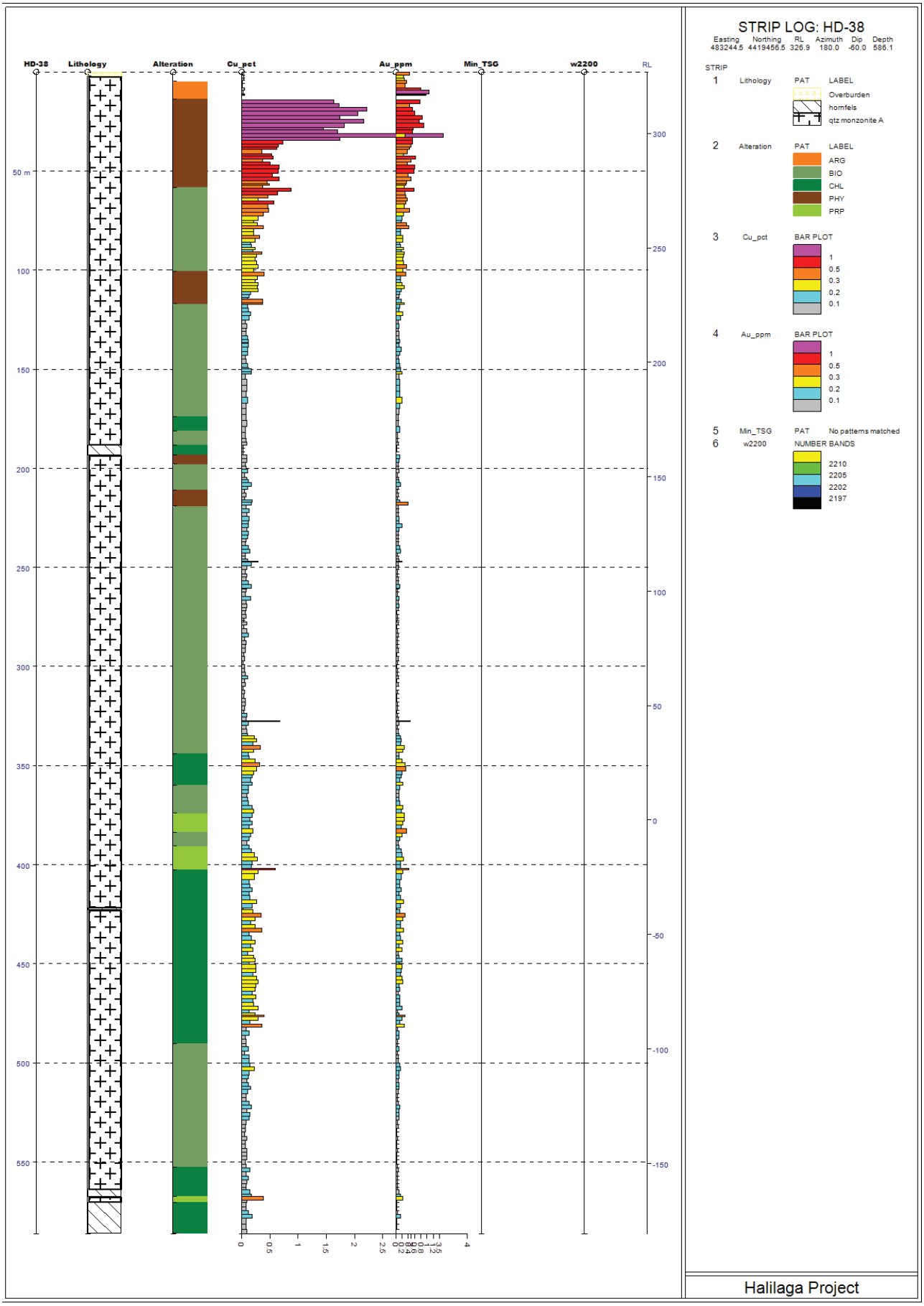

STRIP LOG: HD-38

Easting	Northing	RL	Azimuth	Dip	Depth
483244.5	4419456.5	326.9	180.0	-60.0	586.1

STRIP

1 Lithology — PAT — LABEL
- Overburden
- hornfels
- qtz monzonite A

2 Alteration — PAT — LABEL
- ARG
- BIO
- CHL
- PHY
- PRP

3 Cu_pct — BAR PLOT
- 1
- 0.5
- 0.3
- 0.2
- 0.1

4 Au_ppm — BAR PLOT
- 1
- 0.5
- 0.3
- 0.2
- 0.1

5 Min_TSG — PAT — No patterns matched

6 w2200 — NUMBER BANDS
- 2210
- 2205
- 2202
- 2197

Halilaga Project

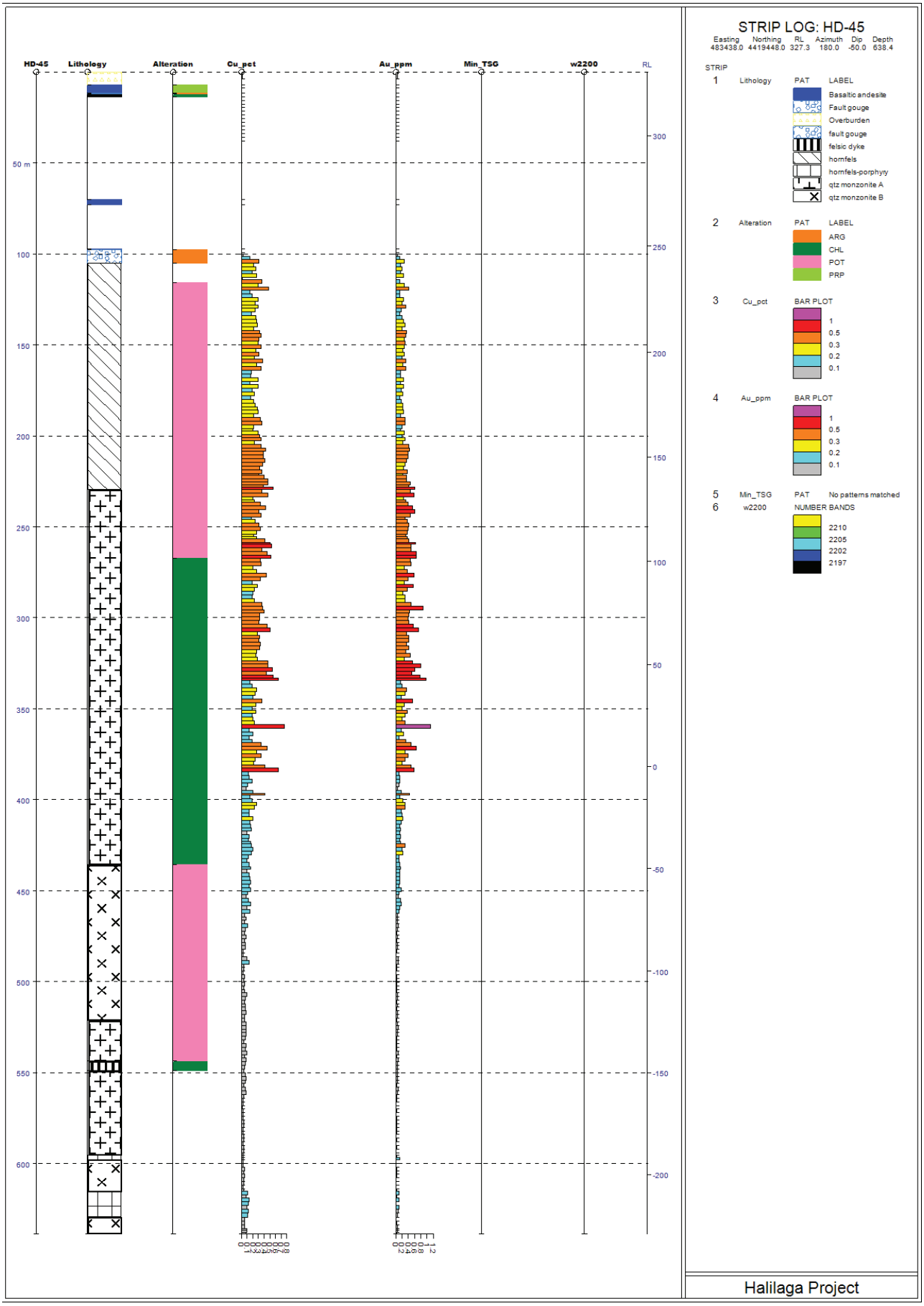
HD-45
Lithology
Alteration
Cu_pct
Au_ppm
Min_TSG
w2200
RL
50 m
STRIP LOG: HD-45
Easting 483438.0
Northing 4419448.0
RL 327.3
Azimuth 180.0
Dip -50.0
Depth 638.4
STRIP
1 Lithology
PAT
LABEL
Basaltic andesite
Fault gouge
Overburden
fault gouge
felsic dyke
hornfels
hornfels-porphyry
qtz monzonite A
qtz monzonite B
2 Alteration
PAT
LABEL
ARG
CHL
POT
PRP
3 Cu_pct
BAR PLOT
1
0.5
0.3
0.2
0.1
4 Au_ppm
BAR PLOT
1
0.5
0.3
0.2
0.1
5 Min_TSG
PAT
No patterns matched
6 w2200
NUMBER BANDS
2210
2205
2202
2197
Halilaga Project

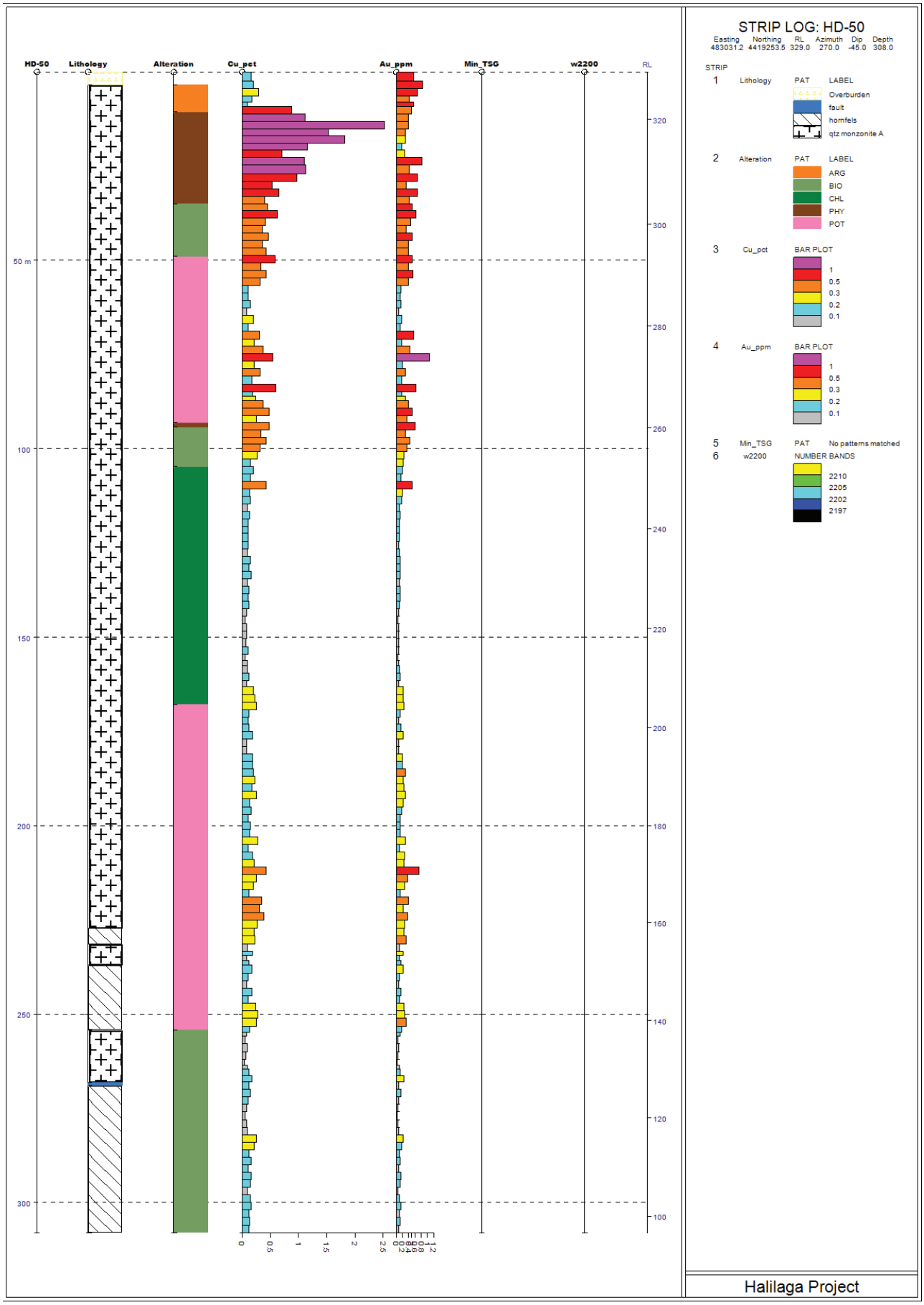
HD-50
Lithology
Alteration
Cu_pct
Au_ppm
Min_TSG
w2200
RL
50 m
100
150
200
250
300
320
300
280
260
240
220
200
180
160
140
120
100
0
0.5
1
1.5
2
2.5
STRIP LOG: HD-50
Easting 483031.2
Northing 4419253.5
RL 329.0
Azimuth 270.0
Dip -45.0
Depth 308.0
STRIP
1 Lithology PAT LABEL
Overburden
fault
hornfels
qtz monzonite A
2 Alteration PAT LABEL
ARG
BIO
CHL
PHY
POT
3 Cu_pct BAR PLOT
1
0.5
0.3
0.2
0.1
4 Au_ppm BAR PLOT
1
0.5
0.3
0.2
0.1
5 Min_TSG PAT No patterns matched
6 w2200 NUMBER BANDS
2210
2205
2202
2197
Halilaga Project

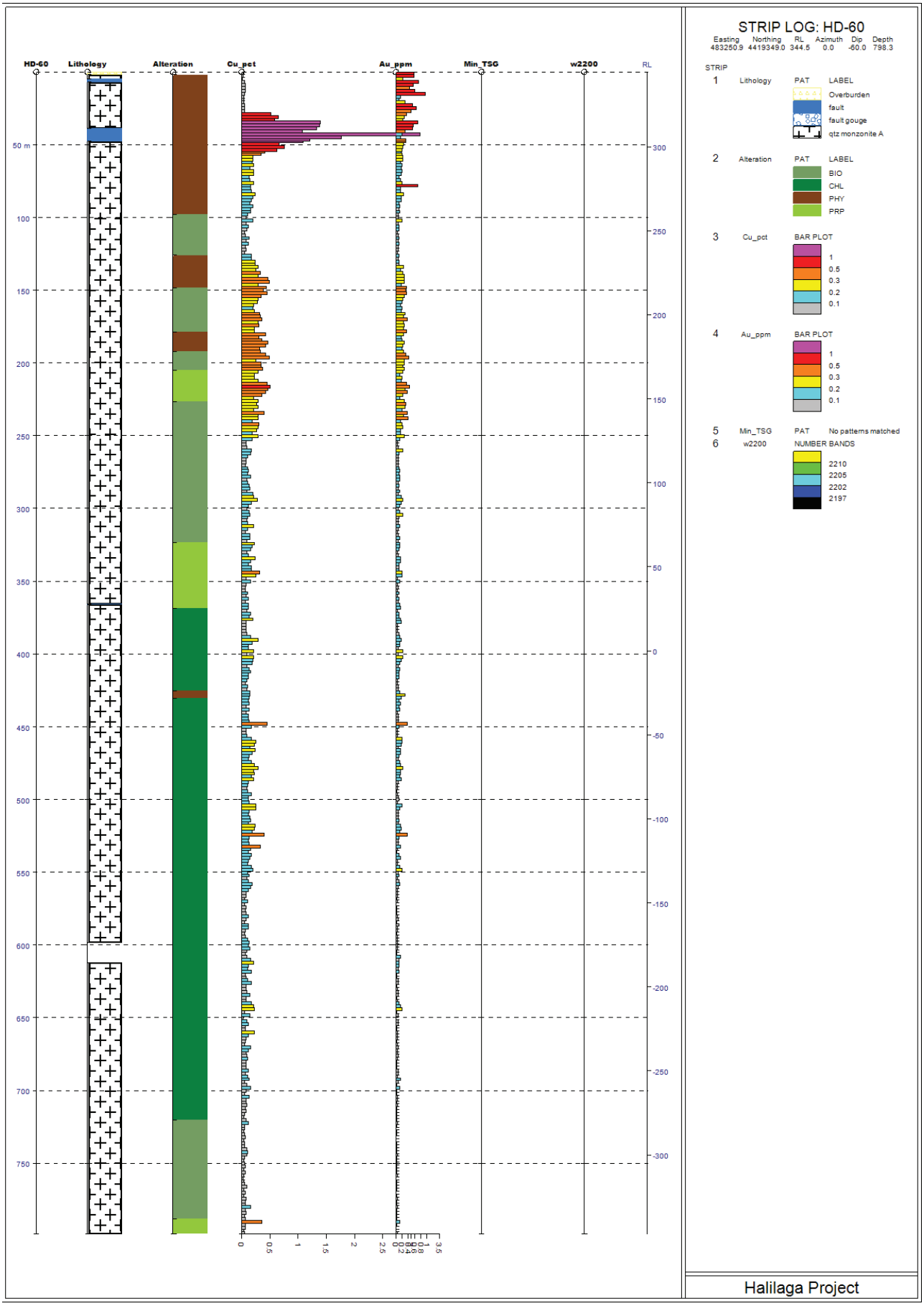
HD-60
Lithology
Alteration
Cu_pct
Au_ppm
Min_TSG
w2200
RL
50 m
100
150
200
250
300
350
400
450
500
550
600
650
700
750
300
250
200
150
100
50
0
-50
-100
-150
-200
-250
-300
0
0.5
1
1.5
2
2.5
0.2
0.4
0.6
0.8
1
3.5
STRIP LOG: HD-60
Easting Northing RL Azimuth Dip Depth
483250.9 4419349.0 344.5 0.0 -60.0 798.3
STRIP
1 Lithology PAT LABEL
Overburden
fault
fault gouge
qtz monzonite A
2 Alteration PAT LABEL
BIO
CHL
PHY
PRP
3 Cu_pct BAR PLOT
1
0.5
0.3
0.2
0.1
4 Au_ppm BAR PLOT
1
0.5
0.3
0.2
0.1
5 Min_TSG PAT No patterns matched
6 w2200 NUMBER BANDS
2210
2205
2202
2197
Halilaga Project

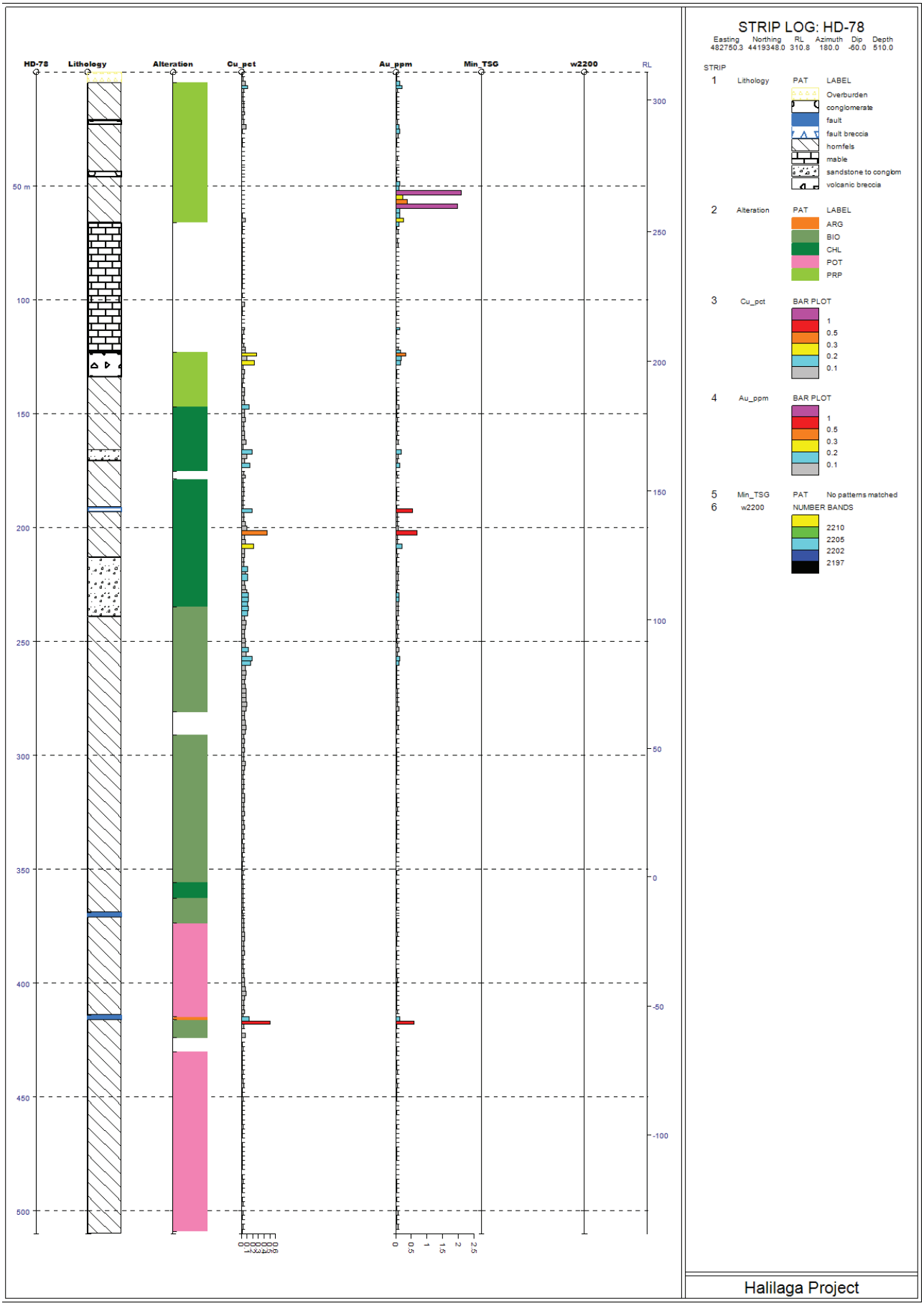
HD-78
Lithology
Alteration
Cu_pct
Au_ppm
Min_TSG
w2200
RL
50 m
300
250
200
150
100
50
0
-50
-100
STRIP LOG: HD-78
Easting Northing RL Azimuth Dip Depth
482750.3 4419348.0 310.8 180.0 -60.0 510.0
STRIP
1 Lithology PAT LABEL
Overburden
conglomerate
fault
fault breccia
hornfels
mable
sandstone to conglom
volcanic breccia
2 Alterstion PAT LABEL
ARG
BIO
CHL
POT
PRP
3 Cu_pct BAR PLOT
1
0.5
0.3
0.2
0.1
4 Au_ppm BAR PLOT
1
0.5
0.3
0.2
0.1
5 Min_TSG PAT No patterns matched
6 w2200 NUMBER BANDS
2210
2205
2202
2197
Halilaga Project

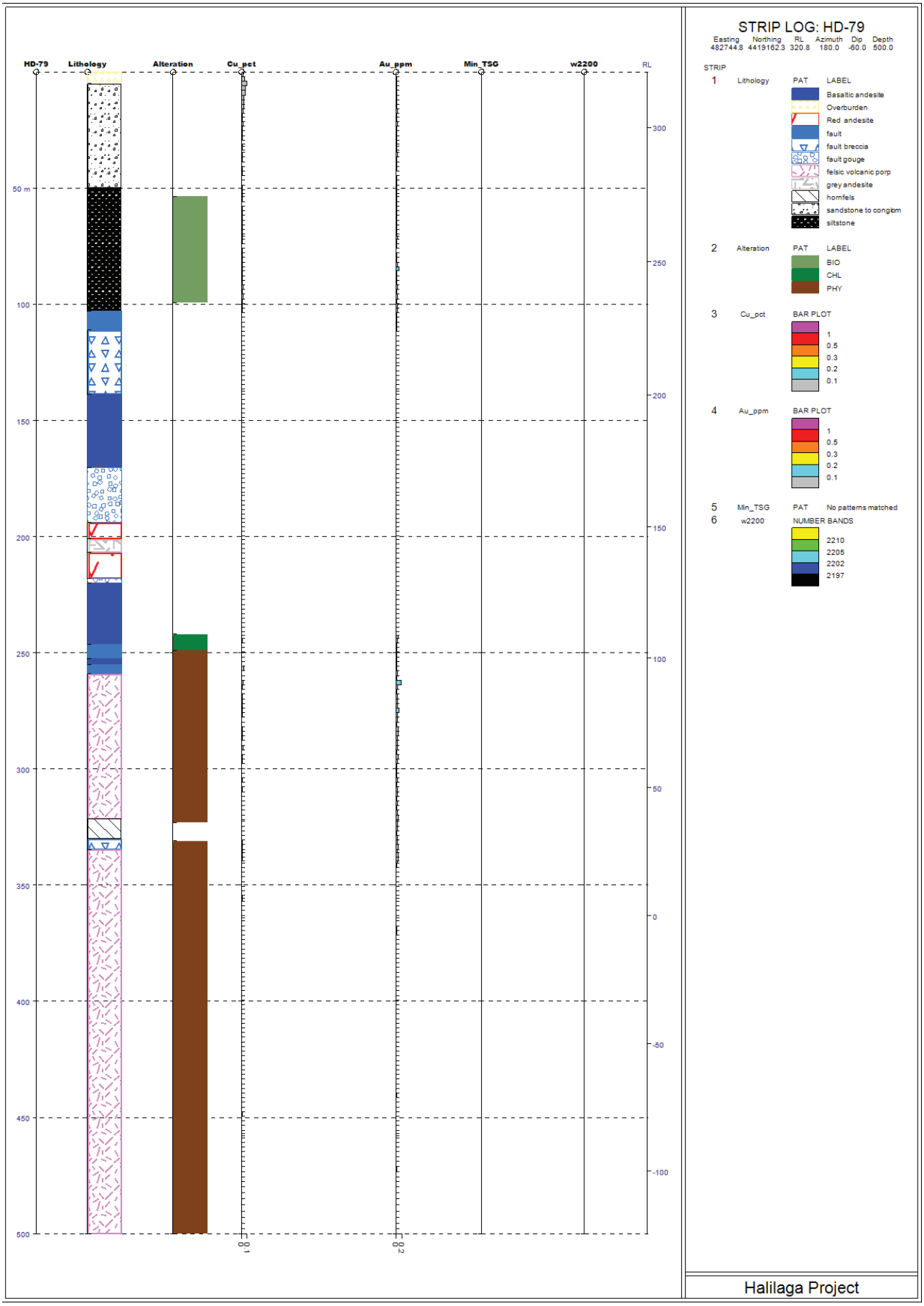
HD-79
Lithology
Alteration
Cu_pct
Au_ppm
Min_TSG
w2200
RL
50 m
100
150
200
250
300
350
400
450
500
300
250
200
150
100
50
0
-50
-100
0.1
0.2
STRIP LOG: HD-79
Easting 482744.8
Northing 4419162.3
RL 320.8
Azimuth 180.0
Dip -60.0
Depth 500.0
STRIP
1 Lithology
PAT
LABEL
Basaltic andesite
Overburden
Red andesite
fault
fault breccia
fault gouge
felsic volcanic porp
grey andesite
hornfels
sandstone to conglom
siltstone
2 Alteration
PAT
LABEL
BIO
CHL
PHY
3 Cu_pct
BAR PLOT
1
0.5
0.3
0.2
0.1
4 Au_ppm
BAR PLOT
1
0.5
0.3
0.2
0.1
5 Min_TSG
PAT
No patterns matched
6 w2200
NUMBER BANDS
2210
2205
2202
2197
Halilaga Project

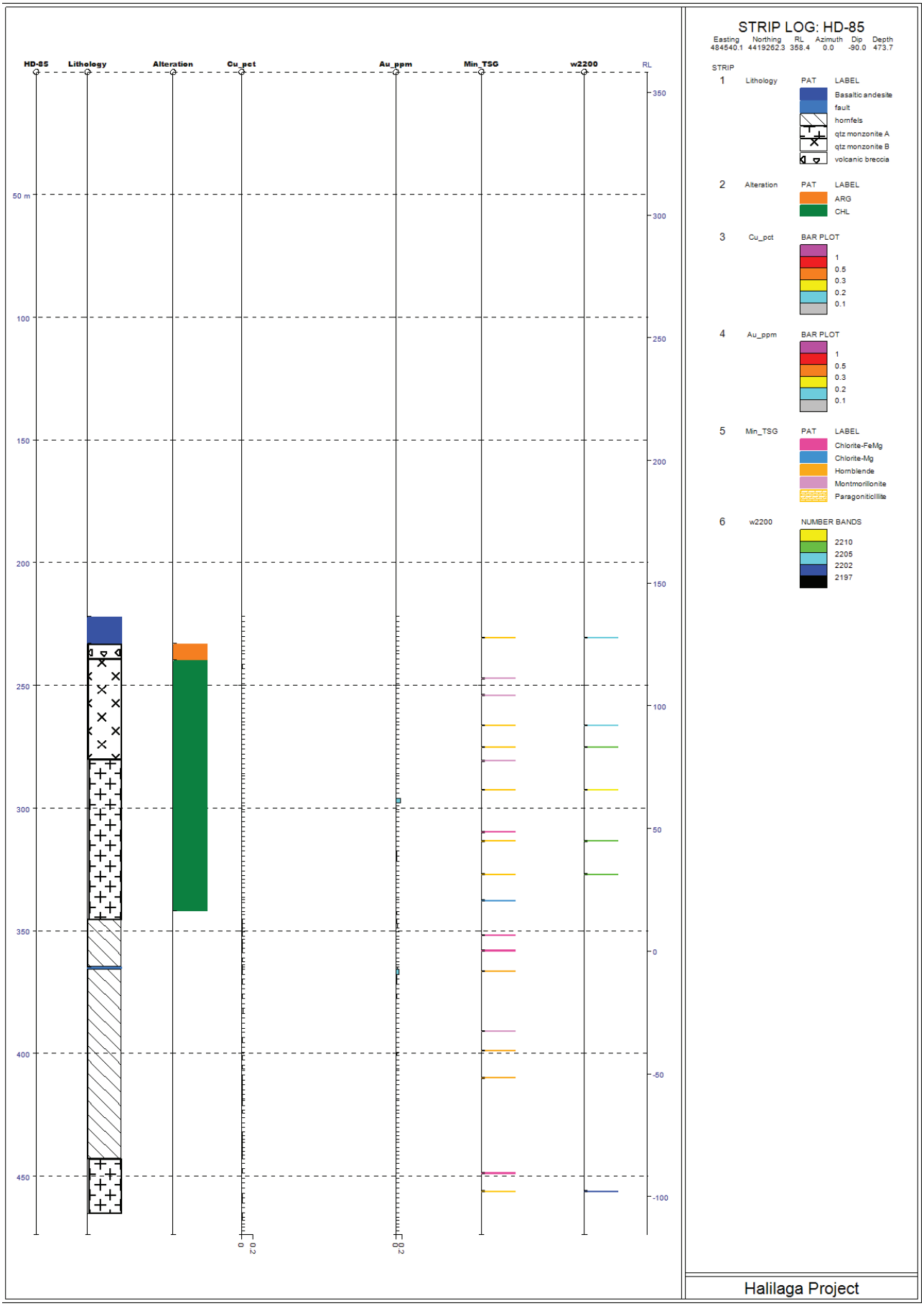
HD-85
Lithology
Alteration
Cu_pct
Au_ppm
Min_TSG
w2200
RL
50 m
100
150
200
250
300
350
400
450
350
300
250
200
150
100
50
0
-50
-100
0
0.2
0
0.2
STRIP LOG: HD-85
Easting Northing RL Azimuth Dip Depth
484540.1 4419262.3 358.4 0.0 -90.0 473.7
STRIP
1 Lithology
PAT LABEL
Basaltic andesite
fault
hornfels
qtz monzonite A
qtz monzonite B
volcanic breccia
2 Alteration
PAT LABEL
ARG
CHL
3 Cu_pct
BAR PLOT
1
0.5
0.3
0.2
0.1
4 Au_ppm
BAR PLOT
1
0.5
0.3
0.2
0.1
5 Min_TSG
PAT LABEL
Chlorite-FeMg
Chlorite-Mg
Hornblende
Montmorillonite
Paragoniticlllite
6 w2200
NUMBER BANDS
2210
2205
2202
2197
Halilaga Project

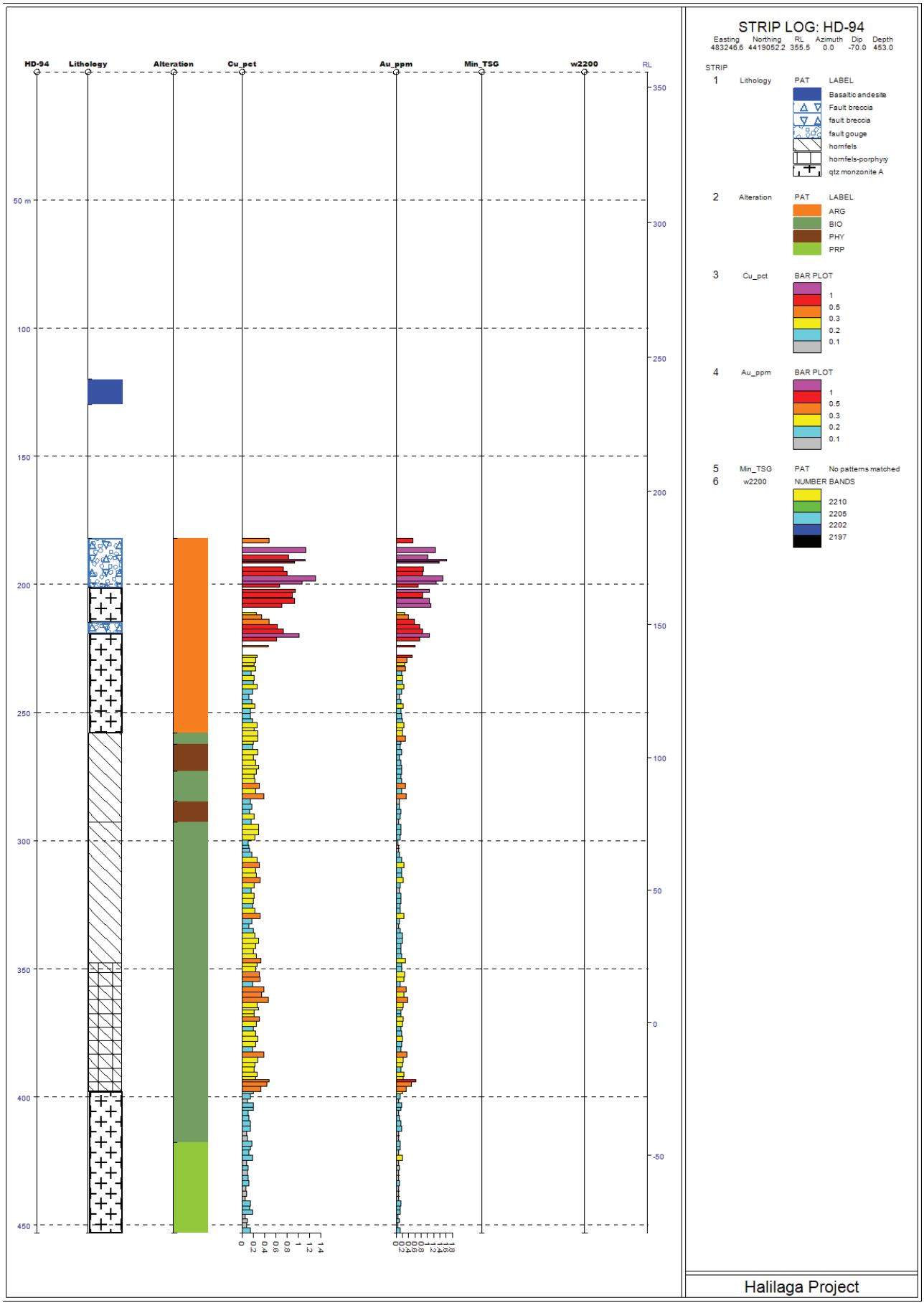
HD-94
Lithology
Alteration
Cu_pct
Au_ppm
Min_TSG
w2200
RL
50 m
350
300
250
200
150
100
50
0
-50
STRIP LOG: HD-94
Easting Northing RL Azimuth Dip Depth
483246.6 4419052.2 355.5 0.0 -70.0 453.0
STRIP
1 Lithology PAT LABEL
Basaltic andesite
Fault breccia
fault breccia
fault gouge
hornfels
hornfels-porphyry
qtz monzonite A
2 Alteration PAT LABEL
ARG
BIO
PHY
PRP
3 Cu_pct BAR PLOT
1
0.5
0.3
0.2
0.1
4 Au_ppm BAR PLOT
1
0.5
0.3
0.2
0.1
5 Min_TSG PAT No patterns matched
6 w2200 NUMBER BANDS
2210
2205
2202
2197
Halilaga Project

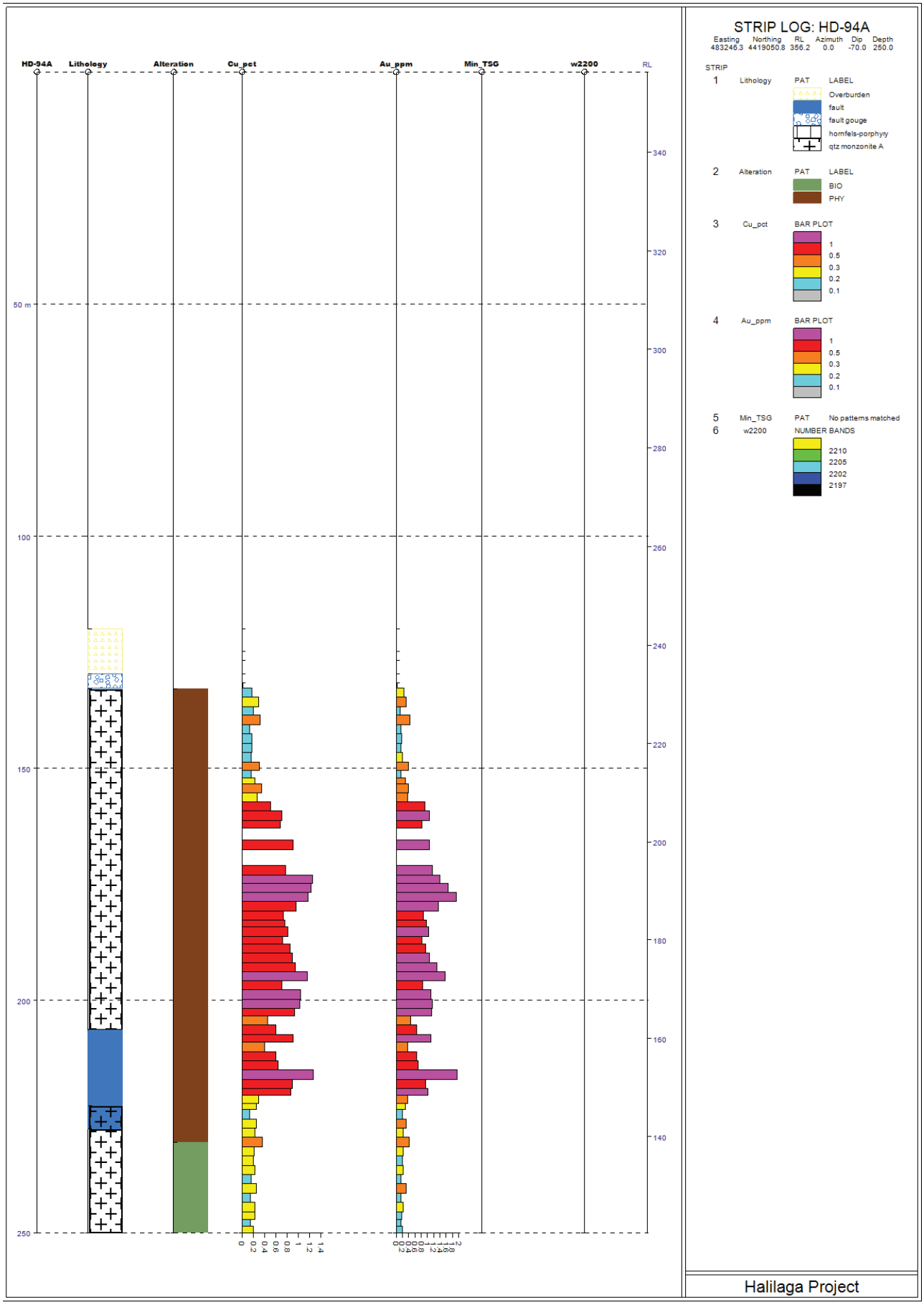
HD-94A
Lithology
Alteration
Cu_pct
Au_ppm
Min_TSG
w2200
RL
340
320
50 m
300
280
100
260
240
150
220
200
200
180
160
250
140
0 0.2 0.4 0.6 0.8 1 1.2 1.4
0 0.2 0.4 0.6 0.8 1 1.2 1.4 1.6 1.8 2
STRIP LOG: HD-94A
Easting Northing RL Azimuth Dip Depth
483246.3 4419050.8 356.2 0.0 -70.0 250.0
STRIP
1 Lithology PAT LABEL
Overburden
fault
fault gouge
hornfels-porphyry
qtz monzonite A
2 Alteration PAT LABEL
BIO
PHY
3 Cu_pct BAR PLOT
1
0.5
0.3
0.2
0.1
4 Au_ppm BAR PLOT
1
0.5
0.3
0.2
0.1
5 Min_TSG PAT No patterns matched
6 w2200 NUMBER BANDS
2210
2205
2202
2197
Halilaga Project

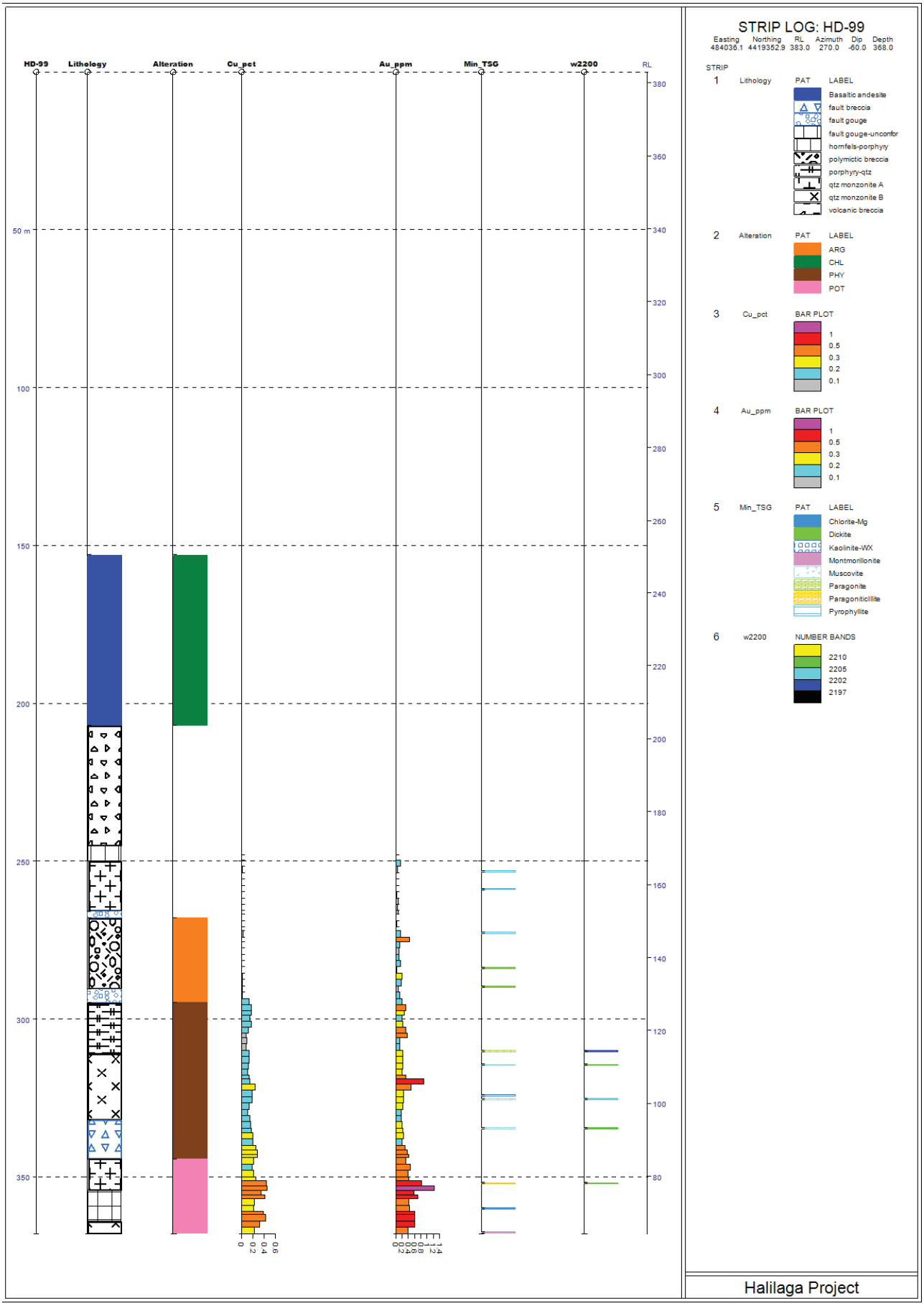
HD-99
Lithology
Alteration
Cu_pct
Au_ppm
Min_TSG
w2200
RL
50 m
100
150
200
250
300
350
380
360
340
320
300
280
260
240
220
200
180
160
140
120
100
80
STRIP LOG: HD-99
Easting 484036.1
Northing 4419352.9
RL 383.0
Azimuth 270.0
Dip -60.0
Depth 368.0
STRIP
1 Lithology
PAT
LABEL
Basaltic andesite
fault breccia
fault gouge
fault gouge-unconfor
hornfels-porphyry
polymictic breccia
porphyry-qtz
qtz monzonite A
qtz monzonite B
volcanic breccia
2 Alteration
PAT
LABEL
ARG
CHL
PHY
POT
3 Cu_pct
BAR PLOT
1
0.5
0.3
0.2
0.1
4 Au_ppm
BAR PLOT
1
0.5
0.3
0.2
0.1
5 Min_TSG
PAT
LABEL
Chlorite-Mg
Dickite
Kaolinite-WX
Montmorillonite
Muscovite
Paragonite
Paragonitic Illite
Pyrophyllite
6 w2200
NUMBER BANDS
2210
2205
2202
2197
Halilaga Project

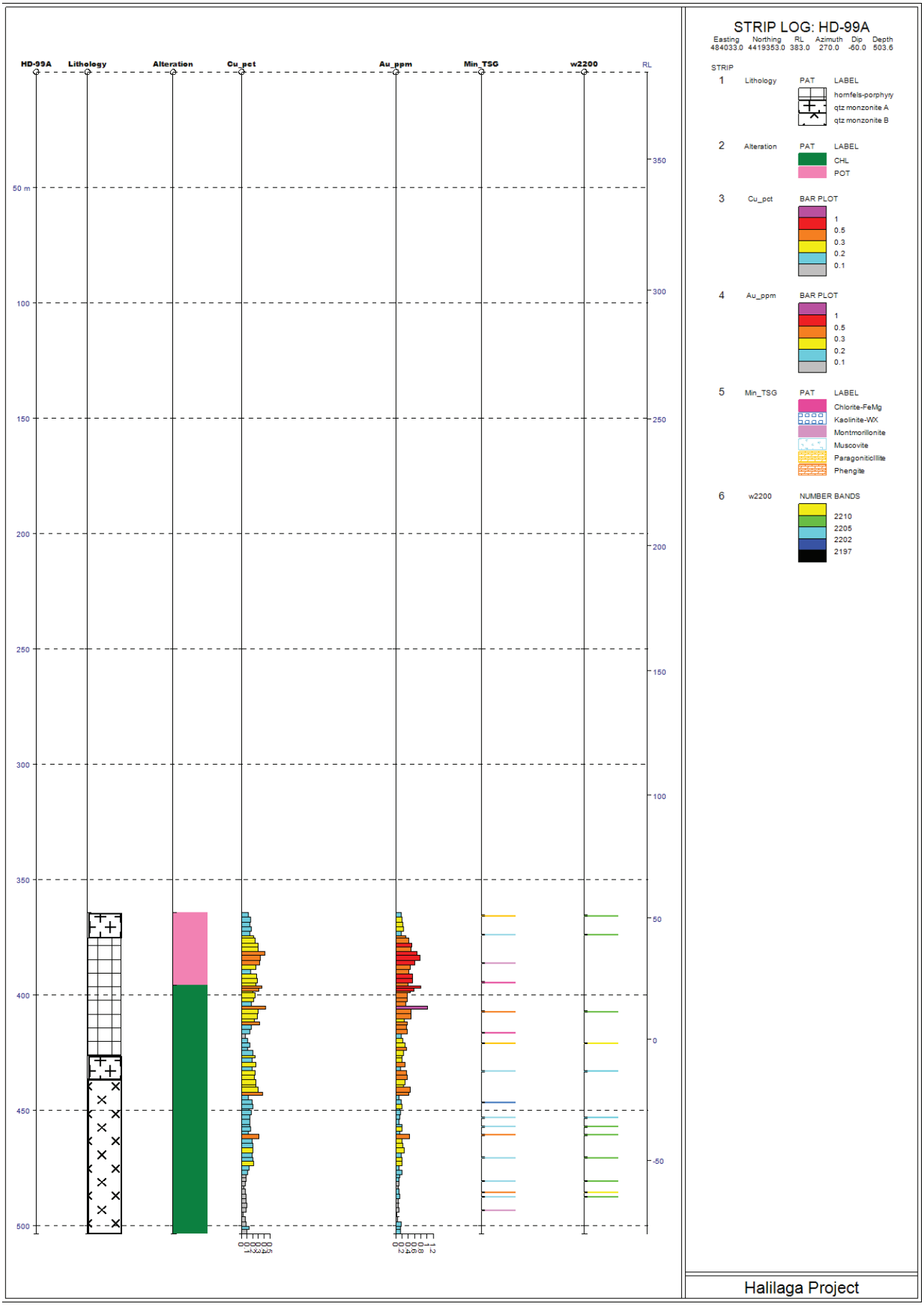
HD-99A
Lithology
Alteration
Cu_pct
Au_ppm
Min_TSG
w2200
RL
50 m
100
150
200
250
300
350
400
450
500
350
300
250
200
150
100
50
0
-50
STRIP LOG: HD-99A
Easting 484033.0
Northing 4419353.0
RL 383.0
Azimuth 270.0
Dip -60.0
Depth 503.6
STRIP
1 Lithology
PAT
LABEL
hornfels-porphyry
qtz monzonite A
qtz monzonite B
2 Alteration
PAT
LABEL
CHL
POT
3 Cu_pct
BAR PLOT
1
0.5
0.3
0.2
0.1
4 Au_ppm
BAR PLOT
1
0.5
0.3
0.2
0.1
5 Min_TSG
PAT
LABEL
Chlorite-FeMg
Kaolinite-WX
Montmorillonite
Muscovite
Paragonitic/Illite
Phengite
6 w2200
NUMBER BANDS
2210
2205
2202
2197
Halilaga Project

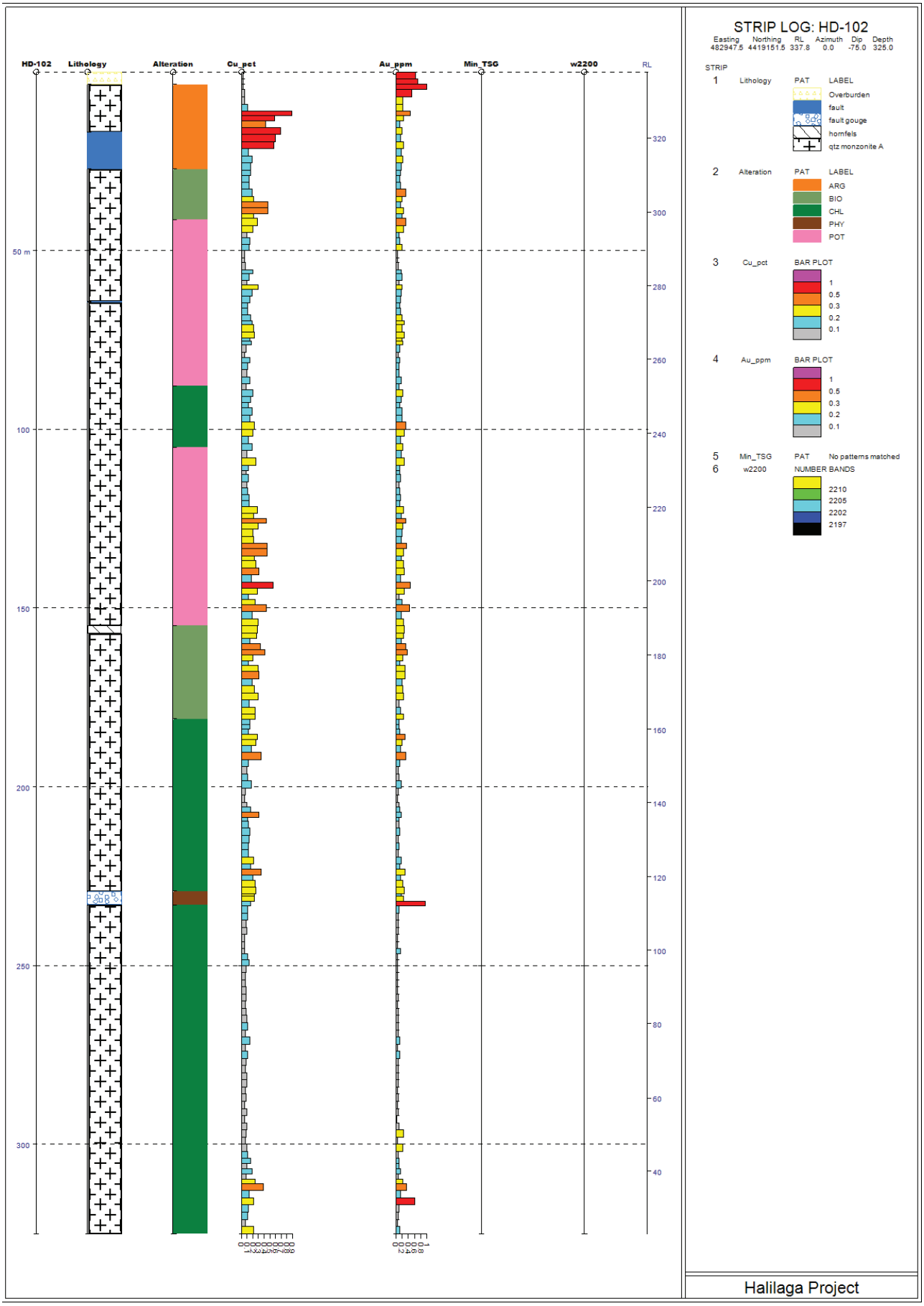
HD-102
Lithology
Alteration
Cu_pct
Au_ppm
Min_TSG
w2200
RL
50 m
100
150
200
250
300
320
300
280
260
240
220
200
180
160
140
120
100
80
60
40
STRIP LOG: HD-102
Easting 482947.5
Northing 4419151.5
RL 337.8
Azimuth 0.0
Dip -75.0
Depth 325.0
STRIP
1 Lithology PAT LABEL
Overburden
fault
fault gouge
hornfels
qtz monzonite A
2 Alteration PAT LABEL
ARG
BIO
CHL
PHY
POT
3 Cu_pct BAR PLOT
1
0.5
0.3
0.2
0.1
4 Au_ppm BAR PLOT
1
0.5
0.3
0.2
0.1
5 Min_TSG PAT No patterns matched
6 w2200 NUMBER BANDS
2210
2205
2202
2197
Halilaga Project

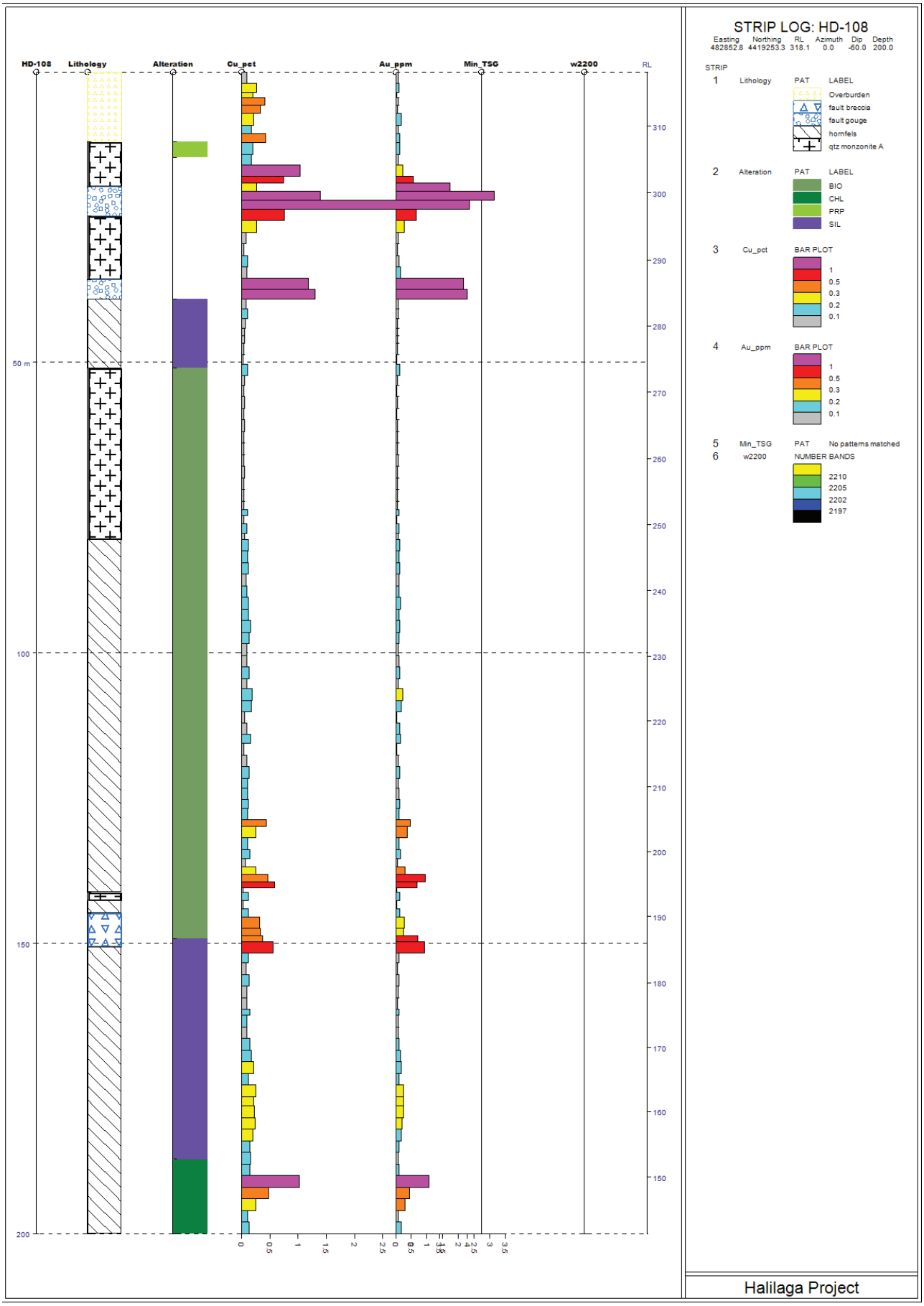
HD-108
Lithology
Alteration
Cu_pct
Au_ppm
Min_TSG
w2200
RL
50 m
100
150
200
310
300
290
280
270
260
250
240
230
220
210
200
190
180
170
160
150
0
0.5
1
1.5
2
2.5
3
3.5
STRIP LOG: HD-108
Easting 482852.8
Northing 4419253.3
RL 318.1
Azimuth 0.0
Dip -60.0
Depth 200.0
STRIP
1 Lithology PAT LABEL
Overburden
fault breccia
fault gouge
hornfels
qtz monzonite A
2 Alteration PAT LABEL
BIO
CHL
PRP
SIL
3 Cu_pct BAR PLOT
1
0.5
0.3
0.2
0.1
4 Au_ppm BAR PLOT
1
0.5
0.3
0.2
0.1
5 Min_TSG PAT No patterns matched
6 w2200 NUMBER BANDS
2210
2205
2202
2197
Halilaga Project

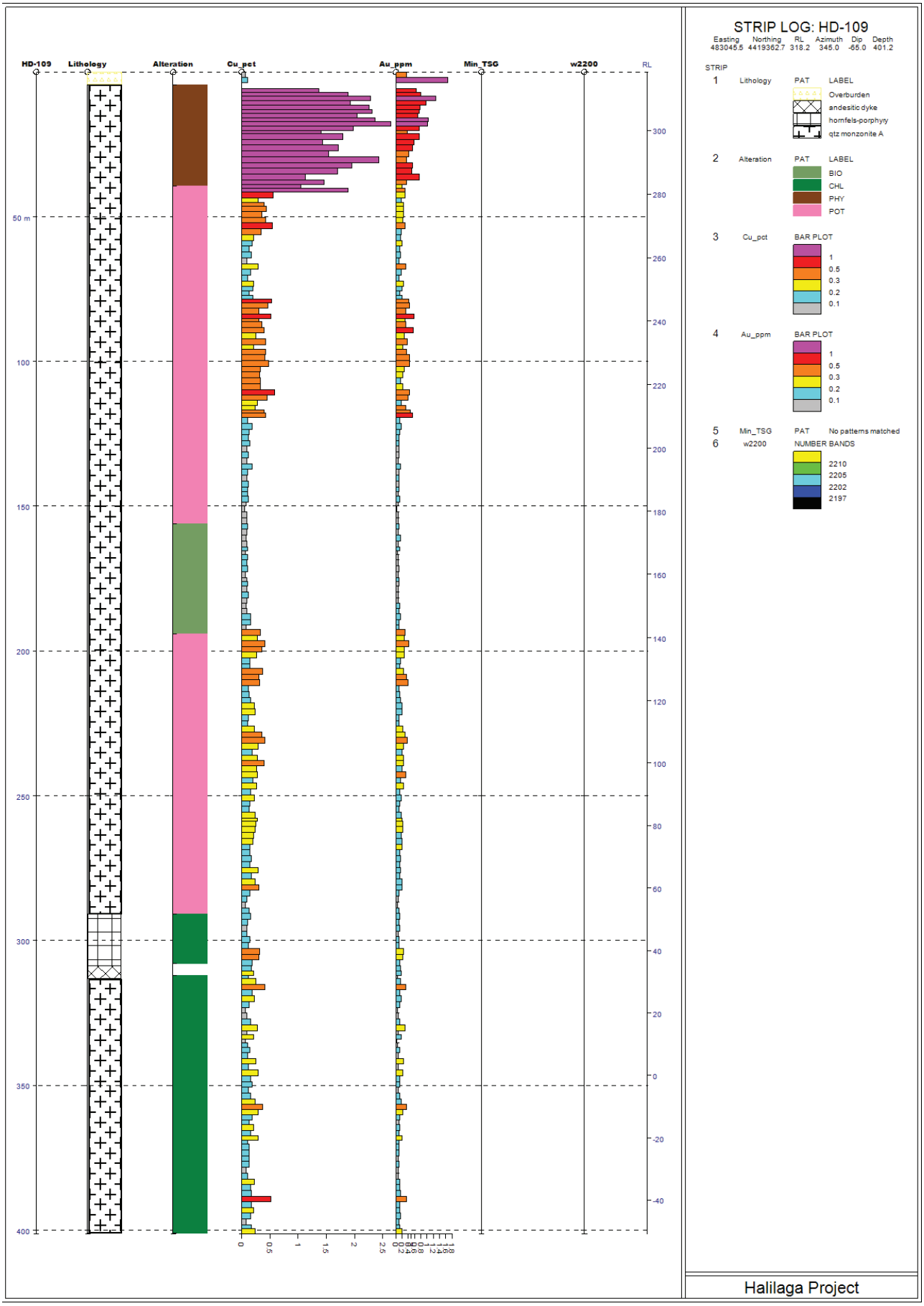
HD-109
Lithology
Alteration
Cu_pct
Au_ppm
Min_TSG
w2200
RL
50 m
100
150
200
250
300
350
400
300
280
260
240
220
200
180
160
140
120
100
80
60
40
20
0
-20
-40
0
0.5
1
1.5
2
2.5
STRIP LOG: HD-109
Easting 483045.5
Northing 4419362.7
RL 318.2
Azimuth 345.0
Dip -65.0
Depth 401.2
STRIP
1 Lithology PAT LABEL
Overburden
andesitic dyke
hornfels-porphyry
qtz monzonite A
2 Alteration PAT LABEL
BIO
CHL
PHY
POT
3 Cu_pct BAR PLOT
1
0.5
0.3
0.2
0.1
4 Au_ppm BAR PLOT
1
0.5
0.3
0.2
0.1
5 Min_TSG PAT No patterns matched
6 w2200 NUMBER BANDS
2210
2205
2202
2197
Halilaga Project

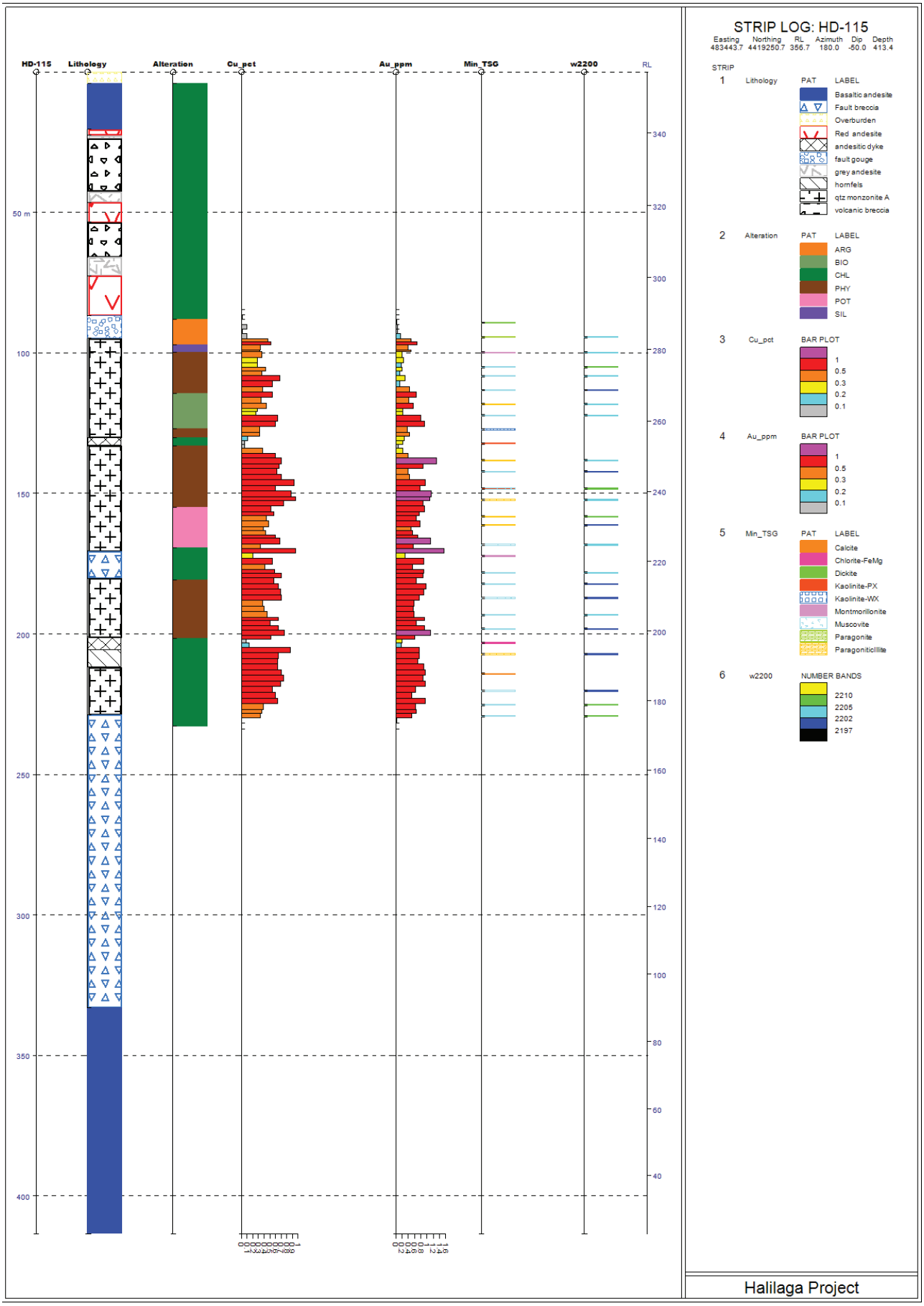

STRIP LOG: HD-115

Easting	Northing	RL	Azimuth	Dip	Depth
483443.7	4419250.7	356.7	180.0	-50.0	413.4

STRIP

1 Lithology

PAT	LABEL
	Basaltic andesite
	Fault breccia
	Overburden
	Red andesite
	andesitic dyke
	fault gouge
	grey andesite
	hornfels
	qtz monzonite A
	volcanic breccia

2 Alteration

PAT	LABEL
	ARG
	BIO
	CHL
	PHY
	POT
	SIL

3 Cu_pct

BAR PLOT

1
0.5
0.3
0.2
0.1

4 Au_ppm

BAR PLOT

1
0.5
0.3
0.2
0.1

5 Min_TSG

PAT	LABEL
	Calcite
	Chlorite-FeMg
	Dickite
	Kaolinite-PX
	Kaolinite-WX
	Montmorillonite
	Muscovite
	Paragonite
	Paragonitic/Illite

6 w2200

NUMBER BANDS

2210
2205
2202
2197

Halilaga Project

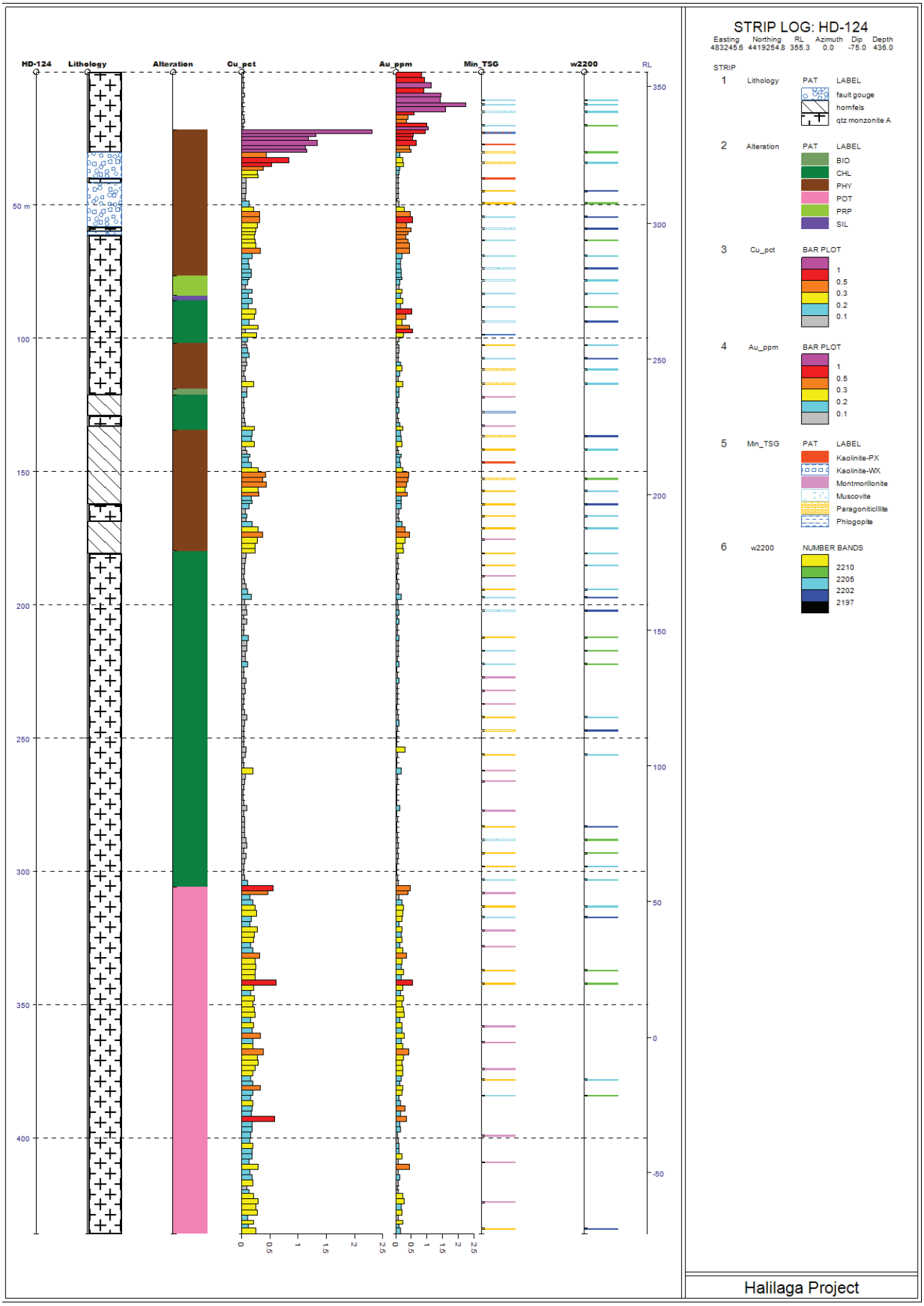
HD-124
Lithology
Alteration
Cu_pct
Au_ppm
Min_TSG
w2200
RL
50 m
100
150
200
250
300
350
400
350
300
250
200
150
100
50
0
-50
0
0.5
1
1.5
2
2.5
STRIP LOG: HD-124
Easting 483245.6
Northing 4419254.8
RL 355.3
Azimuth 0.0
Dip -75.0
Depth 436.0
STRIP
1 Lithology
PAT
LABEL
fault gouge
hornfels
qtz monzonite A
2 Alteration
PAT
LABEL
BIO
CHL
PHY
POT
PRP
SIL
3 Cu_pct
BAR PLOT
1
0.5
0.3
0.2
0.1
4 Au_ppm
BAR PLOT
1
0.5
0.3
0.2
0.1
5 Min_TSG
PAT
LABEL
Kaolinite-PX
Kaolinite-WX
Montmorillonite
Muscovite
Paragoniticllite
Phlogopite
6 w2200
NUMBER BANDS
2210
2205
2202
2197
Halilaga Project

Table A.1. List of logged, checked, and partially logged holes used for cross-section construction and data collection.

Hole ID	Project Name	East	North	Elevation	Depth	Azimuth	Dip	Status
HD-01	Halilaga	483156	4419250	346	298	0	-60	Logged
HD-08	Halilaga	483887	4419361	376	435	270	-60	Logged
HD-09	Halilaga	483818	4418745	530	355	0	-60	Logged
HD-10	Halilaga	484022	4418850	498	298	0	-60	Logged
HD-115	Halilaga	483444	4419251	357	413	180	-50	Logged
HD-12	Halilaga	483406	4418310	532	138	0	-60	Logged
HD-124	Halilaga	483246	4419255	355	436	0	-75	Logged
HD-12A	Halilaga	483406	4418312	532	353	0	-60	Logged
HD-13A	Halilaga	483431	4419113	376	505	315	-60	Logged
HD-37	Halilaga	483139	4419154	336	269	0	-60	Logged
HD-38	Halilaga	483245	4419456	327	586	180	-60	Logged
HD-45	Halilaga	483438	4419448	327	638	180	-50	Logged
HD-47	Halilaga	483243	4419456	327	53	345	-50	Logged
HD-60	Halilaga	483251	4419349	345	798	0	-60	Logged
HD-50	Halilaga	483031	4419254	329	308	270	-45	Logged
HD-70	Halilaga	481945	4418506	285	596	170	-70	Partially Logged
HD-73	Halilaga	484361	4417957	545	632	0	-60	Partially Logged
HD-78	Halilaga	482750	4419348	311	510	180	-60	Logged
HD-79	Halilaga	482745	4419162	321	500	180	-60	Logged
HD-80	Halilaga	483140	4419453	332	857	0	-65	Partially Logged
HD-85	Halilaga	484540	4419262	358	474	0	-90	Logged
HD-94	Halilaga	483247	4419052	355	453	0	-70	Logged
HD-94A	Halilaga	483246	4419051	356	250	0	-70	Logged
HD-99	Halilaga	484036	4419353	383	368	270	-60	Logged
HD-99A	Halilaga	484033	4419353	383	504	270	-60	Logged
HD-102	Halilaga	482947	4419151	338	325	0	-75	Logged
HD-108	Halilaga	482853	4419253	318	200	0	-60	Logged
HD-109	Halilaga	483046	4419363	318	401	345	-65	Logged
PD-03	Pirentepe	480698	4421383	412	59	355	-60	Checked
PD-17	Pirentepe	480562	4421460	373	168	90	-60	Checked
PD-21	Pirentepe	480453	4419126	298	412	285	-50	Partially Logged
PD-22	Pirentepe	480694	4419165	321	201	20	-60	Partially Logged
PD-23	Pirentepe	480656	4421183	359	190	25	-50	Checked

Appendix B: Sample Descriptions

Table B.1 List of samples used in this thesis, description, classification, analysis and SWIR interpretation if corresponds. Units abbreviation are: A=andesite, AD=andesitic dyke, AFP=altered feldspar porphyry, D=dacite, DCT=dacitic crystal tuff, EP=Evciler Pluton, GA=green andesite, KS=Kocakisla Stock, PA=purple andesite, PA_D=purple andesite Dereoba, QMP-A=Quartz Monzonite A (Kestane Stock), QMP-B=Quartz Monzonite B(Kestane Stock), VS=volcanic sandstone, VT=vitreous tuff.; Type abbreviations are P=plutonic, V=volcanic; Age abbreviations are E=Eocene and O=Oligocene; Analysis abbreviations are P=petrography, S=SWIR, G=geochemistry, St=staining.

Sample	East	North	Hole	From	Unit	Type	Age	Location	Description	Analysis	Alteration	Interpreted
HD-01_297.5	483156	4419250	HD-01	298	AD	P	E	Kestane	green porphyritic fine grained andesite	G	Chlorite	
HD-09_216.2	483818	4418745	HD-09	216	D	V	E	Kunk	Phenocryst/ground mass is 70/30. Average size of phenocrysts 3mm. Feldspars 10%, quartz 5%, pyrite (in mafic site) 15%. Pink colour ground mass.	G	Argillic	
HD-09_354.3	483818	4418745	HD-09	354	D	V	E	Kunk	light grey-pink, advanced argillic medium porphyritic dacite	S, G	Adv. Argillic	Pyrophyllite
HD-09_95.55	483818	4418745	HD-09	96	D	V	E	Kunk	light grey-hematitite, coarse porphyritic dacite	S, G	Adv. Argillic	Pyrophyllite
HD-115_23.65	483444	4419251	HD-115	24	PA	V	O	Kestane	greenish argilized, porphyritic medium grained andesite.	P, S, G	Chlorite	Smectite
HD-115_146.7	483444	4419251	HD-115	147	QMP-A	P	E	East Kestane	yellow, sericited quartz monzonite	P, S, St	Quartz, sericite	Muscovite
HD-115_280	483444	4419251	HD-115	280	PA	V	O	Kestane	greenish porphyritic medium grained andesite	P, S, G	Chlorite	Smectite
HD-12_61.35	483406	4418310	HD-12	61	D	V	E	Kunk	Porphyritic dacite, ground mass 65%, phenocrysts 35% (quartz eyes 5%, feldspar 30%).	G	Argillic	
HD-124_373.1	483246	4419255	HD-124	373	QMP-A	P	E	Kestane	leucocratic porphyric medium grained quartz monzonite	P, S	Biotite, chlorite	Paragoniti-cIllite
HD-13A_106.9	483431	4419113	HD-13A	107	QMP-A	P	E	Kestane	yellow-orange porphyritic granodiorite	P, S, G	Sericite	Muscovite
HD-13A_311.1	483431	4419113	HD-13A	311,1	VS	V	E	South Kestane	grey, fine grained hornfels	P, S	Sericite	Illite+phlogo-pite
HD-13A_335.7	483431	4419113	HD-13A	336	VS	V	E	South Kestane	grey, fine grained hornfels	P, S	Biotite, magnetite, chlorite	Phlogopite
HD-13A_415.2	483431	4419113	HD-13A	415	QMP-B	P	E	Kestane	leucocratic, medium grained quartz monzonite	P, S, G, St,	Chlorite, sericite	Chlorite

Table B.1 (cont)

Sample	East	North	Hole	From	Unit	Type	Age	Location	Description	Analysis	Alteration	Interpreted
HD-13A_471.5	483431	4419113	HD-13A	472	QMP-B	P	E	South Kestane	green-white medium grained quartz monzonite	P, S, St	Chlorite, biotite, epidote in mafic site; Sericite in felsic site	Aspectral
HD-13A_488.6	483431	4419113	HD-13A	489	QMP-B	P	E	Kestane	leucocratic, medium grained quartz monzonite	P, S, G, U-Pb	Chlorite, sericite	Chlorite
HD-24_186.2	486604	4417709	HD-24	186	EP	P	O	Bakirlik	light grey to pinkish, medium grained quartz monzonite	S, G, St	Chlorite	Illite
HD-28_138.5	486789	4417441	HD-28	139	EP	P	O	Bakirlik	pinkish to greenish, medium to coarse, amphibole granite	S, G, St	Chlorite	Illite
HD-29_204.5	486781	4417735	HD-29	205	EP	P	O	Bakirlik	light grey to pinkish, medium grained quartz monzonite	S, G	Chlorite	Illite
HD-29_86.6	486781	4417735	HD-29	87	EP	P	O	Bakirlik	light grey porphyric medium grained quartz monzonite	P, S, G, U-Pb	Chlorite	Montmoril-lonite
HD-37_112.7	483139	4419154	HD-37	113	QMP-A	P	E	Kestane	black porphyric medium grained quartz monzonite	P, S, G, St, U-Pb	Biotite, magnetite	Illite
HD-37_127.3	483139	4419154	HD-37	127	QMP-A	P	E	Kestane	Green-Black, Biotitized medium grained monzonite.	P, S, G	Biotite, chlorite	Illite
HD-37_254.3	483139	4419154	HD-37	254	QMP-B	P	E	Kestane	light grey porphyric medium grained quartz monzonite	P, S, G, St,	Chlorite, Sericite	Montmoril-lonite
HD-37_95.35	483139	4419154	HD-37	95	QMP-A	P	E	Kestane	black porphyric medium grained quartz monzonite	P, S, G	Biotite, chlorite	
HD-38_190.4	483245	4419456	HD-38	190	AD	P	E	Kestane	green porphyritic fine grained andesite	P, S, G	Chlorite	Chlorite
HD-38_310	483245	4419456	HD-38	310	QMP-B	P	E	Kestane	light grey porphyric medium grained quartz monzonite	P, S, G, St	Biotite, chlorite	Chlorite
HD-38_396.5	483245	4419456	HD-38	397	QMP-A	P	E	Kestane	light grey porphyric medium grained quartz monzonite	P,	Chlorite, biotite, epidote in mafic site	Paragoniti-cIllite
HD-45_459.45	483438	4419448	HD-45	459	QMP-B	P	E	Kestane	light grey porphyric to phaneritic medi-um grain quartz monzonite	P, S, G, St	Biotite, chlorite	Chlorite
HD-38_396.5	483245	4419456	HD-38	397	QMP-A	P	E	Kestane	Poprhyritic texture; phenocrysts are plagioclases (30%), mafic relicts (7%, altered to chlorite).	P, S	Chlorite	Illite

Table B.1 (cont)

Sample	East	North	Hole	From	Unit	Type	Age	Location	Description	Analysis	Alteration	Interpreted
HD-45_580.15	483438	4419448	HD-45	580	QMP-B	P	E	Kestane	Porphyritic texture: ground mass 60%, phenocrysts 40%. Secondary biotite after hornblende (10%, up to 10mm long), feldspar (20%, white), quartz (10%, gray)	S, G	Biotite, chlorite	FeChlorite
HD-60_720	483251	4419349	HD-60	720	QMP-A	P	E	Kestane	light grey porphyric medium grained quartz monzonite	P, S, G	Chlorite	Phlogopite
HD-60_750.45	483251	4419349	HD-60	750	QMP-A	P	E	Kestane	light grey porphyric medium grained quartz monzonite	G, St	Chlorite	
HD-60_780.25	483251	4419349	HD-60	780	QMP-A	P	E	Kestane	light grey porphyric medium grained quartz monzonite	G	Chlorite	
HD-73_179.1	484361	4417957	HD-73	179	D	V	E	Guvem-tasi	pink-light grey aphanitic dacite	P,	Silice, clays	Kaolinite
HD-78_16	482750	4419348	HD-78	16	VS	V	E	Kestane	black fine grained hornfels	P, S, G	Skarn	Smectite
HD-78_289.2	482750	4419348	HD-78	289	VS	V	E	Kestane	black fine grained hornfels	P, S, G	Chlorite, epidote	Phlogopite
HD-78_39.4	482750	4419348	HD-78	39	VS	V	E	Kestane	black fine grained hornfels	P, S, G	Skarn	Smectite
HD-80_30	483140	4419453	HD-80	30	QMP-A	P	E	Kestane	sericited porphyritic medium grained quartz monzonite	P, S, G	Sericite	Muscovite
HD-80_99	483140	4419453	HD-80	91	QMP-A	P	E	Kestane	light grey porphyric medium grain quartz monzonite	P, S, G, St	Biotite, chlorite	Muscovite
HD-85_253.7	484540	4419262	HD-85	254	QMP-B	V	E	Kestane	Porphyritic rock; phenocyryst 25% and ground mass 75%. Brown biotite (10 %, 3mm), feldspars (15%).	P, S, G	Chlorite	Illite
HD-85_313.1	484540	4419262	HD-85	313	QMP-B	P	E	Kestane	Porphyritic rock; phenocyryst 35% and ground mass 65%. Biotite (10 %, 3mm), feldspars (20 %), quartz (5%). Chlorite in mafic site.	G	Chlorite	
HD-85_246.8	484540	4419262	HD-85	247	QMP-B	P	E	East Kestane	leucocratic, porphyric medium grain quartz monzonite	P, St	Chlorite	Chlorite+illite
HD-94_265.9	483247	4419052	HD-94	266	QMP-A	P	E	South Kestane	yellow porphyric medium grain quartz monzonite	P,	Sericite, biotite	Paragoniti-cIllite
HD-94_274.8	483247	4419052	HD-94	275	VS	P	E	Kestane	Fine grained hornfels with intense sericite alteration.	P, S, G	Sericite	Illite
HD-94_402.6	483247	4419052	HD-94	403	QMP-A	P	E	Kestane	grey to greenish medium grained quartz monzonite	Re-Os	Biotite, chlorite	

Table B.1 (cont)

Sample	East	North	Hole	From	Unit	Type	Age	Location	Description	Analysis	Alteration	Interpreted
HD-96_242.6	483022	4419765	HD-96	243	A	V	O	Kestane	reddish to purple, medium grained andesite	S, G	Clay	Montmoril-lonite
HD-96_270.5	483022	4419765	HD-96	271	A	V	O	Kestane	reddish to purple, medium grained andesite	P, S, G, St	Clay	Montmoril-lonite
HD-96_302	483022	4419765	HD-96	302	A	V	O	Kestane	purple to greenish, medium grained andesite	S, G	Chlorite	Montmoril-lonite
HD-99_204.3	484033	4419353	HD-99	204	A	V	O	Kestane	green-dark grey porphyritic andesite	P, S, G	Chlorite	Muscovite
PB2013004	484233	4418209	Sur-face		D	V	E	Guvem-tasi	hematite argyllized altered; aphanitic dacite	P, S	Clay	Parago-nite+pyro-phyllite
PB2013007	483347	4418414	Sur-face		D	V	E	Guvem-tasi	hematite argyllized porphyritic dacite	P, S	Clay	Paragonite
PB2013011	483573	4418185	Sur-face		D	V	E	Guvem-tasi	hematite argyllized porphyritic dacite	P, S	Clay	Parago-nite+pyro-phyllite
PB2013013	484923	4417815	Sur-face		D	V	E	Guvem-tasi	Siliciefied; aphanitic dacite	P, S	Clays, alunite?	
PB2013017	483502	4418635	Sur-face		D	V	E	Kunk	pink-light grey dacitic to ryodacitic tuff	P, S	Silice, alunite?	Alunite-Na
PB2013018	483406	4418781	Sur-face		D	V	E	Kunk	hematite argyllized porphyritic dacite	P, S, U-Pb	Clays, alunite?	Pyrophyllite
PB2013021	484252	4419672	Sur-face		PA	V	O	Kestane	Dark grey-purple porphyritic fine grained basaltic andesite. Plagioclase phyric in an aphanitic ground mass.	P, S, G	Chlorite	Aspectral
PB2013022	481716	4418405	Sur-face		PA	V	O	W Kes-tane	Basaltic andesite to andesite, with plagioclases partially altered to epidote. Purple aphanitic ground mass.	P, S, G, St,	Chlorite	Aspectral
PB2013023	482160	4418829	Sur-face		GA	V	E	Kestane	Green-dark gray porphyritic medium grained andesite. Subhedral to anhedral feldspars and magnetite disseminated. Aphanitic ground mass.	P, S, G	Chlorite, epidote	Chlorite
PB2013036	483063	4419217	Sur-face		QMP-A	P	E	Kestane	yellow-brown (goethite) medium grained porphyritic quartz monzonite	P,	Sericite	Muscovite
PB2013043	482352	4418909	Sur-face		GA	V	E	Kocakis-la	green-dark grey porphyritic medium grained andesite	P, S	Clay	Chlorite

Table B.1 (cont)

Sample	East	North	Hole	From	Unit	Type	Age	Location	Description	Analysis	Alteration	Interpreted
PB2013044A	481134	4419786	Surface		VS	V	E	Kocakisla	brownish to creamy orange conglomerate	P, S	Clay	
PB2013044B	481134	4419786	Surface		VS	V	E	Kocakisla	greenish porphyritic fine grained andesite	P, S	Epidote	Montmorillonite+Epidote
PB2013046	482697	4421349	Surface		A	V	O	Pirentepe	Porphyritic rock. Phenocrysts of plagioclases, rounded quartz, biotite, amphibole and amphibole. Epidote in plagioclase fresh biotite and hornblendes. Fragmentary texture with lithic clasts	P, S, G, U-Pb	Clay	Montmorillonite
PB2014004	482644	4423143	Surface		DCT	V	O	Pirentepe	Pale grey porphyritic volcanic with coarse phenocryst. Sub ehudral to ehudral Plagioclases (5 mm), reddish tabular hornblende, rounded quartz.	P, S, G, St	Clay	Montmorillonite
PB2014007	490312	4420766	Surface		PA_D	V	O	Dereoba	grey to purple fine grained lithic tuff	S, G	Clay	Montmorillonite
PB2014010	489035	4421835	Surface		VT	V	O	Dereoba	dark grey to greenish fine grained andesite	S, G	Clay	Montmorillonite
PB2014011	489757	4421973	Surface		DCT	V	O	Dereoba	light grey medium grained dacitic crystal tuff	P, S, G	Clay	Montmorillonite
PB2014014	489442	4421141	Surface		PA_D	V	O	Dereoba	dark grey to greenish fine grained andesite	S, G	Clay	Montmorillonite
PB2014021	493726	4419893	Surface		PA_D	V	O	Dereoba	purple to reddish fine grained andesite	S, G	Chlorite	Ankerite
PB2014023	479194	4419081	Surface		GA	V	E	W Kestane	greenish medium grained andesite	S, G	Chlorite, epidote	Chlorite
PB2014032	491373	4423097	Surface		AFP	V	O	Dereoba	pinkish to reddish medium grained dacite	S, G	Clay	Montmorillonite
PB2014052	489402	4421571	Surface		PA_D	V	O	Dereoba	purple to dark grey medium grained andesite	S, G	Clay	Aspectral
PB2014061	480296	4421529	Surface		AFP	V	O	Pirentepe	Porphyrytic andesite. Plagioclase-phyric and aphanitic purple ground mass. Argillized Plagioclases. 30% up to 0.5 mm.	P, S	Argillic	Kaolinite
PB2014092	484230	4417477	Surface		D	V	E	S Kunk	light grey to whitish medium grained dacite	S, G	Clay	Illite
PB2014106	482281	4418910	Surface		GA	V	E	Kestane	green-dark grey porphyritic medium grained andesite	G, U-Pb	Chlorite, epidote	

Table B.1 (cont)

Sample	East	North	Hole	From	Unit	Type	Age	Location	Description	Analysis	Alteration	Interpreted
PB2014107c	481213	4419851	Surface		VS	V	E	Kestane	grey to dark greenish, tufficeous sandstone	P, S, G	Chlorite	Illite
PB2014113	480236	4419531	Surface		VS	V	E	Kestane	grey to pinkish, aphanitic rhyolite	S, G	Clay	Muscovite
PB2014125	479980	4421589	Surface		VT	V	O	Pirentepe	dark grey to purple andesitic crystal tuff	G, St	Clay	
PB2014127	482583	4421893	Surface		A	V	O	Pirentepe	Grey to orange, andesiitc crystal tuff	S, G	Clay	Aspectral
PD-07_101.9	481458	4421848	PD-07	102	A	V	O	Pirentepe	medium grey, medium grained andesite	P, S, G	Chlorite, clay	Aspectral
PD-07_24.5	481458	4421848	PD-07	25	AFP	V	O	Pirentepe	light grey to purple, medium grained andesite	S, G	Clay	Kaolinite
PD-07_55.3	481458	4421848	PD-07	55	A	V	O	Pirentepe	purple to greenish, medium grained andesite	S, G	Chlorite, clay	Halloysite
PD-17_59.8	480562	4421460	PD-17	60	AFP	V	O	Pirentepe	grey to light greenish, medium grained andesite	P, S, G	Clay	Kaolinite
PD-19_171.1	480844	4419223	PD-19	171	VS	V	E	Kocakisla	medium to fine grained quartz monzonite	P, S, G	Chlorite, Sericite	Illite
PD-19_54.2	480844	4419223	PD-19	54	D	V	E	Kocakisla	pinkish to greenish, medium grained andesite	S, G	Chlorite, epidote	Illite
PD-19_64.3	480844	4419223	PD-19	64	VS	V	E	Kocakisla	yellowish, fine grained andesite?	S, G	Sericite	Epidote
PD-19_74.5	480844	4419223	PD-19	75	VS	V	E	Kocakisla	grey to greenish fine grained sandstone?	P, S, G	Sericite	Muscovite
PD-21_113.1	480453	4419126	PD-21	113	KS	P	E	Kocakisla	light grey, medium grained quartz monzonite	S, G	Chlorite, Sericite	Muscovite
PD-21_170.1	480453	4419126	PD-21	170	KS	P	E	Kocakisla	light grey, medium grained quartz monzonite	S, G, St	Chlorite, epidote	Montmorillonite
PD-21_229.5	480453	4419126	PD-21	230	KS	P	E	Kocakisla	light grey, medium grained quartz monzonite	P, S, G	Chlorite, Sericite	Aspectral
PD-22_31.7	480453	4419126	PD-22	32	KS	P	E	Kocakisla	grey to greenish, fine to medium grained monzonite	S, G	Chlorite	Montmorillonite
PD-23_186.7	480656	4421183	PD-23	187	PA	V	O	Pirentepe	dark grey to greenish, fine to medium grained andesite	P, S, G	Chlorite	Aspectral

B2: Geochronology Samples. PB2013018

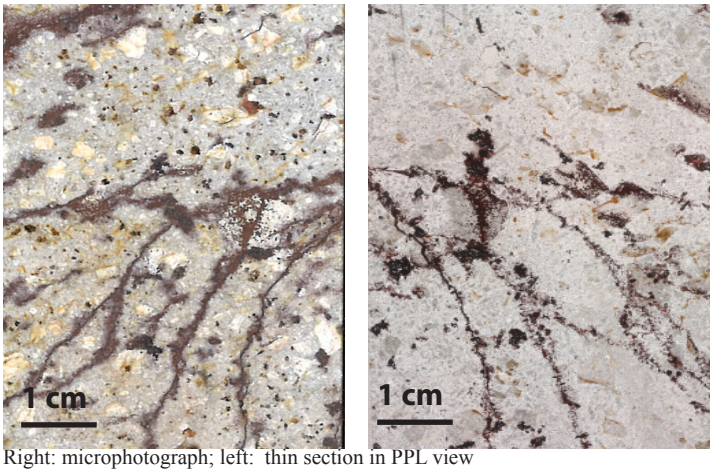

Right: microphotograph; left: thin section in PPL view

Unit: Dacite
Area: Kunk
Assay grade: -
Estimated age: Eocene (40 Ma)

Lithology Description: Feldspar phyric dacitic rock with irregular hematite veining.

Alteration: Plagioclase phenocrysts are intense altered to white mica. White mica is orange to pinkish colour with pearly luster.
Specular and earthy hematite are present in veins and after phenocrysts in a vuggy texture.

Sample type: Geochronology

Petrographic Summary:
The rock presents a porphyritic texture with micro-crystalline ground mass. The phenocrysts/ground mass ratio is 30/70. Only feldspar pseudomorph are observed altered to white mica and no quartz phenocrysts. The ground mass is a fine granular aggregate of feldspars with weak silicification. v

Mineral	pct	style	Size
Feldspars	20	phenocryst	subhedral to anhedral size up to 3 mm
Feldspars	60	groundmass	up to 0.05 mm. Micro-crystalline granular aggregate.
White mica	30	alteration	fine grained in felsic site (phenocrysts and ground mass)
Hematite	15	alteration	Veinlets and associated to felsic phenocrysts
Quartz	15	alteration	In ground mass crystals up to 0.1 mm

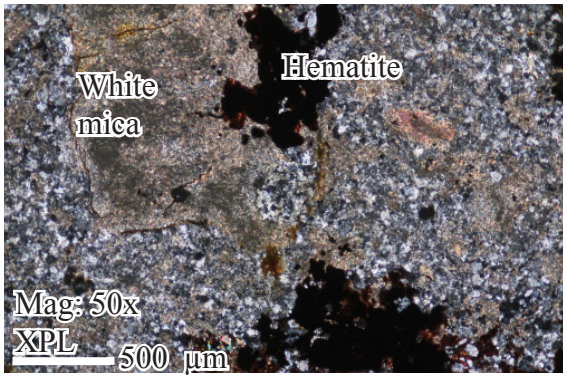

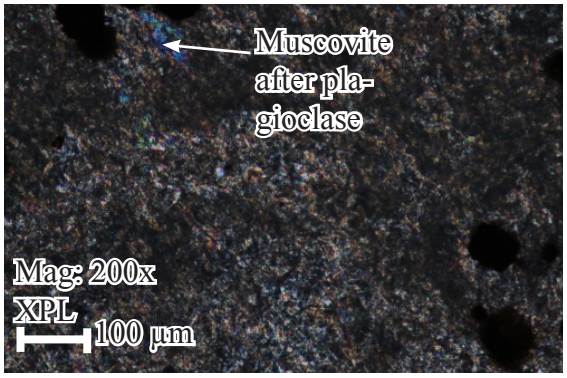

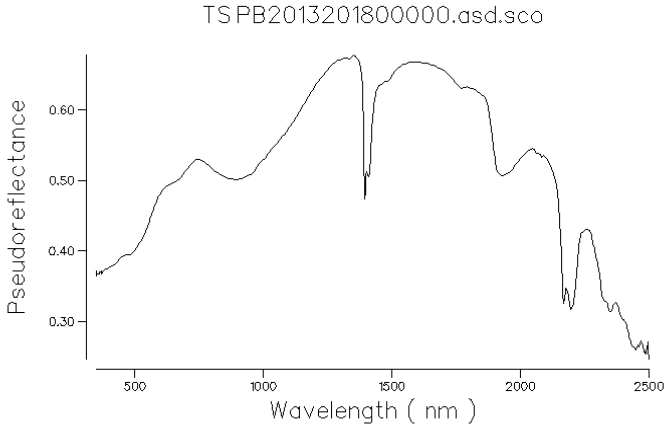

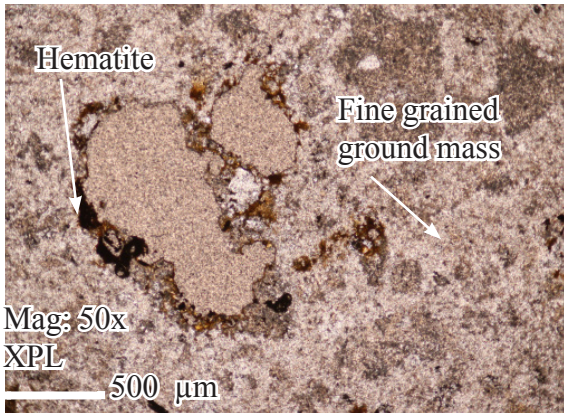

B2: Geochronology Samples. HD-29 86.6

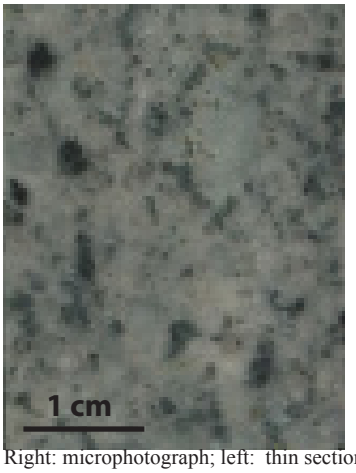

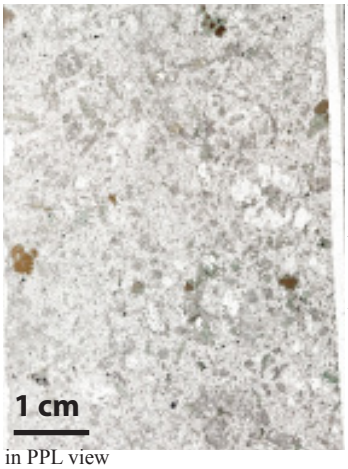

Right: microphotograph; left: thin section in PPL view

Unit: Evçiler pluton
Area: Bakirlik
Assay grade: 173.6 ppm Cu, 1 ppb Au
Estimated age: 26 Ma

Lithology Description: Granodiorite. 30% Phenocrysts; 70% Ground Mass. Fine grained quartz and k-feldspar ground mass (with crystals up to 0.3 mm). Phenocrysts are biotite (3%), quartz (7%), and plagioclases (15%)

Alteration: Chlorite, smectite, epidote.

Sample type: Geochronology

Petrographic Summary:

A fine grained ground mass (with crystals up to 0.3 mm) is formed by a quartz and k-feldspar aggregate and zoned plagioclases phenocrysts with polysynthetic twinning. Biotite exhibits brown-caramel colour with intense pleochroism and birds-eye extinction is partially to totally altered to grey- brownish chlorite.

`

Mineral	pct	style	Size
Plagioclases	25	phenocryst	up to 3 mm
Biotite	8	phenocryst	up to 2.5 mm
Quartz	15	phenocryst	up to 3 mm
Quartz	7	ground-mass	up to 3 mm
K-feldspar	10	ground-mass	up to 3 mm
Chlorite	5	alteration	up to 2 mm
Epidote	1	alteration	up to 0.2 mm
Calcite	1	alteration	up to 0.1

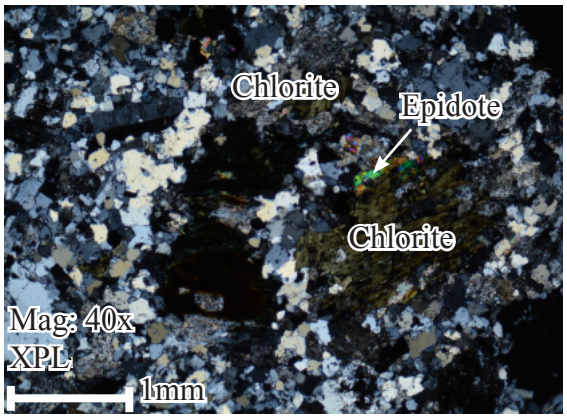

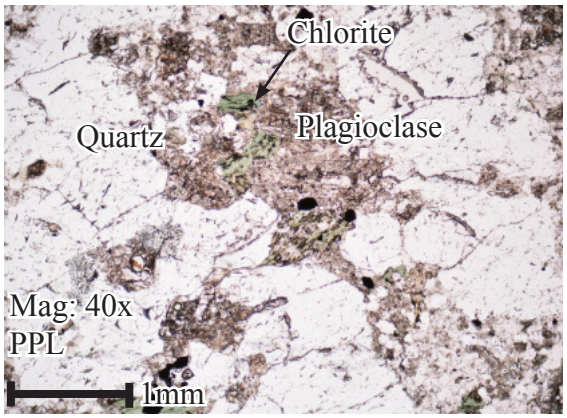

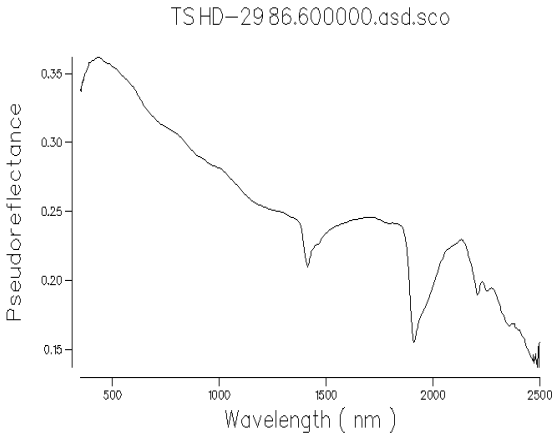

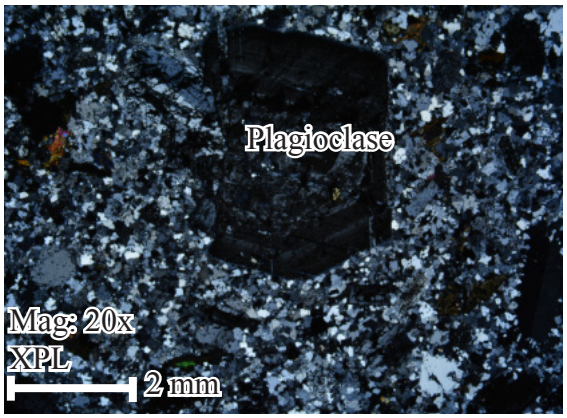

1. B2: Geochronology Samples. HD-13A 488

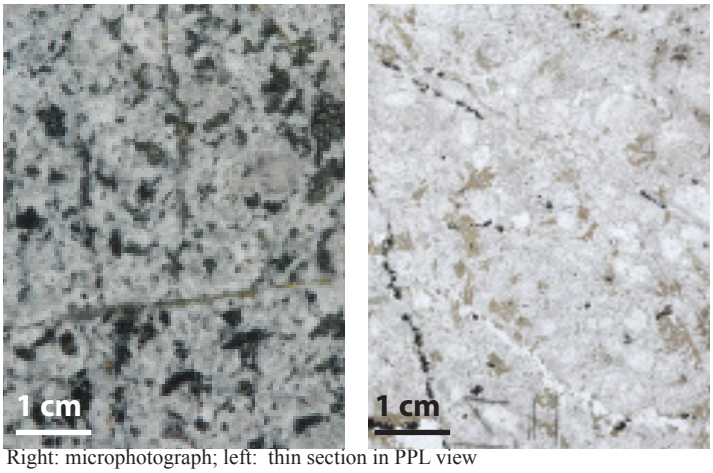

Right: microphotograph; left: thin section in PPL view

Unit: Kestane stock (Phase B)
Area: Kestane
Assay grade:940 ppm Cu; 36.9 ppb Au
Estimated age: 37.79 ± 0.36 (U-Pb)

Lithology Description: Porphyritic texture, ground mass/ phenocrysts: 40/60. Recrystallized and embayed quartz phenocrysts. Plagioclases phenocrysts are zoned and show polysynthetic twining. Ground mass is a granular quartz and feldspar aggregate with dusty feldspars.

Alteration: Chlorite after secondary biotite is weak to moderate. Magnetite is distributed in ground mass and mafics.

Sample type: Geochronology

Petrographic Summary:

Porphyritic texture with megacryst of hornblendes altered to secondary biotite. Recrystallized and embayed quartz phenocrysts. Plagioclases phenocrysts are zoned and show polysynthetic twining. Ground mass is a granular quartz and feldspar aggregate with dusty feldspars. Chlorite after secondary biotite is weak to moderate. Magnetite is distributed in ground mass and mafics. Chalcopyrite is included in pyrite veins and ground mass

Mineral	pct	style	Size
Plagioclases	30	phenocrysts	Phenocrysts 2.5 -1 mm, euhedral tabular shape.
Horn-blendes?	7	phenocrysts	Megacryst (up to 4 mm, av-erage 2.5) , anhedral altered to secondary biotite
Quartz	2	phenocrysts	Embayed crystals up to 2 mm.
Quartz	30	groundmass	0.05 mm. rounded crystals in a granular aggregate
K-feldspar	7	groundmass	0.05 mm. rounded crystals in a granular aggregate
Opaques	4-6	groundmass	Pyrite veins with inclusion of chalcopyrite.
Chlorite	5	alteration	Up tp 0.6 mm. After biotite and locally associated with rutile
Biotite	20	alteration	In mafic site. Fine crystals 0.1 mm.
Clays	2-3	alteration	In felsic site.

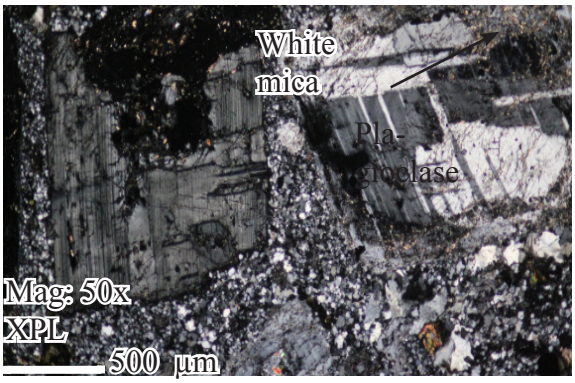

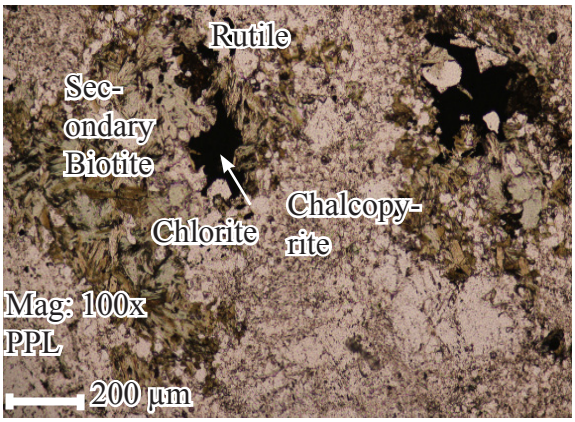

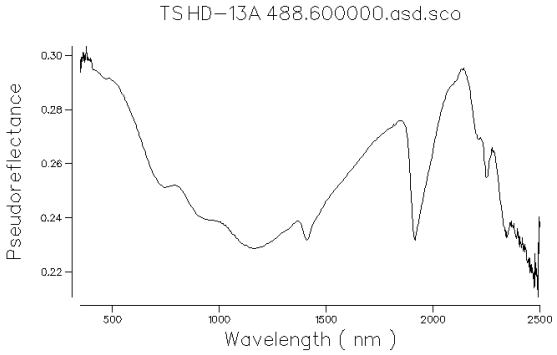

1. B2: Geochronology Samples. PB2014061

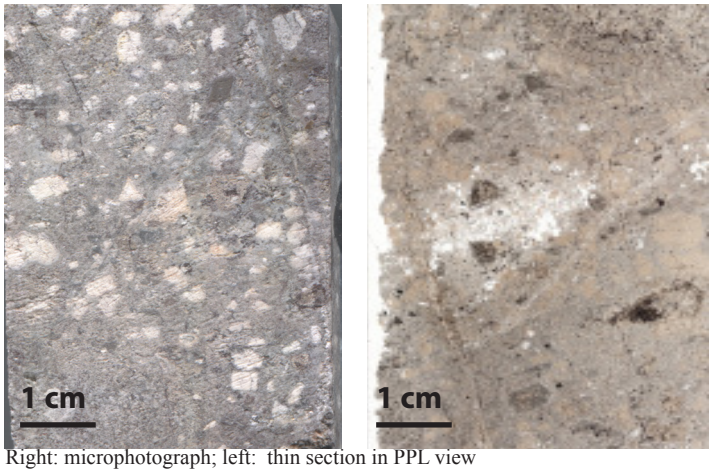

Right: microphotograph; left: thin section in PPL view

Unit: Andesitic porphyry
Area: Pirentepe
Assay grade:-
Estimated age: 28 Ma

Lithology Description: grey to purple medium grained andesite

Alteration: Kaolinite and silicification.

Sample type: Geochronology

Petrographic Summary:

Intense altered sample, porphyritic rock with lithic fragments. Phenocrysts have a brown colour due to alteration overprinting of earthy hematite and clays. Mineral identification based in crystals shape. Non-spectral response on SWIR.

Mineral	pct	style	Size
quartz	5-10	phenocrysts	un-altered/rounded 1mm
plagiclase	15-20	phenocrysts	tabular shape 1-2 mm
hornblende	5-10	phenocrysts	2mm
lithic fragment	15	fragment	10 mm
K-fedspar	20	groundmass	0.025 mm
quartz	10	groundmass	0.025 mm
silica	15	alteration	in groundmass
hematite	15	alteration	pervasive overprinting

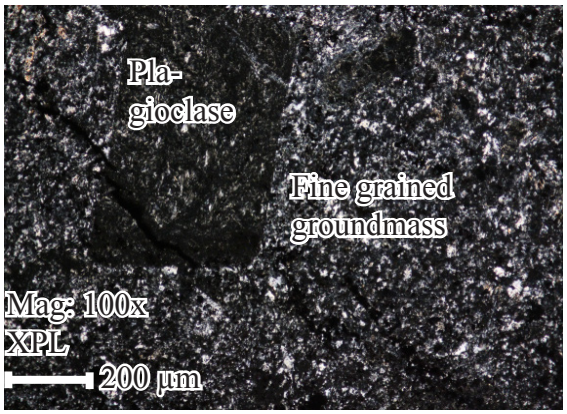

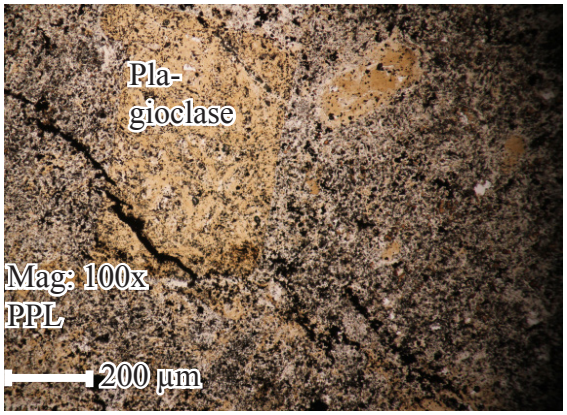

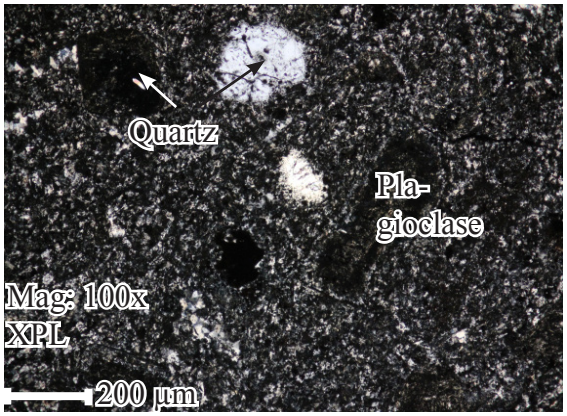

B2: Geochronology Samples. HD-37 112

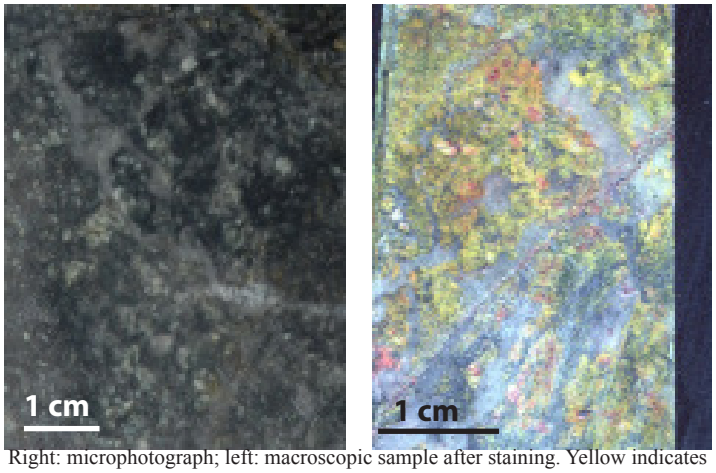

Right: microphotograph; left: macroscopic sample after staining. Yellow indicates K-bearing minerals and red Na- Plagioclase.

Unit: Kestane Stock (Phase A)
Area: Kestane
Assay grade:
Estimated age: 39.19 ± 0.47 (U-Pb)

Lithology Description: Porphyritic texture: quartz, mafics (hornblende altered to biotite), and plagioclases phenocrysts . Fine grained ground mass composed by quartz and k-feldspar.

Alteration: Intense K-altered wall rock.

Sample type: Geochronology

Petrographic Summary:

Intense K-altered wall rock. Quartz-pyrite-magnetite-chalcopyrite.veins are cross cutted by later pyrite veins. Mineralization is also observed after mafic phenocrysts.

Mineral	pct	style	Size
Plagioclase	7	phenocrysts	Altered phenocrysts (0.5-1.2 mm) to clay. Sub euhedral to anhedral.
Quartz	3	phenocrysts	Rounded phenocrysts.
Hornblende?	7	phenocrysts	Altered to secondary biotite, anhedral crystals
Quartz	10	groundmass	Fine grained in ground mass (0.025-0.1 mm)
K-feldspar	15	groundmass	In ground mass (0.025-0.1 mm).
Biotite	15	alteration	Fine secondary biotite (up to 200 µm) is replacing mafic minerals.
Chlorite	5	alteration	Size between 0.05-1 mm. Associated with sulphides and locally with secondary biotite.
Clays	15	alteration	Fine clays are altering feldspars.
Sericite	5	alteration	Felsic site, replacing plagioclases and in association with clays. up to 0.05 mm.

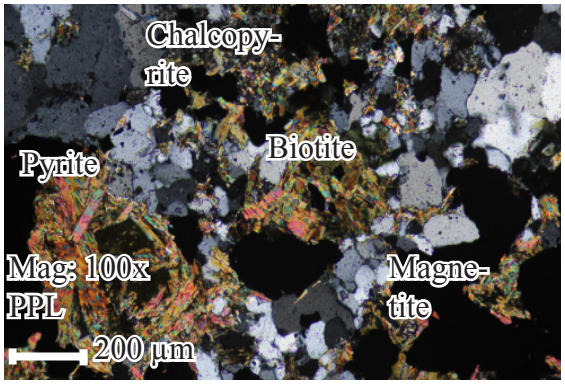

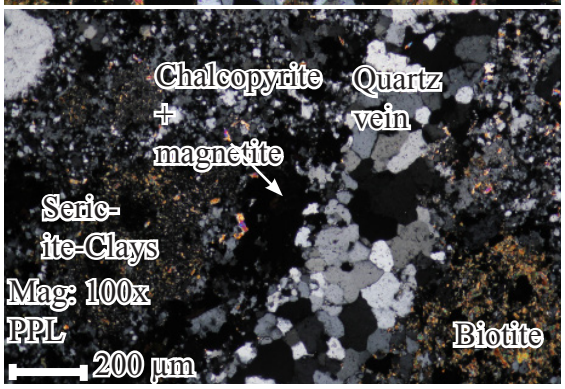

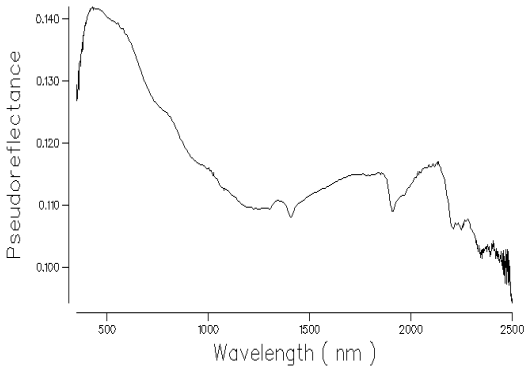

B2: Geochronology Samples. PB2014106

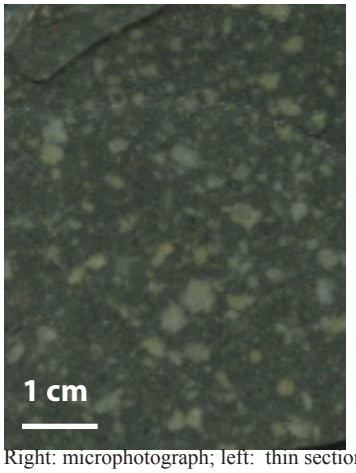

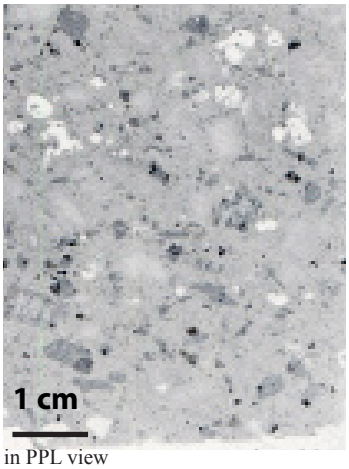

Right: microphotograph; left: thin section in PPL view

Unit: Green andesite
Area: W Kestane
Assay grade:5.1 ppm Cu; 1.9 ppb Au
Estimated age: 38.79 ± 0.32 (U-Pb)

Lithology Description: Porphyritic andesite, plagioclase and quartz phyric, greenish and microcrystalline ground mass. Not good bedding but E-W trending fractures

Alteration: Chlorite and epidote.

Sample type: Geochronology

Petrographic Summary: (Description based on sample PB2013043)

Plagioclase, quartz phyric dacite to rhyodacite. Pseudomorphs of biotite and hornblende. The ground mass is a fine aggregate of feldspars and mafic minerals. Intense and selective carbonate replacement.

Mineral	pct	style	Size
Feldspar	25	phenocrysts	subhedral (tabular) and anhedral. Up to 5 mm (average size 3 mm)
Hornblende	5	phenocrysts	Pseudomorphs. Euhedral diamond and tabular. Up to 2 mm
Quartz	10	phenocrysts	Rounded and embayed, up to 3 mm.
Biotite	7	phenocrysts	Pseudomorphs. Euhedral tabular and hexagonal crystals, altered. Up to 4 mm
Feldspar	40	groundmass	Fine aggregate. Size 0.05 mm.
Magnetite	3	groundmass	Disseminated and associated with biotite.
Sericite	5	alteration	Incipient alteration after plagioclase
Calcite	10	alteration	Incipient to total alteration of crystals. After plagioclase and hornblende.
Rutile	3		In mafic phenocryst

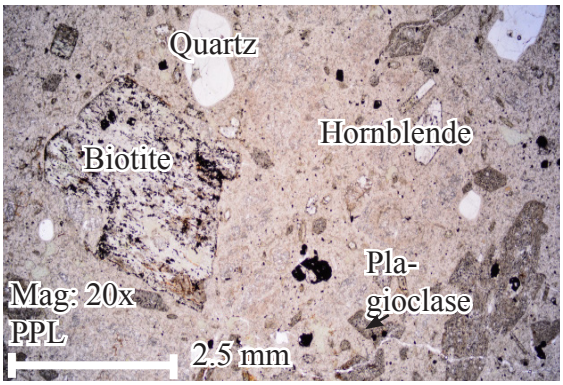

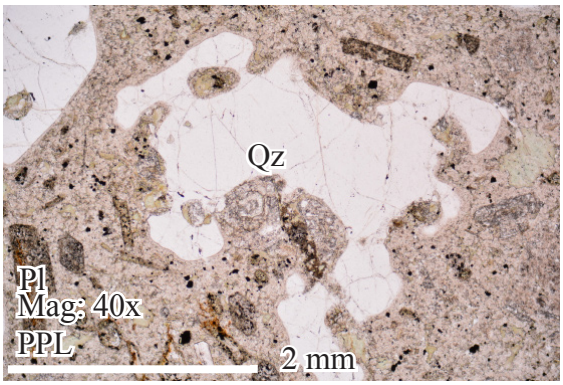

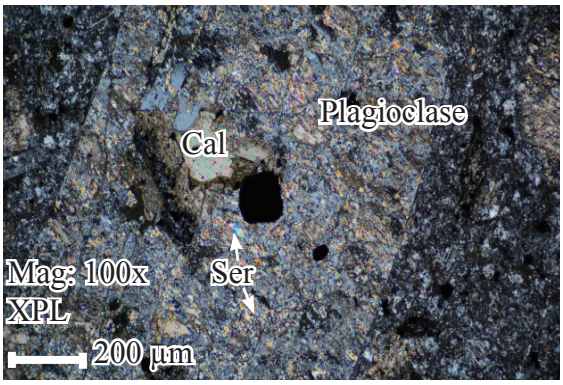

B2: Geochronology Samples. PB2013046

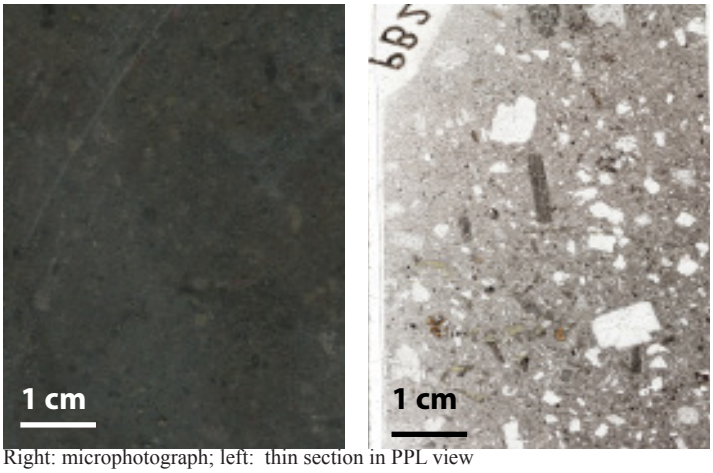

Right: microphotograph; left: thin section in PPL view

Unit: Crystal tuff
Area: Pirentepe
Assay grade: 38.3 ppm Cu; 1.,1 ppb Au
Estimated age: 28.54 ± 0.26 (U-Pb)

Lithology Description: Porphyritic rock. Phenocrysts of plagioclases, rounded quartz, biotite, amphibole and amphibole. Epidote in plagioclase fresh biotite and hornblendes. Fragmentary texture with lithic clasts

Alteration: Weak and selective. Montmorillonite and minor chlorite and epidote.

Sample type: Geochronology

Petrographic Summary:
Ground mass is fine grained with average crystals size 0.25 mm. Trachytic texture is observed in plagioclase microphenocryst.Orthopyroxene has pale green colour and first order yellowish colour, which indicates low Fe contents in the solid solution. The extinction angle is about 80°. Clinopyroxene crystals are smaller than orthopyroxene. Clinopyroxene is colorless in PPL and present second order interference colour. Euhedral to subhedral biotite present brown pleochroism and bird-eye extinction. Hornblende exhibits an intense brown pleochroism and cleavage close to 60 and 120°.

Mineral	pct	style	Size
Plagioclases	20	phenocrysts	up to 4.5mm (average 2 mm)
Clinopyroxene	1	phenocrysts	up to 0.3 mm
Biotite	2	phenocrysts	up to 2 mm
Hornblende	3	phenocrysts	up to 4 mm
Orthopyroxene	3	phenocrysts	up to 2 mm
Plagioclases	50	groundmass	up to 0.2 mm

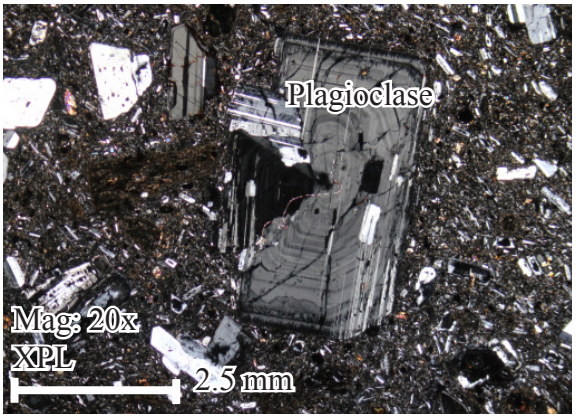

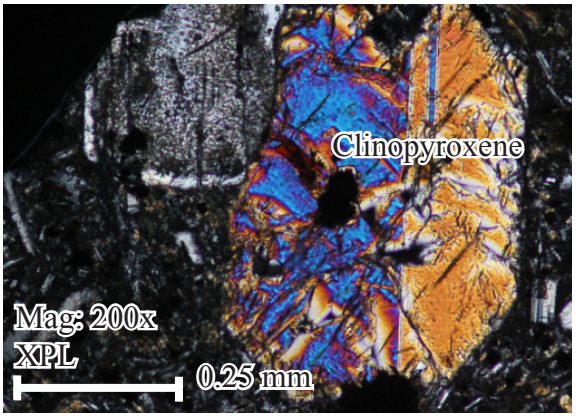

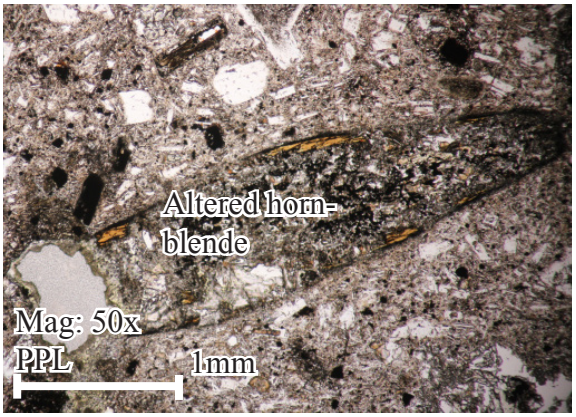

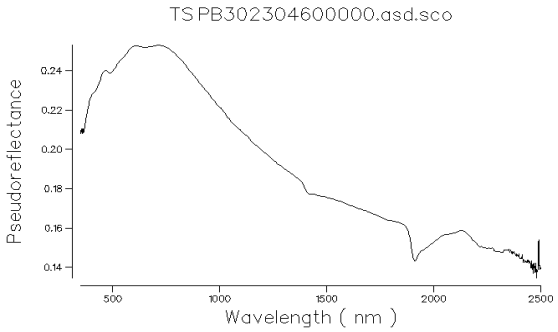

B2b. Geochemistry of geochronology Samples

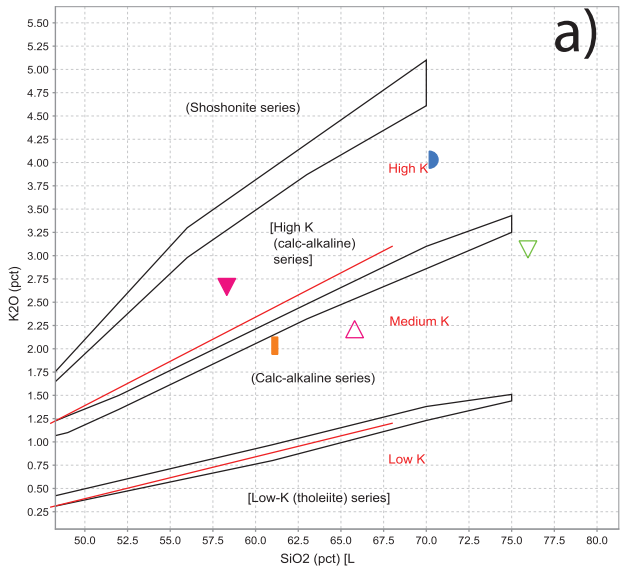

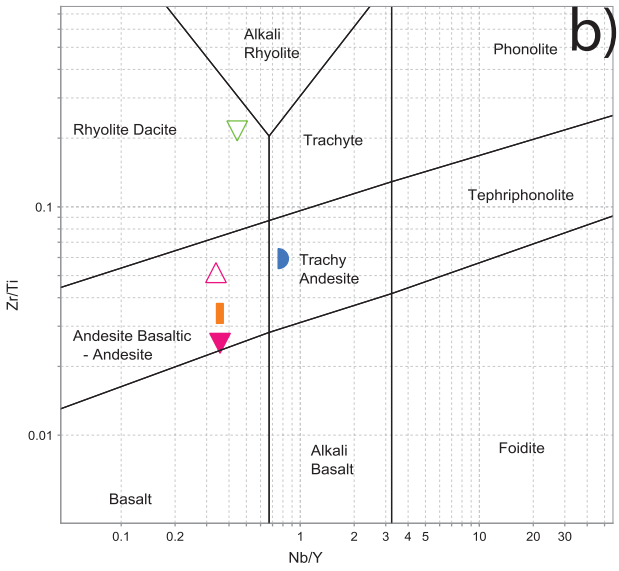

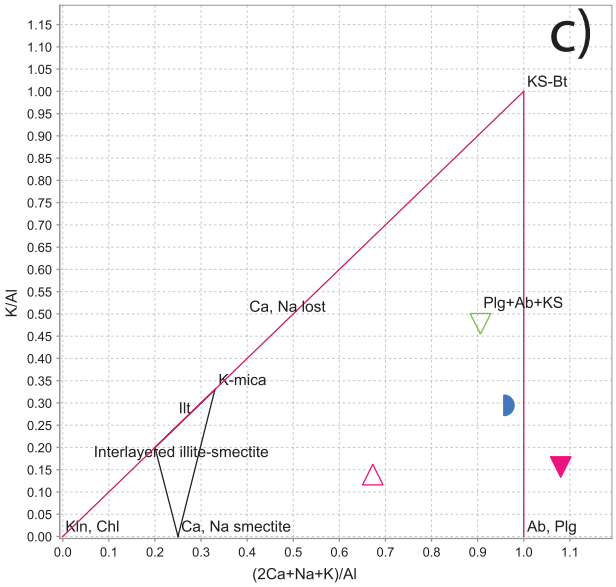

Legend

- PB2014106
- HD-13A 488.6
- HD-37 112
- HD-29 86
- PB2013046

B3. Lithogeochemistry Samples. HD-09 354.1

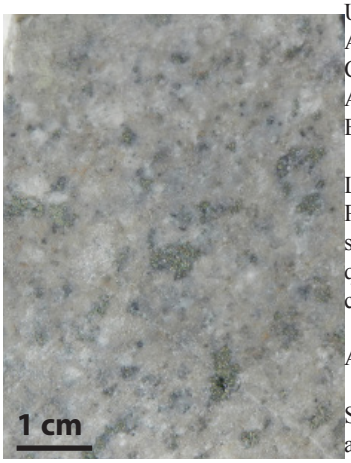

Unit: Dacite
Area: Kunk
Coordinates: 483817 4418744
Assay grade:26.3ppm Cu; 84.4 ppb Au
Estimated age: 40 Ma

Lithology Description: Porphyritic texture. Phenocryst/ground mass is 70/30. Average size of phenocrysts 3mm. Feldspars 10%, quartz 5%, pyrite (in mafic site) 15%. Pink colour ground mass

Alteration: Pyrophyllite

Sample type: Kunk advanced argillic alteration

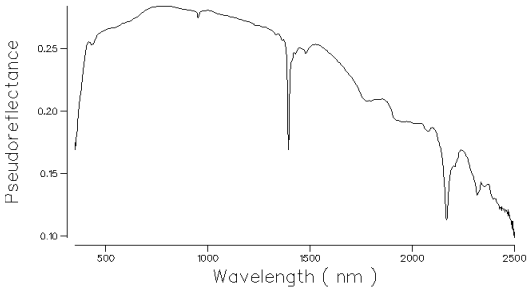

B3. Lithogeochemistry Samples. HD-09 95

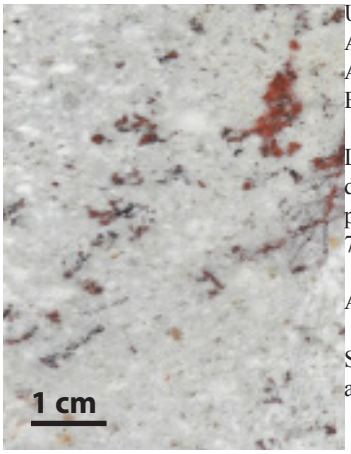

Unit: Dacite
Area:Kunk
Assay grade: 10.2 Cu; 12.72 Au
Estimated age: 40 Ma

Lithology Description: Porphyritic dacite with 5 mm quartz “eyes”, 3-4 mm plagioclases. Phenocryst/ground mass is 70/30. Ground mass is cryptocrystalline.

Alteration: White mica, pyrophyllite.

Sample type: Kunk advanced argillic alteration

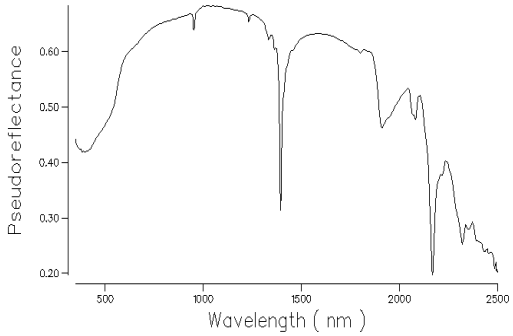

B3. Lithogeochemistry Samples. HD-13A 415

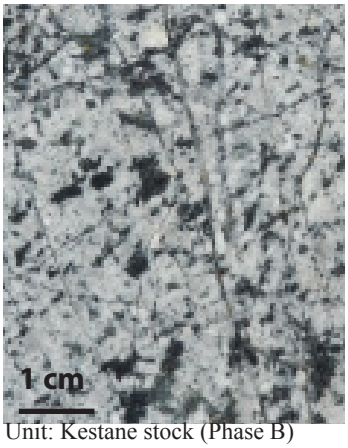

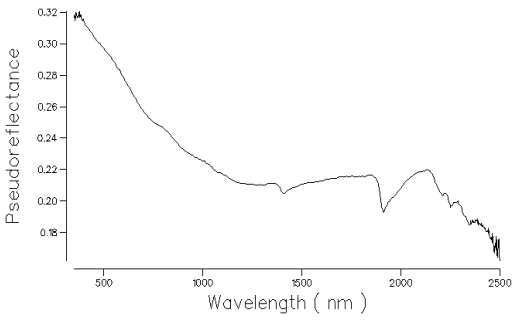

Right: microphotograph; left: macroscopic sample after staining. Yellow indicates K-bearing minerals and red Na- Plagioclase.

Unit: Kestane stock (Phase B)
Area: Kestane
Assay grade:2040.9 ppm Cu; 710 ppb Au
Estimated age: 37 Ma
Sample Type: Chlorite after secondary biotite alteration .

Lithology Description: porphyritic texture (Phenocrysts/ground mass is 45/55) with medium grained crystals 2mm; plagioclases (35%), k-feldspar (20%), quartz (15%), hornblendes (altered to biotite, 30%).
Alteration: Secondary biotite after hornblende and chlorite overprinting.

B3. Lithogeochemistry Samples. HD-13A 311

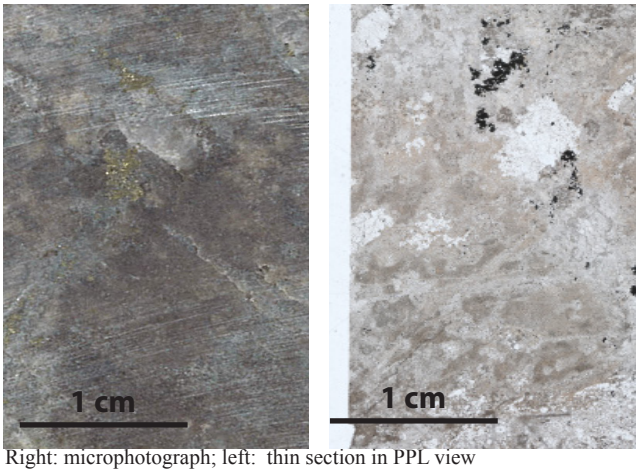

Right: microphotograph; left: thin section in PPL view

Unit: Hornfels
Area: South Kestane
Assay grade:0.424 ppm Au; 0.17% Cu
Estimated age: 40 Ma

Lithology Description: Dark grey, fine grained to aphanitic rock.

Alteration: Pervasive biotite hornfels alteration. White mica is overprinting the biotite alteration.

Petrographic Summary:
Biotite hornfels. Strongly altered to white mica (paragonite, illite) after biotite (phlogopite). The primary texture is overprinted, however it displays quartz porphyroblasts and a probably volcano-sedimentary origin is inferred. Opaques (pyrite and chalcopyrite) are distributed in ground mass and in veins. Rutile is associated to white mica and pyrite

Mineral	pct	Style	Size
Quartz	3	phenocrysts	up to 0.25 mm, rounded crystals
Feldspar	25	groundmass	Fine grained anhedral aggregate partially silicified and altered to white mica .
Pyrite	1	groundmass	up to 1 mm
Chalcopyrite	tr	groundmass	crystals up to 0.1 mm
White mica	15	alteration	Finely distributed in ground mass
Silica	7	alteration	Alteration in ground mass
Biotite	25	alteration	In ground mass, fine grained ? Size

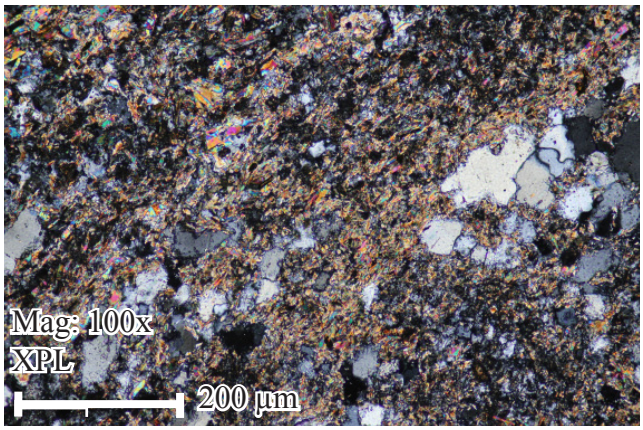

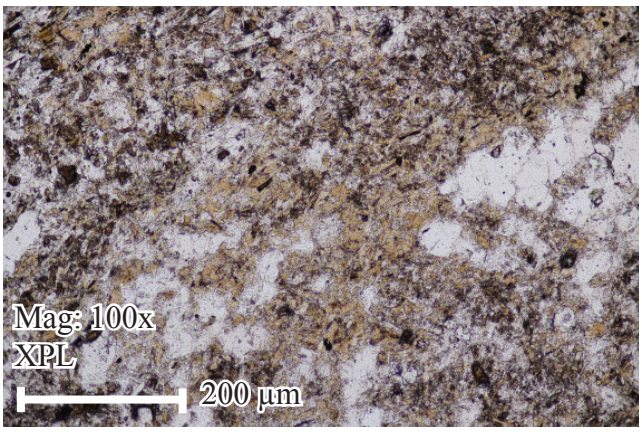

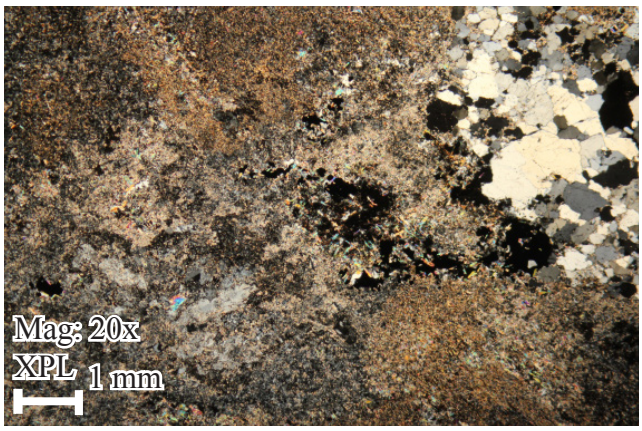

B3. Lithogeochemistry Samples. HD-37 254.3

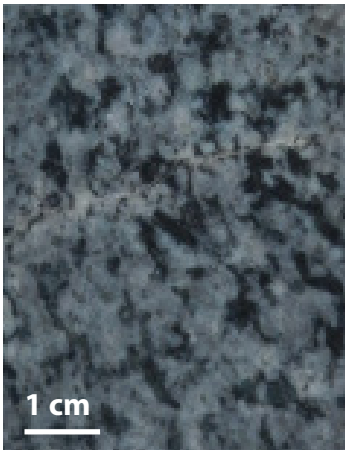

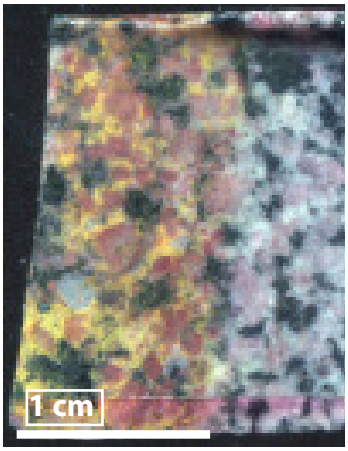

Right: microphotograph; left: macroscopic sample after staining. Yellow indicates K-bearing minerals and red Na- Plagioclase.

Unit: Kestane stock (Phase B)
Area: Kestane
Assay grade:778 ppm Cu; 82 ppb Au
Estimated age: 37 Ma

Lithology Description: Porphyritic to equigranular rock, phenocrysts/ground mass ratio is 50/50. Plagioclase, embayed quartz, and amphibole phyric rock in a micro-crystalline ground mass (quartz and K-feldspar).

Alteration: Secondary biotite after hornblende, chlorite overprints alteration. White mica/clay in felsic site (smectite).

Sample Type: Kestane Stock-Phase B

Petrographic Summary:

Mineral	pct	style	Size
Plagioclases	15	phenocrysts	lath -shape and tabular with zoning and twining size up to 2 mm
Biotite	3	phenocrysts	Up to 1.5 mm subhedral shape
Hornblende?	15	phenocrysts	Completely altered to secondary biotite, up to 5 mm
Magnetite	1	phenocrysts	Associated to secondary biotite, up to 0.5 mm
Quartz	3	phenocrysts	Embayed megacryst (up to 3.5 mm),
Quartz	30	groundmass	Average size 0.1 mm, micro-crystalline granular aggregate
Feldspar	20	groundmass	Average size 0.1 mm, micro-crystalline granular aggregate
Pyrite	2	groundmass	Up to 1 mm, disseminated
Chalcopyrite	<1	groundmass	In ground mass and with secondary biotite
Biotite	20	alteration	after hornblende
Chlorite	3	alteration	In ground mass size up to 0.5 mm
White mica	3	alteration	Fine grained
Calcite	1	alteration	up to 0.1 mm

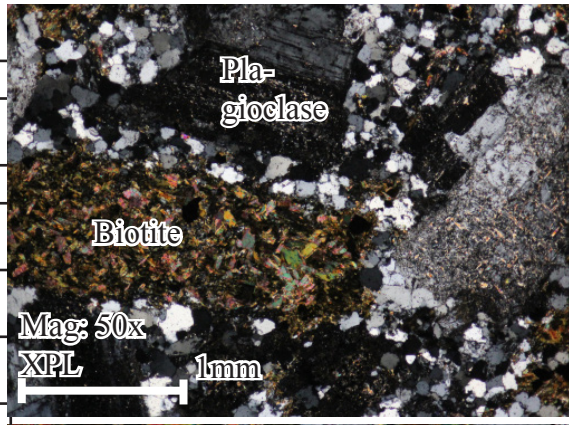

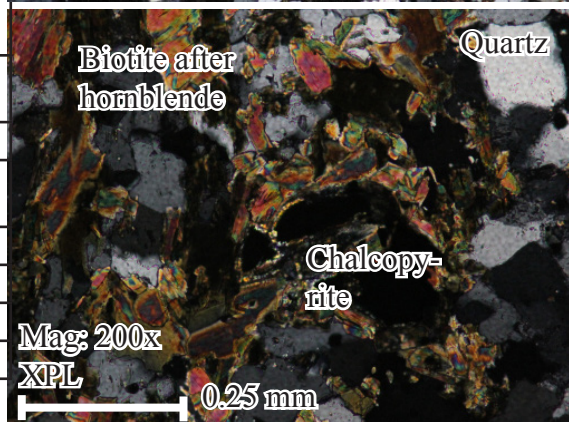

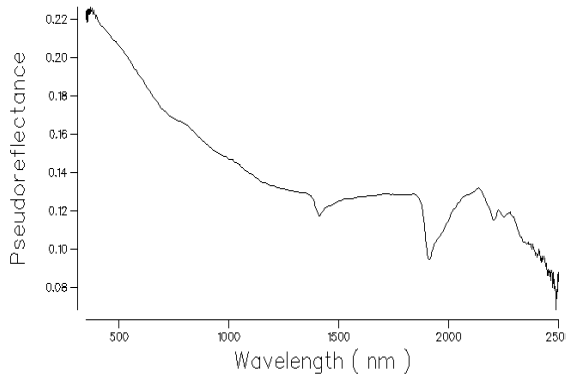

B3. Lithogeochemistry Samples. HD-38 190

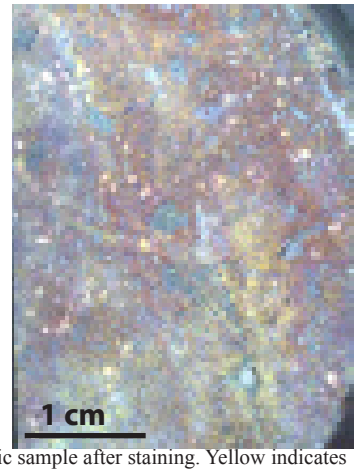

Right: microphotograph; left: macroscopic sample after staining. Yellow indicates K-bearing minerals and red Na- Plagioclase.

Unit: Andesitic dyke
Area: Kestane
Assay grade: 91.4 ppm Cu; 54.7 ppb Au.
Estimated age: Post 37 Ma

Lithology Description: Porphyritic rock, ground mass/ phenocrysts: 70/30. Plagioclases, amphiboles, and pyroxene phyric, microcrystalline ground mass (plagioclases, K-feldspar and fine mafics.

Alteration: Chlorite and epidote in mafic site and ground mass.

Petrographic Summary:
Porphyritic rock. Plagioclases, amphiboles, and pyroxenes phyric and microcrystalline ground mass (plagioclases, K-feldspar and fine mafics (biotite and amphiboles?). Magnetite and pyrite are observed in ground mass. Also minor chalcopyrite is disseminated in ground mass.

Mineral	pct	style	Size/Shape
Plagioclases	30	phenocrysts	0.5-3 mm, altered to clays
Amphiboles	15	phenocrysts	(0.1-0.3 mm) , altered to epidote.
Clinopyroxene	5	phenocrysts	euhedral shape (elongated crystals).
Feldspars	30	groundmass	Dusty -subhedral aggregate
Biotite	7	groundmass	Fine in ground mass and with amphiboles (0.1-0.3 mm) sub-euhedral to . Brown with pleochroism. Masked interference colour with high birefringence.
Pyrite	3	mineralization	(0.1-1 mm) Disseminated.
Magnetite	<1	mineralization	(0.1-0.8 mm) Associated to chalcopyrite and disseminated in ground mass
Chalcopyrite	<1	mineralization	(0.05-0.1 mm) In ground mass and mafics.
Clays	20	alteration	up to Disseminated in ground mass and phenocrysts.
Calcite	7	alteration	up to 0.2 mm
Epidote	7	alteration	In mafic phrnocryst
Chlorite	3	alteration	In phenocryst and ground mass.

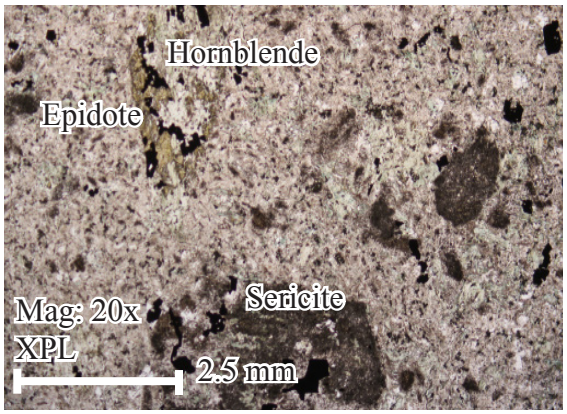

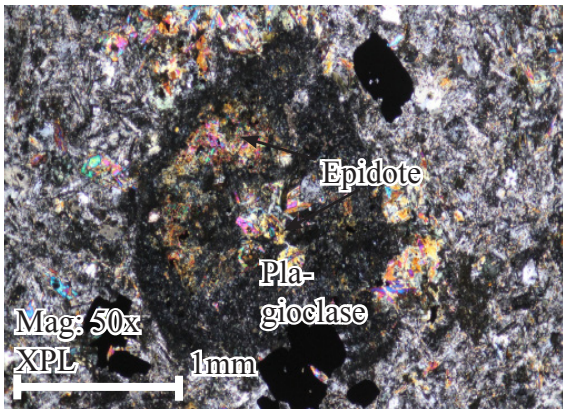

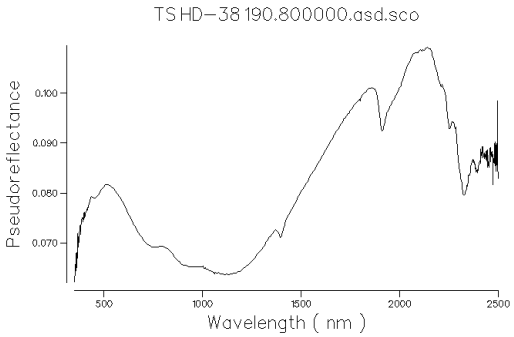

B3. Lithogeochemistry Samples. HD-38 310

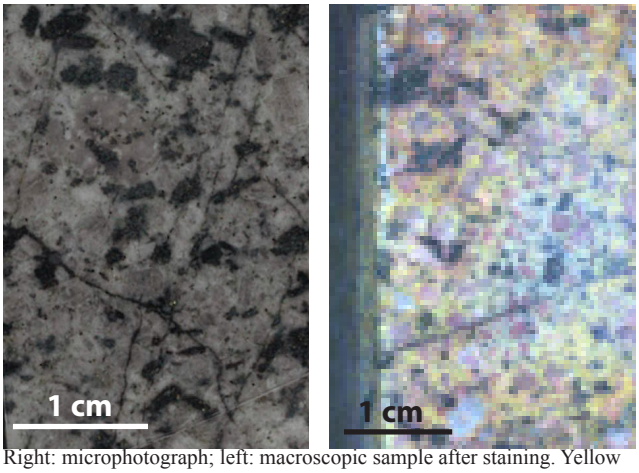

Right: microphotograph; left: macroscopic sample after staining. Yellow indicates K-bearing minerals and red Na- Plagioclase.

Unit: Kestane stock (Phase B)
Area: Kestane
Assay grade: 464 ppm Cu; 109.9 ppb Au
Estimated age: 37 Ma

Lithology Description: Porphyritic rock, ground mass/phenocrysts: 60/40. Phenocrysts are plagioclases, amphiboles (altered to secondary biotite), and rounded quartz. Microcrystalline ground mass (quartz and K-feldspar).

Alteration: Chlorite after secondary biotite.

Petrographic Summary:
Groundmass/phenocrysts ratio 50/50. Minor opaque minerals (magnetite, chacopyrite). Biorite presents green to brown pleochroism.

Mineral	pct	style	Size
Plagioclase	30	phenocrysts	40 mm (20-50 mm)
Biotite	3	phenocrysts	0.5 mm
Hornblende	17	phenocrysts	average 50 mm
K-feldspar	30	groundmass	0.05 mm
Quartz	20	groundmass	0.05 mm
Chlorite	<1	alteration	fine crystals
Biotite		alteration	after hornblende
Epidote	<1	alteration	minor in groundmass 0.05 mm

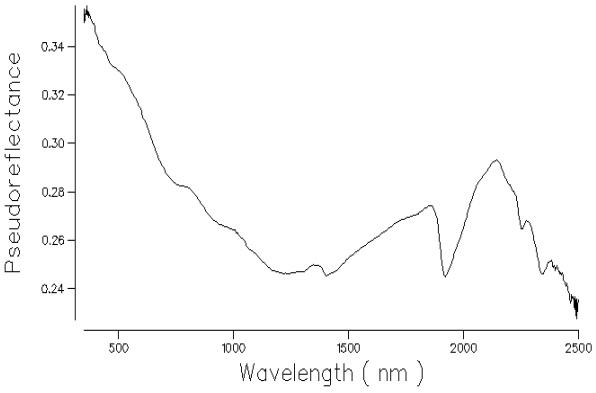

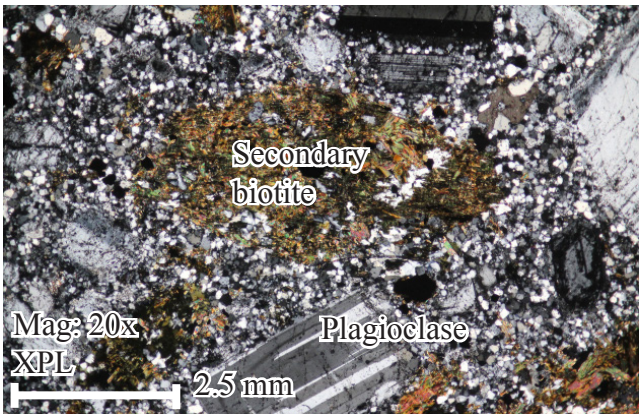

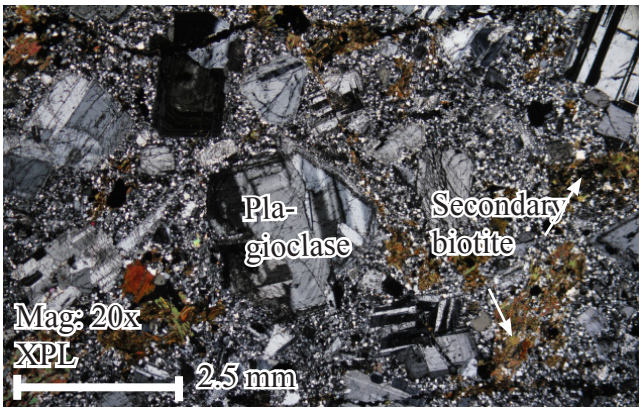

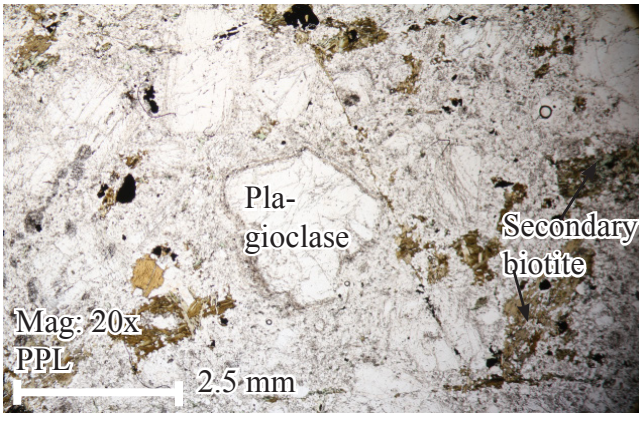

B3. Lithogeochemistry Samples. HD-45 459

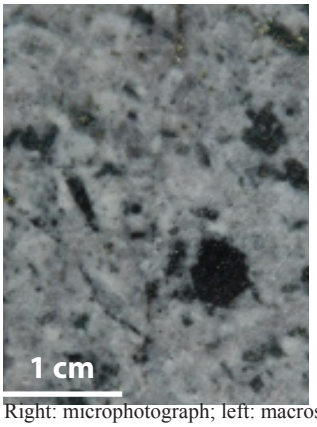

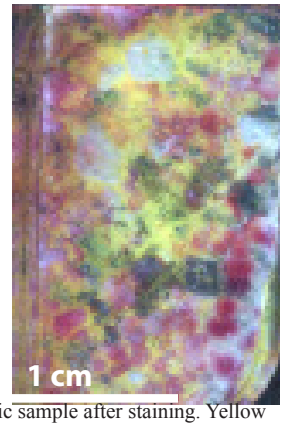

Right: microphotograph; left: macroscopic sample after staining. Yellow indicates K-bearing minerals and red Na- Plagioclase.

Unit: Kestane stock (Phase B)
Area: Kestane
Assay grade:582 ppm Cu; 69.7 ppb Au
Estimated age: 37 Ma

Lithology Description: The rock exhibits a porphyritic texture with primary phenocrysts of plagioclase, quartz, hornblende and minor biotite. The ground mass is a fine granular aggregate of quartz and K-feldspar.

Alteration: Chlorite in mafic site, illite in felsic and minor epidote.

Petrographic Summary:
Porphyritic texture with coarse hornblendes phenocrysts altered to secondary biotite, embayed quartz and fresh to moderate altered plagioclases with twining. Pyrite is the most dominant sulphide, minor chalcopyrite is distributed in ground mass.

Mineral	pct	style	Size
Biotite	2	phenocrysts	subhedral hexagonal crystals with a size up to 3 mm
Hornblende	10*	phenocrysts	size 1-5 mm prismatic relict crystals
Plagioclases	15	phenocrysts	size 1-4 mm tabular and prismatic
Quartz	7	phenocrysts	size 1-4 mm rounded to sub-rounded, some embayed crystals
Quartz and K-feldspar	25	groundmass	fine granular aggregate (0.05 mm)
Clays	3	alteration	After plagioclase
Chlorite	10	alteration	After secondary biotite and replacing primary crystals of biotite.
Biotite	15	alteration	Pseudomorphs of hornblende. Fine grained crystals up to 0.1 mm size.
Titanite	2	alteration	3 mm euhedral rhombic shape
Chalcopyrite	<1	mineralization	fine and disseminated in ground mass
Magnetite	2	mineralization	anhedral crystals size up to 0 .5 mm (average 0.2)

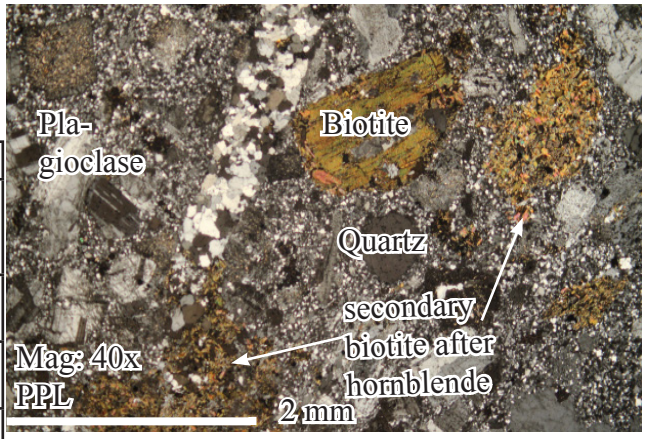

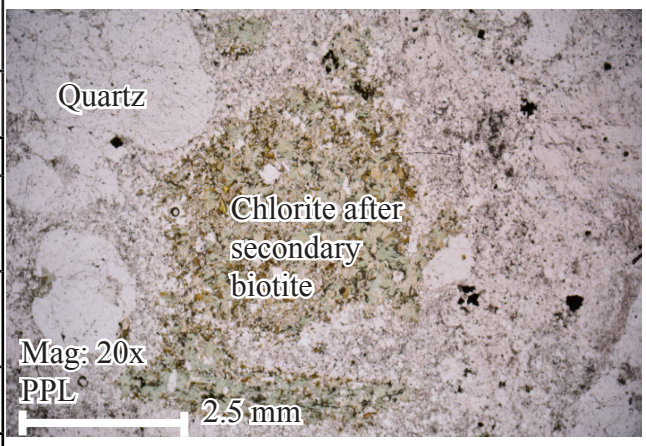

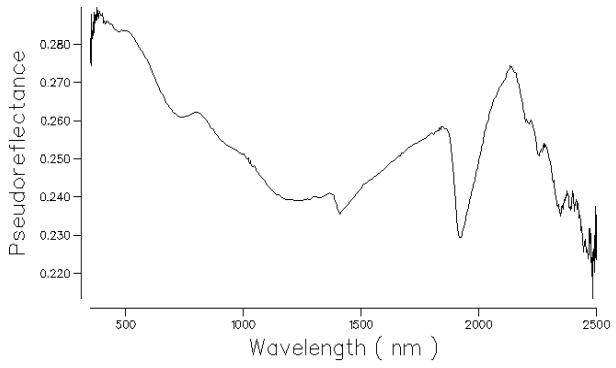

B3. Lithogeochemistry Samples. HD-60 720

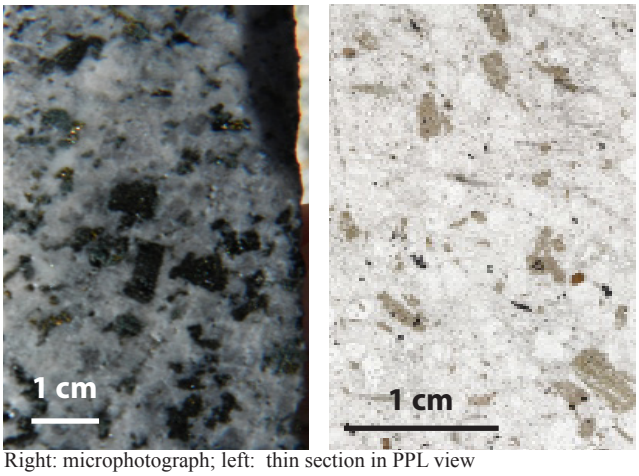

Right: microphotograph; left: thin section in PPL view

Unit: Kestane stock (Phase A)
Area: Kestane
Assay grade: 1828.5 ppb Cu; 131.9 ppb Au
Estimated age: 39 Ma

Lithology Description: Porphyritic to equigranular texture. Ground mass/phenocrysts is 70/30. Phenocrysts are: plagioclases (20%), quartz (5%), hornblende (15%)

Alteration: Secondary biotite after hornblende.

Petrographic Summary:

Groundmass/phenocrysts ratio 60/40. Chlorite alteration in mafics with evidences of rutile. Plagioclase with polysynthetic twining. Replacement textures in mafics: chlorite after secondary biotite after hornblende.

Mineral	pct	style	Size
Biotite	1	phenocrysts	1 mm
Plagioclases	25	phenocrysts	angular and sub-hedral 2 mm
Hornblende	10	phenocrysts	tabular 2.5 mm
Quartz	5	phenocrysts	rounded 1 mm
K-feldspar	40	groundmass	0.05 mm
Quartz	20	groundmass	0.05 mm
Biotite	11	alteration	replacing horn-blende
Chlorite	5	alteration	Incipient alter-ation in biotite

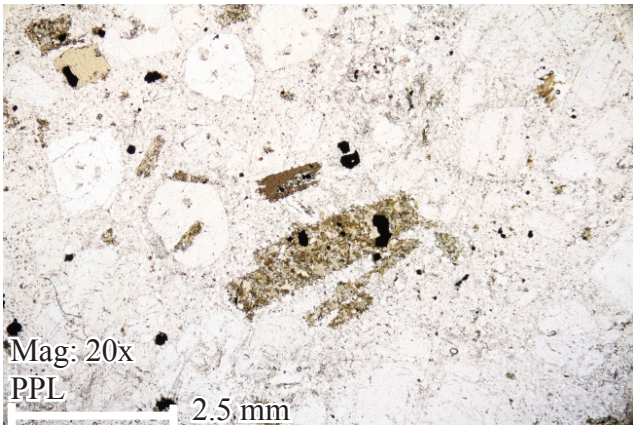

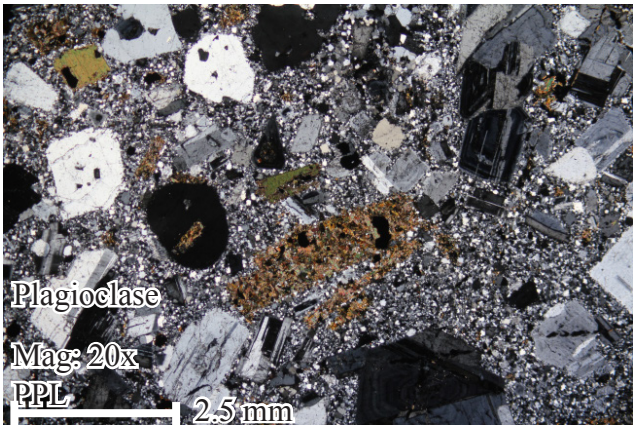

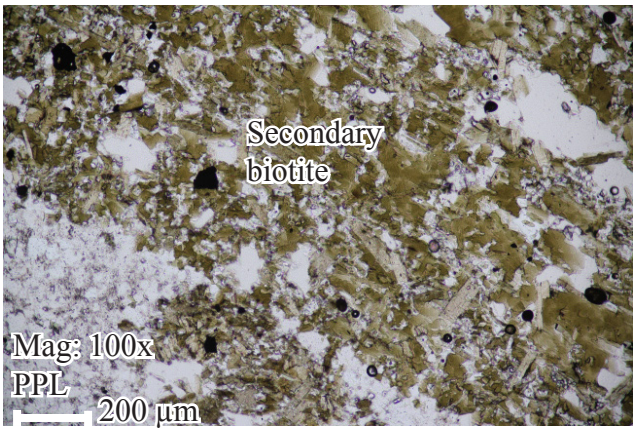

B3. Lithogeochemistry Samples. HD-78 39.4

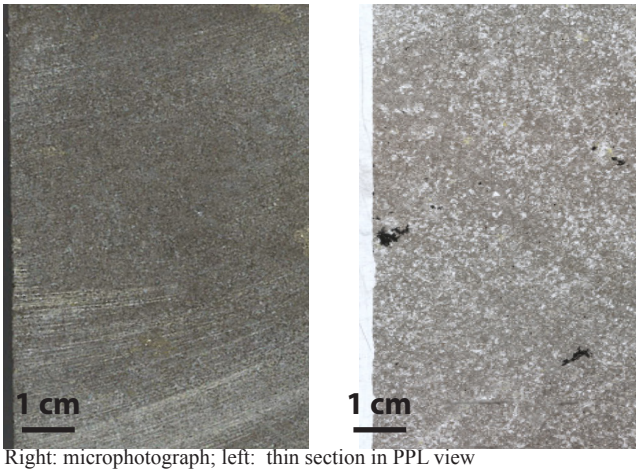

Right: microphotograph; left: thin section in PPL view

Unit: Volcanic sandstone (hornfels)
Area: W Kestane
Assay grade: 31 ppm Cu, 2.3 ppb Au
Estimated age: Pre- Eocene (Pre- 39 Ma)

Lithology Description: Fine grained volcano-sedimentary rock. Igneous texture is obliterated by hydrothermal alteration.

Alteration: Skarn alteration (garnet, epidote, calcite)

Petrographic Summary:
Fine grained rock, primary texture overprinted by calcic-skarn alteration.

Mineral	pct	style	Size
Quartz	20	phenocrysts	up to 0.1 mm
Feldspar	10	phenocrysts	up to 0.1 mm
Pyrite	1	mineralization	up to 0.20 mm
Epidote		alteration	up to 0.20 mm
Calcite	15	alteration	up to 0.30 mm
Clinopyroxene	5	alteration	up to 0.20 mm
Garnet	25	alteration	Anhedral, size up to

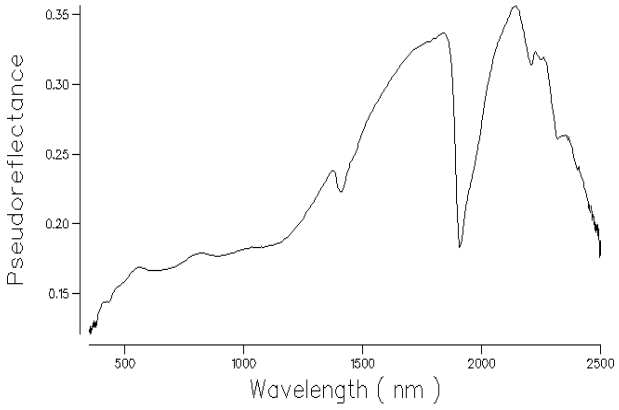

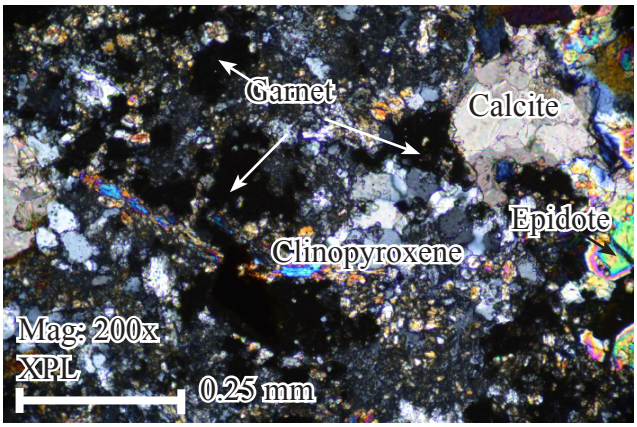

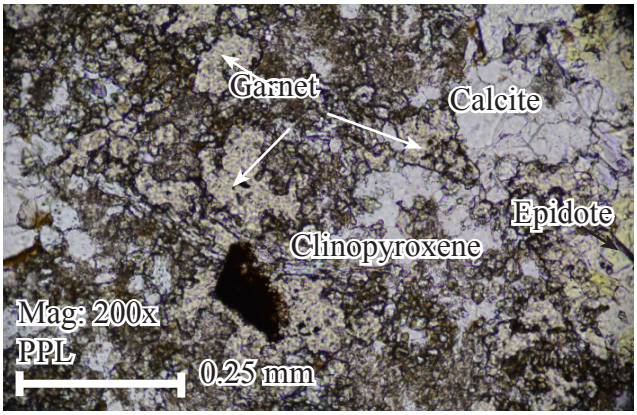

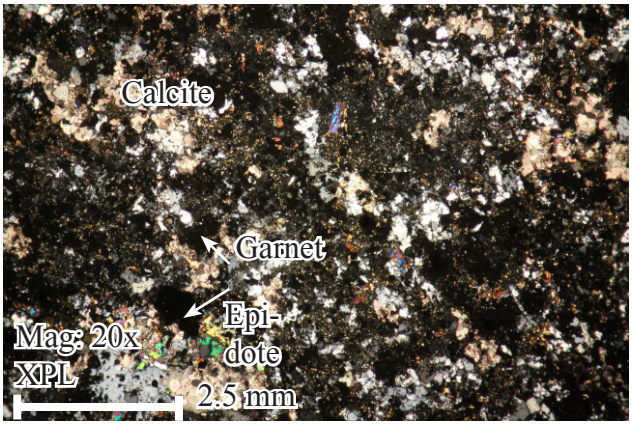

B3. Lithogeochemistry Samples. HD-80 30

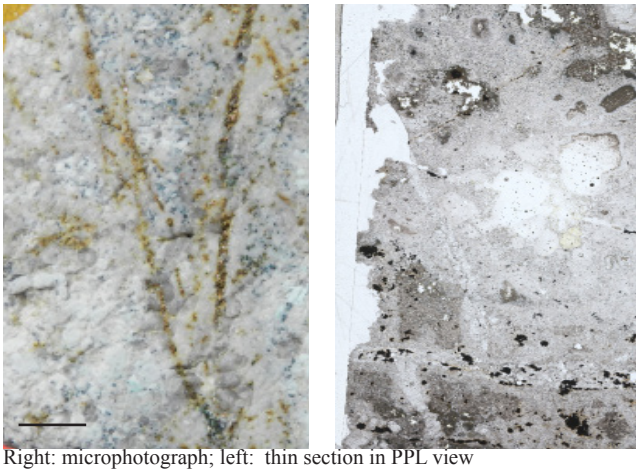

Right: microphotograph; left: thin section in PPL view

Unit: Kestane stock (Phase A)
Area: Kestane
Assay grade: 10000 ppm Cu; 463.4 ppb Au
Estimated age: 39 Ma

Lithology Description: Porphyritic texture, partially obliterated by sericite alteration. Phenocrysts are plagioclases (10%), quartz (2%). Groundmass is a fine grained aggregate of k-feldspar and quartz.

Alteration: Pervasive sericite

Petrographic Summary:

Porphyritic texture of rock with intense sericite alteration. Covellite and Chalcocite are replacing chalcopyrite. Replacement textures observed in thin section includes reaction borders.

Mineral	pct	style	Size
Plagioclases	10	phenocrysts	Completely altered except some relict up to 2.5 mm.
Quartz	2	phenocrysts	Rounded to subrounded size up to 0.8 mm.
Feldspars-Quartz	20	groundmass	Microcrystalline ground mass. Crystals size up to 0.05 mm
Sericite	40	alteration	In veins envelopes and replacing feldspars and mafics. up to 0.05 mm
Limonites	5	ateration	Brownish with anomalous birefringence colour
Rutile	3	alteration	Fine grained and disseminated in ground mass
Covellite	1	alteration	Replacing chalcopyrite, generally associated to goethite.
Chalcopyrite	<1	mineralization	Some relict with covellite borders.

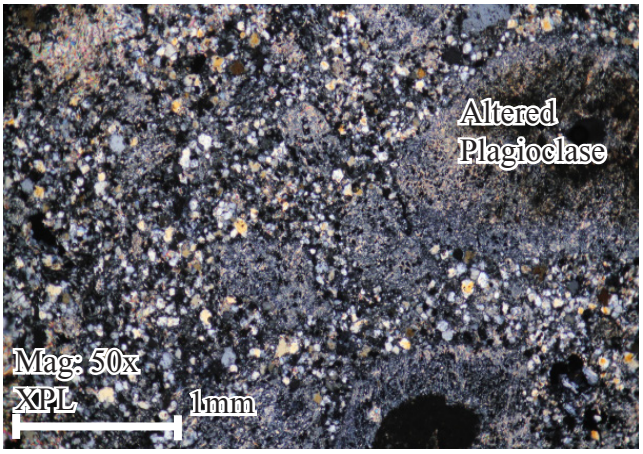

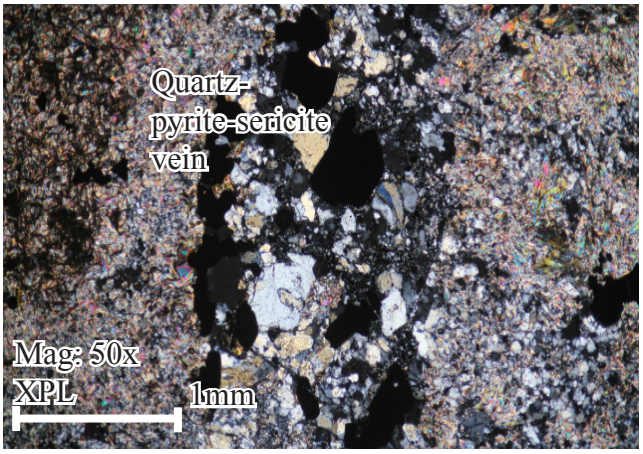

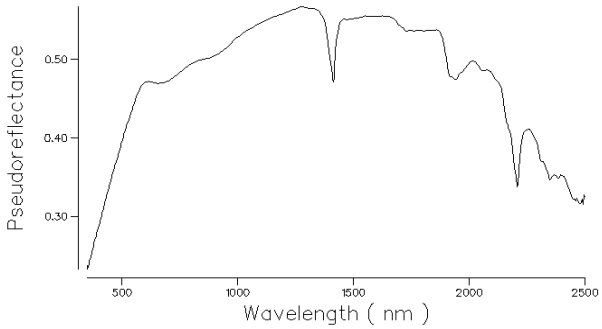

B3. Lithogeochemistry Samples. HD-80 99

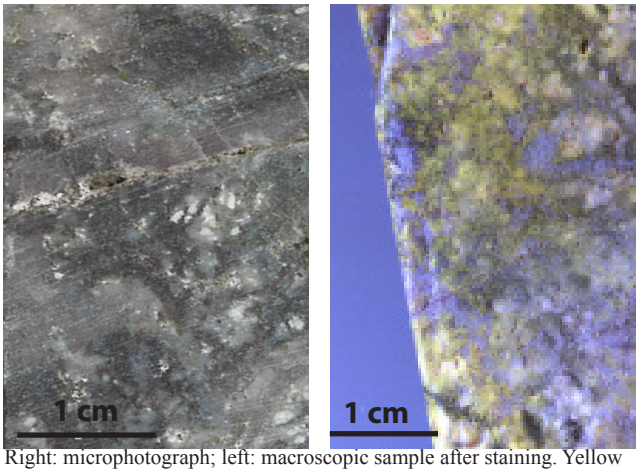

Right: microphotograph; left: macroscopic sample after staining. Yellow indicates K-bearing minerals and red Na- Plagioclase.

Unit: Kestane stock (Phase A)
Area: Kestane
Assay grade: 6812 ppm Cu; 734 ppb Au
Estimated age: 39 Ma

Lithology Description: Porphyritic granitic rock. Plagioclase phenocrysts without twining are in a fine grained quartz and K-feldspar aggregate.

Alteration: sericite and chlorite overprint the K-silicate alteration.

Petrographic Summary:

Porphyritic rock feldspar -phyric with incipient biotite brecciation. Intense biotite -magnetite alteration. In thin section sericite and chlorite appear to be overprinting the K-silicate alteration. The distribution of sulfides is generally in veins. Sulphides veins have chalcopyrite>pyrite.

Mineral	pct	style	Size
Plagioclases	10	phenocrysts	Subhedral to anhedral crystals with size range from 0.5 to 3 mm. Altered to clays
Quartz	20	groundmass	
K-feldspar	20	groundmass	
Clays	5	alteration	Replacing feldspars
Biotite	10	alteration	In mafic site and also in micro-veins locally cementing the rock
Chlorite	2	alteration	After secondary biotite and associated to sericite
Sericite	2	alteration	up to 50 µm
Magnetite	<1	mineralization	In mafic site
Pyrite	2	mineralization	Anhedral crystals up to 1 mm (in veins)
Chalcopyrite	3	mineralization	In vein with 1.5 mm width
Quartz	15	vein	Coarse-grained up to 1mm

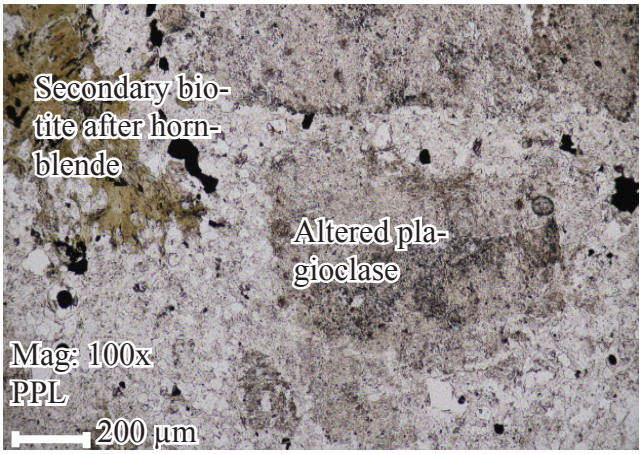

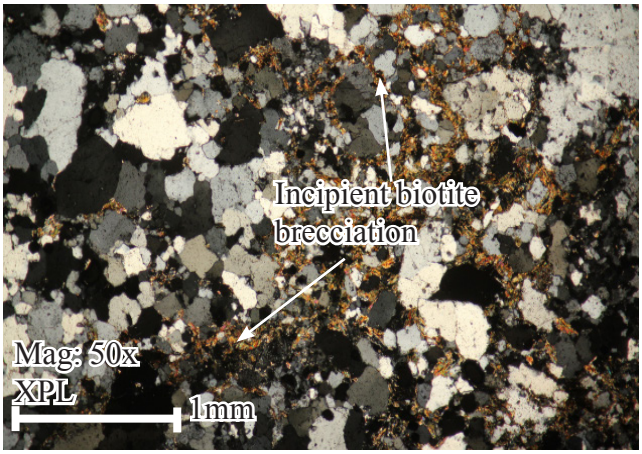

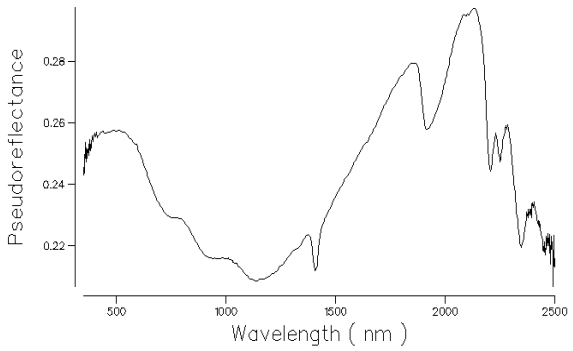

B3. Lithogeochemistry Samples. PB2014004

Right: microphotograph; left: macroscopic sample after staining. Yellow indicates K-bearing minerals and red Na- Plagioclase.

Unit: Crystal tuff
Area: Pirentepe
Assay grade: 8.5 ppm Cu; 0.6 ppb Au
Estimated age: 28 Ma

Lithology Description: Pale grey porphyritic volcanic with coarse phenocryst. Sub ehudral to ehudral Plagioclases (5 mm), reddish tabular hornblende, rounded quartz.

Alteration: Clay in plagioclases.

Petrographic Summary:

Ground mass is hypocrystalline and cryptocrystalline. Rounded to sub-rounded quartz crystals. Some crystals have embayed borders. Diamond-shape hornblende are altered and the primary optical features (colour, pleochroism, interference colour) are not preserved. Fe- oxides replacement? Zonation and twining is common in plagioclases.

Mineral	pct	style	Size
Plagioclases	25	phenocrysts	up to 4 mm
Quartz	7	phenocrysts	up to 2.5 mm
Biotite	5	phenocrysts	up to 2mm
Hornblende	10	phenocrysts	up to 3.5 mm (average size 1.5 mm)
Magnetite	2	groundmass	up to 0.5 mm
Glass	25	groundmass	
Clays	20	alteration	In mafic site and ground mass
Fe-Oxides?	5	alteration	In mafic site

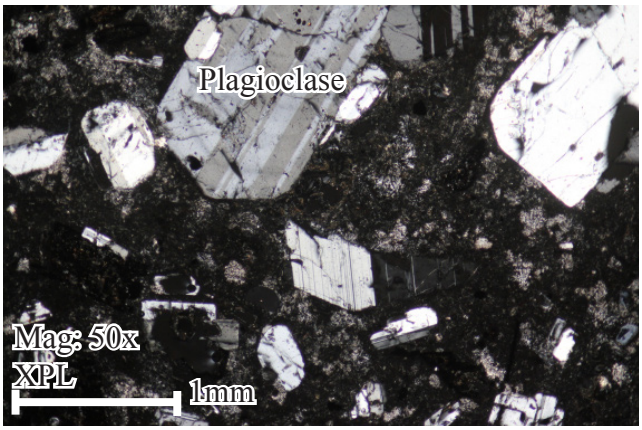

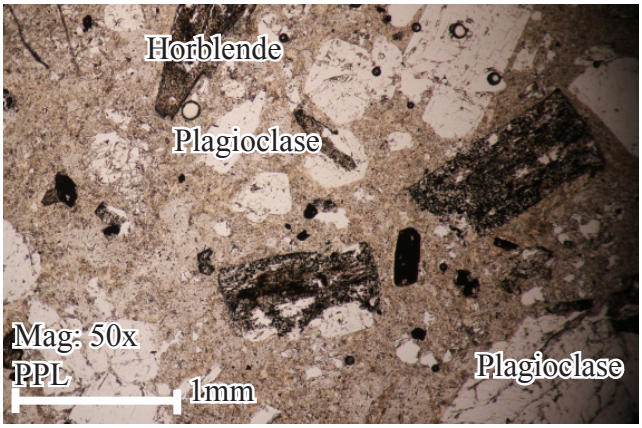

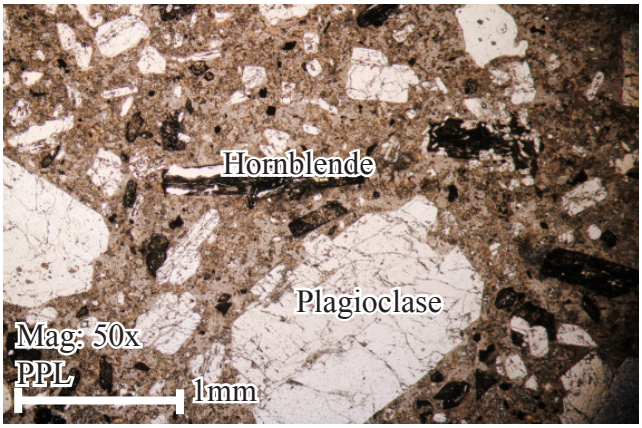

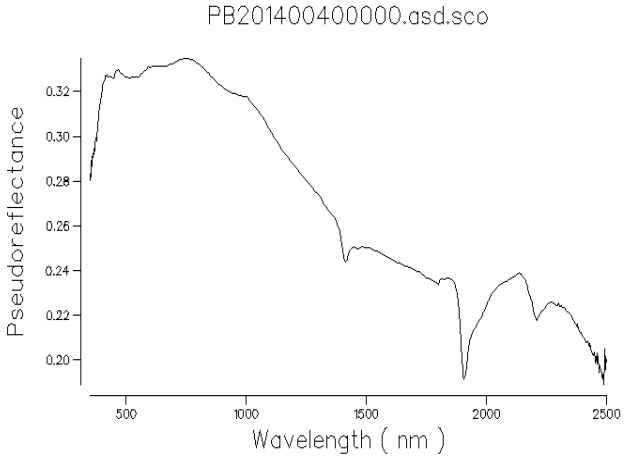

B3. Lithogeochemistry Samples. PB2013021

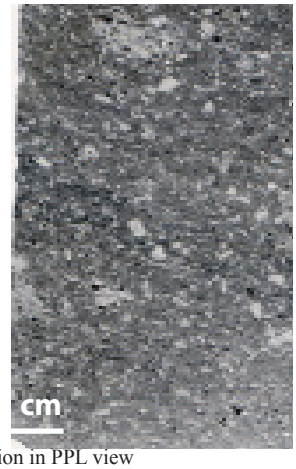

Right: microphotograph; left: thin section in PPL view

Unit: Basaltic andesite
Area: Kestane
Assay grade: 4.3 ppm Cu, 0.8 ppb Au
Estimated age: 37-28 Ma

Lithology Description: Dark grey-purple porphyritic fine grained basaltic andesite. Plagioclase phyric in an aphanitic ground mass.

Alteration: Weak to moderate chlorite in mafics. Plagioclase with clay and calcite replacement.

Petrographic Summary:

Amygdaloidal andesite altered to calcite. Fine grained ground mass (glass and plagioclases). No twining in plagioclase is observed and intense calcite replacement is affecting plagioclases phencrysts.

Mineral	pct	style	Size
Plagioclases	30	phenocrysts	up to 1.5 mm, partially altered to calcite
Amygdules ?	10	phenocrysts	rounded filled with recrystallized feldspar, some of them present euhedral heptagonal shape.
Pyroxene ?	2	phenocrysts	up to 1.25 mm, relict altered to calcite
Feldspar?	25	groundmass	Fine grained
Glass	25	groundmass	Isotropic, disseminated in ground mass.
Calcite	15	alteration	After plagioclase and in veinlets
White mica	7	alteration	After plagioclase

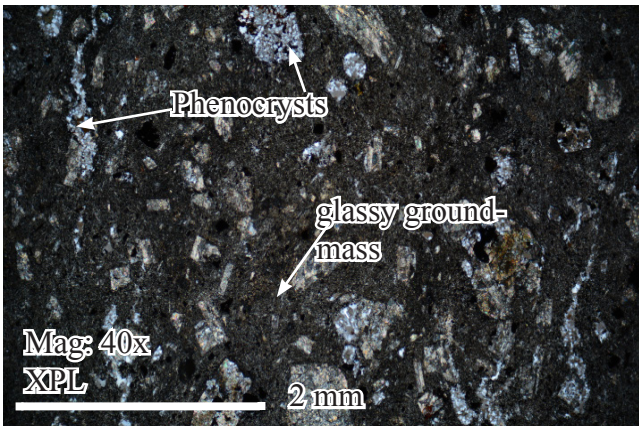

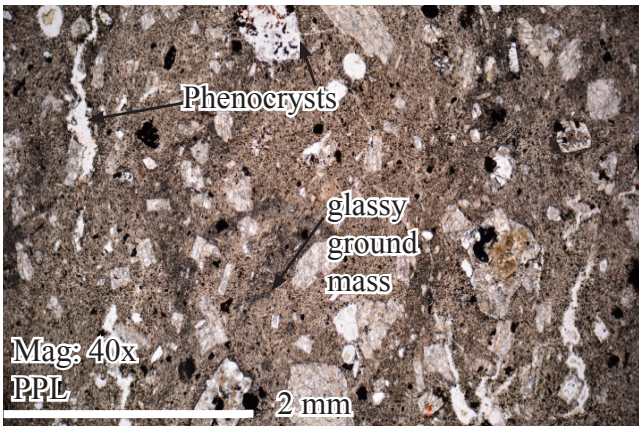

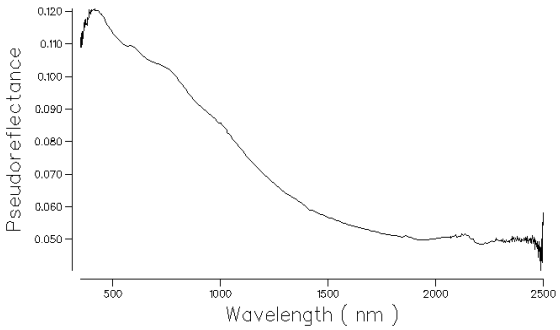

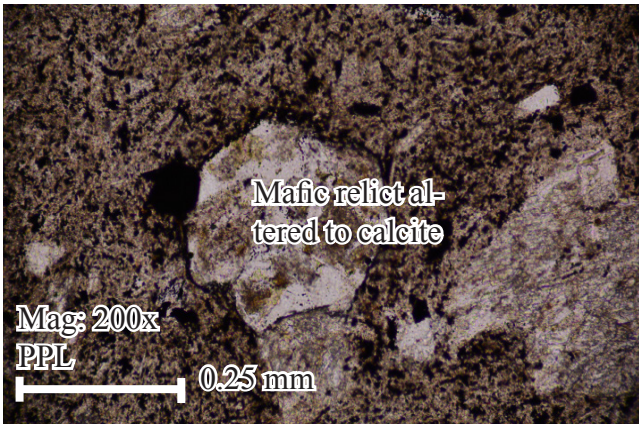

B3. Lithogeochemistry Samples. PB2013004

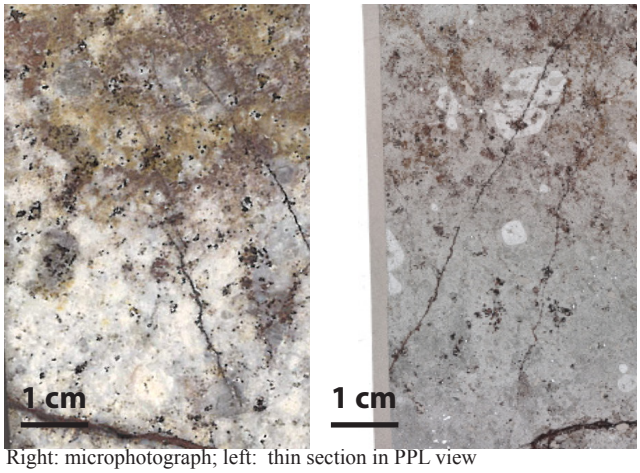

Right: microphotograph; left: thin section in PPL view

Unit: Dacite
Area: Kunk
Assay grade:-
Estimated age: 40 Ma
Coordinates: 484233E; 4418209N

Lithology Description: porphyritic dacite to rhyodacite. 4 mm Rounded quartz phenocrysts. Ground mass dominated by feldspar.

Alteration: White mica in phenocrysts. Hematite and goethite are overprinting primary texture. Fine hematite veins.

Petrographic Summary:

The rock presents a porphyritic texture with micro-crystalline ground mass. The phenocrysts/ground mass ratio is 30/70. Quartz and plagioclase phyric dacite. Limonites in veins and in ground mass and also in vugs. Local hematite brecciation in ground mass.
Feldspars phenocrysts are altered to fine grained white mica, this presents a orange to yellow first order dominant interference colour with second order purple to pinkish. Some laths shaped crystals (plagioclases?) are removed in a vuggy texture. The SWIR spectra indicates montmorillonite, paragonite, and hematite.

Mineral	pct	style	Size
Quartz	5	phenocrysts	Rounded and some embayed crystals up to 5 mm, average size 2 mm
Feldspar	10	phenocrysts	Generally anhedral and some laths-shape pseudomorph. Intense altered to white mica.
Quartz	5	groundmass	Anhedral granular aggregate, average size 0.05
Feldspar	35	groundmass	Anhedral granular aggregate, average size 0.05
White mica	20	alteration	In felsic site, after plagioclases? phenocryst
Limonites	15	alteration	Disseminated in ground mass, local cement of incipient breccia. Also in vugs.
Quartz	30	alteration	Silicification in ground mass.

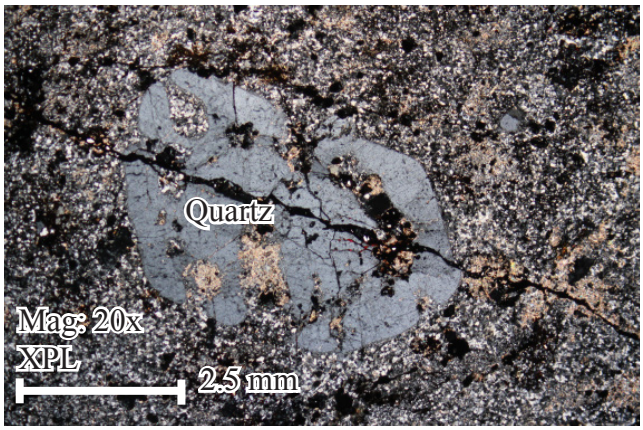

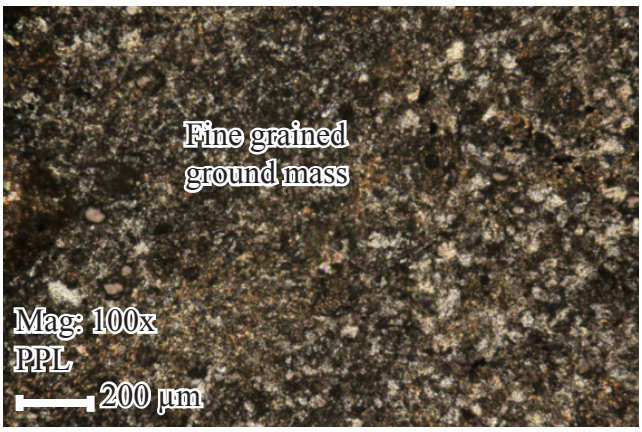

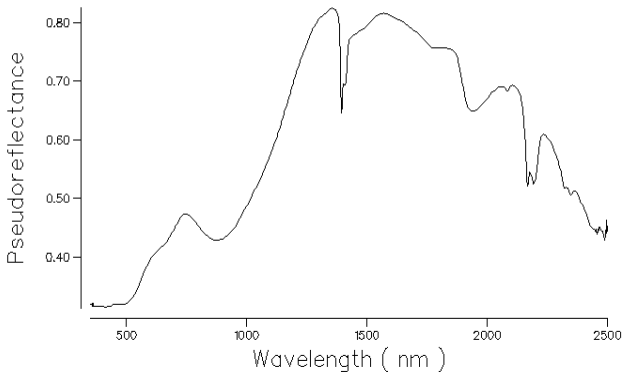

B3. Lithogeochemistry Samples. PB2014107c

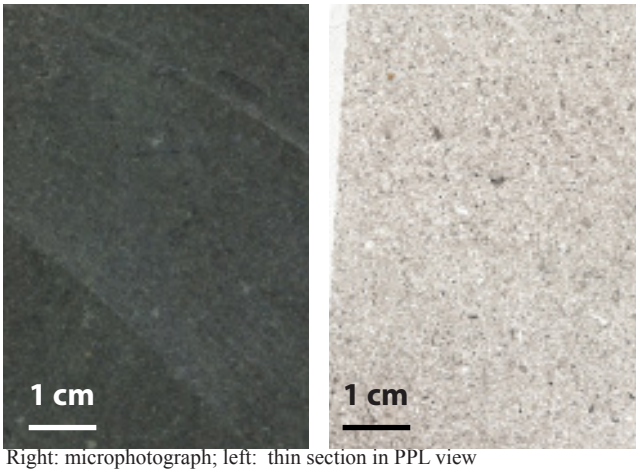

Right: microphotograph; left: thin section in PPL view

Unit: Volcanic sandstone
Area: Kestane
Assay grade:21 ppm Cu, 0.25 ppb Au
Estimated age: Pre- Eocene (Pre- 39 Ma)

Lithology Description: Grey to dark greenish tufficeous sandstone

Alteration: illite, calcite, chlorite

Petrographic Summary:

Sedimentary texture with rounded and angular quartz crystals. Other minerals exhibit fragmentary shape (plagioclases). The groundmass is a fine crystalline aggregate. Calcite is replacing plagioclases total and partially. The rock also exhibit fine grained lithic fragments.

Mineral	pct	style	Size
Quartz	25	phenocryst	up to 0.4 mm
Muscovite	8	phenocryst	up to 0.4 mm
Lithics	15	phenocryst	up to 1.25 mm
Plagioclases	7	phenocryst	up to 0.3 mm
K-feldspar	10	phenocryst	up to 0.3 mm
clays	5	alteration	
chlorite	3	alteration	up to 0.1 mm
calcite	10	alteration	up to 0.25 mm

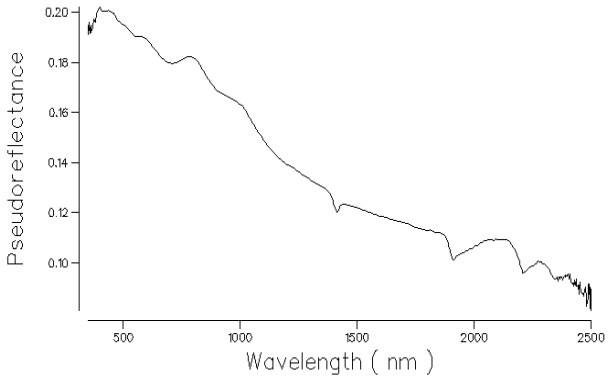

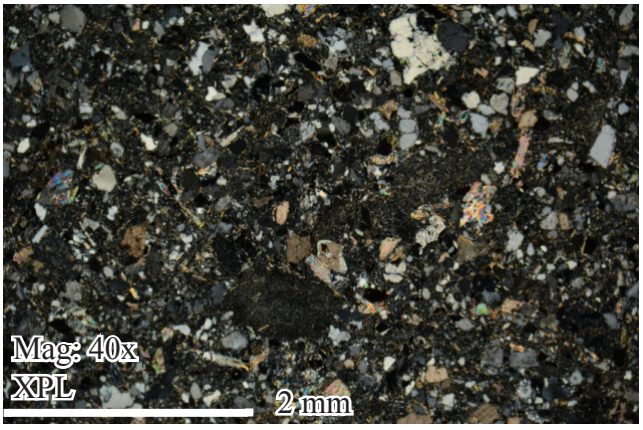

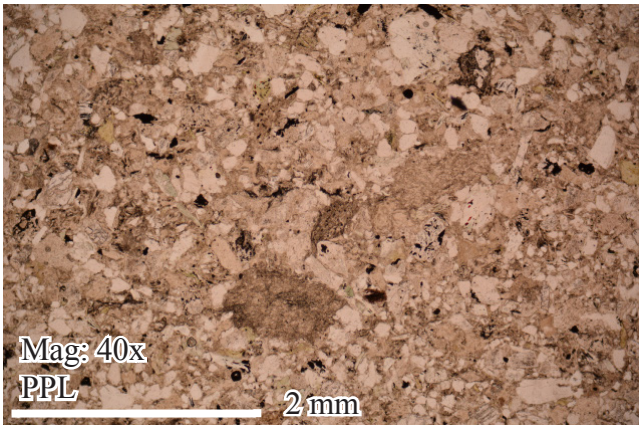

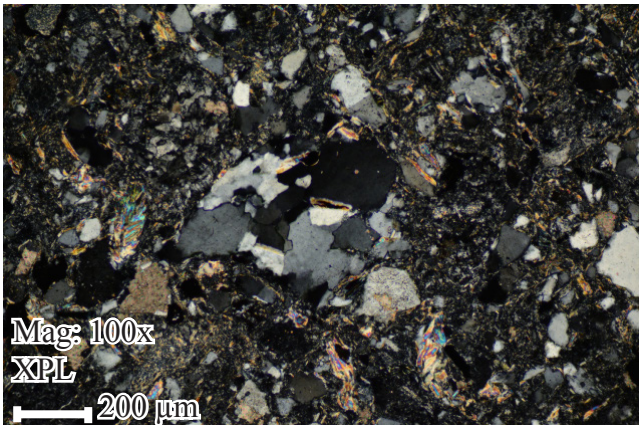

B3. Lithogeochemistry Samples. PB2014125

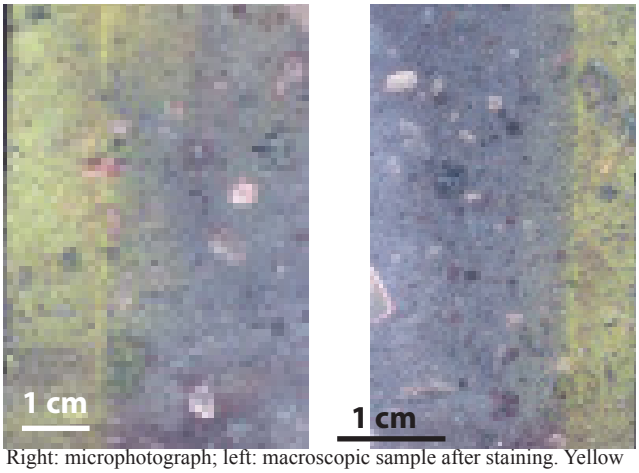

Right: microphotograph; left: macroscopic sample after staining. Yellow indicates K-bearing minerals and red Na- Plagioclase.

Unit: Vitreous tuff
Area: Pirentepe
Assay grade: 19.2 ppm Cu; 0.6 ppb Au
Estimated age: Younger than 28 Ma

Lithology Description: Argillic crystalline tuff with biotite, hornblende, and feldspar crystals. Reddish purple ground mass.

Alteration: Clays in feldspar phenocrysts.

Petrographic Summary: (from similar sample PB2013068)

The sample has a pyroclastic texture. Volcanic fragments with abundant plagioclases and trachytic texture are the main clast. Hornblendes exhibit a intense brown colour and pleochroism in brown to brown-greenish. The crystals shows the classical hornblende cleavage. Biotite have birds eye extinction. In PPL exhibits a reddish -brown colour and pleochroism. Plagioclases are zoned and have carlsbad and polysynthetic twinning. Anti-perthitic exolution texture is observed in plagioclase. Replacement textures are observed within the mafic crystals. However, the relationships are not very clear product of the alteration.

Mineral	pct	style	Size
Plagioclases	30	phenocrysts	up to 5 mm (average 2 mm)
Biotite	7	phenocrysts	up to 0.8 mm
Hornblende	7	phenocrysts	up to 2 mm
Lithic fragments	10	phenocrysts	up to 3 mm
Glass	40	groundmass	
Clays	15	alteration	Selective alteration in mafic phenocrysts.
Calcite	5	alteration	up to 0.5 mm

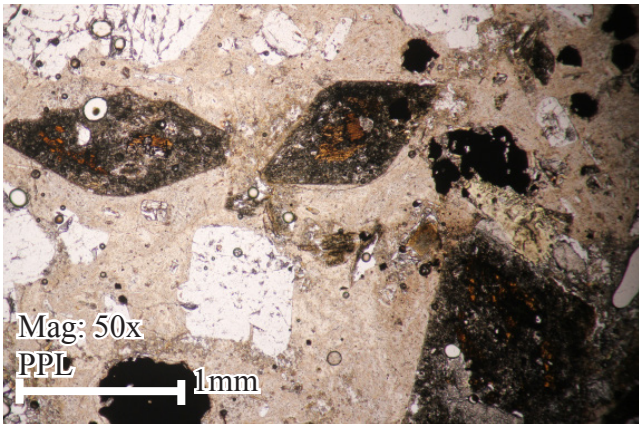

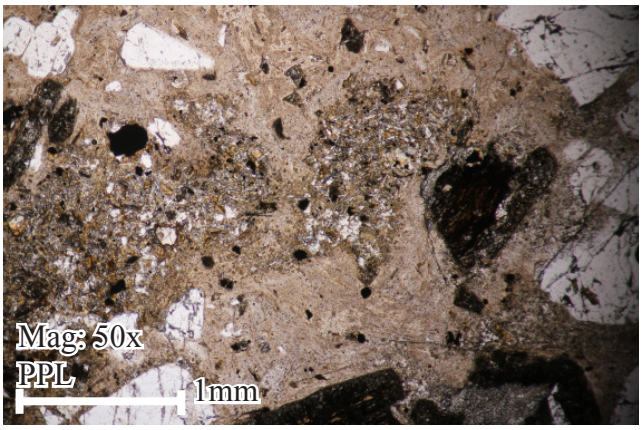

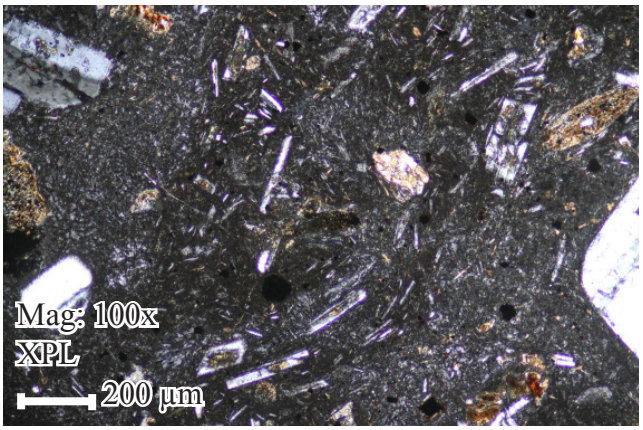

B3. Lithogeochemistry Samples. PD-07_101.9

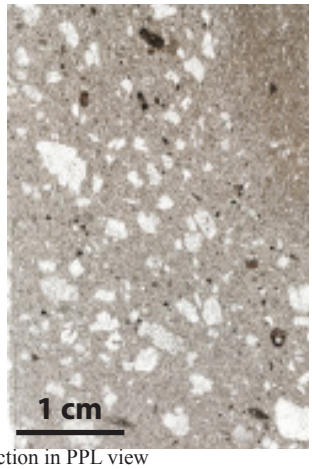

Right: microphotograph; left: thin section in PPL view

Unit: Andesite
Area: Pirentepe
Assay grade:23 ppm Cu, 2 ppb Au
Estimated age: Oligocene

Lithology Description: Dark gray porphyritic andesite with lithic fragment.

Alteration: Clays

Petrographic Summary:
Completely clay altered mafic minerals with brown colour. Groundmass/phenocrysts ratio is 65/45.

Mineral	pct	style	Size
Plagioclase	20	phenocrysts	2mm and 0.3 mm
Pyroxene	5	phenocrysts	up tp 1.5 mm
Lithic fragment	20	fragment	15 mm
Plagioclase	40	groundmass	0.1 mm
Mafics	25	groundmass	
Clay	-	alteration	In mafic minerals

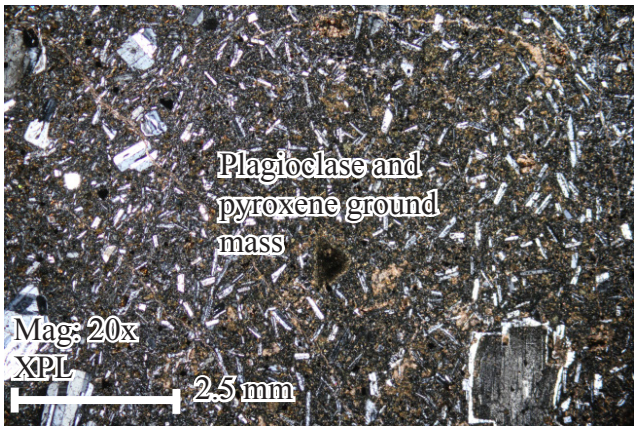

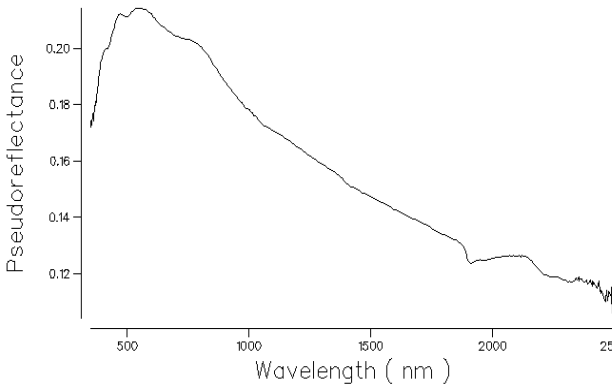

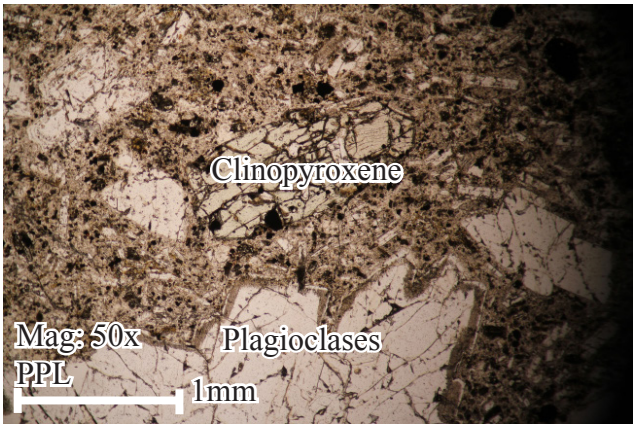

B3. Lithogeochemistry Samples. PD-17 59.8

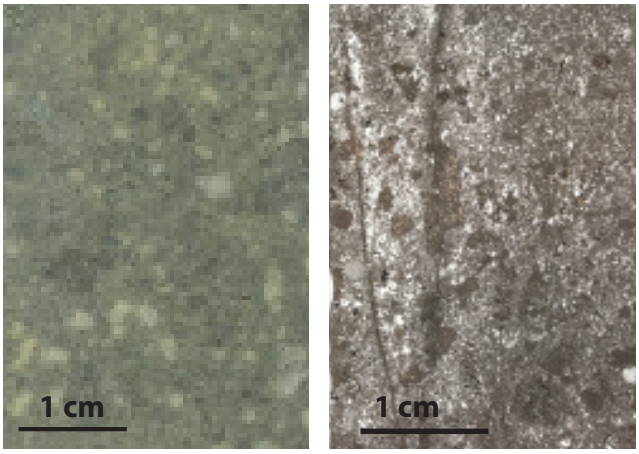

Unit: Feldspar quartz poprhyry (andesite)
Area: Pirentepe
Assay grade:63.8 ppm Cu, 11.5 ppb Au
Estimated age: Oligocene

Lithology Description: Overprinted by alteration

Alteration: Kaolinite overprint in felsic site and ground mass.

Right: microphotograph; left: thin section in PPL view

Petrographic Summary:

Internse altered porphyrytic rock. Quartz exhibits diverse shapes (rounded to angular) and sizes (from 0.03-0.1 mm). The extinction in the grains is not uniform. There are amygdules filled with quartz. Intense hydrothermal alteration: silicification in ground mass and white mica in feldspars.

Mineral	pct	style	Size
Quartz	10	phenocrysts	up to 0.1 mm
Mafic crystals	20	phenocrysts	altered, up to 0.6 mm
K-feldspar	7	phenocrysts	
Cryptocrystalline	20	groundmass	
Silica	15	alteration	
Kaolinite	20	alteration	very fine grained in phenocrysts and ground mass
Pyrite	4	mineralization	up to 0.5 mm

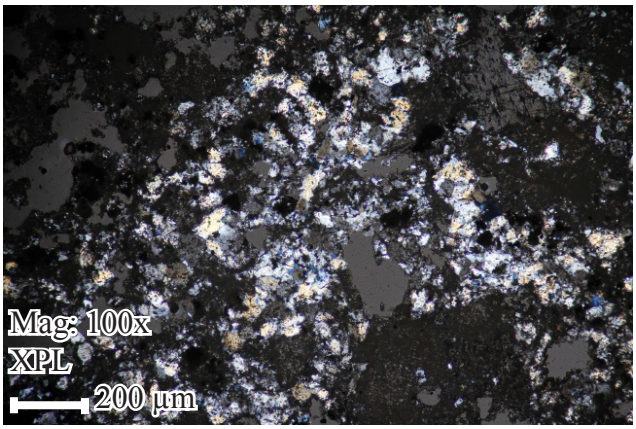

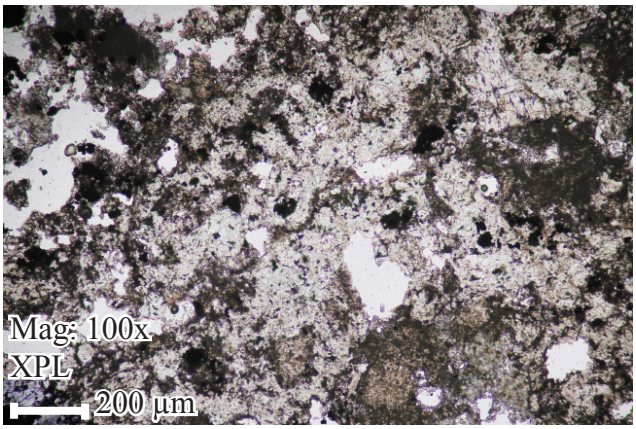

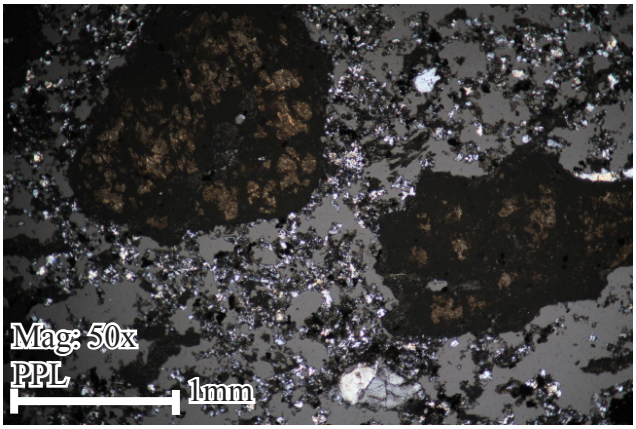

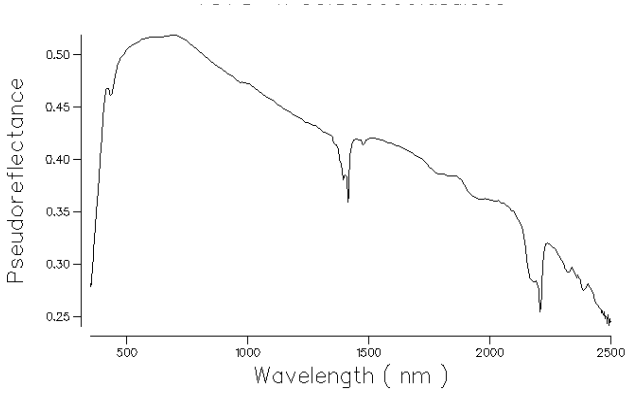

B3. Lithogeochemistry Samples. PD-21 229.5

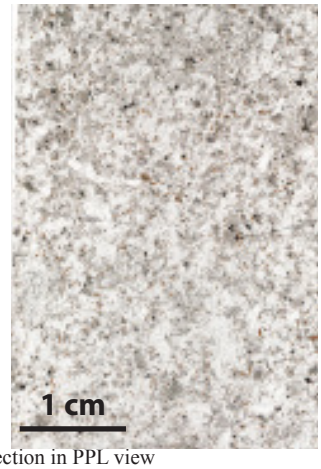

Right: microphotograph; left: thin section in PPL view

Unit: Kocakisla stock
Area: Kocakisla
Assay grade:27.8 ppm Cu; 0.6 ppb Au
Estimated age: Eocene?

Lithology Description: Equigranular texture. Biotite, hornblende, plagioclases, K-feldspar, and quartz

Alteration: Calcite, chlorite, epidote.

Petrographic Summary:

Equigranular texture. However, two sizes of plagioclases. The hornblendes are anhedral with green colour and pleochroism, generally only one cleavage direction is observed.

Mineral	pct	style	Size
Biotite	15	phenocrysts	up to 1 mm, average 0.5 mm
Hornblende	20	phenocrysts	0.5 mm
Plagioclases	35	phenocrysts	Average 2 mm
K-feldspar	20	phenocrysts	up to 0.8 mm
Quartz	10	phenocrysts	0.4 mm
Calcite	tra	alteration	

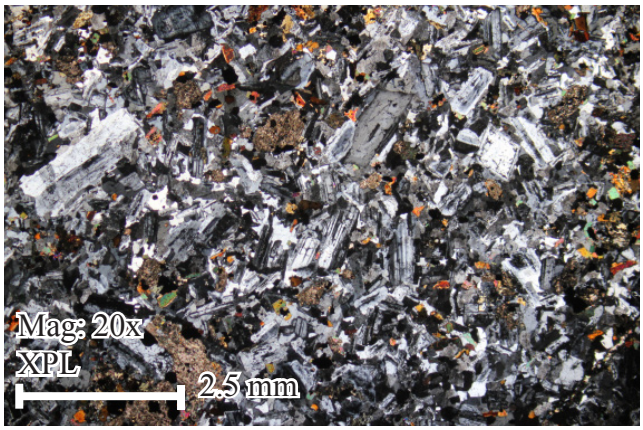

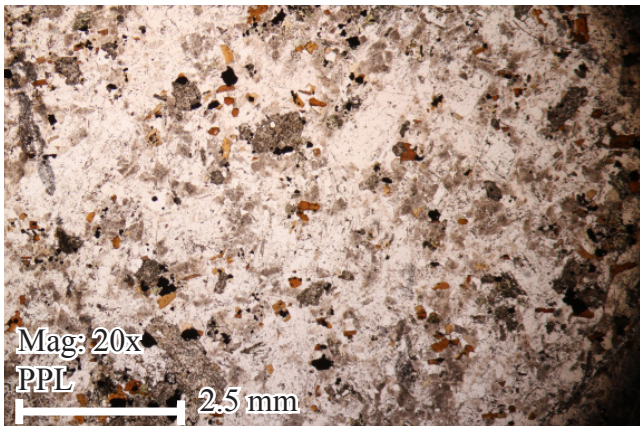

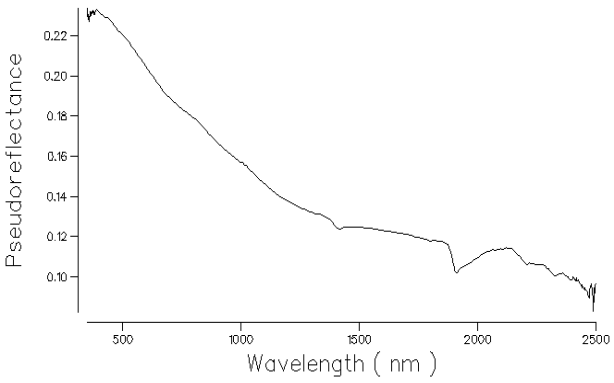

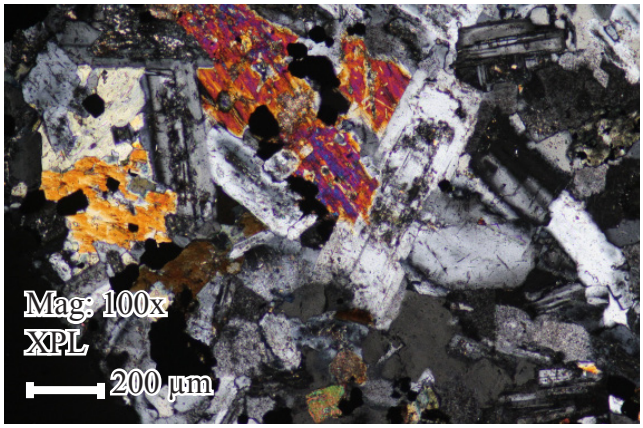

B3. Lithogeochemistry Samples. PD-23 186.7

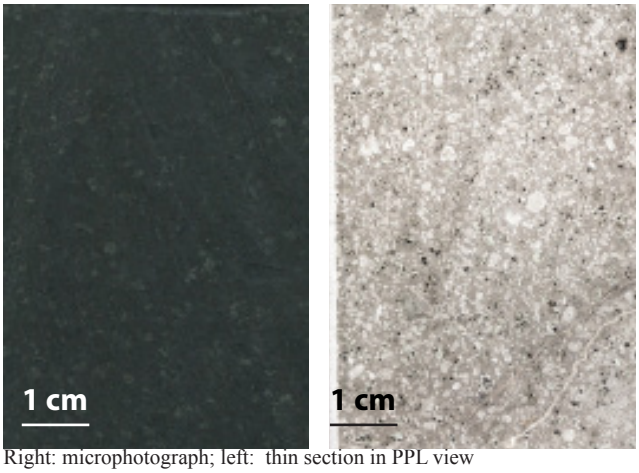

Right: microphotograph; left: thin section in PPL view

Unit: Aphanitic andesite
Area: Pirentepe
Assay grade:8.9 ppm Cu, 1.1 ppb Au.
Estimated age: 37-28 Ma

Lithology Description: Dark gray andesite with aphanitic ground mass and plagioclase phenocrysts.

Alteration: weak carbonates and clays in felsic site.

Petrographic Summary:
Horblende exhibits blue intereference colour due to alteration. Parallel extinction of pyroxene suggest othopyroxene.

Mineral	pct	style	Size
Plagioclase	30	phenocrysts	average size 1 mm
Pyroxene	10	phenocrysts	altered to carbonates
Hornblende	7	phenocrysts	0.05 mm
Plagioclase	35	groundmass	up to 0.05 mm
Pyroxene	15	groundmass	up to 0.025 mm
Rutile	3	alteration	up to 0.025 mm
Carbonates	20	alteration	overprinting mafic minerals

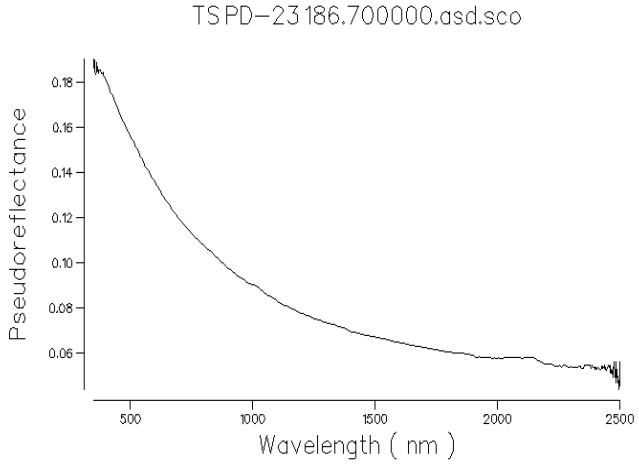

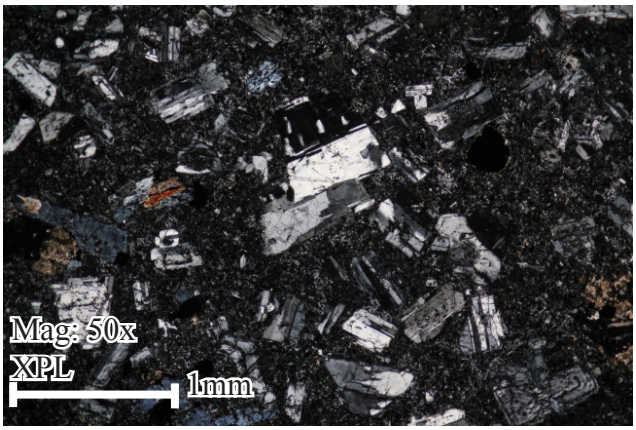

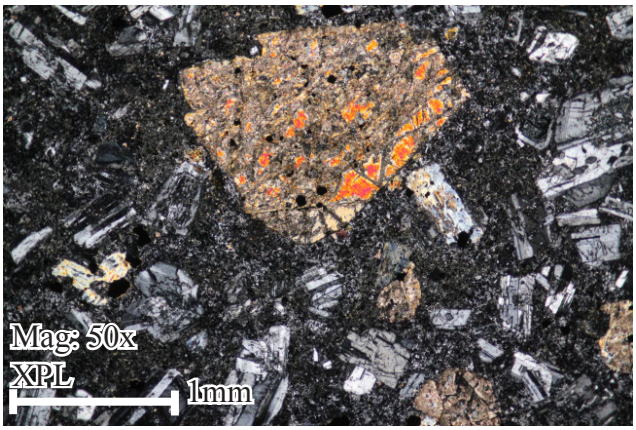

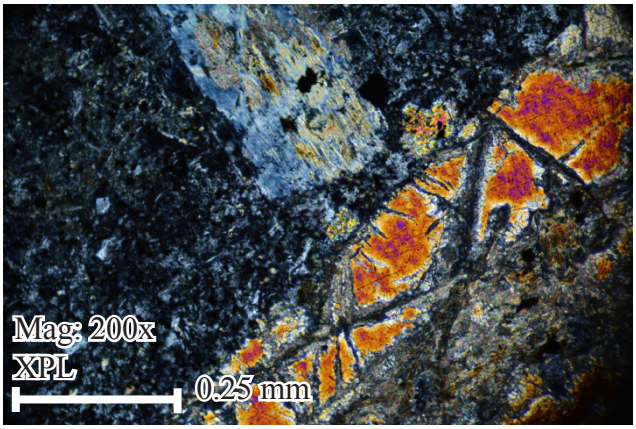

B3.b Geochemistry of samples shown in B3

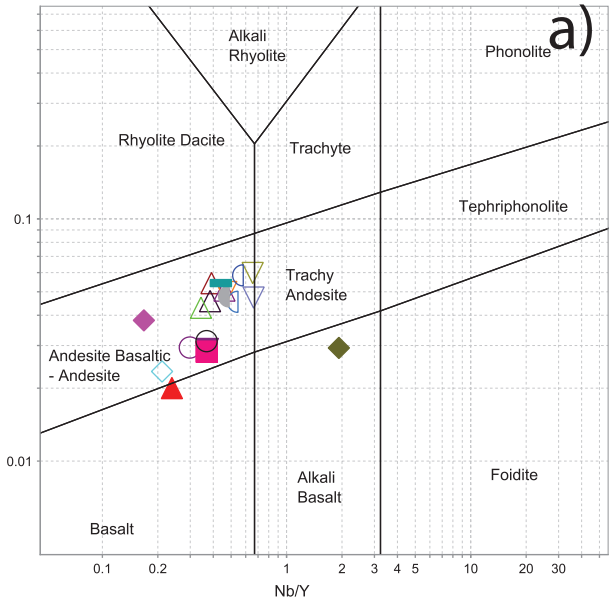

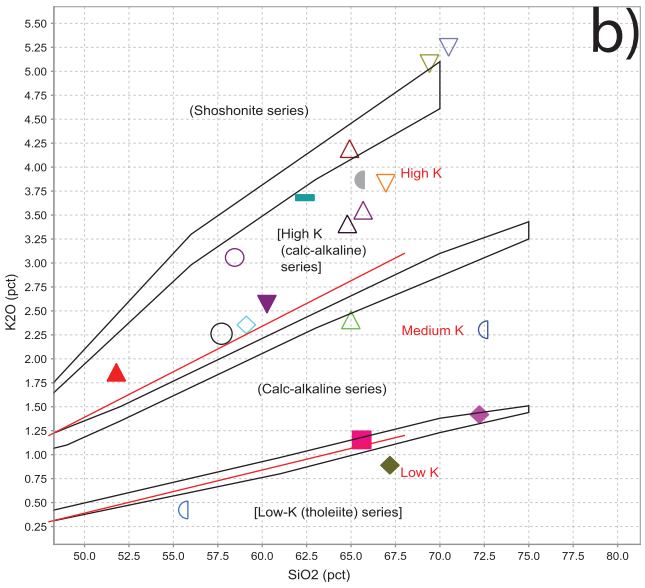

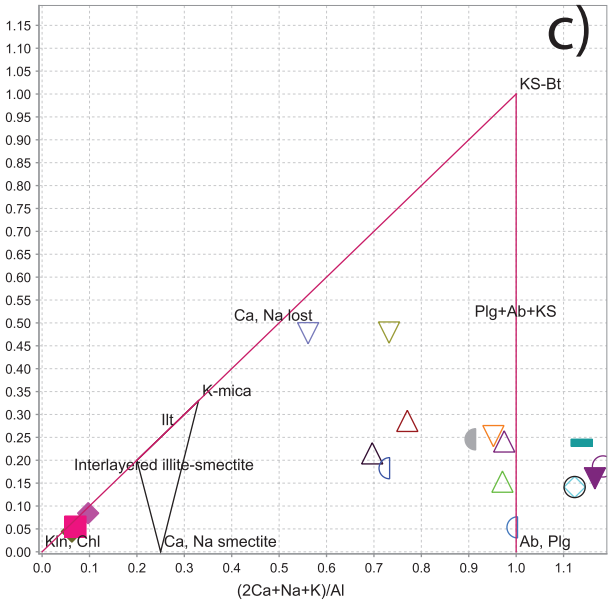

Legend

- HD-09 354
- HD-09 95.55
- HD-13A 415.2
- HD-37 254
- HD-38 190
- HD-38 310
- HD-45 459
- HD-60 720
- HD-78 39
- HD-80 30
- HD-80 90
- PB2013021
- PB2014004
- PB2014107c
- PB2014125
- PD-07 101
- PD-17 59.8
- PD-21 229.5
- PD-23 186.7

Appendix C: Lithogeochemistry Results

Introduction

The lithogeochemical dataset considers six different batches. Four of those batches (ANK12000288, ANK12000289, ANK12000290, ANK12000875) were submitted by Teck in 2012 at Bureau Veritas (formerly ACME Lab). In this study two batches were submitted in 2014; VAN14000527 and VAN14003543-2.

Elements analyzed, analytical packages, and detection limits of samples collected in this work (UBC Method) and previously by Teck are indicated in Table C1.

Tables C2 and C3 show lithogeochemical results used for petrogenesis and alteration geochemistry respectively.

Summary of QA/QC.

First of all, it is important to determine the percentage of analysis out of detection limit by batch (Table C.4).

Field duplicates and reference materials were inserted in batch VAN14003543-2, while reference materials were inserted in VAN14000527 and VAN14003543-2. Batches submitted by Teck contain reference material certified for Au and Cu only and granite blanks. Because of the data available, only field duplicates and field reference materials will be discussed in the next QA/QC analysis. Laboratory duplicates, reference materials and blanks were analyzed by Acme Labs (Now Bureau Veritas for all six batches and will be revised when field materials are not available or present problems.

In order to ensure the quality of the data precision and accuracy will be discussed for the dataset.

Precision

Can be measured by duplicates or by reference materials. Two field duplicated are available only for batch VAN14003543-2. Those correspond to a surface sample (green andesite) and a drill core sample (andesite). For the rest of the batches reference materials were used to determine precision, following the approach of Piercey, 2014.

Precision is calculated using the relative standard deviation (%RSD; Jenner, 1996), calculated as:

$$\%RSD_i = 100 \times (s_i / \mu_i).$$

Where $\%RSD_i$=percent relative standard deviation for element i; s_i=standard deviation of the mean from the series of analytical runs for element i; and μ_i=mean value of element i over a series of

analytical runs. According with Jenner (1996) %RSD between 0-3% is Excellent, between 3-7% is Very good, between 7-10% is good, and greater than 10% is not precise.

Table C5 present the precision test for lithogeochemistry data

Accuracy

Is measured with reference materials and in this case the use of field standard or laboratory standards variates according with the batch. For VAN batches, in-house MDRU reference materials were used (BAS-1, P-1, WP-1). For ANK batches, only ANK12000875 has certified values for Mo and Cu. For the rest of ANK batches it was necessary to use laboratory standards to determine accuracy of the analysis.

Accuracy was calculated using the percent relative difference (%RD), calculated as:

$$\%RD=100 \times (\mu_i-STD_i/STD_i).$$

Where μ_i=mean value of element iin the standard over a number of analysis; and STD_i= certified value of the i element in the reference material. According with Jenner (1996) |%RD | between 0-3% is Excellent, between 3-7% is Very good, between 7-10% is good, and greater than 10% is not accurate.

Table C6 present the accuracy test for lithogeochemistry data.

References

Jenner, G. A. (1996). Trace element geochemistry of igneous rocks: geochemical nomenclature and analytical geochemistry. Trace element geochemistry of volcanic rocks: applications for massive sulfide exploration. Edited by DA Wyman. Geological Association of Canada, Short Course Notes, 12, 51-77.

Piercey, S. J. 2014. Modern Analytical Facilities 2. A review of quality assurance and quality control (QA/QC) procedures for lithogeochemical data. Geoscience Canada, 41(1), 75-88.

Table C.1. Elements and detection limits of samples used in this work with the analytical packages; this study (UBC Method) and by Teck at Bureau Veritas (formerly ACME Labs) . In parenthesis is indicated the original code of the analysis.

Element	Unit	UBC Method	LDL	Teck Method	LDL
Au	ppb	FA130	1	-	-
SiO2	%	LF700	0.01	LF300 (4A-4B)	0.01
Al2O3	%	LF700	0.01	LF300 (4A-4B)	0.01
Fe2O3	%	LF700	0.01	LF300 (4A-4B)	0.04
CaO	%	LF700	0.01	LF300 (4A-4B)	0.01
MgO	%	LF700	0.01	LF300 (4A-4B)	0.01
Na2O	%	LF700	0.01	LF300 (4A-4B)	0.01
K2O	%	LF700	0.01	LF300 (4A-4B)	0.01
MnO	%	LF700	0.01	LF300 (4A-4B)	0.01
TiO2	%	LF700	0.01	LF300 (4A-4B)	0.01
P2O5	%	LF700	0.01	LF300 (4A-4B)	0.01
Cr2O3	%	LF700	0.001	LF300 (4A-4B)	0.002
Ba	%	LF700	0.01	LF300 (4A-4B)	1
LOI	%	LF700	0.1	LF300 (4A-4B)	-5.1
Cu	%	LF700	0.01	-	
Ni	%	LF700	0.01	LF300 (4A-4B)	20
Pb	%	LF700	0.01	-	
SO3	%	LF700	0.002	-	
Sr	%	LF700	0.002	-	
V2O5	%	LF700	0.002	-	
Zn	%	LF700	0.001	-	
Zr	%	LF700	0.002	-	
SUM	%	LF700	0.01	LF300 (4A-4B)	0.01
TOT/C	%	TC000	0.02	TC003 (2A Leco)	0.02
TOT/S	%	TC000	0.02	TC003 (2A Leco)	0.02
Ba	ppm	LF100	1	LF100 (4A-4B)	1
Be	ppm	LF100	1	LF100 (4A-4B)	1
Co	ppm	LF100	0.2	LF100 (4A-4B)	0.2
Cs	ppm	LF100	0.1	LF100 (4A-4B)	0.1
Ga	ppm	LF100	0.5	LF100 (4A-4B)	0.5
Hf	ppm	LF100	0.1	LF100 (4A-4B)	0.1
Nb	ppm	LF100	0.1	LF100 (4A-4B)	0.1
Rb	ppm	LF100	0.1	LF100 (4A-4B)	0.1
Sn	ppm	LF100	1	LF100 (4A-4B)	1
Sr	ppm	LF100	0.5	LF100 (4A-4B)	0.5
Ta	ppm	LF100	0.1	LF100 (4A-4B)	0.1
Th	ppm	LF100	0.2	LF100 (4A-4B)	0.2
U	ppm	LF100	0.1	LF100 (4A-4B)	0.1
V	ppm	LF100	8	LF100 (4A-4B)	8
W	ppm	LF100	0.5	LF100 (4A-4B)	0.5
Zr	ppm	LF100	0.1	LF100 (4A-4B)	0.1
Y	ppm	LF100	0.1	LF100 (4A-4B)	0.1
La	ppm	LF100	0.1	LF100 (4A-4B)	0.1
Ce	ppm	LF100	0.1	LF100 (4A-4B)	0.1
Pr	ppm	LF100	0.02	LF100 (4A-4B)	0.02
Nd	ppm	LF100	0.3	LF100 (4A-4B)	0.3
Sm	ppm	LF100	0.05	LF100 (4A-4B)	0.05
Eu	ppm	LF100	0.02	LF100 (4A-4B)	0.02
Gd	ppm	LF100	0.05	LF100 (4A-4B)	0.05
Tb	ppm	LF100	0.01	LF100 (4A-4B)	0.01
Dy	ppm	LF100	0.05	LF100 (4A-4B)	0.05

Table C.1 (cont)

Element	Unit	UBC Method	LDL	Teck Method	LDL
Ho	ppm	LF100	0.02	LF100 (4A-4B)	0.02
Er	ppm	LF100	0.03	LF100 (4A-4B)	0.03
Tm	ppm	LF100	0.01	LF100 (4A-4B)	0.01
Yb	ppm	LF100	0.05	LF100 (4A-4B)	0.05
Lu	ppm	LF100	0.01	LF100 (4A-4B)	0.01
Mo	ppm	AQ200	0.1	AQ200 (1DX)	0.1
Cu	ppm	AQ200	0.1	AQ200 (1DX)	0.1
Pb	ppm	AQ200	0.1	AQ200 (1DX)	0.1
Zn	ppm	AQ200	1	AQ200 (1DX)	1
Ni	ppm	AQ200	0.1	AQ200 (1DX)	0.1
As	ppm	AQ200	0.5	AQ200 (1DX)	0.5
Cd	ppm	AQ200	0.1	AQ200 (1DX)	0.1
Sb	ppm	AQ200	0.1	AQ200 (1DX)	0.1
Bi	ppm	AQ200	0.1	AQ200 (1DX)	0.1
Ag	ppm	AQ200	0.1	AQ200 (1DX)	0.1
Au	ppb	AQ200	0.5	AQ200 (1DX)	0.5
Hg	ppm	AQ200	0.01	AQ200 (1DX)	0.01
Tl	ppm	AQ200	0.1	AQ200 (1DX)	0.1
Se	ppm	AQ200	0.5	AQ200 (1DX)	0.5
Sc	ppm	AQ200	0.1	LF 300(4A-4B)	1
Te	ppm	AQ200	0.2	-	

Table C.2a Lithogeochemical Results for Petrogenesis Analysis. (Major elements). Batch is abbreviated as follows: 288= ANK12000288, 289= ANK12000289, 290=ANK12000290, 875= ANK12000875, VAN1=VAN14000527, VAN2=VAN143543-2. Observations regarding to geochemistry is: (1) Alteration, (2) Fresh based on LOI only, **(3) Fresh based on LOI and S**, (**4) Fresh based in LOI and included in petrogenesis calculations**, (5) LOI>3.5%. **Notice that only samples with (3) and (4) were used for petrogenesis**. Lithology abbreviations are: A=andesite, AD=andesitic dyke, AFP=altered feldspar porphyry, D=dacite, DCT=dacitic crystal tuff, EP=Evciler Pluton, GA=green andesite, KS=Kocakisla Stock, PA=purple andesite, PA_D=purple andesite Dereoba, QMP-A=Quartz Monzonite A (Kestane Stock), QMP-B=Quartz Monzonite B(Kestane Stock), VS=volcanic sandstone, VT=vitreous tuff.

Sample	BATCH	Obs	Unit	WGHT	LOI_ pct	Sum_%	SiO2_ pct	Al2O3_ pct	Fe2O3_ pct	MgO_ pct	CaO_ pct	Na2O_ pct	K2O_ pct	TiO2_ pct	P2O5_ pct	MnO_ pct	Cr2O3_ pct
HD-01_297.5	289	5	AD	0.25	4	99.68	52.38	17.79	8.17	5.73	9.43	3.22	1.60	0.96	0.25	0.18	0.01
HD-09_216.2	290	5	D	0.32	7.3	99.87	70.62	18.88	6.19	0.12	0.12	0.20	2.71	0.79	0.19	0.01	0.00
HD-09_354.3	290	5	D	0.36	8.9	99.86	67.19	21.78	8.71	0.02	0.15	0.08	0.89	0.83	0.22	0.01	0.00
HD-09_95.55	290	5	D	0.3	4.1	99.95	72.22	18.21	7.02	0.14	0.06	0.07	1.42	0.78	0.07	0.01	0.00
HD-115_23.65	VAN1	5	PA		10.57	100.88	55.74	18.58	8.88	9.32	1.78	2.47	2.23	1.03	0.30	0.16	5.59E-4
HD-115_280	VAN1	5	PA	0.44	3.79	100.78	54.55	19.75	9.13	7.50	2.91	3.84	1.07	1.08	0.31	0.17	5.20E-4
HD-12_61.35	290	5	D	0.36	5	99.88	66.74	20.73	9.51	0.14	0.19	0.16	1.25	0.93	0.25	0.01	0.00
HD-13A_106.9	VAN1	1	QMP-A	0.33	5.72	100.52	80.05	9.25	11.78	0.28	0.42	0.01	2.91	0.09	0.22	0.16	0.00
HD-13A_415.2	VAN1	4	QMP-B	0.28	1.26	100.21	64.92	15.87	6.47	2.91	1.58	2.93	4.19	0.42	0.19	0.07	5.06E-4
HD-13A_488.6	VAN1	2	QMP-B	0.43	2.29	100.37	65.80	17.21	4.54	3.99	1.89	3.49	2.21	0.48	0.17	0.06	5.12E-4
HD-24_186.2	VAN2	3	EP	0.27	2.08	100.08	69.14	14.92	2.80	1.29	3.76	2.98	4.37	0.31	0.11	0.04	0.00
HD-28_138.5	VAN2	3	EP	0.41	1.84	100.2	64.38	16.08	5.05	2.44	4.28	3.28	3.63	0.52	0.20	0.06	0.00
HD-29_204.5	VAN2	3	EP	0.44	1.1	100.37	67.64	15.27	3.88	1.78	3.71	3.06	4.14	0.39	0.16	0.05	0.00
HD-29_86.6	VAN2	3	EP	0.29	1.75	100.22	70.43	14.81	3.00	1.49	2.75	3.02	4.03	0.33	0.12	0.03	0.00
HD-37_112.7	VAN1	1	QMP-A		1.44	100.82	75.95	6.95	13.04	0.15	1.34	0.33	3.07	0.04	0.24	0.05	0.00
HD-37_127.3	288	1	QMP-A	0.35	3.8	99.17	67.44	11.58	9.24	1.42	0.43	0.14	4.57	0.31	0.13	0.11	0.00
HD-37_254.3	VAN1	3	QMP-B	0.27	2	100.34	64.79	17.15	4.67	4.13	1.92	2.90	3.41	0.45	0.18	0.07	5.10E-4
HD-37_268.1	288	2	QMP-B	0.32	2.3	99.77	66.30	16.60	4.79	1.79	3.80	3.00	2.83	0.44	0.15	0.06	0.00
HD-37_95.35	288	1	QMP-A	0.21	2.8	99.08	69.08	8.26	12.4	0.96	0.17	0.64	4.37	0.28	0.08	0.05	0.00
HD-38_190.4	288	4	AD	0.34	2.8	99.71	51.79	17.16	7.2	5.4	9.23	2.87	1.86	0.92	0.24	0.21	0.01
HD-38_310	288	4	QMP-B	0.29	1.9	99.74	64.99	16.99	4.85	1.78	4.53	3.45	2.41	0.48	0.17	0.07	0.00

Table C.2a (cont)

Sample	BATCH	Obs	Unit	WGHT	LOI_ pct	Sum_%	SiO2_ pct	Al2O3_ pct	Fe2O3_ pct	MgO_ pct	CaO_ pct	Na2O_ pct	K2O_ pct	TiO2_ pct	P2O5_ pct	MnO_ pct	Cr2O3_ pct
HD-38_400.05	288	2	QMP-A	0.28	3.3	99.57	63.18	14.14	7.69	1.57	2.11	2.12	4.95	0.37	0.13	0.06	0.00
HD-38_461.1	288	4	QMP-A	0.3	1.9	99.7	69.49	13.36	6.76	1.39	2.44	1.98	3.74	0.37	0.14	0.07	0.00
HD-38_490.85	288	2	QMP-A	0.32	2	99.69	65.47	15.86	5.88	1.49	3.67	2.96	3.66	0.42	0.15	0.09	0.00
HD-38_550.7	288	4	QMP-A	0.27	1.6	99.71	65.28	16.50	5.15	1.68	3.38	3.45	3.60	0.43	0.16	0.07	0.00
HD-45_459.45	875	2	QMP-B	0.18	1.7	99.72	65.68	15.94	4.16	1.39	3.51	3.23	3.55	0.39	0.15	0.06	0.03
HD-45_580.15	875	2	QMP-B	0.3	1.8	99.75	64.86	17.22	4.99	1.80	4.30	3.42	2.38	0.48	0.18	0.05	0.03
HD-60_720	289	2	QMP-A	0.18	1.6	99.56	66.96	16.41	3.68	1.50	3.33	3.29	3.83	0.42	0.14	0.05	0.00
HD-78_16	VAN1	1	VS	0.17	2.4	100.94	52.04	15.65	5.97	15.39	6.26	2.90	0.31	0.85	0.08	0.14	0.10
HD-78_289.2	VAN1	1	VS	0.16	1.42	100.28	66.04	17.13	3.09	3.16	3.75	3.52	2.28	0.77	0.23	0.03	0.02
HD-78_39.4	VAN1	1	VS		5.55	100.88	55.56	8.58	9.25	20.05	3.98	0.50	0.42	0.58	0.05	0.58	0.21
HD-80_119.7	288	1	QMP-A	0.29	3.7	99.04	65.81	14.2	6.45	1.2	0.44	0.99	5.55	0.43	0.2	0.04	0.00
HD-80_30	288	1	QMP-A	0.17	4.4	98.72	70.49	11.9	5.46	0.27	0.14	0.45	5.25	0.3	0.03	0.01	0.00
HD-80_90.65	288	1	QMP-A	0.28	2.4	99.03	69.41	11.48	7.27	1.15	0.33	1.4	5.08	0.31	0.12	0.06	0.00
HD-94_274.8	289	1	VS	0.33	2.8	99.59	65.18	15.87	2.96	2.28	1.85	2.65	5.05	0.78	0.12	0.04	0.01
HD-96_242.6	VAN2	5	A	0.25	5.54	99.32	58.78	19.47	7.13	1.63	5.04	3.16	2.82	0.77	0.20	0.11	0.00
HD-96_270.5	VAN2	5	A	0.32	4.13	99.75	62.59	17.22	6.67	1.21	3.31	2.77	4.57	0.70	0.16	0.31	0.00
HD-96_302	VAN2	3	A	0.36	2.54	99.63	60.65	17.32	6.54	1.85	5.34	3.25	3.43	0.69	0.18	0.10	0.00
HD-99_204.3	VAN1	5	A	0.28	5.62	99.25	59.57	18.58	5.54	5.20	1.77	3.98	2.84	0.70	0.37	0.17	5.30E-4
PB2013021	VAN2	5	PA	1.21	7.46	100.25	58.45	17.75	7.62	1.73	6.61	3.45	3.06	0.89	0.29	0.17	0.00
PB2013022	VAN2	3	PA	1.37	3.12	100.59	57.69	18.35	8.00	2.14	7.39	3.70	1.78	0.96	0.20	0.11	0.00
PB2013023	VAN2	5	GA	2.25	5.56	99.2	61.13	16.44	5.68	2.86	6.37	3.62	2.03	0.64	0.16	0.14	0.00
PB2013046	VAN2	3	A	1.36	2.78	100.5	58.31	18.48	7.36	2.55	6.30	3.41	2.66	0.78	0.20	0.13	0.00
PB2014004	VAN2	3	DCT	0.57	3.03	100.06	65.48	17.04	5.61	0.66	3.37	3.08	3.87	0.53	0.14	0.04	0.00
PB2014007	VAN2	5	PA_D	0.79	6.48	99.58	60.22	15.69	7.55	4.57	4.33	4.10	1.75	0.82	0.24	0.16	0.00
PB2014010	VAN2	3	VT	0.94	1.98	100.65	60.08	16.67	6.41	2.92	6.89	3.24	2.98	0.68	0.27	0.10	0.01
PB2014011	VAN2	3	DCT	0.7	3.5	100.36	65.38	17.01	4.33	1.84	4.41	3.21	3.09	0.59	0.21	0.06	0.01
PB2014014	VAN2	3	PA_D	0.55	1.68	100.91	59.69	17.27	8.22	2.13	5.63	3.36	3.11	0.72	0.19	0.40	0.00

Table C.2a (cont)

Sample	BATCH	Obs	Unit	WGHT	LOI_ pct	Sum_%	SiO2_ pct	Al2O3_ pct	Fe2O3_ pct	MgO_ pct	CaO_ pct	Na2O_ pct	K2O_ pct	TiO2_ pct	P2O5_ pct	MnO_ pct	Cr2O3_ pct
PB2014021	VAN2	5	PA_D	0.75	17.54	100.04	45.72	13.47	7.98	2.32	25.38	2.17	1.61	0.62	0.15	0.45	0.01
PB2014023	VAN2	3	GA	0.9	2.81	99.86	61.74	16.58	6.29	2.59	5.09	3.84	2.56	0.66	0.15	0.14	0.00
PB2014032	VAN2	1	AFP	0.5	7.12	99.32	74.33	15.35	3.11	0.41	0.34	1.13	3.08	0.94	0.10	0.01	0.00
PB2014052	VAN2	3	PA_D	0.41	1.75	99.89	60.46	17.32	6.38	2.29	6.01	3.45	2.73	0.75	0.18	0.08	0.00
PB2014092	VAN2	3	D	1.41	2.95	99.54	75.64	17.42	1.02	0.09	0.05	0.21	4.32	0.68	0.02	0.01	0.00
PB2014106	VAN2	5	GA	0.99	6.56	99.28	62.64	16.67	5.55	2.90	5.10	3.16	2.22	0.64	0.16	0.14	0.00
PB2014107c	VAN2	5	VS	1.02	3.62	99.64	72.43	13.66	4.12	1.98	1.62	2.69	2.30	0.57	0.07	0.05	0.02
PB2014113	VAN2	5	VS	1.25	4.67	101.39	72.23	14.59	5.67	3.60	0.16	0.10	3.61	0.85	0.10	0.12	0.05
PB2014125	VAN2	3	VT	0.94	2.75	101.36	59.10	18.01	7.31	3.18	6.80	3.23	2.35	0.85	0.16	0.09	0.00
PB2014127	VAN2	3	A	1.22	1.91	100.28	56.27	16.91	8.41	5.40	8.01	2.17	1.57	0.99	0.18	0.14	0.01
PD-07_101.9	VAN2	3	A	0.34	1.94	100.27	60.27	17.34	6.22	2.67	6.61	3.29	2.57	0.74	0.19	0.09	0.00
PD-07_24.5	VAN2	1	AFP	0.19	16.84	99.62	63.06	24.26	7.49	0.23	0.11	0.08	2.74	0.87	0.19	0.01	0.00
PD-07_55.3	VAN2	5	A	0.27	4.09	100.11	64.02	18.29	5.61	1.40	3.86	2.82	2.90	0.74	0.20	0.09	0.00
PD-17_59.8	VAN2	1	AFP	0.24	15.09	100.01	65.60	22.80	8.70	0.07	0.12	0.08	1.15	0.75	0.29	0.01	0.00
PD-19_171.1	VAN2	5	VS	0.23	6.04	100.15	66.19	14.92	5.65	1.82	4.54	0.10	3.65	0.71	0.06	0.07	0.02
PD-19_54.2	VAN2	5	D	0.14	7.54	99.56	63.94	16.99	4.85	1.95	5.46	2.58	2.92	0.45	0.16	0.09	0.00
PD-19_74.5	VAN2	2	VS	0.26	3.18	101.15	68.97	14.62	4.90	3.31	4.44	0.46	3.40	0.61	0.09	0.06	0.02
PD-21_113.1	VAN2	2	KS	0.45	3.48	99.73	70.77	15.39	3.90	0.75	0.18	0.17	6.89	0.34	0.09	0.01	0.00
PD-21_170.1	VAN2	3	KS	0.33	1.8	100.41	62.93	17.44	5.19	1.57	4.48	3.82	3.78	0.66	0.20	0.10	0.00
PD-21_229.5	VAN2	3	KS	0.21	1.13	100.03	62.40	16.73	5.43	1.97	4.89	3.75	3.68	0.62	0.19	0.14	0.00
PD-22_31.7	VAN2	3	KS	0.23	2.28	100.3	59.55	17.18	7.30	3.41	6.46	3.17	1.88	0.83	0.18	0.15	0.00
PD-23_186.7	VAN2	3	PA	0.19	2.35	99.55	57.66	16.97	7.58	4.28	6.76	2.60	2.23	0.92	0.18	0.13	0.01

Table C.2b. Lithogeochemical Results for Petrogenesis Analysis. (Trace elements). Batch, observations, and unit in Table C.2a.

Sample	Sc_ ppm	Ba_ ppm	Be_ ppm	Co_ ppm	Cs_ ppm	Ga_ppm	Hf_ ppm	Nb_ ppm	Rb_ ppm	Sn_ ppm	Sr_ ppm	Ta_ ppm	Th_ ppm	U_ ppm	V_ppm	W_ ppm	Zr_ppm	Y_ ppm
HD-01_297.5	24	309	2	15.5	4.8	17.4	2.6	7.4	66.8	3	588.1	0.4	6.3	2.3	227	10.3	108.5	25.2
HD-09_216.2	14.03	459.59	0.54	14.67	1.19	18.23	3.45	7.88	62.36	4.32	272.52	0.76	14.35	4.10	172.62	1.73	146.72	11.00
HD-09_354.3	10.98	562.10	0.55	18.11	0.66	19.32	3.84	8.23	7.25	7.68	562.10	0.77	12.19	4.17	163.58	2.96	146.67	4.28
HD-09_95.55	11.47	234.62	0.52	0.94	0.83	19.40	5.01	8.66	52.35	3.13	138.79	0.63	10.22	4.90	178.31	1.88	178.63	51.51
HD-115_23.65		555	2	24.2	3.8	16.8	3.5	8	68.9	1	415.9	0.5	6.3	2.3	239	1	138	30.9
HD-115_280		390	2	21.6	3.3	17.3	4.4	8.3	24.3	2	579.2	0.4	7.4	2	179	0.7	166.1	34.4
HD-12_61.35	16.84	538.98	2.11	0.32	0.84	23.16	4.42	10.11	43.06	2.11	79.79	1.05	16.00	4.63	227.38	2.95	183.70	64.11
HD-13A_106.9		501	0.5	31.4	2.5	10.2	1.8	2.4	76.6	2	19.2	0.2	5.3	0.7	69	3.6	65.1	9.6
HD-13A_415.2		760	2	11.2	3.8	16.8	3.4	6.3	113.5	0.5	497.9	0.6	12	2.9	88	2	135.1	16.1
HD-13A_488.6		560	0.5	7.9	3.4	17	3.3	6.8	89.6	1	563.3	0.7	13.3	2.8	95	1.6	148.5	20.1
HD-24_186.2	2.7	1025	2	5.5	6.3	11.7	3	7.8	147.5	2	465	0.8	25.4	7.7	68	1.2	109.9	11.4
HD-28_138.5	2.2	978	1	13.8	7.3	15.5	3.6	10.3	168.7	0.5	591.3	0.9	28.6	9.6	118	0.7	140.5	17.9
HD-29_204.5	1.4	1003	2	9.1	8.8	12.6	3.6	9.5	175	1	523	0.9	36.5	10.9	86	1.3	144.3	16.1
HD-29_86.6	3.1	976	2	8.4	10	13.1	3.1	9.4	187.4	0.5	401	0.8	27.9	9.3	68	0.9	115.8	11.7
HD-37_112.7		396	0.5	8.6	3.6	9.9	1.5	2.8	63.5	2	73.4	0.3	6	0.7	73	0.25	53.1	6.3
HD-37_127.3	4	768	0.5	9.8	6.7	14.2	2.6	3.7	121.4	2	136.8	0.3	9.3	2	65	3.3	96.8	9.6
HD-37_254.3		738	1	7.6	10.4	14	3.2	6.8	101.6	0.5	456.9	0.4	12.5	2.6	78	1.5	123.1	17.7
HD-37_268.1	7	594	0.5	5.2	10.2	14.7	3.5	7.5	92.5	0.5	485.2	0.6	14.6	5	78	2.4	136.7	16.4
HD-37_95.35	5	590	0.5	16.7	1.7	12.1	1.5	4.4	77.6	1	100.2	0.3	7.4	1.1	81	2.5	64.9	9.4
HD-38_190.4	23	383	0.5	12.6	2.8	20	2.7	6.2	52.8	3	654.1	0.4	6.3	3	247	0.5	110.4	26
HD-38_310	7	664	2	8.3	3.5	16.3	3.3	6	86.1	1	609.5	0.4	12.6	4.5	88	1.9	123.4	17.5
HD-38_400.05	5	740	0.5	11.6	5.8	13.9	2.5	4.7	115.7	0.5	466.4	0.4	10.9	2.5	76	2.3	111.7	14.4
HD-38_461.1	5	706	2	9.7	3.1	13.5	2.3	4	84.5	1	406.5	0.4	10.4	3	82	1.5	93.7	14.5
HD-38_490.85	6	704	0.5	17.6	3.1	14.7	2.6	6.4	90.1	0.5	501.7	0.5	13.5	4.4	72	3	108	17
HD-38_550.7	6	702	0.5	7.8	3.6	15.2	2.9	6.4	92.1	0.5	483	0.5	11.6	4.2	76	2.6	125	16.9
HD-45_459.45	6	818	0.5	8.8	3.2	17.2	3.6	6.9	108.8	0.5	511.7	0.6	15	5.8	75	1.9	118.3	15
HD-45_580.15	7	681	2	6.3	5.9	17.8	3.5	7.6	101.1	1	592	0.7	12.8	4.8	91	1.3	136.3	18.4

Table C.2b. (cont)

Sample	Sc_ ppm	Ba_ ppm	Be_ ppm	Co_ ppm	Cs_ ppm	Ga_ppm	Hf_ ppm	Nb_ ppm	Rb_ ppm	Sn_ ppm	Sr_ ppm	Ta_ ppm	Th_ ppm	U_ ppm	V_ppm	W_ ppm	Zr_ppm	Y_ ppm
HD-60_720	6	873	4	6.2	5.5	15.8	3.3	8.1	112.2	0.5	543.7	0.7	13.8	4.4	71	4.7	124.6	17.2
HD-78_16		24	0.5	45.9	2.6	15	3.1	12.7	15	3	213.3	1	8.5	2	167	1.2	122.4	20.5
HD-78_289.2		137	0.5	4.8	10.1	16.4	4.5	9	115.3	2	339.7	0.6	9.3	2.6	152	3.3	168	20.2
HD-78_39.4		9	0.5	12.5	5.1	7.9	4.2	7.7	32.2	5	44	0.6	5.1	1.4	90	2	158.6	15.1
HD-80_119.7	6	744	1	26.3	5.3	13.4	3.4	6.6	166.8	1	142.6	0.4	10.4	2	84	5	118.9	15.4
HD-80_30	5	686	1	13.8	2	11.5	2.4	5.1	101.5	2	111.4	0.4	8.9	1.3	56	3.2	85.1	7.7
HD-80_90.65	4	757	0.5	11.8	2.6	13.3	2.9	5.5	99.8	0.5	181.5	0.3	9.4	1.9	65	3.5	111.1	8.4
HD-94_274.8	16	555	3	14.3	5	17.8	4.2	10.3	149.4	1	202.3	0.9	8.6	2.5	122	6.5	175.6	19.8
HD-96_242.6	6.3	903	2	16.3	4.4	17.1	4.8	12.6	51.9	1	688.2	0.9	19.8	3.8	140	1.2	187.8	27.3
HD-96_270.5	4.6	926	2	26.4	4.6	16.2	4.3	11.9	154.6	0.5	517	0.7	19	4.3	124	1.6	174.7	21.9
HD-96_302	5.5	829	4	15.6	8.3	16.1	4.7	12.2	118.3	1	597.6	0.8	19.9	5.8	173	2.3	181.5	42.5
HD-99_204.3		468	0.5	11	17.9	16.2	5.1	10.4	101.5	2	441.6	0.5	11.9	3.7	69	1	211	32
PB2013021	6.8	792	0.5	17.7	18.5	15.4	3.8	8	93.8	1	440.8	0.4	10.3	2.8	180	1.4	156.3	26.8
PB2013022	7.8	466	0.5	14.9	9.3	16.2	3.7	6.5	52.8	1	521.4	0.4	6.6	2.1	176	1.3	146.8	25.4
PB2013023	2.9	401	0.5	12.8	4.6	14.5	3.4	6.9	77.8	0.5	491.7	0.5	11.5	3.9	126	4	130.1	19.4
PB2013046	10.8	685	0.5	24.3	3.9	16.2	3.1	7.2	85.7	0.5	624.8	0.6	15.7	4.2	207	1.3	118.3	20.2
PB2014004	3.3	904	2	12.1	7.1	14.4	4	9.5	132	0.5	481.9	0.9	24	5.4	99	4	150.9	20.8
PB2014007	7.6	555	0.5	19.7	3.2	13.5	4.5	9.9	61.4	2	233.2	0.7	13.2	3.7	171	1.3	175.2	29.8
PB2014010	3.6	1045	0.5	18.7	4	14.6	3.9	8.2	98.6	0.5	865	0.7	21.3	6.7	183	2.3	158.2	22.8
PB2014011	5	1013	2	9.4	7.9	15.9	3.7	8.4	115.8	1	568.5	0.7	22.6	7.2	149	2.1	141.4	19.6
PB2014014	5.6	740	1	18.2	7.5	18.1	4.2	10.9	106.8	2	574.9	0.7	16.7	5	190	2	168.7	29.2
PB2014021	8.8	264	2	25.7	4.8	11.7	3.1	6.6	51.5	4	318.9	0.4	8	2.7	136	1	123.8	22
PB2014023	3	636	1	13.8	2.4	16	3.7	6.4	81.1	1	455.5	0.5	10.9	3.7	141	1.8	149.5	20.7
PB2014032	4.5	2884	1	0.7	6.9	16.3	4	11.3	105.3	1	323.3	0.9	14.5	4.8	145	2.2	158.6	9.4
PB2014052	4.1	770	8	23.1	4.3	16.1	4.3	9.3	85	1	559.8	0.7	16.4	4.8	181	1.8	148	46.5
PB2014092	0.5	744	0.5	0.1	3.6	18.3	4	9.3	154.5	4	102.3	0.7	7.5	2.4	91	1.7	160.1	5.8
PB2014106	3.9	454	0.5	12.5	7.4	15.5	2.9	6.9	87.6	0.5	303.9	0.5	10.8	3.6	132	1.6	108.3	18.1
PB2014107c	1.3	357	0.5	12.1	8.1	12.6	5	11.6	90.7	2	92.3	0.7	10.8	2.8	73	1.4	200	21.3
PB2014113	2.6	472	0.5	23.2	13.7	13	4.5	10.7	164.7	2	15.9	0.8	10.4	3.7	136	2	183.3	13.7
PB2014125	7.2	636	0.5	20.5	7.8	15.4	3.1	6.2	71.9	0.5	538.4	0.4	12.6	4.2	249	1.5	119.9	29.4
PB2014127	3.6	505	0.5	20.6	107.2	16.3	4	10	65.1	0.5	494.7	0.5	5.5	1.1	255	0.6	162.6	35.1

Table C.2b. (cont)

Sample	Sc_ ppm	Ba_ ppm	Be_ ppm	Co_ ppm	Cs_ ppm	Ga_ppm	Hf_ ppm	Nb_ ppm	Rb_ ppm	Sn_ ppm	Sr_ ppm	Ta_ ppm	Th_ ppm	U_ ppm	V_ppm	W_ ppm	Zr_ppm	Y_ ppm
PD-07_101.9	5.4	669	0.5	17.3	3.5	15.6	3.4	8	80.5	0.5	585.2	0.6	15.3	4.6	178	1.6	129.5	21.4
PD-07_24.5	3.3	1693	0.5	0.9	7.1	16.3	3.8	9.3	20.2	0.5	503.3	0.7	12.9	4.1	163	4	140.7	13.4
PD-07_55.3	4.4	865	6	24.9	13.3	15.5	3.8	8.8	97.3	0.5	473.2	0.6	17.8	6.6	168	1.5	145.1	86.6
PD-17_59.8	0.9	824	0.5	20	0.6	15.6	3.4	7.1	6.1	2	1275.7	0.6	20.7	5.2	194	1.7	127.9	19.3
PD-19_171.1	1.1	558	3	10.8	8.1	12.9	4.2	9.3	140.4	2	74.9	0.5	6.2	3	94	2.4	185.6	20.1
PD-19_54.2	3.6	222	0.5	14.4	22.7	14.6	3.1	7.1	107.6	0.5	284.8	0.6	13.9	5.5	107	1.4	114.1	16.6
PD-19_74.5	2.5	579	2	14.4	19	14.2	4.3	10.3	213.7	2	93.5	0.8	11	3.3	97	1.6	172.9	18.6
PD-21_113.1	0.4	720	2	4.7	8	14	5	12.6	303.1	2	73.6	0.9	21	8.6	50	28.8	197.9	26.6
PD-21_170.1	1.9	773	0.5	5.5	5	16.2	5.3	12.6	130.1	1	513.7	0.8	17.7	6.3	128	2.1	210.3	28
PD-21_229.5	3	807	2	13.8	6.1	15.7	4.8	11.7	133.7	1	506.7	0.7	20	5.9	118	1.3	200.9	26.6
PD-22_31.7	2.4	562	1	19.6	3.8	15.8	4.1	11.8	64.2	0.5	484.4	0.6	8.7	1.3	163	0.7	174.5	25.8
PD-23_186.7	9.1	625	0.5	17.7	8.1	16	4.5	9.8	60.3	0.5	449.6	0.6	9.1	2.4	216	1	177	27

Table C.2c. Lithogeochemical Results for Petrogenesis Analysis. (Trace elements continuation and Total C and Total S).Batch, observations, and unit in Table C.2a.

Sample	La_ ppm	Ce_ ppm	Pr_ ppm	Nd_ ppm	Sm_ ppm	Eu_ ppm	Gd_ ppm	Tb_ ppm	Dy_ ppm	Ho_ ppm	Er_ ppm	Tm_ ppm	Yb_ ppm	Lu_ ppm	C_pct	S_pct
HD-01_297.5	26.2	54	6.7	29.7	5.78	1.62	5.25	0.78	4.59	0.92	2.57	0.38	2.49	0.35	0.08	2.48
HD-09_216.2	26.86	52.65	5.55	19.53	3.89	0.78	2.21	0.27	1.73	0.36	1.38	0.26	1.92	0.32	0.01	5.03
HD-09_354.3	32.83	66.42	6.81	22.62	3.88	0.77	1.68	0.16	0.69	0.14	0.49	0.09	0.64	0.16	0.02	7.15
HD-09_95.55	21.90	36.60	4.12	15.43	3.33	1.19	6.32	1.27	8.69	1.82	5.59	0.77	4.87	0.64	0.01	0.06
HD-115_23.65	27.4	52.3	6.37	24.3	5.13	1.34	5.05	0.79	4.88	1.02	2.92	0.46	2.83	0.42	1.85	0.01
HD-115_280	27.6	51.9	6.72	27.2	5.88	1.73	5.86	0.91	5.71	1.17	3.5	0.48	3.1	0.49	0.43	0.01
HD-12_61.35	36.53	71.06	7.25	25.05	4.64	1.65	8.71	1.73	9.87	2.17	5.99	0.82	4.83	0.71	0.01	0.17
HD-13A_106.9	10.6	20.6	2.38	9.7	1.79	0.43	1.8	0.24	1.66	0.34	0.96	0.13	0.93	0.16	0.3	5.36
HD-13A_415.2	20.7	36.1	4.32	16.8	3.28	0.88	3.05	0.42	2.71	0.55	1.57	0.23	1.68	0.24	0.05	0.39
HD-13A_488.6	18.8	34.7	4.66	18	3.9	1.03	3.37	0.5	3.22	0.62	1.95	0.28	1.87	0.3	0.05	1.35
HD-24_186.2	26.4	46.2	4.65	15.5	2.66	0.77	2.27	0.31	1.83	0.37	1.09	0.19	1.32	0.23	0.29	0.04
HD-28_138.5	40.1	70.3	7.38	26.3	4.37	1.12	3.59	0.49	2.92	0.56	1.7	0.25	1.78	0.29	0.16	0.01
HD-29_204.5	36.5	65.1	7.03	24	4.08	1.12	3.43	0.47	2.81	0.51	1.52	0.25	1.84	0.29	0.08	0.01
HD-29_86.6	38.1	60.2	5.79	18.5	2.87	0.71	2.26	0.31	1.84	0.36	1.1	0.18	1.23	0.21	0.11	0.01
HD-37_112.7	3.6	6.4	0.75	3.4	0.78	0.21	0.83	0.14	0.88	0.19	0.59	0.09	0.65	0.11	0.05	1.27
HD-37_127.3	8.6	16.9	1.89	7.4	1.53	0.48	1.52	0.28	1.58	0.34	1.07	0.18	1.09	0.2	0.1	2.22
HD-37_254.3	23.1	42	5.01	19.6	3.54	1	3.38	0.46	3.27	0.59	1.77	0.27	1.8	0.26	0.14	0.23
HD-37_268.1	25.7	50.3	4.96	19.2	3.46	0.84	2.99	0.45	2.83	0.54	1.62	0.25	1.69	0.3	0.07	0.38
HD-37_95.35	10.3	22.8	2.51	8.6	1.99	0.5	1.86	0.28	1.61	0.31	0.88	0.15	0.79	0.14	0.06	2.94
HD-38_190.4	27.2	56.2	6.48	23.9	5.45	1.86	5.22	0.81	4.68	0.97	2.5	0.4	2.51	0.39	0.04	1.24
HD-38_310	26.9	53	5.33	19.6	3.62	0.98	3.54	0.52	2.7	0.6	1.88	0.29	1.91	0.3	0.04	0.64
HD-38_400.05	19	40.2	4.17	16.2	3.12	0.77	2.61	0.41	2.44	0.45	1.41	0.22	1.41	0.26	0.09	1.65
HD-38_461.1	19	36.9	3.9	14.4	2.88	0.78	2.51	0.41	2.23	0.49	1.36	0.23	1.34	0.24	0.05	0.83
HD-38_490.85	21.5	42.9	4.57	18	3.1	0.89	2.91	0.46	2.63	0.55	1.76	0.26	1.69	0.29	0.05	1.3
HD-38_550.7	21.1	41.3	4.4	17.6	3.16	0.9	2.86	0.46	2.51	0.57	1.69	0.27	1.67	0.29	0.06	0.73
HD-45_459.45	24.4	41.1	4.71	17.3	3.25	0.89	2.82	0.45	2.65	0.53	1.66	0.24	1.76	0.25	0.01	0.69
HD-45_580.15	27.3	50.8	6.04	22.1	4.24	1.15	3.74	0.61	3.12	0.69	2.15	0.31	2.57	0.34	0.06	0.51

Table C.2c. (cont)

Sample	La_ ppm	Ce_ ppm	Pr_ ppm	Nd_ ppm	Sm_ ppm	Eu_ ppm	Gd_ ppm	Tb_ ppm	Dy_ ppm	Ho_ ppm	Er_ ppm	Tm_ ppm	Yb_ ppm	Lu_ ppm	C_pct	S_pct
HD-60_720	31.9	58.2	6.06	20.3	3.69	1	3.37	0.53	2.99	0.58	1.93	0.3	2	0.3	0.05	0.59
HD-78_16	19.1	39.2	4.83	20.3	4.06	0.92	3.82	0.58	3.84	0.81	2.32	0.38	2.21	0.33	0.25	2.02
HD-78_289.2	29.6	55.3	6.66	26.2	4.85	1.08	4.12	0.55	3.68	0.69	2.22	0.34	2.31	0.36	0.03	0.38
HD-78_39.4	11	28.1	4.14	18.1	3.38	0.83	2.67	0.4	2.65	0.56	1.54	0.24	1.55	0.23	1.1	0.28
HD-80_119.7	22.7	42.8	4.61	17.7	3	0.83	3.06	0.46	2.61	0.55	1.75	0.24	1.6	0.27	0.01	2.55
HD-80_30	11.4	20.6	2.22	8.6	1.62	0.48	1.6	0.26	1.52	0.33	0.81	0.12	0.78	0.13	0.06	3.73
HD-80_90.65	11.5	21.6	2.34	9.9	1.7	0.47	1.7	0.27	1.28	0.31	0.82	0.15	0.96	0.15	0.01	1.5
HD-94_274.8	29.2	59.3	6.68	27.1	4.5	1.08	4.08	0.59	3.6	0.69	2.01	0.34	2.46	0.34	0.18	0.75
HD-96_242.6	39.3	72.9	8.48	31.9	6.07	1.42	5.46	0.76	4.63	0.93	2.7	0.41	2.86	0.45	0.06	0.01
HD-96_270.5	36	71.3	7.55	27.5	5.15	1.2	4.47	0.66	3.89	0.79	2.25	0.37	2.28	0.38	0.07	0.01
HD-96_302	44	82.4	9.47	36.8	7.59	1.65	7.26	1.07	6.3	1.35	3.77	0.6	3.92	0.65	0.04	0.01
HD-99_204.3	42.1	78.4	9.25	36.3	6.7	1.7	6.32	0.9	5.79	1.1	3.29	0.52	3.29	0.51	0.92	0.01
PB2013021	33.4	64.1	7.5	28.4	5.61	1.56	5.33	0.79	4.52	0.93	2.49	0.39	2.55	0.4	1.29	0.02
PB2013022	18.5	37.2	4.59	19.9	4.1	1.25	4.62	0.7	4.42	0.92	2.57	0.42	2.6	0.42	0.68	0.01
PB2013023	27.1	46	5.27	19.5	3.83	1.09	3.65	0.52	3.26	0.65	1.81	0.27	1.8	0.3	1.02	0.01
PB2013046	27.2	50.2	5.89	23.5	4.56	1.23	4.39	0.63	3.99	0.73	2.22	0.33	2.16	0.33	0.01	0.01
PB2014004	33	59.6	6.37	23.1	4.25	1.08	4.03	0.6	3.78	0.76	2.27	0.36	2.41	0.41	0.01	0.01
PB2014007	26.7	54.9	6.29	25.1	5.16	1.18	5.3	0.8	4.93	1.04	3.03	0.48	3.35	0.53	0.77	0.01
PB2014010	44.1	76.4	8.69	32.7	5.92	1.49	5.26	0.69	4.1	0.79	2.18	0.32	2.08	0.34	0.01	0.01
PB2014011	39.7	63.2	7.16	25.6	4.48	1.2	4.22	0.57	3.23	0.69	1.82	0.28	2.06	0.31	0.04	0.01
PB2014014	35.8	67.2	7.91	29.6	5.87	1.37	5.74	0.87	4.98	1.08	3.04	0.49	3.13	0.52	0.06	0.01
PB2014021	26.8	44.5	5.16	18.7	3.77	0.81	3.59	0.56	3.5	0.7	2.04	0.32	2.15	0.35	4.24	0.01
PB2014023	24.1	43.1	4.99	18.8	3.91	1.05	3.69	0.58	3.45	0.7	2.02	0.33	2.17	0.36	0.22	0.01
PB2014032	28.2	50	5.53	19.9	3.36	0.69	2.9	0.39	1.98	0.36	1	0.14	1.01	0.16	0.06	0.1
PB2014052	51.4	102	13.58	56.5	12.35	2.98	12.27	1.82	10.06	1.95	5.24	0.77	5.24	0.84	0.01	0.01
PB2014092	30.6	53.7	5.92	22	3.19	0.76	1.69	0.2	1	0.2	0.73	0.12	0.9	0.17	0.01	0.1
PB2014106	26.4	43.2	5.24	19.1	3.6	1.09	3.75	0.54	3	0.68	1.84	0.3	2.02	0.32	0.96	0.01
PB2014107c	26.2	33.3	5.05	17.9	3.6	0.8	3.31	0.57	3.42	0.74	2.22	0.33	2.25	0.35	0.26	0.01
PB2014113	13.3	26.3	3.09	11.1	2.28	0.47	2.13	0.34	2.09	0.47	1.57	0.24	1.74	0.3	0.01	2.79
PB2014125	24	42.8	5.29	20.3	4.4	1.26	4.82	0.75	4.59	1.01	2.9	0.43	2.73	0.43	0.01	0.01

Table C.2c. (cont)

Sample	La_ ppm	Ce_ ppm	Pr_ ppm	Nd_ ppm	Sm_ ppm	Eu_ ppm	Gd_ ppm	Tb_ ppm	Dy_ ppm	Ho_ ppm	Er_ ppm	Tm_ ppm	Yb_ ppm	Lu_ ppm	C_pct	S_pct
PB2014127	25.8	50.9	6.29	25.7	5.64	1.52	6.65	1.02	6.25	1.29	3.67	0.54	3.26	0.52	0.01	0.01
PD-07_101.9	27.7	51.1	5.61	21.1	4.25	1.17	4.08	0.58	3.8	0.77	2.16	0.32	2.27	0.36	0.07	0.05
PD-07_24.5	18.6	34.1	3.59	12.9	2.12	0.49	1.84	0.34	2.21	0.48	1.41	0.24	1.59	0.28	0.01	3.01
PD-07_55.3	43.9	87.1	10.41	43	9.99	3	12.72	2.05	13.13	2.81	8.15	1.22	7.86	1.26	0.01	0.01
PD-17_59.8	35.6	68.8	7.96	30.3	5.12	1.2	4.16	0.55	3.24	0.67	1.86	0.28	2.01	0.32	0.01	7.08
PD-19_171.1	22.3	39.6	4.29	15.6	2.95	0.94	3.08	0.5	3.19	0.66	2.04	0.32	2.02	0.32	0.74	3.35
PD-19_54.2	32.3	57	6.31	23.5	3.86	1.16	3.4	0.46	2.66	0.51	1.57	0.22	1.55	0.26	1.26	0.03
PD-19_74.5	29.6	54.3	5.68	20.4	3.73	0.82	3.51	0.53	3.12	0.63	1.96	0.3	1.9	0.34	0.01	2.38
PD-21_113.1	41.4	71.4	7.56	26.4	4.81	0.9	4.55	0.68	4.25	0.85	2.63	0.4	2.73	0.45	0.01	2.6
PD-21_170.1	39.3	71.9	8.14	29.9	5.7	1.31	5.3	0.79	4.51	0.95	2.64	0.41	2.76	0.44	0.03	0.07
PD-21_229.5	37.3	69.3	7.7	27.4	5.2	1.29	4.77	0.73	4.34	0.86	2.52	0.41	2.7	0.41	0.13	0.01
PD-22_31.7	31.5	57.2	6.4	24.8	4.91	1.31	4.84	0.7	4.37	0.87	2.57	0.38	2.56	0.4	0.01	0.01
PD-23_186.7	29.5	56.3	6.67	26.5	5.29	1.32	5.26	0.77	4.62	1	2.78	0.41	2.61	0.41	0.31	0.01

Table C.2d. Lithogeochemical Results for Petrogenesis Analysis. (Pathfinder elements). Batch, observations, and unit in Table C.2a.

Sample	Mo_ppm	Cu_ppm	Pb_ppm	Zn_ppm	Ni_ppm	As_ppm	Cd_ppm	Sb_ppm	Bi_ppm	Ag_ppm	Au_ppb	Hg_ppm	Tl_ppm	Se_ppm
HD-01_297.5	0.4	529.4	5.8	25	30.3	6.8	0.1	0.5	2.3	0.2	24.2	0.01	0.05	0.8
HD-09_216.2	0.86	53.51	15.00	4.32	9.49	45.31	0.05	0.05	0.76	0.05	34.52	0.02	0.43	2.16
HD-09_354.3	1.10	26.35	14.05	83.44	12.84	13.06	0.55	0.22	4.83	0.11	84.42	0.11	0.44	5.38
HD-09_95.55	1.15	10.22	18.67	2.09	0.31	71.95	0.05	0.21	2.40	0.05	12.72	0.01	0.21	1.56
HD-115_23.65	0.4	14.2	7.7	58	14.9	28.9	0.2	0.1	0.05	0.05	1.6	0.02	0.05	0.25
HD-115_280	0.9	26.5	3.8	56	6.3	7.6	0.1	0.3	0.05	0.05	1.5	0.01	0.05	0.25
HD-12_61.35	1.16	25.79	10.11	0.53	0.11	29.69	0.05	0.05	2.00	0.05	4.63	0.01	0.11	1.37
HD-13A_106.9	2.3	7906.8	10.5	62	14.2	5.8	0.4	1.2	1.3	1.9	1849.9	0.03	0.1	7.2
HD-13A_415.2	9.5	2040.9	3.5	36	7	0.9	0.05	0.8	0.8	0.5	710	0.01	0.7	2.3
HD-13A_488.6	6.2	904.3	3.3	37	2.2	2.2	0.05	0.2	0.8	0.4	36.9	0.01	0.2	1.2
HD-24_186.2	1.5	399	3.9	12	3.3	2	0.05	0.1	0.2	0.1	3.3	0.01	0.05	0.25
HD-28_138.5	0.5	17.7	3.1	21	6.2	1.7	0.05	0.05	0.05	0.05	1.4	0.01	0.2	0.25
HD-29_204.5	0.7	79.5	4.3	11	4.1	2.2	0.05	0.1	0.05	0.05	0.8	0.01	0.2	0.25
HD-29_86.6	0.7	173.6	3.1	13	4.1	2.2	0.05	0.1	0.05	0.05	1	0.01	0.2	0.25
HD-37_112.7	3.7	6979	9.1	60	6.1	0.25	0.2	0.4	0.4	1.8	492.1	0.03	0.4	4.5
HD-37_127.3	4.5	5759	21.7	128	9.8	2.4	0.7	0.7	1.4	1.7	818.4	0.01	1.1	4.8
HD-37_254.3	2.4	778.9	3.9	31	3.2	1.4	0.05	0.3	0.6	0.3	82	0.01	0.7	0.25
HD-37_268.1	6.1	486	3.4	27	3.3	1.4	0.05	0.1	0.4	0.2	53.9	0.01	0.8	0.5
HD-37_95.35	9.1	6958	13.2	61	6.2	1.4	0.4	0.7	0.9	1.9	666	0.02	0.6	4.3
HD-38_190.4	0.2	91.4	11.5	29	22.5	7.1	0.1	1.1	46.7	0.1	54.7	0.01	0.3	0.25
HD-38_310	3.8	464.2	4.6	39	3.2	1.2	0.05	0.05	0.6	0.2	109.9	0.01	0.5	0.6
HD-38_400.05	9.1	2124.2	7	46	5.5	1	0.2	0.1	0.6	0.7	159.2	0.01	0.5	2.8
HD-38_461.1	6.9	1095	3.7	34	3.7	1.4	0.05	0.2	0.3	0.3	115	0.01	0.2	1.7
HD-38_490.85	41.4	976.5	8.4	64	3.9	1.6	0.4	0.2	0.5	0.4	85.2	0.01	0.3	2.1
HD-38_550.7	2.2	854.5	5.4	45	5.3	1.4	0.1	0.1	0.2	0.4	70.1	0.01	0.5	1.2
HD-45_459.45	4.2	582.8	8.5	48	4.6	2	0.2	0.1	0.7	0.2	69.7	0.01	0.4	1.2
HD-45_580.15	2.2	287.4	3.1	33	5.4	2	0.05	0.2	0.2	0.1	202.8	0.01	0.3	0.6
HD-60_720	5	1828.5	3.7	23	2.6	0.9	0.1	0.05	0.1	0.8	131.9	0.01	0.5	1.5
HD-78_16	4	482.4	34.4	41	590.8	12.4	0.2	0.9	1.2	0.3	36	0.01	0.05	5.9
HD-78_289.2	0.4	75.3	1	19	70.1	1.7	0.05	0.2	0.05	0.05	2.7	0.01	1.6	0.25
HD-78_39.4	1.9	31	14.2	46	87.2	7.7	0.1	0.4	0.3	0.05	2.3	0.01	0.05	0.25

Table C.2d. (cont)

Sample	Mo_ppm	Cu_ppm	Pb_ppm	Zn_ppm	Ni_ppm	As_ppm	Cd_ppm	Sb_ppm	Bi_ppm	Ag_ppm	Au_ppb	Hg_ppm	Tl_ppm	Se_ppm
HD-80_119.7	36.3	6903.2	38.6	98	21.4	233.5	0.4	20.9	1.6	1.6	708.3	0.43	0.6	3.7
HD-80_30	22.4	10000.1	6.5	5	5.6	1.1	0.05	0.6	1.7	2.1	463.4	0.01	0.5	5.2
HD-80_90.65	69.1	6812	76.8	85	5.7	1.3	0.2	1.3	1.8	1.7	734.1	0.01	0.5	3.3
HD-94_274.8	108.4	1994.5	16.4	53	43.4	2.6	0.3	0.4	0.2	0.5	82	0.01	0.6	0.8
HD-96_242.6	0.2	23.5	4.3	28	4.5	2.7	0.05	0.05	0.05	0.05	0.25	0.01	0.05	0.25
HD-96_270.5	0.2	8.6	3.2	27	4.8	12.1	0.2	0.2	0.05	0.05	0.6	0.01	0.05	0.25
HD-96_302	1.3	20.1	5.6	64	6.3	11.5	0.05	0.3	0.05	0.05	0.25	0.03	0.05	0.25
HD-99_204.3	1.1	1.2	5.6	67	2.6	2.1	0.05	0.2	0.05	0.05	1.5	0.01	0.2	0.25
PB2013021	0.05	4.3	10	51	6.4	3.6	0.05	0.1	0.05	0.05	0.8	0.01	0.05	0.25
PB2013022	0.3	21.2	8.7	79	4	17.7	0.05	0.2	0.05	0.05	0.25	0.01	0.05	0.25
PB2013023	1.4	7.1	4	60	4.2	3.5	0.05	0.2	0.05	0.05	1	0.01	0.05	0.25
PB2013046	0.9	38.3	3.1	71	11.7	2.3	0.1	0.2	0.05	0.05	1.1	0.01	0.05	0.25
PB2014004	0.2	8.5	2.2	17	2.4	2.4	0.05	0.3	0.05	0.05	0.6	0.01	0.05	0.25
PB2014007	0.2	14.4	10.6	72	10.3	5.4	0.2	0.05	0.6	0.05	1.1	0.24	0.05	0.25
PB2014010	0.9	44	5.3	52	13.4	3	0.05	0.3	0.1	0.05	2.1	0.01	0.05	0.25
PB2014011	0.3	25.5	2.1	43	5	0.7	0.05	0.05	0.05	0.05	1.3	0.01	0.1	0.25
PB2014014	0.9	25.9	3.7	160	6.4	8.8	0.4	0.2	0.05	0.05	0.25	0.01	0.05	0.25
PB2014021	0.5	30.7	17.7	52	18.8	2.9	0.5	0.05	0.6	0.05	0.25	0.01	0.05	0.25
PB2014023	0.4	18.6	3.7	68	5.1	4.4	0.05	0.2	0.05	0.05	0.25	0.01	0.05	0.25
PB2014032	0.4	13.3	7	6	0.4	5	0.05	0.2	0.05	0.05	0.25	0.01	0.05	0.25
PB2014052	1.5	26.3	8	138	17.5	5.1	1.1	0.2	0.05	0.05	0.25	0.01	0.05	0.25
PB2014092	0.4	22.8	56.8	2	0.3	12.3	0.05	1.2	3.8	1.9	31	2.33	0.3	0.8
PB2014106	0.1	5.1	9.5	74	4.5	17.5	0.05	0.4	0.05	0.05	1.9	0.01	0.1	0.25
PB2014107c	0.05	21.1	7.1	49	90.2	4	0.05	0.1	0.2	0.05	0.25	0.01	0.05	0.25
PB2014113	0.5	4.9	17	41	138.4	16.7	0.2	0.6	1.1	0.05	6.9	0.01	0.3	0.7
PB2014125	0.8	19.2	3.8	118	7.2	1.7	0.05	0.2	0.05	0.05	0.6	0.01	0.05	0.25
PB2014127	0.4	7.9	3.5	64	1.3	0.8	0.3	0.2	0.05	0.05	0.25	0.01	0.5	0.25
PD-07_101.9	0.7	23.1	4	48	7.4	2.5	0.05	0.05	0.05	0.05	2	0.01	0.05	0.25
PD-07_24.5	1.6	2.5	3.5	1	0.2	24.3	0.05	0.3	0.05	0.05	0.25	0.01	0.1	1
PD-07_55.3	0.7	13.3	3.3	68	6.4	2.4	0.1	0.1	0.05	0.05	1.4	0.01	9.2	0.25
PD-17_59.8	1.4	63.8	9.1	40	10.1	52.2	0.9	0.5	3.1	0.05	11.5	0.03	1.6	4.4

Table C.2d.(cont)

Sample	Mo_ppm	Cu_ppm	Pb_ppm	Zn_ppm	Ni_ppm	As_ppm	Cd_ppm	Sb_ppm	Bi_ppm	Ag_ppm	Au_ppb	Hg_ppm	Tl_ppm	Se_ppm
PD-19_171.1	0.2	61.5	54.8	40	50.8	14.6	0.4	1.9	1.2	0.1	19.3	0.01	0.2	1.6
PD-19_54.2	0.9	28.7	10.4	34	5.3	2	0.05	0.5	0.3	0.05	0.25	0.01	0.2	0.25
PD-19_74.5	0.3	7.3	8.2	31	69.6	20.9	0.05	0.6	0.8	0.05	7.3	0.01	1.7	0.7
PD-21_113.1	1.9	14.9	5715.5	3447	2.7	18.2	44.9	1.7	2	3.3	8.9	0.21	0.2	0.25
PD-21_170.1	1.9	30.9	24.1	95	6.1	6.7	0.3	1	0.05	0.05	0.7	0.01	0.3	0.25
PD-21_229.5	1.8	27.8	21.5	39	5.4	3.1	0.1	0.6	0.05	0.05	0.6	0.01	0.2	0.25
PD-22_31.7	0.1	17.9	9	58	20.6	2.2	0.05	0.2	0.05	0.05	1.5	0.01	0.5	0.25
PD-23_186.7	1	8.9	6.3	46	6.5	5.7	0.05	0.05	0.05	0.05	1.1	0.01	0.05	0.25

Table C.3a. Litogeochemical Results for Alteration Geochemistry Analysis. (Major elements)Batch is abbreviated as follows: 288= ANK12000288, 289= ANK12000289, 290=ANK12000290. Lithology abbreviations are, QMP-A=Quartz Monzonite A (Kestane Stock) and QMP-B=Quartz Monzonite B(Kestane Stock). Alteration K=Biotite+ magnetite ± K-feldspar, P= Chlorite + epidote + calcite, S=Sericite ± quartz, SC=Chlorite ± sericite.

Sample	Batch	Lithology	Alt.	Wght	SiO2_ pct	Al2O3_ pct	Fe2O3_ pct	MgO_ pct	CaO_ pct	Na2O_ pct	K2O_ pct	TiO2_ pct	P2O5_ pct	MnO_ pct	Cr2O3_ pct	Ni_ ppm	Sc_ ppm	LOI_ pct	Sum_%
HD-37_3.65	288	QMP-A	S	0.2	72.01	13.08	9.12	0.74	0.04	0.11	4.03	0.42	0.01	0.01	0.00	10.45	6.27	4.3	99.59
HD-37_34	288	QMP-A	S	0.22	78.50	8.64	8.34	0.36	0.07	0.04	2.42	0.21	0.03	0.01	0.00	31.60	4.21	5	98.67
HD-37_64.6	288	QMP-A	K	0.36	71.51	8.86	12.12	1.00	0.14	0.57	4.52	0.26	0.06	0.04	0.00	10.22	4.09	2.1	99.05
HD-37_95.35	288	QMP-A	K	0.21	71.09	8.50	12.76	0.99	0.17	0.66	4.50	0.29	0.08	0.05	0.00	10.29	5.15	2.8	99.08
HD-37_127.3	288	QMP-A	K	0.35	70.13	12.04	9.61	1.48	0.45	0.15	4.75	0.32	0.14	0.11	0.00	10.40	4.16	3.8	99.17
HD-37_156.55	288	QMP-A	K	0.32	73.84	10.02	7.81	1.65	1.19	0.27	4.23	0.27	0.07	0.14	0.00	10.32	5.16	3.1	99.52
HD-37_186.8	288	QMP-A	K	0.34	68.04	14.28	7.50	1.75	1.70	1.22	4.68	0.40	0.09	0.08	0.00	10.48	6.29	4.6	99.75
HD-37_215.3	288	QMP-B	K	0.43	68.63	14.80	6.53	2.01	2.32	1.60	3.22	0.39	0.16	0.05	0.00	10.54	6.32	5.1	99.7
HD-37_245.15	288	QMP-B	S-C	0.27	67.57	16.09	4.81	1.68	3.34	2.59	3.05	0.43	0.16	0.05	0.00	10.42	6.25	4	99.74
HD-37_268.1	288	QMP-B	F	0.32	66.30	16.60	4.79	1.79	3.80	3.00	2.83	0.44	0.15	0.06	0.00	10.24	7.17	2.3	99.77
HD-38_38.75	288	QMP-A	S	0.26	76.40	14.08	3.91	0.24	0.15	0.66	3.33	0.40	0.06	0.01	0.00	10.51	6.30	4.8	99.27
HD-38_69.4	288	QMP-A	K	0.25	73.55	13.38	3.69	1.01	0.56	1.75	5.12	0.37	0.04	0.01	0.00	10.34	5.17	3.3	99.44
HD-38_100.95	288	QMP-A	K	0.23	71.48	14.92	4.09	1.37	0.42	1.06	5.64	0.36	0.14	0.03	0.00	10.40	5.20	3.8	99.49
HD-38_129.9	288	QMP-A	S-C	0.26	68.77	16.14	4.59	2.09	2.21	2.44	2.83	0.46	0.16	0.03	0.00	10.43	8.34	4.1	99.72
HD-38_160.1	288	QMP-A	S-C	0.28	65.83	17.07	5.71	2.01	2.95	3.01	2.47	0.48	0.18	0.04	0.00	10.42	7.29	4	99.76
HD-38_221	288	QMP-A	S-C	0.27	65.20	16.93	5.67	2.15	3.26	3.02	2.85	0.47	0.19	0.05	0.00	10.52	7.36	4.9	99.73
HD-38_250.65	288	QMP-A	S-C	0.33	67.50	15.57	4.20	1.74	4.29	2.74	3.02	0.42	0.15	0.05	0.00	10.32	6.19	3.1	99.67

Table C.3a (cont)

Sample	Batch	Lithology	Alt.	Wght	SiO2_ pct	Al2O3_ pct	Fe2O3_ pct	MgO_ pct	CaO_ pct	Na2O_ pct	K2O_ pct	TiO2_ pct	P2O5_ pct	MnO_ pct	Cr2O3_ pct	Ni_ ppm	Sc_ ppm	LOI_ pct	Sum_%
HD-38_280	288	QMP-A	S-C	0.24	65.48	16.87	5.33	2.09	3.47	2.72	2.95	0.51	0.22	0.04	0.00	10.40	7.28	3.8	99.74
HD-38_310	288	QMP-A	F	0.29	64.99	16.99	4.85	1.78	4.53	3.45	2.41	0.48	0.17	0.07	0.00	10.19	7.14	1.9	99.74
HD-38_341.6	288	QMP-A	K	0.31	62.43	14.16	12.60	1.40	1.91	2.00	4.43	0.37	0.13	0.05	0.00	10.56	5.28	5.3	99.45
HD-38_371	288	QMP-A	K	0.32	62.41	14.63	11.56	1.26	1.59	2.50	5.07	0.46	0.07	0.06	0.00	10.31	5.16	3	99.61
HD-38_400.05	288	QMP-A	S-C	0.28	65.35	14.62	7.95	1.62	2.18	2.19	5.12	0.38	0.13	0.06	0.00	10.34	5.17	3.3	99.57
HD-38_431	288	QMP-A	K	0.27	66.30	11.85	12.81	1.00	1.35	1.33	4.32	0.30	0.11	0.05	0.00	10.42	5.21	4	99.43
HD-38_461.1	288	QMP-A	F	0.3	69.49	13.36	6.76	1.39	2.44	1.98	3.74	0.37	0.14	0.07	0.00	10.19	5.10	1.9	99.7
HD-38_490.85	288	QMP-A	F	0.32	65.47	15.86	5.88	1.49	3.67	2.96	3.66	0.42	0.15	0.09	0.00	10.20	6.12	2	99.69
HD-38_521	288	QMP-A	S-C	0.31	61.22	14.64	12.82	1.11	3.13	2.13	4.00	0.39	0.14	0.07	0.00	10.62	5.31	5.8	99.64
HD-38_550.7	288	QMP-A	F	0.27	65.28	16.50	5.15	1.68	3.38	3.45	3.60	0.43	0.16	0.07	0.00	10.16	6.10	1.6	99.71
HD-80_1.55	288	QMP-A	S	0.21	74.75	12.56	6.64	0.71	0.21	0.08	4.17	0.32	0.02	0.01	0.00	10.38	5.19	3.6	99.44
HD-80_30	288	QMP-A	S	0.17	73.78	12.46	5.71	0.28	0.15	0.47	5.49	0.31	0.03	0.01	0.00	10.47	5.23	4.4	98.72
HD-80_60.7	288	QMP-A	S	0.19	72.23	14.84	4.60	1.51	0.31	1.23	4.03	0.43	0.03	0.02	0.00	10.41	6.25	3.9	99.21
HD-80_90.65	288	QMP-A	S	0.28	71.13	11.77	7.45	1.18	0.34	1.43	5.21	0.32	0.12	0.06	0.00	10.25	4.10	2.4	99.03
HD-80_119.7	288	QMP-A	K	0.29	68.36	14.75	6.70	1.25	0.46	1.03	5.77	0.45	0.21	0.04	0.00	31.16	6.23	3.7	99.04
HD-80_149.55	288	QMP-A	K	0.26	70.28	13.64	6.82	1.31	0.53	1.21	5.32	0.37	0.11	0.02	0.00	10.41	5.20	3.9	99.63
HD-80_181.3	288	QMP-A	K	0.2	67.12	16.21	6.58	1.67	0.97	1.13	5.32	0.42	0.16	0.10	0.00	10.57	6.34	5.4	99.66
HD-80_209.8	288	QMP-A	K	0.28	69.09	15.55	5.58	1.61	0.76	0.62	5.90	0.40	0.14	0.03	0.00	10.52	5.26	4.9	99.68
HD-80_238.7	288	QMP-A	K	0.33	68.10	15.14	5.56	1.86	1.84	1.67	4.76	0.40	0.14	0.05	0.00	10.51	5.25	4.8	99.55
HD-80_268.6	288	QMP-A	K	0.28	69.32	11.97	7.35	1.20	3.00	0.58	5.19	0.34	0.15	0.10	0.00	10.62	4.25	5.8	99.24

Table C.3a (cont)

Sample	Batch	Lithology	Alt.	Wght	SiO2_ pct	Al2O3_ pct	Fe2O3_ pct	MgO_ pct	CaO_ pct	Na2O_ pct	K2O_ pct	TiO2_ pct	P2O5_ pct	MnO_ pct	Cr2O3_ pct	Ni_ ppm	Sc_ ppm	LOI_ pct	Sum_%
HD-80_298.85	288	QMP-A	K	0.3	66.08	15.48	7.25	1.73	1.92	1.65	4.80	0.50	0.16	0.03	0.00	10.56	6.34	5.3	99.56
HD-80_328.7	288	QMP-A	K	0.24	69.68	16.13	3.96	1.59	1.55	1.34	4.74	0.44	0.15	0.03	0.00	10.48	6.29	4.6	99.64
HD-80_362.3	288	QMP-A	S-C	0.25	67.43	15.80	5.01	1.44	2.76	2.70	3.88	0.39	0.10	0.03	0.00	10.46	5.23	4.4	99.5
HD-80_383.9	288	QMP-A	S-C	0.31	64.49	16.64	6.31	1.92	3.21	2.77	3.73	0.47	0.16	0.03	0.00	10.48	6.29	4.6	99.75
HD-80_421.35	288	QMP-A	K	0.32	62.52	13.42	15.13	1.09	2.00	1.44	3.73	0.35	0.13	0.02	0.00	10.92	5.46	8.4	99.82
HD-80_451.75	288	QMP-A	S-C	0.33	66.88	16.48	4.06	1.63	3.41	3.33	3.36	0.44	0.16	0.05	0.00	10.29	6.17	2.8	99.76
HD-80_477.3	288	QMP-A	S-C	0.24	67.70	15.51	4.05	1.57	3.82	2.15	4.18	0.40	0.15	0.05	0.00	10.50	5.25	4.7	99.62
HD-80_510.95	288	QMP-A	S-C	0.31	66.41	16.78	3.78	1.64	3.93	2.99	3.62	0.45	0.15	0.06	0.00	10.27	6.16	2.6	99.78
HD-80_542.1	288	QMP-A	S-C	0.36	64.96	17.07	4.46	1.94	3.95	4.28	2.29	0.49	0.19	0.05	0.00	10.29	8.23	2.8	99.63
HD-80_570.6	288	QMP-A	F	0.32	67.48	17.28	2.63	1.62	3.41	4.83	1.94	0.47	0.16	0.03	0.00	10.20	6.12	2	99.81
HD-80_601.7	288	QMP-A	S-C	0.26	66.43	17.41	3.43	1.85	4.03	4.22	1.71	0.51	0.18	0.03	0.00	10.35	8.28	3.4	99.79
HD-80_632	288	QMP-A	P	0.25	64.51	16.35	2.48	1.74	8.72	4.14	1.22	0.47	0.17	0.03	0.00	10.44	7.31	4.2	99.81
HD-80_661.15	288	QMP-A	P	0.29	66.73	15.97	4.18	1.70	5.21	3.83	1.57	0.45	0.17	0.04	0.00	10.55	7.38	5.2	99.81
HD-80_691.6	288	QMP-A	S-C	0.23	65.76	17.29	3.94	1.78	3.49	3.73	3.03	0.51	0.16	0.03	0.00	10.26	8.21	2.5	99.77
HD-80_721.05	288	QMP-A	P	0.27	64.40	16.83	4.25	1.65	5.68	3.89	2.53	0.45	0.14	0.03	0.00	10.54	6.32	5.1	99.79
HD-80_752.55	288	QMP-A	S-C	0.29	63.81	16.42	6.50	1.77	4.24	3.31	3.02	0.46	0.16	0.05	0.00	10.52	6.31	4.9	99.78
HD-80_778.8	288	QMP-A	P	0.24	64.72	16.52	5.38	1.82	4.43	3.71	2.57	0.45	0.15	0.05	0.00	10.61	6.36	5.7	99.83

Table C.3a (cont)

Sample	Batch	Lithology	Alt.	Wght	SiO2_ pct	Al2O3_ pct	Fe2O3_ pct	MgO_ pct	CaO_ pct	Na2O_ pct	K2O_ pct	TiO2_ pct	P2O5_ pct	MnO_ pct	Cr2O3_ pct	Ni_ ppm	Sc_ ppm	LOI_ pct	Sum_%
HD-99_311.65	288	QMP-A	K	0.21	77.02	11.77	5.45	0.39	1.20	0.20	3.00	0.63	0.11	0.01	0.04	48.03	8.54	6.3	99.79
HD-99A_367.8	288	QMP-A	K	0.4	67.15	14.80	6.92	1.52	1.82	2.96	4.01	0.38	0.13	0.05	0.00	10.29	6.17	2.8	99.76
HD-99A_428.3	288	QMP-A	K	0.35	72.74	10.27	8.21	0.38	1.42	1.72	4.83	0.20	0.01	0.03	0.00	10.31	2.06	3	99.81
HD-99A_460.1	288	QMP-A	K	0.27	70.65	11.91	7.84	0.89	1.57	2.11	4.49	0.28	0.04	0.04	0.00	10.30	4.12	2.9	99.77
HD-99A_491.8	288	QMP-A	S-C	0.15	66.24	14.90	7.84	1.27	3.62	2.43	2.95	0.39	0.11	0.04	0.00	10.58	5.29	5.5	99.75
HD-94A_120.15	289	QMP-A	P	0.26	59.99	16.65	7.60	2.22	8.02	0.61	3.27	0.69	0.21	0.55	0.00	11.46	13.75	12.7	99.81
HD-94A_155.05	289	QMP-A	S	0.21	65.44	16.55	9.42	2.13	0.35	0.10	4.96	0.47	0.18	0.05	0.00	10.35	6.21	3.4	99.66
HD-94A_185	289	QMP-A	S	0.24	73.43	8.43	11.67	1.11	0.21	0.10	3.47	0.25	0.08	0.04	0.00	10.31	4.13	3	98.81
HD-94A_245	289	QMP-A	K	0.26	66.52	15.53	4.82	2.52	3.78	0.21	5.42	0.45	0.17	0.08	0.00	10.83	6.50	7.6	99.51
HD-94_423.9	289	QMP-A	K	0.29	68.69	13.86	6.56	1.33	1.92	2.03	4.87	0.35	0.12	0.06	0.00	10.21	5.11	2.1	99.79
HD-94_450.7	289	QMP-A	K	0.28	68.44	16.76	5.54	1.31	1.99	0.56	4.50	0.46	0.17	0.06	0.00	10.64	6.38	6	99.75
HD-01_31.8	289	QMP-A	S	0.23	79.60	9.57	4.92	0.16	0.03	0.06	2.40	0.23	0.03	0.01	0.00	10.52	4.21	4.8	97.02
HD-01_62.5	289	QMP-A	K	0.22	79.31	4.80	11.24	0.51	0.05	0.21	2.38	0.15	0.02	0.02	0.00	10.14	2.03	1.4	98.73
HD-01_92.6	289	QMP-A	K	0.27	75.09	6.97	12.31	1.14	0.05	0.08	3.26	0.17	0.03	0.04	0.00	10.49	2.10	4.6	99.13
HD-01_121.1	289	QMP-A	K	0.26	66.64	15.98	7.11	1.69	1.08	2.24	4.44	0.43	0.11	0.08	0.00	10.34	6.21	3.3	99.76
HD-01_154.4	289	QMP-A	K	0.27	68.33	12.84	8.94	1.44	0.74	1.79	5.05	0.33	0.10	0.06	0.00	10.24	5.12	2.3	99.62
HD-01_187	289	QMP-A	K	0.28	69.32	14.15	6.61	1.74	0.74	0.79	5.11	0.41	0.19	0.06	0.00	10.43	6.26	4.1	99.13
HD-01_214.85	289	QMP-A	K	0.33	48.37	12.62	27.16	1.64	1.13	1.59	5.81	0.76	0.26	0.07	0.00	23.21	7.39	5.2	99.39
HD-01_244.4	289	QMP-A	K	0.27	69.23	14.06	6.61	1.46	1.10	1.25	5.16	0.39	0.16	0.03	0.00	10.50	5.25	4.7	99.5

Table C.3a (cont)

Sample	Batch	Lithology	Alt.	Wght	SiO2_ pct	Al2O3_ pct	Fe2O3_ pct	MgO_ pct	CaO_ pct	Na2O_ pct	K2O_ pct	TiO2_ pct	P2O5_ pct	MnO_ pct	Cr2O3_ pct	Ni_ ppm	Sc_ ppm	LOI_ pct	Sum_%
HD-01_271.6	289	QMP-A	K	0.23	67.73	15.48	5.91	1.79	2.69	1.26	3.69	0.44	0.17	0.06	0.00	10.58	6.35	5.4	99.23
HD-60_3.6	289	QMP-A	S	0.31	73.00	10.29	12.32	0.41	0.06	0.07	2.99	0.65	0.06	0.01	0.00	10.40	6.24	3.8	99.84
HD-60_28.25	289	QMP-A	S	0.28	73.30	14.80	6.61	0.43	0.03	0.08	3.94	0.47	0.05	0.01	0.00	10.59	6.36	5.6	99.74
HD-60_60.15	289	QMP-A	S	0.2	67.14	17.20	6.05	1.94	1.03	1.79	3.78	0.48	0.17	0.06	0.00	10.47	6.28	4.5	99.67
HD-60_95.9	289	QMP-A	S	0.34	68.38	18.05	5.32	2.34	0.79	0.94	3.14	0.51	0.19	0.04	0.00	24.76	6.46	7.1	99.64
HD-60_125	289	QMP-A	S-C	0.32	67.61	17.04	5.31	2.00	2.25	2.40	2.43	0.48	0.19	0.05	0.00	10.47	6.28	4.5	99.8
HD-60_150.1	289	QMP-A	K	0.33	68.74	15.34	4.65	1.83	0.97	2.11	5.18	0.42	0.15	0.06	0.00	10.39	6.23	3.7	99.46
HD-60_181.7	289	QMP-A	S	0.27	69.25	14.78	7.36	1.77	0.60	0.42	4.57	0.38	0.14	0.12	0.00	23.62	5.37	6.8	99.43
HD-60_211.7	289	QMP-A	K	0.35	70.82	15.11	4.34	0.89	0.52	1.99	5.00	0.37	0.15	0.01	0.00	10.38	5.19	3.6	99.2
HD-60_241.7	289	QMP-A	K	0.33	68.20	15.02	7.14	1.39	1.06	1.31	4.90	0.38	0.13	0.02	0.00	10.54	5.27	5.1	99.54
HD-60_270.35	289	QMP-A	K	0.38	67.59	16.55	3.50	1.63	2.72	2.49	4.72	0.38	0.11	0.03	0.00	10.33	5.17	3.2	99.75
HD-60_300.5	289	QMP-A	K	0.27	67.58	16.29	3.32	1.64	2.58	1.98	5.60	0.42	0.12	0.04	0.00	10.40	6.24	3.8	99.6
HD-60_329.3	289	QMP-A	P	0.41	65.03	16.53	4.61	0.77	6.77	0.09	4.79	0.46	0.18	0.67	0.00	10.94	6.57	8.6	99.84
HD-60_360.05	289	QMP-A	S-C	0.33	67.17	16.30	4.17	1.03	5.05	0.27	4.95	0.43	0.15	0.24	0.00	10.73	6.44	6.8	99.73
HD-60_389.45	289	QMP-A	S-C	0.28	67.28	16.07	4.56	1.79	3.51	2.67	3.23	0.44	0.13	0.06	0.00	10.36	5.18	3.5	99.71
HD-60_420	289	QMP-A	S-C	0.28	65.70	16.86	4.63	2.02	3.66	3.01	3.25	0.45	0.17	0.04	0.00	10.35	6.21	3.4	99.74
HD-60_453	289	QMP-A	S-C	0.38	67.89	15.16	5.52	1.78	2.98	2.24	3.54	0.40	0.17	0.04	0.00	10.51	6.30	4.8	99.71
HD-60_482.1	289	QMP-A	K	0.27	73.59	13.23	4.62	1.30	1.20	1.36	3.94	0.35	0.13	0.04	0.00	10.46	4.18	4.4	99.76
HD-60_510	289	QMP-A	S-C	0.33	69.06	15.56	3.68	1.50	3.26	2.05	4.04	0.41	0.15	0.05	0.00	10.42	5.21	4	99.73

Table C.3a (cont)

Sample	Batch	Lithology	Alt.	Wght	SiO2_ pct	Al2O3_ pct	Fe2O3_ pct	MgO_ pct	CaO_ pct	Na2O_ pct	K2O_ pct	TiO2_ pct	P2O5_ pct	MnO_ pct	Cr2O3_ pct	Ni_ ppm	Sc_ ppm	LOI_ pct	Sum_%
HD-60_540.3	289	QMP-A	S-C	0.2	69.95	14.60	3.45	1.45	2.79	2.51	4.32	0.36	0.12	0.05	0.00	10.38	5.19	3.6	99.6
HD-60_570.4	289	QMP-A	S-C	0.26	68.78	15.56	3.81	1.30	3.34	2.84	3.54	0.39	0.12	0.05	0.00	10.28	5.14	2.7	99.71
HD-60_600	289	QMP-A	S-C	0.28	66.88	15.67	5.72	1.34	2.97	2.30	4.24	0.37	0.12	0.04	0.00	10.34	5.17	3.3	99.62
HD-60_630.35	289	QMP-A	S-C	0.41	67.42	15.44	4.13	1.43	4.13	2.79	3.77	0.39	0.13	0.06	0.00	10.34	5.17	3.3	99.7
HD-60_660.5	289	QMP-A	S-C	0.2	67.68	13.83	7.19	1.31	2.78	2.20	4.01	0.37	0.14	0.06	0.00	25.06	4.18	4.2	99.55
HD-60_690	289	QMP-A	S-C	0.2	81.24	8.71	2.65	0.79	1.82	1.33	2.96	0.22	0.08	0.04	0.00	10.27	3.08	2.6	99.8
HD-60_720	289	QMP-A	F	0.18	66.96	16.41	3.68	1.50	3.33	3.29	3.83	0.42	0.14	0.05	0.00	10.16	6.10	1.6	99.56
HD-60_750.45	289	QMP-A	F	0.18	66.76	15.87	4.65	1.38	3.59	3.15	3.68	0.41	0.13	0.05	0.00	10.19	5.10	1.9	99.66
HD-60_780.25	289	QMP-A	F	0.18	66.65	15.95	4.72	1.46	3.50	3.11	3.62	0.41	0.14	0.05	0.00	10.16	6.10	1.6	99.61
HD-60_797.9	289	QMP-A	S-C	0.18	65.12	17.06	6.23	0.71	4.04	0.57	4.87	0.46	0.18	0.31	0.00	10.74	6.45	6.9	99.59
HD-85_253.7	290	QMP-B	S-C	0.33	65.03	16.85	5.22	1.83	4.47	3.67	1.95	0.54	0.19	0.01	0.00	10.40	7.28	3.8	99.79
HD-85_283.8	290	QMP-B	S-C	0.3	64.44	17.20	5.06	1.86	4.45	4.16	1.86	0.57	0.20	0.02	0.00	10.36	8.29	3.5	99.8
HD-85_313.1	290	QMP-B	P	0.35	65.05	16.91	4.31	1.77	5.09	3.58	2.32	0.54	0.18	0.03	0.00	10.26	7.18	2.5	99.78
HD-85_465.55	290	QMP-B	P	0.34	57.12	16.51	8.31	3.73	7.29	3.79	1.69	0.93	0.25	0.10	0.01	69.58	14.54	3.7	99.72

Table C.3b. Litogeochemical Results for Alteration Geochemistry Analysis (Trace elements).Batch, observations, and unit in Table C.3a.

Sample	Ba_ppm	Be_ ppm	Co_ ppm	Cs_ ppm	Ga_ ppm	Hf_ ppm	Nb_ ppm	Rb_ ppm	Sn_ ppm	Sr_ppm	Ta_ ppm	Th_ ppm	U_ ppm	V_ppm	W_ ppm	Zr_ ppm	Y_ ppm	La_ ppm	Ce_ ppm	Pr_ ppm
HD-37_3.65	1038.85	3.14	7.32	2.19	15.36	2.93	5.75	85.49	4.18	27.28	0.42	6.90	1.88	95.11	12.02	110.37	9.20	12.44	23.41	2.50
HD-37_34	332.87	1.05	21.80	2.00	13.90	1.58	1.90	53.41	3.16	49.30	0.21	5.06	0.74	60.04	4.21	61.94	7.06	5.37	12.43	1.49
HD-37_64.6	616.06	2.04	12.26	2.25	14.00	1.63	2.55	84.18	0.51	88.37	0.20	7.05	1.12	79.69	1.53	74.99	8.79	11.03	21.56	2.36
HD-37_95.35	607.16	0.51	17.19	1.75	12.45	1.54	4.53	79.86	1.03	103.11	0.31	7.62	1.13	83.36	2.57	66.79	9.67	10.60	23.46	2.58
HD-37_127.3	798.60	0.52	10.19	6.97	14.77	2.70	3.85	126.24	2.08	142.25	0.31	9.67	2.08	67.59	3.43	100.66	9.98	8.94	17.57	1.97
HD-37_156.55	654.38	0.52	7.23	6.71	11.87	1.45	2.89	99.91	2.06	192.50	0.31	7.12	1.65	66.06	2.06	64.10	8.15	5.37	10.63	1.33
HD-37_186.8	778.92	4.19	6.92	6.29	13.31	2.73	4.72	120.35	1.05	277.81	0.42	7.97	1.99	78.63	3.25	105.36	14.68	11.22	22.43	2.50
HD-37_215.3	588.08	0.53	11.70	8.96	14.12	3.69	5.69	102.76	1.05	233.97	0.42	12.44	3.27	89.58	2.53	121.09	15.07	17.60	34.78	3.84
HD-37_245.15	618.82	3.13	6.98	5.73	15.21	3.33	7.29	101.78	1.04	399.52	0.52	13.23	4.48	71.88	1.67	130.12	14.90	23.86	46.36	4.70
HD-37_268.1	608.02	0.51	5.32	10.44	15.05	3.58	7.68	94.68	0.51	496.65	0.61	14.94	5.12	79.84	2.46	139.93	16.79	26.31	51.49	5.08
HD-38_38.75	608.42	0.53	7.88	2.52	12.92	2.84	6.73	83.64	1.05	201.44	0.42	10.51	3.36	78.81	3.05	115.38	12.08	21.33	42.77	4.72
HD-38_69.4	751.95	0.52	10.45	4.14	11.89	3.41	7.65	117.60	1.03	293.54	0.52	11.69	4.86	54.82	2.90	119.77	21.00	15.20	32.99	3.56
HD-38_100.95	1000.20	0.52	9.98	4.68	13.83	3.33	7.07	133.71	2.08	211.06	0.52	11.64	2.50	54.07	5.61	112.81	20.27	33.89	67.37	6.98
HD-38_129.9	727.93	2.09	11.26	4.28	13.77	3.96	6.15	92.29	1.04	400.36	0.52	13.45	3.96	88.64	5.32	145.48	18.35	28.78	54.96	5.44
HD-38_160.1	477.13	0.52	6.88	4.38	16.46	3.75	7.60	86.26	0.52	477.24	0.52	13.23	3.85	86.47	1.67	156.99	20.31	21.46	43.44	5.04
HD-38_221	641.52	3.16	8.41	9.57	15.04	3.68	7.78	107.17	1.05	419.20	0.53	12.94	4.31	88.34	2.31	125.89	17.14	28.18	53.64	5.42
HD-38_250.65	745.18	0.52	7.74	4.85	14.24	3.61	7.33	107.85	0.52	494.07	0.52	15.58	4.75	73.28	1.55	130.66	17.55	33.65	62.44	6.17
HD-38_280	782.82	0.52	11.44	4.57	14.76	3.85	8.52	110.61	0.52	550.37	0.62	13.00	4.26	92.53	4.26	145.44	18.71	34.00	64.25	6.98
HD-38_310	676.89	2.04	8.46	3.57	16.62	3.36	6.12	87.77	1.02	621.34	0.41	12.84	4.59	89.71	1.94	125.80	17.84	27.42	54.03	5.43
HD-38_341.6	837.64	0.53	20.07	4.54	14.15	2.64	4.01	121.68	2.11	331.78	0.42	11.30	2.11	72.88	4.75	107.85	12.04	11.41	24.19	2.64

Table C.3b. (cont)

Sample	Ba_ppm	Be_ ppm	Co_ ppm	Cs_ ppm	Ga_ ppm	Hf_ ppm	Nb_ ppm	Rb_ ppm	Sn_ ppm	Sr_ppm	Ta_ ppm	Th_ ppm	U_ ppm	V_ppm	W_ ppm	Zr_ ppm	Y_ ppm	La_ ppm	Ce_ ppm	Pr_ ppm
HD-38_371	742.36	0.52	12.17	3.71	17.63	2.37	3.30	113.42	1.03	435.72	0.31	9.07	2.06	121.66	2.17	102.07	8.15	9.38	18.04	1.90
HD-38_400.05	765.37	0.52	12.00	6.00	14.38	2.59	4.86	119.67	0.52	482.39	0.41	11.27	2.59	78.61	2.38	115.53	14.89	19.65	41.58	4.31
HD-38_431	668.91	0.52	37.61	4.38	13.96	2.29	2.92	115.55	2.08	243.18	0.31	8.75	2.19	80.23	3.13	88.67	9.38	8.86	17.92	1.92
HD-38_461.1	719.72	2.04	9.89	3.16	13.76	2.34	4.08	86.14	1.02	414.40	0.41	10.60	3.06	83.59	1.53	95.52	14.78	19.37	37.62	3.98
HD-38_490.85	718.41	0.51	17.96	3.16	15.00	2.65	6.53	91.94	0.51	511.97	0.51	13.78	4.49	73.47	3.06	110.21	17.35	21.94	43.78	4.66
HD-38_521	639.21	0.53	25.91	5.52	12.42	2.97	5.95	102.89	2.12	374.29	0.42	12.95	4.14	80.70	3.19	105.76	16.56	23.68	47.57	5.00
HD-38_550.7	713.45	0.51	7.93	3.66	15.45	2.95	6.50	93.60	0.51	490.88	0.51	11.79	4.27	77.24	2.64	127.04	17.18	21.44	41.97	4.47
HD-80_1.55	4621.30	0.52	0.52	1.97	14.11	3.01	4.77	112.47	4.15	31.65	0.31	7.26	0.62	95.46	5.81	99.92	3.01	11.21	17.33	1.68
HD-80_30	718.00	1.05	14.44	2.09	12.04	2.51	5.34	106.23	2.09	116.60	0.42	9.32	1.36	58.61	3.35	89.07	8.06	11.93	21.56	2.32
HD-80_60.7	634.96	0.52	15.30	4.27	13.84	3.44	6.66	117.42	1.04	156.76	0.52	11.03	2.81	83.27	3.33	112.42	17.18	25.81	47.78	5.06
HD-80_90.65	775.80	0.51	12.09	2.66	13.63	2.97	5.64	102.28	0.51	186.01	0.31	9.63	1.95	66.61	3.59	113.86	8.61	11.79	22.14	2.40
HD-80_119.7	772.87	1.04	27.32	5.51	13.92	3.53	6.86	173.27	1.04	148.13	0.42	10.80	2.08	87.26	5.19	123.51	16.00	23.58	44.46	4.79
HD-80_149.55	792.00	0.52	10.93	4.06	12.91	3.02	5.41	129.47	1.04	177.45	0.42	10.72	2.08	77.01	3.33	105.64	11.55	18.53	32.68	3.61
HD-80_181.3	945.22	2.11	11.63	8.56	13.74	3.91	7.61	153.94	1.06	232.39	0.53	13.43	3.81	69.78	7.40	131.10	14.59	50.64	86.70	8.14
HD-80_209.8	830.84	1.05	14.09	5.68	13.78	3.47	6.73	159.23	2.10	170.16	0.63	12.94	3.26	58.90	6.84	118.84	15.57	27.03	48.80	5.10
HD-80_238.7	778.54	2.10	15.55	5.67	13.45	3.78	6.51	138.90	0.53	274.22	0.53	12.40	3.36	61.99	5.78	123.66	15.13	24.69	47.81	4.95
HD-80_268.6	770.00	0.53	16.67	4.67	10.09	2.23	4.89	136.48	0.53	265.41	0.32	12.21	2.55	62.66	5.63	86.35	16.36	28.99	55.65	6.36
HD-80_298.85	794.28	0.53	27.25	3.80	14.05	3.27	7.18	131.18	2.11	272.30	0.53	11.83	2.43	108.79	7.92	113.65	16.05	21.55	42.04	4.66
HD-80_328.7	894.29	0.52	9.85	3.88	12.58	4.51	8.39	143.11	2.10	169.32	0.63	13.21	3.35	71.29	11.11	153.59	15.20	27.78	48.02	4.82

Table C.3b. (cont)

Sample	Ba_ppm	Be_ ppm	Co_ ppm	Cs_ ppm	Ga_ ppm	Hf_ ppm	Nb_ ppm	Rb_ ppm	Sn_ ppm	Sr_ppm	Ta_ ppm	Th_ ppm	U_ ppm	V_ppm	W_ ppm	Zr_ ppm	Y_ ppm	La_ ppm	Ce_ ppm	Pr_ ppm
HD-80_362.3	814.00	1.05	15.48	5.34	13.60	3.45	7.11	100.13	0.52	385.86	0.52	12.03	3.87	64.87	7.22	124.40	16.11	26.05	47.61	5.02
HD-80_383.9	819.81	2.10	16.56	11.01	15.31	3.35	7.65	112.91	1.05	445.44	0.52	13.63	4.72	80.72	5.45	109.55	16.14	26.42	48.22	5.27
HD-80_421.35	791.62	0.55	27.73	7.21	11.46	2.84	5.90	111.81	1.09	281.05	0.55	11.57	3.28	64.42	7.42	108.10	14.85	30.79	56.67	5.67
HD-80_451.75	687.29	2.06	5.25	3.81	14.61	2.98	7.20	101.65	0.51	500.45	0.62	14.20	4.01	76.14	3.50	114.62	16.67	29.43	53.71	5.71
HD-80_477.3	960.31	0.52	13.96	6.19	11.23	3.25	7.24	147.25	2.10	546.69	0.52	13.64	4.93	66.12	9.97	120.80	24.87	50.38	86.27	8.63
HD-80_510.95	798.81	4.11	6.06	8.32	15.71	4.21	8.32	121.88	0.51	534.02	0.62	15.09	5.24	77.01	4.21	137.79	17.76	37.27	59.55	5.75
HD-80_542.1	399.22	2.06	13.68	4.22	16.87	4.22	7.10	84.27	0.51	550.47	0.62	12.14	4.73	87.46	6.79	169.26	17.08	21.81	40.23	4.87
HD-80_570.6	281.64	3.06	6.22	3.37	14.80	3.16	7.14	71.53	0.51	500.73	0.51	12.86	7.14	77.55	9.49	116.02	20.72	30.92	62.15	6.70
HD-80_601.7	230.87	2.07	20.60	4.45	15.94	3.93	6.63	81.06	1.04	496.00	0.62	13.04	4.14	96.28	9.52	143.70	17.70	18.12	41.10	5.05
HD-80_632	231.75	2.09	7.10	2.61	15.24	3.76	7.20	58.36	0.52	605.17	0.63	12.42	4.59	86.65	8.04	150.12	20.04	24.74	55.85	5.98
HD-80_661.15	370.29	4.22	16.56	3.59	13.61	3.16	6.44	63.83	0.53	512.50	0.53	10.66	5.38	73.85	8.12	114.15	21.31	23.31	44.84	5.46
HD-80_691.6	915.95	0.51	9.95	2.77	15.18	3.80	6.15	93.34	1.03	486.59	0.51	11.49	5.85	90.26	12.10	128.73	17.85	30.57	55.18	5.75
HD-80_721.05	635.48	0.53	10.43	4.43	14.44	2.53	7.06	86.84	0.53	579.73	0.53	10.96	5.59	81.15	7.90	123.41	17.07	27.08	49.32	5.43
HD-80_752.55	628.88	0.53	12.62	4.10	14.93	2.94	7.57	100.75	0.53	389.42	0.63	10.73	4.52	83.08	5.89	124.51	15.88	23.14	41.33	4.69
HD-80_778.8	508.01	0.53	16.33	5.30	13.47	3.39	7.11	91.74	0.53	440.66	0.42	10.71	4.35	83.78	7.00	127.27	14.64	21.00	34.15	3.99
HD-99_311.65	543.30	1.07	8.43	3.42	12.06	3.20	11.42	111.86	2.13	75.25	0.85	5.66	2.35	122.75	4.38	119.55	22.20	24.55	47.29	5.04
HD-99A_367.8	663.63	0.51	4.42	4.73	15.64	3.50	6.69	103.40	0.51	383.57	0.51	10.49	2.37	73.05	2.47	127.07	15.12	13.07	29.22	3.30

Table C.3b. (cont)

Sample	Ba_ppm	Be_ ppm	Co_ ppm	Cs_ ppm	Ga_ ppm	Hf_ ppm	Nb_ ppm	Rb_ ppm	Sn_ ppm	Sr_ppm	Ta_ ppm	Th_ ppm	U_ ppm	V_ppm	W_ ppm	Zr_ ppm	Y_ ppm	La_ ppm	Ce_ ppm	Pr_ ppm
HD-99A_428.3	641.27	0.52	8.04	3.51	10.93	2.47	1.34	97.94	0.52	162.17	0.21	5.15	0.93	47.43	1.65	77.12	3.61	3.92	6.39	0.65
HD-99A_460.1	844.55	0.51	7.11	4.53	14.21	2.57	3.30	108.04	0.51	154.80	0.41	10.71	1.75	61.80	4.22	107.22	8.75	5.25	10.20	1.21
HD-99A_491.8	498.49	0.53	15.77	10.16	15.98	3.60	7.62	84.46	0.53	289.99	0.53	13.12	4.45	69.85	2.75	133.67	15.56	21.80	42.65	4.29
HD-94A_120.15	737.89	0.57	11.23	4.81	17.99	5.27	12.15	107.25	0.57	230.76	0.80	19.13	3.78	167.29	1.83	175.99	31.39	31.74	66.69	8.04
HD-94A_155.05	858.28	3.11	5.07	5.69	19.98	3.62	7.14	126.52	0.52	34.79	0.62	12.53	2.38	93.18	33.96	148.88	16.67	21.33	41.83	4.80
HD-94A_185	545.56	5.16	15.47	2.27	13.82	1.65	1.86	77.86	1.03	57.34	0.21	6.08	0.72	61.88	2.17	64.46	6.81	4.85	9.38	1.20
HD-94A_245	982.00	0.54	9.09	26.31	16.46	3.46	6.71	185.14	1.08	170.63	0.54	12.45	3.68	90.95	3.57	143.89	17.65	26.20	50.45	5.53
HD-94_423.9	701.77	3.06	6.44	4.29	12.97	2.96	3.17	103.48	1.02	336.17	0.31	9.50	2.04	61.29	4.29	85.60	11.03	8.99	17.98	2.29
HD-94_450.7	901.21	3.19	8.09	7.87	15.75	3.51	5.85	128.96	0.53	216.20	0.64	12.77	3.40	80.86	3.72	127.79	17.34	14.36	30.32	3.70
HD-01_31.8	446.07	2.10	31.25	1.16	11.15	1.37	3.26	46.08	2.10	61.44	0.32	4.84	1.47	57.86	1.89	50.08	7.15	12.84	26.20	3.10
HD-01_62.5	303.30	0.51	11.46	1.22	9.43	0.71	1.72	42.50	1.01	51.94	0.10	3.35	0.51	54.78	1.83	32.66	2.64	2.33	4.67	0.51
HD-01_92.6	420.51	2.10	21.50	2.83	11.54	1.15	1.89	80.75	3.15	42.37	0.21	4.61	0.73	50.34	2.20	54.85	4.51	3.46	6.50	0.79
HD-01_121.1	694.99	0.52	5.79	5.90	15.93	3.52	6.41	113.35	2.07	275.10	0.62	11.27	2.59	63.09	5.69	136.83	12.72	13.34	26.27	3.10
HD-01_154.4	832.21	2.05	6.24	5.94	13.31	3.38	4.09	102.77	1.02	251.40	0.41	12.28	1.84	62.44	2.56	105.64	10.85	8.91	16.99	2.04
HD-01_187	934.66	2.09	16.38	4.80	16.27	3.34	7.20	140.41	2.09	163.98	0.63	10.54	2.61	87.62	6.15	127.99	15.86	19.82	37.45	4.32
HD-01_214.85	694.33	4.22	29.02	5.59	21.42	2.43	5.70	138.65	3.17	201.54	0.42	15.62	2.00	250.08	4.01	100.88	20.05	11.92	26.91	3.58
HD-01_244.4	689.57	0.52	12.18	3.36	11.65	2.83	5.67	129.41	2.10	164.57	0.52	10.60	3.57	71.37	3.36	115.98	15.95	16.06	31.17	3.87
HD-01_271.6	743.46	4.23	14.59	6.24	14.38	3.49	6.45	122.57	3.17	258.68	0.53	12.27	2.86	78.26	3.81	131.03	15.55	20.30	39.66	4.67
HD-60_3.6	438.70	2.08	0.31	2.29	13.83	3.74	9.77	66.01	4.16	24.33	0.62	7.90	1.25	123.71	9.88	115.81	11.44	19.34	35.45	3.93

Table C.3b. (cont)

Sample	Ba_ppm	Be_ ppm	Co_ ppm	Cs_ ppm	Ga_ ppm	Hf_ ppm	Nb_ ppm	Rb_ ppm	Sn_ ppm	Sr_ppm	Ta_ ppm	Th_ ppm	U_ ppm	V_ppm	W_ ppm	Zr_ ppm	Y_ ppm	La_ ppm	Ce_ ppm	Pr_ ppm
HD-60_28.25	785.08	2.12	9.01	2.33	17.38	3.07	4.56	88.89	3.18	128.73	0.53	10.49	2.33	87.94	4.98	108.39	6.99	10.28	20.66	2.86
HD-60_60.15	648.27	0.52	11.10	5.86	14.03	3.25	7.12	121.80	1.05	289.99	0.63	10.26	3.35	70.17	2.83	112.16	17.07	20.32	39.90	4.61
HD-60_95.9	741.86	2.15	14.32	8.72	16.37	4.31	7.75	104.98	1.08	200.92	0.54	13.24	5.06	81.83	2.37	146.22	33.92	23.15	49.31	5.99
HD-60_125	542.46	2.09	8.17	7.54	15.29	4.08	8.06	96.55	2.09	371.76	0.52	12.99	4.61	91.11	3.35	129.02	16.23	25.87	49.95	5.89
HD-60_150.1	735.36	0.52	11.74	4.78	14.23	3.32	7.58	121.42	2.08	284.38	0.62	12.15	2.49	62.32	5.09	128.69	11.74	17.03	34.28	4.04
HD-60_181.7	609.70	3.22	19.64	15.03	11.27	3.97	6.12	137.83	3.22	171.96	0.43	12.24	2.15	50.45	4.08	132.57	11.16	22.00	43.15	4.91
HD-60_211.7	641.27	0.52	13.70	5.50	13.90	3.42	6.23	138.63	1.04	181.28	0.52	12.14	2.39	49.81	5.50	111.86	12.87	17.54	34.76	4.01
HD-60_241.7	739.91	0.53	16.65	3.48	11.80	3.79	7.27	138.07	2.11	179.08	0.53	12.02	2.42	62.19	5.90	124.58	10.96	14.23	27.40	3.44
HD-60_270.35	831.68	0.52	6.20	4.65	13.95	3.51	5.99	121.39	0.52	363.46	0.41	8.68	2.69	58.89	3.31	109.93	8.37	18.08	32.44	3.52
HD-60_300.5	932.58	0.52	7.59	3.95	14.04	3.43	8.53	163.23	1.04	348.08	0.52	12.06	3.74	75.90	3.74	136.51	17.15	36.49	62.90	6.46
HD-60_329.3	263.72	0.55	9.85	15.32	18.06	3.17	8.21	321.49	0.55	29.33	0.55	12.58	4.71	96.29	5.36	143.89	14.99	24.07	42.89	4.94
HD-60_360.05	389.56	2.15	12.88	10.84	15.99	3.22	7.30	331.50	0.54	67.18	0.54	10.62	3.33	85.85	5.37	126.21	14.92	24.04	43.79	4.90
HD-60_389.45	806.30	2.07	21.87	4.97	15.23	3.32	7.05	92.44	0.52	438.28	0.52	12.44	4.56	76.69	2.90	134.52	16.69	26.53	48.09	5.29
HD-60_420	747.48	0.52	9.94	7.14	16.88	3.93	7.45	105.81	0.52	468.57	0.62	12.11	3.83	84.89	3.00	126.41	17.91	24.85	48.45	5.28
HD-60_453	767.97	0.53	14.71	3.26	15.02	3.36	7.14	100.43	0.53	382.20	0.53	11.98	3.05	78.79	3.36	127.33	20.91	35.93	67.66	7.60
HD-60_482.1	654.88	0.52	11.19	3.35	12.66	2.30	5.54	112.04	1.05	157.23	0.42	13.08	3.03	66.95	6.07	91.75	11.30	18.20	32.95	3.77
HD-60_510	855.30	0.52	5.52	5.73	15.42	2.92	8.23	127.83	2.08	451.30	0.63	12.50	3.85	73.97	3.33	130.74	17.40	25.32	47.30	5.38
HD-60_540.3	863.2	5.19	7.47	4.25	14.11	2.91	7.47	133.53	0.52	404.31	0.52	9.96	3.01	62.25	2.70	121.70	14.73	24.49	44.09	4.99
HD-60_570.4	921.97	0.51	6.78	6.27	16.55	3.39	10.07	109.05	2.06	474.86	0.62	15.52	5.14	68.86	3.29	121.80	15.11	36.90	62.90	6.29
HD-60_600	1183.19	2.07	7.45	10.65	16.03	3.62	8.27	145.52	1.03	401.19	0.62	12.82	4.14	70.33	4.96	119.25	15.41	32.37	58.54	5.86

Table C.3b. (cont)

Sample	Ba_ppm	Be_ ppm	Co_ ppm	Cs_ ppm	Ga_ ppm	Hf_ ppm	Nb_ ppm	Rb_ ppm	Sn_ ppm	Sr_ppm	Ta_ ppm	Th_ ppm	U_ ppm	V_ppm	W_ ppm	Zr_ ppm	Y_ ppm	La_ ppm	Ce_ ppm	Pr_ ppm
HD-60_630.35	1061.12	0.52	6.41	6.41	16.24	3.41	8.07	110.66	0.52	610.30	0.62	12.62	4.45	74.46	2.28	124.00	16.96	28.23	52.23	5.53
HD-60_660.5	1076.41	0.52	13.68	8.87	12.84	3.24	8.56	132.18	1.04	436.31	0.42	13.16	3.24	75.17	5.95	122.36	16.81	34.35	62.33	6.42
HD-60_690	711.54	1.03	5.96	4.52	7.91	1.85	6.47	87.79	0.51	207.20	0.51	7.60	1.64	35.94	4.11	77.11	10.47	18.79	34.19	3.52
HD-60_720	887.26	4.07	6.30	5.59	16.06	3.35	8.23	114.03	0.51	552.58	0.71	14.03	4.47	72.16	4.78	126.64	17.48	32.42	59.15	6.16
HD-60_750.45	920.55	1.02	12.64	4.38	15.19	3.57	7.75	104.90	1.02	583.02	0.61	14.99	5.10	68.30	3.47	121.31	16.41	37.52	64.33	6.41
HD-60_780.25	864.89	3.05	6.50	3.35	14.13	3.35	7.62	106.71	0.51	546.07	0.51	14.03	4.57	74.19	6.30	125.11	16.26	30.49	53.76	5.43
HD-60_797.9	354.57	0.54	5.59	28.04	16.98	3.12	6.88	308.58	4.30	84.99	0.43	16.22	5.16	74.14	7.31	126.57	17.73	39.54	67.58	6.84
HD-85_253.7	808.80	4.16	11.02	2.81	17.05	3.95	8.52	49.07	2.08	550.77	0.73	13.20	4.47	89.40	1.77	156.56	20.58	32.12	62.58	6.42
HD-85_283.8	690.21	2.07	8.29	3.73	17.62	4.04	10.05	51.09	0.52	570.20	0.62	10.88	4.04	94.31	1.97	146.33	20.31	33.89	67.05	6.77
HD-85_313.1	845.18	0.51	6.56	1.33	16.82	3.49	9.13	53.75	0.51	545.77	0.62	13.95	4.82	88.21	1.44	145.96	20.51	33.44	66.36	6.73
HD-85_465.55	594.04	2.08	24.51	1.56	17.45	3.63	12.05	41.33	1.04	623.33	0.62	10.90	3.95	171.36	2.39	155.78	31.05	36.76	72.49	8.04

Table C.3c. Litogeochemical Results for Alteration Geochemistry Analysis (Trace elements continuation and Total C and S).Batch, observations, and unit in Table C.3a.

Sample	Nd_ppm	Sm_ppm	Eu_ppm	Gd_ppm	Tb_ppm	Dy_ppm	Ho_ppm	Er_ppm	Tm_ppm	Yb_ppm	Lu_ppm	C_pct	S_pct
HD-37_3.65	10.66	1.78	0.30	1.62	0.24	1.54	0.30	1.07	0.17	1.13	0.19	0.03	2.22
HD-37_34	6.21	1.30	0.32	1.27	0.21	1.14	0.25	0.81	0.12	0.81	0.11	0.01	5.88
HD-37_64.6	9.40	1.75	0.43	1.63	0.25	1.40	0.32	0.98	0.10	0.85	0.14	0.01	1.74
HD-37_95.35	8.85	2.05	0.51	1.91	0.29	1.66	0.32	0.91	0.15	0.81	0.14	0.06	3.03
HD-37_127.3	7.69	1.59	0.50	1.58	0.29	1.64	0.35	1.11	0.19	1.13	0.21	0.10	2.31
HD-37_156.55	5.47	1.29	0.38	1.19	0.24	1.29	0.30	1.00	0.17	1.20	0.19	0.14	1.34
HD-37_186.8	10.38	2.26	0.73	2.35	0.38	2.44	0.48	1.69	0.24	1.70	0.30	0.16	3.17
HD-37_215.3	14.54	2.97	0.80	2.86	0.45	2.75	0.56	1.76	0.27	1.61	0.30	0.15	3.22
HD-37_245.15	19.59	3.09	0.90	2.94	0.47	2.56	0.56	1.63	0.28	1.70	0.30	0.19	1.86
HD-37_268.1	19.65	3.54	0.86	3.06	0.46	2.90	0.55	1.66	0.26	1.73	0.31	0.07	0.39
HD-38_38.75	19.33	3.68	0.98	3.11	0.46	2.60	0.54	1.36	0.21	1.39	0.24	0.01	2.41
HD-38_69.4	15.20	3.42	1.07	3.90	0.69	3.64	0.80	2.32	0.34	2.01	0.34	0.03	1.83
HD-38_100.95	26.41	4.90	1.06	4.03	0.59	3.16	0.62	1.77	0.28	1.60	0.28	0.03	1.76
HD-38_129.9	22.11	3.83	1.01	3.16	0.51	3.16	0.62	1.79	0.30	1.93	0.34	0.01	1.81
HD-38_160.1	20.94	3.99	1.03	3.17	0.56	3.45	0.70	2.06	0.34	2.14	0.38	0.05	1.98
HD-38_221	19.98	3.48	0.91	3.09	0.47	2.40	0.57	1.87	0.28	1.71	0.28	0.13	2.38
HD-38_250.65	22.40	3.83	0.94	3.46	0.50	2.64	0.60	1.75	0.26	1.82	0.28	0.23	0.56
HD-38_280	26.30	4.72	1.08	4.01	0.61	3.50	0.72	2.30	0.31	2.11	0.32	0.04	1.34
HD-38_310	19.98	3.69	0.10	3.61	0.53	2.75	0.61	1.92	0.30	1.95	0.31	0.04	0.65
HD-38_341.6	11.20	2.20	0.61	2.07	0.35	2.02	0.43	1.33	0.21	1.53	0.25	0.05	5.77
HD-38_371	8.15	1.57	0.62	1.56	0.26	1.62	0.27	0.92	0.16	0.84	0.18	0.05	2.32
HD-38_400.05	16.76	3.23	0.80	2.70	0.42	2.52	0.47	1.46	0.23	1.46	0.27	0.09	1.71
HD-38_431	8.86	1.47	0.45	1.58	0.25	1.26	0.33	0.88	0.14	1.13	0.17	0.08	3.90
HD-38_461.1	14.68	2.94	0.80	2.56	0.42	2.27	0.50	1.39	0.23	1.37	0.24	0.05	0.85
HD-38_490.85	18.37	3.16	0.91	2.97	0.47	2.68	0.56	1.80	0.27	1.72	0.30	0.05	1.33
HD-38_521	17.41	3.60	0.87	3.28	0.50	2.85	0.53	1.66	0.28	1.45	0.32	0.17	5.91
HD-38_550.7	17.89	3.21	0.91	2.91	0.47	2.55	0.58	1.72	0.27	1.70	0.29	0.06	0.74
HD-80_1.55	4.77	0.85	0.09	0.77	0.11	0.61	0.13	0.29	0.05	0.40	0.07	0.06	0.11
HD-80_30	9.00	1.70	0.50	1.67	0.27	1.59	0.35	0.85	0.13	0.82	0.14	0.06	3.90
HD-80_60.7	20.82	3.73	1.05	3.37	0.56	3.12	0.58	1.83	0.23	1.55	0.29	0.01	1.83

Table C.3c. (cont)

Sample	Nd_ppm	Sm_ppm	Eu_ppm	Gd_ppm	Tb_ppm	Dy_ppm	Ho_ppm	Er_ppm	Tm_ppm	Yb_ppm	Lu_ppm	C_pct	S_pct
HD-80_90.65	10.15	1.74	0.48	1.74	0.28	1.31	0.32	0.84	0.15	0.98	0.15	0.01	1.54
HD-80_119.7	18.39	3.12	0.86	3.18	0.48	2.71	0.57	1.82	0.25	1.66	0.28	0.01	2.65
HD-80_149.55	12.59	2.44	0.69	2.08	0.36	1.95	0.43	1.28	0.20	1.40	0.17	0.01	3.37
HD-80_181.3	27.38	4.24	1.06	3.47	0.51	2.48	0.60	1.70	0.27	1.79	0.27	0.13	3.17
HD-80_209.8	19.04	3.09	0.91	2.90	0.44	2.43	0.53	1.52	0.26	1.56	0.27	0.16	3.02
HD-80_238.7	18.91	3.41	0.91	2.88	0.47	2.44	0.54	1.73	0.25	1.55	0.28	0.19	2.20
HD-80_268.6	23.90	4.34	0.91	3.76	0.54	2.80	0.52	1.62	0.24	1.77	0.23	0.46	3.93
HD-80_298.85	17.43	3.64	0.90	3.02	0.49	2.38	0.58	1.90	0.24	1.81	0.30	0.15	3.34
HD-80_328.7	17.09	2.95	0.91	2.86	0.44	2.40	0.52	1.78	0.26	1.89	0.28	0.22	1.85
HD-80_362.3	17.47	3.37	0.93	2.65	0.45	2.35	0.53	1.73	0.24	1.54	0.27	0.23	2.25
HD-80_383.9	18.35	3.52	0.91	2.99	0.48	2.83	0.62	1.79	0.27	1.95	0.30	0.13	2.97
HD-80_421.35	20.09	3.48	0.81	3.20	0.47	2.54	0.57	1.41	0.21	1.75	0.26	0.11	10.68
HD-80_451.75	20.99	3.75	0.99	3.37	0.50	2.91	0.60	1.75	0.29	1.85	0.31	0.11	0.81
HD-80_477.3	33.16	5.30	1.44	4.73	0.72	4.09	0.85	2.50	0.39	2.46	0.43	0.22	1.81
HD-80_510.95	21.87	3.58	0.98	3.28	0.51	2.77	0.64	1.87	0.29	2.14	0.33	0.13	0.79
HD-80_542.1	18.83	3.93	0.98	3.20	0.54	2.58	0.67	1.90	0.28	2.09	0.32	0.06	1.50
HD-80_570.6	24.08	4.52	1.26	4.07	0.62	3.10	0.72	1.89	0.34	2.16	0.36	0.07	0.81
HD-80_601.7	20.50	4.39	1.02	3.43	0.59	2.99	0.64	2.02	0.29	1.74	0.31	0.06	1.46
HD-80_632	24.11	4.45	1.05	3.77	0.58	2.81	0.70	1.93	0.32	2.23	0.32	0.40	2.29
HD-80_661.15	21.84	5.00	0.97	4.26	0.71	3.72	0.72	2.30	0.36	2.10	0.34	0.09	2.64
HD-80_691.6	21.13	3.81	0.99	3.74	0.55	2.82	0.65	1.93	0.30	2.18	0.36	0.05	1.61
HD-80_721.05	19.60	3.56	1.06	3.39	0.50	2.58	0.53	1.59	0.22	1.58	0.24	0.05	2.73
HD-80_752.55	19.03	3.47	0.84	3.10	0.47	2.60	0.54	1.49	0.22	2.09	0.25	0.25	3.08
HD-80_778.8	15.27	2.78	0.74	2.88	0.42	2.81	0.55	1.50	0.22	1.53	0.25	0.19	2.87
HD-99_311.65	19.00	3.68	0.95	3.78	0.69	4.00	0.88	2.60	0.39	2.55	0.37	0.01	3.93
HD-99A_367.8	13.27	2.74	0.77	2.75	0.41	2.41	0.49	1.49	0.24	1.50	0.26	0.06	1.23
HD-99A_428.3	2.99	0.54	0.35	0.48	0.07	0.52	0.13	0.33	0.04	0.51	0.07	0.28	2.32
HD-99A_460.1	5.66	1.16	0.46	1.22	0.22	1.36	0.29	1.08	0.15	1.18	0.16	0.30	1.11
HD-99A_491.8	17.04	3.01	0.96	2.74	0.46	2.68	0.48	1.53	0.21	1.74	0.25	0.53	3.32
HD-94A_120.15	28.87	6.16	1.43	5.34	0.85	4.54	1.04	2.82	0.44	2.56	0.46	1.76	0.25
HD-94A_155.05	18.74	3.59	0.87	3.14	0.46	2.57	0.53	1.59	0.23	1.78	0.23	0.04	0.30

Table C.3c. (cont)

Sample	Nd_ppm	Sm_ppm	Eu_ppm	Gd_ppm	Tb_ppm	Dy_ppm	Ho_ppm	Er_ppm	Tm_ppm	Yb_ppm	Lu_ppm	C_pct	S_pct
HD-94A_185	5.05	1.09	0.28	1.14	0.17	0.84	0.23	0.65	0.09	0.83	0.11	0.06	3.24
HD-94A_245	19.92	3.82	0.94	3.53	0.52	3.11	0.55	1.71	0.26	1.79	0.28	0.57	1.36
HD-94_423.9	8.27	2.03	0.62	2.06	0.37	2.26	0.46	1.33	0.23	1.47	0.23	0.08	1.18
HD-94_450.7	14.68	3.03	0.80	2.86	0.47	2.80	0.63	1.70	0.29	2.21	0.30	0.29	1.88
HD-01_31.8	12.62	2.31	0.55	1.79	0.27	1.17	0.24	0.72	0.11	0.75	0.13	0.04	3.90
HD-01_62.5	2.54	0.39	0.14	0.42	0.07	0.36	0.09	0.24	0.04	0.29	0.04	0.11	1.67
HD-01_92.6	3.46	0.70	0.21	0.76	0.12	0.73	0.17	0.45	0.06	0.56	0.07	0.01	6.71
HD-01_121.1	12.93	2.62	0.72	2.36	0.36	2.19	0.48	1.50	0.22	1.80	0.26	0.21	0.74
HD-01_154.4	8.60	1.89	0.55	1.80	0.31	1.84	0.35	1.21	0.18	1.23	0.24	0.11	0.96
HD-01_187	15.96	2.95	0.82	2.96	0.43	2.49	0.48	1.32	0.22	1.50	0.23	0.05	2.72
HD-01_214.85	14.14	3.41	0.61	3.39	0.56	3.28	0.64	2.16	0.31	2.30	0.34	0.07	6.66
HD-01_244.4	15.53	3.10	0.79	2.68	0.42	2.20	0.50	1.47	0.24	1.60	0.24	0.10	3.73
HD-01_271.6	18.51	3.44	0.84	2.94	0.44	2.75	0.49	1.50	0.23	1.70	0.23	0.24	2.84
HD-60_3.6	15.28	2.37	0.41	2.06	0.31	1.81	0.36	1.26	0.18	1.44	0.21	0.03	0.04
HD-60_28.25	12.93	3.68	1.12	3.34	0.37	1.49	0.33	0.96	0.14	1.03	0.21	0.01	3.05
HD-60_60.15	18.96	3.60	1.03	3.41	0.52	3.20	0.67	2.05	0.30	2.39	0.34	0.02	2.14
HD-60_95.9	25.95	5.92	1.70	6.57	1.06	6.01	1.23	3.49	0.53	3.31	0.47	0.02	2.06
HD-60_125	20.53	3.97	1.05	3.41	0.57	3.18	0.65	1.83	0.29	2.19	0.30	0.01	1.85
HD-60_150.1	15.48	2.96	0.79	2.49	0.36	2.19	0.41	1.26	0.21	1.39	0.22	0.14	1.70
HD-60_181.7	18.36	2.98	0.82	2.72	0.40	2.39	0.44	1.28	0.18	1.38	0.23	0.32	2.92
HD-60_211.7	16.29	3.04	0.78	2.68	0.38	2.06	0.45	1.36	0.22	1.35	0.25	0.03	2.37
HD-60_241.7	12.54	2.28	0.72	2.11	0.33	1.82	0.44	1.26	0.19	1.42	0.22	0.07	3.94
HD-60_270.35	11.78	2.20	0.77	1.84	0.30	1.91	0.32	1.14	0.15	1.21	0.20	0.11	1.11
HD-60_300.5	22.25	3.68	1.05	3.20	0.47	2.61	0.52	1.71	0.24	1.68	0.24	0.18	1.06
HD-60_329.3	18.82	3.32	0.95	2.81	0.44	2.72	0.50	1.39	0.25	1.53	0.24	1.47	2.89
HD-60_360.05	19.53	3.11	0.92	2.88	0.41	2.55	0.52	1.31	0.20	1.65	0.25	1.01	2.29
HD-60_389.45	19.28	3.54	0.88	3.10	0.46	2.46	0.55	1.50	0.25	1.84	0.27	0.12	0.98
HD-60_420	19.36	3.72	0.96	3.03	0.46	2.76	0.62	1.70	0.26	1.70	0.28	0.10	1.05
HD-60_453	31.83	4.95	1.13	4.07	0.59	3.52	0.75	2.08	0.34	2.16	0.35	0.13	1.70
HD-60_482.1	12.24	2.41	0.63	2.44	0.32	2.08	0.39	1.10	0.17	1.36	0.20	0.15	2.23
HD-60_510	20.11	3.38	0.98	3.00	0.47	2.59	0.54	1.63	0.26	1.78	0.26	0.18	0.73

Table C.3c. (cont)

Sample	Nd_ppm	Sm_ppm	Eu_ppm	Gd_ppm	Tb_ppm	Dy_ppm	Ho_ppm	Er_ppm	Tm_ppm	Yb_ppm	Lu_ppm	C_pct	S_pct
HD-60_540.3	19.61	3.33	0.86	2.79	0.43	2.27	0.49	1.50	0.22	1.53	0.25	0.21	0.77
HD-60_570.4	20.35	3.30	0.91	3.21	0.48	2.58	0.56	1.68	0.27	1.56	0.29	0.16	0.65
HD-60_600	22.13	3.81	0.94	3.06	0.51	2.65	0.58	1.69	0.30	1.71	0.30	0.11	2.40
HD-60_630.35	21.41	3.71	0.99	3.16	0.52	2.65	0.58	1.79	0.27	1.80	0.34	0.24	0.75
HD-60_660.5	22.55	3.72	1.02	3.38	0.48	2.99	0.53	1.60	0.25	1.82	0.26	0.16	2.70
HD-60_690	12.83	2.29	0.62	2.01	0.31	1.70	0.32	1.15	0.16	0.95	0.16	0.23	0.64
HD-60_720	20.63	3.75	1.02	3.43	0.54	3.04	0.59	1.96	0.30	2.03	0.30	0.05	0.60
HD-60_750.45	23.45	3.89	1.03	3.27	0.51	2.70	0.59	1.83	0.28	1.89	0.32	0.05	1.25
HD-60_780.25	19.21	3.43	1.02	3.19	0.50	3.12	0.58	1.67	0.28	1.78	0.32	0.05	1.28
HD-60_797.9	26.00	4.35	1.46	3.81	0.59	2.87	0.66	2.00	0.31	1.99	0.32	0.80	3.80
HD-85_253.7	25.89	4.48	1.20	4.02	0.61	3.72	0.69	2.14	0.34	2.20	0.33	0.08	3.43
HD-85_283.8	26.74	4.50	1.41	3.99	0.59	3.75	0.74	2.03	0.35	1.90	0.33	0.11	2.93
HD-85_313.1	25.23	4.40	1.22	3.87	0.62	3.64	0.78	2.04	0.33	2.23	0.35	0.02	2.10
HD-85_465.55	30.12	6.48	1.69	6.14	0.93	5.61	1.12	2.92	0.48	3.24	0.49	0.12	3.35

Table C.3d. Lithogeochemical Results for Alteration Geochemistry Analysis (Pathfinder elements).Batch, observations, and unit in Table C.3a.

Sample	Mo_ppm	Cu_ppm	Pb_ppm	Zn_ppm	Ni2_ppm	As_ppm	Cd_ppm	Sb_ppm	Bi_ppm	Ag_ppm	Au_ppb	Hg_ppm	Tl_ppm	Se_ppm
HD-37_3.65	29.37	2515.20	9.72	9.41	4.18	47.34	0.05	1.67	2.40	6.27	569.70	0.13	0.21	31.88
HD-37_34	1.05	10533.89	8.01	14.75	27.60	10.96	0.63	1.90	0.95	3.37	772.65	0.02	2.21	10.01
HD-37_64.6	9.81	8053.34	5.41	58.23	4.39	1.43	0.20	0.51	0.72	2.35	716.80	0.01	0.61	4.39
HD-37_95.35	9.36	7160.35	13.58	62.77	6.38	1.44	0.41	0.72	0.93	1.96	685.37	0.02	0.62	4.43
HD-37_127.3	4.68	5988.47	22.56	133.10	10.19	2.50	0.73	0.73	1.46	1.77	851.01	0.01	1.14	4.99
HD-37_156.55	5.37	2929.04	19.92	196.11	5.26	1.24	0.93	0.83	1.03	0.93	388.30	0.01	0.93	2.17
HD-37_186.8	7.55	654.06	13.94	71.29	3.98	1.15	0.21	0.42	0.84	0.31	45.18	0.01	0.94	2.83
HD-37_215.3	26.03	1488.02	9.91	49.53	3.90	1.58	0.21	0.32	2.00	0.74	124.68	0.01	0.74	3.48
HD-37_245.15	6.56	906.87	16.25	57.30	4.27	1.56	0.21	0.42	1.46	0.52	106.37	0.01	0.52	1.67
HD-37_268.1	6.24	497.47	3.48	27.64	3.38	1.43	0.05	0.10	0.41	0.20	55.17	0.01	0.82	0.51
HD-38_38.75	3.15	5331.07	6.41	8.41	3.05	0.26	0.42	0.21	0.42	1.16	369.57	0.01	0.84	2.94
HD-38_69.4	24.00	3690.57	10.34	23.79	6.00	0.26	1.03	0.62	0.31	0.62	312.37	0.01	1.24	2.90
HD-38_100.95	29.53	2767.61	10.81	63.42	6.55	0.26	0.21	0.21	0.52	0.62	283.32	0.01	0.52	3.64
HD-38_129.9	7.30	751.19	6.36	22.94	5.11	0.63	0.05	0.21	0.31	0.21	45.05	0.01	0.83	1.98
HD-38_160.1	5.73	643.50	8.13	37.50	4.48	1.77	0.21	0.42	0.52	0.31	95.32	0.01	0.63	1.25
HD-38_221	46.06	682.53	9.25	38.91	3.16	1.37	0.05	0.32	1.16	0.21	75.09	0.01	0.32	2.42
HD-38_250.65	63.16	1032.10	3.82	27.87	3.10	1.44	0.05	0.05	0.41	0.41	71.11	0.01	0.62	1.24
HD-38_280	4.78	369.79	4.16	24.95	3.85	1.14	0.05	0.05	0.31	0.10	47.51	0.01	0.73	1.66
HD-38_310	3.87	473.21	4.69	39.76	3.26	1.22	0.05	0.05	0.61	0.20	112.03	0.01	0.51	0.61
HD-38_341.6	44.47	3447.32	7.39	35.91	8.45	0.85	0.11	0.11	1.80	1.27	179.99	0.01	0.53	5.39
HD-38_371	15.88	1994.67	7.11	52.58	7.32	1.55	0.21	0.31	1.24	0.93	480.88	0.01	0.31	3.09
HD-38_400.05	9.41	2197.01	7.24	47.58	5.69	1.03	0.21	0.10	0.62	0.72	164.66	0.01	0.52	2.90
HD-38_431	10.63	3973.87	5.21	33.34	9.06	0.73	0.10	0.05	1.15	1.35	181.29	0.01	0.21	4.69
HD-38_461.1	7.03	1116.27	3.77	34.66	3.77	1.43	0.05	0.20	0.31	0.31	117.23	0.01	0.20	1.73
HD-38_490.85	42.25	996.49	8.57	65.31	3.98	1.63	0.41	0.20	0.51	0.41	86.94	0.01	0.31	2.14
HD-38_521	4.46	1939.71	11.15	63.71	12.21	2.12	0.42	0.11	1.49	0.96	115.74	0.01	0.21	6.37
HD-38_550.7	2.24	868.44	5.49	45.73	5.39	1.42	0.10	0.10	0.20	0.41	71.24	0.01	0.51	1.22
HD-80_1.55	290.52	371.14	23.66	3.11	2.80	17.22	0.05	1.87	1.56	19.51	829.12	0.15	0.21	12.87
HD-80_30	23.44	10466.60	6.80	5.23	5.86	1.15	0.05	0.63	1.78	2.20	485.02	0.01	0.52	5.44
HD-80_60.7	258.46	5503.96	14.57	65.58	6.25	0.26	0.73	0.94	0.73	1.56	471.22	0.01	0.83	3.64
HD-80_90.65	70.82	6981.19	78.71	87.11	5.84	1.33	0.20	1.33	1.84	1.74	752.33	0.01	0.51	3.38

Table C.3d. (cont).

Sample	Mo_ppm	Cu_ppm	Pb_ppm	Zn_ppm	Ni2_ppm	As_ppm	Cd_ppm	Sb_ppm	Bi_ppm	Ag_ppm	Au_ppb	Hg_ppm	Tl_ppm	Se_ppm
HD-80_119.7	37.71	7171.10	40.10	101.80	22.23	242.56	0.42	21.71	1.66	1.66	735.79	0.45	0.62	3.84
HD-80_149.55	120.00	2169.73	6.14	36.43	3.95	2.81	0.21	1.14	0.73	0.62	295.26	0.01	0.62	3.23
HD-80_181.3	416.89	1077.17	19.56	72.95	2.75	13.96	0.05	1.59	0.85	0.42	118.42	0.01	0.74	2.75
HD-80_209.8	97.70	1630.87	8.20	36.81	3.58	1.68	0.05	3.26	0.74	0.42	114.11	0.01	0.42	3.37
HD-80_238.7	123.14	2746.00	6.09	42.03	3.68	1.47	0.05	1.47	0.32	0.74	222.63	0.01	0.42	3.05
HD-80_268.6	3.50	5638.33	32.07	73.28	5.95	1.27	0.53	1.38	1.70	2.44	628.43	0.01	0.11	6.05
HD-80_298.85	4.75	2757.18	3.59	23.24	4.86	0.26	0.05	1.06	0.42	0.84	267.01	0.01	0.63	5.70
HD-80_328.7	19.81	1962.19	9.85	25.16	2.83	0.73	0.05	0.84	0.31	0.52	154.22	0.01	0.21	2.52
HD-80_362.3	2.09	3120.70	4.60	18.83	4.29	1.36	0.10	1.36	0.31	0.94	142.82	0.01	0.21	3.35
HD-80_383.9	2.20	695.37	3.77	23.06	3.04	2.83	0.05	0.63	0.21	0.21	73.17	0.01	0.63	2.31
HD-80_421.35	24.24	564.50	6.22	10.92	3.71	4.04	0.05	0.55	5.02	0.22	51.97	0.01	0.22	8.95
HD-80_451.75	4.22	820.43	3.60	26.75	2.47	1.13	0.05	0.21	0.10	0.31	54.22	0.01	0.21	0.62
HD-80_477.3	191.85	1409.60	6.61	20.99	3.99	1.47	0.05	0.31	0.52	0.52	102.22	0.01	0.10	3.15
HD-80_510.95	5.03	411.11	4.11	25.67	2.57	0.92	0.05	0.31	0.05	0.21	33.37	0.01	0.51	1.23
HD-80_542.1	14.10	1942.08	3.60	39.10	4.42	1.13	0.31	0.62	0.10	0.72	91.06	0.01	0.62	2.26
HD-80_570.6	92.55	522.88	7.86	27.55	2.65	1.63	0.20	1.33	0.05	0.20	30.72	0.01	0.31	0.92
HD-80_601.7	43.17	788.26	4.97	22.78	6.73	1.66	0.05	1.14	0.05	0.31	45.45	0.01	0.31	2.07
HD-80_632	62.11	410.06	4.59	20.88	3.13	1.15	0.05	0.21	0.05	0.21	60.03	0.01	0.21	0.94
HD-80_661.15	14.66	467.45	7.91	23.21	3.80	1.27	0.05	0.63	0.05	0.21	35.24	0.01	0.11	2.95
HD-80_691.6	13.95	375.10	12.62	31.80	3.08	0.82	0.21	0.10	0.05	0.10	17.64	0.01	0.51	3.08
HD-80_721.05	32.14	429.24	3.90	18.97	2.63	0.95	0.05	0.21	0.05	0.11	21.29	0.01	0.42	2.11
HD-80_752.55	7.47	564.31	19.14	37.86	3.37	1.05	0.21	0.32	0.11	0.21	32.81	0.01	0.21	3.05
HD-80_778.8	8.17	483.61	7.53	23.33	3.50	1.06	0.05	0.32	0.21	0.21	16.01	0.01	0.11	3.18
HD-99_311.65	51.88	1271.36	14.73	11.74	44.30	15.48	0.05	0.43	1.07	0.43	242.72	0.05	0.21	2.88
HD-99A_367.8	9.88	1003.26	7.00	28.81	8.64	3.19	0.05	0.51	0.41	0.41	71.92	0.01	0.51	0.72
HD-99A_428.3	3.61	1150.89	15.16	11.34	12.58	0.52	0.05	0.05	0.52	0.52	160.22	0.01	0.21	1.55
HD-99A_460.1	12.36	1014.80	6.69	24.72	7.11	0.62	0.05	0.05	0.21	0.31	108.56	0.01	0.21	1.13
HD-99A_491.8	5.19	1318.29	17.67	25.40	7.94	1.16	0.05	0.11	1.06	0.53	107.11	0.01	0.21	1.80
HD-94A_120.15	1.60	32.43	4.35	61.87	6.07	2.64	0.06	0.06	0.06	0.06	2.29	0.01	0.06	0.29
HD-94A_155.05	9.94	1446.14	11.49	88.00	5.28	1.97	0.05	0.52	0.31	0.41	151.36	0.01	1.55	0.72
HD-94A_185	12.79	10037.24	7.73	57.75	5.47	0.83	0.21	1.13	0.93	2.58	986.45	0.06	0.83	5.78

Table C.3d. (cont)

Sample	Mo_ppm	Cu_ppm	Pb_ppm	Zn_ppm	Ni2_ppm	As_ppm	Cd_ppm	Sb_ppm	Bi_ppm	Ag_ppm	Au_ppb	Hg_ppm	Tl_ppm	Se_ppm
HD-94A_245	79.58	2658.11	9.53	46.56	4.66	3.57	0.05	1.41	0.65	0.65	180.48	0.01	0.87	1.84
HD-94_423.9	7.66	582.46	16.04	31.67	6.44	1.23	0.05	0.31	0.31	0.31	65.99	0.01	0.51	0.92
HD-94_450.7	3.94	755.87	21.81	40.43	5.00	2.98	0.05	0.11	0.64	0.32	46.71	0.02	0.21	0.74
HD-01_31.8	3.68	10520.60	45.24	6.31	3.79	1.58	0.05	0.21	0.53	3.47	2037.19	0.02	0.21	8.21
HD-01_62.5	5.68	10143.94	5.58	48.69	4.67	0.25	0.51	0.71	0.91	3.45	4461.26	0.03	0.20	5.27
HD-01_92.6	8.91	7793.97	6.50	55.58	8.07	0.26	0.52	0.42	1.57	2.52	6007.57	0.01	1.26	8.07
HD-01_121.1	2.38	726.33	11.48	61.02	5.17	1.55	0.10	0.41	0.21	0.21	74.57	0.01	0.41	1.03
HD-01_154.4	8.19	2092.92	7.57	53.23	4.20	1.23	0.20	0.31	0.51	0.82	164.50	0.01	0.31	1.74
HD-01_187	95.66	6260.43	7.20	55.29	6.47	0.83	0.42	0.31	1.56	2.40	399.52	0.01	0.83	4.69
HD-01_214.85	14.46	4065.82	10.66	70.70	11.92	3.59	0.32	0.32	3.59	1.58	672.69	0.01	1.27	5.49
HD-01_244.4	8.40	3170.04	7.98	33.59	6.93	2.31	0.21	0.21	1.57	1.15	246.86	0.01	0.63	3.67
HD-01_271.6	3.91	5817.90	13.85	86.72	6.24	1.37	0.53	0.21	1.80	2.54	224.10	0.01	0.53	5.18
HD-60_3.6	101.88	541.82	23.08	5.20	1.77	24.74	0.05	0.73	2.29	0.83	796.41	0.10	0.21	15.80
HD-60_28.25	5.72	1366.42	8.79	5.30	4.66	0.26	0.05	0.32	0.32	0.85	307.78	0.19	0.21	18.65
HD-60_60.15	4.08	1500.34	34.98	146.62	6.39	1.15	1.05	0.63	0.63	0.52	181.81	0.01	0.52	2.62
HD-60_95.9	41.67	1537.99	55.67	267.03	11.95	2.58	0.43	0.75	0.43	0.43	160.00	0.01	0.54	2.15
HD-60_125	2.72	435.64	7.96	33.51	4.50	1.26	0.05	0.42	0.31	0.10	31.00	0.01	0.63	1.68
HD-60_150.1	39.57	3451.19	13.92	78.94	8.62	0.73	0.21	0.52	0.31	0.62	389.28	0.01	0.73	3.43
HD-60_181.7	91.99	4222.58	18.57	91.24	12.56	3.97	0.43	2.25	0.54	0.97	263.41	0.01	0.54	4.83
HD-60_211.7	13.80	6507.67	19.92	21.79	7.68	0.26	0.21	0.31	0.52	1.66	727.40	0.01	0.31	5.08
HD-60_241.7	5.27	3091.07	5.16	20.03	6.01	0.26	0.05	0.84	0.74	0.74	141.66	0.01	0.95	5.16
HD-60_270.35	14.46	705.12	9.71	22.73	4.44	2.69	0.10	0.10	0.21	0.21	175.32	0.01	0.72	1.34
HD-60_300.5	40.55	1844.58	5.20	31.19	3.64	2.08	0.05	1.46	0.31	0.62	173.10	0.01	0.62	1.98
HD-60_329.3	1.31	417.46	125.84	176.18	3.28	101.33	0.88	34.69	0.11	2.08	74.96	0.78	0.66	0.98
HD-60_360.05	15.13	1083.48	248.65	134.15	3.54	167.63	1.29	58.81	0.32	1.50	51.94	0.38	0.54	2.90
HD-60_389.45	3.21	841.75	5.70	26.95	3.73	3.01	0.05	1.04	0.21	0.31	74.83	0.01	0.52	1.66
HD-60_420	1.76	580.90	4.87	24.85	3.42	1.35	0.05	0.72	0.05	0.21	45.76	0.01	0.83	1.55
HD-60_453	4.73	1028.83	5.46	28.37	4.31	1.26	0.05	0.21	0.11	0.32	77.43	0.01	0.63	3.05
HD-60_482.1	8.58	1050.43	16.53	27.20	3.87	0.26	0.21	0.10	0.21	0.42	133.70	0.01	0.21	2.51
HD-60_510	6.04	816.03	3.85	22.92	3.13	1.04	0.05	0.05	0.10	0.31	102.09	0.01	0.05	1.25
HD-60_540.3	3.01	2065.97	5.91	24.9	3.11	1.66	0.05	0.10	0.10	0.73	116.41	0.01	0.10	1.56

Table C.3d. (cont)

Sample	Mo_ppm	Cu_ppm	Pb_ppm	Zn_ppm	Ni2_ppm	As_ppm	Cd_ppm	Sb_ppm	Bi_ppm	Ag_ppm	Au_ppb	Hg_ppm	Tl_ppm	Se_ppm
HD-60_570.4	2.88	850.63	4.11	27.75	2.57	1.03	0.10	0.41	0.21	0.31	53.34	0.01	0.31	1.34
HD-60_600	4.45	1381.57	4.03	21.72	3.41	0.93	0.05	0.21	0.62	0.52	26.06	0.01	0.31	1.97
HD-60_630.35	5.38	469.96	4.55	32.06	2.38	1.65	0.05	0.10	0.10	0.21	334.57	0.01	0.21	1.34
HD-60_660.5	6.58	2172.04	7.62	29.23	3.13	2.19	0.05	0.31	0.63	0.84	163.29	0.01	0.10	3.65
HD-60_690	6.06	813.49	3.80	13.35	2.26	1.64	0.05	2.05	0.10	0.41	101.03	0.02	0.21	0.92
HD-60_720	5.08	1858.37	3.76	23.38	2.64	0.91	0.10	0.05	0.10	0.81	134.05	0.01	0.51	1.52
HD-60_750.45	7.24	961.63	4.69	32.62	2.96	1.73	0.05	0.20	0.20	0.41	128.96	0.01	0.31	1.63
HD-60_780.25	7.01	1488.92	4.07	30.49	4.57	1.22	0.05	0.20	0.10	0.61	84.15	0.01	0.30	3.76
HD-60_797.9	5.37	383.04	1167.81	1390.33	3.33	428.17	9.03	18.05	0.21	3.98	52.43	0.09	0.43	1.07
HD-85_253.7	1.46	8.73	6.97	12.48	3.74	8.52	0.05	0.31	0.42	0.05	8.32	0.01	0.42	0.83
HD-85_283.8	1.55	5.80	4.87	12.44	3.42	1.76	0.05	0.05	0.21	0.05	3.42	0.01	0.41	0.26
HD-85_313.1	1.54	21.85	5.54	15.39	2.87	9.64	0.05	0.05	0.51	0.05	7.49	0.01	0.21	0.82
HD-85_465.55	1.35	230.35	4.36	19.73	69.79	11.11	0.05	0.05	0.62	0.21	63.04	0.01	0.05	0.26

Table C.4. Percentage of analysis out of detection limit by batch.

Element	Unit	VAN14 000527	VAN14 003543-2	ANK12 000288	ANK12 000289	ANK12 000290	ANK12 000875
Au	ppb		1.8519				
SiO2	%	0	0	0	0	0	0
Al2O3	%	0	0	0	0	0	0
Fe2O3	%	0	0	0.3731	0	0	0
CaO	%	1.8868	0.3731	0	0	0	0.4695
MgO	%	4.7170	0.7463	0	0	0	0.4695
Na2O	%	5.6604	5.2239	1.4925	0	1.8182	0.9390
K2O	%	0.9434	3.3582	0	0	1.0909	0.4695
MnO	%	6.6038	7.8358	6.3433	3.0189	16	3.2864
TiO2	%	0	1.4925	0.3731	0	1.0909	0.4695
P2O5	%	1.8868	7.8358	2.6119	0	0.3636	0.9390
Cr2O3	%	37.7358	42.9104	52.2388	43.3962	46.1818	17.3709
Ba	%	6.6038	20.1493				
LOI	%	0	0	0	0	0	0
Cu	%	67.9245	89.9254				
Ni	%	85.8491	94.7761	57.0896	57.7358	56.3636	53.9906
Pb	%	91.5094	93.6567				
SO3	%	15.0943	48.8806				
Sr	%	0	20.8955				
V2O5	%	2.8302	8.5821				
Zn	%	8.4906	16.0448				
Zr	%	5.6604	13.8060				
SUM	%	0	0	0	0	0	0
TOT/C	%	14.7059	35.5872	13.9535	3.8911	13.2404	6.1224
TOT/S	%	53.9216	64.7687	1.9380	0.7782	11.4983	1.0204
Ba	ppm	0	0.3745	0	0	0	0.4695
Be	ppm	47.0588	46.4419	49.2537	43.7736	42.5455	32.3944
Co	ppm	0	5.6180	0	0	0.3636	0
Cs	ppm	4.9020	7.4906	0	0	1.0909	0.9390
Ga	ppm	3.9216	4.1199	1.4925	0	1.4545	0
Hf	ppm	0	2.2472	0.7463	0	1.4545	2.3474
Nb	ppm	0	2.6217	0.3731	0	0.3636	0
Rb	ppm	0	0	0	0	0	0
Sn	ppm	28.4314	35.2060	29.4776	24.9057	20.7273	32.8638
Sr	ppm	0	0	0	0	0	0
Ta	ppm	0.9804	10.4869	1.1194	0.3774	1.4545	1.8779
Th	ppm	0	7.4906	0.3731	0	0.3636	0
U	ppm	0	5.2434	0	0	0	0
V	ppm	0.9804	2.6217	1.4925	0	2.5455	0
W	ppm	31.3725	26.5918	1.4925	1.1321	1.8182	0.4695
Zr	ppm	0	0	0	0	0	0
Y	ppm	0	0	0	0	0	0
La	ppm	0	0	0	0	0	0
Ce	ppm	0	0	0	0	0	0

Table C.4. (cont).

Element	Unit	VAN14 000527	VAN14 003543-2	ANK12 000288	ANK12 000289	ANK12 000290	ANK12 000875
Pr	ppm	0	0.7491	0	0	0	0
Nd	ppm	1.9608	1.4981	0	0	0	0.4695
Sm	ppm	1.9608	1.1236	0	0	0	0
Eu	ppm	2.9412	2.2472	0	0	0	0.4695
Gd	ppm	0	0.3745	0	0	0	0
Tb	ppm	0	1.1236	0	0.3774	0	0
Dy	ppm	0	0	0	0	0	0
Ho	ppm	0.9804	1.4981	0	0.3774	0	0
Er	ppm	0	0	0	0	0	0
Tm	ppm	0.9804	1.4981	1.1194	0.3774	0	0
Yb	ppm	0	1.4981	0	0	0	0
Lu	ppm	0.9804	1.4981	0	0.3774	0.3636	0
Mo	ppm	14.8515	21.7228	0	0.3831	1.7422	0.5076
Cu	ppm	0.9901	0	1.1628	1.9157	1.7422	0
Pb	ppm	0	0.3745	0	0	0	0
Zn	ppm	2.9703	2.9963	0.7752	0	0.3484	1.0152
Ni	ppm	0.9901	0	1.1628	0	0.3484	0.5076
As	ppm	25.7426	15.7303	6.2016	4.2146	5.5749	1.5228
Cd	ppm	70.2970	71.5356	39.1473	43.6782	50.1742	39.0863
Sb	ppm	44.5545	40.0749	17.8295	13.7931	17.4216	7.1066
Bi	ppm	63.3663	69.2884	9.3023	11.4943	19.1638	5.5838
Ag	ppm	73.2673	83.5206	9.6899	15.3257	41.1150	7.1066
Au	ppb	29.7030	42.3221	1.9380	4.9808	6.6202	2.0305
Hg	ppm	64.3564	66.2921	64.7287	59.3870	53.6585	68.0203
Tl	ppm	63.3663	64.7940	6.5891	9.9617	16.7247	9.6447
Se	ppm	62.3762	83.8951	10.4651	19.5402	31.0105	8.6294
Sc	ppm		0	1.4925	0	1.8182	0.9390
Te	ppm		84.2697				

Table C.5a. Precision test for ANK batches.

	ANK12000288				ANK12000289				ANK12000290				ANK12000875			
	s	u	%RSDi	Precision	sv	u	%RSDi	Precision	s	u	%RSDi	Precision	s	u	%RSDi	Precision
SiO2	0.41	59.08	0.70	Excellent	0.13	58.80	0.23	Excellent	0.20	58.96	0.34	Excellent	0.12	63.17	0.19	Excellent
Al2O3	0.20	16.02	1.25	Excellent	0.12	16.14	0.75	Excellent	0.15	16.12	0.94	Excellent	0.09	15.58	0.60	Excellent
Fe2O3	0.13	6.98	1.80	Excellent	0.09	6.97	1.29	Excellent	0.07	6.93	0.95	Excellent	0.09	6.12	1.45	Excellent
MgO	0.02	1.85	0.83	Excellent	0.02	1.86	1.11	Excellent	0.02	1.86	0.85	Excellent	0.02	1.27	1.82	Excellent
CaO	0.02	0.65	2.36	Excellent	0.01	0.66	0.88	Excellent	0.01	0.64	0.85	Excellent	0.03	3.38	0.75	Excellent
Na2O	0.03	1.95	1.78	Excellent	0.03	1.95	1.62	Excellent	0.01	1.97	0.56	Excellent	0.07	3.89	1.90	Excellent
K2O	0.11	7.84	1.42	Excellent	0.08	7.86	1.01	Excellent	0.12	7.97	1.45	Excellent	0.05	2.94	1.77	Excellent
TiO2	0.02	0.77	1.98	Excellent	0.01	0.77	0.65	Excellent	0.01	0.77	1.09	Excellent	0.01	0.37	1.57	Excellent
P2O5	0.01	0.25	2.28	Excellent	0.01	0.26	1.94	Excellent	0.01	0.26	2.14	Excellent	0.0	0.19	0.0	Excellent
MnO	0	0.06	0	Excellent	0	0.06	0	Excellent	0	0.06	0	Excellent	0.0	0.09	0.0	Excellent
Cr2O3	0.00	0.01	9.09	Good	0.00	0.01	7.82	good	0.00	0.01	5.89	Very good	0.00	0.00	41.66	Not precise
Ni	3	42	7.14	Good	1.26	42.75	2.94	Excellent	2.77	44.2	6.28	Very good	0	10	0	Excellent
Sc	0	18	0	Excellent	0	18	0	Excellent	0.45	17.8	2.51	Excellent	0	6	0	Excellent
LOI	0.06	3.93	1.47	Excellent	0.17	4.03	4.24	Very good	0.07	3.8	1.86	Excellent	0.12	2.43	4.75	Very good
Sum	0.04	99.37	0.04	Excellent	0.01	99.34	0.01	Excellent	0.01	99.38	0.01	Excellent	0.02	99.43	0.02	Excellent
Ba	10.82	653	1.66	Excellent	26.03	625.5	4.16	Very good	24.24	614.4	3.95	Very good	39.27	1707.33	2.30	Excellent
Be	1.32	1.5	88.19	Not precise	0.75	1.38	54.55	Not precise	1.08	1.1	98.54	Not precise	0.87	1	86.60	Not precise
Co	0.26	20.9	1.27	Excellent	1.71	20.08	8.51	good	0.47	20.14	2.32	Excellent	0.62	7.9	7.91	Good
Cs	0.26	4.6	5.75	Very Good	0.17	4.53	3.77	Very good	0.24	4.28	5.58	Very good	0.15	0.57	26.96	Not precise
Ga	0.70	16.47	4.27	Very Good	0.86	16.73	5.15	Very good	0.80	15.98	5.03	Very good	0.31	17.23	1.77	Excellent
Hf	0.1	3	3.33	Very Good	0.22	2.9	7.45	good	0.30	3.08	9.85	Good	0.35	2.77	12.69	Not precise
Nb	0.53	7.4	7.15	Good	0.52	7.05	7.37	good	0.77	6.78	11.40	Not precise	0.67	6.43	10.35	Not precise
Rb	5.42	169.23	3.20	Very Good	7.18	169.58	4.23	Very good	7.29	162.58	4.48	Very good	3.82	65.83	5.80	Very good
Sn	0.58	2.67	21.65	Not precise	0.5	2.25	22.22	Not precise	0.55	2.6	21.07	Not precise	0.58	2.67	21.65	Not precise
Sr	13.93	282.67	4.93	Very Good	9.54	277.68	3.44	Very good	9.88	272.2	3.63	Very good	51.56	766.6	6.73	Very good
Ta	0.06	0.43	13.32	Not precise	0.06	0.45	12.83	Not precise	0.05	0.44	12.45	Not precise	0.06	0.33	17.32	Not precise
Th	0.25	3.07	8.21	Good	0.26	3.28	8.03	good	0.24	3.26	7.39	Good	0.21	4.73	4.40	Very good
U	0.06	1.83	3.15	Very Good	0.17	1.85	9.36	good	0.07	1.8	3.93	Very good	0.12	1.07	10.83	Not precise
V	9.02	219.67	4.11	Very Good	18.48	223.75	8.26	good	16.43	214.6	7.65	Good	13.65	78.67	17.35	Not precise
W	1.42	23.7	5.98	Very Good	1.99	23.68	8.41	good	1.23	24.7	4.97	Very good	0.20	0.48	41.81	Not precise
Zr	1.46	107.23	1.36	Excellent	6.26	107.05	5.85	Very good	3.21	105.36	3.05	Very good	6.54	104.83	6.23	Very good

Table C.5a. (cont)

	ANK12000288				ANK12000289				ANK12000290				ANK12000875			
	s	u	%RSDi	Precision	s	u	%RSDi	Precision	s	u	%RSDi	Precision	s	u	%RSDi	Precision
Y	0.57	19.83	2.87	Excellent	0.66	19.15	3.45	Very good	0.77	19.02	4.06	Very good	0.15	9.33	1.64	Excellent
La	1.00	21.53	4.65	Very Good	0.80	20.68	3.88	Very good	0.51	20.74	2.47	Excellent	1.33	16.23	8.20	Good
Ce	2.59	38.7	6.68	Very Good	2.39	37.88	6.32	Very good	1.29	37.5	3.43	Very good	1.82	30.57	5.96	Very good
Pr	0.18	4.45	4.12	Very Good	0.18	4.33	4.20	Very good	0.12	4.23	2.73	Excellent	0.01	3.3	0.30	Excellent
Nd	1.31	17.67	7.39	Good	1.70	17.13	9.94	good	0.67	16.6	4.02	Very good	0.87	11.5	7.58	Good
Sm	0.31	3.89	7.92	Good	0.17	3.72	4.46	Very good	0.16	3.88	4.07	Very good	0.16	2.37	6.58	Very good
Eu	0.05	1.12	4.72	Very Good	0.06	1.06	5.77	Very good	0.05	1.06	5.08	Very good	0.03	0.64	3.95	Very good
Gd	0.12	3.90	2.97	Excellent	0.11	3.81	2.94	Excellent	0.12	3.70	3.17	Very good	0.16	2	7.76	Good
Tb	0.04	0.61	6.59	Very Good	0.01	0.61	1.56	Excellent	0.04	0.59	6.56	Very good	0.02	0.31	5.59	Very good
Dy	0.26	3.51	7.39	Good	0.22	3.51	6.31	Very good	0.34	3.66	9.22	Good	0.06	1.67	3.29	Very good
Ho	0.02	0.74	2.70	Excellent	0.03	0.71	4.41	Very good	0.07	0.71	9.53	Good	0.02	0.35	4.95	Very good
Er	0.19	2.32	8.15	Good	0.04	2.15	2.03	Excellent	0.03	2.01	1.35	Excellent	0.10	0.97	9.83	Good
Tm	0.02	0.33	6.06	Very Good	0.01	0.32	1.57	Excellent	0.03	0.30	10.31	Not precise	0.02	0.16	9.75	Good
Yb	0.17	2.26	7.52	Good	0.14	2.09	6.53	Very good	0.14	2.19	6.19	Very good	0.02	1.03	2.03	Excellent
Lu	0.02	0.34	4.54	Very Good	0.01	0.34	3.73	Very good	0.04	0.31	14.23	Not precise	0.02	0.16	9.75	Good
TOT/C	0.01	0.20	5.68	Very Good	0.01	0.21	2.41	Excellent	0.01	0.21	4.02	Very good	0.01	0.31	1.88	Excellent
TOT/S	0.22	1.99	11.02	Not precise	0.05	2	2.74	Excellent	0.22	1.88	11.42	Not precise	0.02	0.25	6.19	Very good
Mo	8.91	123.47	7.22	Good	7.09	138.18	5.13	Very good	7.97	126.4	6.31	Very good	3.28	153.3	2.14	Excellent
Cu	83.40	3756.93	2.22	Excellent	119.22	3914.45	3.05	Very good	132.35	3728.76	3.55	Very good	75.57	1762.77	4.29	Very good
Pb	1.02	23.37	4.37	Very Good	1.93	25.18	7.65	good	1.32	23.68	5.56	Very good	0.42	5.23	7.96	Good
Zn	2.89	64.67	4.46	Very Good	7.33	71.5	10.25	Not precise	1.52	63.4	2.39	Excellent	2.65	73	3.62	Very good
Ni_1	1.82	36.1	5.05	Very Good	1.77	38.55	4.60	Very good	1.76	37.54	4.68	Very good	3.59	16.77	21.44	Not precise
As	2.66	54.43	4.89	Very Good	2.17	56.45	3.85	Very good	2.97	53.88	5.51	Very good	0.1	2.5	4	Very good
Cd	0.0	0.4	0.0	Excellent	0.08	0.3	27.22	Not precise	0.15	0.27	54.93	Not precise	0.13	0.15	88.19	Not precise
Sb	0.35	2.33	15.05	Not precise	0.15	2.43	6.19	Very good	0.48	2.52	18.91	Not precise	0.1	0.3	33.33	Not precise
Bi	0.0	0.4	0.0	Excellent	0.10	0.38	25.53	Not precise	0.13	0.34	39.46	Not precise	0	0.3	0	Excellent
Ag	0.06	2.47	2.34	Excellent	0.13	2.75	4.69	Very good	0.16	2.38	6.90	Very good	0.06	0.67	8.66	Good
Au	158.65	381.3	41.61	Not precise	291.20	629.18	46.28	Not precise	78.05	385	20.27	Not precise	67.80	245.73	27.59	Not precise
Hg	0.0	0.05	0.0	Excellent	0.01	0.08	6.06	Very good	0.01	0.07	19.17	Not precise	0	0.03	0	Excellent
Tl	0.12	0.57	20.38	Not precise	0.06	0.55	10.50	Not precise	0.04	0.52	8.60	Good	0.06	0.17	34.64	Not precise
Se	0.35	6.67	5.27	Very Good	0.74	7.13	10.40	Not precise	0.55	6.66	8.33	Good	0.25	0.87	29.04	Not precise

Table C.5b. Precision test for VAN batches.

	VAN14000527				VAN14003543-2			
	s	u	%RSDi	Precision	s	u	%RSDi	Precision
Au					0	2	0	Excellent
SiO2	0.2	70.6	0.28	Excellent	0.28	57.9	0.49	Excellent
Al2O3	0.07	14.39	0.46	Excellent	0.02	15.54	0.14	Excellent
Fe2O3	0.05	3.76	1.38	Excellent	0.04	5.39	0.79	Excellent
CaO	0.01	3.41	0.34	Excellent	0.30	5.8	5.12	Very good
MgO	0.01	1.03	0.56	Excellent	0.10	2.77	3.57	Very good
Na2O	0.01	3.79	0.26	Excellent	0.03	3.4	0.83	Excellent
K2O	0.01	2.11	0.27	Excellent	0.01	1.92	0.37	Excellent
MnO	0.01	0.07	7.87	Good	0.01	0.14	5.24	Very good
TiO2	0.03	0.39	8.88	Good	0	0.6	0	Excellent
P2O5	0.01	0.08	7.53	Good	0	0.15	0	Excellent
Cr2O3	0.00	0.02	12.60	Not precise	0	0.00	0	Excellent
Ba	0.01	0.07	7.87	Good	0.01	0.05	15.71	Not precise
LOI	0.02	0.45	3.37	Very Good	0.11	5.49	1.93	Excellent
Cu	0	0.01	0	Excellent	0	0.01	0	Excellent
Ni	0	0.01	0	Excellent	0	0.01	0	Excellent
Pb	0	0.01	0	Excellent	0	0.01	0	Excellent
SO3	0	0.00	0	Excellent	0.00	0.01	23.57	Not precise
Sr	0.00	0.03	3.33	Very Good	0.00	0.04	9.96	Good
V2O5	0.00	0.01	17.32	Not precise	0.00	0.02	3.14	Very good
Zn	0.0	0.00	0.0	Excellent	0.00	0.01	10.88	Not precise
Zr	0.00	0.01	10.83	Not precise	0.00	0.01	24.96	Not precise
SUM	0.25	100.25	0.25	Excellent	0.01	99.21	0.01	Excellent
TOT/C	0.01	0.01	43.30	Not precise	0.07	0.97	7.29	Good
TOT/S	0	0.01	0	Excellent	0	0.01	0	Excellent
Ba	22.81	771.33	2.96	Excellent	12.02	409.5	2.94	Excellent
Be	0.58	1.67	34.64	Not precise	0	0.5	0	Excellent
Co	0.25	7.23	3.48	Very Good	0.35	12.55	2.82	Excellent
Cs	0.12	0.97	11.95	Not precise	0.21	4.45	4.77	Very good
Ga	0.61	13.53	4.51	Very Good	0.14	14.4	0.98	Excellent
Hf	0.12	3.73	3.09	Very Good	0.35	3.65	9.69	Good
Nb	0.49	3.17	15.58	Not precise	0.14	7	2.02	Excellent
Rb	1.76	46.27	3.80	Very Good	0.07	77.85	0.09	Excellent
Sn	0	2	0	Excellent	0	0.5	0	Excellent
Sr	7.71	223.13	3.46	Very Good	12.16	483.1	2.52	Excellent
Ta	0.06	0.27	21.65	Not precise	0	0.5	0	Excellent
Th	0.25	4.13	6.09	Very Good	0.14	11.6	1.22	Excellent
U	0.15	1.37	11.18	Not precise	0	3.9	0	Excellent
V	4.04	64.67	6.25	Very Good	4.24	129	3.29	Very good
W	0.25	0.73	34.32	Not precise	1.48	2.95	50.34	Not precise
Zr	7.76	134.93	5.75	Very Good	21.92	145.6	15.06	Not precise
Y	0.84	19.33	4.34	Very Good	0.64	18.95	3.36	Very good
La	1.00	13.23	7.57	Good	0.21	26.95	0.79	Excellent

Table C.5b. (cont)

	VAN14000527				VAN14003543-2			
	s	u	%RSDi	Precision	s	u	%RSDi	Precision
Ce	1.57	24.6	6.39	Very Good	0.49	46.35	1.07	Excellent
Pr	0.19	3.03	6.18	Very Good	0.01	5.26	0.27	Excellent
Nd	0.91	11.87	7.65	Good	0.49	19.85	2.49	Excellent
Sm	0.14	2.61	5.43	Very Good	0.10	3.76	2.63	Excellent
Eu	0.02	0.72	2.88	Excellent	0.06	1.05	5.39	Very good
Gd	0.19	2.79	6.72	Very Good	0.08	3.60	2.16	Excellent
Tb	0.01	0.46	2.17	Excellent	0.01	0.52	1.37	Excellent
Dy	0.26	3.00	8.67	Good	0.11	3.19	3.33	Very good
Ho	0.02	0.66	2.33	Excellent	0.02	0.64	3.34	Very good
Er	0.08	2.04	3.69	Very Good	0.05	1.78	2.79	Excellent
Tm	0.01	0.31	1.84	Excellent	0.01	0.28	2.57	Excellent
Yb	0.05	2.09	2.41	Excellent	0.04	1.83	1.94	Excellent
Lu	0.01	0.35	2.86	Excellent	0.01	0.30	2.40	Excellent
Mo	0.06	0.43	13.32	Not precise	0.85	0.8	106.07	Not precise
Cu	1.37	8.23	16.58	Not precise	0.07	7.05	1.00	Excellent
Pb	0.06	2.33	2.47	Excellent	0	4	0	Excellent
Zn	1	33	3.03	Very Good	2.83	62	4.56	Very good
Ni	0.51	2.87	17.90	Not precise	0.14	4.3	3.29	Very good
As	0.33	0.62	53.99	Not precise	0.21	3.65	5.81	Very good
Cd	0.0	0.05	0.0	Excellent	0	0.05	0	Excellent
Sb	0.03	0.08	34.64	Not precise	0	0.2	0	Excellent
Bi	0.0	0.05	0.0	Excellent	0	0.05	0	Excellent
Ag	0.0	0.05	0.0	Excellent	0	0.05	0	Excellent
Au	0.38	0.47	80.42	Not precise	0.57	1.4	40.41	Not precise
Hg	0.01	0.02	57.74	Not precise	0	0.01	0	Excellent
Tl	0.0	0.2	0.0	Excellent	0	0.05	0	Excellent
Se	0	0.25	0	Excellent	0	0.25	0	Excellent
Sc					0.07	2.95	2.40	Excellent
Te					0	0.1	0	Excellent

Table C.6a. Accuracy test for ANK batches. N/A: Not analyzed, BDL: Below detection limit.

	ANK12000288		ANK12000289		ANK12000290		ANK12000875	
	%RDi	Accuracy	%RDi	Accuracy	%RDi	Accuracy	%RDi	Accuracy
SiO2	-0.49	Excellent	-0.43	Excellent	-0.60	Excellent	-0.68	Excellent
Al2O3	-0.82	Excellent	-0.86	Excellent	-0.86	Excellent	-0.79	Excellent
Fe2O3	-1.26	Excellent	-1.14	Excellent	-0.48	Excellent	-0.58	Excellent
MgO	1.08	Excellent	0.09	Excellent	0.84	Excellent	0.88	Excellent
CaO	-1.25	Excellent	-1.57	Excellent	-1.37	Excellent	-1.40	Excellent
Na2O	-1.28	Excellent	-1.27	Excellent	-1.40	Excellent	-0.55	Excellent
K2O	-1.99	Excellent	-2.11	Excellent	-1.30	Excellent	-1.69	Excellent
TiO2	0.38	Excellent	-0.43	Excellent	-0.17	Excellent	0.07	Excellent
P2O5	0.82	Excellent	-0.78	Excellent	0.21	Excellent	0.46	Excellent
MnO	2.02	Excellent	1.06	Excellent	2.26	Excellent	2.32	Excellent
Cr2O3	-0.92	Excellent	-0.96	Excellent	-0.45	Excellent	1.23	Excellent
Ni	3.23	Very Good	6.82	Very Good	10.43	Not accurate	12.66	Not accurate
Sc	-4.21	Very Good	-5.41	Very Good	-4.71	Very good	-3.62	Very good
LOI	-0.0	Excellent	-0.0	Excellent	-0.0	Excellent	-0.0	Excellent
Sum	N/A	N/A	N/A	N/A	N/A	N/A	N/A	N/A
Ba	-0.52	Excellent	0.18	Excellent	-1.43	Excellent	0.23	Excellent
Be	BDL	BDL	BDL	BDL	BDL	BDL	BDL	BDL
Co	1.25	Excellent	4.76	Very Good	1.06	Excellent	0.24	Excellent
Cs	-2.67	Excellent	-4.23	Very Good	-6.38	Very good	-4.69	Very good
Ga	-0.24	Excellent	0	Excellent	-2.37	Excellent	0.22	Excellent
Hf	-4.94	Very Good	-6.36	Very Good	-6.66	Very good	-6.95	Very good
Nb	-6.52	Very Good	-4.45	Very Good	-6.93	Very good	-5.01	Very good
Rb	-1.58	Excellent	-0.55	Excellent	-4.30	Very good	-2.65	Excellent
Sn	-4.56	Very Good	-1.96	Excellent	-3.53	Very good	-6.35	Very good
Sr	4.42	Very Good	3.35	Very Good	0.99	Excellent	1.28	Excellent
Ta	-8.11	Good	-10.89	No accurate	-10.33	Not accurate	-9.72	Good
Th	0.80	Excellent	-1.72	Excellent	-1.19	Excellent	-1.64	Excellent
U	-2.41	Excellent	-2.12	Excellent	-3.16	Very good	-2.56	Excellent
V	0.63	Excellent	4.38	Very Good	0.41	Excellent	-2.93	Excellent
W	-2.95	Excellent	-2.54	Excellent	-2.46	Excellent	-2.03	Excellent
Zr	-1.40	Excellent	0.16	Excellent	-1.63	Excellent	-0.37	Excellent
Y	6.24	Very Good	7.22	Good	5.74	Very good	3.30	Very good
La	3.00	Excellent	1.63	Excellent	2.87	Excellent	2.71	Excellent
Ce	2.21	Excellent	-1.37	Excellent	-0.82	Excellent	-3.06	Very good
Pr	-2.68	Excellent	-3.14	Very Good	-2.93	Excellent	-4.76	Very good
Nd	-4.81	Very Good	-5.50	Very Good	-6.30	Very good	-7.14	Good
Sm	-2.93	Excellent	-4.12	Very Good	-3.59	Very good	-4.97	Very good
Eu	-4.20	Very Good	-3.83	Very Good	-2.84	Excellent	-6.21	Very good
Gd	-0.34	Excellent	0.26	Excellent	0.56	Excellent	-3.01	Very good
Tb	-6.65	Very Good	-8.88	Good	-7.21	Good	-8.63	Good
Dy	-0.12	Excellent	-0.80	Excellent	-1.71	Excellent	-2.84	Excellent
Ho	2.72	Excellent	-0.85	Excellent	-1.52	Excellent	-0.92	Excellent

Table C.6a. (cont)

	ANK12000288		ANK12000289		ANK12000290		ANK12000875	
	%RDi	Accuracy	%RDi	Accuracy	%RDi	Accuracy	%RDi	Accuracy
Er	1.52	Excellent	-1.63	Excellent	-3.26	Very good	-1.04	Excellent
Tm	1.36	Excellent	-3.05	Very Good	4.36	Very good	-0.88	Excellent
Yb	-0.94	Excellent	-2.40	Excellent	-1.41	Excellent	-3.09	Very good
Lu	-0.58	Excellent	-4.36	Very Good	-0.87	Excellent	-2.29	Excellent
TOT/C	-0.75	Excellent	1.07	Excellent	0.38	Excellent	0	Excellent
TOT/S	-3.28	Very Good	-1.01	Excellent	-4.58	Very good	0.09	Excellent
Mo	-8.23	Good	2.68	Excellent	-2.16	Excellent	-17.71	Not accurate
Cu	-2.20	Excellent	0.95	Excellent	1.23	Excellent	-1.96	Excellent
Pb	-1.15	Excellent	5.62	Very Good	2.62	Excellent	5.51	Very good
Zn	-1.39	Excellent	4.85	Very Good	0.84	Excellent	-3.59	Very good
Ni_1	0.70	Excellent	2.77	Excellent	0.85	Excellent	6.40	Very good
As	-7.56	Good	-2.64	Excellent	-6.06	Very good	-3.23	Very good
Cd	-7.56	Good	0.84	Excellent	-5.46	Very good	-2.52	Excellent
Sb	-11.11	Not accurate	-11.61	No accurate	-11.98	Not accurate	3.33	Very good
Bi	-11.29	Not accurate	-10.47	No accurate	-13.23	Not accurate	6.75	Very good
Ag	-0.39	Excellent	7.35	Good	0.59	Excellent	8.88	Good
Au	16.96	Not accurate	26.60	No accurate	16.03	Not accurate	20.41	Not accurate
Hg	3.30	Very Good	8.63	Good	10.03	Not accurate	10.42	Not accurate
Tl	0.93	Excellent	7.14	Good	3.94	Very good	1.11	Excellent
Se	1.34	Excellent	5.71	Very Good	1.82	Excellent	6.69	Very good

Table C.6b. Accuracy test for VAN batches. N/A: Not analyzed,

	VAN14000527		VAN14003543-2	
	%RDi	Accuracy	%RDi	Accuracy
Au (Fire Assay)			-0.40	Excellent
SiO2	2.40	Excellent	2.96	Excellent
Al2O3	0.75	Excellent	0.10	Excellent
Fe2O3	-0.12	Excellent	0.10	Excellent
CaO	-0.65	Excellent	-1.46	Excellent
MgO	-5.09	Very good	-3.24	Very good
Na2O	-0.99	Excellent	2.41	Excellent
K2O	-2.11	Excellent	1.66	Excellent
MnO	-5.09	Very good	1.85	Excellent
TiO2	-0.70	Excellent	-2.87	Excellent
P2O5	-4.58	Very good	-1.72	Excellent
Cr2O3	N/A	N/A	N/A	N/A
Ba	N/A	N/A	N/A	N/A
LOI	0	Excellent	0	Excellent
Cu	N/A	N/A	N/A	N/A
Ni	N/A	N/A	N/A	N/A
Pb	N/A	N/A	N/A	N/A
SO3	N/A	N/A	N/A	N/A
Sr	N/A	N/A	N/A	N/A
V2O5	N/A	N/A	N/A	N/A
Zn	N/A	N/A	N/A	N/A
Zr	N/A	N/A	N/A	N/A
SUM	N/A	N/A	N/A	N/A
TOT/C	0.65	Excellent	1.89	Excellent
TOT/S	-1.99	Excellent	-1.09	Excellent
Ba	2.01	Excellent	1.51	Excellent
Be				
Co	2.54	Excellent	3.35	Very good
Cs	0.0	Excellent	-1.21	Excellent
Ga	-0.28	Excellent	-4.71	Very good
Hf	-0.51	Excellent	-5.17	Very good
Nb	-6.73	Very good	-8.12	Good
Rb	-0.87	Excellent	-2.59	Excellent
Sn	2.22	Excellent	-1.43	Excellent
Sr	-1.48	Excellent	1.80	Excellent
Ta	-4.50	Very good	-11.00	Not accurate
Th	-0.51	Excellent	-2.60	Excellent
U	-7.83		-4.22	Very good
V	11.67	Not accurate	8.96	Good
W	0.45	Excellent	-1.74	Excellent
Zr	5.21	Very good	3.04	Very good
Y	9.37	Good	2.51	Excellent

Table C.6b. Accuracy test for VAN batches. N/A: Not analyzed,

	VAN14000527		VAN14003543-2	
	%RDi	Accuracy	%RDi	Accuracy
La	11.65	Not accurate	3.43	Very good
Ce	-3.87	Very good	-5.32	Very good
Pr	-2.37	Excellent	-6.58	Very good
Nd	1.31	Excellent	-6.68	Very good
Sm	-2.94	Excellent	-6.64	Very good
Eu	-4.31	Very good	-6.90	Very good
Gd	5.75	Very good	-1.97	Excellent
Tb	-10.06	Not accurate	-11.19	Not accurate
Dy	1.39	Excellent	-2.40	Excellent
Ho	0.81	Excellent	-2.65	Excellent
Er	-1.27	Excellent	-4.58	Very good
Tm	1.23	Excellent	-1.85	Excellent
Yb	-1.02	Excellent	-5.79	Very good
Lu	2.47	Excellent	-0.26	Excellent
Mo	0	Excellent	-9.56	Good
Cu	-6.84	Very good	2.68	Excellent
Pb	-4.51	Very good	6.13	Very good
Zn	-7.57	Good	3.63	Very good
Ni	-4.69	Very good	5.82	Very good
As	-7.58	Good	3.46	Very good
Cd	-8.40	Good	-0.76	Excellent
Sb	-16.67	Not accurate	-8.10	Good
Bi	-3.86	Very good	10.24	Not accurate
Ag	-7.59	Good	1.13	Excellent
Au	30.76	Not accurate	3.72	Very good
Hg	-3.33	Very good	7.14	Good
Tl	-7.84	Good	6.16	Very good
Se	18.84	Not accurate	12.42	Not accurate
Sc	N/A	N/A	2.55	Excellent
Te	N/A	N/A	-0.48	Excellent

Table C.7. Element gain and losses in the Kestane stock for hydrothermal alteration.

HOLEID	HD-80	HD-01	HD-01	HD-01	HD-60	HD-85
SAMPFROM	661.15	31.8	62.5	271.6	150.1	283.8
Alteration	Propylitic	Sericite	Intense Potassic	Sericite-Chlorite	Moderate Potassic	Chlorite
SiO2_pct	-5.6629	76.3497	150.2540	-3.4197	1.9864	-19.8466
Al2O3_pct	-1.7422	0.8223	-3.2739	-1.8889	-1.0273	-3.8371
Fe2O3_pct	0.1584	5.1851	27.1009	1.8669	0.9879	0.0181
MgO_pct	0.0560	-1.2201	-0.1152	0.1725	0.3293	-0.1480
CaO_pct	1.4536	-3.2768	-3.1947	-0.8136	-2.3648	-0.0833
Na2O_pct	0.2248	-3.1793	-2.7095	-2.1123	-1.1782	-0.2548
K2O_pct	-2.3877	0.4869	2.6967	-0.3690	1.3667	-2.4754
P2O5_pct	0.0128	-0.0855	-0.0867	0.0165	0.0036	0.0017
MnO_pct	-0.0121	-0.0413	0.0047	0.0087	0.0117	-0.0357
Sc_ppm	0.6854	1.4783	-0.5420	-0.1452	0.1524	-0.0370
C_pct	0.0364	0.0249	0.2548	0.1774	0.0846	0.0325
S_pct	1.8230	6.4274	3.9840	2.0692	1.1088	1.5445
Ba_ppm	-547.1182	-84.1709	-56.6436	-189.7881	-149.7059	-382.6772
Co_ppm	8.9130	49.9528	25.0899	7.3902	5.4704	-0.2402
Cs_ppm	-2.2950	-3.5063	-2.2563	0.2638	-0.7978	-2.8624
Ga_ppm	-3.5572	4.0191	9.7771	-2.5650	-1.7862	-3.1784
Hf_ppm	-0.4467	-0.8916	-1.4093	-0.0799	-0.0203	-0.3991
Nb_ppm	-2.3210	-2.3607	-3.5097	-2.1803	-0.6276	-0.8833
Rb_ppm	-55.4043	-31.0721	2.3647	0.9558	7.7470	-76.6814
Sr_ppm	-81.8101	-441.9663	-410.3479	-309.9042	-267.3515	-135.7322
Ta_ppm	-0.2269	-0.1432	-0.4336	-0.2154	-0.0864	-0.2569
Th_ppm	-4.2379	-5.3127	-4.8581	-2.5166	-1.8370	-6.0703
U_ppm	0.4703	-1.8202	-3.0829	-1.7931	-1.9717	-1.5171
V_ppm	-4.3253	32.0145	77.8511	1.2583	-9.6552	-3.2153
W_ppm	2.6850	-1.3674	0.2236	-1.2051	0.3278	-3.3373
Zr_ppm	-21.7826	-36.4771	-37.1842	-3.7096	2.4367	-19.6577
Y_ppm	2.0941	-4.6012	-10.2582	-2.8965	-5.7093	-2.6314
La_ppm	-11.0048	-9.3133	-26.0317	-13.3720	-15.3365	-7.6465
Ce_ppm	-17.9655	-11.9881	-46.3719	-21.9455	-24.7731	-10.1319
Pr_ppm	-1.1392	-0.5715	-4.7700	-1.7737	-2.1066	-1.2117
Nd_ppm	-0.5720	2.0973	-13.6866	-3.2692	-5.1096	-1.0847
Sm_ppm	0.8431	0.4167	-2.6946	-0.5258	-0.7813	-0.4622
Eu_ppm	-0.1248	-0.0314	-0.6274	-0.2325	-0.2246	0.0140
Gd_ppm	0.4900	-0.2051	-2.2861	-0.6669	-0.9249	-0.5082
Tb_ppm	0.1106	-0.0462	-0.3442	-0.1220	-0.1740	-0.1068
Dy_ppm	0.3820	-0.9364	-2.0665	-0.4593	-0.8408	-0.2962
Ho_ppm	0.0695	-0.1538	-0.3395	-0.1331	-0.1832	-0.0516
Er_ppm	0.1510	-0.6736	-1.2948	-0.5527	-0.7010	-0.4766
HOLEID	HD-80	HD-01	HD-01	HD-01	HD-60	HD-85
SAMPFROM	661.15	31.8	62.5	271.6	150.1	283.8
HOLEID	HD-80	HD-01	HD-01	HD-01	HD-60	HD-85
SAMPFROM	661.15	31.8	62.5	271.6	150.1	283.8

Table C.7. (cont)

Alteration	Propylitic	Sericite	Intense Potassic	Sericite-Chlorite	Moderate Potassic	Chlorite
Tm_ppm	0.0246	-0.1155	-0.1938	-0.0866	-0.0966	-0.0473
Yb_ppm	-0.1042	-0.6879	-1.2271	-0.4353	-0.6367	-0.6462
Lu_ppm	0.0052	-0.0776	-0.1938	-0.0866	-0.0861	-0.0625
Mo_ppm	8.3883	1.5476	10.4750	-1.4108	34.6087	-3.9452
Cu_ppm	-1428.9739	17082.5792	25921.6866	3599.6659	1603.1335	-1854.1225
Pb_ppm	3.5075	77.6848	11.5184	9.2365	10.1989	-0.1996
Zn_ppm	-2.0563	-12.0112	109.9673	57.9794	55.7967	-14.2841
Ni_ppm	0.8462	4.1762	10.1362	3.2111	6.0040	-0.1423
As_ppm	0.2482	1.9264	-0.2202	0.3751	-0.1855	0.3733
Cd_ppm	-0.0532	-0.0069	1.2874	0.3944	0.1067	-0.0638
Sb_ppm	0.5306	0.3280	1.8938	0.1476	0.4701	-0.0129
Bi_ppm	-0.0532	0.8454	2.3985	1.5850	0.2109	0.0499
Ag_ppm	-0.6193	5.4374	8.6321	1.5681	-0.1880	-0.7752
Au_ppb	-101.6877	3533.6335	12083.4903	76.1790	256.3904	-131.5542
Hg_ppm	-0.0002	0.0328	0.0783	0.0048	0.0001	-0.0013
Tl_ppm	-0.4113	-0.1294	0.0474	-0.0121	0.2211	-0.2051
Se_ppm	1.1889	13.2493	12.9210	3.3370	1.9132	-1.3351
Ra_ppm	2.3311	0.0201	0.2185	0.3085	0.3940	1.6675

Appendix D: Geochronology Results

Table D.1. U-Pb geochronology results for 6 samples. Concordia diagrams are shown in Figure 3.6 and 3.7. (*)=Excluded zircons, ρ=error correlation

Sample ID	207Pb/235U				206Pb/238U				ρ
	Ratio	2σ	Age (Ma)	2σ	Ratio	2σ	Age (Ma)	2σ	
HD_29_1	0.0265	0.0026	26.6	2.5	0.0042	0.0003	27.1	1.9	0.2983
HD_29_2	0.026	0.0026	26.1	2.6	0.0042	0.0003	26.7	1.9	0.1770
HD_29_3	0.0288	0.0029	28.8	2.9	0.0043	0.0003	27.6	2	0.2430
HD_29_4	0.0265	0.0026	26.5	2.6	0.0042	0.0003	27.3	1.8	0.1990
HD_29_5	0.026	0.0026	26	2.5	0.0041	0.0003	26.1	1.8	0.1211
HD_29_6	0.0259	0.0026	25.9	2.6	0.0040	0.0003	25.9	1.8	0.1178
HD_29_7	0.0259	0.0026	26	2.6	0.0040	0.0003	25.9	1.8	0.0936
HD_29_8	0.0251	0.0025	25.1	2.5	0.0039	0.0003	25	1.8	0.2750
HD_29_9	0.0263	0.0025	26.3	2.5	0.0040	0.0003	26	1.8	0.2180
HD_29_10	0.0236	0.0024	23.7	2.4	0.0040	0.0003	25.5	1.7	0.0415
PB2014061_1	0.0263	0.0028	26.3	2.7	0.0042	0.0003	27	1.9	0.0921
PB2014061_2	0.0309	0.0036	30.8	3.5	0.0046	0.0003	29.7	2.2	0.1391
PB2014061_3	0.0273	0.003	27.2	3	0.0043	0.0003	27.5	2	0.2696
PB2014061_4	0.0293	0.003	29.2	3	0.0043	0.0003	27.7	2.1	0.1902
PB2014061_5	0.0284	0.0029	28.3	2.9	0.0044	0.0003	28	1.9	0.0928
PB2014061_6	0.0282	0.0027	28.2	2.7	0.0045	0.0003	28.6	2	0.1746
PB2014061_7	0.0277	0.0029	27.7	2.8	0.0045	0.0003	28.8	2	0.1048
PB2014061_8	0.03	0.0031	30	3.1	0.0046	0.0003	29.3	2.1	0.1515
PB2014061_9	0.0296	0.003	29.7	2.9	0.0045	0.0003	28.6	2	0.2336
PB2013_046_1	0.0297	0.0019	29.7	1.9	0.0046	0.0002	29.5	1.4	0.1223
PB2013_046_2	0.03	0.0018	30	1.8	0.0045	0.0002	29.2	1.4	0.2281
PB2013_046_3	0.0293	0.0018	29.3	1.7	0.0044	0.0002	28.5	1.4	0.1947
PB2013_046_4	0.0292	0.0014	29.2	1.4	0.0045	0.0002	28.8	1.3	0.2324
PB2013_046_5	0.0277	0.0014	27.8	1.4	0.0044	0.0002	28.4	1.3	0.2118
PB2013_046_6	0.0293	0.0015	29.4	1.5	0.0045	0.0002	28.7	1.3	0.2033
PB2013_046_7	0.0298	0.0015	29.9	1.5	0.0045	0.0002	28.7	1.3	0.1750
PB2013_046_8	0.0273	0.0016	27.3	1.6	0.0044	0.0002	28	1.3	0.2200
PB2013_046_9	0.0297	0.0017	29.7	1.7	0.0046	0.0002	29.3	1.5	0.2588
PB2013_046_10	0.0284	0.0015	28.5	1.5	0.0044	0.0002	28.3	1.3	0.0214
PB2013_046_11	0.0278	0.0015	27.8	1.5	0.0044	0.0002	28.3	1.3	0.1350
PB2013_046_12	0.0281	0.0016	28	1.5	0.0043	0.0002	27.8	1.3	0.2645
PB2013_046_13	0.0293	0.0023	29.3	2.3	0.0045	0.0002	29	1.5	0.2081
PB2013_046_14	0.03	0.0016	30	1.6	0.0045	0.0002	29.3	1.3	0.2313
PB2013_046_15	0.0283	0.0015	28.3	1.5	0.0044	0.0002	28.2	1.3	0.2823
PB2013_046_16	0.0286	0.0016	28.6	1.6	0.0045	0.0002	28.8	1.4	0.0831
PB2013_046_17	0.0287	0.0022	28.7	2.1	0.0044	0.0003	28.3	1.7	0.2396
PB2013_046_18	0.0275	0.0014	27.5	1.3	0.0042	0.0002	27.1	1.2	0.2795
PB2013_046_19	0.027	0.0015	27	1.5	0.0043	0.0002	27.6	1.2	0.1561
PB2013_046_20*	0.0268	0.0022	26.8	2.2	0.0040	0.0002	25.4	1.3	0.0803
PB2014_106_1	0.0385	0.002	38.4	2	0.0063	0.0003	40.1	1.8	0.1443
PB2014_106_2	0.039	0.002	38.8	1.9	0.0061	0.0003	39	1.7	0.1821
PB2014_106_3	0.0382	0.0019	38.1	1.9	0.0060	0.0003	38.3	1.7	0.0736

Table D.1. (cont)

Sample ID	207Pb/235U				206Pb/238U				ρ
	Ratio	2σ	Age (Ma)	2σ	Ratio	2σ	Age (Ma)	2σ	
PB2014_106_4	0.0386	0.0021	38.4	2.1	0.0062	0.0003	40	1.8	0.1384
PB2014_106_5	0.0398	0.002	39.6	2	0.0060	0.0003	38.7	1.7	0.1527
PB2014_106_6	0.0376	0.0018	37.4	1.8	0.0060	0.0003	38.5	1.7	0.2092
PB2014_106_7	0.0396	0.0023	39.4	2.3	0.0059	0.0003	38.2	1.8	0.166
PB2014_106_8	0.0395	0.0017	39.3	1.7	0.0060	0.0003	38.7	1.7	0.2727
PB2014_106_9	0.0384	0.0018	38.2	1.7	0.0060	0.0003	38.3	1.7	0.4030
PB2014_106_10	0.0367	0.0021	36.6	2	0.0059	0.0003	38	1.7	0.0277
PB2014_106_11	0.0393	0.0018	39.1	1.7	0.0060	0.0003	38.4	1.7	0.2854
PB2014_106_12	0.0395	0.0018	39.5	1.7	0.0061	0.0003	39.1	1.7	0.2131
PB2014_106_13	0.039	0.0019	38.7	1.8	0.0061	0.0003	38.9	1.7	0.1935
PB2014_106_14	0.0374	0.0018	37.2	1.8	0.0060	0.0003	38.4	1.7	0.0816
PB2014_106_15	0.0399	0.0021	39.6	2	0.0060	0.0003	38.7	1.7	0.1661
PB2014_106_16	0.0389	0.002	38.8	1.9	0.0061	0.0003	39	1.8	0.1364
PB2014_106_17*	0.0422	0.0027	42.1	2.6	0.0062	0.0003	39.6	1.9	0.1970
PB2014_106_18	0.0398	0.0025	39.5	2.5	0.0063	0.0003	40.2	1.9	0.1240
PB2014_106_19	0.0408	0.0022	40.5	2.1	0.0063	0.0003	40.2	1.8	0.1823
PB2014_106_20	0.0388	0.002	38.6	1.9	0.0060	0.0003	38.7	1.7	0.0663
HD-13A_488_1	0.04	0.02			0.0058	0.0002	37.1	1.2	0.2376
HD-13A_488_2	0.036	0.018			0.0059	0.0002	38.1	1.4	0.0737
HD-13A_488_3	0.036	0.018			0.0058	0.0002	37	1.3	0.0621
HD-13A_488_4	0.039	0.019			0.0058	0.0002	37.1	1.3	0.0705
HD-13A_488_5	0.037	0.018			0.0058	0.0003	37.5	1.6	0.0492
HD-13A_488_6	0.037	0.019			0.0059	0.0002	37.7	1.4	0.0072
HD-13A_488_7	0.042	0.021			0.0061	0.0002	39	1.4	0.1425
HD-13A_488_8	0.044	0.022			0.0059	0.0002	37.7	1.4	0.116
HD-13A_488_9	0.038	0.019			0.0060	0.0002	38.2	1.6	0.1709
HD-13A_488_10	0.039	0.019			0.0059	0.0002	37.8	1.4	0.0854
HD-13A_488_11	0.04	0.021			0.0059	0.0002	38	1.3	0.0738
HD-13A_488_12	0.042	0.022			0.0059	0.0003	37.6	1.9	0.0186
HD-13A_488_13	0.038	0.02			0.0061	0.0002	38.9	1.5	0.0302
HD-13A_488_14	0.045	0.022			0.0060	0.0002	38.3	1.3	0.0028
HD-13A_488_15	0.04	0.02			0.0058	0.0002	37.2	1.6	0.2975
HD-37_112_1	0.0412	0.0036			0.0063	0.0003	40.2	1.6	0.0573
HD-37_112_2	0.0378	0.0032			0.0062	0.0003	39.8	1.6	0.1419
HD-37_112_3	0.0363	0.003			0.0062	0.0002	39.6	1.4	0.0947
HD-37_112_4	0.0413	0.0031			0.0059	0.0002	37.8	1.3	0.0769
HD-37_112_5	0.0787	0.0079			0.0112	0.0005	71.5	3	0.1478
HD-37_112_6	0.0422	0.0032			0.0061	0.0002	39	1.3	0.2950
HD-37_112_7	0.0691	0.0087			0.0110	0.0006	70.7	3.5	0.1734
HD-37_112_8	0.069	0.0038			0.0114	0.0004	72.7	2.3	0.1799
HD-37_112_9	0.078	0.0071			0.0114	0.0005	72.9	3.1	0.1936
HD-37_112_10	0.0375	0.0035			0.0064	0.0003	41.2	1.7	0.1247
HD-37_112_11	0.0398	0.0029			0.0062	0.0002	40	1.4	0.1460

Table D.1. (cont)

Sample ID	207Pb/235U				206Pb/238U				ρ
	Ratio	2σ	Age (Ma)	2σ	Ratio	2σ	Age (Ma)	2σ	
HD-37_112_12	0.0372	0.0038			0.0061	0.0003	39.3	1.7	0.1013
HD-37_112_13	0.0393	0.0032			0.0063	0.0003	40.2	1.8	0.2247
HD-37_112_14	0.0404	0.0038			0.0059	0.0002	37.8	1.5	0.1564
PB2013018_1	0.0413	0.0038			0.0062	0.0002	40	1.5	0.0802
PB2013018_2	0.0396	0.0037			0.0062	0.0002	39.8	1.5	0.1252
PB2013018_3	0.0346	0.0029			0.0063	0.0002	40.3	1.3	0.0213
PB2013018_4	0.0403	0.0031			0.0061	0.0002	38.9	1.3	0.0555
PB2013018_5	0.0416	0.0041			0.0064	0.0003	40.8	1.8	0.2744
PB2013018_6	0.0402	0.0027			0.0063	0.0002	40.3	1.2	0.0745
PB2013018_7	0.0364	0.0034			0.0061	0.0002	39.1	1.5	0.0795
PB2013018_8	0.0413	0.0035			0.0062	0.0002	39.7	1.4	0.1209
PB2013018_9	0.04	0.0049			0.0063	0.0003	40.8	1.8	0.0328
PB2013018_10	0.0391	0.0029			0.0062	0.0002	40.1	1.3	0.0815
PB2013018_11	0.0392	0.0028			0.0064	0.0002	40.8	1.3	0.0933
PB2013018_12	0.0433	0.0028			0.0064	0.0002	41	1.3	0.0846
PB2013018_13	0.0391	0.0035			0.0064	0.0002	41.1	1.5	0.0214
PB2013018_14	0.0424	0.0032			0.0063	0.0002	40.2	1.3	0.2182
PB2013018_15	0.0395	0.003			0.0063	0.0002	40.4	1.4	0.0193
PB2013018_16	0.041	0.0031			0.0061	0.0002	39.4	1.3	0.2142

Appendix E: Analytical Methods

Geochronological Analytical Methods

Re-Os

After mineral separation, the molybdenite samples were dissolved and equilibrated with a known amount of ^{185}Re and isotopically normal Os in inverse aqua regia (2:1 16 N HNO3 and 12 N HCl, 3 mL) at 240°C for 24 h in a Carius-tube (Selby and Creaser, 2004). Rhenium and Os were isolated and purified by solvent extraction, microdistillation, and anion exchange chromatography, and analyzed by negative thermal ionization mass spectrometry (NTIMS).

U-Pb

Methodology

Seven U-Pb (zircon) samples were processed in the Pacific Centre for Isotopic and Geochemical Research (PCIGR) at the University of British Columbia (UBC). The samples include: two phases of the Kestane stock, Evçiler pluton, dacite from Kunk, andesite in the Kestane graben, andesite from the base of Pirentepe hill, and an altered andesite from the top of Pirentepe hill.

Refer to Appendix B1 for descriptions and petrography of the geochronological samples. Sample processing completed at UBC was as follows:

- Crushing and grinding the sample by using a Rhino jaw crusher and Bico disk grinder
- Pulverized fragments were then separated by density using heavy liquids stage.
- Further sorting by magnetic separation allowed separation of zircon, pyrite, barite, and apatite after four passes with different side slopes (ranging from 20 to 2°) and electric current (0.6-1.8 A) in a ramp Frantz.
- Final zircon picking was done with a stereomicroscope and the zircons obtained were imaged by cathodoluminescence on the scanning electron microscopy (SEM).
- The zircons were analyzed by using laser ablation mass spectrometry (LA-ICP-MS). Additionally the standards Temora (416.8 ± 1.1 Ma; Black et al., 2003) and Plešovice (338 ± 1.0 Ma; Sláma et al., 2008) were analyzed.
- Data reduction was using Iolite software.

Samples

Sample PB2013018 is part of the dacitic volcanic sequence at the Kunk hill, this sample is the oldest of the seven samples with a 40.20 ± 0.35 Ma concordia age from fourteen of sixteen

zircons. Two zircons were excluded from this concordia age because they were slightly discordant.

Sample HD-37 112 corresponds to the mineralized and intensely biotite-magnetite altered phase of the stock (Phase A), which yielded a concordia age of 39.19 ± 0.47 Ma from nine of fourteen zircons. Four zircons present inheritance with a concordia age of 71.9 ± 1.3 and one zircon, that presented the oldest age from the concordant zircons, was rejected.

The un-mineralized Phase B of Kestane stock is represented in sample HD-13A 488 and yields an age of 37.79 ± 0.36. The fifteen zircons are all concordant.

PB2014106 corresponds to a green plagioclase and rounded quartz phyric andesite, located in the Kestane graben. The analysis from nineteen of twenty zircons yielded a concordia age of 38.79 ± 0.32. One zircon was excluded due to high 207Pb/235U ratios.

Sample PB2014061corresponds to an argillized plagioclase-phyric andesite from the top of Pirentepe in the Büyükdağ hill. Nine zircons indicated a concordia age of 28.36 ± 0.59.

PB2014046 is a biotite, hornblende, plagioclase-phyric andesite from the base of Pirentepe. Nineteen of twenty zircons provide a concordia age of 28.54 ± 0.26. The zircon excluded showed the lowest 206Pb/238U radios and consequently was interpreted as having a significantly younger age.

The sample HD-29: is from the Evçiler pluton in the Bakirlik area. Ten zircons yield a late Oligocene age of 26.13± 0.51 Ma.

References

Black, L.P., Kamo, S.L., Allen, C.M., Aleinikoff, J.N., Davis, D.W., Korsch, R.J., Foudoulis, C., 2003. TEMORA 1: a new Zircon standard for phanerozoic U-Pb geochronology. Chemical Geology 200, 155-170.

Selby, D., and Creaser, R.A. (2004). Macroscale NTIMS and microscale LA-MC-ICP-MS Re-Os isotopic analysis of molybdenite: Testing spatial restrictions for reliable Re-Os age determinations, and implications for the decoupling of Re and Os within molybdenite. *Geochimica et Cosmochimica Acta*, *68*(19), 3897-3908.

Slama, J., Kosler, J., Condon, D.J., Crowley, J.L., Gerdes, A., Hanchar, J.M., Horstwood, M.S.A., Morris, G.A., Nasdala, L., Norberg, N., Schaltegger, U., Schoene, N., Tubrett, M.N., Whitehouse, M.J., 2008. Plesovice zircon - a new natural reference material for U-Pb and Hf isotopic microanalysis. Chemical Geology, 249, 1-2, 1-35